



Université de Liège - Faculty of Applied Sciences

# Principal static wind loads within a rigorous methodology to the envelope reconstruction problem

Thesis submitted in partial fulfillment of the requirements for the degree of  
Doctor of Philosophy in Applied Sciences by

**Nicolas Blaise, Ir.**

February 2016



© Copyright by Nicolas J. L. Blaise 2016  
All Rights Reserved



---

**Author's contact details**

Nicolas Jacques Lambert BLAISE, Ir.

Structural & Stochastic Dynamics  
Research Unit of The Structural Engineering Division  
Dept. of Architecture, Geology, Environment and Constructions

Bât. B52/3 Analyse sous actions aléatoires en génie civil  
Quartier Polytech 1,  
Allée de la Découverte 9,  
4000 Liège, Belgium

Email: [n.blaise0@gmail.com](mailto:n.blaise0@gmail.com)

Phone: +32 4 97927913

---



---

### **Members of the Doctoral Jury**

Prof. Vincent TERRAPON (President of the Jury)  
Université de Liège

Prof. Vincent DENOËL (Supervisor)  
Université de Liège  
Email: v.denoel@ulg.ac.be

Dr. Ir. Thomas ANDRIANNE  
Université de Liège

Prof. Luigi CARASSALE  
University degli Studi di Genova  
Italy

Prof. Vincent DE VILLE DE GOYET  
Université de Liège

Prof. Michael KASPERSKI  
Ruhr-Universität Bochum  
Germany

---





## Abstract

Static wind loads are used for the design of large civil structures such as high-rise buildings, large roofs and long-span bridges. Once static wind loads are known, they are used through the iterative design process without repeating cumbersome dynamical analyses. In this framework, structural engineers can effectively focus on the structural sizing since static analyses are straightforward. No codified wind loads, however, exist for those large structures with unique shapes and there is no consensual view on how to formally derived them. For each new major project, the challenge consists therefore in deriving a relevant set of static wind loads. Obviously, these loads must provide the actual envelope values of structural responses of interest. This states the objective of the *envelope reconstruction problem* and constitutes the core of this thesis. The proposed developments to solve this problem are relevant for structures responding with a linear dynamic behavior to the buffeting action of synoptic winds in a stationary framework.

The pioneering concept of *Equivalent Static Wind Load* is normally considered for the design. An extensive review points out three main limitations of the current formulations. They have been originally established in a Gaussian context, are associated with either a nodal or nodal-modal basis and do not have a formal definition. The proposed *Conditional Expected Load method* overcomes these three drawbacks by defining a *Conditional Expected Static Wind Load*. This novel approach presents a general rigorous formulation for linear structural behavior, irrespective of the basis used for the analysis and relevant in a non-Gaussian context. The method is particularized for a certain class of non-Gaussian processes through a *bicubic translation model*. This model covers a large range of non-Gaussianity in the random processes and therefore paves the way for the formal establishment of “non-Gaussian” static wind loads with a physical interpretation.

Other kinds of static loads such as the covariance proper transformation loading modes and the modal inertial loads are additionally studied. Unfortunately, both sets of loads are simply relevant for two limit structural behaviors, quasi-static and resonant, respectively. Moreover, they do not adapt to the set of structural responses of interest. From both points of view, one key result from our study is the innovative concept of *Principal Static Wind Load* as a sound solution for the envelope reconstruction problem. The concept relies upon a robust mathematical foundation. These loads are determined by the singular value decomposition of a large set of equivalent static wind loads. This decomposition can be seen as a way to rank the most relevant load patterns for the envelope reconstruction problem. The principal static wind loads have also the added distinctive advantage to be flexible. They are, indeed, able to naturally adapt to the set of structural responses of interest.

Finally, a complete methodology to solve the envelope reconstruction problem irrespective of the structure, its load-bearing system and its susceptibility to vibrations in a Gaussian or non-Gaussian context is rigorously conceptualized. The intrinsic controllability of a set of pertinent parameters provides a smart balance between over and underestimation of the actual envelope. Moreover, combinations of static wind loads are computed to speed-up the reconstruction of the envelope values. The problem of determining these combination coefficients is formulated as a constrained nonlinear optimization. Equivalent and principal static wind loads, covariance proper transformation loading modes and modal inertial loads are implemented within the proposed methodology. Three examples, a four-span bridge, a real-life large stadium roof and a low-rise building demonstrate that the envelope reconstruction accuracy is considerably improved with principal static wind loads and with combinations thereof.



## Résumé

Des chargements de vent statiques sont utilisés couramment pour le dimensionnement d'ouvrages imposants du génie civil tel que gratte-ciels, toitures de grandes dimensions et ponts de grande portée. Lorsque ces chargements de vent statiques sont connus, ils sont utilisés de manière itérative durant le dimensionnement sans devoir réaliser une analyse dynamique formelle à chaque modification d'élément au sein de la structure. Etant donné la simplicité d'une analyse statique linéaire, les ingénieurs de structures peuvent se focaliser efficacement sur le dimensionnement et non sur des analyses structurelles. Cependant, pour des ouvrages de dimensions hors normes aux formes souvent uniques et pouvant répondre de manière dynamique, il n'existe pas de chargements de vent codifiés ni même d'une méthodologie claire afin de les dériver. Pour chaque nouveau projet d'envergure, le défi consiste alors à établir un ensemble de chargements de vent statiques pertinents pour le dimensionnement. A l'évidence, ces chargements doivent reproduire les valeurs enveloppes réelles des réponses structurelles, c.-à-d. celles provenant d'une analyse dynamique, et ce de manière sécuritaire. Cela établit l'objectif du *problème de reconstruction de l'enveloppe* et constitue le noyau central des recherches entreprises au sein de cette thèse. Les développements proposés afin d'apporter des solutions à ce problème sont applicables aux structures ayant un comportement linéaire dynamique à l'action de vents turbulents synoptiques en faisant l'hypothèse de processus aléatoires stationnaires.

Le concept de *chargement de vent statique équivalent* est souvent considéré pour le dimensionnement. Un état de l'art exhaustif indique cependant trois limitations des formulations actuelles. Celles-ci ont été originellement établies dans un contexte Gaussien, sont associées à une base nodale ou nodale-modale et n'ont pas de définition formelle. La *méthode de charge moyenne conditionnelle* est développée afin de surmonter ces trois limitations en définissant un *chargement de vent moyen statique conditionnel*. Cette nouvelle approche est basée sur une formulation générale et rigoureuse, pour des structures à comportements linéaires, quelle que soit la base dans laquelle l'analyse est effectuée et applicable dans un contexte non-Gaussien. La méthode est explicitée pour une certaine classe de processus non-Gaussiens au moyen d'un *modèle de translation bicubique*. Ce modèle couvre une large gamme de processus aléatoires et ouvre donc la voie à l'établissement formel de chargements de vent statiques équivalents dits "non-Gaussiens" avec une signification physique.

D'autres types de chargements statiques sont également étudiés tels que, les modes de chargement provenant de la diagonalisation de la matrice de covariance des pressions aérodynamiques et les charges modales inertielles. Cependant, ces deux ensembles de chargements sont valables uniquement pour deux comportements structurels limites, soit quasi-statique, soit résonant, respectivement. De plus, ils ne s'adaptent pas à l'ensemble des réponses étudiées. A partir de ces deux constats, un résultat clé de notre étude est le concept innovant de *chargement de vent statique principal* apportant une solution robuste au problème de reconstruction d'enveloppe. Le concept se base sur des fondements mathématiques rigoureux. Ces chargements sont déterminés par une décomposition en valeurs singulières d'un grand nombre de chargements de vent statiques équivalents. Cette décomposition peut être interprétée comme une manière de classer les chargements les plus importants pour le problème de reconstruction de l'enveloppe. Les chargements de vent statiques principaux ont également l'avantage caractéristique d'être adaptatifs. En effet, ils peuvent naturellement s'adapter à l'ensemble des réponses structurelles considérées.



Finalement, une méthodologie complète pour solutionner le problème de reconstruction d'enveloppe, quelque soit la structure, son système porteur et sa susceptibilité aux vibrations dans un contexte Gaussien ou non-Gaussien est rigoureusement conceptualisée. Un ensemble de paramètres pertinents permet un contrôle intrinsèque du niveau de sur- et sous-estimation de l'enveloppe. De plus, des combinaisons de chargements de vent statiques sont calculées afin de faciliter la reconstruction des valeurs enveloppes. La détermination des coefficients de combinaison est formulée via un problème d'optimisation non linéaire avec contraintes. Les chargements de vents statiques équivalents et principaux, les modes de chargement provenant de la diagonalisation de la matrice de covariance et les charges modales inertielles sont utilisés au sein de la méthodologie proposée. Trois exemples: un pont à quatre travées, une toiture de stade réel ainsi qu'un bâtiment de type industriel de faible hauteur démontrent que la reconstruction de l'enveloppe est considérablement améliorée avec les chargements de vent statiques principaux ainsi qu'avec des combinaisons de ceux-ci.



## Acknowledgements

Je me souviens très bien de mon premier jour en tant que doctorant au sein de mon institution. Je me réjouissais alors de découvrir la vie de chercheur. Durant les cinq années, j'ai vécu bien plus d'expériences enrichissantes tant d'un point de vue intellectuel que d'un point de vue humain que ce que j'attendais. Cette période restera une référence pour ma vie future.

Ce choix d'entreprendre une thèse dans le domaine des effets du vent sur les structures de génie civil a été initié par mon professeur et promoteur de travail de fin d'études : Vincent Denoël. Vincent, je tiens à t'exprimer ici ma gratitude pour avoir cru en mes possibilités. Tu m'as donné l'opportunité de travailler à tes côtés sur ce sujet si passionnant et sur d'autres matières. Ton ardeur au travail et ton enthousiasme m'ont énormément soutenu et ont aidé à l'aboutissement de cette thèse. Je te remercie aussi de m'avoir ouvert largement ton réseau et dès le début de mon travail de doctorant, d'avoir suggéré d'aller présenter mes recherches dans des conférences internationales. Ces voyages et présentations m'ont beaucoup apporté. J'ai trouvé en toi les qualités d'un mentor.

Je tiens également à remercier Vincent De Ville de Goyet. Cher Vincent, déjà présent au sein de mon jury de travail de fin d'études, je te remercie d'avoir formulé cette question en apparence anodine: "Comment établirais-tu des cas de charges de vent pour le dimensionnement d'un stade?". Elle a participé à éveiller mon intérêt pour ce passionnant sujet. Je pense qu'en lisant cette thèse tu trouveras des éléments de réponse.

Dear members of the committee, thank you for accepting the reading and assessment of this thesis. I hope your lecture will be enjoyable.

Chers Thomas, Alexandre et Benjamin, après avoir fait nos études ensemble, nous avons tous les trois entamé un doctorat. Je suis très heureux d'avoir partagé cette étape en votre chaleureuse compagnie. Avec Thomas, pouvoir échanger sur nos recherches respectives et même avoir pu travailler ensemble avec publications à la clé a été un plaisir supplémentaire. Mon cher Alex, je vais regretter l'excellente ambiance de bureau que nous avons installée, elle a contribué à maintenir un climat de travail toujours motivant.

Ma très chère Capucine, j'aimerais t'exprimer au moyen de ces quelques mots tout l'amour et l'admiration que je te porte depuis que je t'ai rencontrée lors de nos études d'ingénieur. Après deux ans et demi de travaux nous voilà bien installés dans notre maison. Ce projet comme celui de faire un doctorat, je n'aurais pu le faire sans ta patience et ton soutien. Avec tout mon amour, merci.

Chers Papa et Maman, le chemin que j'ai parcouru jusqu'à aujourd'hui, j'ai su le faire grâce à votre amour et votre soutien inconditionnel. Merci de m'avoir si bien entouré, guidé, et encouragé depuis mes premiers pas.

Finalement, je remercie ma famille, ma belle-famille ainsi que mes amis pour m'avoir soutenu en me posant cette question: "Et ta thèse, elle avance bien?". Je peux maintenant vous le dire après cinq ans d'efforts: "Oui, elle est bel et bien terminée, et si on parlait d'autres choses?".





*“Quand on me contrarie, on éveille mon attention, non pas ma colère.”*

Essais, III, 8, De l’art de conférer

Michel de Montaigne



## ELECTRIC LIGHT ORCHESTRA (ELO)

**"Hold On Tight"**

Hold on tight to your dream,  
Hold on tight to your dream,  
When you see your ship go sailing,  
When you feel your heart is breaking,  
Hold on tight to your dream.

It's a long time to be gone,  
Time just rolls on and on,  
When you need a shoulder to cry on,  
When you get so sick of trying,  
Just hold on tight to your dream.

When you get so down that you can't get up,  
And you want so much but you're all out of luck,  
When you're so downhearted and misunderstood,  
Just over & over & over you could.

Accroche-toi à ton rêve,  
Accroche-toi à ton rêve,  
Quand tu vois ton bateau partir,  
Quand tu sents ton coeur se briser,  
Accroche-toi à ton rêve.

Hold on tight to your dream,  
Hold on tight to your dream,  
When you see the shadows falling,  
When you hear that cold wind calling,  
Hold on tight to your dream.

Lyrics: Jeff Lynne

Copyright: 1981 JET Records



# Contents

|  |            |
|--|------------|
| <b>Abstract</b>  | <b>i</b>   |
| <b>Résumé</b>  | <b>iii</b> |
| <b>Acknowledgements</b>  | <b>vii</b> |
| <b>Nomenclature</b>  | <b>xix</b> |
| <b>I Introduction</b>  | <b>1</b>   |
| I.1 Context  | 2          |
| I.2 Motivations  | 4          |
| I.3 Personal contributions   | 6          |
| I.4 Outline  | 7          |
| <b>II Buffeting analysis of civil structures</b>                   | <b>11</b>  |
| II.1 Introduction  | 12         |
| II.2 Theory of probability   | 12         |
| II.2.1 Random variables  | 12         |
| II.2.2 Stochastic processes  | 15         |
| II.2.3 Random vectors  | 17         |
| II.3 Representative extreme values                                 | 19         |
| II.3.1 Gaussian framework  | 20         |
| II.3.2 Non-Gaussian framework - Hermite moment model               | 23         |
| II.4 Equation of motion  | 28         |
| II.4.1 Structural responses  | 29         |
| II.4.2 Envelope of structural responses                            | 30         |
| II.5 Modal basis   | 31         |
| II.6 Gaussian spectral analysis                                    | 35         |
| II.6.1 Nodal basis analysis  | 35         |
| II.6.2 Modal basis analysis  | 36         |
| II.6.3 Hybrid analysis   | 37         |
| II.7 Davenport's white noise approximation and extensions          | 40         |
| II.7.1 Timescale separation condition                              | 40         |
| II.7.2 Resonant contribution to the variance of modal amplitudes   | 41         |
| II.7.3 Resonant contribution to the covariance of modal amplitudes | 42         |
| II.7.4 Advanced method   | 45         |
| II.8 Proper orthogonal decomposition                               | 50         |

|            |  |           |
|------------|--|-----------|
| II.8.1     | Wind field . . . . .   | 50        |
| II.8.2     | Aerodynamic pressure field . . . . .   | 51        |
| II.8.3     | Structural analysis . . . . .  | 52        |
| <b>III</b> | <b>The envelope reconstruction problem . . . . .</b>   | <b>55</b> |
| III.1      | Introduction . . . . .   | 56        |
| III.2      | Review of available methods . . . . .  | 58        |
| III.2.1    | Equivalent static wind loads . . . . .   | 59        |
| III.2.2    | One-sided envelope reconstruction problem . . . . .  | 59        |
| III.2.3    | Two-sided envelope reconstruction problem . . . . .  | 61        |
| III.2.4    | Limitations and objectives . . . . .   | 62        |
| III.3      | Proposed general methodology . . . . .   | 63        |
| III.3.1    | Underestimation of the envelope . . . . .  | 63        |
| III.3.2    | Reconstruction rate . . . . .  | 64        |
| III.3.3    | Preponderant factors . . . . .   | 65        |
| III.3.4    | Number of static wind loads for an overall reconstruction . . . . .                                    | 67        |
| III.3.5    | Number of static wind loads ensuring no underestimation of the envelope . . . . .                      | 68        |
| III.4      | Basic static wind loads . . . . .  | 70        |
| III.4.1    | Normalization . . . . .  | 70        |
| III.4.2    | Envelope reconstruction . . . . .  | 71        |
| III.5      | Combinations of basic static wind loads . . . . .  | 73        |
| III.5.1    | Constrained nonlinear optimization problem . . . . .   | 73        |
| III.5.2    | Combination coefficients . . . . .   | 76        |
| III.6      | Summary . . . . .  | 77        |
| <b>IV</b>  | <b>Equivalent static wind loads . . . . .</b>  | <b>81</b> |
| IV.1       | Introduction . . . . .   | 82        |
| IV.2       | Concept . . . . .  | 84        |
| IV.3       | Conditional sampling technique . . . . .   | 86        |
| IV.4       | Load-Response Correlation method . . . . .   | 87        |
| IV.5       | Modal inertial loads-based ESWLs . . . . .   | 88        |
| IV.6       | Hybrid-based ESWLs . . . . .   | 89        |
| IV.7       | Conditional Expected Load method . . . . .   | 91        |
| IV.7.1     | Conditional Expected Static Wind Load . . . . .  | 91        |
| IV.7.2     | Gaussian framework . . . . .   | 94        |
| IV.7.3     | Non-Gaussian framework . . . . .   | 94        |
| IV.7.4     | Covariance matrix of elastic forces . . . . .  | 95        |
| IV.7.5     | Review of the LRC-, CST-, MIL- and hybrid-based methods in the perspective of the CEL method . . . . . | 98        |
| IV.8       | Non-Gaussian joint probability density function . . . . .  | 104       |
| IV.9       | Two-step adjustment method . . . . .   | 109       |
| IV.10      | Envelope reconstruction problem using ESWLs . . . . .  | 110       |
| IV.10.1    | Normalization . . . . .  | 110       |
| IV.10.2    | Ranking of the equivalent static wind loads . . . . .  | 110       |
| IV.11      | Summary . . . . .  | 113       |

|           |  |     |
|-----------|--|-----|
| <b>V</b>  | <b>Principal static wind loads</b>   | 115 |
| V.1       | Introduction   | 116 |
| V.2       | Singular value decomposition   | 117 |
| V.3       | Principal static wind loads  | 120 |
| V.3.1     | Concept  | 120 |
| V.3.2     | LRC-based ESWLs with CPT loading modes   | 121 |
| V.3.3     | MIL-based ESWLs  | 123 |
| V.3.4     | Hybrid-based ESWLs   | 124 |
| V.4       | Envelope reconstruction problem using PSWLs  | 126 |
| V.5       | Summary  | 131 |
| <b>VI</b> | <b>Illustrations</b>   | 133 |
| VI.1      | Introduction   | 133 |
| VI.2      | Four span bridge   | 135 |
| VI.2.1    | CEL-based ESWLs for the case $\xi = 1.5\%$   | 143 |
| VI.2.2    | Envelope reconstruction with ESWLs ( $\xi = 1.5\%$ )                               | 145 |
| VI.2.3    | PSWLs  | 149 |
| VI.2.4    | Limiting cases of PSWLs: CPT loading modes and MILs                                | 151 |
| VI.2.5    | Envelope reconstruction with PSWLs $\xi = 1.5\%$                                   | 160 |
| VI.2.6    | Comparison of envelope reconstruction with combinations of basic static wind loads | 165 |
| VI.2.7    | Summary  | 172 |
| VI.3      | Lille's stadium (unique peak factor)   | 173 |
| VI.3.1    | Description of the structure   | 173 |
| VI.3.2    | Description of the wind loading  | 176 |
| VI.3.3    | Buffeting analysis (Gaussian assumption)   | 178 |
| VI.3.4    | Envelope of structural responses   | 185 |
| VI.3.5    | Envelope reconstruction with ESWLs   | 190 |
| VI.3.6    | Envelope reconstruction with PSWLs   | 194 |
| VI.3.7    | Envelope reconstruction with CPT loading modes and MILs                            | 209 |
| VI.3.8    | Summary  | 212 |
| VI.4      | Lille's stadium (Automatic procedure)  | 213 |
| VI.4.1    | Introduction   | 213 |
| VI.4.2    | Automatic procedure to obtain SWLs ensuring no underestimation                     | 221 |
| VI.4.3    | Summary  | 225 |
| VI.5      | Low-rise gable roof building   | 226 |
| VI.5.1    | Two-step adjustment method   | 231 |
| VI.5.2    | Bicubic model  | 232 |
| VI.5.3    | ESWLs  | 236 |
| VI.5.4    | Envelope reconstruction with PSWLs   | 243 |
| VI.5.5    | Automatic procedure to obtain SWLs ensuring no underestimation                     | 251 |
| VI.5.6    | Summary  | 254 |
| VI.6      | Summary  | 255 |

|            |  |     |
|------------|--|-----|
| <b>VII</b> | <b>Conclusions</b>   | 257 |
|            | VII.1 Introduction   | 258 |
|            | VII.2 Theoretical implications                                       | 258 |
|            | VII.3 Practical implications   | 259 |
|            | VII.4 Limitations of the study                                       | 260 |
|            | VII.5 Recommendations for further research                           | 260 |
|            | VII.6 Conclusion   | 261 |
| <b>A</b>   | <b>Alternative estimation of extreme values</b>                      | 275 |
|            | A.1 Introduction   | 275 |
|            | A.2 Methodology communicated by Dr. Kasperski                        | 275 |
|            | A.3 Lille's stadium example  | 277 |
|            | A.3.1 Establishment of the envelope (Reference period 1 hour)        | 277 |
|            | A.3.2 Automatic procedure (Kareem-Zhao model for peak factors)       | 284 |
|            | A.3.3 Automatic procedure (Kasperski's methodology for peak factors) | 285 |
|            | A.4 Low-rise gable roof building example                             | 288 |
|            | A.4.1 Establishment of the envelope (reference period 1 hour)        | 288 |
|            | A.4.2 Automatic procedure (Kareem-Zhao model for peak factors)       | 289 |
|            | A.4.3 Automatic procedure (Kasperski's methodology for peak factors) | 291 |
|            | A.5 Conclusion   | 294 |
| <b>B</b>   | <b>Curriculum vitae</b>  | 297 |







# Nomenclature

## Acronyms

|          |  |        |
|----------|--|--------|
| PDF      | Probability Density Function             | II.2.1 |
| CDF      | Cumulative Distribution Function         | II.2.1 |
| PSD      | Power Spectral Density                   | II.2.2 |
| MIL(s)   | Modal Inertial Load(s)                   | II.5   |
| POD      | Proper Orthogonal Decomposition          | II.8   |
| CPT      | Covariance Proper Transformation         | II.8   |
| SPT      | Spectral Proper Transformation           | II.8   |
| ERP      | Envelope Reconstruction Problem          | III    |
| SWL(s)   | Static Wind Load(s)                      | III    |
| ESWL(s)  | Equivalent Static Wind load(s)           | IV     |
| LRC      | Load-Response Correlation method         | IV.4   |
| CESWL(s) | Conditional Expected Static Wind Load(s) | IV.7   |
| CEL      | Conditional Expected Load method         | IV.7   |
| PSWL(s)  | Principal Static Wind Load(s)            | V      |
| SVD      | Singular Value Decomposition             | V.2    |

## One random process

|                              |  |           |
|------------------------------|--|-----------|
| $x(t)$                       | Any Latin letter may signify a stationary random process     | (II.2.1)  |
| $x'(t)$                      | The superscript ' indicates the mean component is included   | (II.2.1)  |
| $\psi_x(x)$                  | Probability density function of $x$                          | (II.2.2)  |
| $\Psi_x(x)$                  | Cumulative distribution function of $x$                      | (II.2.3)  |
| $\psi_x^N(x)$                | PDF (normal process)   | (II.2.17) |
| $\psi_x^C(x)$                | PDF (non-normal process, cubic model)                        | (II.3.24) |
| $\mu_{k,x'}$                 | The $k$ -th <i>raw moment</i> of $x$                         | (II.2.5)  |
| $\mu_{k,x}$                  | The $k$ -th <i>central moment</i> of $x$                     | (II.2.5)  |
| $\kappa_{k,x}$               | The $k$ -th <i>cumulant</i> of $x$                           | (II.2.6)  |
| $\gamma_{3,x}, \gamma_{e,x}$ | Skewness and excess coefficients of $x$ , respectively       | (II.2.7)  |
| $R_{xx}(\tau)$               | Autocorrelation function                                     | (II.2.24) |
| $S_{xx}(\omega)$             | Univariate power spectral density                            | (II.2.25) |
| $m_{i,x}$                    | $i$ -th spectral moment of $x$                               | (II.2.28) |
| $\varepsilon, \delta$        | Spectral and spreading parameters, respectively              | (II.3.14) |
| $\nu_0$                      | Zero up-crossing rate with a positive slope (Rice's formula) | (II.3.15) |
| $\nu_{\max}$                 | Maxima crossing rate (Rice's formula)                        | (II.3.16) |

## Two random processes

|                                  |  |           |
|----------------------------------|--|-----------|
| $\psi_{xy}(x, y)$                | Joint PDF of two normal processes $x$ and $y$              | (II.2.8)  |
| $\psi_{xy}^{\mathcal{N}}(x, y)$  | Joint PDF (normal processes)                               | (II.2.18) |
| $\psi_{xy}^{\mathcal{B}}(x, y)$  | Joint PDF (non-normal processes, bicubic model)            | (IV.8.3)  |
| $\psi_{x y}(x, y)$               | Conditional PDF of $x$ on the condition that $y$ is given  | (II.2.15) |
| $\psi_{x y}^{\mathcal{N}}(x, y)$ | Conditional PDF (normal process)                           | (II.2.19) |
| $\psi_{x y}^{\mathcal{B}}(x, y)$ | Conditional PDF (non-normal processes, bicubic model)      | (IV.8.3)  |
| $\mu_{x y}(y)$                   | Conditional mean of $x$ on the condition that $y$ is given | (II.2.16) |
| $\mu_{x y}^{\mathcal{N}}(y)$     | Conditional mean (normal process)                          | (II.2.20) |
| $\mu_{x y}^{\mathcal{B}}(y)$     | Conditional mean (non-normal processes, bicubic model)     | (IV.8.8)  |
| $\sigma_{xy}$                    | Covariance coefficient between $x$ and $y$                 | (II.2.13) |
| $\rho_{xy}$                      | Correlation coefficient between $x$ and $y$                | (II.2.14) |
| $S_{xy}(\omega)$                 | Cross power spectral density function                      | (II.2.33) |
| $R_{xy}(\tau)$                   | Cross-correlation function                                 | (II.2.34) |
| $\Gamma_{xy}(\omega)$            | Coherence function   | (II.2.37) |

## $m$ random processes

|   |   |           |
|---|---|-----------|
| $\mathbf{x}$  | Vector of random processes                                | (II.2.38) |
| $\boldsymbol{\mu}_{\mathbf{x}}, \boldsymbol{\sigma}_{\mathbf{x}}$ | Vector of the means and standard deviations, respectively | (II.2.39) |
| $\boldsymbol{\Sigma}^{\mathbf{x}}$                                | Covariance matrix   | (II.2.40) |
| $\boldsymbol{\mathcal{R}}^{\mathbf{x}}$                           | Correlation matrix  | (II.2.41) |
| $\mathbf{S}^{\mathbf{x}}(\omega)$                                 | Power spectral density matrix                             | (II.2.42) |

## Operators and notation conventions

|   |   |
|---|---|
| $E[\cdot]$  | Expectation operator  |
| $\mathcal{F}[\cdot], \mathcal{F}^{-1}[\cdot]$     | Fourier transform and inverse Fourier transform, respectively                                     |
| $\dot{x}(t), \ddot{x}(t)$                         | First and second time derivatives, respectively   |
| $\circ$   | Hadamard product  |
| $\square^{\text{b}}$                              | Quantity related to quasi-static contribution (buffeting analysis)                                |
| $\square^{\text{r}}$                              | Quantity related to resonant contribution (buffeting analysis)                                    |
| $\square^{(\text{m})}$                            | Quantity related to the envelope ( $\text{m} \equiv \text{min}$ or $\text{m} \equiv \text{max}$ ) |
| $ \square $                                       | Absolute value  |
| $\mathbf{A}^{\text{T}}$                           | The transpose of matrix $\mathbf{A}$  |
| $\mathbf{A}^{-1}$                                 | The inverse of matrix $\mathbf{A}$  |
| $\mathbf{A}^{\star}$                              | The Hermitian of matrix $\mathbf{A}$  |
| $\mathbf{A}_j$                                    | The $j$ -th column of the matrix $\mathbf{A}$   |
| $\mathbf{A}_{i\circ} = (\mathbf{A}^{\text{T}})_i$ | The $i$ -th row of the matrix $\mathbf{A}$  |

**Scalars**

|  |   |            |
|--|---|------------|
| $n_b$  | Number of basic static wind loads                                   | (II.2.20)  |
| $n_t$  | Number of degrees of freedom  | (II.4.1)   |
| $n_l$  | Number of aerodynamic pressures                                     | (II.4.2)   |
| $n_r$  | Number of structural responses                                      | (II.4.9)   |
| $n_m$  | Number of modes retained for the analysis                           | (II.5.4)   |
| $n_{cpt}$                                    | Number of CPT loading modes   | (II.8.2)   |
| $n_s$  | Number of static wind loads considered for the ERP                  | (III.3.1)  |
| $n_q$  | Number of static wind loads retained for combinations               | (III.5.2)  |
| $n_c$  | Number of initial sets of combination coefficients                  | (III.5.1)  |
| $n_p$  | Number of PSWL bases considered for the ERP                         | V.4        |
| $\omega_m$                                   | Natural circular frequency of the $m$ -th mode                      | (II.5.3)   |
| $\xi_m$                                      | Damping ratio in the $m$ -th mode                                   | (III.3.1)  |
| $f, \omega$                                  | frequency and circular frequency, respectively                      |            |
| $i$  | The imaginary number  |            |
| $\tilde{\epsilon}_{(k)}$                     | Largest relative error indicator                                    | (III.3.3)  |
| $\mathcal{R}_{(k)}$                          | Overall reconstruction indicator                                    | (III.3.6)  |
| $\overline{\rho}_r$                          | Overall indicator of (absolute) correlation                         | (III.3.8)  |
| $\hat{\epsilon}$                             | Acceptable overestimation   | (III.3.10) |
| $\tilde{\epsilon}^t$                         | Acceptable underestimation  | (III.3.13) |
| $\hat{\epsilon}'$                            | Overestimation associated with no underestimation of the envelope   | III.3.5    |
| $\mathcal{R}^t$                              | Acceptable overall reconstruction                                   | (III.3.12) |
| $\alpha_{(k)}^{(b,1)}, \alpha_{(k)}^{(b,2)}$ | Coefficients that normalize the $k$ -th basic static wind loads     | (III.4.2)  |
| $\gamma$                                     | Parameter in the cost function                                      | (III.5.5)  |
| $\Psi_{(k)}^{(\gamma)}$                      | Cost function for the constrained nonlinear optimization algorithm  | (III.5.6)  |
| $\alpha_{(k)}^{(e,m,1)}$                     | Coefficient that normalizes the $k$ -th equivalent static wind load | (IV.10.1)  |
| $\alpha_{(k)}^{(e,m)}$                       | Coefficient that scales the $k$ -th equivalent static wind load     | (VI.5.2)   |
| $\alpha^{(e)}$                               | Amplification factor ensuring no underestimation of the envelope    | (VI.3)     |

**Vectors**

|   |  |            |
|---|--|------------|
| $\mathbf{x}(t)$                                 | Nodal displacements  | (II.4.1)   |
| $\mathbf{q}(t)$                                 | Modal amplitudes   | (II.5.5)   |
| $\mathbf{p}(t), \mathbf{c}_p(t)$                | Aerodynamic pressures and pressure coefficients, respectively    | (II.4.2)   |
| $\mathbf{f}(t)$                                 | External nodal forces (wind forces)                              | (II.4.2)   |
| $\mathbf{f}^e(t)$                               | Elastic forces   | (II.4.3)   |
| $\mathbf{f}^i(t)$                               | Inertial forces  | (II.4.5)   |
| $\mathbf{f}^d(t)$                               | Damping forces   | (II.4.6)   |
| $\mathbf{g}(t)$                                 | Generalized modal forces   | (II.5.6)   |
| $\mathbf{f}^{(s)}$                              | Static nodal forces for the ERP                                  | (III.3.1)  |
| $\mathbf{f}^{(c)}$                              | Static nodal forces ensuring no underestimation of the envelope  | (III.3.20) |
| $\mathbf{r}(t)$                                 | Structural responses   | (II.4.9)   |
| $\mathbf{r}^{(m)}$                              | Envelope of structural responses                                 | (II.4.15)  |
| $\tilde{\mathbf{r}}^{(m)}$                      | Approximation of the envelope with $k$ static wind loads         | (III.1.2)  |
| $\varepsilon^{(m)}$                             | Relative errors of the $k$ -th reconstructed envelope            | (III.3.2)  |
| $\mathbf{r}'^{(m)}$                             | Total envelope of structural responses                           | (II.4.19)  |
| $\mathbf{r}'^{(d,\min)}$                        | Design envelope of structural responses                          | (II.4.20)  |
| $\mathbf{g}^{(m)}$                              | Peak factors of structural responses                             | (II.3.5)   |
| $\mathbf{f}^{(e,m)}$                            | Equivalent static wind load (dynamic analysis)                   | (IV.2.1)   |
| $\mathbf{p}^{(e,m)}, \mathbf{c}_p^{(e,m)}$      | Equivalent static wind load (quasi-static analysis)              | (II.4.1)   |
| $\mathbf{r}^{(e,m)}$                            | Static structural responses under ESWL                           | (IV.2.2)   |
| $\beta^{(e,m)}$                                 | Coefficients to adjust ESWL                                      | (VI.5.3)   |
| $\mathbf{f}^{(\mathcal{E},m)}$                  | ( $e \equiv \mathcal{E}$ ) Conditional expected SWL              | (IV.7.2)   |
| $\mathbf{p}^{(\mathcal{S},m)}$                  | ( $e \equiv \mathcal{S}$ ) CST-based ESWL                        | (IV.3.2)   |
| $\mathbf{p}^{(\mathcal{L},m)}$                  | ( $e \equiv \mathcal{L}$ ) LRC-based ESWL                        | (IV.4.3)   |
| $\mathbf{f}^{(\mathcal{M},m)}$                  | ( $e \equiv \mathcal{M}$ ) MIL-based ESWL                        | (IV.5.6)   |
| $\mathbf{f}^{(\mathcal{L}^b \mathcal{M}^r, m)}$ | ( $e \equiv \mathcal{L}^b \mathcal{M}^r$ ) Hybrid-based ESWL     | (IV.6.4)   |
| $\mathbf{f}^{(\mathcal{E}^N, m)}$               | ( $e \equiv \mathcal{E}^N$ ) CEL-method ESWL, Gaussian framework | (IV.7.11)  |
| $\mathbf{f}^{(\mathcal{E}^B, m)}$               | ( $e \equiv \mathcal{E}^B$ ) CEL-method ESWL, bicubic model      | (IV.7.15)  |

## Matrices

|  |   |           |
|--|---|-----------|
| <b>I</b>                                 | Identity matrix   |           |
| <b>M, C, K</b>                           | Mass, damping and stiffness matrices  | (II.4.1)  |
| <b>A</b>                                 | Linear map from aerodynamic pressures to nodal forces                                   | (II.4.2)  |
| <b>O</b>                                 | Linear map from nodal displacements to structural responses                             | (II.4.9)  |
| <b>L</b>                                 | Linear map from elastic forces to structural responses                                  | (II.4.10) |
| <b>B</b>                                 | Linear map from aerodynamic pressures to structural responses                           | (II.4.13) |
| $\Omega$                                 | Generalized stiffness matrix  | (II.5.3)  |
| $\Phi$                                   | Matrix of mode shapes   | (II.5.3)  |
| <b>D</b>                                 | Generalized damping matrices  | (II.5.5)  |
| $\mathbf{H}(\omega)$                     | Nodal transfer function   | (II.6.3)  |
| $\mathcal{H}(\omega)$                    | Modal transfer function   | (II.6.9)  |
| $\mathcal{K}(\omega)$                    | Residual function   | (II.6.19) |
| $\mathbf{F}^{(b)}, \mathbf{P}^{(b)}$     | Matrix of basic static wind loads   |           |
| $\mathbf{W}^{(b)}$                       | Matrix of weighting factors of the basic static wind loads                              |           |
| $\mathbf{F}^{(\mathcal{M})}$             | Matrix of modal inertial loads ( $b \equiv \mathcal{M}$ )                               | (II.5.11) |
| $\mathbf{P}^{(\mathcal{C})}$             | Matrix of covariance proper transformation loading modes ( $b \equiv \mathcal{C}$ )     | (II.8.1)  |
| $\mathbf{F}^{(b,1)}, \mathbf{F}^{(b,2)}$ | Matrix of normalized basic static wind loads  | (III.4.2) |
| $\mathbf{R}^{(b,1)}, \mathbf{R}^{(b,2)}$ | Matrix of structural responses under the normalized basic SWLs                          | (III.4.3) |
| $\mathbf{F}^{(e)}$                       | Matrix of equivalent static wind loads  | (V.3.1)   |
| $\mathbf{F}^{(\mathcal{P})}$             | Matrix of principal static wind loads, nodal forces ( $b \equiv \mathcal{P}$ )          | (V.3.2)   |
| $\mathbf{P}^{(e)}$                       | Matrix of equivalent static wind loads  | (V.3.5)   |
| $\mathbf{P}^{(\mathcal{P})}$             | Matrix of principal static wind loads, aerodynamic pressures ( $b \equiv \mathcal{P}$ ) | (V.3.6)   |





# Chapter I

## Introduction

- 
- I.1** Context
  - I.2** Motivations
  - I.3** Personal contributions
  - I.4** Outline
- 

◇ “*How can we simplify and generalize wind loads?*”

[Davenport \(1995\)](#)

## I.1 Context

The structural design of buildings is the main mission of structural engineers. They have responsibility for the feasibility with the available materials and techniques, serviceability in regard to the purposes of the building and strength of the structure under various loads. These loads may be regarded as static or time-dependent. The former load may be evaluated with ease while the latter type is more demanding. The primary static load is the self-weight of the structural elements for which the structural response is computed easily whereas dealing with time-dependent loads required advanced techniques of structural analyses.

In our context, we are interested in random loads, in space and time, produced by the wind blowing over civil engineering structures. Wind loads may be decisive for a wide range of constructions and must therefore be predicted adequately in a structural design. Specifically, there exist synoptic and non-synoptic winds associated with severe to extreme wind events. The loading due to synoptic winds, also called atmospheric boundary layer winds, is considered in this work. These winds result from large-scale phenomena and are assumed stationary on a restricted period, representative for the wind effects on structures. Non-synoptic and transient winds such as downbursts and tornadoes are not considered.

For structures with small dimensions, usual shapes and under the assumption of a dynamic response in the fundamental mode, most wind loading codes provide a general set of design guidelines for synoptic winds. For the design of low- and middle-rise buildings, these codes have been developed thanks to intensive wind tunnel measurements establishing the pressure coefficients for the building envelope. As a matter of fact, large structures such as high-rise buildings and large-span roof structures, often exhibit unusual — even unique — shape and may be flexible enough to allow for a significant dynamic response in several, possibly coupled, modes. For instance, the railway station in Liège (Belgium), see the picture below, is beyond the scope of actual standards and advanced methods are required to predict the wind loads for the design.



Figure I.1: Picture freely available at <http://alltrends.over-blog.net/article-gare-des-guillemins-a-liege-79792068.html>

If the structure under investigation is out of the scope of actual standards, structural engineers may opt for either wind tunnel testing or computational fluid dynamics or both to provide the aerodynamic pressure field, not the design wind loads at this stage. When the aerodynamic pressure field is measured or computed, the buffeting analysis of the structure is then performed. This work focuses on the analysis of structures for which a linear behavior under wind actions can be reasonably assumed.

The buffeting analysis may be conducted in time or frequency domain and in a nodal, modal or hybrid basis. Among other considerations, the choice of the type of structural analysis depends on features of the aerodynamic pressure field that may be Gaussian or mildly to strongly non-Gaussian. For example, the buffeting analysis, in a Gaussian framework, is typically tackled as a spectral analysis. The well-known decomposition into mean, background and resonant contributions of the wind-induced responses provides an affordable access to this type of analysis in the everyday practice. As an ultimate outcome of the analysis, representative values of some structural responses, such as displacements, internal forces or stresses, have to be estimated for the design and they constitute the *envelope* of structural responses. These representative values may be defined in various ways for the design, e.g., as the mean of the extremes or in terms of some non-exceedance probabilities ( $p$ -quantiles) of the extremes. Additionally, there exist several methods to estimate at first the extreme value distribution. Actually, the extreme value analysis is an active research field of paramount importance in wind engineering. The development of new methods to estimate extreme value distribution or better definition for representative values is not the scope of the present study and we therefore set back to well-known methods.

For all practical purposes, the buffeting analysis may be separated from the structural design. Indeed, the study of wind effects on large flexible structures is usually tackled by structural engineers with expertise in this field while the sizing of the structure or at least, checking the structural strength is a mission of another team or even engineering office. Naturally, those in charge of the buffeting analysis should provide the structural responses to the structural engineers with responsibility for the design. This approach is however not the common one. Following the checking of structural strength, if structural engineers adapt structural elements to satisfy the design, a new buffeting analysis is performed and then a new verification has to be done. The decoupling of the buffeting analysis and the structural design is, therefore, not really optimal.

Besides, structural engineers seek to design with static wind loads and not blindly with only structural responses. These static wind loads have to replace the time-dependent wind loads and reproduce the dynamic response of the structure. On the practical side, the concept of static wind loads recasts the design procedure into the well-known format of standards and combination with other codified static loads such as self-weight or snow is straightforward. Once static wind loads are known, they are used through the iterative design process without repeating cumbersome dynamical analyses. In this framework, structural engineers can effectively focus on the structural sizing since static analyses are straightforward. Finally, if major modifications of structural elements or adjustments of the load-bearing system have been done, a new buffeting analysis is required to cross-check the design.

For decades, this concept of static wind loads for the analysis of civil structures subjected to wind has aroused interest due to its valuable features. Mainly, such an analysis has to provide structural responses similar to the extreme values that would be provided by a

buffeting analysis. If the structure exhibits a dynamic response in its fundamental mode, most of codes are based on the gust factor approach originally introduced by Davenport in the early sixties in which the static wind load is the mean wind loading amplified by a factor. Since this pioneering work, a lot of effort has been devoted to developing accurate static wind loads. When they are known, they are readily applied to the structure in a straightforward analysis.

Actually, the wind effects on structures through static loads may be understood as an *envelope reconstruction problem*. This problem consists in deriving a set of static loads targeting the efficient reconstruction of the extreme values of structural responses which are required for the design. The term “efficient” may cover a large range of features that would be desirable for these static wind loads. For instance, a minimum number for an optimum reconstruction would be expected, hence they must be derived very carefully. This issue constitutes the central core of the studies undertaken in this dissertation.

## I.2 Motivations

Since the 1970’s, methods have been developed for reformulating the complex time-space-dependent distribution of the fluctuating wind load into deterministic space-only dependent distributions, so-called *Static Wind Loads* (SWLs), with the purpose to handle the envelope reconstruction problem.

### Equivalent static wind loads

A first method is the *Equivalent Static Wind Load* (ESWL) such that the application of this type of loading provides responses in the structure and the same extreme value of a chosen one as what would result from the buffeting analysis. Formulations of ESWLs are available for quasi-static and dynamic structural behavior. For dynamic behavior, these ESWLs are expressed as weighted combinations of background and resonant parts computed in the nodal and modal basis, respectively. Actually, the methods formulating ESWLs are associated with a specific basis, nodal or nodal-modal (hybrid). Moreover, no formulation is given if the dynamic analysis is conducted in the nodal basis, see Table I.1. This has motivated the investigation of an alternative method, so-called *Conditional Expected Load* (CEL), developed no matter the basis in which the structural analysis is conducted: nodal, modal or hybrid (nodal-modal).

| Framework:           | Gaussian     |         | non-Gaussian |         |
|----------------------|--------------|---------|--------------|---------|
| Structural behavior: | Quasi-static | Dynamic | Quasi-static | Dynamic |
| Nodal basis          | ✓            | ✗       | ?            | ?       |
| Hybrid basis         | -            | ✓       | ?            | ?       |

Table I.1: Limitations of the current methods formulating ESWLs.

Furthermore, several methods developed hitherto to establish ESWLs assume Gaussian aerodynamic pressures and Gaussian structural responses. Actually, it is tempting to avoid a formal extension to non-Gaussian processes arguing that current ESWL formulations provide a very close approximation to the actual static load pattern even if the aerodynamic pressure field is non-Gaussian.

Notwithstanding this belief, disharmony has been shown between the ‘‘Gaussian’’ ESWLs and those obtained with a statistical treatment of wind-tunnel measurements. This has especially conducted to the study of a non-Gaussian formulation for ESWLs undertaken in this work. For this purpose a bicubic model for the joint and conditional PDFs of two non-Gaussian random processes has been derived.

### The envelope reconstruction problem

**Equivalent static wind loads** A first approach to tackle the envelope reconstruction problem consists in computing the ESWLs associated with all structural responses. For large and complex structures, the resulting set of loadings is huge but it ensures that the entire envelope is recovered. The size of this set is expected to be prohibitive, as the application of an ESWL related to a specific structural response may reconstruct a certain fraction of the envelope, with an acceptable tolerance. Thus it appears that a more suitable approach could be to identify, for instance from influence surfaces and engineering judgment, some representative structural responses along with their corresponding ESWLs. However, considering only a few ESWLs may lead to important underestimation of the envelope, especially if representative structural responses are not selected judiciously. This is feasible for simple structures but remains hazardous for large ones. Therefore, we foresee that other kinds of static wind loads are better suited. Nonetheless, this common and elementary option is considered for comparison in the illustrations.

**Basic static wind loads** A kind of static wind load, that we called *basic*, holds two distinctive features. They are not associated with specific structural responses, and are naturally ordered by decreasing importance.

For quasi-static structural behaviors, basic SWLs may be obtained, for instance, with the *Covariance Proper Transformation* (CPT) method producing wind modes related to the aerodynamic pressure field, so-called CPT loading modes. For dynamic structural behaviors, *Modal Inertial Loads* (MILs) are such that the deflection under those ones gives the modal shapes. They can be classified as basic SWLs, as well. The former kind focuses on the wind loading and disregards the load bearing system while the latter only depends on the modal characteristics. Accordingly to their features, they should be good candidates for the envelope reconstruction problem.

Though the concept is appealing, two drawbacks are underlined. First, they are more than ‘‘not associated with’’ specific structural responses since they are completely independent of the set of structural responses to be reconstructed. Second, the case of hybrid structural behavior, i.e., the quasi-static and resonant contributions to the variance of structural responses are similar, is problematic since we can not simply select one kind or the other, see Table I.2.

| Structural behavior: | Quasi-static | Hybrid | Resonant |
|----------------------|--------------|--------|----------|
| CPT loading modes    | ✓            | ✗      | ✗        |
| Modal inertial loads | ✗            | ✗      | ✓        |

Table I.2: Scope of application of CPT loading modes and modal inertial loads in the framework of the envelope reconstruction problem.

**Principal static wind loads** Since the aforementioned equivalent and basic SWLs are not really optimal for the envelope reconstruction problem, a novel kind relevant for any dynamic behavior is introduced, so-called Principal Static Wind Loads (PSWLs), as an important contribution of this thesis.

### I.3 Personal contributions

The essential contributions of this thesis are:

1. **Estimation of modal correlation coefficients using the white noise approximation**

Formulations for the estimation of modal covariances are already available. Those existing formulations are enhanced with a proper inclusion of the imaginary part of coherence functions of generalized forces. Indeed, this imaginary part is not always negligible in spite of some practical habits. The formulation is derived thanks to the white noise approximation and multiple timescale spectral analysis.

2. **Conditional Expected Load (CEL) method**

This formulation of ESWLs is able to handle quasi-static, mixed and resonant behaviors within a unique formulation. The proposed method is general and is relevant for Gaussian and non-Gaussian processes.

3. **Bicubic model for the joint and conditional PDFs**

A parametric model for the joint and conditional PDFs of two non-Gaussian processes is derived based on the Hermite moment model. It is an extension of the well-known cubic translation model and is the cornerstone to establish ESWLs for a certain class of non-Gaussian processes.

4. **General methodology for the Envelope Reconstruction Problem (ERP)**

A complete methodology to apprehend the envelope reconstruction problem is formalized. The procedure consists in the successive application of static wind loads to accurately approximate the envelope with a minimum range of discrepancy. The procedure, seen as an iterative procedure, is a general concept no matter the structure, its load-bearing system and structural behavior. Also, it is relevant for Gaussian and non-Gaussian structural responses.

5. **Principal Static Wind Loads (PSWLs)**

The principal static wind loads are determined by singular value decomposition. Their definition makes them naturally suitable to solve the envelope reconstruction problem. They are still dependent upon the set of structural responses that we want to reconstruct, though they are not associated with specific structural responses, making a notable difference. Moreover, they form a suitable orthogonal basis for linear combinations. In addition, they adapt for Gaussian and non-Gaussian structural responses. Finally, under several circumstances, these loadings degenerate into the CPT loading modes and modal inertial loads, which thence acts as limit cases.

## 6. Formulation of a constrained nonlinear optimization problem

A more elaborated approach to tackle the envelope reconstruction problem is based on combinations of static wind loads. The combination coefficients are determined with a constrained nonlinear optimization algorithm formally conceptualized.

The developments numbered 3 to 6 can be found in (Blaise et al., 2012; Blaise and Denoël, 2013a,b; Blaise et al., 2016).

## I.4 Outline

The present manuscript is divided into an introduction, five chapters and a conclusion. Briefly, the organization is as follows.

**Chapter I** presents the context in which the study was undertaken. Objectives and potential developments are identified. The personal contributions are listed and the outline of the manuscript is given.

**Chapter II** reviews the concepts from the theory of probability used in this dissertation. The models used to compute the envelope of structural responses are detailed. It describes also the Gaussian spectral analysis of structures derived in nodal basis, modal basis or hybrid basis with the background-resonant decomposition. As well, the well-known concept of white noise approximation is applied to the estimation of modal correlation coefficients. Finally, applications of the proper orthogonal decomposition technique in the field of wind engineering are described.

**Chapter III** formally introduces the envelope reconstruction problem and reviews several current methods to handle it. A general methodology consisting in an iterative procedure is proposed. Combinations of static wind loads are considered to speed-up the reconstruction of the envelope values. The problem of finding these combination coefficients is formulated as a constrained nonlinear optimization.

**Chapter IV** is devoted to the concept of equivalent static wind load. A first part is devoted to current methods such as the load-response correlation method, conditional sampling technique and hybrid method. The second part focuses on the development of a novel formulation relevant for various structural behaviors and for Gaussian or non-Gaussian structural responses. The third part customizes the methodology to handle the envelope reconstruction problem introduced in Chapter III to the equivalent static wind loads.

**Chapter V** is dedicated to the novel concept of principal static wind loads. Since they are determined by singular value decomposition, this matrix factorization is detailed. Under specific circumstances, limit cases of PSWLs for quasi-static and resonant structural behaviors are studied. The methodology to handle the envelope reconstruction problem introduced in Chapter III is enhanced thanks to a distinctive feature of principal static wind loads.

**Chapter VI** provides the illustrations of the concepts discussed in this thesis using three examples: a four-span bridge, a real-life stadium roof and a low-rise building. In the preceding Chapters, the reader is invited to refer to this one to gain understanding of the concepts and methods discussed in the thesis.

**Chapter VII** summarizes the major outcomes of this work in terms of theoretical and practical implications and gives recommendations for further investigations.

The glossary of symbols and initials used in the thesis is reported in the nomenclature on page **xix**.







# Chapter II

## Buffeting analysis of civil structures

---

- II.1 Introduction
  - II.2 Theory of probability
  - II.3 Representative extreme values
  - II.4 Equation of motion
  - II.5 Modal basis
  - II.6 Gaussian spectral analysis
  - II.7 Davenport's white noise approximation and extensions
  - II.8 Proper orthogonal decomposition
-

## II.1 Introduction

This Chapter describes some usual methods for the buffeting analysis of structures. This thesis focuses on either the quasi-static analysis in a non-Gaussian framework or the dynamic analysis in a Gaussian framework. The former is tackled with time-domain analysis and the latter with a proper recourse to spectral analysis.

Section II.2 discusses probability and stochastic tools to characterize the random response of structures to random excitations. For sake of brevity, only the materials and concepts used in the thesis are discussed and this Section is based on well-known references (Papoulis, 1965; Lin, 1976; Preumont, 1994). It also serves to introduce our notations.

As an ultimate outcome of the buffeting analysis, extreme values of some structural responses, have to be established. They are usually expressed with peak factors, for which there exists various models, depending on the properties of the considered random process (Rice, 1945; Kareem and Zhao, 1994; Floris and Iseppi, 1998). In Section II.3 two models of peak factors for the extreme values of Gaussian and non-Gaussian random processes are respectively detailed.

The equation of motion is reviewed in Section II.4 and Section II.4.2 introduces the definitions of *envelope* and *total envelope*. The properties of the modal analysis are given in Section II.5: truncation (Maddox, 1975; Hansteen and Bell, 1979), background-resonant decomposition along with the modal acceleration method (Dickens et al., 1997).

Section II.6 provides the elementary steps of a Gaussian spectral analysis (Clough and Penzien, 1993; Preumont, 1994). Section II.7 presents the white noise approximation (Dav-enport, 1964b, 1967) and its extensions (Denoël, 2009a, 2015). At last, the relevance of the white noise approximation for the covariance of modal amplitudes that take into account the imaginary part of the cross-PSD of generalized forces is assessed.

Finally, Section II.8 reviews the Proper Orthogonal Decomposition (POD) which has been widely applied in wind engineering as an understanding, simplification, modeling and simulation tool for the structural analysis (Gurley et al., 1997; Solari et al., 2007; Carassale et al., 2007).

## II.2 Theory of probability

### II.2.1 Random variables

We use the prime symbol ' to indicate a random variable  $x$  with a non-zero mean  $\mu_{x'}$ , while the centered random variable is devoid of this symbol, that yields

$$x' = \mu_{x'} + x. \quad (\text{II.2.1})$$

The *probability density function*  $\psi_x(x)$  is a Lebesgue-integrable function that fulfills the first and second axioms of Kolmogorov

$$\psi_x(x) \geq 0 \quad , \quad \int_{\mathbb{R}} \psi_x(x) dx = 1, \quad (\text{II.2.2})$$

and the product  $\psi_x(x)dx$  represents the probability that the random variable  $x$  takes a value between  $x$  and  $x+dx$ . The *cumulative distribution function*  $\Psi_x(x)$  gives the probability that the random variable takes a value lower than a value  $x$

$$\Psi_x(x) = \int_{-\infty}^x \psi_x(a) da \iff \psi_x(x) = \frac{d\Psi_x(x)}{dx}, \quad (\text{II.2.3})$$

and it is a monotonically nondecreasing function with the conditions

$$\Psi_x(-\infty) = 0 \quad , \quad \Psi_x(+\infty) = 1. \quad (\text{II.2.4})$$

The  $k$ -th *raw moment*  $\mu_{k,x'}$  and *central moment*  $\mu_{k,x}$  of the random variable  $x$  are defined by

$$\mu_{k,x'} = E[(x')^k] = \int_{\mathbb{R}} (x')^k \psi_{x'}(x') dx' \quad , \quad \mu_{k,x} = E[x^k] = \int_{\mathbb{R}} x^k \psi_x(x) dx, \quad (\text{II.2.5})$$

and correspond to the expected value (or mathematical expectation) of  $x'$  and  $x$  to the power  $k$ , respectively. The first raw moment is the mean,  $\mu_{1,x'} \equiv \mu_{x'}$ , and the second central moment is the variance,  $\mu_{2,x} \equiv \sigma_x^2$  with  $\sigma_x$  the standard deviation. The standard deviation divided by the mean  $\sigma_x/\mu_{x'}$  is a measure of the dispersion of the random variable around its mean. The first four *cumulants*  $\kappa_{k,x}$  of the random variable  $x$  are expressed in terms of the central moments, as

$$\kappa_{1,x} = 0 \quad , \quad \kappa_{2,x} = \mu_{2,x} \quad , \quad \kappa_{3,x} = \mu_{3,x} \quad , \quad \kappa_{4,x} = \mu_{4,x} - 3(\mu_{2,x})^2. \quad (\text{II.2.6})$$

The skewness and excess coefficients are respectively defined as the ratio of the third and fourth cumulants to the third and fourth powers of  $\sigma_x$

$$\gamma_{3,x} = \frac{\kappa_{3,x}}{\sigma_x^3} \quad , \quad \gamma_{e,x} = \frac{\kappa_{4,x}}{\sigma_x^4}. \quad (\text{II.2.7})$$

If the random variable is Gaussian, the skewness and excess coefficients are both equal to 0, otherwise they indicate the level of departure from a Gaussian distribution of the random variable.

**Two random variables** The *joint probability density function*  $\psi_{xy}(x, y)$  is a Lebesgue-integrable function that fulfills the first and second axioms of Kolmogorov,

$$\psi_{xy}(x, y) \geq 0 \quad , \quad \iint_{\mathbb{R}^2} \psi_{xy}(x, y) dx dy = 1, \quad (\text{II.2.8})$$

and  $\psi_{xy}(x, y) dx dy$  represents the probability that the random variables  $x$  and  $y$  take values between  $x$  and  $x + dx$ ,  $y$  and  $y + dy$ , respectively. The *joint cumulative distribution function*  $\Psi_{xy}(x, y)$  is defined by

$$\Psi_{xy}(x, y) = \int_{-\infty}^x \int_{-\infty}^y \psi_{xy}(a, b) da db \iff \psi_{xy}(x, y) = \frac{\partial^2 \Psi_{xy}(x, y)}{\partial x \partial y}, \quad (\text{II.2.9})$$

where  $\Psi_{xy}(x, y)$  is a monotonically nondecreasing function with the conditions

$$\Psi_{xy}(-\infty, y) = \Psi_{xy}(x, -\infty) = 0 \quad , \quad \Psi_{xy}(+\infty, +\infty) = 1, \quad (\text{II.2.10})$$

and

$$\Psi_{xy}(x, +\infty) = \Psi_x(x) \quad , \quad \Psi_{xy}(+\infty, y) = \Psi_y(y). \quad (\text{II.2.11})$$

The cross-central moments of the random variables  $x$  and  $y$  are given by

$$E[x^m y^n] = \iint_{\mathbb{R}^2} x^m y^n \psi_{xy}(x, y) dx dy, \quad (\text{II.2.12})$$

where  $m$  and  $n$  are the orders of  $x$  and  $y$ , respectively. The covariance of the two random variables is defined as

$$\sigma_{xy} = E[xy] = \iint_{\mathbb{R}^2} x y \psi_{xy}(x, y) dx dy. \quad (\text{II.2.13})$$

The correlation coefficient, defined as

$$\rho_{xy} = \frac{\sigma_{xy}}{\sigma_x \sigma_y}, \quad (\text{II.2.14})$$

is a measure of the degree of linear dependence between the two random variables. The *conditional probability density function* of  $x$  given  $y$  is expressed as

$$\psi_{x|y}(x, y) = \frac{\psi_{xy}(x, y)}{\psi_y(y)}. \quad (\text{II.2.15})$$

The *conditional expected value* of  $x$  given  $y$  is obtained as

$$\mu_{x|y}(y) = \int_{\mathbb{R}} x \psi_{x|y}(x, y) dx. \quad (\text{II.2.16})$$

**Gaussian framework** The probability density function of a zero-mean Gaussian random variable  $x$  reads

$$\psi_x^{\mathcal{N}}(x) = \frac{1}{\sqrt{2\pi}\sigma_x} \exp\left(-\frac{1}{2} \frac{x^2}{\sigma_x^2}\right), \quad (\text{II.2.17})$$

and the joint probability density function of two zero-mean Gaussian variables  $x$  and  $y$  is expressed as

$$\psi_{xy}^{\mathcal{N}}(x, y) = \frac{1}{2\pi\sigma_x\sigma_y\sqrt{1-\rho_{xy}^2}} \exp\left[-\frac{\left(\frac{x^2}{\sigma_x^2} - 2\rho_{xy}\frac{xy}{\sigma_x\sigma_y} + \frac{y^2}{\sigma_y^2}\right)}{2(1-\rho_{xy}^2)}\right], \quad (\text{II.2.18})$$

with  $\rho_{xy}$  the correlation coefficient between these two variables. Following definition (II.2.15), the conditional PDF of  $x$  given  $y$  is a Gaussian variable as well, given by

$$\psi_{x|y}^{\mathcal{N}}(x, y) = \frac{1}{\sqrt{1-\rho_{xy}^2}} \psi_x^{\mathcal{N}}\left(\frac{x - \frac{y}{\sigma_y}\rho_{xy}\sigma_x}{\sqrt{1-\rho_{xy}^2}}\right), \quad (\text{II.2.19})$$

with a standard deviation  $\sigma_{x|y}^{\mathcal{N}} = \sqrt{1-\rho_{xy}^2}$  and a conditional expected value equal to

$$\mu_{x|y}^{\mathcal{N}}(y) = \frac{y}{\sigma_y} \rho_{xy} \sigma_x. \quad (\text{II.2.20})$$

This relation is used for developments in Chapter IV.

## II.2.2 Stochastic processes

The developments in this thesis apply to *homogeneous random processes*. Also called *stationary random processes*, this kind of process exhibits several important features for the structural analysis. The *first rank probability density function*

$$\psi_x(x), \quad (\text{II.2.21})$$

of the random process  $x(t)$  is not a function of time  $t$  and  $\psi_x(x)dx$  represents the probability that the process takes a value between  $x$  and  $x + dx$  at any time  $t$ . So, at the first rank, the random process may be seen as a random variable.

However, to adequately characterize the random process in a Gaussian framework, two different times have to be considered. For this purpose, the *second rank probability density function*

$$\psi_x(x_1, t_1; x_2, t_2), \quad (\text{II.2.22})$$

is introduced such that  $\psi_x(x_1, t_1; x_2, t_2)dx_1dx_2$  represents the probability that the process  $x$  takes a value between  $x_1$  and  $x_1 + dx_1$  at time  $t_1$  and a value between  $x_2$  and  $x_2 + dx_2$  at time  $t_2$ . Since stationary implies that

$$\psi_x(x_1, t_1; x_2, t_2) = \psi_x(x_1, t_1 + \tau; x_2, t_2 + \tau) \quad \forall \tau \in \mathbb{R}, \quad (\text{II.2.23})$$

the second order probability density only depends on the time lag  $t_2 - t_1$ . The *autocorrelation function*, defined as

$$R_{xx}(\tau) = \text{E}[x(0)x(\tau)] = \iint_{\mathbb{R}^2} \psi_x(x_1, 0; x_2, \tau)dx_1dx_2, \quad (\text{II.2.24})$$

gives the correlation between values of the process at different times. By definition, this function is symmetric, i.e.,  $R_{xx}(\tau) = R_{xx}(-\tau)$  and attains its maximum at the origin  $R_{xx}(0) \geq R_{xx}(\tau)$  that is equal to the variance  $R_{xx}(0) = \sigma_x^2$ .

The Fourier transform of the autocorrelation function defines the (mean-square) *univariate power spectral density*

$$S_{xx}(\omega) = \mathcal{F}[R_{xx}(\tau)] = \frac{1}{2\pi} \int_{\mathbb{R}} R_{xx}(\tau)e^{-i\omega\tau}d\tau, \quad (\text{II.2.25})$$

of the random process  $x(t)$ . For stationary random processes, the *Wiener-Khintchine theorem* asserts that the autocorrelation function and the power spectral density function form a Fourier transform pair. The inverse Fourier transform of the power spectral density

$$R_{xx}(\tau) = \mathcal{F}^{-1}[S_{xx}(\omega)] = \int_{\mathbb{R}} S_{xx}(\omega)e^{i\omega\tau}d\omega, \quad (\text{II.2.26})$$

returns the autocorrelation function. The value at the origin of the autocorrelation function, i.e., at  $\tau = 0$ , reveals the fundamental property of the power spectral density: its integral over the frequency domain gives the variance of the random process

$$\sigma_x^2 = \int_{\mathbb{R}} S_{xx}(\omega)d\omega. \quad (\text{II.2.27})$$

In other words, the power spectral density gives the distribution of the variance over the frequency domain. By extension, the  $i$ -th *spectral moment* is defined as

$$m_{i,x} = \int_{\mathbb{R}} |\omega|^i S_{xx}(\omega) d\omega, \quad (\text{II.2.28})$$

where  $m_{0,x} = \sigma_x^2$ ,  $m_{2,x} = \sigma_{\dot{x}}^2$  and  $m_{4,x} = \sigma_{\ddot{x}}^2$  are the variances of the random process  $x$ , of its first time derivative  $\dot{x}(t) = \frac{dx(t)}{dt}$ , and of its second time derivative  $\ddot{x}(t) = \frac{d^2x(t)}{dt^2}$ , respectively.

**Two random processes** The *first rank joint probability density function* of two random processes  $x(t)$  and  $y(t)$  is written

$$\psi_{xy}(x, y), \quad (\text{II.2.29})$$

and  $\psi_{xy}(x, y) dx dy$  represents the probability that  $x(t)$  and  $y(t)$  take values between  $x$  and  $x + dx$  and  $y$  and  $y + dy$  at any time  $t$ . As before, to adequately characterize these two random processes in a Gaussian framework, two different instants have to be considered. We introduce the *second rank joint probability density function*

$$\psi_{xy}(x, t_1; y, t_2), \quad (\text{II.2.30})$$

such that  $\psi_{xy}(x, t_1; y, t_2) dx dy$  represents the probability that the processes  $x(t_1)$  and  $y(t_2)$  take values between  $x$  and  $x + dx$  at time  $t_1$  and a value between  $y$  and  $y + dy$  at time  $t_2$ . Since stationary implies that

$$\psi_{xy}(x, t_1; y, t_2) = \psi_{xy}(x, t_1 + \tau; y, t_2 + \tau) \quad \forall \tau \in \mathbb{R}, \quad (\text{II.2.31})$$

the second rank joint probability density function only depends on the time lag  $t_2 - t_1$ . The *cross-correlation function*, defined as

$$R_{xy}(\tau) = E[x(0) y(\tau)] = \iint_{\mathbb{R}^2} \psi_{xy}(x, 0; y, \tau) dx dy, \quad (\text{II.2.32})$$

gives the correlation between values of the two random processes at different times. Its value at the origin is equal to the covariance  $R_{xy}(0) = \sigma_{xy}$ .

The Fourier transform of the cross-correlation function defines the (mean-square) *cross-power spectral density*

$$S_{xy}(\omega) = \mathcal{F}[R_{xy}(\tau)] = \frac{1}{2\pi} \int_{\mathbb{R}} R_{xy}(\tau) e^{-i\omega\tau} d\tau, \quad (\text{II.2.33})$$

of two random processes  $x(t)$  and  $y(t)$ . Unlike the univariate one, the cross-power spectral density is a complex function. The inverse Fourier transform of the cross-power spectral density

$$R_{xy}(\tau) = \mathcal{F}^{-1}[S_{xy}(\omega)] = \int_{\mathbb{R}} S_{xy}(\omega) e^{i\omega\tau} d\omega, \quad (\text{II.2.34})$$

gives the cross-correlation function. The value at the origin of the cross-correlation function, i.e., at  $\tau = 0$ , reveals the fundamental property of the cross-power spectral density: its integral over the frequency domain gives the covariance between the two random processes

$$\sigma_{xy} = \int_{\mathbb{R}} S_{xy}(\omega) d\omega. \quad (\text{II.2.35})$$



The cross-power spectral density satisfies

$$|S_{xy}(\omega)|^2 \leq S_y(\omega)S_x(\omega), \quad (\text{II.2.36})$$

and the relation

$$\Gamma_{xy}(\omega) = \frac{S_{xy}(\omega)}{\sqrt{S_y(\omega)S_x(\omega)}}, \quad (\text{II.2.37})$$

defines the complex-valued *coherence function*  $\Gamma_{xy}(\omega)$ .

### II.2.3 Random vectors

An  $m \times 1$  random vector  $\mathbf{x}$  is a vector of  $m$  stationary random processes, denoted by

$$\mathbf{x}(t) = \begin{Bmatrix} x_1(t) \\ \vdots \\ x_i(t) \\ \vdots \\ x_m(t) \end{Bmatrix}, \quad (\text{II.2.38})$$

and the  $m \times 1$  vectors  $\boldsymbol{\mu}_{\mathbf{x}'}$  and  $\boldsymbol{\sigma}_{\mathbf{x}}$

$$\boldsymbol{\mu}_{\mathbf{x}'} = \begin{Bmatrix} \mu_{x'_1} \\ \vdots \\ \mu_{x'_i} \\ \vdots \\ \mu_{x'_m} \end{Bmatrix}, \quad \boldsymbol{\sigma}_{\mathbf{x}} = \begin{Bmatrix} \sigma_{x_1} \\ \vdots \\ \sigma_{x_i} \\ \vdots \\ \sigma_{x_m} \end{Bmatrix}, \quad (\text{II.2.39})$$

collect the mean and standard deviation of each stationary random process, respectively. The covariance matrix is denoted by

$$\boldsymbol{\Sigma}^{\mathbf{x}} = \begin{bmatrix} \Sigma_{11}^{\mathbf{x}} & \cdots & \Sigma_{1i}^{\mathbf{x}} & \cdots & \Sigma_{1m}^{\mathbf{x}} \\ & \ddots & & & \vdots \\ & & \Sigma_{ii}^{\mathbf{x}} & & \Sigma_{im}^{\mathbf{x}} \\ \text{Sym.} & & \ddots & & \vdots \\ & & & \Sigma_{mm}^{\mathbf{x}} & \end{bmatrix} = \begin{bmatrix} \sigma_{x_1}^2 & \cdots & \rho_{x_1x_i}\sigma_{x_1}\sigma_{x_i} & \cdots & \rho_{x_1x_m}\sigma_{x_1}\sigma_{x_m} \\ & \ddots & & & \vdots \\ & & \sigma_{x_i}^2 & & \rho_{x_ix_m}\sigma_{x_i}\sigma_{x_m} \\ \text{Sym.} & & \ddots & & \vdots \\ & & & \sigma_{x_m}^2 & \end{bmatrix}, \quad (\text{II.2.40})$$

and collects the variance on its diagonal and the covariance on the off-diagonal elements, while the correlation matrix reads

$$\boldsymbol{\mathcal{R}}^{\mathbf{x}} = \begin{bmatrix} 1 & \cdots & \rho_{x_1x_i} & \cdots & \rho_{x_1x_m} \\ & \ddots & & & \vdots \\ & & 1 & & \rho_{x_ix_m} \\ \text{Sym.} & & \ddots & & \vdots \\ & & & & 1 \end{bmatrix}. \quad (\text{II.2.41})$$

Also, the PSD matrix is denoted by

$$\mathbf{S}^{\mathbf{x}}(\omega) = \begin{bmatrix} S_{11}^{\mathbf{x}}(\omega) & \cdots & S_{1i}^{\mathbf{x}}(\omega) & \cdots & S_{1m}^{\mathbf{x}}(\omega) \\ & \ddots & & & \vdots \\ & & S_{ii}^{\mathbf{x}}(\omega) & & S_{im}^{\mathbf{x}}(\omega) \\ \text{Sym.} & & & \ddots & \vdots \\ & & & & S_{mm}^{\mathbf{x}}(\omega) \end{bmatrix}, \quad (\text{II.2.42})$$

and collects the auto-PSD on its diagonal, while the cross-PSD are the off-diagonal elements.

## II.3 Representative extreme values

In structural engineering, representative extreme values of a zero-mean random process  $x(t)$  are usually derived from extreme value theory. The maximum (resp. minimum) representative value is usually based on the statistics of the largest maximum (resp. smallest minimum) of  $x(t)$  over a reference period  $T$ .

Mathematically, the  $i$ -th maximum  $x(t) = \hat{\xi}_i$ , positive or negative, occurs in the interval  $[t; t + dt]$  if the following three conditions are fulfilled

$$\ddot{x}(t) < 0, \dot{x}(t) > 0, \dot{x}(t + dt) < 0. \quad (\text{II.3.1})$$

The maximum of the  $n_{\max}$  maxima occurring in the observation period, is defined as the largest maximum (positive extreme)  $\hat{x}$

$$\hat{x} = \max_{i=1, \dots, n_{\max}} \hat{\xi}_i, \quad (\text{II.3.2})$$

which is seen as a random variable. The  $i$ -th minimum  $x(t) = \check{\xi}_i$ , positive or negative, occurs in the interval  $[t; t + dt]$  if the following three conditions are fulfilled

$$\ddot{x}(t) > 0, \dot{x}(t) < 0, \dot{x}(t + dt) > 0. \quad (\text{II.3.3})$$

The minimum of the  $n_{\min}$  minima occurring in the observation period, is defined as the smallest minimum (negative extreme)  $\check{x}$

$$\check{x} = \min_{i=1, \dots, n_{\min}} \check{\xi}_i, \quad (\text{II.3.4})$$

which is seen as a random variable.

In a Gaussian framework, [Cartwright and Longuet-Higgins \(1956\)](#) derived the PDFs of the positive extreme  $\hat{x}$  (resp. negative extreme  $\check{x}$ ) assuming that the  $n_{\max}$  maxima (resp.  $n_{\min}$  minima) occur independently of each other (Poisson assumption). This is described in Section [II.3.1](#).

In a non-Gaussian framework, several methods exist to estimate the extreme value PDF such as the block maxima method, the peaks-over-threshold method, the average conditional exceedance rate method and translation process method, see [Ding and Chen \(2014\)](#) for a review. The translation process method based on the works of [Winterstein \(1988\)](#) is selected in this work and described in Section [II.3.2](#). The method is well-known and accurate for slightly to mildly softening Gaussian processes. It is therefore relevant for the examples treated in Chapter [VI](#). In case of strongly non-Gaussian processes, the translation process method is less accurate and a mixture distribution model ([Ding and Chen, 2014](#)) is recommended instead.

When the extreme value distribution is estimated, a choice of the representative value has to be made. This value is termed “the envelope value” in this work.

### Envelope values

The envelope value of the largest maximum over a reference period  $T$  is commonly expressed by

$$x^{(\max)} = g^{(\max)} \sigma_x + \hat{\kappa} \sigma_{\hat{x}}, \quad (\text{II.3.5})$$

where  $g^{(\max)}$  is called the *peak factor* for the mean largest maximum

$$E[\hat{x}] = g^{(\max)}\sigma_x, \quad (\text{II.3.6})$$

and  $\hat{\kappa}$  is a coefficient that multiplies the standard deviation  $\sigma_{\hat{x}}$  of the largest maximum variable (II.3.2). The same definition holds for the envelope value of the largest minimum over a reference period  $T$

$$x^{(\min)} = g^{(\min)}\sigma_x + \check{\kappa}\sigma_{\check{x}}, \quad (\text{II.3.7})$$

where  $g^{(\min)}$  is called the *peak factor* for the mean smallest minimum

$$E[\check{x}] = g^{(\min)}\sigma_x, \quad (\text{II.3.8})$$

and  $\check{\kappa}$  is a coefficient that multiplies the standard deviation  $\sigma_{\check{x}}$  of the smallest minimum variable (II.3.4).

For instance, if the largest maximum PDF is considered as a Gumbel distribution, the coefficients  $\hat{\kappa} = 0, 0.636$  and  $1.025$  correspond to the  $p$ -quantiles (or non-exceedance probabilities) of 57%, 78% and 86%. These three statistics are often used to compare the accuracy of methods developed in the framework of the extreme value theory. As stated in the introduction of Chapter I, it is not the purpose of this work to compare different definitions for the representative value. It is therefore not discussed further, and we follow the same objectives as those presented by [Chen and Zhou \(2007\)](#) who stress that “*The precise choice of the characteristic value is rather arbitrary provided it is consistent, convenient and useful for practical design applications.*”

For the sake of illustration, it is therefore arbitrarily chosen to consider the mean largest maximum (resp. mean smallest minimum) for the envelope value of the largest maximum (resp. smallest minimum)

$$x^{(\max)} = g^{(\max)}\sigma_x \quad ; \quad x^{(\min)} = g^{(\min)}\sigma_x, \quad (\text{II.3.9})$$

and only this representative value is discussed in Sections II.3.1 and II.3.2. It is emphasized that this arbitrary choice does not necessarily ease the envelope reconstruction problem, which is the scope of Chapter III and illustrated in Chapter VI. It is just a choice among others. Additionally, the formulation of the envelope reconstruction problem discussed in Chapter III is not associated with a specific choice of the representative value and other models can also be used (see Appendix A).

### II.3.1 Gaussian framework

Assuming the standardized random process  $\eta = x/\sigma_x$  is Gaussian, [Rice \(1945\)](#) derived the probability density functions of its maxima and minima

$$\psi_{\eta^{\max}}^{\mathcal{N}}(\eta) = \frac{1}{(2\pi)^{\frac{1}{2}}} \left[ \varepsilon e^{-\frac{1}{2}\eta^2/\varepsilon^2} + (1 - \varepsilon^2)^{\frac{1}{2}} \eta e^{-\frac{1}{2}\eta^2} \int_{-\infty}^{\eta(1-\varepsilon^2)^{\frac{1}{2}}/\varepsilon} e^{-\frac{1}{2}t^2} dt \right], \quad (\text{II.3.10})$$

$$\psi_{\eta^{\min}}^{\mathcal{N}}(\eta) = \frac{1}{(2\pi)^{\frac{1}{2}}} \left[ \varepsilon e^{-\frac{1}{2}\eta^2/\varepsilon^2} - (1 - \varepsilon^2)^{\frac{1}{2}} \eta e^{-\frac{1}{2}\eta^2} \int_{-\infty}^{-\eta(1-\varepsilon^2)^{\frac{1}{2}}/\varepsilon} e^{-\frac{1}{2}t^2} dt \right], \quad (\text{II.3.11})$$

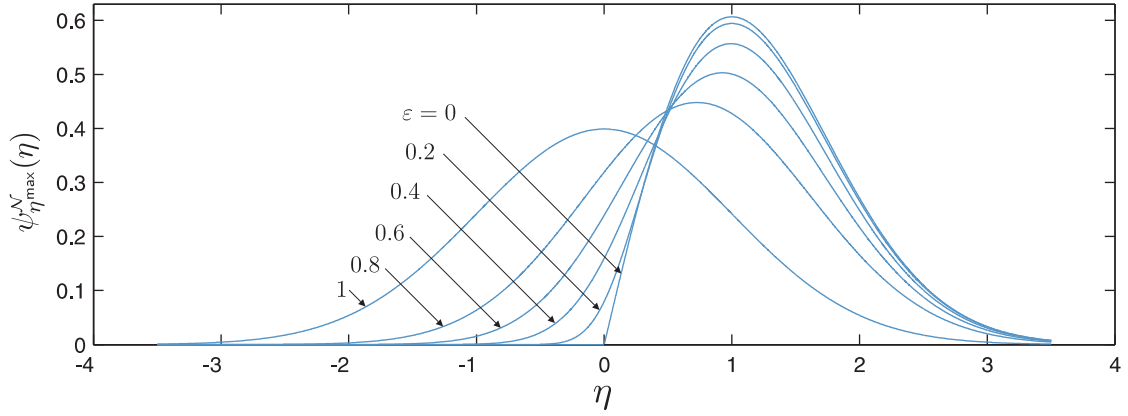


Figure II.1: PDF of maxima for six values of the spectral parameter. Figure reproduced from [Cartwright and Longuet-Higgins \(1956\)](#).

and the associated cumulative distribution functions

$$\Psi_{\eta^{\max}}^{\mathcal{N}}(\eta) = \frac{1}{(2\pi)^{\frac{1}{2}}} \left[ \int_{-\infty}^{\eta/\varepsilon} e^{-\frac{1}{2}t^2} dt - (1 - \varepsilon^2)^{\frac{1}{2}} e^{-\frac{1}{2}\eta^2} \int_{-\infty}^{\eta(1-\varepsilon^2)^{\frac{1}{2}}/\varepsilon} e^{-\frac{1}{2}t^2} dt \right], \quad (\text{II.3.12})$$

$$\Psi_{\eta^{\min}}^{\mathcal{N}}(\eta) = \frac{1}{(2\pi)^{\frac{1}{2}}} \left[ \int_{-\infty}^{\eta/\varepsilon} e^{-\frac{1}{2}t^2} dt + (1 - \varepsilon^2)^{\frac{1}{2}} e^{-\frac{1}{2}\eta^2} \left( (2\pi)^{\frac{1}{2}} - \int_{-\infty}^{\eta(1-\varepsilon^2)^{\frac{1}{2}}/\varepsilon} e^{-\frac{1}{2}t^2} dt \right) \right]. \quad (\text{II.3.13})$$

The PDF and CDF of the maxima depend on a single parameter  $\varepsilon$ , so-called *spectral parameter*, defined by

$$\varepsilon^2 = 1 - \frac{(m_{2,x})^2}{m_{0,x}m_{4,x}}. \quad (\text{II.3.14})$$

It is a dimensionless number,  $0 \leq \varepsilon \leq 1$ , indicating the relative bandwidth of the power spectral density of  $x$ . Narrow and large band-processes have a spectral parameter close to 0 and 1, respectively. Two limiting cases for  $\psi_{\eta^{\max}}^{\mathcal{N}}(\eta)$  are (i)  $\varepsilon = 0$ , a Rayleigh distribution and (ii)  $\varepsilon = 1$ , a Gaussian distribution. Figure II.1 depicts the PDF of maxima for six values of the spectral parameter.

[Rice \(1945\)](#) derived the formulation of the frequency of zero up-crossings with a positive slope (known as Rice's formula), given by

$$\nu_0 = \frac{1}{2\pi} \left( \frac{m_{2,x}}{m_{0,x}} \right)^{\frac{1}{2}} = \frac{1}{2\pi} \frac{\sigma_{\dot{x}}}{\sigma_x}, \quad (\text{II.3.15})$$

and the frequency of maxima as

$$\nu_{\max} = \frac{1}{2\pi} \left( \frac{m_{4,x}}{m_{2,x}} \right)^{\frac{1}{2}} = \frac{1}{2\pi} \frac{\sigma_{\ddot{x}}}{\sigma_{\dot{x}}}. \quad (\text{II.3.16})$$

The zero up-crossing rate  $\nu_0$  is also named the *central frequency* where the energy is concentrated in the random process.

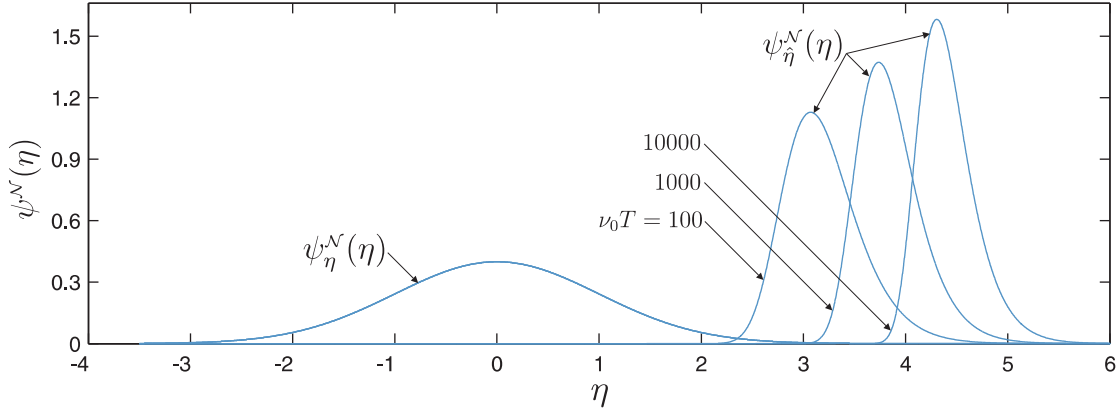


Figure II.2: PDFs of the random process and of its largest maximum for three values of  $\nu_0 T = 100, 1000$  and  $10000$ . Figure reproduced from [Davenport \(1964a\)](#).

[Cartwright and Longuet-Higgins \(1956\)](#) derived the probability density functions of the largest of  $n_{\max}$  maxima and of the smallest of  $n_{\min}$  minima, respectively as

$$\psi_{\hat{\eta}}^{\mathcal{N}}(\eta) = \frac{d}{d\eta} [\Psi_{\eta^{\max}}^{\mathcal{N}}(\eta)]^{n_{\max}} = n_{\max} [\Psi_{\eta^{\max}}^{\mathcal{N}}(\eta)]^{n_{\max}-1} \psi_{\eta^{\max}}^{\mathcal{N}}(\eta), \quad (\text{II.3.17})$$

$$\psi_{\hat{\eta}}^{\mathcal{N}}(\eta) = \frac{d}{d\eta} [\Psi_{\eta^{\min}}^{\mathcal{N}}(\eta)]^{n_{\min}} = n_{\min} [1 - \Psi_{\eta^{\min}}^{\mathcal{N}}(\eta)]^{n_{\min}-1} \psi_{\eta^{\min}}^{\mathcal{N}}(\eta), \quad (\text{II.3.18})$$

assuming that the  $n_{\max}$  maxima (resp.  $n_{\min}$  minima) occur independently of each other (Poisson assumption) over the observation period  $T$ . Figure II.2 depicts the PDF of  $\eta$  and PDFs of its largest maximum  $\hat{\eta}$  for three values of  $\nu_0 T$ .

An asymptotic expression of the peak factor, valid for values of  $n_{\max}$  greater than 50 and  $0 \leq \varepsilon \ll 1$ , is given by

$$g^{(\max)} = E[\hat{\eta}] = \sqrt{2 \ln \left( (1 - \varepsilon^2)^{\frac{1}{2}} n_{\max} \right)} + \frac{\gamma}{\sqrt{2 \ln \left( (1 - \varepsilon^2)^{\frac{1}{2}} n_{\max} \right)}}, \quad (\text{II.3.19})$$

where  $\gamma = 0.5772$  is Euler's constant. This approximation is applicable to most of the random processes encountered in wind engineering, assuming they are Gaussian.

Using (II.3.14), (II.3.15) and (II.3.16), [Davenport \(1964a\)](#) formulated the number of maxima during a reference period as

$$n_{\max} = \frac{\nu_0 T}{(1 - \varepsilon^2)^{\frac{1}{2}}}, \quad (\text{II.3.20})$$

and inserting (II.3.20) into (II.3.19), the peak factor reads

$$g^{(\max)} = \sqrt{2 \ln(\nu_0 T)} + \frac{\gamma}{\sqrt{2 \ln(\nu_0 T)}}. \quad (\text{II.3.21})$$

Under the assumption of Gaussianity, the peak factors for the mean smallest minimum and the mean largest maximum only differ by their sign, i.e.,

$$g^{(\min)} = -g^{(\max)}. \quad (\text{II.3.22})$$

Figure II.3 illustrates the evolution of the peak factor as a function of  $\nu_0 T$ . In wind engineering and for observation periods of 10 minutes, the typical value of  $\nu_0 T$  lies between 50 and 1000 that gives a range for the peak factor of [3, 3.9].

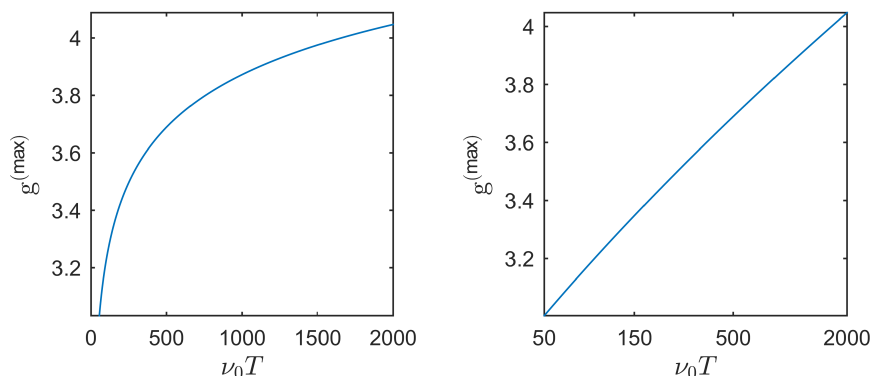


Figure II.3: Peak factor as a function of  $\nu_0 T$ . The graph on the right is given as a semi-log plot.

### II.3.2 Non-Gaussian framework - Hermite moment model

In the Hermite moment model, the PDF of a non-Gaussian random variable is modeled thanks to a cubic transformation of a Gaussian variable. This model fits the first four cumulants. Actually, in wind engineering applications, the statistical knowledge of non-Gaussian random processes is usually limited to the first four cumulants. Moreover, *softening* random processes, i.e.,  $\gamma_{e,x} > 0$ , are more common than *hardening* random processes, i.e.,  $\gamma_{e,x} < 0$ , since the non-Gaussian aerodynamic pressures are usually softening ones. Winterstein (1988) suggested the use of Hermite series instead of Charlier or Edgeworth series, that can exhibit limitations, especially in the tail regions. Thence, the Hermite moment model is adopted in the thesis.

The proposed polynomial transformation method is a 3-parameter model and consists in a cubic monotonic transformation  $g(\cdot)$  of a standard Gaussian random variable  $u$ , such as

$$x = g(u) = \frac{\alpha}{b} \left( \frac{u^3}{3} + au^2 + (b-1)u - a \right), \quad (\text{II.3.23})$$

where the parameters  $\alpha$ ,  $a$  and  $b$  are tuned to match the variance  $\sigma_x^2$ , skewness coefficient  $\gamma_{3,x}$  and excess coefficient  $\gamma_{e,x}$  of the zero-mean random variable  $x$ . Provided  $g(u)$  is monotonic, the PDF of the variable  $x$  reads

$$\psi_x^{\mathcal{C}}(x) = \frac{\psi_u^{\mathcal{N}}(u(x))}{\left| \frac{dg}{du}(u(x)) \right|}, \quad (\text{II.3.24})$$

where symbol “ $\mathcal{C}$ ” stands for “*Cubic translation model*” and  $u(x) = g^{-1}(x)$  is explicitly given as

$$u(x) = \left[ \zeta(x) + \sqrt{c + \zeta^2(x)} \right]^{1/3} + \left[ \zeta(x) - \sqrt{c + \zeta^2(x)} \right]^{1/3} - a, \quad (\text{II.3.25})$$

with  $c = (b - 1 - a^2)^3$  and  $\zeta(x) = \frac{3}{2}b \left( a + \frac{x}{\alpha} \right) - a^3$ . Writing (II.3.24) and (II.3.25) require that the cubic transformation (II.3.23) is monotonic. This is ensured by the *monotone limitation*  $b - 1 - a^2 \geq 0$  (Choi and Sweetman, 2010).

Introducing the convenient variables  $h_3$  and  $h_4$  to satisfy the variance  $\sigma_x^2$  leads to

$$a = \frac{h_3}{3h_4}, \quad b = \frac{1}{3h_4}, \quad \alpha = \frac{\sigma_x}{\sqrt{1 + 2h_3^2 + 6h_4^2}}, \quad (\text{II.3.26})$$

resulting in a set of nonlinear equations in two variables (Gurley et al., 1997)

$$\gamma_{3,x} = \frac{2h_3(3 + 4h_3^2 + 18h_4 + 54h_4^2)}{(\sqrt{1 + 2h_3^2 + 6h_4^2})^3}, \quad (\text{II.3.27})$$

$$\gamma_{4,x} = \frac{3(1 + 20h_3^4 + 8h_4 + 84h_4^2 + 432h_3^3 + 1116h_4^4 + 4h_3^2(5 + 48h_4 + 186h_4^2))}{(1 + 2h_3^2 + 6h_4^2)^2}, \quad (\text{II.3.28})$$

for the skewness and kurtosis coefficients, respectively. The solution of equations (II.3.27)-(II.3.28) may be computed using Newton's iterative method. Alternatively, several approximate solutions are given in (Winterstein, 1988; Winterstein and Kashef, 2000; Yang et al., 2013).

The monotone limitation limits the effective region of skewness and excess coefficients where the approximation of random variables using the cubic transformation is applicable. In case of slight deviations from the monotone limitation, adjustments are nevertheless proposed in (Peng et al., 2014). This limitation is illustrated by the curve in Figure II.4-(a). The dot and plus markers (in orange) identify two sets of 4 couples of  $(\gamma_{3,x}, \gamma_{e,x})$  for which the PDFs, computed with (II.3.24), are illustrated in Figure II.5 along with the normal distribution.

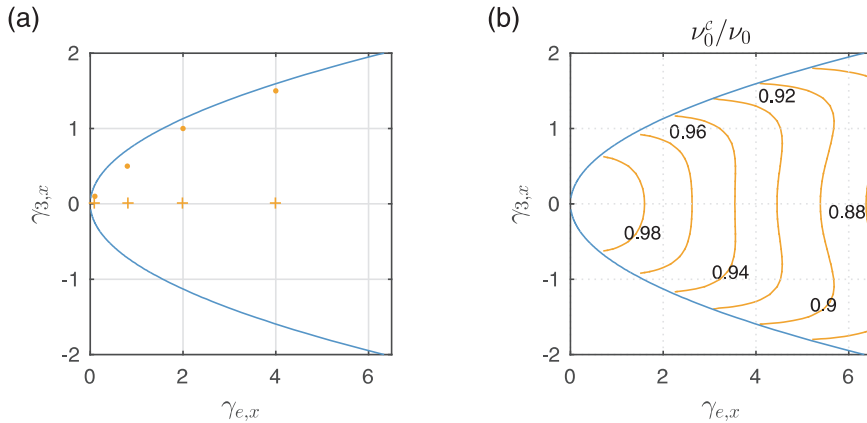


Figure II.4: (a) Monotone limitation (in blue). The domain of applicability of the Hermite moment model (in its original formulation) is inside the two lines. (b) Contour plot of non-Gaussian to Gaussian ratio of mean zero up-crossing rate.

The set of couples  $(\gamma_{3,x}, \gamma_{e,x})$  identified with dot markers gives couples of increasing skewness and excess coefficients while the set of couples  $(\gamma_{3,x}, \gamma_{e,x})$  identified with plus markers gives increasing excess coefficients with the skewness coefficient equal to 0.



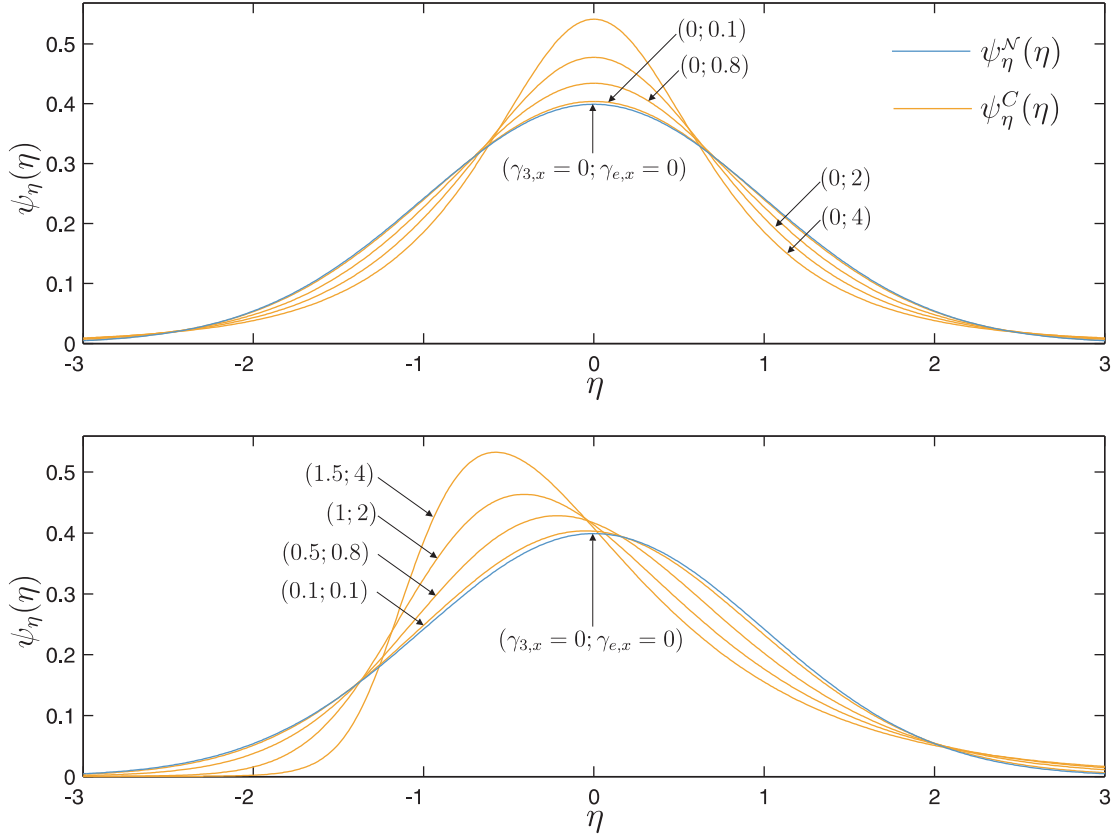


Figure II.5: Examples of probability density functions, Gaussian (in blue) and non-Gaussian (in orange) obtained with the Hermite moment model for 4 sets of values of  $(\gamma_{3,x}, \gamma_{e,x})$ .

The zero up-crossing rate with cubic transformation is expressed as

$$\nu_0^c = \nu_0 \frac{1}{(\alpha/\sigma_x)^2 (1 + 4h_3^2 + 18h_4^2)}, \quad (\text{II.3.29})$$

and the ratio  $\nu_0^c/\nu_0$  is illustrated in Figure II.4-(b).

The PDFs of the largest maximum and smallest minimum of a non-Gaussian random process, modeled with the cubic transformation (II.3.23), are respectively given by

$$\psi_{\tilde{\eta}}^c(\eta) = \frac{\psi_{\tilde{\eta}}^N(g^{-1}(\eta))}{\left| \frac{dg}{du}(g^{-1}(\eta)) \right|}, \quad \psi_{\tilde{\eta}}^c(\eta) = \frac{\psi_{\tilde{\eta}}^N(g^{-1}(\eta))}{\left| \frac{dg}{du}(g^{-1}(\eta)) \right|}. \quad (\text{II.3.30})$$

Figure II.6 illustrates the PDFs of largest maximum and smallest minimum when the random process is Gaussian (in blue) and non-Gaussian modeled with the cubic transformation (in orange). The upper graph of Figure II.6 illustrates PDFs for increasing values of the excess coefficient while the skewness is set equal to 0. The PDFs for the largest maximum and minimum for the non-Gaussian process are similar, as in the Gaussian case. However they are more spread and displaced towards larger values when the excess coefficient increases. Peak factors are still equal in absolute value, i.e.,  $g^{(\min)} = -g^{(\max)}$ , since odd cumulants are zero.

The lower graph of Figure (II.6) illustrates PDFs for increasing values of both the skewness and excess coefficients. In this case, the PDFs of largest maxima and minima are no longer similar and the non-Gaussian peak factors are different in absolute values, i.e.,

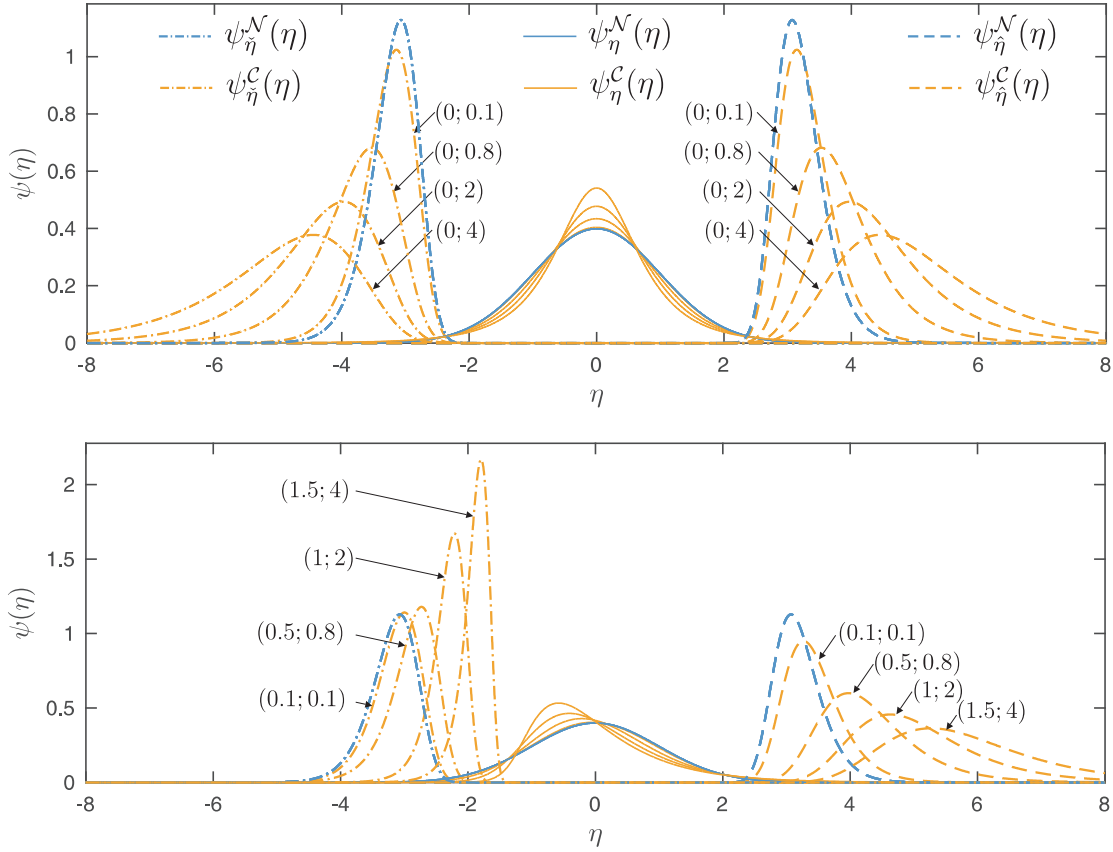


Figure II.6: PDFs of the Gaussian process (in blue) and non-Gaussian process (in orange) and PDFs of the largest maximum and minimum for values of  $\nu_0 T = 100$ .

$g^{(\min)} \neq -g^{(\max)}$ . For positive skewness coefficient, the peak factor for the mean largest maximum is larger than the peak factor for the mean smallest minimum (in absolute value), i.e.,  $g^{(\max)} > -g^{(\min)}$ .

Kareem and Zhao (1994) derived a peak factor formulation for the mean largest maximum and minimum of a non-Gaussian process modeled as a cubic transformation of a Gaussian one. The peak factor for the mean largest maximum is given by

$$g^{(\max)} = \alpha \left\{ \left( \beta + \frac{\gamma}{\beta} \right) + h_3 (\beta^2 + 2\gamma - 1) + h_4 \left[ \beta^3 + 3\beta(\gamma - 1) + \frac{3}{\beta} \left( \frac{\pi^2}{12} - \gamma + \frac{\gamma^2}{2} \right) \right] \right\}, \quad (\text{II.3.31})$$

and the peak factor for the mean smallest minimum reads

$$g^{(\min)} = -\alpha \left\{ \left( \beta + \frac{\gamma}{\beta} \right) - h_3 (\beta^2 + 2\gamma - 1) + h_4 \left[ \beta^3 + 3\beta(\gamma - 1) + \frac{3}{\beta} \left( \frac{\pi^2}{12} - \gamma + \frac{\gamma^2}{2} \right) \right] \right\}, \quad (\text{II.3.32})$$

where  $\beta = \sqrt{2 \ln(\nu_0^C T)}$ . If the skewness coefficient takes values different from 0, i.e.,  $h_3 \neq 0$  in the above two equations, the peak factors for the mean smallest minima and the mean largest maximum are not equal in absolute value

$$g^{(\min)} \neq -g^{(\max)}. \quad (\text{II.3.33})$$

The values of the “non-Gaussian” peak factor for the mean largest maximum associated with  $\nu_0 T = 50, 100$  and  $600$  are illustrated in Figure II.7.

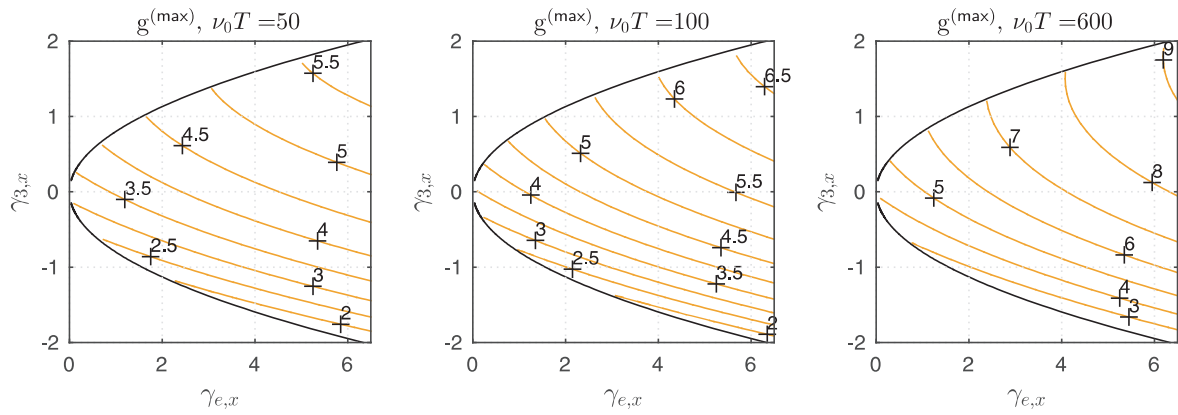


Figure II.7: Contour plots of the non-Gaussian peak factor for three values of  $\nu_0 T$ .

## II.4 Equation of motion

The equation of motion of a linear dynamic structure modeled with finite elements is

$$\mathbf{M}\ddot{\mathbf{x}}(t) + \mathbf{C}\dot{\mathbf{x}}(t) + \mathbf{K}\mathbf{x}(t) = \mathbf{f}(t), \quad (\text{II.4.1})$$

where  $\mathbf{M}$ ,  $\mathbf{C}$  and  $\mathbf{K}$  denote  $n_t \times n_t$  mass, damping and stiffness matrices, respectively with  $n_t$  the number of degrees of freedom (DOFs). The  $n_t \times 1$  vectors  $\mathbf{x}(t)$ ,  $\dot{\mathbf{x}}(t)$  and  $\ddot{\mathbf{x}}(t)$  collect nodal displacements (that comprise both deflections and rotations), velocities and accelerations, respectively. The  $n_t \times 1$  vector  $\mathbf{f}(t)$  collects the applied nodal forces.

The matrices  $\mathbf{M}$ ,  $\mathbf{C}$  and  $\mathbf{K}$  are obtained with standard finite element techniques and this is not further discussed here, see e.g., (Zienkiewicz and Taylor, 1991) for details.

### Applied nodal forces

The stationary random aerodynamic pressures modeling wind actions are gathered in an  $n_l \times 1$  vector  $\mathbf{p}(t)$ . The external nodal forces are obtained by linear combinations of  $\mathbf{p}(t)$  through

$$\mathbf{f} = \mathbf{A}\mathbf{p}, \quad (\text{II.4.2})$$

with  $\mathbf{A}$  an  $n_t \times n_l$  rectangular transformation matrix of local influence areas.

### Elastic forces

Elastic forces  $\mathbf{f}^e(t)$ , also called “internal forces”, are defined as the product  $\mathbf{K}\mathbf{x}$  and thence, equation for the nodal displacements (II.4.1) may be rewritten

$$\mathbf{K}\mathbf{x} = \mathbf{f}^e, \quad (\text{II.4.3})$$

where elastic forces  $\mathbf{f}^e(t)$  are also expressed by

$$\mathbf{f}^e = \mathbf{f} - \mathbf{f}^i - \mathbf{f}^d, \quad (\text{II.4.4})$$

with inertial forces  $\mathbf{f}^i(t)$  defined as

$$\mathbf{f}^i = \mathbf{M}\ddot{\mathbf{x}}, \quad (\text{II.4.5})$$

and damping forces  $\mathbf{f}^d(t)$  given by

$$\mathbf{f}^d = \mathbf{C}\dot{\mathbf{x}}. \quad (\text{II.4.6})$$

The superscripts “e, i and d” stand for “elastic”, “inertial” and “damping” forces, respectively.

### Quasi-static behavior of the structure

If the inertial and damping terms in (II.4.1) are negligible or neglected, the *quasi-static* nodal displacements  $\mathbf{x}^b(t)$  are obtained by solving

$$\mathbf{K}\mathbf{x}^b = \mathbf{f}, \quad (\text{II.4.7})$$

where the superscript “b” stands for “background”.

### Resonant component

For structures with a dynamic structural behavior, the nodal displacements derived from (II.4.1) may be seen as an addition of a quasi-static (background) component  $\mathbf{x}^b(t) = \mathbf{K}^{-1}\mathbf{f}(t)$  and a *resonant* component  $\mathbf{x}^r(t)$ , such that

$$\mathbf{x} = \mathbf{x}^b + \mathbf{x}^r, \quad (\text{II.4.8})$$

where the superscript “r” stands for “resonant”.

#### II.4.1 Structural responses

Structural responses, sometimes referred to as “load effects”, “wind-induced responses”, or simply “responses” in the literature, are required for the structural design. For instance, they include displacements, internal forces, reactions or stresses. Figure II.8 illustrates some structural responses in three kinds of structures: (a) top displacement and support reactions of a tower, (b) mid-span displacement, shear force, bending moment and reaction in a multi-span beam and (c) support reactions and bending moments in a frame. These design quantities are referred to as *structural responses* in this document.

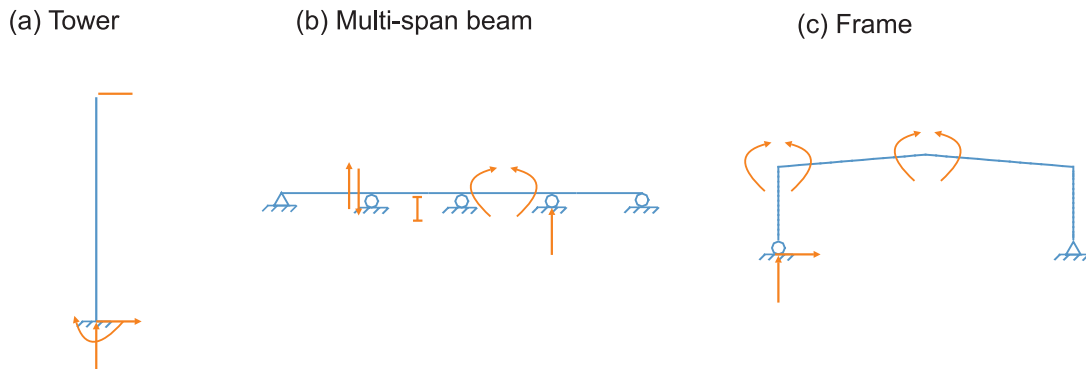


Figure II.8: Examples of structural responses in three kinds of structures: (a) a tower, (b) a multi-span beam and (c) a frame.

We only consider in this work structural responses  $\mathbf{r}(t)$  that are obtained by linear combinations of the nodal displacements

$$\mathbf{r} = \mathbf{O}\mathbf{x}, \quad (\text{II.4.9})$$

where  $\mathbf{r}(t)$  is an  $n_r \times 1$  vector and  $\mathbf{O}$  is an  $n_r \times n_t$  matrix of influence coefficients. Note that the vector of structural responses  $\mathbf{r}(t)$  may simply collect the nodal displacements, in which case the matrix of influence coefficients degenerates in the identity matrix:  $\mathbf{O} = \mathbf{I}$ .

The structural responses may also be expressed in terms of elastic forces as

$$\mathbf{r} = \mathbf{L}\mathbf{f}^e, \quad (\text{II.4.10})$$

where  $\mathbf{L} = \mathbf{O}\mathbf{K}^{-1}$  is another  $n_r \times n_t$  matrix gathering influence coefficients.

With (II.4.9), the covariance matrices of structural responses and their first time derivative are given by

$$\Sigma^{\mathbf{r}} = \mathbf{O}\Sigma^{\mathbf{x}}\mathbf{O}^{\top} \quad , \quad \Sigma^{\dot{\mathbf{r}}} = \mathbf{O}\Sigma^{\dot{\mathbf{x}}}\mathbf{O}^{\top}, \quad (\text{II.4.11})$$

or alternatively with (II.4.10)

$$\Sigma^{\mathbf{r}} = \mathbf{L}\Sigma^{\mathbf{f}^e}\mathbf{L}^{\top} \quad , \quad \Sigma^{\dot{\mathbf{r}}} = \mathbf{L}\Sigma^{\dot{\mathbf{f}}^e}\mathbf{L}^{\top}. \quad (\text{II.4.12})$$

### Quasi-static structural behavior

The background structural responses are directly obtained by linear combinations of the aerodynamic pressures through

$$\mathbf{r}^{\text{b}} = \mathbf{B}\mathbf{p}, \quad (\text{II.4.13})$$

with  $\mathbf{B} = \mathbf{L}\mathbf{A}$  being an  $n_r \times n_l$  matrix of influence coefficients.

The covariance matrices of the structural responses and their first time derivative are given by

$$\Sigma^{\mathbf{r}^{\text{b}}} = \mathbf{B}\Sigma^{\mathbf{p}}\mathbf{B}^{\top} \quad , \quad \Sigma^{\dot{\mathbf{r}}^{\text{b}}} = \mathbf{B}\Sigma^{\dot{\mathbf{p}}}\mathbf{B}^{\top}. \quad (\text{II.4.14})$$

## II.4.2 Envelope of structural responses

Thanks to the developments made in Section II.3, the extreme values of structural responses can be established. Actually, these extreme values for the (zero-mean) fluctuating part of structural responses, minima and maxima (abbreviated to **min** and **max**, respectively), define an *envelope* denoted by

$$(\mathbf{r}^{(\text{min})}, \mathbf{r}^{(\text{max})}),$$

and the envelope value associated with the  $i$ -th structural response is obtained by

$$r_i^{(\text{m})} = g_i^{(\text{m})} \sigma_{r_i}, \quad (\text{II.4.15})$$

where the superscript (m) refers to either (min) or (max). The envelope value  $r_i^{(\text{min})}$  (resp.  $r_i^{(\text{max})}$ ) corresponds to the mean smallest minimum (II.3.7) (resp. the mean largest maximum (II.3.5)) occurring on an reference period  $T$  during which the wind is considered as stationary. Under the assumption of Gaussianity and linearity of the response, the mean smallest minimum and the mean largest maximum only differ by their sign, i.e.,

$$\mathbf{r}^{(\text{min})} = -\mathbf{r}^{(\text{max})}, \quad (\text{II.4.16})$$

leading to a *symmetric envelope*. Non-Gaussianity of the structural responses (with  $\gamma_3 \neq 0$ ) leads to an *asymmetric envelope*, i.e.,

$$\mathbf{r}^{(\text{min})} \neq -\mathbf{r}^{(\text{max})}. \quad (\text{II.4.17})$$

The *total envelope*

$$(\mathbf{r}'^{(\text{min})}, \mathbf{r}'^{(\text{max})}), \quad (\text{II.4.18})$$

(including the mean component) is obtained by a shift of the envelope of the fluctuating part

$$\mathbf{r}'^{(\text{m})} = \boldsymbol{\mu}_{\mathbf{r}'} + \mathbf{r}^{(\text{m})}. \quad (\text{II.4.19})$$

Ultimately, the design of structural members is considered by adding to this *total envelope*, the structural responses resulting from permanent loads, e.g., the self-weight. In the context of the Eurocodes, a single *design envelope* ( $\mathbf{r}'^{(d,\min)}, \mathbf{r}'^{(d,\max)}$ ) is then obtained by

$$\mathbf{r}'^{(d,m)} = \gamma_{pl}\mathbf{r}^{(pl)} + \gamma_q\mathbf{r}'^{(m)}, \quad (\text{II.4.20})$$

where  $\gamma_{pl}$  and  $\gamma_q$  are the partial safety factors for the permanent and the variable loads, respectively and  $\mathbf{r}^{(pl)}$  is an  $n_r \times 1$  vector collecting the structural responses under the permanent loads.

## II.5 Modal basis

The normal modes of vibration constitute an optimum basis for the representation of flexible structures under a broadband loading (Gérardin and Rixen, 2014). They are obtained by solving the generalized undamped eigenvalue problem

$$(\mathbf{K} - \omega_j^2\mathbf{M})\boldsymbol{\Phi}_j = \mathbf{0}, \quad (\text{II.5.1})$$

where  $\boldsymbol{\Phi}_j$  is the  $j$ -th normal mode of vibration (mode shape) and the eigenvalue  $\omega_j^2$  is the square of the  $j$ -th natural circular frequency. The mode shapes are orthogonal in the metric space of  $(\mathbf{K}, \mathbf{M})$  that yields the following square diagonal matrices

$$\boldsymbol{\Phi}^T\mathbf{M}\boldsymbol{\Phi} = \text{diag}(m_j) \quad , \quad \boldsymbol{\Phi}^T\mathbf{K}\boldsymbol{\Phi} = \text{diag}(\omega_j^2 m_j), \quad (\text{II.5.2})$$

where  $m_j$  is the modal mass of the  $j$ -th mode.

### Scaling of the mode shapes

The normal mode of vibrations derived from (II.5.1) are unity-scaled or mass-normalized if for each mode, a unit value is assigned to the largest (in absolute value) translational displacements or the modal mass, respectively. The latter normalization is adopted here and (II.5.2) reads

$$\boldsymbol{\Phi}^T\mathbf{M}\boldsymbol{\Phi} = \mathbf{I} \quad , \quad \boldsymbol{\Phi}^T\mathbf{K}\boldsymbol{\Phi} = \boldsymbol{\Omega}, \quad (\text{II.5.3})$$

where  $\boldsymbol{\Omega} = \text{diag}(\omega_j^2)$  is an  $n_t \times n_t$  diagonal matrix collecting on its diagonal the squares of the natural circular frequencies.

In a modal basis, the nodal displacements are approximated by

$$\mathbf{x} \simeq \boldsymbol{\Phi}\mathbf{q}, \quad (\text{II.5.4})$$

where  $\boldsymbol{\Phi}$  is the  $n_t \times n_m$  matrix of mode shapes ( $n_m \ll n_t$ ) collecting the  $n_m$  retained normal modes of vibration and  $\mathbf{q}(t)$  is an  $n_m \times 1$  vector collecting their amplitudes. Projection of the equation of motion (II.4.1) into the new modal coordinates  $\mathbf{q}(t)$  reads

$$\mathbf{I}\ddot{\mathbf{q}} + \mathbf{D}\dot{\mathbf{q}} + \boldsymbol{\Omega}\mathbf{q} = \mathbf{g}, \quad (\text{II.5.5})$$

where  $\mathbf{I} = \boldsymbol{\Phi}^T\mathbf{M}\boldsymbol{\Phi}$ ,  $\mathbf{D} = \boldsymbol{\Phi}^T\mathbf{C}\boldsymbol{\Phi}$ ,  $\boldsymbol{\Omega} = \boldsymbol{\Phi}^T\mathbf{K}\boldsymbol{\Phi}$  are the  $n_t \times n_m$  modal mass (normalized to unity), damping and stiffness matrices, respectively, and

$$\mathbf{g}(t) = \boldsymbol{\Phi}^T\mathbf{f}(t), \quad (\text{II.5.6})$$

is an  $n_m \times 1$  vector of generalized forces and where  $\mathbf{q}(t)$ ,  $\dot{\mathbf{q}}(t)$  and  $\ddot{\mathbf{q}}(t)$  are the modal displacements, velocities and accelerations, respectively.

### Truncation

The efficiency of the modal basis is attributable to the fact that it usually requires a small to moderate amount of mode shapes to provide a reliable estimation of the resonant component of nodal displacements  $\mathbf{x}^r$ , see (II.4.8). In the analysis of large scale civil structures with a number of degrees of freedom larger than or similar to  $10^4$ , the size of the modal matrices is much smaller than the original structural matrices. The truncation of the modal basis only retains modal amplitudes with a significant resonant contribution in the overall dynamic of the structure.

### Modal acceleration method

Actually, the truncated modal basis is not well-suited to provide a reliable estimation of the background component of structural responses. Indeed, a larger number of mode is usually required than for the resonant component (Maddox, 1975; Hansteen and Bell, 1979). To circumvent this issue, the modal acceleration method (Dickens et al., 1997) computes the background component of nodal displacements in the nodal basis by means of (II.4.7) and the resonant component in the modal basis using

$$\mathbf{x}^r = \mathbf{K}^{-1} \left( -\mathbf{M} \sum_{i=1}^{n_m} \Phi_i \ddot{q}_i - \mathbf{C} \sum_{i=1}^{n_m} \Phi_i \dot{q}_i \right). \quad (\text{II.5.7})$$

Differently, the resonant component of nodal displacements may be obtained with

$$\mathbf{x}^r = \Phi \mathbf{q}^r, \quad (\text{II.5.8})$$

where  $\mathbf{q}^r$  is the resonant component of modal displacements given by

$$\mathbf{q}^r = \mathbf{q} - \mathbf{q}^b, \quad (\text{II.5.9})$$

with quasi-static modal displacements found as

$$\mathbf{q}^b = \Omega^{-1} \mathbf{g}. \quad (\text{II.5.10})$$

### Modal inertial loads

For later developments, the *Modal Inertial Loads* (MILs) are introduced here. They are defined as

$$\mathbf{F}^{(\mathcal{M})} = \mathbf{K} \Phi, \quad (\text{II.5.11})$$

with  $\mathbf{F}^{(\mathcal{M})}$  an  $n_t \times n_m$  matrix such that the  $k$ -th column  $\mathbf{F}_k^{(\mathcal{M})}$  is a modal inertial load. When it is statically applied to the structure, it produces the exact  $k$ -th modal shape  $\Phi_k$ . The symbol “ $\mathcal{M}$ ” stands for “ $\mathcal{M}$ odal” (inertial loads).



### Decoupling of the equations of motion in the modal basis

For proportional damping, i.e., the modal damping matrix  $\mathbf{D}$  is diagonal, the system of equations (II.5.5) is decoupled and we simply solve for each mode

$$\ddot{q}_m + 2\xi_m\omega_m\dot{q}_m + \omega_m^2q_m = g_m. \quad (\text{II.5.12})$$

With this assumption, the solution of (II.5.5) is greatly speeded-up. The reduction of the computing time is especially relevant for large structures. Models such as the Rayleigh-type damping, described hereinafter and the modal damping provide such a damping and are used in this document.

Although the structural damping in a structure is commonly supposed to be proportional, this assumption cannot always be made (Morzfeld et al., 2009). Recently, an approximation based on an asymptotic expansion of the modal transfer matrix has been proposed to partially account for off-diagonal terms of the modal damping matrix, but still with a set of uncoupled equations (Denoël and Degée, 2009; Canor, Blaise and Denoël, 2012).

### Rayleigh damping

In classical structural mechanics, the Rayleigh damping model is often used (Rayleigh, 1945). In this model, the damping matrix  $\mathbf{C}$  is constructed through a linear combination of the mass and stiffness matrices

$$\mathbf{C} = \alpha\mathbf{M} + \beta\mathbf{K}, \quad (\text{II.5.13})$$

where the Rayleigh damping coefficients  $\alpha, \beta$  are real positive scalars with [rad/s] and [s/rad] units, respectively. With (II.5.13), the modal damping matrix  $\mathbf{D}$  is diagonal and said to be proportional. The damping coefficient in the  $m$ -th mode defined by

$$\xi_m = \frac{D_{mm}}{2\omega_m}, \quad (\text{II.5.14})$$

is, in the Rayleigh model, given by

$$\xi_m = \frac{\alpha}{2\omega_m} + \frac{\beta\omega_m}{2}. \quad (\text{II.5.15})$$

The two coefficients  $\alpha, \beta$  are obtained by imposing the damping coefficients in two modes, let say the  $n$ -th and  $m$ -th modes with  $\omega_n > \omega_m$ , that yields

$$\alpha = 2\omega_m\omega_n \frac{\omega_m\xi_n - \omega_n\xi_m}{\omega_m^2 - \omega_n^2}, \quad (\text{II.5.16})$$

$$\beta = 2 \frac{\omega_m\xi_m - \omega_n\xi_n}{\omega_m^2 - \omega_n^2}. \quad (\text{II.5.17})$$

### Damping and inertial forces

In the modal basis, the damping (II.4.6) and inertial (II.4.5) forces are respectively given by

$$\mathbf{f}^d = \mathbf{C}\Phi\dot{\mathbf{q}}, \quad \mathbf{f}^i = \mathbf{M}\Phi\ddot{\mathbf{q}}. \quad (\text{II.5.18})$$

For proportional damping, we have the following equality ([Dickens et al., 1997](#))

$$\mathbf{C}\Phi = \mathbf{M}\Phi\mathbf{D}, \quad (\text{II.5.19})$$

and [\(II.5.7\)](#) can be rewritten as

$$\mathbf{x}^r = \mathbf{K}^{-1}(-\mathbf{M}\Phi\ddot{\mathbf{q}} - \mathbf{M}\Phi\mathbf{D}\dot{\mathbf{q}}) = \mathbf{K}^{-1}(-\mathbf{M}\Phi(\ddot{\mathbf{q}} - \mathbf{D}\dot{\mathbf{q}})). \quad (\text{II.5.20})$$

## II.6 Gaussian spectral analysis

The spectral analysis (Papoulis, 1965; Grigoriu, 2013) helps to have a better understanding of systems that behave randomly, e.g., identify the nature of the random processes and if they are governed by a unique or several timescales (Denoël, 2015). This knowledge is pushed forward with the concept of white noise approximation that provides convenient formulations for the variance and covariance of modal amplitudes, as detailed in the sequel. Also, when realizations are available and a series of processing has to be realized to the recorded data, this can be practically done in the frequency-domain with the possibility to fit probabilistic models (Blaise and Denoël, 2011a).

Sections II.6.1 and II.6.2 introduce the spectral analysis in a full nodal and modal bases, respectively. Since none of these bases is really optimum (nodal basis is too large, modal basis hardly captures quasi-static components), the quasi-static and dynamic spectral analyses are developed in the nodal and modal bases, respectively, see Section II.6.3.

### II.6.1 Nodal basis analysis

Applying the Fourier Transform to (II.4.1), the equations of motion in the nodal basis and in the frequency domain are rewritten as

$$\mathbf{G}\hat{\mathbf{x}} = \hat{\mathbf{f}}, \quad (\text{II.6.1})$$

with  $\hat{\mathbf{x}}(\omega) = \mathcal{F}[\mathbf{x}(t)]$ ,  $\hat{\mathbf{f}}(\omega) = \mathcal{F}[\mathbf{f}(t)]$  and

$$\mathbf{G} = -\omega^2\mathbf{M} + i\omega\mathbf{C} + \mathbf{K}. \quad (\text{II.6.2})$$

The inverse of the matrix  $\mathbf{G}(\omega)$  is the nodal transfer function  $\mathbf{H}(\omega)$

$$\mathbf{H} = \mathbf{G}^{-1} = (-\omega^2\mathbf{M} + i\omega\mathbf{C} + \mathbf{K})^{-1}, \quad (\text{II.6.3})$$

and the nodal displacements are obtained with

$$\hat{\mathbf{x}} = \mathbf{H}\hat{\mathbf{f}}. \quad (\text{II.6.4})$$

The PSD matrix of nodal displacements reads

$$\mathbf{S}^{\mathbf{x}} = \mathbf{H}\mathbf{S}^{\mathbf{f}}\mathbf{H}^*, \quad (\text{II.6.5})$$

where  $\mathbf{S}^{\mathbf{f}}$  is the PSD matrix of nodal forces.

The covariance matrices of nodal displacements, nodal velocities and nodal accelerations are derived from

$$\Sigma^{\mathbf{x}} = \int_{\mathbb{R}} \mathbf{S}^{\mathbf{x}} d\omega \quad , \quad \Sigma^{\dot{\mathbf{x}}} = \int_{\mathbb{R}} \omega^2 \mathbf{S}^{\mathbf{x}} d\omega \quad , \quad \Sigma^{\ddot{\mathbf{x}}} = \int_{\mathbb{R}} \omega^4 \mathbf{S}^{\mathbf{x}} d\omega. \quad (\text{II.6.6})$$

### Background structural behavior

The PSD and covariance matrices of  $\mathbf{x}^{\mathbf{b}}$ , see (II.4.7), read

$$\mathbf{S}^{\mathbf{x}^{\mathbf{b}}} = \mathbf{K}^{-1}\mathbf{S}^{\mathbf{f}}\mathbf{K}^{-1} \quad , \quad \Sigma^{\mathbf{x}^{\mathbf{b}}} = \mathbf{K}^{-1}\Sigma^{\mathbf{f}}\mathbf{K}^{-1}, \quad (\text{II.6.7})$$

where  $\Sigma^{\mathbf{f}}$  is the covariance matrix of nodal forces.

## II.6.2 Modal basis analysis

For large structures and in the context of a spectral analysis, all PSDs of structural responses are usually not computed and especially not stored due to the computational cost. Instead, the spectral moments, which are the important quantities for the design, are directly computed. However, these spectral moments are obtained with integration of the PSDs. This is a reason why the modal basis is usually preferred to the nodal basis to perform a spectral analysis. For example in a modal basis, the potentially high-dimensional covariance matrix of displacements is obtained with the low-dimensional covariance matrix of modal amplitudes which requires the integration of a few number of PSDs of modal displacements.

Applying the Fourier Transform to (II.5.5), the equations of motion in the modal basis and in the frequency domain read

$$(-\omega^2 \mathbf{I} + i\omega \mathbf{D} + \mathbf{\Omega}) \hat{\mathbf{q}} = \hat{\mathbf{g}}, \quad (\text{II.6.8})$$

with  $\hat{\mathbf{q}}(\omega) = \mathcal{F}[\mathbf{q}(t)]$  and  $\hat{\mathbf{g}}(\omega) = \mathcal{F}[\mathbf{g}(t)]$ . Introducing the modal transfer function  $\mathcal{H}(\omega)$

$$\mathcal{H} = (-\omega^2 \mathbf{I} + i\omega \mathbf{D} + \mathbf{\Omega})^{-1}, \quad (\text{II.6.9})$$

the PSD matrix of the modal amplitudes  $\mathbf{S}^q(\omega)$  is expressed by

$$\mathbf{S}^q = \mathcal{H} \mathbf{S}^g \mathcal{H}^*, \quad (\text{II.6.10})$$

with  $\mathbf{S}^g = \mathbf{\Phi}^T \mathbf{S}^f \mathbf{\Phi}$ , the PSD matrix of the generalized forces. Finally, the PSD matrix of nodal displacements is found as

$$\mathbf{S}^x = \mathbf{\Phi} \mathbf{S}^q \mathbf{\Phi}^T. \quad (\text{II.6.11})$$

The covariance matrices of modal displacements, modal velocities and modal accelerations are derived from

$$\Sigma^q = \int_{\mathbb{R}} \mathbf{S}^q d\omega \quad , \quad \Sigma^{\dot{q}} = \int_{\mathbb{R}} \omega^2 \mathbf{S}^q d\omega \quad , \quad \Sigma^{\ddot{q}} = \int_{\mathbb{R}} \omega^4 \mathbf{S}^q d\omega. \quad (\text{II.6.12})$$

The covariance matrices of nodal displacements, nodal velocities and nodal accelerations are simply obtained with

$$\Sigma^x = \mathbf{\Phi} \Sigma^q \mathbf{\Phi}^T \quad , \quad \Sigma^{\dot{x}} = \mathbf{\Phi} \Sigma^{\dot{q}} \mathbf{\Phi}^T \quad , \quad \Sigma^{\ddot{x}} = \mathbf{\Phi} \Sigma^{\ddot{q}} \mathbf{\Phi}^T. \quad (\text{II.6.13})$$

### Background structural behavior

The PSD matrices of  $\mathbf{q}^b$  (II.5.10) and  $\mathbf{x}^b$  (II.4.7) read

$$\mathbf{S}^{q^b} = \mathbf{\Omega}^{-1} \mathbf{S}^g \mathbf{\Omega}^{-1}, \quad (\text{II.6.14})$$

$$\mathbf{S}^{x^b} = \mathbf{\Phi} \mathbf{S}^{q^b} \mathbf{\Phi}^T, \quad (\text{II.6.15})$$

and the covariance matrices of  $\mathbf{q}^b$  and  $\mathbf{x}^b$  may be obtained directly from the covariance matrix of the nodal forces, as

$$\Sigma^{\mathbf{q}^b} = \Omega^{-1} \Phi^T \Sigma^f \Phi \Omega^{-1}, \quad (\text{II.6.16})$$

$$\Sigma^{\mathbf{x}^b} = \Phi \Omega^{-1} \Phi^T \Sigma^f \Phi \Omega^{-1} \Phi^T. \quad (\text{II.6.17})$$

It is recalled that the truncated modal basis is not well-suited to provide a reliable estimation of the background contribution to the covariance matrix of nodal displacements.

### II.6.3 Hybrid analysis

Usually, the background contribution to the covariance matrix of nodal displacements is not well estimated in the modal basis. This contribution is usually computed in the nodal basis with (II.6.7) and the *residual* contribution to the covariance matrix of nodal displacements

$$\Sigma^{\mathbf{x}^{\text{re}}} = \underbrace{\Sigma^{\mathbf{x}}}_{(\text{II.6.13})} - \underbrace{\Sigma^{\mathbf{x}^b}}_{(\text{II.6.17})}, \quad (\text{II.6.18})$$

is computed in the modal basis and where the superscript “re” stands for “residual”.

#### Residual modal analysis

By subtracting (II.6.14) from (II.6.10) and introducing a residual function as

$$\mathcal{K}_{mn}(\omega) = \mathcal{H}_{mm}(\omega) \mathcal{H}_{nn}^*(\omega) - \frac{1}{\Omega_{mm} \Omega_{nn}}, \quad (\text{II.6.19})$$

the residual contribution to the PSD of the  $m$ -th modal amplitude is given by

$$S_{mm}^{\text{qre}}(\omega) = S_{mm}^{\text{q}}(\omega) - S_{mm}^{\text{qb}}(\omega) = \mathcal{K}_{mm}(\omega) S_{mm}^{\text{g}}(\omega), \quad (\text{II.6.20})$$

with  $\mathcal{K}_{mm}(\omega) = |\mathcal{H}_{mm}(\omega)|^2 - \frac{1}{\Omega_{mm}^2}$  from (II.6.19). Also, the residual contribution to the cross-PSD of the  $m$ -th and  $n$ -th modal amplitudes is evaluated as

$$S_{mn}^{\text{qre}}(\omega) = S_{mn}^{\text{q}}(\omega) - S_{mn}^{\text{qb}}(\omega) = \mathcal{K}_{mn}(\omega) S_{mn}^{\text{g}}(\omega). \quad (\text{II.6.21})$$

The residual contribution to the covariance matrices of modal and nodal displacements are derived from

$$\Sigma^{\mathbf{q}^{\text{re}}} = \int_{\mathbb{R}} \mathbf{S}^{\mathbf{q}^{\text{re}}} d\omega \quad , \quad \Sigma^{\mathbf{x}^{\text{re}}} = \Phi \Sigma^{\mathbf{q}^{\text{re}}} \Phi^T. \quad (\text{II.6.22})$$

Figure II.9 depicts both contributions, background and residual to a unilateral PSD of modal amplitude.

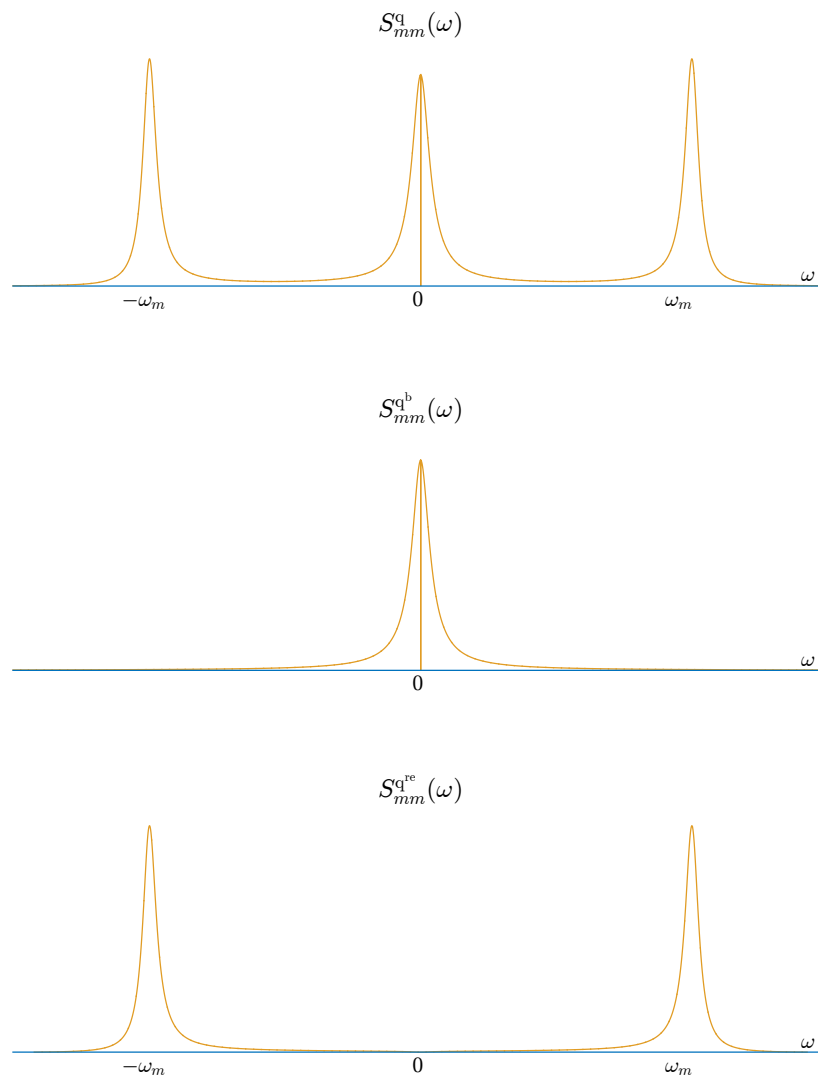


Figure II.9: Typical example of a unilateral PSD of modal amplitude. The background and residual contributions are also depicted.

### Contributions to the covariance matrix of modal displacements

With (II.5.10) and (II.5.9), the modal displacements can be seen as the addition of quasi-static  $\mathbf{q}^b$  and resonant  $\mathbf{q}^r$  components, such as

$$\mathbf{q} = \mathbf{q}^b + \mathbf{q}^r. \quad (\text{II.6.23})$$

Therefore, the variance of the  $i$ -th modal displacement,  $\Sigma_{ii}^a = \sigma_{q_i}^2$ , reads

$$\sigma_{q_i}^2 = \sigma_{q_i^b}^2 + \sigma_{q_i^r}^2 + 2\sigma_{q_i^b q_i^r}, \quad (\text{II.6.24})$$

where  $\sigma_{q_i^b}^2 = \text{E}[(q_i^b)^2] = \Sigma_{ii}^{q^b}$  is the background contribution,  $\sigma_{q_i^r}^2 = \text{E}[(q_i^r)^2] = \Sigma_{ii}^{q^r}$  is the resonant contribution and  $\sigma_{q_i^b q_i^r} = \text{E}[q_i^b q_i^r] = \Sigma_{ii}^{q^b q^r}$  is the mixed background/resonant contribution. Not only the diagonal, but the whole covariance matrix of modal displacements is also split into background  $\Sigma^{q^b}$ , resonant  $\Sigma^{q^r}$  and mixed background/resonant  $\Sigma^{q^b q^r}$  contributions, such as

$$\Sigma^a = \Sigma^{q^b} + \Sigma^{q^r} + \Sigma^{q^b q^r} + \Sigma^{q^r q^b}, \quad (\text{II.6.25})$$

with  $\Sigma_{ij}^{q^r} = \sigma_{q_i^r q_j^r} = \text{E}[q_i^r q_j^r]$ ,  $\Sigma_{ij}^{q^b q^r} = \sigma_{q_i^b q_j^r} = \text{E}[q_i^b q_j^r]$  and  $\Sigma^{q^r q^b} = \left(\Sigma^{q^b q^r}\right)^\top$ .

From (II.6.25), the residual contribution to the covariance matrix of modal displacements

$$\Sigma^{q^r e} = \Sigma^a - \Sigma^{q^b} = \Sigma^{q^r} + \Sigma^{q^b q^r} + \Sigma^{q^r q^b}, \quad (\text{II.6.26})$$

collects the resonant and mixed background/resonant contributions.

### Covariance matrices of nodal velocities and accelerations

The covariance matrices of nodal velocities  $\Sigma^{\dot{\mathbf{x}}}$  and nodal accelerations  $\Sigma^{\ddot{\mathbf{x}}}$  are given by (II.6.13) in the modal basis. For these quantities, there is no need for separating background and residual contributions since the former one is usually negligible (Denoël, 2015) and thus the modal analysis is suitable.

## II.7 Davenport's white noise approximation, advanced application and novel contribution

In a hybrid analysis, the integration of the residual contribution to the PSDs of modal displacements, see (II.6.22), is rendered useless thanks to the white noise approximation. This well-known approximation is used in many wind engineering applications and was introduced by Davenport (1967). In its original work, the approximation is only developed for the residual contribution to the variance of modal amplitudes. It took almost 40 years to have an approximation developed for the residual contribution to the covariance of modal amplitudes thanks to the works of Denoël (2009a). Independently, Gu and Zhou (2009) proposed another formulation for the same purpose, which is not discussed here for sake of brevity.

### II.7.1 Timescale separation condition

A condition on the applicability of the white noise approximation concept is the timescale separation, see Figure II.10. In wind engineering and for linear dynamical system, the timescales associated with resonant components  $\{T^*\}$  are usually significantly different from those of the background components  $\{t^*\}$  which are related to those of the loading. In other words, the energy of the loading is contained in a frequency band much lower than the natural frequencies. This timescale separation allows us to postulate that the mixed background/resonant contributions to the covariance matrix in (II.6.26) is negligible. Consequently, the residual contribution to the covariance matrix of  $\mathbf{q}$  reduces to the resonant contribution.

$$\Sigma^{\mathbf{q}^e} \simeq \Sigma^{\mathbf{q}^f}, \quad (\text{II.7.1})$$

which is evaluated thanks to the white noise approximation concept, as detailed next.

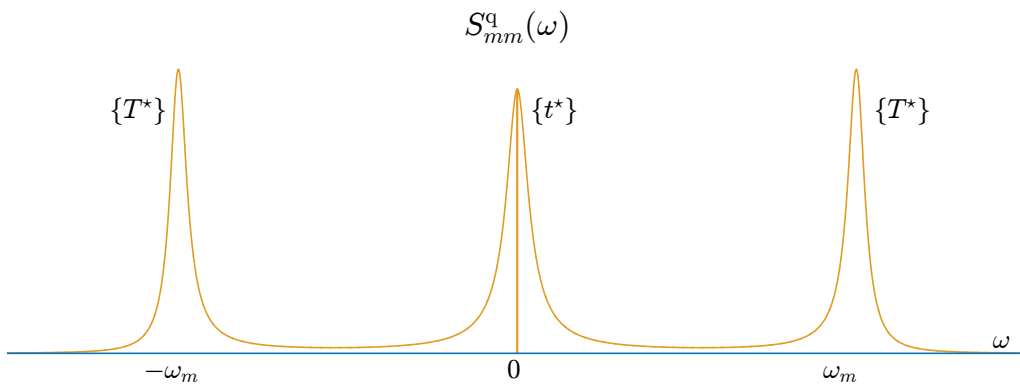


Figure II.10: Example of a unilateral PSD of modal amplitude. Figure inspired from (Denoël, 2015).



## II.7.2 Resonant contribution to the variance of modal amplitudes

In (II.6.20), the PSD of the  $m$ -th generalized force is replaced by a white noise

$$S_{mm}^{(\text{wn})} = S_{mm}^g(\omega_m), \quad (\text{II.7.2})$$

which takes its value at the resonant frequency of the  $m$ -th mode (Davenport, 1964b, 1967). In order to ensure integrability of (II.6.20) since  $\mathcal{K}_{mm}(\pm\infty) = -1/\Omega_{mm}^2$ , the resonant contribution to the PSD of the  $m$ -th modal amplitude is then approximated with

$$S_{mm}^{\text{qf}}(\omega) \simeq \mathcal{K}_{mm}^{\text{da}}(\omega)S_{mm}^{(\text{wn})}, \quad (\text{II.7.3})$$

with

$$\mathcal{K}_{mm}^{\text{da}}(\omega) = |\mathcal{H}_{mm}(\omega)|^2, \quad (\text{II.7.4})$$

the approximation of the residual function  $\mathcal{K}_{mn}(\omega)$  given in (Davenport, 1967). The resonant contribution to the variance of the  $m$ -th modal amplitude, is expressed by

$$(\Sigma_{mm}^{\text{qf}})^{(\text{d})} \simeq f_{mm}^{(\text{Re,d})}S_{mm}^{(\text{wn})} = \frac{\pi\omega_m}{2\xi_m\Omega_{mm}^2} S_{mm}^{(\text{wn})}, \quad (\text{II.7.5})$$

with

$$f_{mm}^{(\text{Re,d})} = \int_{\mathbb{R}} \mathcal{K}_{mm}^{\text{da}}(\omega)d\omega = \frac{\pi\omega_m}{2\xi_m\Omega_{mm}^2}. \quad (\text{II.7.6})$$

Figure II.11 shows the white noise approximation for the resonant contribution to the unilateral PSD of modal amplitude. The approximation matches almost perfectly the residual contribution  $S_{mm}^{\text{qre}}(\omega)$ . An additional condition on the applicability is that the magnitude of the unilateral PSD of the generalized force  $S_{mm}^g(\omega)$  does not change significantly over the width of the resonant peaks in the modal transfer function.

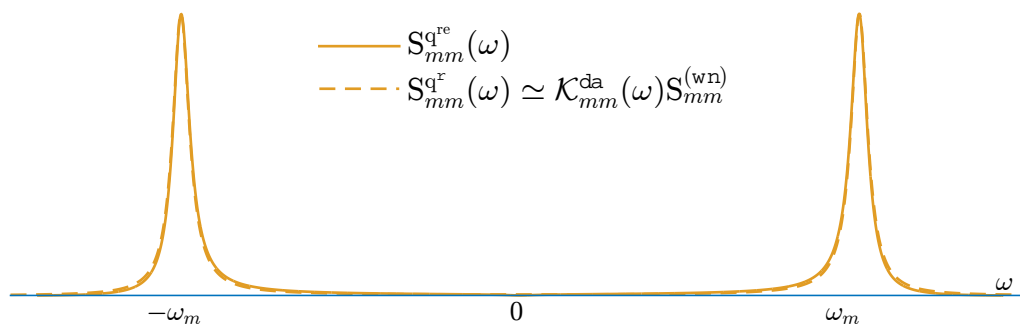


Figure II.11: Illustration of the white noise approximation for the resonant contribution to the unilateral PSD of modal amplitude.

### II.7.3 Resonant contribution to the covariance of modal amplitudes

The real part of the cross-PSD of the  $m$ -th and  $n$ -th generalized forces in (II.6.21) is replaced by a white noise

$$S_{mn}^{(\text{Re},\text{wn})} = \Gamma_{mn}^{(\text{Re},\text{wn})} \sqrt{S_{mm}^g(\omega_m) S_{nn}^g(\omega_n)}, \quad (\text{II.7.7})$$

with  $\Gamma_{mn}^{(\text{Re},\text{wn})}$  obtained as a mean of the real part of the coherence functions evaluated at the natural circular frequencies of the  $m$ -th and  $n$ -th modes, such that

$$\Gamma_{mn}^{(\text{Re},\text{wn})} = \frac{\text{Re}[\Gamma_{mn}^g(\omega_m)] + \text{Re}[\Gamma_{mn}^g(\omega_n)]}{2}. \quad (\text{II.7.8})$$

In order to ensure integrability of (II.6.21), the resonant contribution to the cross-PSD of the  $m$ -th and  $n$ -th modal amplitudes is approached by

$$S_{mn}^{\text{qr}}(\omega) \simeq \text{Re}[\mathcal{K}_{mn}^{\text{de}}(\omega)] S_{mn}^{(\text{Re},\text{wn})}, \quad (\text{II.7.9})$$

with

$$\mathcal{K}_{mn}^{\text{de}}(\omega) = \mathcal{H}_{mm}(\omega) \mathcal{H}_{nn}^*(\omega), \quad (\text{II.7.10})$$

the approximation of the residual function  $\mathcal{K}_{mm}(\omega)$  given in (Denoël, 2009a) and inspired from the original approximation of Davenport (II.7.3). The dimensionless number  $\epsilon \in [-1; 1]$

$$\epsilon = \frac{\omega_n - \omega_m}{\omega_n + \omega_m}, \quad (\text{II.7.11})$$

measures the relative distance between the two resonant frequencies. Figure II.12 and II.13 show the real and imaginary parts of  $\mathcal{K}_{mn}(\omega)$  and its approximation  $\mathcal{K}_{mn}^{\text{de}}(\omega)$  for three values of  $\epsilon$  corresponding to distinct peaks  $\epsilon = 0.2$ , close peaks  $\epsilon = 0.091$ , and almost merged peaks  $\epsilon = 0.0025$ . Two distinct damping ratios of 1% and 1.5% are used for the illustrations. For both the real and imaginary parts, the approximation  $\mathcal{K}_{mn}^{\text{de}}(\omega)$  matches almost perfectly the residual function in the vicinity of the peaks, validating its adequacy.

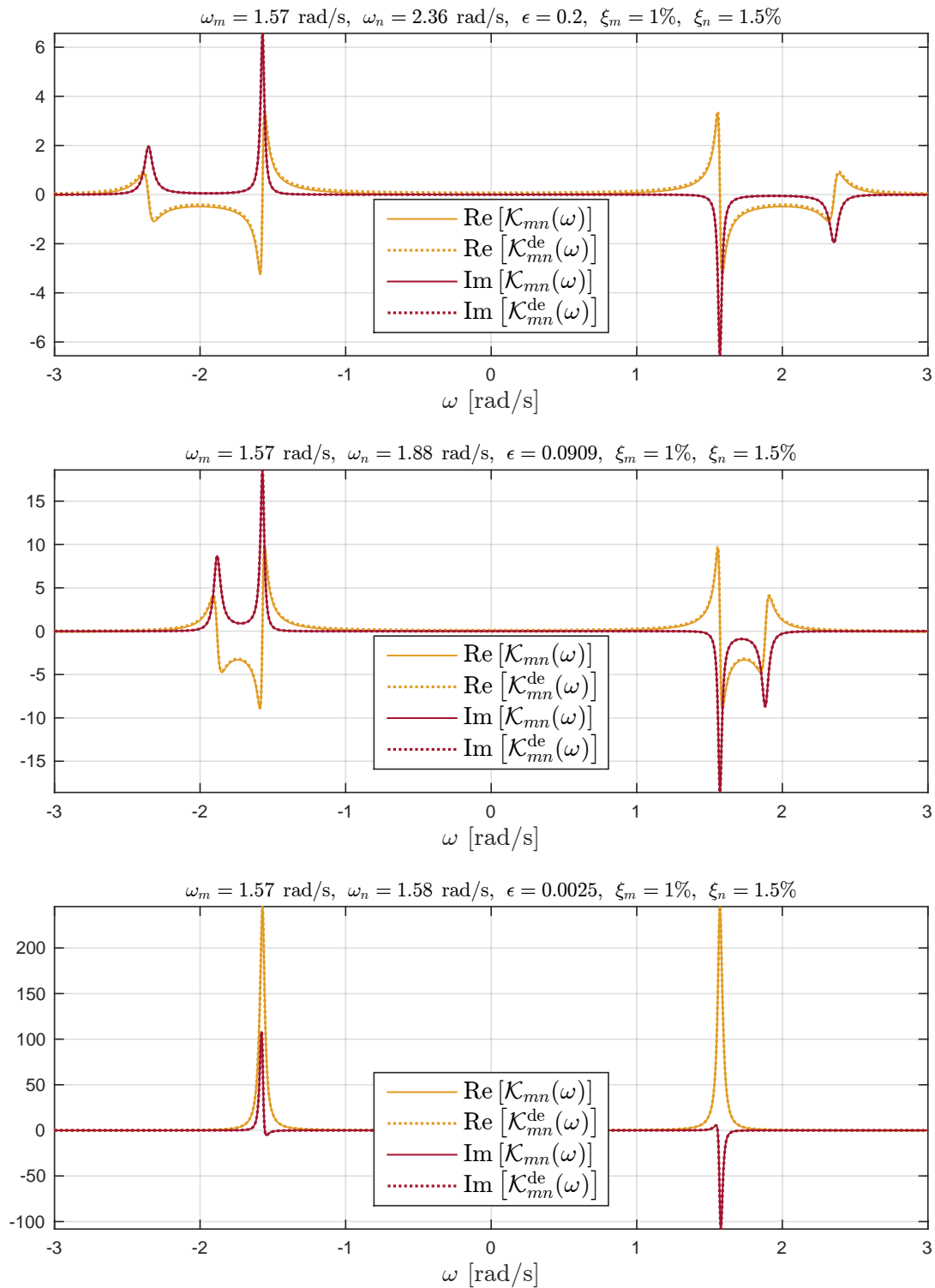


Figure II.12: Approximations of the real and imaginary parts of the residual function  $\mathcal{K}_{mn}(\omega)$  for three values of  $\epsilon = [0.2, 0.091, 0.0025]$ .

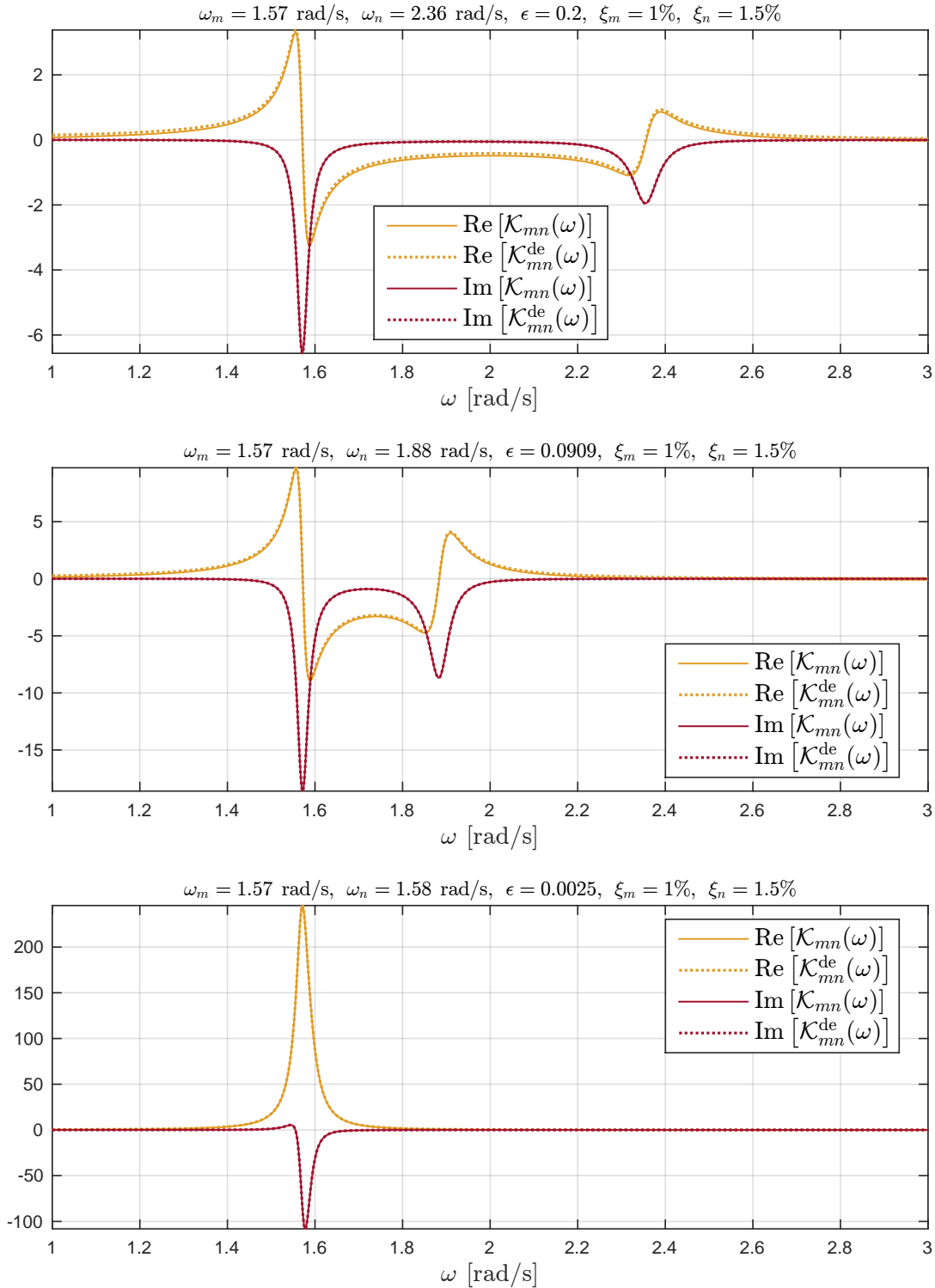


Figure II.13: Approximations of the real and imaginary parts of the residual function  $\mathcal{K}_{mn}(\omega)$  for three values of  $\epsilon = [0.2, 0.091, 0.0025]$ . (Closeup view of Figure II.12).

The resonant contribution to the covariance and correlation between the  $m$ -th and  $n$ -th modal amplitudes are then obtained by integration. They respectively read

$$\left(\Sigma_{mn}^{qr}\right)^{(Re,d)} = \frac{\pi\sqrt{\omega_m\omega_n}}{2\sqrt{\xi_m\xi_n}} \frac{S_{mn}^{(Re,wn)}}{\Omega_{mm}\Omega_{nn}} h_{mn}^{(Re,d)}, \quad (\text{II.7.12})$$

$$\rho_{q_m^r, q_n^r}^{(Re,d)} = \Gamma_{mn}^{(Re,wn)} h_{mn}^{(Re,d)}, \quad (\text{II.7.13})$$

with

$$\begin{aligned} h_{mn}^{(Re,d)} &= \left( \int_{\mathbb{R}} \text{Re} [\mathcal{K}_{mn}^{de}(\omega)] d\omega \right) / \left( \sqrt{f_{mm}^{(Re,d)} f_{nn}^{(Re,d)}} \right), \\ &= \left( \int_{\mathbb{R}} \text{Re} [\mathcal{K}_{mn}^{de}(\omega)] d\omega \right) / \left( \frac{\pi\sqrt{\omega_m\omega_n}}{2\sqrt{\xi_m\xi_n}\Omega_{mm}\Omega_{nn}} \right), \\ &= \frac{8(\omega_m\omega_n)^{3/2}(\xi_m\omega_m + \xi_n\omega_n)\sqrt{\xi_m\xi_n}}{(\omega_m^2 - \omega_n^2)^2 + 4\omega_m\omega_n(\xi_m\omega_m + \xi_n\omega_n)(\xi_m\omega_n + \xi_n\omega_m)}. \end{aligned} \quad (\text{II.7.14})$$

If  $\xi_m = \xi_n = \xi$ , (II.7.14) degenerates into

$$h_{mn}^{(Re,d)} = \frac{8(\omega_m\omega_n)^{3/2}\xi^2(\omega_m + \omega_n)}{(\omega_m^2 - \omega_n^2)^2 + 4\omega_m\omega_n\xi^2(\omega_m + \omega_n)^2}. \quad (\text{II.7.15})$$

This approximation method is used in the first example of the Chapter illustrations, see Section VI.2.

## II.7.4 Advanced method for the resonant contribution of the covariance of modal amplitudes

Noticing that only the real part of the cross-PSD of the  $m$ -th and  $n$ -th generalized forces is considered in the previous method, a method to handle the imaginary part as well is next derived. Indeed, as illustrated in (Blaise and Denoël, 2011b), the imaginary part of the coherence functions of generalized forces is not necessary negligible.

In a general case, the residual contribution to the cross-PSD of the  $m$ -th and  $n$ -th modal amplitudes is evaluated as

$$S_{mn}^{q^{re}}(\omega) = \text{Re} [\mathcal{K}_{mn}(\omega)] \text{Re} [S_{mn}^g(\omega)] - \text{Im} [\mathcal{K}_{mn}(\omega)] \text{Im} [S_{mn}^g(\omega)]. \quad (\text{II.7.16})$$

With (II.7.16), the residual contribution to the covariance of the  $m$ -th and  $n$ -th modal amplitudes is written as

$$\Sigma_{mn}^{q^{re}} = \left(\Sigma_{mn}^{q^{re}}\right)^{(Re)} + \left(\Sigma_{mn}^{q^{re}}\right)^{(Im)}, \quad (\text{II.7.17})$$

with

$$\left(\Sigma_{mn}^{q^{re}}\right)^{(Re)} = \int_{\mathbb{R}} \text{Re} [\mathcal{K}_{mn}(\omega)] \text{Re} [S_{mn}^g(\omega)] d\omega,$$

and

$$\left(\Sigma_{mn}^{q^{re}}\right)^{(Im)} = \int_{\mathbb{R}} -\text{Im} [\mathcal{K}_{mn}(\omega)] \text{Im} [S_{mn}^g(\omega)] d\omega.$$

The real part of the cross-PSD of the  $m$ -th and  $n$ -th generalized forces in (II.7.16) is replaced by (II.7.7) and the imaginary part is also replaced by a white noise

$$S_{mn}^{(\text{Im},\text{wn})} = \Gamma_{mn}^{(\text{Im},\text{wn})} \sqrt{S_{mm}^g(\omega_m) S_{nn}^g(\omega_n)}, \quad (\text{II.7.18})$$

where  $\Gamma_{mn}^{(\text{Im},\text{wn})}$  is obtained as a mean of the imaginary part of the coherence functions evaluated at the natural circular frequencies of the  $m$ -th and  $n$ -th modes, such that

$$\Gamma_{mn}^{(\text{Im},\text{wn})} = \frac{\text{Im} [\Gamma_{mn}^g(\omega_m)] + \text{Im} [\Gamma_{mn}^g(\omega_n)]}{2}. \quad (\text{II.7.19})$$

Thus the resonant contribution to the cross-PSD of the  $m$ -th and  $n$ -th modal amplitudes is approximated by

$$S_{mn}^{\text{qr}}(\omega) = \begin{cases} \text{Re} [\mathcal{K}_{mn}(\omega)] S_{mn}^{(\text{Re},\text{wn})} - \text{Im} [\mathcal{K}_{mn}(\omega)] S_{mn}^{(\text{Im},\text{wn})}, & \forall \omega \geq 0 \\ \text{Re} [\mathcal{K}_{mn}(\omega)] S_{mn}^{(\text{Re},\text{wn})} + \text{Im} [\mathcal{K}_{mn}(\omega)] S_{mn}^{(\text{Im},\text{wn})}, & \forall \omega < 0 \end{cases}. \quad (\text{II.7.20})$$

### Approximation of the residual function $\mathcal{K}_{mn}(\omega)$ given in

In order to ensure integrability of (II.7.20), the approximation (II.7.10) is used such that

$$S_{mn}^{\text{qr}}(\omega) \simeq \begin{cases} \text{Re} [\mathcal{K}_{mn}^{\text{de}}(\omega)] S_{mn}^{(\text{Re},\text{wn})} - \text{Im} [\mathcal{K}_{mn}^{\text{de}}(\omega)] S_{mn}^{(\text{Im},\text{wn})}, & \forall \omega \geq 0 \\ \text{Re} [\mathcal{K}_{mn}^{\text{de}}(\omega)] S_{mn}^{(\text{Re},\text{wn})} + \text{Im} [\mathcal{K}_{mn}^{\text{de}}(\omega)] S_{mn}^{(\text{Im},\text{wn})}, & \forall \omega < 0 \end{cases}. \quad (\text{II.7.21})$$

With (II.7.21), the resonant contribution to the covariance of the  $m$ -th and  $n$ -th modal amplitudes is evaluated as

$$(\Sigma_{mn}^{\text{qr}})^{(\text{d})} = (\Sigma_{mn}^{\text{qr}})^{(\text{Re},\text{d})} + (\Sigma_{mn}^{\text{qr}})^{(\text{Im},\text{d})}, \quad (\text{II.7.22})$$

where  $(\Sigma_{mn}^{\text{qr}})^{(\text{Re},\text{d})}$  is given by (II.7.12) and the ‘‘imaginary’’ contribution  $(\Sigma_{mn}^{\text{qr}})^{(\text{Im},\text{d})}$  is derived from

$$(\Sigma_{mn}^{\text{qr}})^{(\text{Im},\text{d})} = S_{mn}^{(\text{Im},\text{wn})} \left( \int_{\mathbb{R}^-} \text{Im} [\mathcal{K}_{mn}^{\text{de}}(\omega)] d\omega - \int_{\mathbb{R}^+} \text{Im} [\mathcal{K}_{mn}^{\text{de}}(\omega)] d\omega \right), \quad (\text{II.7.23})$$

$$= -2 S_{mn}^{(\text{Im},\text{wn})} \int_{\mathbb{R}^+} \text{Im} [\mathcal{K}_{mn}^{\text{de}}(\omega)] d\omega, \quad (\text{II.7.24})$$

$$= \frac{\pi \sqrt{\omega_m \omega_n}}{2 \sqrt{\xi_m \xi_n}} \frac{S_{mn}^{(\text{Im},\text{wn})}}{\Omega_{mm} \Omega_{nn}} h_{mn}^{(\text{Im},\text{d})}, \quad (\text{II.7.25})$$

where the factor 2 in (II.7.24) appears since  $\int_{\mathbb{R}^-} \text{Im} [\mathcal{K}_{mn}^{\text{de}}(\omega)] d\omega = - \int_{\mathbb{R}^+} \text{Im} [\mathcal{K}_{mn}^{\text{de}}(\omega)] d\omega$  and we introduce

$$\begin{aligned} h_{mn}^{(\text{Im},\text{d})} &= \left( -2 \int_{\mathbb{R}^+} \text{Im} [\mathcal{K}_{mn}^{\text{de}}(\omega)] d\omega \right) / \left( \frac{\pi \sqrt{\omega_m \omega_n}}{2 \sqrt{\xi_m \xi_n} \Omega_{mm} \Omega_{nn}} \right), \\ &= - \frac{\sqrt{1 - \xi_m^2} \omega_m [\omega_m^2 + \omega_n (2\omega_m \xi_m \xi_n + \omega_n (2\xi_m^2 - 1))]}{(\omega_m^2 - \omega_n^2)^2 + 4\omega_m \omega_n (\xi_m \omega_m + \xi_n \omega_n) (\xi_m \omega_n + \xi_n \omega_m)} \\ &\quad + \frac{\sqrt{1 - \xi_n^2} \omega_n [\omega_n^2 + \omega_m (2\omega_n \xi_m \xi_n + \omega_m (2\xi_n^2 - 1))]}{(\omega_m^2 - \omega_n^2)^2 + 4\omega_m \omega_n (\xi_m \omega_m + \xi_n \omega_n) (\xi_m \omega_n + \xi_n \omega_m)}. \end{aligned} \quad (\text{II.7.26})$$

If  $\xi_m = \xi_n = \xi$ , (II.7.26) degenerates into

$$h_{mn}^{(\text{Im,d})} = \frac{\sqrt{1 - \xi^2} (\omega_n - \omega_m)}{(\omega_m^2 - \omega_n^2)^2 + 4\omega_m\omega_n\xi^2 (\omega_m + \omega_n)^2}. \quad (\text{II.7.27})$$

By substituting (II.7.12) and (II.7.23) into (II.7.22), the resonant contribution to the covariance of the  $m$ -th and  $n$ -th modal amplitudes is given by

$$(\Sigma_{mn}^{\text{qr}})^{(\text{d})} = \frac{\pi\sqrt{\omega_m\omega_n}}{2\sqrt{\xi_m\xi_n}} \frac{1}{\Omega_{mm}\Omega_{nn}} (S_{mn}^{(\text{Re,wn})} h_{mn}^{(\text{Re,d})} + S_{mn}^{(\text{Im,wn})} h_{mn}^{(\text{Im,d})}). \quad (\text{II.7.28})$$

The resonant contribution to the correlation of the  $m$ -th and  $n$ -th modal amplitudes is approximated by

$$\rho_{q_m^r q_n^r}^{(\text{d})} = \Gamma_{mn}^{(\text{Re,wn})} h_{mn}^{(\text{Re,d})} + \Gamma_{mn}^{(\text{Im,wn})} h_{mn}^{(\text{Im,d})}, \quad (\text{II.7.29})$$

$$= \rho_{q_m^r q_n^r}^{(\text{Re,d})} + \rho_{q_m^r q_n^r}^{(\text{Im,d})}, \quad (\text{II.7.30})$$

with  $\rho_{q_m^r q_n^r}^{(\text{Re,d})} = \Gamma_{mn}^{(\text{Re,wn})} h_{mn}^{(\text{Re,d})}$  and  $\rho_{q_m^r q_n^r}^{(\text{Im,d})} = \Gamma_{mn}^{(\text{Im,wn})} h_{mn}^{(\text{Im,d})}$ .

The weighting functions  $h_{mn}^{(\text{Re,d})}$  and  $h_{mn}^{(\text{Im,d})}$  for the real and imaginary parts of the coherence functions are shown in Figure II.14 as a function of  $\epsilon$ . The weighting function  $h_{mn}^{(\text{Re,d})}$  is monotonically decreasing with the relative distance between the natural frequencies and has a maximum for  $\omega_m = \omega_n$  ( $\epsilon = 0$ ). As expected the weighting function  $h_{mn}^{(\text{Im,d})}$  is null when  $\omega_m = \omega_n$  since there is no phase shift between the modes, then increases to attain a maximum before a decreasing to zero. Before the maximum it may be noted that  $h_{mn}^{(\text{Im,d})} < h_{mn}^{(\text{Re,d})}$  and then  $h_{mn}^{(\text{Im,d})} > h_{mn}^{(\text{Re,d})}$ . Also the condition on  $\mathcal{R}_{mn}^{\text{qr}} \in [-1, 1]$  is fulfilled since it can be noted that  $h_{mn}^{(\text{Re,d})} + h_{mn}^{(\text{Im,d})} \leq 1$ .

This approximation method is used in the second example of the Chapter illustrations, see Section VI.3.

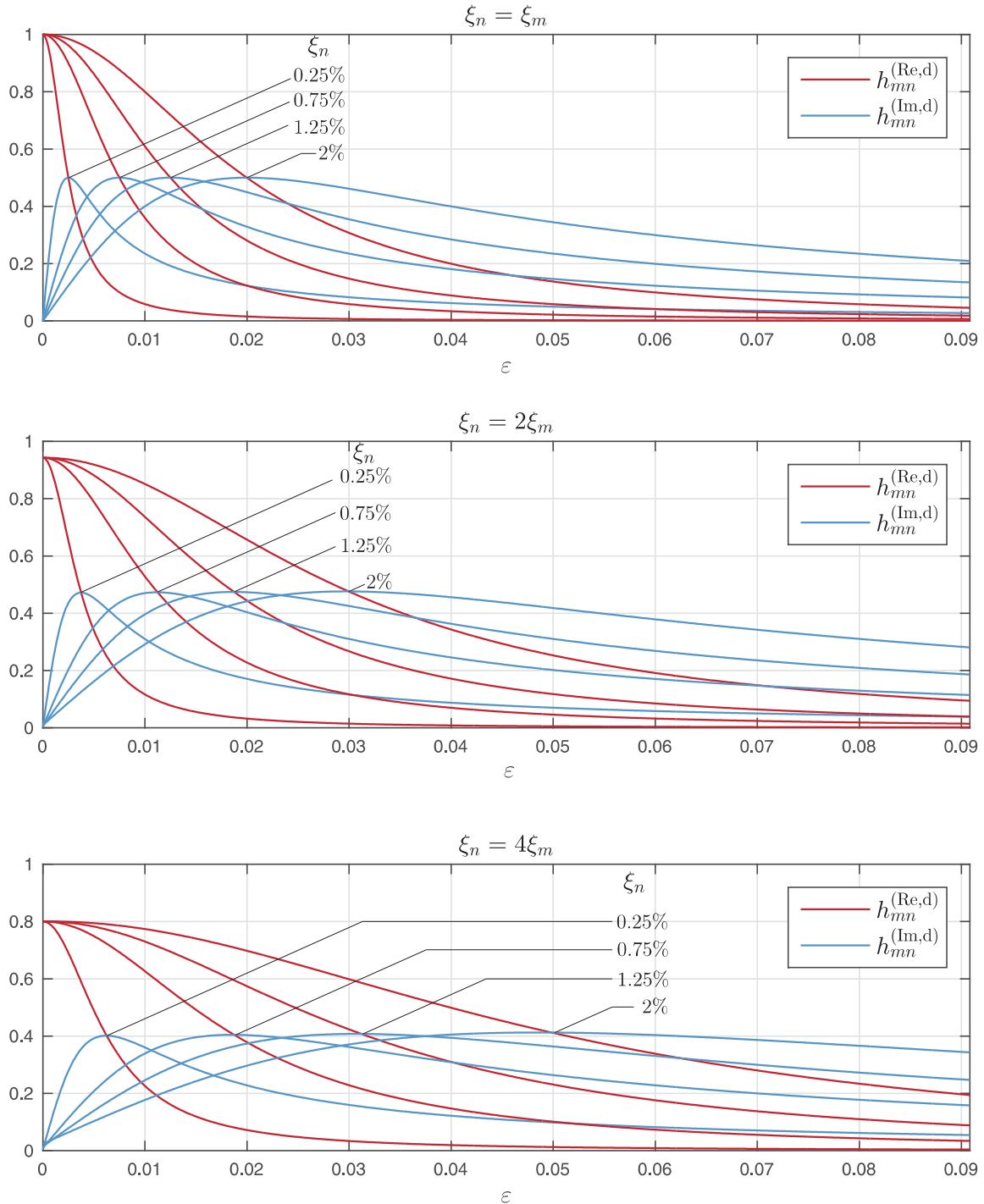


Figure II.14: Weighting functions for the real and imaginary parts of the coherence function for four sets of modal damping coefficients with  $\xi_n = \xi_m$ ,  $\xi_n = 2\xi_m$  and  $\xi_n = 4\xi_m$ .



### Correlation coefficient of modal amplitudes

Thanks to the previous developments, the approximation for the correlation coefficient of modal amplitudes  $\rho_{q_m q_n}$  is established (Denoël, 2009a). They are evaluated as a weighted combination of the correlation coefficient of generalized forces  $\rho_{g_m g_n}$  and resonant contribution to the correlation coefficient of modal amplitudes

$$\rho_{q_m q_n}^{(d)} = \gamma_{mn}^b \rho_{g_m g_n} + \gamma_{mn}^r \rho_{q_m^r q_n^r}^{(d)}, \quad (\text{II.7.31})$$

where  $\rho_{q_m^r q_n^r}^{(d)}$  is given by (II.7.13) or (II.7.30) if the imaginary part of the coherence functions is neglected or not, respectively.

The background  $\gamma_{mn}^b$  and resonant  $\gamma_{mn}^r$  weighting coefficients respectively defined as

$$\gamma_{mn}^b = \frac{1}{\sqrt{1+b_m^{-1}}\sqrt{1+b_n^{-1}}} \quad , \quad \gamma_{mn}^r = \frac{1}{\sqrt{1+b_m}\sqrt{1+b_n}}, \quad (\text{II.7.32})$$

where  $b_m$  and  $b_n$  are the background-to-resonant ratio in mode  $m$  and  $n$ , respectively defined as

$$b_m = \Sigma_{mm}^{q^b} / \Sigma_{mm}^{q^r} \quad , \quad b_n = \Sigma_{nn}^{q^b} / \Sigma_{nn}^{q^r}. \quad (\text{II.7.33})$$

This formulation of correlation coefficient of modal amplitudes is used in the first two examples of the Chapter VI.

### Higher spectral moments of modal amplitudes (Der Kiureghian, 1980)

The variances of the  $m$ -th modal velocity and modal accelerations are respectively expressed by the resonant contribution

$$\Sigma_{mm}^{\dot{q}} \simeq \Sigma_{mm}^{\dot{q}^r} \simeq \omega_m^2 \Sigma_{mm}^{q^r} \quad , \quad \Sigma_{mm}^{\ddot{q}} \simeq \Sigma_{mm}^{\ddot{q}^r} \simeq \omega_m^4 \Sigma_{mm}^{q^r}. \quad (\text{II.7.34})$$

The covariance between the  $m$ -th and  $n$ -th modal velocities and modal accelerations are respectively derived from the resonant contribution

$$\Sigma_{mn}^{\dot{q}} \simeq \Sigma_{mn}^{\dot{q}^r} \simeq \omega_m \omega_n \Sigma_{mn}^{q^r} \quad , \quad \Sigma_{mn}^{\ddot{q}} \simeq \Sigma_{mn}^{\ddot{q}^r} \simeq \omega_m^2 \omega_n^2 \Sigma_{mn}^{q^r}, \quad (\text{II.7.35})$$

instead of the integrals given in (II.6.12). Also, (II.7.35) is used in Section IV.7.4 to assess the magnitude of damping forces compared to inertial forces.

## II.8 Proper orthogonal decomposition

The proper orthogonal decomposition is a technique that expresses a set of correlated random processes as a combination of orthogonal functions modulated by uncorrelated stochastic processes (Papoulis, 1965; Lumley, 1967). This method is also termed the Karhunen-Loeve expansion (Loeve, 1977) and belongs to Principal Component Analysis (PCA) (Jolliffe, 2005).

In wind engineering, data processing techniques based on the proper orthogonal decomposition (POD) may be sorted into two families depending on the correlated random field on which POD is applied: the oncoming wind velocities or the aerodynamic pressures acting on the structure. In both cases, deterministic orthogonal shapes are extracted from the complex time-space representation of a wind turbulence (resp. loading) field that may be obtained with wind tunnel measurements, computational fluid dynamics or full-scale measurements. These modes are sometimes termed wind blowing modes (Di Paola, 1998) or wind loading modes, respectively. Each wind mode is amplified by its principal component, uncorrelated with the others. Linear combinations of a limited number of wind modes reproduce accurately, in a mean square sense, the entire wind (resp. loading) field in time and space.

Although partly driven by the drastic need to compress wind-tunnel data in 1960's-1980's due to computer storage limitations, POD has been constantly used in order to provide a sound understanding of the wind and aerodynamic pressure fields.

### II.8.1 Wind field

First applications crystallized with the Covariance Proper Transformation (CPT) consisting in the diagonalization of the zero-lag covariance matrix of the wind field. The CPT produces wind modes that are only space-dependent with principal components uncorrelated only for a zero-time lag. The Spectral Proper Transformation (SPT) consisting in the diagonalization of the power spectral matrix of the wind field produces space-frequency dependent wind modes and principal components that are uncorrelated for any time lag. Therefore, the SPT provides a higher reconstruction rate of the original wind field than the CPT does. Nevertheless, under some circumstances, CPT and SPT may produce similar wind modes (Carassale, 2005) with a much heavier computational cost for SPT, though.

A short description of POD applied to the turbulence field is first discussed. Usually, the turbulence field is modeled by a zero mean weakly stationary Gaussian 3-V (variate) (longitudinal, lateral and vertical turbulence components) and 4-D (dimensional) (three spatial coordinates plus time) random process. In the frequency domain, the cross-power spectral density functions describe the space-time characteristics. Several authors have proposed models using POD for simulation of 1-V 4-D (Shinozuka et al., 1990; Di Paola, 1998; Di Paola and Gullo, 2001), 1-V 2-D (Carassale and Solari, 2002) and 3-V 4-D (Solari and Tubino, 2002; Tubino and Solari, 2005) wind velocity fields.

These simulation methods based on POD are typically well suited to line-like structures such as buildings or bridges. Indeed, using well-known closed-form expressions of aerodynamic admittances (Scanlan and Jones, 1999), aerodynamic pressures may be computed with the simulated turbulence wind field. For instance, an aerodynamic admittance is given in (Uematsu et al., 2008) for a circular flat roof. Also, Han and Li (2009) used the CPT to reconstruct and interpolate wind velocities on a tensile cable-membrane large roof structure, the Foshan Century Lotus Stadium (outside diameter of 300 m). Actually for wide-span enclosures, the wide variety of shapes, the 3-D geometry of the structure, and the particular

aerodynamic signature of such large structures, conspire to make the determination of a general expression for the aerodynamic admittance quite challenging, if not vain. Consequently, a proper recourse to the aerodynamic pressure field is preferred.

## II.8.2 Aerodynamic pressure field

Application of the POD directly to the aerodynamic pressure field on a bluff body was first investigated by [Armitt \(1968\)](#). Using the CPT truncation of wind-tunnel measurements, [Best and Holmes \(1983\)](#) reduced the computational effort implementing their covariance integration method for static analysis of low-rise buildings. For the same type of structures, effects of integration of only a part of or all panel pressures for the CPT ([Bienkiewicz et al., 1993](#)), possible simplifications of the CPT modes based on the influence functions ([Ho et al., 1995](#)) and presence of internal pressures due to openings in the buildings ([Holmes et al., 1997](#)) were investigated. This latter study compared the experimental CPT blowing modes with those resulting from the modeling of the covariance matrix with a decreasing exponential and identical variances on the diagonal ([Van Trees, 1968](#); [Spanos and Ghanem, 1989](#)). [Tamura et al. \(1999\)](#) clarified that the application of the CPT must be made on the fluctuating aerodynamic pressure without the mean values which otherwise would introduce distortion in the loading modes.

### CPT loading modes

For later developments, the covariance proper transformation applied to the aerodynamic pressure field is detailed. The CPT method consists in the diagonalization of the zero-lag covariance matrix of the aerodynamic pressures  $\Sigma^{\mathbf{P}}$ , that reads as a generalized eigenvalue problem

$$\Sigma^{\mathbf{P}}\mathbf{P}^{(c)} = \mathbf{P}^{(c)}\Sigma^c, \quad (\text{II.8.1})$$

where  $\Sigma^c$  is a diagonal covariance matrix of principal components ordered by decreasing variances and  $\mathbf{P}^{(c)}$  collects the CPT loading modes. The CPT produces wind modes that are only space-dependent with principal components uncorrelated only for a zero-time lag. Also, the set of loadings  $\mathbf{P}^{(c)}$  forms an orthonormal basis and the aerodynamic pressures are expressed by

$$\mathbf{p}(t) = \sum_{m=1}^{n_{cpt}} \mathbf{P}_m^{(c)} a_m(t), \quad (\text{II.8.2})$$

with  $n_{cpt}$  the number of CPT modes retained and  $a_m(t)$  the principal component of the  $m$ -th CPT mode. Note that  $\Sigma_{mm}^c = \text{E}[a_m^2(t)] = \lambda_m^c$  gives a relative contribution of each mode on the covariance matrix of aerodynamic pressures since we have

$$\Sigma^{\mathbf{P}} = \mathbf{P}^{(c)}\Sigma^c(\mathbf{P}^{(c)})^T. \quad (\text{II.8.3})$$

Numerous studies have shown that a small number of modes is adequate to capture the whole aerodynamic pressure field, in a mean square sense.

### II.8.3 Structural analysis

Davenport (1995) and Bienkiewicz (1996) highlighted the importance of the POD tool in understanding wind loads in a generalized and simplified way. Wind-induced dynamic behavior on single-layer latticed dome was investigated by Uematsu et al. (1997) using CPT loading modes. Nine configurations of dome geometry with three different increasing rise-span ratios were considered to model low-, middle- and high-rise domes, respectively. Physical interpretations of the CPT loading modes are done using the quasi-steady theory (Letchford et al., 1993) and analytical equations for the loading modes are proposed with expressions that could be generalized to other dome shapes. The wind pressures acting on the structure for the analysis were generated using proposed formulations of symmetric and anti-symmetric loading modes. Combination coefficients are necessary to derive the loading modes and they have been tuned for the specific experiment. The LRC method allows to compute ESWLs and for the background contribution of several large roofs, Holmes and Wood (2001) simplify the computation of the correlation coefficient between load and response using the CPT. Rizzo et al. (2009) compute CPT wind modes on hyperbolic paraboloid shaped roofs from wind tunnel measurements. For the Shenzhen Citizen Center, Liu et al. (2011) compare aerodynamic pressures measured in full scale and those reconstructed with CPT modes derived from recorded pressures in wind-tunnel.

Benfratello and Muscolino (1999) used the SPT method to perform the stochastic analysis of an MDOF structure in order to evaluate the statistical moments with possible inclusion of the quadratic terms in the aerodynamic forces. Solari and Carassale (2000) introduced the Double Modal Transformation (DMT) method to analyze the structure in the modal basis using loading modes obtained with CPT or SPT methods. The DMT method allows to compute the dynamic response of each structural mode under each loading mode and finally, the structural response is obtained, in an elegant way, with a double linear combination of some pairs of structural and loading modes (Carassale et al., 2001). Although apparently optimal, from a computational point of view, it appears to be efficient only if the mode shapes and loading modes are known in closed form. Essentially, this concerns line-like structures for which aerodynamic pressures may be directly obtained with a turbulence field characterized by a simple analytical model. The DMT method has been applied to tall buildings (Chen and Kareem, 2005), and long-span bridges (Tubino and Solari, 2007). Concerning wide-span enclosure, Blaise and Denoël (2011b) discussed different structural analysis methods, including the DMT, from wind-tunnel pressures on the stadium roof of Lille (France). It is reported that the cross-modal participation matrix mixed between structural and CPT loading modes is fully populated. Interesting orthogonality properties between the structural and wind modes are thus hardly exploitable. Moreover, they suggest to fit probabilistic models on the principal components of the SPT. This idea is appealing since no coherence function has to be considered in that case; however the fitting of the space-frequency dependent loading modes appears to be difficult to fit with a general analytical model.

As a matter of fact, concerning applications of the POD as a tool for the analysis of wide-span enclosures, few studies are reported. As mentioned by Chen et al. (2011), the environment and the shape of the wide-span roof play a determining role in the characterization of the wind loads and every new wide-span roof requires specific studies.





# Chapter III

## The envelope reconstruction problem

---

### III.1 Introduction

### III.2 Review of available methods

### III.3 Proposed general methodology

### III.4 Basic static wind loads

### III.5 Combinations of basic static wind loads

### III.6 Summary

---

- ◇ *“The dynamic effects of gusts and vortex shedding are represented by equivalent static loads producing the same maximum deflections and stresses.”* Davenport (1967)
- ◇ *“[...] if a single distribution is used for design it must be a conservative one for most effects.”* Holmes (1988)
- ◇ *“An approximation to the [...] load distribution that is independent of the [...] load effect is given.”* Holmes (1996)
- ◇ *“For potential application in design practice, it is necessary to limit the number of distributions to only critical response components [...]”* Chen and Kareem (2001)
- ◇ *“[...] by defining a global and unique loading condition able to furnish [...] a correct scenario of all load effects.”* Repetto and Solari (2004)
- ◇ *“It would be useful to have a universal wind load distribution that simultaneously reproduces largest load effects for all structural members [...]”* Katsumura et al. (2007)

### III.1 Introduction

This Chapter poses the problem related to the main scope of this thesis: the envelope reconstruction problem. It consists in deriving a relevant set of static wind loads providing the actual envelope values of structural responses of interest. Two options to solve the envelope reconstruction problem are identified.

Section III.2 reviews existing methods. Their limitations are pointed out and the objectives of this Chapter are stated. Section III.3 rigorously conceptualizes a complete methodology to solve the envelope reconstruction problem. Section III.4 identifies a kind of static wind loads, named *basic*, and provides the methodology to use them for the envelope reconstruction problem. Instead of applying them successively without combination, Section III.5 describes a more elaborated approach based on some combinations of a subset of basic static wind loads to speed-up the reconstruction of the envelope.

#### Envelope of structural responses (Section II.4.1)

Figure III.1 illustrates the mean component, envelope and total envelope of different kinds of structural responses in a cantilever vertical structure, a four-span bridge and a frame in a low-rise building.

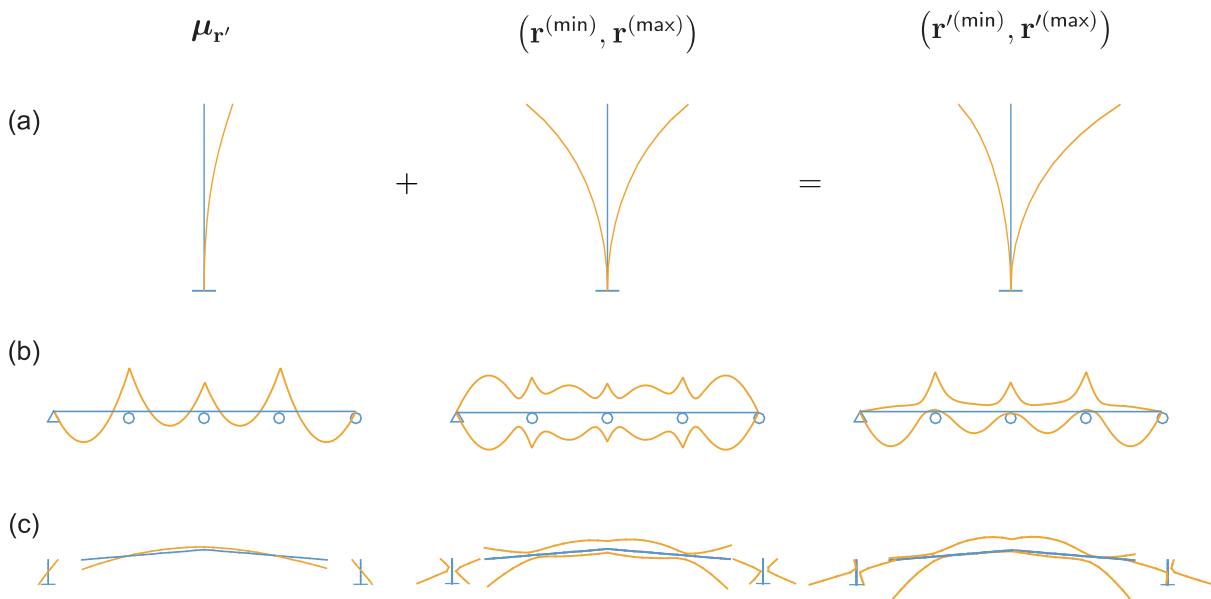


Figure III.1: Conceptual examples of mean, envelope and total envelope (in orange) of (a) along-wind displacements in a cantilever vertical structure, (b) bending moments under aerodynamic lift forces in a four-span bridge and (c) bending moments in a frame (exploded view) under aerodynamic pressures acting on the cladding of a low-rise building. Each structure is represented in blue.

#### The envelope reconstruction problem

For decades, the concept of *static wind analysis* for design of civil structures has aroused interest due to its valuable features. By essence, such a static analysis should produce



structural responses similar to envelope values that would be provided by a buffeting analysis. We will henceforth refer to the concept of structural analysis by means of static loads as the *envelope reconstruction problem*. This problem consists in deriving a set  $n_s$  of static wind loads efficiently reconstructing the envelope values of structural responses everywhere in the structure or at least for some structural responses of interest. Notice we only focus on the reconstruction of the envelope. Indeed, the total envelope simply evaluated as the envelope plus the mean component provided by the static analysis under the mean aerodynamic loading, which is known.

The envelope reconstruction problem (ERP) focuses on the reconstruction of the *envelope*

$$\left( \mathbf{r}^{(\min)}, \mathbf{r}^{(\max)} \right),$$

with:

- **Option 1**, a basis of an  $n_s$ –dimensional vector space of static wind loads

$$\left\{ \mathbf{f}_{(1)}^{(s)}, \mathbf{f}_{(2)}^{(s)}, \dots, \mathbf{f}_{(n_s)}^{(s)} \right\},$$

- **Option 2**, only two static wind loads

$$\left\{ \mathbf{f}_{(1)}^{(s)}, \mathbf{f}_{(2)}^{(s)} \right\},$$

to be determined adequately. The superscript “s” stands for “static” (wind loads).

**Iterative procedure (Option 1)** The static analysis under the  $k$ -th static wind load  $\mathbf{f}_{(k)}^{(s)}$  produces a  $k$ -th vector of static structural responses

$$\mathbf{r}_{(k)}^{(s)} = \mathbf{L} \mathbf{f}_{(k)}^{(s)}. \quad (\text{III.1.1})$$

Considering the first  $k$  static wind loads, the  $k$ -th approximation of the envelope is expressed by the recursive relations

$$\tilde{\mathbf{r}}_{(k)}^{(\min)} = \min \left( \tilde{\mathbf{r}}_{(k-1)}^{(\min)}; \mathbf{r}_{(k)}^{(s)} \right); \quad \tilde{\mathbf{r}}_{(k)}^{(\max)} = \max \left( \tilde{\mathbf{r}}_{(k-1)}^{(\max)}; \mathbf{r}_{(k)}^{(s)} \right), \quad (\text{III.1.2})$$

where  $\min(\cdot)$  and  $\max(\cdot)$  are element-by-element operators and  $\tilde{\mathbf{r}}_{(0)}^{(\min)}$  and  $\tilde{\mathbf{r}}_{(0)}^{(\max)}$  are  $n_r \times 1$  vectors filled with zeros (no static wind load has already been applied). The reconstructed envelope after  $k$  iterations

$$\left( \tilde{\mathbf{r}}_{(k)}^{(\min)}, \tilde{\mathbf{r}}_{(k)}^{(\max)} \right), \quad (\text{III.1.3})$$

is the result of a sequential reconstruction process, see Figure III.2 for an example.

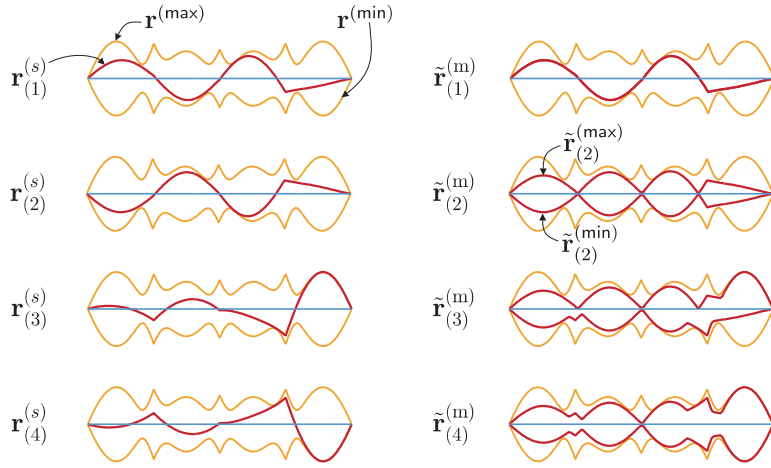


Figure III.2: Conceptual example: bending moments under aerodynamic lift forces in a four-span bridge. Illustration of the iterative reconstruction of the envelope (in orange). The diagrams are taken from Figure VI.15.

Finally, the *total envelope*  $(\mathbf{r}'^{(\min)}, \mathbf{r}'^{(\max)})$  is approximated by the reconstructed total envelope after  $k$  iterations  $(\tilde{\mathbf{r}}'^{(\min)}, \tilde{\mathbf{r}}'^{(\max)})$  using

$$\tilde{\mathbf{r}}'^{(\min)} = \boldsymbol{\mu}_{\mathbf{r}'} + \tilde{\mathbf{r}}^{(\min)}; \quad \tilde{\mathbf{r}}'^{(\max)} = \boldsymbol{\mu}_{\mathbf{r}'} + \tilde{\mathbf{r}}^{(\max)}, \quad (\text{III.1.4})$$

under total static wind loads given by

$$\mathbf{f}'^{(s)} = \boldsymbol{\mu}_{\mathbf{f}'} + \mathbf{f}^{(s)}. \quad (\text{III.1.5})$$

The number  $n_s$  of static wind loads necessary to get a satisfactory approximation of the envelope depends on several parameters detailed later.

**Two static wind loads (Option 2)** This option is a particular case of the first one where  $n_s = 2$ , i.e., the envelope is approximated with only two static wind loads. At first sight, this option may appear attractive though it is really conceivable for a specific class of structures and structural responses. However, most works, detailed in Section III.2, try to solve the ERP with only two static wind loads.

## III.2 Review of available methods

One common approach described in Section III.2.1 is to consider ESWLs associated with some specific responses of major importance. Instead of using ESWLs, many studies derived SWLs that are no longer associated with specific responses but aim at recovering several ones at the same time. In general, the envelope reconstruction problem focuses on both sides of the envelope since each side of the total envelope usually lead the design. In such cases, the methods have to deal with a *two-sided envelope reconstruction problem*, as presented in the introduction. However, for a specific set of structural responses, only one side of the envelope may be required for the design. For such responses, the methods deals with a *one-sided envelope reconstruction problem* and the option 2 reduces to the determination of a

unique static wind load. In the sequel, the methods are classified if they aim at approximating one side (Section III.2.2) or both sides (Section III.2.3) of the (total) envelope.

### III.2.1 Equivalent static wind loads

For each specific response, application of the ESWL provides the associated extreme value. At the early beginning, this approach has been used for the design of frames in low-rise buildings. In (Kasperski, 1993), the static wind load aims at reproducing the base reactions of such a kind of building. In addition to base reactions, the focus is also made in (Holmes, 1988; Holmes et al., 1995) on ESWLs targeting the knee and ridge bending moments for fixed-based and pin-based frames, respectively. In (Holmes and Wood, 2001), hundreds of ESWLs were computed for the design of very large roofs.

This approach is conceivable if the responses that should guide the structural design are easy to identify. Otherwise, the manual selection of representative structural responses (left to the structural engineers) may become tricky. As a consequence, the ESWLs associated with a user-defined set of responses may not safely reproduce other responses in the entire structure, eventually important for the design. This is particularly expected for complex load-bearing systems and large structures. Unfortunately, to our knowledge, no general methodology to adequately select ESWLs has been proposed.

### III.2.2 One-sided envelope reconstruction problem

#### Option 2: Gust factor technique,...

Originally, Davenport (1967) defined a unique ( $n_s=1$ ) static wind load as a deterministic load pattern reproducing with a static analysis several extreme dynamic structural responses. Its first formulation was developed for the along-wind responses of cantilever vertical structures. The total static wind load used for the design is expressed as the mean wind load amplified by a single Gust Loading Factor (GLF)

$$\mathbf{f}'_{(1)}{}^{(s)} = G\boldsymbol{\mu}_{\mathbf{f}'},$$

where this factor  $G$  incorporates the background and resonant behaviors of the structure (Vickery, 1970; Simiu, 1973). In the original version, Davenport (1967) proposed a unique static wind load since only one side of the total envelope may be of interest for the design of vertical structures, see Figure III.1-(a). For example, if the envelope collects the — positive-definite — along-wind displacements, a side of the envelope is larger in absolute value:  $\mathbf{r}'^{(\max)} \geq |\mathbf{r}'^{(\min)}|$  and only one side of the total envelope is relevant for the design and has to be approximated

$$\tilde{\mathbf{r}}'_{(1)}{}^{(s)} \approx \mathbf{r}'^{(\max)}.$$

Initially, the concept was developed for the along-wind response of buildings that mainly exhibit vibrations in their first mode (Holmes, 2007). In this case, the GLF is taken equal to the Gust Response Factor (GRF) defined as the ratio of the extreme modal amplitude in the first mode and its mean value (Vellozzi and Cohen, 1968). Seminal developments on the formulation of such gust loading factors were reported in (Solari, 1993a,b; Holmes, 1994; Simiu and Scanlan, 1996).

The obvious simplicity of the formulation made it suitable for codification and most standards are based on this approach for the design of vertical structures under several assumptions (Eurocode, 1991b; Solari and Kareem, 1998; International Standards Organization, 2009; Zhou et al., 2002).

### ...its extensions,

Several studies pushed forward the original idea: Zhou et al. (1999) proposed to focus on the base bending moment for the determination of the gust factor, Piccardo and Solari (2002) and Kareem and Zhou (2003) extended it to more complicated (3D) loading models, Seo and Caracoglia (2010) recourse to a database-assisted-design approach.

Application of the mean wind load amplification concept for rigid and elastic beams supporting flat roof was done by Tamura et al. (1992) with wind tunnel tests. Empirical GRFs are provided for displacements, bending moments and shear forces for several building models with increasing span ratio and five wind models. Large-span (up to 200 m) elastic beams mainly vibrate in their first mode shape which is more or less similar to the mean displacement validating the applicability of the gust factor approach. For the same type of bearing system of flat roof, Uematsu et al. (1997) derived empirical formulas for the ratio of root-mean square and mean modal force coefficient in the first mode. These integrate the influence of the height-span ratio, damping-height ratio and turbulence intensity. For long span roofs behaving like elastic flat plates simply supported on four edges under wind loading, Uematsu et al. (1996) gave empirical GLFs equal to the GRF of the first modal amplitude. Uematsu et al. (1999) applied the same approach for circular flat roofs, modeled as an elastic plate, with span up to 150 m under the same assumptions that the structure mainly vibrates in its first mode.

### ...and limitations.

Actually, the gust factor technique can not be applied to zero-mean wind loadings and/or responses. Typical examples are across-wind forces, due to vortex shedding, and zero-mean modal amplitude for asymmetrical modal shapes as in roof structures. Zhou et al. (1999) indicated that the original method gives reliable values for extreme deflections but not for other components, e.g., bending moments and shear forces. In fact, the GRFs may exhibit large sensitivity to the shape of influence functions (Tamura et al., 1992; Huang and Chen, 2007).

To sum up, the important inherent limitations are (i) the modal truncation to the first mode, (ii) the need for a mode shape similar to the mean displacement of the structure, in other words the static loading reproducing the mode shape has to be similar to the mean loading and (iii) the range of structural responses essentially restricted to nodal displacements. For the type of structures studied with the concept of GLF, a resonant response in the first mode is not a priori necessary for the applicability of the method, i.e., the GLF method may be applied in case of quasi-static structural behavior only. This makes use of GRF and GLF rather difficult in a systematic way for any type of structure and structural responses. For example, wide span enclosures are usually unique complex structures with complex influence functions (with positive and negative parts) and responding in several low-frequency modes for which other methods have to be investigated to produce reliable SWLs.

### Option 2: Global loading technique

A global loading technique producing a unique ( $n_s = 1$ ) total SWL with the same objective that several responses have to reach simultaneously their maximum total envelope values has been derived in (Repetto and Solari, 2004). The technique is based on the fitting of coefficients that multiply assumed forms of loadings (expressed as polynomial expansions) to obtain the global loading. The number of coefficients corresponds to the number of structural responses investigated and under the global loading, the side of the total envelope considered for reconstruction is recovered

$$\tilde{\mathbf{r}}'_{(1)}^{(s)} = \mathbf{r}'^{(\max)}.$$

Unfortunately, this method is only valid for vertical structures with a dynamic behavior in the fundamental mode.

For bridges, Fiore and Monaco (2009) proposed a combination of SPT loading modes using the global loading technique. In this study, a drawback remains the preselection of a user-defined number of structural responses to tune the combination coefficients.

## III.2.3 Two-sided envelope reconstruction problem

### Option 2: Universal SWLs,...

Most recent works focus on combinations of the CPT loading modes  $\mathbf{P}^{(c)}$  to establish two representative SWLs. In a quasi-static framework, the universal SWL introduced by Katsumura et al. (2007) is a combination of CPT loading modes. The combination coefficients are obtained as a least-square approximate solution through a pseudo-inverse.

Prior to this, a selection of envelope values, min or max for each structural response, is required to establish the so-called universal SWL. Contrary to the two aforementioned methods, a universal static wind load is thus not associated to a side of the envelope to be approximated. At least, two universal SWLs are derived to approximate the two sides of the total envelope

$$\left( \tilde{\mathbf{r}}'_{(2)}^{(\min)}, \tilde{\mathbf{r}}'_{(2)}^{(\max)} \right) \approx \left( \mathbf{r}'^{(\min)}, \mathbf{r}'^{(\max)} \right).$$

### ...and limitations

Although the concept is appealing at first sight, the method is not straightforward. This is mostly due to the selection of envelope values required to compute each universal static wind load. In fact, this selection is based on engineering judgment and not on an automatic procedure. Also, former studies (Chen and Zhou, 2007; Li et al., 2009; Kasperski, 2009; Zhou et al., 2011; Li et al.) revealed several drawbacks of the universal SWL as erratic load patterns without physical meaning, important deficient response estimations and suggest some ways to improve its reliability. Recent applications of the universal SWL (Katsumura et al., 2011; Tamura and Katsumura, 2012), however attempt to confirm its effectiveness and applicability to a wide class of structures.

### III.2.4 Limitations and objectives

To sum up, several limitations of the methods developed so far are worth being noticed, see Table III.1. The methods are either associated with (i) specific structures or (ii) relevant for a kind of structural behavior, quasi-static or dynamic. It is also our opinion that (iii) handling the envelope reconstruction problem with option 2 is not well-suited. Indeed, it is not natural to impose that a set of some structural responses reach their extreme values under a unique static wind load. Actually, for responses that are mildly or even negatively correlated, this unique loading may exhibit an erratic pattern since responses are forced to reach their extreme values under the same load case.

|                          | Structures | Structural behavior | Process  |
|--------------------------|------------|---------------------|----------|
| ESWLs                    | -          | Dynamic             | -        |
| Gust loading factor      | Limited    | Dynamic             | -        |
| Global loading technique | Cantilever | Dynamic             | Gaussian |
| Universal SWLs           | -          | Quasi-static        | -        |

Table III.1: Features of the methods applied for the envelope reconstruction problem.

#### Objectives

Addressing the aforementioned issues, this Chapter formalizes an alternative manner to apprehend the envelope reconstruction problem. Instead of deriving a unique static wind load targeting several structural responses simultaneously with varying success, the iterative procedure presented as the first option for the envelope reconstruction problem is formally detailed. This procedure consists in the successive application of static wind loads to accurately approximate the envelope with a minimum range of discrepancy. It is relevant in both Gaussian and non-Gaussian frameworks.

It is emphasized that our purpose is not the wind load codification, in the strict sense, since the iterative procedure is a numerical approach that would provide specific SWLs for each new envelope reconstruction problem. Despite this, the procedure to rank static wind loads, in the format described hereinafter, is well-suited for codification. Anyhow, a general procedure for any kinds of structure, its load-bearing system and dynamical structural behavior and for non-Gaussian structural responses is sought.

As appealing as the concept could be, combinations of a set of SWLs is more efficient than applying them separately. A reliable method for the establishment of combination coefficients is required. Hence, an additional objective is the formalization of a constrained nonlinear optimization, to derive combination coefficients in an automatic procedure. This adaptive formulation is relevant to meet specific envelope reconstruction requirements.

### III.3 Proposed general methodology

As introduced above, a set of static wind loads has to be determined for design purposes in order to accurately reproduce each side of the envelope.

The envelope reconstruction problem focuses on the reconstruction of the *envelope*

$$\left(\mathbf{r}^{(\min)}, \mathbf{r}^{(\max)}\right),$$

based on a particular basis of an  $n_s$ -dimensional vector space of static wind loads

$$\{\mathbf{f}_{(1)}^{(s)}, \mathbf{f}_{(2)}^{(s)}, \dots, \mathbf{f}_{(n_s)}^{(s)}\}. \quad (\text{III.3.1})$$

Considering the first  $k$  static wind loads, the  $k$ -th approximation of the envelope is expressed as

$$\left(\tilde{\mathbf{r}}_{(k)}^{(\min)}, \tilde{\mathbf{r}}_{(k)}^{(\max)}\right).$$

Different strategies may be adopted to determine the minimum number  $n_s$  of static wind loads ensuring a reliable reconstruction of the envelope.

#### III.3.1 Underestimation of the envelope

The level of underestimation of each part of the envelope with its  $k$ -th approximation has to be first assessed. In order to compute this discrepancy for each envelope value, we choose to compute the relative errors rather than the absolute errors. The absolute errors are indeed not suitable because envelope values may have large difference of order of magnitude between them since different kinds of responses are collected in the envelope, e.g., displacements and internal forces. The relative errors ( $\mathbf{m} \equiv \mathbf{max}$  or  $\mathbf{m} \equiv \mathbf{min}$ ) are given by

$$\boldsymbol{\varepsilon}_{(k)}^{(\mathbf{m})} = \left(\tilde{\mathbf{r}}_{(k)}^{(\mathbf{m})} - \mathbf{r}^{(\mathbf{m})}\right) \div \mathbf{r}^{(\mathbf{m})}, \quad (\text{III.3.2})$$

where the symbol  $\div$  means the division is performed element by element. For  $\varepsilon_{i,(k)}^{(\mathbf{m})} = -100\%$ ,  $-100\% < \varepsilon_{i,(k)}^{(\mathbf{m})} < 0\%$ ,  $\varepsilon_{i,(k)}^{(\mathbf{m})} = 0\%$  and  $\varepsilon_{i,(k)}^{(\mathbf{m})} > 0\%$ , the  $i$ -th envelope value is not approximated, underestimated, perfectly reconstructed or overestimated, respectively. The *largest relative error indicator*, defined as

$$\check{\varepsilon}_{(k)} = \min \left[ \min \left( \boldsymbol{\varepsilon}_{(k)}^{(\min)} \right); \min \left( \boldsymbol{\varepsilon}_{(k)}^{(\max)} \right) \right], \quad (\text{III.3.3})$$

is used for the *acceptable underestimation condition* described in Section III.3.4. Figure III.3 illustrates the relative errors and the largest relative error indicator with the second example of Figure III.1. Figure III.6 depicts an example of the series  $\check{\varepsilon}_{(k)}$ .

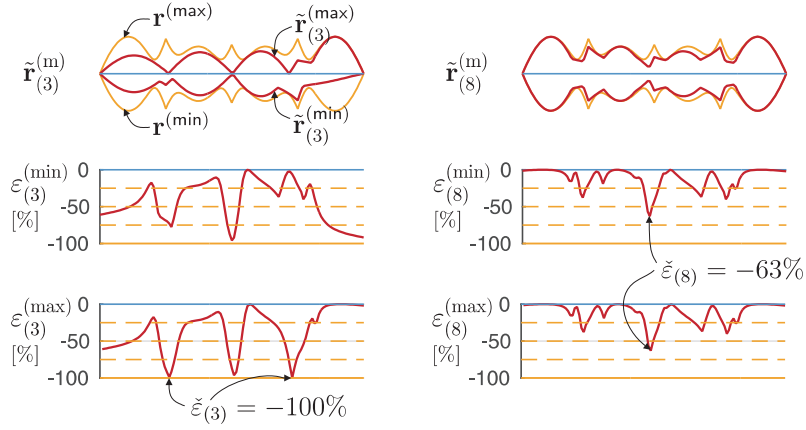


Figure III.3: Conceptual example: bending moments under aerodynamic lift forces in a four-span bridge. Illustration of the relative errors of reconstruction of the envelope and the largest relative error indicator. The diagrams are taken from Figures VI.15 and VI.16.

### III.3.2 Reconstruction rate

Furthermore, we assess the *envelope reconstruction accuracy* for each side of the envelope by computing the indicators

$$\mathcal{R}_{(k)}^{(\min)} = \frac{1}{n_r} \sum_{i=1}^{n_r} \left[ \max \left( \tilde{r}_{i,(k)}^{(\min)}, r_i^{(\min)} \right) \right] / r_i^{(\min)}, \quad (\text{III.3.4})$$

$$\mathcal{R}_{(k)}^{(\max)} = \frac{1}{n_r} \sum_{i=1}^{n_r} \left[ \min \left( \tilde{r}_{i,(k)}^{(\max)}, r_i^{(\max)} \right) \right] / r_i^{(\max)}, \quad (\text{III.3.5})$$

chosen here as the percentage of reconstruction for each side of the envelope in average. The operations  $\max \left( \tilde{r}_{i,(k)}^{(\min)}, r_i^{(\min)} \right)$  and  $\min \left( \tilde{r}_{i,(k)}^{(\max)}, r_i^{(\max)} \right)$  in (III.3.4) and (III.3.5) ensure that positive relative errors, i.e., overestimations of the envelope, are not taken into account in these indicators. An *overall reconstruction indicator* for the envelope is expressed by

$$\mathcal{R}_{(k)} = \frac{\mathcal{R}_{(k)}^{(\min)} + \mathcal{R}_{(k)}^{(\max)}}{2}. \quad (\text{III.3.6})$$

Note  $\mathcal{R}_{(k)}$  is a monotonic series:  $0\% < \mathcal{R}_{(k)} \leq \mathcal{R}_{(k+1)} \leq 100\%$  with  $\mathcal{R}_{(k)} = 100\%$  when the entire envelope is perfectly reconstructed, see Figure III.5 for an example of the series. As well, the inequality

$$\mathcal{R}_{(k)} \geq 1 - \tilde{\xi}_{(k)}, \quad (\text{III.3.7})$$

holds at each iteration.



### III.3.3 Preponderant factors

The evolution of the largest relative error indicator  $\tilde{\varepsilon}_{(k)}$  and the envelope reconstruction rate  $\mathcal{R}_{(k)}$  are highly dependent on the considered problem. This is a statement that we try to capture with the following four factors. It is also illustrated with the examples of Chapter VI.

#### 1. Correlation between responses

The correlation between the structural responses considered in the envelope is a preponderant factor. Obviously, the more correlated the structural responses, the easier the reconstruction of the envelope is. To assess the correlation between all structural responses, we define an *overall indicator of (absolute) correlation*

$$\begin{aligned}\bar{\rho}_r &= \frac{1}{(n_r^2 - n_r)/2} \sum_{i=1}^{n_r} \sum_{j=i+1}^{n_r} |\rho_{r_i r_j}|, \\ &= \frac{1}{n_r} \sum_{i=1}^{n_r} \bar{\rho}_{r_i},\end{aligned}\tag{III.3.8}$$

where  $\bar{\rho}_{r_i}$  is the average of the (absolute) correlations between the structural response  $r_i$  and all other investigated responses defined as

$$\bar{\rho}_{r_i} = \frac{1}{(n_r - 1)} \left( \sum_{j=1}^{n_r} |\rho_{r_i r_j}| - 1 \right).\tag{III.3.9}$$

The overall correlation indicator lies between 0 and 1 for a set of responses without any correlation or perfectly correlated with each other, respectively. In the latter case of perfect correlation, only two static loads are necessary for a perfect reconstruction of the envelope, one for each side of the envelope. The correlation between structural responses depends on (i) the aerodynamic pressure field that develops on the structural envelope, mildly to strongly correlated, (ii) the load bearing system and (iii) the structural behavior, quasi-static, mostly resonant or in between (hybrid). In a modal analysis and neglecting a quasi-static contribution, if the structure behaves in a unique mode, the correlation  $\bar{\rho}_r$  is maximum and equal to one. If several modes are activated,  $\bar{\rho}_r$  is no longer maximum and decreases depending on the magnitude of modal correlations. Same interpretation holds for structures with quasi-static behaviors.

#### 2. Number of structural responses

A second relevant factor is the number  $n_r$  of structural responses considered in the envelope. For a same overall correlation, more load cases are required as the number of structural responses increases. This is particularly expected for low values of overall correlation and should be rather limited for high values of overall correlation.

#### 3. Gaussian or non-Gaussian framework

A third factor is the Gaussian or non-Gaussian properties of the structural responses. This does not influence the correlation between responses but the envelope may be significantly

modified and therefore the envelope reconstruction rate too. Clearly, the envelope reconstruction for the min and max sides of the envelope are different in a non-Gaussian context.

#### 4. Overestimations of the envelope

At last, a fourth factor is the level of acceptable overestimation of the envelope. From our point of view, this discussion is crucial even if the level of overestimation is usually not regarded. An expected property of the formulation is that the overestimation of the envelope is controllable. The *acceptable overestimation*, noted  $\hat{\varepsilon}$ , of the envelope is such that the static responses  $\mathbf{r}_{(k)}^{(s)}$  under the  $k$ -th SWL  $\mathbf{f}_{(k)}^{(s)}$ , fulfills

$$(1 + \hat{\varepsilon}) \mathbf{r}_i^{(\min)} \leq \mathbf{r}_{i(k)}^{(s)} \leq (1 + \hat{\varepsilon}) \mathbf{r}_i^{(\max)} \quad \forall i \in [1, n_r], \quad (\text{III.3.10})$$

or in terms of relative errors

$$\varepsilon_{i,(k)}^{(m)} \leq \hat{\varepsilon} \quad \forall i \in [1, n_r], \quad (\text{III.3.11})$$

see Figure III.4 for an example. By setting  $\hat{\varepsilon} = 0$ , there is no overestimation of the envelope anywhere. In the proposed procedure, the level of acceptable overestimation is an important parameter of the problem. Although it reduces the burden of the envelope's reconstruction, an increase of the acceptable overestimation lessens the design's performances. This consideration needs to be put into perspective of the general design where other loads are taken into account. In this way, the more the structural design is guided by the wind load cases, the lower the acceptable overestimation should be. Finally, it could also depend on the structural design phase, at the early stages of pre-design or at the final stages of structural verification.

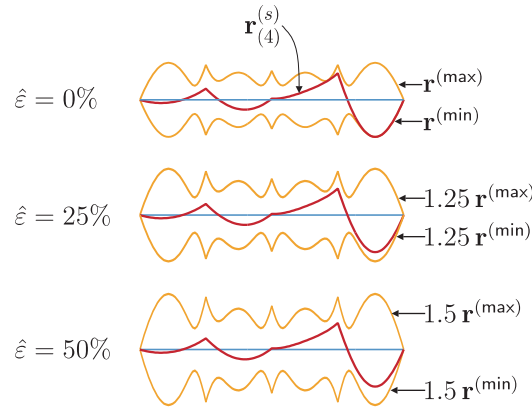


Figure III.4: Conceptual example: bending moments under aerodynamic lift forces in a four-span bridge. Illustration of the acceptable overestimation of the envelope (in orange).

### III.3.4 Number of static wind loads for an overall reconstruction

The number  $n_s$  of SWLs is formally obtained when the following two conditions are fulfilled:

#### 1. Acceptable overall reconstruction

An acceptable overall reconstruction, noted  $\mathcal{R}^t$ , is chosen such that the condition writes

$$\mathcal{R}_{(n_s^{(1)})} \geq \mathcal{R}^t, \quad (\text{III.3.12})$$

where  $n_s^{(1)}$  is the number of SWLs required to fulfill (III.3.12), see Figure III.5 for an example.

#### 2. Acceptable underestimation of the envelope

An acceptable underestimation, noted  $\check{\varepsilon}^t$  and regarded as reliable for all responses, is chosen such that

$$\varepsilon_{i,(n_s^{(2)})}^{(\min)} \geq \check{\varepsilon}^t \quad \& \quad \varepsilon_{i,(n_s^{(2)})}^{(\max)} \geq \check{\varepsilon}^t \quad \forall i \in [1, n_r], \quad (\text{III.3.13})$$

where  $n_s^{(2)}$  is the number of SWLs required to fulfill (III.3.13). Alternatively, (III.3.13) is rewritten with the largest relative error indicator defined in (III.3.3)

$$\check{\varepsilon}_{(n_s^{(2)})} \geq \check{\varepsilon}^t, \quad (\text{III.3.14})$$

see Figure III.6 for an example.

The condition (III.3.7) also holds for the acceptable overall reconstruction and underestimation

$$\mathcal{R}^t \geq 1 - \check{\varepsilon}^t, \quad (\text{III.3.15})$$

and  $\mathcal{R}^t = 100\%$  with  $\check{\varepsilon}^t = 0\%$ .

#### Optimization of the basis of static wind loads

To sum up, the number  $n_s$  is obtained by

$$n_s = \max(n_s^{(1)}; n_s^{(2)}), \quad (\text{III.3.16})$$

with  $n_s^{(1)}$  and  $n_s^{(2)}$  the numbers of SWLs required to fulfill the overall reconstruction  $\mathcal{R}^t$  and the acceptable underestimation of the envelope  $\check{\varepsilon}^t$ , respectively. From our point of view, the two conditions are essentials since we could have a good overall reconstruction indicator with however large relative errors. With (III.3.15), the number of SWLs required to fulfill the overall reconstruction is always lower than the number to fulfill the acceptable underestimation of the envelope

$$n_s^{(1)} \leq n_s^{(2)}. \quad (\text{III.3.17})$$

The more the basis of static wind loads provides a number of SWLs  $n_s^{(2)}$  close to  $n_s^{(1)}$ , the more it is well-suited for the envelope reconstruction problem. In others words, the basis of SWLs must provide a good overall reconstruction for each envelope value.

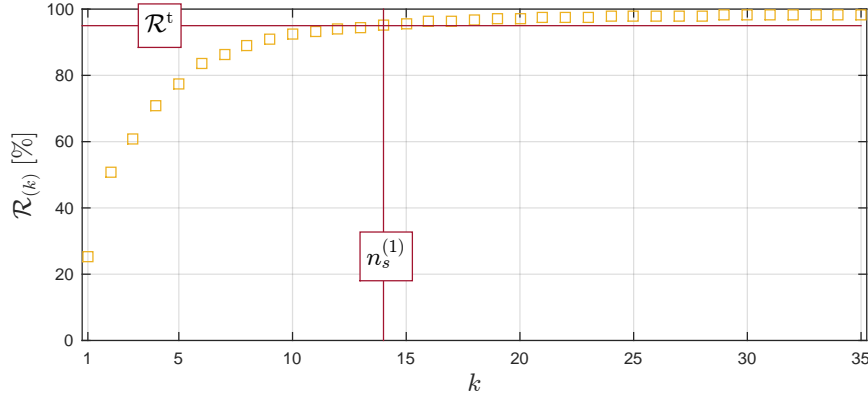


Figure III.5: Example of the evolution of the overall reconstruction indicator  $\mathcal{R}_{(k)}$  as a function of the number of load cases with  $\mathcal{R}^t = 95\%$ . The diagram is taken from Figure VI.17.

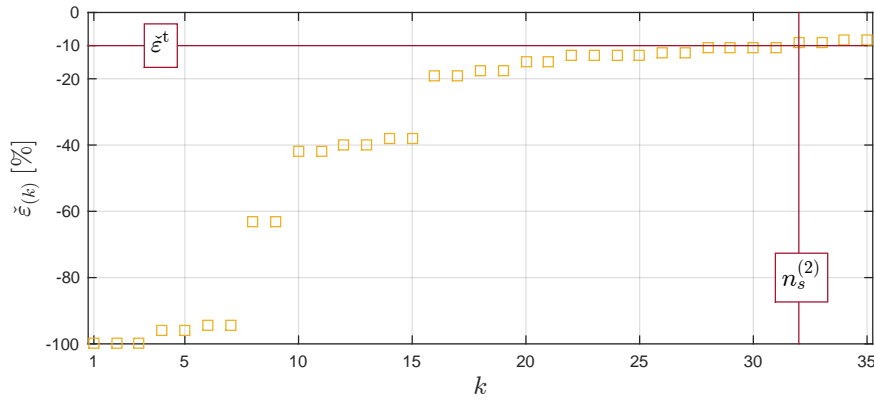


Figure III.6: Example of the evolution of the largest relative error indicator  $\check{\epsilon}_{(k)}$  as a function of the number of load cases with  $\check{\epsilon}^t = -10\%$ . The diagram is taken from Figure VI.18.

### III.3.5 Number of static wind loads ensuring no underestimation of the envelope

For given acceptable underestimation  $\check{\epsilon}^t$  and overestimation  $\hat{\epsilon}$  parameters, the particular basis of  $n_s$  static wind loads

$$\{\mathbf{f}_{(1)}^{(s)}, \mathbf{f}_{(2)}^{(s)}, \dots, \mathbf{f}_{(n_s)}^{(s)}\}, \quad (\text{III.3.18})$$

is established to meet the requirements of the ERP. Conservatively, it could be required that all responses have reached, at least, their envelope values, i.e., there is no underestimation of the envelope. To do so, the SWLs of (III.3.18) are multiplied by an amplification factor

$$\alpha^{(c)} = \frac{1}{1 + \check{\epsilon}_{(n_s)}}, \quad (\text{III.3.19})$$

to obtain the SWLs  $\{\mathbf{f}_{(1)}^{(c)}, \mathbf{f}_{(2)}^{(c)}, \dots, \mathbf{f}_{(n_s)}^{(c)}\}$  ensuring no underestimation of the envelope

$$\{\mathbf{f}_{(1)}^{(c)}, \mathbf{f}_{(2)}^{(c)}, \dots, \mathbf{f}_{(n_s)}^{(c)}\} = \alpha^{(c)} \{\mathbf{f}_{(1)}^{(s)}, \mathbf{f}_{(2)}^{(s)}, \dots, \mathbf{f}_{(n_s)}^{(s)}\}. \quad (\text{III.3.20})$$

As a result, the maximum overestimation is changed from  $\hat{\varepsilon}$  to

$$\hat{\varepsilon}' = \frac{1 + \hat{\varepsilon}}{1 + \check{\varepsilon}_{(n_s)}} - 1, \quad (\text{III.3.21})$$

the ‘‘final’’ overestimation obtained with the scaled SWL basis (III.3.20). It is thus clear that the solution of the ERP with  $\check{\varepsilon}^t$  and  $\hat{\varepsilon}$  is also a solution of the problem with no underestimation and  $\hat{\varepsilon}'$ . The solutions of the two problems are however not identical since the ERP is solved with a nonlinear solver that may find optimized solutions in different zones of the parameter space. Three options are thus discussed, and later compared in the illustrations.

**Option A.** The ERP is simply solved with  $\check{\varepsilon}^t = 0$  and  $\hat{\varepsilon} = \hat{\varepsilon}'$ . With this option, the basis of SWLs (III.3.18) is the one ensuring no underestimation and the amplification factor is equal to one.

**Option B.** The ERP is solved without overestimation, i.e.,  $\hat{\varepsilon} = 0$ , and with underestimation

$$\check{\varepsilon}^t = \frac{1}{1 + \hat{\varepsilon}'} - 1. \quad (\text{III.3.22})$$

**Option C.** The ERP is solved with overestimation and underestimation such that

$$\check{\varepsilon}^t = -\hat{\varepsilon} = \frac{\hat{\varepsilon}'}{(2 + \hat{\varepsilon}')}. \quad (\text{III.3.23})$$

### Amplification factor

Table III.2 gives the numerical values for the parameters  $\check{\varepsilon}^t$ ,  $\hat{\varepsilon}$  and  $\alpha^{(c)}$  associated with the three options for two values of the final overestimation  $\hat{\varepsilon}' = 25\%$  and  $\hat{\varepsilon}' = 10\%$ .

| Options:                | $\hat{\varepsilon}' = 25\%$ |      |      | $\hat{\varepsilon}' = 10\%$ |       |        |
|-------------------------|-----------------------------|------|------|-----------------------------|-------|--------|
|                         | A                           | B    | C    | A                           | B     | C      |
| $\check{\varepsilon}^t$ | 0%                          | -20% | -11% | 0%                          | -9.1% | -4.76% |
| $\hat{\varepsilon}$     | 25%                         | 0%   | 11%  | 10%                         | 0%    | 4.76%  |
| $\alpha^{(c)}$          | 1                           | 1.20 | 1.10 | 1                           | 1.10  | 1.05   |

Table III.2: Numerical values for the parameters  $\check{\varepsilon}^t$ ,  $\hat{\varepsilon}$  and  $\alpha^{(c)}$  associated with  $\hat{\varepsilon}' = 25\%$  and  $\hat{\varepsilon}' = 10\%$ .

Several considerations are given to guide the choice of the final overestimation  $\hat{\varepsilon}'$ .

- Firstly, the relative importance of the wind load case (associated with the fluctuating component of the wind) in comparison with the mean load case. Indeed, the final overestimation applies only to the fluctuating component of the responses. Proportionally, the larger the mean load, the lower the overestimation on the total envelope values (II.4.19).
- Secondly, the relative importance of the total wind load case in comparison with other permanent load cases, e.g., self-weight and variable load cases, e.g., snow.

- Thirdly, in the design process, the required cross-sections or required resistance of the materials can usually not be exactly selected due to technological limitations (selection in a catalogue and limitation of the number of different sections in a single project). It implies that the elements and the properties of the materials with which they are built in are more or less over-resistant.

## III.4 Basic static wind loads

We define a set of basic static wind loads as wind loads that are (i) not associated with specific structural responses, (ii) defined up to a multiplicative constant and (iii) naturally ordered by decreasing importance in an  $n_t \times n_b$  matrix  $\mathbf{F}^{(b)}$ . The superscript “b” stands for “basic” (static wind loads). The CPT loading modes, modal inertial loads and principal static wind loads are three examples of basic SWLs. Obviously, ESWLs can not be categorized as basic ones.

Structural responses produced by these static wind loads are collected in an  $n_r \times n_b$  matrix given by

$$\mathbf{R}^{(b)} = \mathbf{L}\mathbf{F}^{(b)}. \quad (\text{III.4.1})$$

### III.4.1 Normalization

These SWLs require *normalization* before the envelope reconstruction. Two *normalized* SWLs are defined for each of these SWL by

$$\mathbf{F}_k^{(b,1)} = \alpha_{(k)}^{(b,1)} \mathbf{F}_k^{(b)}, \quad \mathbf{F}_k^{(b,2)} = \alpha_{(k)}^{(b,2)} \left( -\mathbf{F}_k^{(b)} \right), \quad (\text{III.4.2})$$

where  $\alpha_{(k)}^{(b,1)}$  and  $\alpha_{(k)}^{(b,2)}$  are two positive coefficients applied to satisfy the acceptable overestimation of the envelope (III.3.10) and *the tangency condition* (Blaise and Denoël, 2013a). The tangency condition is such that the static responses  $\mathbf{R}_k^{(b,1)}$  and  $\mathbf{R}_k^{(b,2)}$  under the  $k$ -th normalized SWLs  $\mathbf{F}_k^{(b,1)}$  and  $\mathbf{F}_k^{(b,2)}$ , defined as

$$\mathbf{R}_k^{(b,1)} = \mathbf{L}\mathbf{F}_k^{(b,1)} \quad , \quad \mathbf{R}_k^{(b,2)} = \mathbf{L}\mathbf{F}_k^{(b,2)}, \quad (\text{III.4.3})$$

are somewhere tangent to the envelope amplified by the acceptable overestimation  $\hat{\varepsilon}$ . Mathematically, we may write the tangency condition as

$$\forall k, \quad (\exists j \in [1, n_r] : \mathbf{R}_{jk}^{(b,1)} = (1 + \hat{\varepsilon})r_j^{(\max)} \quad \text{or} \quad \mathbf{R}_{jk}^{(b,1)} = (1 + \hat{\varepsilon})r_j^{(\min)}), \quad (\text{III.4.4})$$

with the acceptable overestimation of the envelope expressed by

$$(1 + \hat{\varepsilon})r_j^{(\min)} \leq \mathbf{R}_{jk}^{(b,1)} \leq (1 + \hat{\varepsilon})r_j^{(\max)} \quad \forall j \in [1, n_r]. \quad (\text{III.4.5})$$

The same definition holds for  $\mathbf{R}_k^{(b,2)}$ . Note that in a Gaussian framework, the envelope is symmetric:  $\alpha_k^{(b,1)} = \alpha_k^{(b,2)}$  and  $\mathbf{F}_k^{(b,1)} = -\mathbf{F}_k^{(b,2)}$ .

### III.4.2 Envelope reconstruction

Since the basic SWLs are ordered by decreasing importance, a straightforward approach is to successively apply them. The sequential approximation  $(\tilde{\mathbf{r}}_{(k)}^{(\min)}, \tilde{\mathbf{r}}_{(k)}^{(\max)})$  of the *envelope*  $(\mathbf{r}^{(\min)}, \mathbf{r}^{(\max)})$  after considering the first  $k$  normalized basic static wind loads is expressed by the recursive relations for  $k$  odd

$$\tilde{\mathbf{r}}_{(k)}^{(\min)} = \min \left( \tilde{\mathbf{r}}_{(k-1)}^{(\min)}; \mathbf{R}_{\frac{k+1}{2}}^{(b,1)} \right); \quad \tilde{\mathbf{r}}_{(k)}^{(\max)} = \max \left( \tilde{\mathbf{r}}_{(k-1)}^{(\max)}; \mathbf{R}_{\frac{k+1}{2}}^{(b,1)} \right); \quad (\text{III.4.6})$$

$$\tilde{\mathbf{r}}_{(k+1)}^{(\min)} = \min \left( \tilde{\mathbf{r}}_{(k)}^{(\min)}; \mathbf{R}_{\frac{k+1}{2}}^{(b,2)} \right); \quad \tilde{\mathbf{r}}_{(k+1)}^{(\max)} = \max \left( \tilde{\mathbf{r}}_{(k)}^{(\max)}; \mathbf{R}_{\frac{k+1}{2}}^{(b,2)} \right),$$

with  $\tilde{\mathbf{r}}_{(0)}^{(m)} = \mathbf{0}$ .

It is worth noticing that this approach leads to an approximation of the actual envelope

$$\left( \tilde{\mathbf{r}}_{(n_b)}^{(\min)}, \tilde{\mathbf{r}}_{(n_b)}^{(\max)} \right) \approx \left( \mathbf{r}^{(\min)}, \mathbf{r}^{(\max)} \right), \quad (\text{III.4.7})$$

even by considering the maximum number of basic SWLs that could be derived in a general case, i.e.,  $n_b = n_l$  with  $b \equiv \mathcal{C}$  (CPT loading modes, see (II.8.1)),  $n_b = n_m$  with  $b \equiv \mathcal{M}$  (Modal inertial loads, see (II.5.11)) and  $n_b = 2n_r$  with  $b \equiv \mathcal{P}$  (Principal static wind loads, see Chapter V). However, this simple approach is already able to provide a significant reconstruction rate, as a first insight of the envelope reconstruction. Figure III.7 depicts the flowchart of the ERP with basic SWLs that are applied successively. If a too large acceptable overestimation or number of static wind loads is required to fulfill the two conditions (III.3.12)-(III.3.13), combinations of static wind loads, described in Section III.5, have to be considered.

**Gaussian framework** The  $n_b$ -dimensional vector space of basic static wind loads has an important feature if structural responses are Gaussian processes. For  $k$  odd, the  $k$ -th and  $(k+1)$ -th SWLs are identical in distribution and just differ by their sign

$$\mathbf{f}_{(k)}^{(s)} = \mathbf{F}_{\frac{k+1}{2}}^{(b,1)}, \quad (\text{III.4.8})$$

$$\mathbf{f}_{(k+1)}^{(s)} = -\mathbf{f}_{(k)}^{(s)}. \quad (\text{III.4.9})$$

This result holds because of the symmetry of the envelope and each side of the envelope has the same approximation for  $k$  even, mathematically it reads

$$\tilde{\mathbf{r}}_{(k)}^{(\min)} = -\tilde{\mathbf{r}}_{(k)}^{(\max)}. \quad (\text{III.4.10})$$

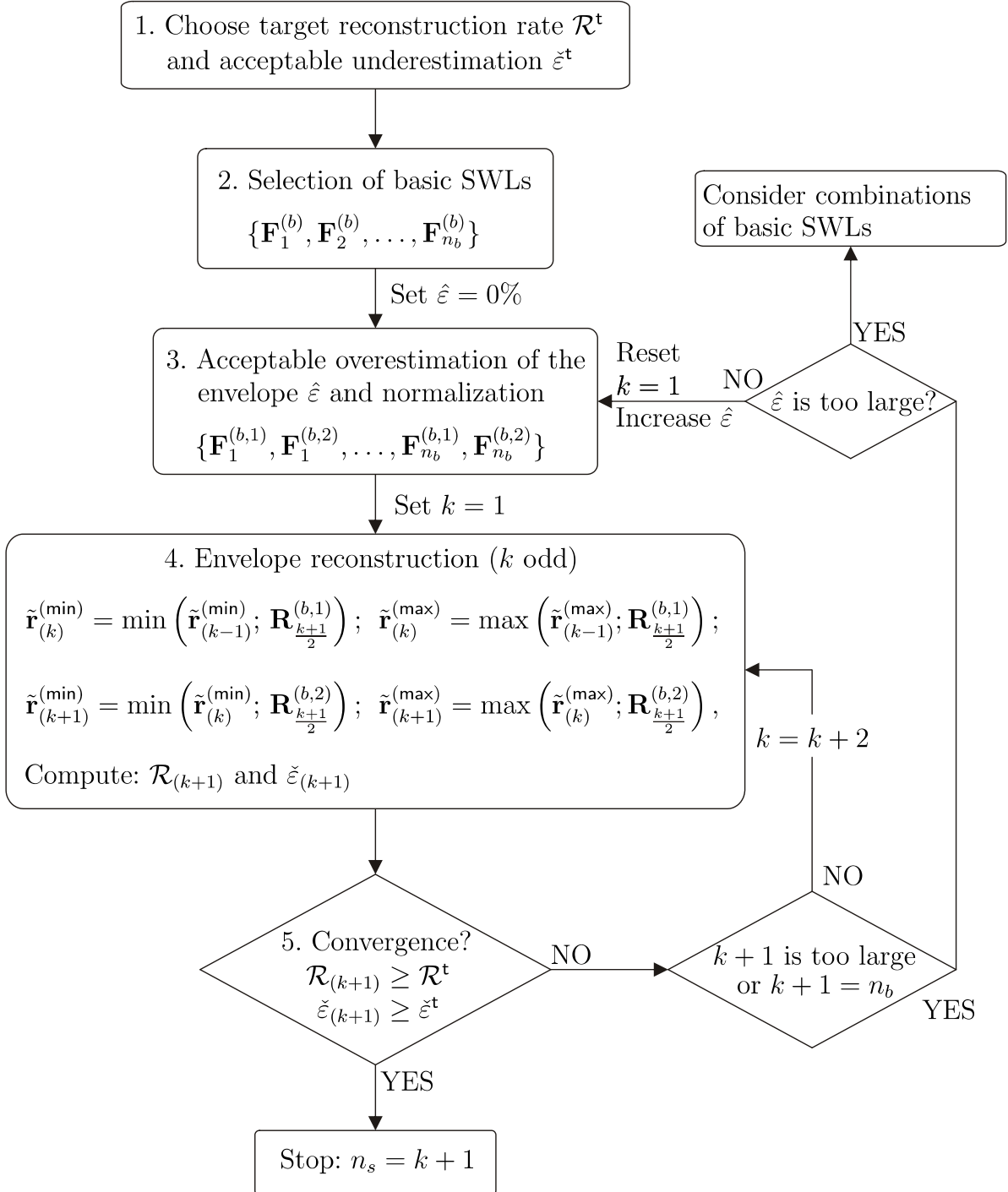


Figure III.7: Flowchart of the envelope reconstruction problem. Basic SWLs are applied successively without combination.



### III.5 Combinations of basic static wind loads

A more elaborated approach is based on some combinations of a subset of basic SWLs to produce the sequence of static wind loads in the ERP. Mathematically, the way to establish the particular basis

$$\{\mathbf{f}_{(1)}^{(s)}, \mathbf{f}_{(2)}^{(s)}, \dots, \mathbf{f}_{(n_s)}^{(s)}\}, \quad (\text{III.5.1})$$

is to consider combinations in another  $n_q$ -dimensional basis

$$\{\mathbf{F}_1^{(b)}, \mathbf{F}_2^{(b)}, \dots, \mathbf{F}_{n_q}^{(b)}\}, \quad (\text{III.5.2})$$

which collects the first  $n_q$  basic static wind loads. Combining basic SWLs performs better for the envelope reconstruction than applying successively each normalized ones separately. For these reasons, only the first few  $n_q$  basic SWLs are retained and combinations of them are considered instead

$$\mathbf{f}_{(k)}^{(s)} = [\mathbf{F}_1^{(b)}, \mathbf{F}_2^{(b)}, \dots, \mathbf{F}_{n_q}^{(b)}] \mathbf{q}_{(k)}^{(b)}, \quad (\text{III.5.3})$$

with  $\mathbf{q}_{(k)}^{(b)}$  an  $n_q \times 1$  vector of combination coefficients and  $\mathbf{f}_{(k)}^{(s)}$  an  $n_t \times 1$  vector representing a static wind load obtained by combinations of the first  $n_q$  basic SWLs. The combination coefficients in  $\mathbf{q}_{(k)}^{(b)}$  are such that the static responses

$$\mathbf{r}_{(k)}^{(s)} = \mathbf{L} \mathbf{f}_{(k)}^{(s)}, \quad (\text{III.5.4})$$

associated with the combinations of basic SWLs satisfy the level of acceptable overestimation and the tangency condition. The envelope reconstruction problem requires combinations of a sufficient number of basic SWLs such that the reconstructed envelope  $(\tilde{\mathbf{r}}_{(k)}^{(\min)}, \tilde{\mathbf{r}}_{(k)}^{(\max)})$  of the structural responses be close enough to the actual envelope. At each step, the combination that will appropriately fill the gaps between the actual envelope and the envelope reconstructed with the former iterations is sought.

#### III.5.1 Constrained nonlinear optimization problem

In this document, we choose a cost function  $f$  of the envelope  $(\mathbf{r}^{(\min)}, \mathbf{r}^{(\max)})$  and its current approximation  $(\tilde{\mathbf{r}}_{(k)}^{(\min)}, \tilde{\mathbf{r}}_{(k)}^{(\max)})$ , that reads

$$f \left( (\tilde{\mathbf{r}}_{(k)}^{(\min)}, \tilde{\mathbf{r}}_{(k)}^{(\max)}), (\mathbf{r}^{(\min)}, \mathbf{r}^{(\max)}) \right) := \left| \Psi_{(k)}^{(\gamma)} \right|, \quad (\text{III.5.5})$$

which aims at the minimization, at each iteration, of the *overall error indicator*  $\Psi_{(k)}^{(\gamma)}$ . This indicator is given by

$$\Psi_{(k)}^{(\gamma)} = \frac{\Psi_{(k)}^{(\min, \gamma)} + \Psi_{(k)}^{(\max, \gamma)}}{2}, \quad (\text{III.5.6})$$

with

$$\Psi_{(k)}^{(\min, \gamma)} = \frac{1}{n_r} \sum_{i=1}^{n_r} - \left| \left[ \max \left( \tilde{r}_{i, (k)}^{(\min)}, r_i^{(\min)} \right) - r_i^{(\min)} \right] / r_i^{(\min)} \right|^\gamma, \quad (\text{III.5.7})$$

$$\Psi_{(k)}^{(\max, \gamma)} = \frac{1}{n_r} \sum_{i=1}^{n_r} - \left| \left[ \min \left( \tilde{r}_{i, (k)}^{(\max)}, r_i^{(\max)} \right) - r_i^{(\max)} \right] / r_i^{(\max)} \right|^\gamma, \quad (\text{III.5.8})$$

where  $\gamma \geq 1$  is a parameter that gives more weight to large relative errors in the cost function. For an easier understanding of the cost function we first set  $\hat{\varepsilon} = 0$  and  $\gamma = 1$ , i.e., no overestimation of the envelope is accepted and each relative error has the same weight in the cost function, respectively. In this case, equations (III.5.7) and (III.5.8) degenerate into

$$\Psi_{(k)}^{(\min,1)} = \frac{1}{n_r} \sum_{i=1}^{n_r} \varepsilon_{i,(k)}^{(\min)}, \quad (\text{III.5.9})$$

$$\Psi_{(k)}^{(\max,1)} = \frac{1}{n_r} \sum_{i=1}^{n_r} \varepsilon_{i,(k)}^{(\max)}, \quad (\text{III.5.10})$$

and  $\Psi_{(k)}^{(\min,1)}$  and  $\Psi_{(k)}^{(\max,1)}$  correspond to the average of the relative errors for the min and max sides of the envelope, respectively. Moreover, we have  $\mathcal{R}_{(k)}^{(m)} = 1 + \Psi_{(k)}^{(m,1)}$  and  $\mathcal{R}_{(k)} = 1 + \Psi_{(k)}^{(1)}$ .

The operations  $\max(\tilde{r}_{i,(k)}^{(\min)}, r_i^{(\min)})$  and  $\min(\tilde{r}_{i,(k)}^{(\max)}, r_i^{(\max)})$  in (III.5.7) and (III.5.8) ensure positive relative errors, i.e., overestimations of the envelope, are not taken into account in the cost function. The negative sign is due to the absolute value required for even  $\gamma$ . Note  $\Psi_{(k)}^{(\gamma)}$  is a monotonic series:  $-100\% < \Psi_{(k)}^{(\gamma)} \leq \Psi_{(k+1)}^{(\gamma)} \leq 0\%$  and the bounded value  $\Psi_{(k)}^{(\gamma)} = 0\%$  means that the envelope is perfectly reconstructed.

We recommend to set the parameter  $\gamma$  equal to one as an educated initial value. After solving the envelope reconstruction problem, if the number  $n_s^{(2)}$  of SWLs required to fulfill the acceptable underestimation of the envelope  $\tilde{\varepsilon}^t$  is much larger than the number  $n_s^{(1)}$  to achieve the overall reconstruction  $\mathcal{R}^t$ , then it makes sense to increase the parameter  $\gamma$ .

Figure III.8 depicts the flowchart with combinations of basic SWLs to solve the envelope reconstruction problem. At the  $k$ -th iteration, the convergence (step 6), i.e., fulfillment of (III.3.12) and (III.3.13) is checked. If one or both conditions are not satisfied, the behaviors of the series  $\mathcal{R}_{(k)}$  and  $\tilde{\varepsilon}_{(k)}$  are assessed before the next iteration (step 7). If they do not change through iterations, it means they may have reached asymptotic values. What we define as asymptotic values denoted by  $\mathcal{R}_{(\infty)}$  and  $\tilde{\varepsilon}_{(\infty)}$  are associated with the approximation of the envelope considering all possible combinations  $\mathbf{q}_{(k)}^{(b)}$  generated with a Monte Carlo simulation technique (Blaise and Denoël, 2013a).

Practically, both asymptotic quantities are not computed since it is time-consuming. Instead, if the rate of change of  $\mathcal{R}_{(k)}$  and  $\tilde{\varepsilon}_{(k)}$  through iterations is below a certain threshold, for instance 1%, and  $\mathcal{R}_{(k)} \ll \mathcal{R}^t$  or  $\tilde{\varepsilon}_{(k)} \ll \tilde{\varepsilon}^t$ , it is recommended to increase the number  $n_q$  or the acceptable level of overestimation. Contrary to the series  $\mathcal{R}_{(k)}$ , the series  $\tilde{\varepsilon}_{(k)}$  may exhibit one or several plateau's and the assessment of its rate of change is therefore not straightforward, see Figure III.6 for an example.

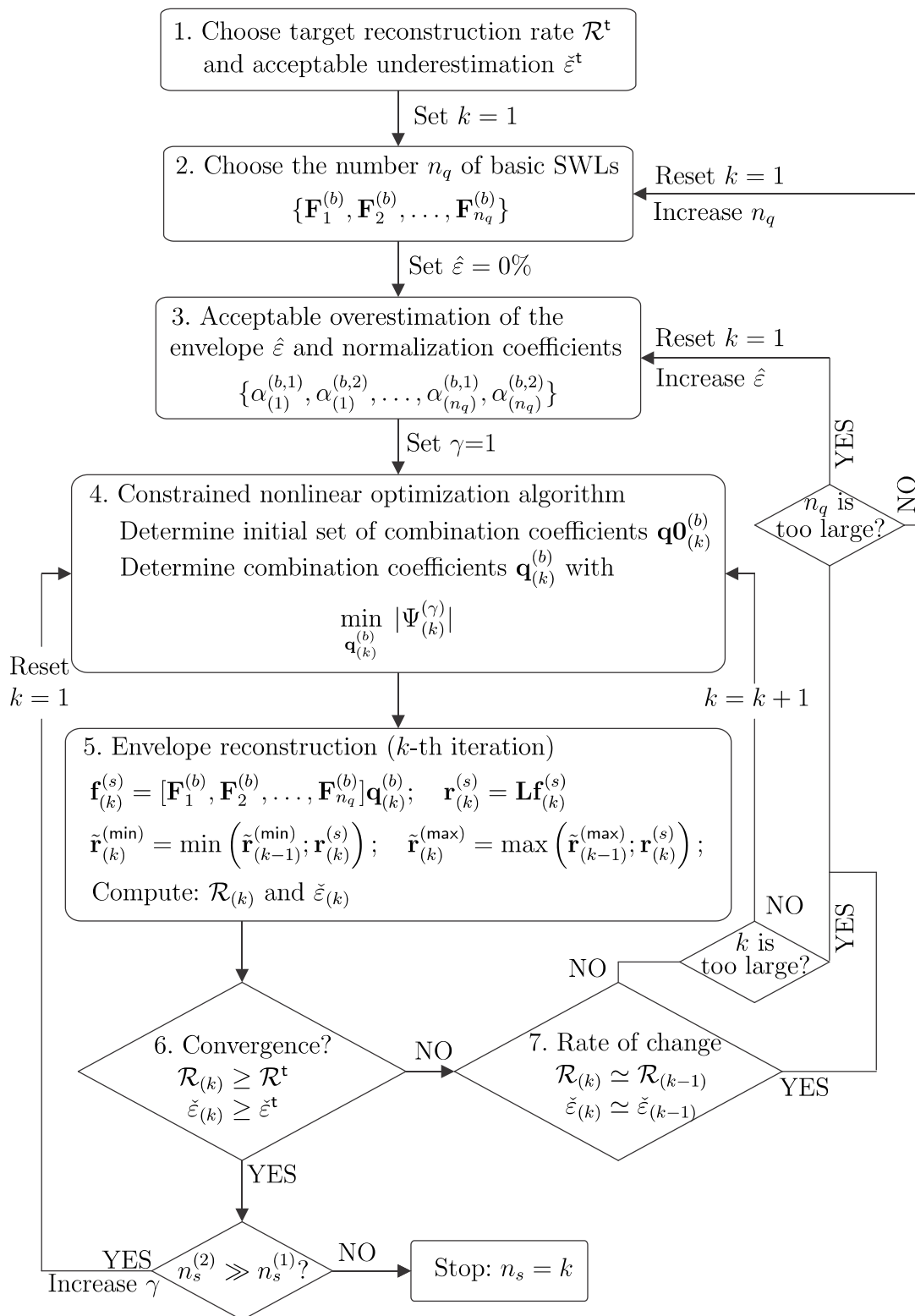


Figure III.8: Flowchart of the envelope reconstruction problem. Combinations of Basic SWLs are considered.

### III.5.2 Combination coefficients

The constrained nonlinear optimization consists in finding a vector of combination coefficients  $\mathbf{q}_{(k)}^{(b)}$  associated with a local minimum to the scalar cost function (III.5.5)

$$\min_{\mathbf{q}_{(k)}^{(b)}} \left| \Psi_{(k)}^{(\gamma)} \right|, \quad (\text{III.5.11})$$

under the linear constraints of the acceptable overestimation conditions

$$\begin{cases} +\mathbf{L}[\mathbf{F}_1^{(b)}, \mathbf{F}_2^{(b)}, \dots, \mathbf{F}_{n_q}^{(b)}] \mathbf{q}_{(k)}^{(b)} - (1 + \hat{\varepsilon}) \mathbf{r}^{(\max)} \leq \mathbf{0}, \\ -\mathbf{L}[\mathbf{F}_1^{(b)}, \mathbf{F}_2^{(b)}, \dots, \mathbf{F}_{n_q}^{(b)}] \mathbf{q}_{(k)}^{(b)} + (1 + \hat{\varepsilon}) \mathbf{r}^{(\min)} \leq \mathbf{0}. \end{cases} \quad (\text{III.5.12})$$

With (III.5.11) the same relative errors for two structural responses have the same weight in the cost function no matter the magnitude of each structural response. If structural responses are stresses, one may be more interested on the accurate reconstruction of the highest stresses than the lower ones. For this purpose, a weighting function integrating the magnitude of structural responses may be incorporated in the cost function. Moreover, only the min or max side of the envelope may be of interest depending on the magnitude of the mean structural responses under the mean wind loading and other loads, e.g., self-weight. Other cost functions may be chosen as well, depending on the specificity of the problem.

Following the optimization, the reconstructed envelope is updated using (III.5.3)-(III.5.4)-(III.1.2) and we proceed to the next iteration. We recommend the Sequential Quadratic Programming method (Boggs and Tolle, 1995) for this constrained nonlinear optimization problem.

The cost function to be minimized possesses many local minima, in the space of the combination coefficients, which makes the optimization algorithm sensitive to the initial set of combination coefficients  $\mathbf{q}\mathbf{0}_{(k)}^{(b)}$ . Two procedures to guess a good initial set of combination coefficients  $\mathbf{q}\mathbf{0}_{(k)}^{(b)}$  before minimization of the cost function are described. This is further discussed in the illustrations.

#### Initial set of combination coefficients (small $n_q$ )

- Each retained basic SWL for combinations is multiplied by the normalization coefficients, see (III.4.2), chosen in the triplet  $\left\{ -\alpha_{(i)}^{(b,2)}, 0, \alpha_{(i)}^{(b,1)} \right\}$ .
- All possible combinations of normalization coefficients of basic SWL are considered. Discarding the trivial combination, for  $n_q$  basic SWLs, the number of possible combinations amounts to  $3^{n_q} - 1$ . For instance, for  $n_q = 2$  basic SWLs, the 8 sets of combination coefficients are given by each column of the matrix below

$$\begin{bmatrix} -\alpha_{(1)}^{(b,2)} & -\alpha_{(1)}^{(b,2)} & -\alpha_{(1)}^{(b,2)} & 0 & 0 & \alpha_{(1)}^{(b,1)} & \alpha_{(1)}^{(b,1)} & \alpha_{(1)}^{(b,1)} \\ -\alpha_{(2)}^{(b,2)} & 0 & \alpha_{(2)}^{(b,1)} & -\alpha_{(2)}^{(b,2)} & \alpha_{(2)}^{(b,1)} & -\alpha_{(2)}^{(b,2)} & 0 & \alpha_{(2)}^{(b,1)} \end{bmatrix}.$$

- Finally, each set of combination coefficients (each column above) is scaled by a scalar to fulfill again the level of acceptable overestimation and the tangency condition. The cost function is evaluated for each set of combination coefficients and the set providing the minimum cost function is selected as the initial value  $\mathbf{q}\mathbf{0}_{(k)}^{(b)}$  for the optimization (III.5.11).

In practice, if the CPU time to evaluate the cost function (III.5.11) for one set of initial combination coefficients is denoted by  $t_c$ , the total CPU time to determine the initial set  $\mathbf{q}\mathbf{0}_{(k)}^{(b)}$  from  $3^{n_q} - 1$  initial combination coefficients is equal to  $t_c \times (3^{n_q} - 1)$ . Hence, the total CPU time to choose the initial set is proportional to three to the power  $n_q$ . If this CPU time is prohibitive, another procedure is described next in case of large  $n_q$ .

### Initial set of combination coefficients (large $n_q$ )

In case of large  $n_q$ , the procedure described above might be time consuming and is better suited to small  $n_q$ . For large  $n_q$ , we recommend instead to randomly generate  $n_c$  sets of combination coefficients as described next.

- For each retained basic SWL,  $n_c$  coefficients uniformly distributed between  $-\alpha_{(i)}^{(b,2)}$  and  $\alpha_{(i)}^{(b,1)}$  are randomly generated and denoted by  $\alpha_{(i)}^{(rg)}$ .
- For instance, for  $n_q = 40$  basic SWLs and  $n_c = 10000$ , the 10000 sets of combination coefficients are given by each column of the matrix below

$$\begin{bmatrix} \alpha_{(1)}^{(rg)} & \cdots & \alpha_{(1)}^{(rg)} \\ \vdots & \ddots & \vdots \\ \alpha_{(40)}^{(rg)} & \cdots & \alpha_{(40)}^{(rg)} \end{bmatrix}_{40 \times 10000} .$$

- Finally, each set of combination coefficients (each column above) is scaled by a scalar to fulfill again the level of acceptable overestimation and the tangency condition. The cost function is evaluated for each set of combination coefficients and the set providing the minimum cost function is selected as the initial value  $\mathbf{q}\mathbf{0}_{(k)}^{(b)}$  for the optimization (III.5.11).

### Gaussian framework

The  $n_s$ -dimensional vector space of static wind loads (III.3.1) has an important feature if structural responses are Gaussian processes. For  $k$  odd, the  $k$ -th and  $(k + 1)$ -th static wind loads are identical in distribution and just differ by their sign

$$\mathbf{f}_{(k)}^{(s)} = -\mathbf{f}_{(k+1)}^{(s)}. \quad (\text{III.5.13})$$

This result holds because of the symmetry of the envelope and if the reconstruction of each side of the envelope has the same weight in the cost function.

## III.6 Summary

A complete methodology to solve the envelope reconstruction problem irrespective of the structure, its load-bearing system and its susceptibility to vibrations in a Gaussian or non-Gaussian context is rigorously conceptualized. The intrinsic controllability of a set of pertinent parameters makes the methodology flexible to specific envelope reconstruction requirements. In other words, it provides a smart balance between over- and under-estimation of the actual envelope and three options are also discussed to obtain static wind loads ensuring

no underestimation of the envelope. Moreover, combinations of basic static wind loads are computed to speed-up the reconstruction of the envelope values. The problem of determining these combination coefficients is formulated as a constrained nonlinear optimization. The covariance proper transformation loading modes, modal inertial loads and principal static wind loads, categorized as basic static wind loads, can be implemented within the proposed methodology.







# Chapter IV

## Equivalent static wind loads

---

**IV.1 Introduction**

**IV.2 Concept**

**IV.3 Conditional sampling technique**

**IV.4 Load-Response Correlation method**

**IV.5 Modal inertial loads-based ESWLs**

**IV.6 Hybrid-based ESWLs**

**IV.7 Conditional Expected Load method**

**IV.8 Non-Gaussian joint probability density function**

**IV.9 Two-step adjustment method**

**IV.10 Envelope reconstruction problem using ESWLs**

**IV.11 Summary**

---

◇ “The instantaneous load distributions producing the peak load effects were recorded, using a conditional sampling technique.” [Holmes \(1988\)](#)

◇ “Assuming Gaussian properties, the load pattern obtained [...] is the most probable extreme load pattern for the specified maximum response.” [Kasperski \(1992\)](#)

◇ “This approach also allows the peak-load distributions [...] to be reduced to linear combinations [...] of eigenvector modes.” [Holmes \(1992\)](#)

◇ “The equivalent design pressure coefficients which reproduce the maximum load effects are proposed [...]” [Tamura et al. \(1992\)](#)

◇ “[...] the equivalent static load distribution [...] is formulated in terms of either a weighted combination of modal inertial load components, or the background and resonant load components.” [Chen and Kareem \(2001\)](#)

◇ “The load distribution for a given peak response is not necessarily unique simply because that multiple load distributions can result in an identical response.” [Chen and Zhou \(2007\)](#)

## IV.1 Introduction

An Equivalent Static Wind Load (ESWL) is a loading such that its application provides the same extreme value of a given structural response as what would result from the buffeting analysis. Their usual designation is equivalent static wind loads although they are sometimes referred as “peak wind loads” (Holmes, 1988), “extreme load distributions” or “unfavorable wind load distributions” (Kasperski and Niemann, 1992), “effective static load distributions” (Holmes, 1996) and “equivalent static buffeting loads” (Zhou et al., 2000), to name but a few. In this document, the former designation is adopted.

The static wind loads obtained with the GLF and GRF concepts may be assimilated as equivalent one. They are not presented here since they have been discussed in the previous Chapter where it was decided to disregard them in this thesis.

The main methods formulating ESWLs are next reviewed.

### Conditional Sampling Technique (CST-based ESWLs)

An approach for the formulation of ESWL arose with the studies on the wind loading of low-rise buildings (Holmes and Best, 1981; Stathopoulos, 1984). In Holmes (1988) the notion of peak-load pressure distributions is introduced for specific structural responses referred to as “load effects” in his works. To each structural response corresponds plausible patterns of pressure distributions that maximize or minimize it in the manner of an influence line or influence surface, in a static analysis. The conditional sampling technique (Atta, 1974) identifies these peak-load pressure distributions. This technique has been mainly applied to low-rise buildings (Tamura et al., 1992, 2001).

### Load-Response Correlation method and CPT loading modes (LRC-based ESWLs)

An important breakthrough was achieved with works of Kasperski (1992) who derived a mathematical formulation defining an ESWL as the “most probable wind load pattern associated with an extreme value of a specific response”. The assumption is a Gaussian wind field and the proposed method termed the Load-Response Correlation (LRC) method is limited to structures with a background structural behavior (Kasperski and Niemann, 1992). More precisely, the LRC method gives a load pattern producing an extreme value (min or max) of the (zero-mean) fluctuating response. This work also emphasizes that the total wind load has to incorporate the mean wind loading separately. The LRC method has the main advantage to provide meaningful realistic load for any considered response in the structure. For cantilevered grandstand roofs, improvements of the design load patterns provided in the Australian code were compared with those obtained with the LRC method (Letchford and Killen, 2002). Actually, the LRC method has been incorporated in the ISO-document (International Standards Organization, 2009). It is illustrated with the design of low-rise buildings in (Kasperski, 2009). Finally, it appears that LRC-based ESWLs may be seen as combinations of a small number of the CPT loading modes (Holmes, 1992).

### Methods for dynamic structural behaviors using LRC-based ESWLs and Modal Inertial Loads (Hybrid-based ESWLs)

Even if not formulated as such, Davenport (1985) sketched the use of Modal Inertial Loads (MILs) to derive static wind loads for the dynamic analysis of long-span bridges. A modal

inertial load statically applied to the structure produces a deflection affine to the corresponding mode shape. In the general case of a hybrid background-resonant structural behavior, [Holmes \(1996\)](#) formulated the ESWL as an addition to the mean pressure field of an SRSS combination of the (background) load pattern obtained with the LRC method and a resonant load pattern resulting from the first modal inertial force. This formulation was initially derived for structures that exhibit a dynamic behavior only in their first mode. The design of the *Stadium Australia* and the *Sydney SuperDome* was based on this method ([Holmes and Wood, 2001](#)). For the background component of the ESWL, comparisons are made between a direct approach in which instantaneous pressures producing extreme responses are picked up and those obtained with the LRC method. The authors advised to use the second approach because it produces, from a statistical point of view, more reliable load patterns than those obtained with a single snapshot. The formulation was pushed forward by [Zhou et al. \(2000\)](#) using several MILs for horizontal structures that may exhibit resonant responses in several modes but neglecting modal response correlations. Note, the number of MIL is equal to the number of modes with a resonant response included in the modal analysis. Other ways to combine the different contributions (mean, background and resonant) of an ESWL is a weighted addition of each part. This is discussed in ([Chen and Kareem, 2001](#)) with extension to modal response correlations and these hybrid-based ESWLs have been applied to a wide range of roof structures as cylindrical shell models ([Li and Tamura, 2005](#)) or long-span roof structures, for example to the 486 m long roof of the *Shenzhen Citizens Centerwith* in China ([Fu et al., 2008](#)).

## Objectives

The concept of equivalent static wind loads aiming at reproducing as close as possible specific responses that would be obtained with a formal buffeting approach has been enhanced through the decades mainly assuming Gaussian processes. [Table IV.1](#) shows the domain of applicability of the methods discussed herebefore.

| Framework:           | Gaussian     |              | non-Gaussian |              |
|----------------------|--------------|--------------|--------------|--------------|
| Structural behavior: | Quasi-static | Dynamic      | Quasi-static | Dynamic      |
| With realizations:   | CST-based    | ✗            | CST-based    | ✗            |
| Nodal basis:         | LRC-based    | ✗            | LRC-based    | ✗            |
| Hybrid basis:        | -            | Hybrid-based | -            | Hybrid-based |

Table IV.1: Domain of applicability for the main three actual formulations of equivalent static wind loads.

The conditional sampling technique, by nature, incorporates the non-Gaussian aspects in both aerodynamic loads and structural responses. Conversely, the LRC methods and hybrid-based ESWLs were developed assuming Gaussian processes. Actually, [Kasperski \(1992\)](#) avoids a formal extension to non-Gaussian processes arguing that, the LRC method would provide “[...] a very close approximation to the real load pattern for non-Gaussian load processes [...]”. However, disharmony has been shown between the “Gaussian” ESWLs

obtained with the LRC method and those obtained with statistical treatment of wind-tunnel measurements (Tamura et al., 2002). However, it is emphasized that the LRC- and hybrid-based ESWL formulations are sometimes used for non-Gaussian processes together with non-Gaussian peak factors (Tamura et al., 2002).

In fact, there is today no agreement, to the author's knowledge on how to formally extend the concept of ESWL in a non-Gaussian framework. This has especially motivated a study of a "non-Gaussian" formulation of ESWLs as a main objective of this Chapter.

### Outline of the Chapter

Section IV.2 reports the objective of an equivalent static wind load and formulates the envelope value and non-overestimation conditions. In section IV.3, the conditional sampling technique is discussed and Section IV.4 presents the well-known LRC method. Sections IV.5 and IV.6 detail ESWLs computed with modal inertial loads and as weighted combinations of background and resonant components, respectively.

Section IV.7 introduces a subclass of ESWLs, termed the Conditional Expected SWLs, through a novel method, relevant for any structural behavior, quasi-static, mixed or resonant and for Gaussian and non-Gaussian structural responses. The method is particularized for a certain class of non-Gaussian processes through a *bicubic translation model* of joint probability density derived in Section IV.8. Section IV.9 discusses a two-step adjustment method to ensure that ESWLs satisfy both the envelope value and non-overestimation conditions.

Finally, in Section IV.10, the ESWLs are normalized and a general methodology to rank them for the envelope reconstruction problem is described.

## IV.2 Concept

The following developments are relevant for Gaussian and non-Gaussian structural responses resulting from linear quasi-static and dynamic structural behaviors. To be general, ESWLs are expressed with the nodal forces in the sequel, even if ESWL derived in a quasi-static framework is usually expressed with the aerodynamic pressures, still it may be transformed into nodal forces using (II.4.2).

### Objective of an ESWL

Through a static analysis, the main objective of the  $i$ -th equivalent static wind load, denoted by

$$\mathbf{f}_{(i)}^{(e,m)}, \quad (\text{IV.2.1})$$

is to target one of the two envelope values ( $m \equiv \min$  or  $m \equiv \max$ ) of the  $i$ -th structural response  $r_i^{(m)}$ . The superscript "e" stands for "equivalent" (static wind load).

### Envelope value condition

The static responses under  $\mathbf{f}_{(i)}^{(e,m)}$  are given by

$$\mathbf{r}_{(i)}^{(e,m)} = \mathbf{L}\mathbf{f}_{(i)}^{(e,m)}. \quad (\text{IV.2.2})$$

By invoking the concept of *equivalence*, the  $i$ -th structural response under  $\mathbf{f}_{(i)}^{(e,m)}$  must in principle satisfy

$$\boxed{\mathbf{r}_{i(i)}^{(e,m)} = \mathbf{r}_i^{(m)}}, \quad (\text{IV.2.3})$$

which defines the *envelope value condition*. In other words, an ESWL statically applied to the structure, should exactly produce the targeted structural response for which it has been derived.

### Non-overestimation condition

From the conceptual point of view, it would be desired that the static analysis under  $\mathbf{f}_{(i)}^{(e,m)}$  satisfies (IV.2.3) and the following *non-overestimation condition* (of the envelope)

$$\boxed{\mathbf{r}_j^{(\min)} \leq \mathbf{r}_{j(i)}^{(e,m)} \leq \mathbf{r}_j^{(\max)} \quad \forall j \in [1, n_r]}. \quad (\text{IV.2.4})$$

Indeed, an ESWL derived for a specific response should not produce, in principle, responses in other locations larger than their envelope values.

### Envelope reconstruction problem

The both conditions that an ESWL is expected to fulfill are independent of the type of analysis (background, hybrid or resonant and Gaussian or non-Gaussian) performed to obtain the envelope ( $\mathbf{r}^{(\min)}, \mathbf{r}^{(\max)}$ ). However, depending on the formulation of ESWLs, these two conditions may not be guaranteed. This is studied in Section IV.7. If the two above conditions are met, the reconstructed envelope obtained with a sufficient number  $n_s$  of static analyses should reconstruct the real envelope, at the least with  $2n_r$  ESWLs.

### Total ESWL

Finally, the total ESWL reads

$$\mathbf{f}_{(i)}'^{(e,m)} = \boldsymbol{\mu}_{\mathbf{f}'} + \mathbf{f}_{(i)}^{(e,m)}, \quad (\text{IV.2.5})$$

with  $\boldsymbol{\mu}_{\mathbf{f}'}$  the mean wind load component.

### IV.3 Conditional sampling technique

This Section describes the conditional sampling technique relevant for structures with a quasi-static behavior. In this technique, realizations of aerodynamic pressures, obtained in wind-tunnel, measured in situ or resulting from computational fluid dynamic simulations are required. If the envelope values are obtained from realisations as described next, the envelope value condition is satisfied. In any case, the formulation discussed hereinafter do not ensure that the non-overestimation condition is satisfied.

#### Envelope of structural responses

In a statistical framework, where time series are available, envelope values of structural responses may also be obtained with inferential statistics on realizations instead of the model adopted in the thesis, described in Section II.3. These realizations are computed by time-domain analysis performed with the sampled aerodynamic pressures. The observed extreme values of the  $i$ -th structural response on the  $k$ -th observation window and occurring at time  $t_k$ , denoted by  $r_i^{(\text{ext})}(t_k)$ , are identified on each observation window and with their average,

$$r_i^{(\mathcal{S},\text{m})} = \text{mean}_{t_k} \left[ r_i^{(\text{ext})}(t_k) \right], \quad k \in [1, n_t], \quad (\text{IV.3.1})$$

an observed peak factor  $g_i^{(\mathcal{S},\text{m})} = r_i^{(\mathcal{S},\text{m})} / \sigma_{r_i}$  may be computed as well. The total number of observation window is denoted by  $n_t$ . The symbol “ $\mathcal{S}$ ” stands for (conditional) “Sampling” (technique). The average of the observed extreme values tends to the exact envelope value, as the number of observation windows increases. However, the number of observation windows (in full-scale) usually measured is rather low due to the amount of data to be stored. As a result, the confidence intervals of the observed peak factor may be rather large. This is a reason why estimated peak factors are computed using advanced evaluation methods (Sadek and Simiu, 2002; Gioffrè et al., 2000).

#### Common formulation

Common practice consists in identifying extreme values of structural responses on each observation window and sampling the associated pressure distributions (Holmes, 1988; Tamura et al., 2002). The common sampling formulation of an ESWL ( $\mathbf{p}^{(e,\text{m})} \equiv \mathbf{p}^{(\mathcal{S},\text{m})}$ ) is then defined as the average of these sampled load patterns

$$\mathbf{p}_{(i)}^{(\mathcal{S},\text{m})} = \text{mean}_{t_k} \left[ \mathbf{p}_{(i)}^{(\text{ext})}(t_k) \right], \quad k \in [1, n_t], \quad (\text{IV.3.2})$$

where  $\mathbf{p}_{(i)}^{(\text{ext})}(t_k)$  is the  $k$ -th load pattern associated with the  $i$ -th extreme value  $r_i^{(\text{ext})}(t_k)$  of a structural response on the  $k$ -th observation window and occurring at time  $t_k$ . The superscript **ext** stands for “extreme” (values of structural responses).

## IV.4 Load-Response Correlation method

Under Gaussian loading and in case of structures with a quasi-static behavior, [Kasperski \(1992\)](#) derived the pioneering Load-Response Correlation (LRC) method to compute ESWLs.

### Original demonstration

Using [\(II.4.13\)](#), the variance of the  $i$ -th structural response reads

$$\sigma_{r_i}^2 = \sum_{k=1}^{n_l} \sum_{l=1}^{n_l} B_{ik} B_{il} \rho_{p_k p_l} \sigma_{p_k} \sigma_{p_l}, \quad (\text{IV.4.1})$$

where  $\rho_{p_k p_l}$  is the correlation coefficient between the  $k$ -th and  $l$ -th components of  $\mathbf{p}(t)$ . Substituting [\(IV.4.1\)](#) into [\(II.4.15\)](#), the envelope value associated with the  $i$ -th structural response yields

$$r_i^{(m)} = \sum_{k=1}^{n_l} B_{ik} \left( g_i^{(m)} \sum_{l=1}^{n_l} B_{il} \rho_{p_k p_l} \sigma_{p_k} \frac{\sigma_{p_l}}{\sigma_{r_i^b}} \right), \quad (\text{IV.4.2})$$

and the term in parentheses gives the  $k$ -th component of the ESWL ( $\mathbf{p}^{(e,m)} \equiv \mathbf{p}^{(\mathcal{L},m)}$ ) associated with the  $i$ -th structural response

$$p_{k(i)}^{(\mathcal{L},m)} = g_i^{(m)} \sum_{l=1}^{n_l} B_{il} \rho_{p_k p_l} \sigma_{p_k} \frac{\sigma_{p_l}}{\sigma_{r_i^b}}, \quad (\text{IV.4.3})$$

where symbol “ $\mathcal{L}$ ” stands for “ $\mathcal{L}$ oad” (-response correlation method).

### With CPT loading modes

[Holmes \(1992\)](#) established LRC-based ESWLs using linear combinations of a small number  $n_{cpt}$  of CPT loading modes, introduced in [Section II.8.2](#). The LRC-based ESWL ( $\mathbf{p}^{(e,m)} \equiv \mathbf{p}^{(\mathcal{L}^c,m)}$ ) targeting the  $i$ -th envelope value is given by

$$p_{k(i)}^{(\mathcal{L}^c,m)} = \sum_{m=1}^{n_{cpt}} P_{km}^{(c)} W_{mi}^{(c,m)}, \quad (\text{IV.4.4})$$

with the weighting factors given by

$$W_{mi}^{(c,m)} = \frac{g_i^{(m)}}{\sigma_{r_i^b}} \lambda_m^c \sum_{j=1}^{n_l} B_{ij} P_{jm}^{(c)}. \quad (\text{IV.4.5})$$

The symbol “ $\mathcal{L}^c$ ” stands for “ $\mathcal{L}$ oad” (-response correlation method) with “ $\mathcal{C}$ ovariance” (proper transformation loading modes). In the early nineties, this approach simplified the computation of ESWLs and for large structures for which an important number of ESWLs may be established, it greatly reduces the data storage.

## IV.5 Modal inertial loads-based ESWLs

If ESWLs are only expressed with the modal inertial loads they are so-called *MIL-based* ESWLs and are detailed here. In fact, they are a limit case of the *hybrid-based* ESWLs which are described in the following Section IV.6. Chen and Kareem (2001) formalized hybrid-based ESWLs as weighted combinations of background ESWLs obtained with the LRC method and resonant ESWLs formulated with modal inertial loads.

In the framework of a full modal analysis, Fu et al. (2008) promote the use of MIL-based ESWLs in these terms “[...] the formula derived for the ESWL [...] can be applied to all kinds of structural systems [...]”. However, several required features of the kind of structural system must be formulated before following blindly the hereinbefore assertion. First, the background contribution of structural responses must be well approximated with the  $n_m$  modes retained for the modal analysis or at least the background-resonant ratio should be very low. Second, even if the background contribution of responses is well approximated with the  $n_m$  modes, the contribution of the applied nodal forces  $\mathbf{f}$  to the ESWLs, may be poorly-represented with the same number  $n_m$  of modal inertial loads. In other words, Fu et al. (2008) postulates

$$\sum_{i=1}^{n_m} \mathbf{F}_i^{(\mathcal{M})} \mathbf{q}_i^b \simeq \mathbf{f}, \quad (\text{IV.5.1})$$

which is not guaranteed in the framework of a full modal analysis.

### Original demonstration

Substituting (II.5.4) into (II.4.9), structural responses, in a modal basis, read

$$\mathbf{r} = \mathbf{O}\mathbf{x} = \mathbf{O}\Phi\mathbf{q}, \quad (\text{IV.5.2})$$

and inserting (II.5.11) into (IV.5.2), structural responses become expressed with modal inertial loads

$$\mathbf{r} = \mathbf{L}\mathbf{F}^{(\mathcal{M})}\mathbf{q}. \quad (\text{IV.5.3})$$

The variance of the  $i$ -th structural response is found as

$$\begin{aligned} \sigma_{r_i}^2 &= \sum_{m=1}^{n_m} \sum_{n=1}^{n_m} \left( \sum_{k=1}^{n_t} L_{ik} F_{km}^{(\mathcal{M})} \right) \left( \sum_{l=1}^{n_t} L_{il} F_{ln}^{(\mathcal{M})} \right) \sigma_{q_m q_n}, \\ &= \sum_{m=1}^{n_m} \sum_{n=1}^{n_m} (\mathbf{L}_{i\circ} \mathbf{F}_m^{(\mathcal{M})}) (\mathbf{L}_{i\circ} \mathbf{F}_n^{(\mathcal{M})}) \sigma_{q_m q_n}, \end{aligned} \quad (\text{IV.5.4})$$

with  $\mathbf{L}_{i\circ} \mathbf{F}_m^{(\mathcal{M})} = \sum_k^{n_t} L_{ik} F_{km}^{(\mathcal{M})}$  and  $\mathbf{L}_{i\circ} \mathbf{F}_k^{(\mathcal{M})} = \sum_k^{n_t} L_{ik} F_{kn}^{(\mathcal{M})}$ . The  $i$ -th envelope value  $r_i^{(m)} = g_i^{(m)} \sigma_{r_i}$ , is reformulated using (IV.5.4), that yields



$$\begin{aligned}
r_i^{(m)} &= g_i^{(m)} \sum_{m=1}^{n_m} \sum_{n=1}^{n_m} \mathbf{L}_{i_o} \mathbf{F}_m^{(\mathcal{M})} \mathbf{L}_{i_o} \mathbf{F}_n^{(\mathcal{M})} \frac{\sigma_{q_m q_n}}{\sigma_{r_i}}, \\
&= \mathbf{L}_{i_o} \left( \sum_{m=1}^{n_m} \sum_{n=1}^{n_m} g_i^{(m)} \mathbf{F}_m^{(\mathcal{M})} \mathbf{L}_{i_o} \mathbf{F}_n^{(\mathcal{M})} \frac{\sigma_{q_m q_n}}{\sigma_{r_i}} \right), \tag{IV.5.5}
\end{aligned}$$

and the term in parentheses gives the ESWL ( $\mathbf{f}^{(e,m)} \equiv \mathbf{f}^{(\mathcal{M},m)}$ ) expressed as a weighted combination of the modal inertial loads, such as

$$\begin{aligned}
\mathbf{f}_{(i)}^{(\mathcal{M},m)} &= \sum_{m=1}^{n_m} \sum_{n=1}^{n_m} g_i^{(m)} \mathbf{F}_m^{(\mathcal{M})} \mathbf{L}_{i_o} \mathbf{F}_n^{(\mathcal{M})} \frac{\sigma_{q_m q_n}}{\sigma_{r_i}}, \\
&= \sum_{m=1}^{n_m} \mathbf{F}_m^{(\mathcal{M})} \mathbf{W}_{mi}^{(\mathcal{M},m)}, \tag{IV.5.6}
\end{aligned}$$

with the weighting factors  $\mathbf{W}_{mi}^{(\mathcal{M},m)}$  expressed by

$$\mathbf{W}_{mi}^{(\mathcal{M},m)} = \sum_{n=1}^{n_m} g_i^{(m)} \mathbf{L}_{i_o} \mathbf{F}_n \frac{\sigma_{q_m q_n}}{\sigma_{r_i}}. \tag{IV.5.7}$$

## IV.6 Hybrid-based ESWLS

Chen and Kareem (2001) formalized hybrid-based ESWLS as weighted combinations of background ESWLS obtained with the LRC method, see Section IV.4 and resonant ESWLS formulated with modal inertial loads, see Section IV.5. From our point of view, this method remains in the literature so far the best option to compute ESWLS for structures with a dynamic behavior. The method is relevant for structures responding in several, eventually coupled, modes. Even if the method was originally presented for the buffeting response of bridges it is in fact general.

**Original demonstration** The nodal background modal resonant (hybrid) analysis is performed and the variance of the  $i$ -th structural response is derived from

$$\sigma_{r_i}^2 = \sigma_{r_i^b}^2 + \sigma_{r_i^r}^2, \tag{IV.6.1}$$

considering a timescale separation, i.e., the mixed background/resonant contributions are negligible, see Sections II.6.3 and II.7. Using (IV.6.1), the  $i$ -th envelope value  $r_i^{(m)} = g_i^{(m)} \sigma_{r_i}$ , is expressed by

$$\begin{aligned}
r_i^{(m)} &= g_i^{(m)} \sqrt{\sigma_{r_i^b}^2 + \sigma_{r_i^r}^2}, \\
&= \left( w_i^b g_i^{(m)} \sigma_{r_i^b} + w_i^r g_i^{(m)} \sigma_{r_i^r} \right), \\
&= \mathbf{L}_{i_o} \mathbf{f}_{(i)}^{(\mathcal{L}^b \mathcal{M}^r, m)}, \tag{IV.6.2}
\end{aligned}$$

where  $w_i^b$  and  $w_i^r$  are structural factors given by

$$w_i^b = \frac{\sigma_{r_i^b}}{\sigma_{r_i}} \quad , \quad w_i^r = \frac{\sigma_{r_i^r}}{\sigma_{r_i}}. \quad (\text{IV.6.3})$$

The symbol “ $\mathcal{L}^b\mathcal{M}^r$ ” stands for “ $\mathcal{L}$ oad” (-response correlation method) for the “background” contribution and “ $\mathcal{M}$ odal” (interial loads) for the “resonant” contribution. The hybrid-based ESWL ( $\mathbf{f}^{(e,m)} \equiv \mathbf{f}^{(\mathcal{L}^b\mathcal{M}^r,m)}$ ) in (IV.6.2) is expressed as a weighted combination of LRC-based and MIL-based ESWLs, such as

$$\mathbf{f}_{(i)}^{(\mathcal{L}^b\mathcal{M}^r,m)} = \mathbf{f}_{(i)}^{(\mathcal{L}^b,m)} + \mathbf{f}_{(i)}^{(\mathcal{M}^r,m)}. \quad (\text{IV.6.4})$$

The LRC-based ESWL targets the background contribution of the structural response

$$\mathbf{f}_{k(i)}^{(\mathcal{L}^b,m)} = \sum_{m=1}^{n_c} F_{km}^{(C)} W_{mi}^{(\mathcal{L}^b,m)}, \quad (\text{IV.6.5})$$

with the weighting factors given by

$$W_{mi}^{(\mathcal{L}^b,m)} = w_i^b \left( \frac{g_i^{(m)}}{\sigma_{r_i^b}} \lambda_m^c \sum_{j=1}^{n_l} B_{ij} P_{jm}^{(C)} \right). \quad (\text{IV.6.6})$$

The MIL-based ESWL targets the resonant (and not the dynamic here) contribution ( $\mathbf{f}^{(e,m)} \equiv \mathbf{f}^{(\mathcal{M}^r,m)}$ ) of the structural response and we have

$$\mathbf{f}_{k(i)}^{(\mathcal{M}^r,m)} = \sum_{m=1}^{n_m} F_{km}^{(\mathcal{M})} W_{mi}^{(\mathcal{M}^r,m)}, \quad (\text{IV.6.7})$$

with the weighting factors that read

$$W_{mi}^{(\mathcal{M}^r,m)} = w_i^r \left( \sum_{n=1}^{n_m} g_i^{(m)} \mathbf{L}_{i \circ} \mathbf{F}_n^{(\mathcal{M})} \frac{\sigma_{q_m^r} q_n^r}{\sigma_{r_i^r}} \right). \quad (\text{IV.6.8})$$

## IV.7 Conditional Expected Load method

This section presents the Conditional Expected Load method (CEL) as a unique formulation for structures with (i) various dynamical behaviors, from background to resonant, (ii) analyzed in nodal, or hybrid basis, (iii) in a Gaussian or non-Gaussian framework and (iv) without the assumption of timescale separation. In a Gaussian framework, the proposed method develops the LRC-based ESWLs for quasi-static structural behavior, and the hybrid-based ESWLs for structures with resonant behaviors if there is a clear timescale separation. For the latter case, the proposed formulation does not require separating background and resonant contributions of the ESWL. After the structural analysis is performed, the elastic forces (II.4.3) are the relevant quantities to establish CEL-based ESWLs.

### IV.7.1 Conditional Expected Static Wind Load

Chen and Zhou (2007) stressed that “The load distribution for a given peak response is not necessarily unique simply because that multiple load distributions can result in an identical response.”

The uniqueness of the equivalent static wind load is not ensured by the envelope value and non-overestimation conditions (IV.2.3) and (IV.2.4), respectively. Moreover, even completely unrealistic distributions of elastic forces may satisfy them without being plausible at all. Thinking with possible realisations, there exists an infinite collection of distributions of elastic forces producing static responses satisfying the envelope value condition. To all these plausible static elastic loads might be attributed a certain likelihood, which is measured here as the conditional multivariate PDF of the elastic forces given the structural response  $r_i$

$$\psi_{\mathbf{f}^e|r_i}(\mathbf{f}_1^e, \dots, \mathbf{f}_{n_t}^e, r_i) = \frac{\psi_{\mathbf{f}^e r_i}(\mathbf{f}_1^e, \dots, \mathbf{f}_{n_t}^e, r_i)}{\psi_{r_i}(r_i)}, \quad (\text{IV.7.1})$$

where  $\psi_{\mathbf{f}^e r_i}(\mathbf{f}_1^e, \dots, \mathbf{f}_{n_t}^e, r_i)$  is the joint  $n_t+1$ -dimensional PDF of the elastic forces and the considered structural response and  $\psi_{r_i}(r_i)$  is the marginal PDF of the considered structural response. We introduce the Conditional Expected Static Wind Load (CESWL) as the average of these plausible elastic forces conditioned upon recovery of the considered response. Mathematically, it is defined by

$$\mathbf{f}^{(\mathcal{E},m)} = \mathbb{E} \left[ \mathbf{f}^e | r_i = r_i^{(m)} \right] = \mu_{\mathbf{f}^e|r_i}(r_i^{(m)}), \quad (\text{IV.7.2})$$

where the symbol “ $\mathcal{E}$ ” stands for “conditional  $\mathcal{E}$ xpected value” and the  $k$ -th component of the conditional expected static wind load is simply obtained as

$$\mu_{f_k^e|r_i}(r_i^{(m)}) = \int_{\mathbb{R}} f_k^e \psi_{\mathbf{f}^e|r_i}(\mathbf{f}_k^e, r_i^{(m)}) df_k^e, \quad (\text{IV.7.3})$$

where  $\psi_{f_k^e|r_i}(\mathbf{f}_k^e, r_i^{(m)})$  is the conditional PDF of the  $k$ -th elastic force given the  $i$ -th envelope value  $r_i = r_i^{(m)}$ . The PDF of the elastic force  $f_k^e$  conditioned on the structural response  $r_i$  is obtained by a multi-fold integration of the conditional multivariate PDF (IV.7.1) with respect to all other elastic forces

$$\psi_{f_k^e|r_i}(\mathbf{f}_k^e, r_i) = \int_{-\infty}^{\infty} \dots \int_{-\infty}^{\infty} \psi_{\mathbf{f}^e|r_i}(\mathbf{f}_1^e, \dots, \mathbf{f}_{n_t}^e, r_i) df_1^e \dots df_{k-1}^e df_{k+1}^e \dots df_{n_t}^e. \quad (\text{IV.7.4})$$

As such, each component of the CESWL (IV.7.3) might be derived from the sole knowledge of the conditional distribution (IV.7.4) of each elastic force given a structural response.

The loading given by (IV.7.2) is such that the corresponding static response  $\mathbf{r}^{(\mathcal{E},m)} = \mathbf{L}\mathbf{f}^{(\mathcal{E},m)}$  satisfies the envelope value condition

$$\mathbf{r}_i^{(\mathcal{E},m)} = \sum_{k=1}^{n_l} L_{ik} \mathbf{f}_k^{(\mathcal{E},m)} = \sum_{k=1}^{n_l} L_{ik} \mathbb{E} \left[ \mathbf{f}_k^e | r_i = r_i^{(m)} \right] = \mathbb{E} \left[ \left( \sum_{k=1}^{n_l} L_{ik} \mathbf{f}_k^e \right) | r_i = r_i^{(m)} \right] \quad (\text{IV.7.5})$$

$$= \mathbb{E} \left[ r_i | r_i = r_i^{(m)} \right] = r_i^{(m)}, \quad (\text{IV.7.6})$$

as a consequence of the linearity of the structural behaviour. Also, the non-overestimation condition is an inherent feature of the conditional expected static wind load since we have

$$r_j^{(\min)} \leq \mathbb{E} \left[ r_j | r_i = r_i^{(m)} \right] \leq r_j^{(\max)}, \quad \forall j \in [1, n_r], \quad (\text{IV.7.7})$$

where  $\mathbb{E} \left[ r_j | r_i = r_i^{(m)} \right]$  is the average of the  $j$ -th response conditioned on  $r_i = r_i^{(m)}$ . In a Gaussian-context, Eq. (IV.7.7) reads

$$g_j^{(\min)} \leq g_i^{(m)} \rho_{r_j r_i} \leq g_j^{(\max)}, \quad \forall j \in [1, n_r]. \quad (\text{IV.7.8})$$

Because of the properties (IV.7.5) and (IV.7.7), the envelope value and non-overestimation conditions are in theory fulfilled and the *Conditional Expected Static Wind Load* introduced in (IV.7.2) is a formal kind of ESWL, that is readily applicable in non-Gaussian frameworks.

### Conditional expected aerodynamic pressures

For a quasi-static structural behavior, elastic loads  $\mathbf{f}^e(t)$  are equal to the external nodal forces  $\mathbf{f}(t)$  that can be directly obtained from aerodynamic pressures  $\mathbf{p}(t)$ . If the conditional PDF  $\psi_{\mathbf{p}_k | r_i}(\mathbf{p}_k, r_i^{(m)})$  of the  $k$ -th aerodynamic pressure  $\mathbf{p}_k$  given the  $i$ -th structural response  $r_i^{(m)}$  is known, then the conditional mean value found as

$$\mu_{\mathbf{p}_k | r_i^{(m)}} = \int_{\mathbb{R}} \mathbf{p}_k \psi_{\mathbf{p}_k | r_i}(\mathbf{p}_k, r_i^{(m)}) d\mathbf{p}_k, \quad (\text{IV.7.9})$$

gives the  $k$ -th component of the conditional expected SWL

$$\boxed{\mathbf{p}_{k(i)}^{(\mathcal{E},m)} = \mu_{\mathbf{p}_k | r_i^{(m)}}}, \quad (\text{IV.7.10})$$

in terms of the aerodynamic pressures.

The definition (IV.7.3) is central for the following developments and provides the essential information to extend the classical notions of ESWL in a non-Gaussian framework in Section IV.8. Indeed, this kind of static wind load that Kasperski (1992) and Chen and Kareem (2001) are used to call “[...] *the most probable load* [...]” must actually be understood as the expected load conditioned upon recovery of the considered response. In the Gaussian framework this does not make any difference; it is however of paramount importance in a non-Gaussian one. Extension of “the most probable load” to the non Gaussian setting is therefore seen as the mean, not the mode (most probable), nor the median. Finally, it is worth noticing that the probabilistic definition of a conditional expected SWL is unique, in the sense of the envelope value condition.

### IV.7.2 Gaussian framework

Assuming Gaussian elastic forces and structural responses, the  $k$ -th component of the conditional expected SWL ( $\mathbf{f}^{(e,m)} \equiv \mathbf{f}^{(\mathcal{E}^{\mathcal{N}},m)}$ ) is known in a closed-form as

$$\boxed{\mathbf{f}_{k(i)}^{(\mathcal{E}^{\mathcal{N}},m)} = \mu_{\mathbf{f}_k^e | \mathbf{r}_i^{(m)}}^{\mathcal{N}} = \frac{\mathbf{r}_i^{(m)}}{\sigma_{\mathbf{r}_i}} \rho_{\mathbf{f}_k^e \mathbf{r}_i} \sigma_{\mathbf{f}_k^e} = \mathbf{g}_i^{(m)} \rho_{\mathbf{f}_k^e \mathbf{r}_i} \sigma_{\mathbf{f}_k^e}}, \quad (\text{IV.7.11})$$

where the Gaussian conditional mean value  $\mu_{\mathbf{f}_k^e | \mathbf{r}_i^{(m)}}^{\mathcal{N}}$  is derived from (II.2.20) with  $x \equiv \mathbf{f}_k^e$ ,  $y \equiv \mathbf{r}_i^{(m)}$  and  $\rho_{\mathbf{f}_k^e \mathbf{r}_i}$ , the correlation coefficient between the  $k$ -th elastic force and the  $i$ -th structural response (see Section IV.7.4). The symbol “ $\mathcal{E}^{\mathcal{N}}$ ” stands for CEL-based ESWLs in a Gaussian context.

The  $j$ -th structural response under the conditional expected SWL that targets the  $i$ -th envelope value  $\mathbf{r}_i^{(m)}$  is found as

$$\mathbf{r}_{j(i)}^{(\mathcal{E}^{\mathcal{N}},m)} = \sum_{k=1}^{n_t} \mathbf{L}_{jk} \left( \mathbf{g}_i^{(m)} \sum_{l=1}^{n_t} \mathbf{L}_{il} \rho_{\mathbf{f}_k^e \mathbf{f}_l^e} \sigma_{\mathbf{f}_k^e} \sigma_{\mathbf{f}_l^e} \frac{1}{\sigma_{\mathbf{r}_i}} \right) = \mathbf{g}_i^{(m)} \rho_{\mathbf{r}_j \mathbf{r}_i} \sigma_{\mathbf{r}_j} = \mu_{\mathbf{r}_j | \mathbf{r}_i^{(m)}}^{\mathcal{N}}. \quad (\text{IV.7.12})$$

The previous equation means that the  $j$ -th structural response  $\mathbf{r}_{j(i)}^{(\mathcal{E}^{\mathcal{N}},m)}$  under  $\mathbf{f}_{(i)}^{(\mathcal{E}^{\mathcal{N}},m)}$  takes its value in average conditioned on  $\mathbf{r}_i = \mathbf{r}_i^{(m)}$ . In other words, the conditional expected SWL associated with the  $i$ -th structural response provides the values in average of all other structural responses conditioned on the target envelope value. As a consequence, the non-overestimation condition reads

$$\mathbf{g}_j^{(\min)} \leq \mathbf{g}_i^{(m)} \rho_{\mathbf{r}_j \mathbf{r}_i} \leq \mathbf{g}_j^{(\max)} \quad \forall j \in [1, n_r], \quad (\text{IV.7.13})$$

which is satisfied if a unique peak factor is considered for all structural responses. As seen in Chapter III, peak factors are different for each structural response (unless they are perfectly correlated) and therefore (IV.7.13) is not naturally fulfilled. A unique peak factor may be a good approximation for Gaussian processes since the range of variation should be rather low but cannot be stated for non-Gaussian processes.

### IV.7.3 Non-Gaussian framework

The derivation of the conditional expected SWL requires the conditional PDF  $\psi_{\mathbf{f}_k^e | \mathbf{r}_i}(x)$  of the  $k$ -th elastic force  $\mathbf{f}_k^e$  conditioned on the  $i$ -th structural response  $\mathbf{r}_i$  written as

$$\psi_{\mathbf{f}_k^e | \mathbf{r}_i}(x) = \frac{\psi_{\mathbf{f}_k^e \mathbf{r}_i}(x, y)}{\psi_{\mathbf{r}_i}(y)}, \quad (\text{IV.7.14})$$

where  $\psi_{\mathbf{f}_k^e \mathbf{r}_i}(x, y)$  is their joint PDF and  $\psi_{\mathbf{r}_i}(y)$  is the marginal PDF for the  $i$ -th structural response. As a matter of fact, any non-Gaussian formulation of a conditional expected SWL ( $\mathbf{f}^{(e,m)} \equiv \mathbf{f}^{(\mathcal{E},m)}$ ) can only be an approximation of the actual one, since the methods used to estimate the marginal, joint and conditional PDFs of non-Gaussian processes can only be approximations of the real ones. The symbol “ $\mathcal{E}$ ” stands for CEL-based ESWLs in a non-Gaussian context.

At this stage two distinct approaches may be pointed out. A class of methods consists in non-parametric estimations of these PDFs, for instance, through the maximum entropy method (Shannon and Weaver, 1948; Lang and Mathematician, 1987) or the recourse to kernel density estimation (Rosenblatt, 1956; Azzalini and Bowman, 1997). Another class collects the methods seeking parametric estimations of PDFs. This latter category is adopted in Section IV.8 since our purpose is to find a closed-form estimation for the conditional mean value.

### The bicubic translation model

In Section IV.8 is derived a parametric “*bicubic translation*” model for the joint and conditional PDFs. With this model the  $k$ -th component of the conditional expected SWL ( $\mathbf{f}^{(e,m)} \equiv \mathbf{f}^{(\mathcal{E}^{\mathcal{B}},m)}$ ) targeting the  $i$ -th envelope value  $r_i^{(m)}$  is defined as

$$\boxed{f_{k(i)}^{(\mathcal{E}^{\mathcal{B}},m)} = \mu_{f_k^e|r_i^{(m)}}^{\mathcal{B}}}, \quad (\text{IV.7.15})$$

where  $\mu_{f_k^e|r_i^{(m)}}^{\mathcal{B}}$  is given by (IV.8.8) with  $x \equiv f_k^e$  and  $y \equiv r_i^{(m)}$ . The symbol “ $\mathcal{E}^{\mathcal{B}}$ ” stands for CEL-based ESWLs in a non-Gaussian context computed with the “ $\mathcal{B}$ icubic” model.

#### IV.7.4 Covariance matrix of elastic forces

In order to establish conditional expected SWLs with the CEL-method, the standard deviation of elastic forces and correlation between elastic forces and structural responses are required. The covariance matrix of elastic forces, that reads

$$\Sigma^{\mathbf{f}^e}, \quad (\text{IV.7.16})$$

must be computed first and from (II.4.10), the cross-covariance matrix between structural responses and elastic forces is derived from

$$\Sigma^{\mathbf{r}^{\mathbf{f}^e}} = \mathbf{L}\Sigma^{\mathbf{f}^e}. \quad (\text{IV.7.17})$$

The correlation coefficient between the  $k$ -th elastic force and the  $i$ -th structural response is written

$$\rho_{f_k^e r_i} = \sum_{l=1}^{n_l} L_{il} \rho_{f_k^e f_l^e} \sigma_{f_l^e} / \sigma_{r_i}. \quad (\text{IV.7.18})$$

Two formulations providing the covariance matrix of elastic forces  $\Sigma^{\mathbf{f}^e}$ , to use in (IV.7.17), are detailed next.

##### Formulation 1

Using (II.4.3), the elastic forces are expressed as

$$\mathbf{f}^e = \mathbf{K}\mathbf{x}, \quad (\text{IV.7.19})$$

and the covariance matrix of elastic forces is derived from

$$\Sigma^{\mathbf{f}^e} = \mathbf{K}\Sigma^{\mathbf{x}}\mathbf{K}^T. \quad (\text{IV.7.20})$$

Equation (IV.7.20) requires the covariance matrix  $\Sigma^{\mathbf{x}}$  that is computed according to the type of analysis performed (see Section II.6). The full nodal or nodal background modal resonant (hybrid) analyses are recommended. In a full modal analysis, even if the background contribution of structural responses is accurately evaluated, computing the contribution of the applied forces  $\mathbf{f}$  to the elastic forces  $\mathbf{f}^e$  demands more modes than the structural analysis does. This is illustrated in Chapter VI. To avoid this issue a second formulation is introduced.

### Formulation 2

Using equations (II.4.4)-(II.4.5)-(II.4.6), the covariance matrix  $\Sigma^{\mathbf{f}^e}$  may be also derived from

$$\begin{aligned} \Sigma^{\mathbf{f}^e} &= \Sigma^{\mathbf{f}} + \Sigma^{\mathbf{f}^i} + \Sigma^{\mathbf{f}^d} + \Sigma^{\mathbf{f}^e} + \Sigma^{\mathbf{f}^e} \\ &= \Sigma^{\mathbf{f}} + \Sigma^{\mathbf{f}\ddot{\mathbf{x}}}\mathbf{M}^T + \mathbf{M}\Sigma^{\ddot{\mathbf{x}}\mathbf{f}} + \mathbf{M}\Sigma^{\ddot{\mathbf{x}}}\mathbf{M}^T + \mathbf{C}\Sigma^{\mathbf{x}}\mathbf{C}^T, \end{aligned} \quad (\text{IV.7.21})$$

and the covariance matrices  $\Sigma^{\mathbf{x}}$  and  $\Sigma^{\ddot{\mathbf{x}}}$  may be computed in a nodal or modal basis, see Sections II.6.1 and II.5, respectively.

This second formulation has the advantage to include, naturally, the exact contribution of the applied forces  $\mathbf{f}$  to the elastic forces  $\mathbf{f}^e$ , no matter the type of analysis performed. Also, the contributions from the damping and inertial forces as well as cross terms between the wind forces  $\mathbf{f}$  and the inertial forces  $\mathbf{f}^i$  are enhanced. Equation (IV.7.21) contains many terms. With the objective to simplify this expression, their relative contributions to the covariance matrix of elastic forces are studied next.

**Damping forces** As a matter of fact, the damping forces are usually assumed to be small compared to inertial forces and therefore disregarded (Dickens et al., 1997). In the modal basis, the study of the relative magnitude of damping and inertial forces can be conducted. Assuming the damping to be proportional, the modal damping matrix is diagonal and reads

$$\mathbf{D} = \text{diag}(2\xi_j\omega_j), \quad (\text{IV.7.22})$$

and using the resulting property (II.5.19), damping and inertial forces read

$$\mathbf{f}^d = \mathbf{M}\Phi\mathbf{D}\dot{\mathbf{q}}, \quad (\text{IV.7.23})$$

$$\mathbf{f}^i = \mathbf{M}\Phi\ddot{\mathbf{q}}. \quad (\text{IV.7.24})$$

The modes of vibration have been derived from a generalized eigenvalue problem (II.5.1), rewritten here as

$$\mathbf{K}\Phi = \mathbf{M}\Phi\Omega, \quad (\text{IV.7.25})$$

with  $\Omega = \text{diag}(\omega_j^2)$ , so that the modal inertial loads (II.5.11) also read

$$\mathbf{F}^{(\mathcal{M})} = \mathbf{M}\Phi\Omega, \quad (\text{IV.7.26})$$



and inserting (IV.7.26) into (IV.7.23) and (IV.7.24), damping and inertial forces are found as

$$\mathbf{f}^d = \mathbf{F}^{(\mathcal{M})} \Omega^{-1} \mathbf{D} \dot{\mathbf{q}} = \mathbf{F}^{(\mathcal{M})} \mathbf{W}^d, \quad (\text{IV.7.27})$$

$$\mathbf{f}^i = \mathbf{F}^{(\mathcal{M})} \Omega^{-1} \ddot{\mathbf{q}} = \mathbf{F}^{(\mathcal{M})} \mathbf{W}^i, \quad (\text{IV.7.28})$$

with  $\mathbf{W}^d = \Omega^{-1} \mathbf{D} \dot{\mathbf{q}}$  and  $\mathbf{W}^i = \Omega^{-1} \ddot{\mathbf{q}}$ , the weighting factors of modal inertial loads for the damping and inertial forces, respectively. Based on (IV.7.27) and (IV.7.28), the covariance matrices of  $\mathbf{f}^d$  and  $\mathbf{f}^i$  are expressed as

$$\Sigma^{\mathbf{f}^d} = \mathbf{F}^{(\mathcal{M})} \Sigma^{\mathbf{W}^d} (\mathbf{F}^{(\mathcal{M})})^\top, \quad (\text{IV.7.29})$$

$$\Sigma^{\mathbf{f}^i} = \mathbf{F}^{(\mathcal{M})} \Sigma^{\mathbf{W}^i} (\mathbf{F}^{(\mathcal{M})})^\top, \quad (\text{IV.7.30})$$

with

$$\Sigma^{\mathbf{W}^d} = \Omega^{-1} \mathbf{D} \Sigma^{\dot{\mathbf{q}}} \mathbf{D}^\top \Omega^{-1}, \quad \Sigma^{\mathbf{W}^i} = \Omega^{-1} \Sigma^{\ddot{\mathbf{q}}} \Omega^{-1}.$$

The  $(m, n)$  entries of covariance matrices  $\Sigma^{\dot{\mathbf{q}}}$  and  $\Sigma^{\ddot{\mathbf{q}}}$  are derived from the  $(m, n)$  entries of covariance matrix  $\Sigma^{\mathbf{q}^f}$  as (II.7.35)

$$\Sigma_{mn}^{\dot{\mathbf{q}}} = \omega_m \omega_n \Sigma_{mn}^{\mathbf{q}^f}, \quad \Sigma_{mn}^{\ddot{\mathbf{q}}} = \omega_m^2 \omega_n^2 \Sigma_{mn}^{\mathbf{q}^f}. \quad (\text{IV.7.31})$$

Using (IV.7.31) and (IV.7.22), the  $(m, n)$  entries of covariance matrices of weighting factors  $\Sigma^{\mathbf{W}^d}$  and  $\Sigma^{\mathbf{W}^i}$  are derived from

$$\Sigma_{mn}^{\mathbf{W}^d} = \Omega_{mm}^{-1} \mathbf{D}_{mm} \Sigma_{mn}^{\dot{\mathbf{q}}} \mathbf{D}_{nn} \Omega_{nn}^{-1} = 4 \xi_m \xi_n \omega_m^{-1} \omega_n^{-1} \Sigma_{mn}^{\dot{\mathbf{q}}} = 4 \xi_m \xi_n \Sigma_{mn}^{\mathbf{q}^f}, \quad (\text{IV.7.32})$$

$$\Sigma_{mn}^{\mathbf{W}^i} = \Omega_{mm}^{-1} \Sigma_{mn}^{\ddot{\mathbf{q}}} \Omega_{nn}^{-1} = \Sigma_{mn}^{\mathbf{q}^f}, \quad (\text{IV.7.33})$$

and finally a relation of  $1/(4\xi_m \xi_n)$  between  $\Sigma_{mn}^{\mathbf{W}^i}$  and  $\Sigma_{mn}^{\mathbf{W}^d}$  is highlighted. For usual damping coefficients, the belief that damping forces are negligible compared to inertial forces is thus demonstrated. For example, with damping coefficients  $\xi_m = \xi_n = 1\%$ , the entries  $\Sigma_{mn}^{\mathbf{W}^i}$  are  $2.5 \cdot 10^3$  greater than  $\Sigma_{mn}^{\mathbf{W}^d}$ . Therefore, (IV.7.21) is simplified as

$$\begin{aligned} \Sigma^{\mathbf{f}^e} &\simeq \Sigma^{\mathbf{f}} + \Sigma^{\mathbf{f}^i} + \Sigma^{\mathbf{f}^i \mathbf{f}} + \Sigma^{\mathbf{f}^i}, \\ &\simeq \Sigma^{\mathbf{f}} + \Sigma^{\mathbf{f} \ddot{\mathbf{x}}} \mathbf{M}^\top + \mathbf{M} \Sigma^{\ddot{\mathbf{x}} \mathbf{f}} + \mathbf{M} \Sigma^{\ddot{\mathbf{x}}} \mathbf{M}^\top. \end{aligned} \quad (\text{IV.7.34})$$

**Cross term between inertial forces  $\mathbf{f}^i$  and wind forces  $\mathbf{f}$**  The covariance matrix of inertial and wind forces is expressed by

$$\Sigma^{\mathbf{f}^i \mathbf{f}} = \mathbf{M} \Sigma^{\ddot{\mathbf{x}} \mathbf{f}}. \quad (\text{IV.7.35})$$

In a modal basis, the cross-PSD matrix of nodal accelerations and wind forces is given by

$$\mathbf{S}^{\ddot{\mathbf{x}} \mathbf{f}} = \Phi \mathbf{S}^{\ddot{\mathbf{q}} \mathbf{f}}, \quad (\text{IV.7.36})$$

and the  $(m, i)$  entries of the cross-PSD matrix of modal accelerations and nodal forces is found as

$$\begin{aligned} S_{mi}^{\ddot{\mathbf{q}}\mathbf{f}} &= -\omega^2 \mathcal{H}_{mm} S_{mi}^{\mathbf{g}\mathbf{f}}, \\ &= -\omega^2 \mathcal{H}_{mm} \Phi_m^\top S_{oi}^{\mathbf{f}}. \end{aligned} \quad (\text{IV.7.37})$$

A full integration of  $\mathbf{S}^{\ddot{\mathbf{q}}\mathbf{f}}$  is required to finally obtain the cross-covariance matrix of inertial and wind forces as

$$\Sigma^{\mathbf{f}^i\mathbf{f}} = \mathbf{M}\Phi\Sigma^{\ddot{\mathbf{q}}\mathbf{f}}. \quad (\text{IV.7.38})$$

Therefore, from a computational point of view, formulation 1 should be preferred.

**Timescale separation condition** Considering a timescale separation, the timescales associated with wind forces are expected to be significantly different from timescales of inertial forces. Under this condition, cross term between inertial forces  $\mathbf{f}^i$  and wind forces  $\mathbf{f}$  are neglected and the covariance matrix  $\Sigma^{\mathbf{f}^e}$  given by (IV.7.34) is further simplified as

$$\begin{aligned} \Sigma^{\mathbf{f}^e} &\simeq \Sigma^{\mathbf{f}} + \Sigma^{\mathbf{f}^i}, \\ &\simeq \Sigma^{\mathbf{f}} + \mathbf{M}\Sigma^{\ddot{\mathbf{x}}}\mathbf{M}^\top, \end{aligned} \quad (\text{IV.7.39})$$

with assumption of proportional damping.

## IV.7.5 Review of the LRC-, CST-, MIL- and hybrid-based methods in the perspective of the CEL method

In the light of the definition of a conditional expected SWL (IV.7.2), classic methods to compute ESWLs are next reviewed. A straightforward extension of the common conditional sampling technique to structures with a dynamic behavior is derived. However, it appears that this technique does not provide the conditional expected SWL in a non-Gaussian framework. Also, it is demonstrated that LRC-, MILs- and hybrid-based ESWLs are particular cases of conditional expected SWLs derived from the CEL method in a Gaussian context.

### Review of the LRC-based ESWLs

- The LRC-based ESWL, described in Section IV.4, is the conditional expected SWL, i.e.,  $\mathbf{p}^{(\mathcal{L},m)} = \mathbf{p}^{(\mathcal{E}^{\mathcal{N}},m)}$  in a Gaussian framework. From (IV.7.10), the  $k$ -th component of the LRC-based ESWL targeting the  $i$ -th envelope value  $r_i^{(m)}$  in a Gaussian framework is then alternatively given by

$$p_{k(i)}^{(\mathcal{L},m)} = \mu_{p_k|r_i^{(m)}}^{\mathcal{N}} = \frac{r_i^{(m)}}{\sigma_{r_i}} \rho_{p_k r_i} \sigma_{p_k} = g_i^{(m)} \rho_{p_k r_i} \sigma_{p_k}, \quad (\text{IV.7.40})$$

where  $\mu_{p_k|r_i^{(m)}}^{\mathcal{N}} = g_i^{(m)} \rho_{p_k r_i} \sigma_{p_k}$  is derived from Equation (II.2.20) with  $x \equiv p_k$  and  $y \equiv r_i^{(m)}$  and the correlation  $\rho_{p_k r_i}$  is expressed by

$$\rho_{p_k r_i} = \sum_{l=1}^{n_l} B_{il} \rho_{p_k p_l} \frac{\sigma_{p_l}}{\sigma_{r_i}}. \quad (\text{IV.7.41})$$

- The LRC-based ESWLs may be expressed using linear combinations of a small number of CPT loading modes. An alternative formulation is given here which brings the meaning of the weighting factors of each CPT loading mode applied to have any ESWL. Using (II.8.2), the correlation coefficient between aerodynamic pressures and structural responses is expanded as

$$\begin{aligned}
\rho_{p_k r_i} &= E[p_k(t)r_i(t)]/(\sigma_{p_k}\sigma_{r_i}), \\
&= E\left[\sum_{m=1}^{n_c} P_{km}^{(C)} a_m(t)r_i(t)\right]/(\sigma_{p_k}\sigma_{r_i}), \\
&= \sum_{m=1}^{n_c} E[P_{km}^{(C)} a_m(t)r_i(t)]/(\sqrt{\lambda_m^c}\sigma_{r_i}) \sqrt{\lambda_m^c}/\sigma_{p_k}, \\
&= \sum_{m=1}^{n_c} P_{km}^{(C)} \rho_{a_m r_i} \sqrt{\lambda_m^c}/\sigma_{p_k},
\end{aligned} \tag{IV.7.42}$$

with  $\rho_{a_m r_i} = E[a_m(t)r_i(t)]/(\sqrt{\lambda_m^c}\sigma_{r_i})$  the correlation coefficient between the  $m$ -th principal component and the  $i$ -th structural response. The LRC-based ESWL is rewritten as

$$P_{k(i)}^{(\mathcal{L}^c, m)} = \mu_{p_k | r_i^{(m)}}^{\mathcal{N}} = \sum_{m=1}^{n_c} P_{km}^{(C)} \mu_{a_m | r_i^{(m)}}^{\mathcal{N}}, \tag{IV.7.43}$$

where  $\mu_{a_m | r_i^{(m)}}^{\mathcal{N}}$  is the conditional mean value of the  $m$ -th principal component given  $r_i^{(m)}$ , expressed by

$$\mu_{a_m | r_i^{(m)}}^{\mathcal{N}} = g_i^{(m)} \rho_{a_m r_i} \sqrt{\lambda_m^c}, \tag{IV.7.44}$$

which is equal to the weighting factors (IV.4.5), i.e.,

$$\mu_{a_m | r_i^{(m)}}^{\mathcal{N}} = W_{mi}^{(C, m)}. \tag{IV.7.45}$$

With this alternative formulation, the meaning of the weighting factors for each CPT loading mode appears clearly: they are equal to the conditional expected value given a structural response. Note this probabilistic meaning is not valid in a non-Gaussian framework where (IV.7.10) cannot be written as

$$P_{k(i)}^{(\mathcal{E}, m)} = \mu_{p_k | r_i^{(m)}} \neq \sum_{m=1}^{n_c} P_{km}^{(C)} \mu_{a_m | r_i^{(m)}}. \tag{IV.7.46}$$

### Review of the CST-based ESWLs

- In the common conditional sampling technique, discussed in Section IV.3, the average is made on load patterns producing the extreme values  $r_i^{(\text{ext})}(t_k)$  on each observation window, each one being different from the envelope value, i.e.,  $r_i^{(\text{ext})}(t_k) \neq r_i^{(m)}$ . This has serious consequences on the convergence toward the conditional expected SWL. In a Gaussian framework, the conditional expected SWL  $\mathbf{p}_{(i)}^{(\mathcal{E}^{\mathcal{N}},m)} = \mathbf{p}_{(i)}^{(\mathcal{L},m)}$  associated with the  $i$ -th structural response is linear with respect to the value given to  $r_i$ , see (IV.7.40). Hence, if the peak factor computed is the actual one, i.e.,  $g_i^{(m)} = g_i^{(S,m)}$ , the formulation given by (IV.3.2) tends to the conditional expected SWL, i.e.,  $\mathbf{p}_{(i)}^{(S,m)} \Big|_{n_T \rightarrow \infty} = \mathbf{p}_{(i)}^{(\mathcal{E},m)}$ . In a non-Gaussian framework, the conditional expected SWL  $\mathbf{p}_{(i)}^{(\mathcal{E},m)}$  associated with the  $i$ -th structural response is nonlinear with respect to the value given to  $r_i$  and thus the loading  $\mathbf{p}_{(i)}^{(S,m)}$  does not converge toward the conditional expected SWL, i.e.,  $\mathbf{p}_{(i)}^{(S,m)} \Big|_{n_T \rightarrow \infty} \neq \mathbf{p}_{(i)}^{(\mathcal{E},m)}$ , even if  $g_i^{(m)} = g_i^{(S,m)}$ .
- The actual conditional sampling formulation of the ESWL ( $\mathbf{p}^{(e,m)} \equiv \mathbf{p}^{(S^A,m)}$ ) should be

$$\mathbf{p}_{(i)}^{(S^A,m)} = \text{mean}_k \mathbf{p}_{(i)}^{(m)}(t_k), \quad k \in [1, n_t], \quad (\text{IV.7.47})$$

where  $\mathbf{p}_{(i)}^{(m)}(t_k)$  is a snapshot of the load distribution associated with the  $i$ -th envelope value of a structural response  $r_i^{(m)}$  sampled on the  $k$ -th observation window and occurring at time  $t_k$ . With this formulation and with a large number of observation windows, the loading  $\mathbf{p}_{(i)}^{(S^A,m)}$  tends to the conditional expected SWL, i.e.,  $\mathbf{p}_{(i)}^{(S^A,m)} \Big|_{n_T \rightarrow \infty} = \mathbf{p}_{(i)}^{(\mathcal{E},m)}$ . The method may be applied to non-Gaussian structural responses without limitation. However two drawbacks are pointed out: (i) the envelope value may not be reached during each observation window and (ii) due to the time discretization, the envelope value may not be exactly computed. These drawbacks due to the time sampling support the use of the common formulation described in Section IV.3.

- A straightforward extension of the common conditional sampling technique to structures with a dynamic behavior is next derived. On each observation window, extreme values of the target structural response are identified and the associated elastic forces are computed. The common sampling formulation of an ESWL ( $\mathbf{f}^{(e,m)} \equiv \mathbf{f}^{(S,m)}$ ) is then defined as the average of these sampled elastic forces

$$\mathbf{f}_{(i)}^{(S,m)} = \text{mean}_k \mathbf{f}_{(i)}^{\text{e},(\text{ext})}(t_k), \quad k \in [1, n_t], \quad (\text{IV.7.48})$$

where  $\mathbf{f}_{(i)}^{\text{e},(\text{ext})}(t_k)$  is the  $k$ -th elastic forces pattern associated with the extreme value  $r_i^{(\text{ext})}(t_k)$  of a structural response in the  $k$ -th observation window and occurring at time  $t_k$ . In case of proportional damping, the damping forces are negligible and the sampling formulation may be expressed as

$$\mathbf{f}_{(i)}^{(S,m)} = \text{mean}_k \mathbf{f}^{(\text{ext})}(t_k) + \text{mean}_k \mathbf{f}^{\text{i},(\text{ext})}(t_k), \quad k \in [1, n_t] \quad (\text{IV.7.49})$$

where  $\mathbf{f}_{(i)}^{(\text{ext})}(t_k)$  and  $\mathbf{f}_{(i)}^{\mathbf{i},(\text{ext})}(t_k)$  are respectively the  $k$ -th wind load pattern and the  $k$ -th inertial forces pattern associated with the extreme value  $r_i^{(\text{ext})}(t_k)$  of a structural response on the  $k$ -th observation window and occurring at time  $t_k$ .

### Review of the MIL-based ESWLs

- The MIL-based ESWL, described in Section IV.5, is the conditional expected SWL, i.e.,  $\mathbf{f}^{(\mathcal{M},m)} = \mathbf{f}^{(\mathcal{E}^{\mathcal{N}},m)}$  in a Gaussian framework. In a Gaussian framework, the  $k$ -th component of the ESWL (IV.7.2) can be differently expressed as

$$\mathbf{f}_{k(i)}^{(\mathcal{M},m)} = \mu_{\mathbf{f}_k^e | r_i^{(m)}}^{\mathcal{N}} = \sum_{m=1}^{n_m} \mathbf{F}_{km}^{(\mathcal{M})} \mu_{\mathbf{q}_m | r_i^{(m)}}^{\mathcal{N}}, \quad (\text{IV.7.50})$$

where  $\mu_{\mathbf{q}_m | r_i^{(m)}}^{\mathcal{N}}$  is the conditional mean value of the  $m$ -th modal amplitude given  $r_i^{(m)}$ , equal to the weighting factor (IV.5.7), i.e.,

$$\mu_{\mathbf{q}_m | r_i^{(m)}}^{\mathcal{N}} = \mathbf{W}_{mi}^{(\mathcal{M},m)}. \quad (\text{IV.7.51})$$

This probabilistic meaning is not valid in a non-Gaussian framework where (IV.7.2) cannot be written as

$$\mathbf{f}_{k(i)}^{(\mathcal{E},m)} = \mu_{\mathbf{f}_k^e | r_i^{(m)}}^{\mathcal{E}} \neq \sum_{m=1}^{n_m} \mathbf{F}_{km}^{(\mathcal{M})} \mu_{\mathbf{q}_m | r_i^{(m)}}. \quad (\text{IV.7.52})$$

### Review of the hybrid-based ESWLs

- In a Gaussian framework, the  $k$ -th component of the conditional expected SWL is expressed as

$$\mathbf{f}_{k(i)}^{(\mathcal{E}^{\mathcal{N}},m)} = \mu_{\mathbf{f}_k^e | r_i^{(m)}}^{\mathcal{N}} = \mathbf{g}_i^{(m)} \rho_{\mathbf{f}_k^e r_i} \sigma_{\mathbf{f}_k^e}, \quad (\text{IV.7.53})$$

with  $\rho_{\mathbf{f}_k^e r_i} = \text{E}[\mathbf{f}_k^e r_i] / (\sigma_{\mathbf{f}_k^e} \sigma_{r_i})$ . With the background/resonant decomposition, structural responses are written  $r_i = r_i^b + r_i^r$  and elastic forces are expressed as

$$\mathbf{f}_k^e = \mathbf{f}_k + \mathbf{f}_k^r, \quad (\text{IV.7.54})$$

where  $\mathbf{f}_k^r = -(\mathbf{f}_k^d + \mathbf{f}_k^i)$  is the resonant component of elastic forces that collects damping and inertial forces, see (II.4.4). The correlation coefficient between the  $k$ -th elastic force and the  $i$ -th structural response is expressed by

$$\begin{aligned} \rho_{\mathbf{f}_k^e r_i} \sigma_{\mathbf{f}_k^e} &= \text{E}[\mathbf{f}_k^e r_i] / \sigma_{r_i}, \\ &= \text{E}[(\mathbf{f}_k + \mathbf{f}_k^r)(r_i^b + r_i^r)] / \sigma_{r_i}, \\ &= (\text{E}[\mathbf{f}_k r_i^b] + \text{E}[\mathbf{f}_k r_i^r] + \text{E}[\mathbf{f}_k^r r_i^b] + \text{E}[\mathbf{f}_k^r r_i^r]) / \sigma_{r_i}, \\ &= \mathbf{w}_i^b \left( \rho_{\mathbf{f}_k r_i^b} \sigma_{\mathbf{f}_k} + \rho_{\mathbf{f}_k^r r_i^b} \sigma_{\mathbf{f}_k^r} \right) + \mathbf{w}_i^r \left( \rho_{\mathbf{f}_k r_i^r} \sigma_{\mathbf{f}_k} + \rho_{\mathbf{f}_k^r r_i^r} \sigma_{\mathbf{f}_k^r} \right), \end{aligned} \quad (\text{IV.7.55})$$

where  $w_i^b$  and  $w_i^r$  are structural factors defined by (IV.6.3). By substituting (IV.7.55) into (IV.7.53) and noticing that the LRC-based ESWL (IV.6.5) and MIL-based ESWL (IV.6.7) that target the background and resonant component of the  $i$ -th structural response, respectively, are alternatively expressed as

$$f_{k(i)}^{(\mathcal{L}^b, m)} = g_i^{(m)} w_i^b \rho_{f_k r_i^b} \sigma_{f_k} \quad , \quad f_{k(i)}^{(\mathcal{M}^r, m)} = g_i^{(m)} w_i^r \rho_{f_k r_i^r} \sigma_{f_k} \quad , \quad (\text{IV.7.56})$$

the conditional expected SWL (IV.7.53) may be given by

$$f_{k(i)}^{(\mathcal{E}^N, m)} = f_{k(i)}^{(\mathcal{L}^b \mathcal{M}^r, m)} + w_i^b \rho_{f_k r_i^b} \sigma_{f_k} + w_i^r \rho_{f_k r_i^r} \sigma_{f_k} \quad , \quad (\text{IV.7.57})$$

with  $f_{k(i)}^{(\mathcal{L}^b \mathcal{M}^r, m)}$  the hybrid-based ESWL expressed by (IV.6.4). With (IV.7.57), it is emphasized that the method proposed by Chen and Kareem (2001) neglects mixed background/resonant contributions brought by  $w_i^b \rho_{f_k r_i^b} \sigma_{f_k} + w_i^r \rho_{f_k r_i^r} \sigma_{f_k}$  since the method considered a timescale separation of background and resonant components.

## Summary

In a Gaussian framework, the two conditional expected SWLs for the minimum and maximum envelope values  $\mathbf{f}_{(i)}^{(\mathcal{E}^N, \min)}$  and  $\mathbf{f}_{(i)}^{(\mathcal{E}^N, \max)}$  only differ by their sign, i.e.,  $\mathbf{f}_{(i)}^{(\mathcal{E}^N, \min)} = -\mathbf{f}_{(i)}^{(\mathcal{E}^N, \max)}$  while in a non-Gaussian framework, they are different load patterns, i.e.,  $\mathbf{f}_{(i)}^{(\mathcal{E}, \min)} \neq -\mathbf{f}_{(i)}^{(\mathcal{E}, \max)}$ . However, it is emphasized that nothing prevents the use of the LRC-, MIL- and mixed-based ESWL formulation for non-Gaussian processes together with non-Gaussian peak factors (Tamura et al., 2002). In that case the following equality  $\frac{1}{g_i^{(\min)}} \mathbf{f}_{(i)}^{(e, \min)} = \frac{1}{g_i^{(\max)}} \mathbf{f}_{(i)}^{(e, \max)}$  holds. In this framework, the envelope value condition is still satisfied since this is a feature of the ‘‘Gaussian’’ formulation but these ESWLs are no longer the conditional expected ones.

Table IV.2 summarizes the features of the methods in the perspective of the conditional expected SWL and the envelope value condition.

| Framework       |   | Gaussian | Non-Gaussian | Gaussian        | Non-Gaussian | Structural behavior |
|-----------------|---|----------|--------------|-----------------|--------------|---------------------|
|                 |   | CESWL?   |              | Envelope value? |              |                     |
| LRC-based       | $\mathbf{p}^{(\mathcal{L})}$                | ✓        | -            | ✓               | ✓            | Quasi-static        |
| CST<br>(Common) | $\mathbf{p}^{(\mathcal{S})}$                | →        | ↔            | →               | ↔            | Quasi-static        |
|                 | $\mathbf{f}^{(\mathcal{S})}$                |          |              |                 |              | Dynamic             |
| Hybrid-based    | $\mathbf{f}^{(\mathcal{L}^b\mathcal{M}^r)}$ | ✓        | -            | ✓               | ✓            | Dynamic             |
| CEL-based       | $\mathbf{f}^{(\mathcal{E})}$                | ✓        | ✓            | ✓               | ✓            | Dynamic             |
| Gaussian        | $\mathbf{f}^{(\mathcal{E}^N)}$              | ✓        | -            | ✓               | ✓            | Quasi-static        |
| Bicubic model   | $\mathbf{f}^{(\mathcal{E}^B)}$              | ✓        | ≈            | ✓               | ✗            | Dynamic             |

Table IV.2: Overview of the features of the methods in the perspective of the conditional expected SWL and the envelope value condition. The symbols → and ↔ respectively mean that the formulation tends or not to the conditional expected SWL or tends or not to fulfill the envelope value condition as the number of observation windows increased. The symbol ≈ means that the formulation provides an estimation of the actual conditional expected SWL. The red cross symbol ✗ means that the envelope value condition (IV.2.3) is not necessarily satisfied.

Table IV.3 emphasizes cases where the non-overestimation condition is satisfied or not.

| Framework     |                                | Gaussian                      | Non-Gaussian |
|---------------|--------------------------------|-------------------------------|--------------|
|               |                                | Non-overestimation condition? |              |
| CEL-based     | $\mathbf{f}^{(\mathcal{E})}$   | ✓                             | ✓            |
| Gaussian      | $\mathbf{f}^{(\mathcal{E}^N)}$ | ✓                             | ✗            |
| Bicubic model | $\mathbf{f}^{(\mathcal{E}^B)}$ | ✓                             | ✗            |

Table IV.3: Non-overestimation condition assuming that the mean largest maximum (II.3.6) and the mean smallest minimum (II.3.8) are the actual ones in (IV.7.7). The red cross symbol ✗ means that the non-overestimation condition (IV.2.4) is not necessarily satisfied.

## IV.8 Non-Gaussian joint probability density function

In this Section, we propose a parametric model for the joint and conditional PDFs such that the “non-Gaussian” conditional expected SWL formulation seeks (i) *consistency*, the model should develop into the Gaussian formulation as a limit case, (ii) *applicability*, large ranges of non-Gaussianity in the random processes shall be covered, (iii) *accuracy* with available statistical information and (iv) *simplicity* of the analytical formulation. The latter ensures a computational efficiency which is required for the subsequent envelope reconstruction problem.

In this study, we consider the Hermite moment model introduced by Winterstein (1988) for the approximation of the PDF and discussed in Section II.3.2. We motivate this choice by several reasons. The model is convenient and well-known in the wind engineering community for different applications. Also, it is the cornerstone of the model for non-Gaussian peak factor developed by Kareem and Zhao (1994) which has a large applicability and accuracy. Finally, using this model for non-Gaussian peak factors, a consistent approach requires that the Hermite moment model should be kept for the PDF.

Driven by the definition we give of the conditional expected SWL, the establishment of a non-Gaussian formulation requires the conditional PDF of the loading given an envelope value. This implies to first derive a model of the joint PDF of the loads and responses and then the conditional PDF of the load, given a response.

In its domain of applicability and limitations, it is important to stress that the proposed model described hereinafter for the joint and conditional PDFs is utterly general in the sense that it could be applied to any set of two random processes. For example, one could want to derive the joint PDF of two structural responses or two loads.

**Joint probability density function** In order to provide a simple parametric joint PDF model between zero-mean non-Gaussian variables  $x$  and  $y$ , we model  $x$  and  $y$  as two cubic monotonic transformations, see (II.3.23), of two correlated standard Gaussian variables  $u$  and  $v$ , such as

$$x = g(u) = \frac{\alpha_u}{b_u} \left( \frac{u^3}{3} + a_u u^2 + (b_u - 1)u - a_u \right), \quad (\text{IV.8.1})$$

$$y = h(v) = \frac{\alpha_v}{b_v} \left( \frac{v^3}{3} + a_v v^2 + (b_v - 1)v - a_v \right), \quad (\text{IV.8.2})$$

provided the *monotone limitations*  $b_u - 1 - a_u^2 \geq 0$  and  $b_v - 1 - a_v^2 \geq 0$  for each random variable are fulfilled. The joint PDF is given by

$$\psi_{xy}^{\mathcal{B}}(x, y) = \frac{\psi_{uv}^{\mathcal{N}}(u(x), v(y))}{|J(u(x), v(y))|}, \quad (\text{IV.8.3})$$

where  $\psi_{uv}^{\mathcal{N}}(u, v)$  is the Gaussian joint PDF of  $u$  and  $v$  and  $J(u, v) = \frac{dg}{du} \frac{dh}{dv}$  is the Jacobian of the transformation (Papoulis, 1965). The cross-moments of the random variables  $x$  and  $y$  are defined by

$$\mathbb{E}[x^m y^n] = \iint_{\mathbb{R}^2} g(u)^m h(v)^n \psi^{\mathcal{N}}(u, v) \, du dv, \quad (\text{IV.8.4})$$



where  $m$  and  $n$  are the orders of  $x$  and  $y$ , respectively. We propose to use a bicubic model with 7 parameters,  $\alpha_u, \alpha_v, a_u, a_v, b_u, b_v, \rho_{uv}$  where the subscripts of the three parameters  $\alpha, a, b$  refer to the Gaussian variables  $u$  and  $v$ . These 7 parameters are used to fit 7 statistical moments  $\sigma_x, \sigma_y, \gamma_{3,x}, \gamma_{e,x}, \gamma_{3,y}, \gamma_{e,y}, \rho_{xy}$ . In our bicubic model of joint PDF (IV.8.3), the correlation coefficient  $\rho_{xy}$  is thus the only imposed cross-moment.

The other cross-moments of the joint PDF are relatively close to the real ones if the non-Gaussian random variables are slight perturbations of cubic transformations of Gaussian ones.

To the author knowledge, the fitting of the first four moments of each random variable as well as their correlation coefficient by means of a parametric bivariate distribution, referred as bicubic distribution, constitutes a novel contribution.

For comparison, the bivariate skew-normal distribution (Azzalini and Dalla Valle, 1996) fits 5 statistical moments  $\sigma_x, \sigma_y, \gamma_{3,x}, \gamma_{3,y}, \rho_{xy}$  while the bivariate skew-t distribution (Azzalini and Capitanio, 2003) fits 3 statistical moments  $\sigma_x, \sigma_y, \rho_{xy}$  and approximates  $\gamma_{3,x}, \gamma_{3,y}, \gamma_{e,x}, \gamma_{e,y}$  or fits the 7 statistical moments if  $\gamma_{3,x} = \gamma_{3,y}, \gamma_{e,x} = \gamma_{e,y}$ . Note that in both bivariate distributions, only one cross-central moment, the correlation coefficient, is also set to its real value. For bivariate skew-normal and skew-t distributions, conditioning gives rise to extended skew-normal and skew-t distributions, respectively (Arellano-Valle and Genton, 2010; Adcock, 2010).

Actually, one could want to derive a joint PDF targeting other cross-moments. However, this is not our scope because the mathematical formulations may rapidly become complex. This explanation supports the primary choice to only target the correlation coefficient as a compromise between accuracy and simplicity. After some developments, the correlation coefficient between  $x$  and  $y$  is obtained as a function of the parameters of the bicubic model, including the correlation  $\rho_{uv}$  of the two Gaussian processes  $u$  and  $v$

$$\rho_{xy} = \frac{\alpha_u \alpha_v}{\sigma_x \sigma_y} \rho_{uv} \left( 1 + \frac{2a_u a_v}{b_u b_v} \rho_{uv} + \frac{2}{3b_u b_v} \rho_{uv}^2 \right). \quad (\text{IV.8.5})$$

The single real solution of this cubic equation reads

$$\rho_{uv}(\rho_{xy}) = \left( r + \sqrt{q + r^2} \right)^{1/3} + \left( r - \sqrt{q + r^2} \right)^{1/3} - a_u a_v, \quad (\text{IV.8.6})$$

where  $r = \frac{3}{4} a_u a_v b_u b_v - a_u^3 a_v^3 + \frac{3b_u b_v \rho_{xy} \sigma_x \sigma_y}{4\alpha_u \alpha_v}$  and  $q = \left( \frac{b_u b_v}{2} - a_u^2 a_v^2 \right)^3$  with the condition  $\frac{b_u b_v}{2} - a_u^2 a_v^2 \geq 0$ .

Figure IV.1 illustrates the joint PDFs computed from Equation (IV.8.3) for correlation coefficients, equal to -0.4, 0 and 0.4, and for three sets of  $(\gamma_3, \gamma_e)$ . Figures IV.1-(a), (b) and (c) shows limit cases where the variables are Gaussian. The intermediate case of joint PDFs of a normal variable and another non-Gaussian is illustrated in Figures IV.1-(d), (e) and (f). For two non-Gaussian variables, the joint PDFs are drawn in Figures IV.1-(g), (h) and (f). These illustrations show that a wide variety of joint PDF might be spanned by this bicubic transformation method.

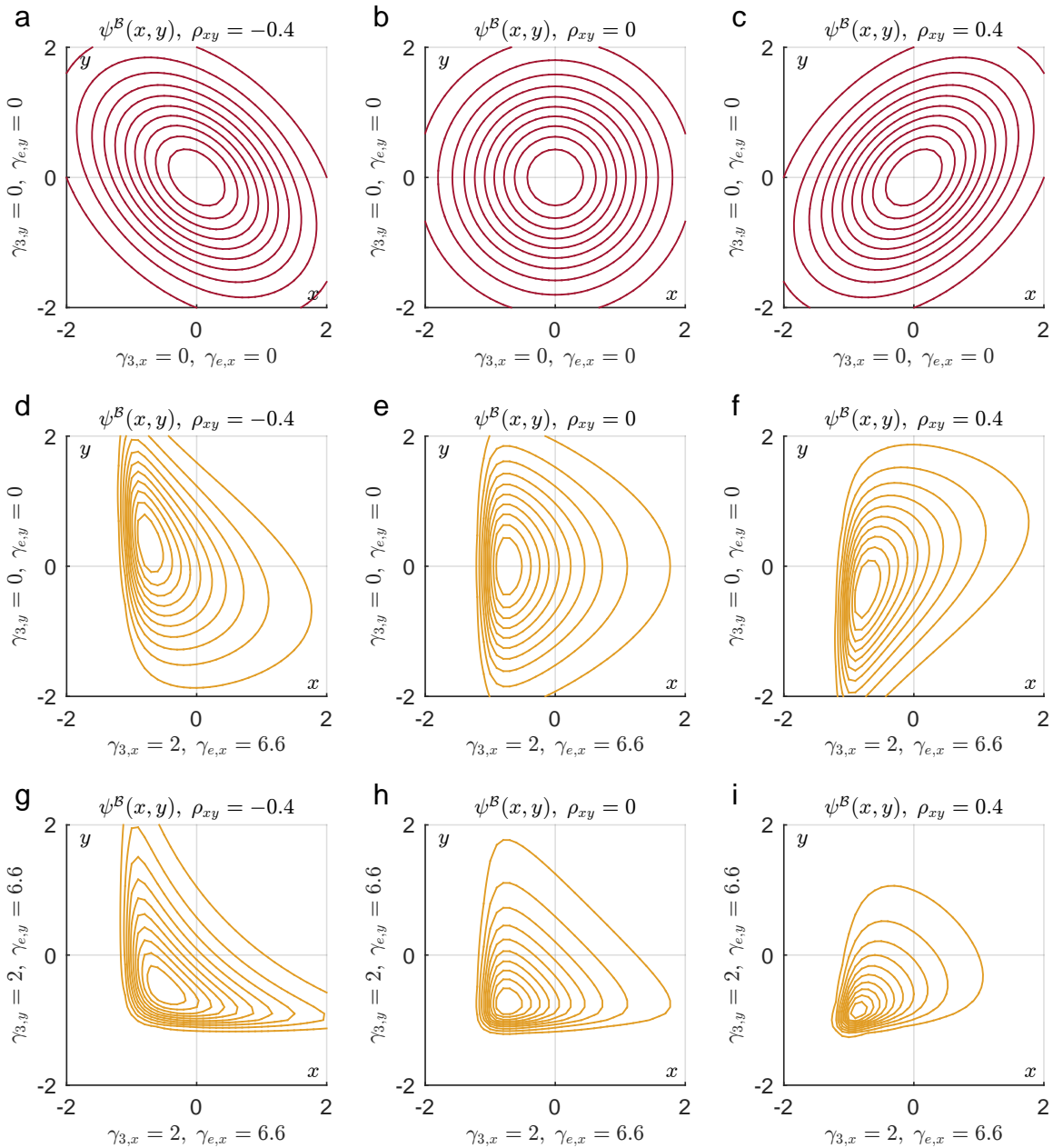


Figure IV.1: Joint PDFs of two standard random variables for different couples  $(\gamma_3, \gamma_e)$  and three correlation coefficients -0.4, 0 and 0.4. The joint Gaussian pdfs are plotted in red and the joint pdfs obtained with the bicubic model, in orange.

**Conditional probability density function** The conditional PDF of  $x$  given  $y$  is written

$$\psi_{x|y}^{\mathcal{B}}(x, y) = \frac{\psi_{u|v}^{\mathcal{N}}(u(x), v(y))}{\left| \frac{dg}{du}(u(x)) \right|}, \quad (\text{IV.8.7})$$

with the conditional mean equal to

$$\mu_{x|y}^{\mathcal{B}}(y) = \frac{\alpha_u}{3b_u} ((v(y))^3 - 3v(y)) \rho_{uv}^3 + 3a_u (v(y)^2 - 1) \rho_{uv}^2 + 3b_u v(y) \rho_{uv}. \quad (\text{IV.8.8})$$

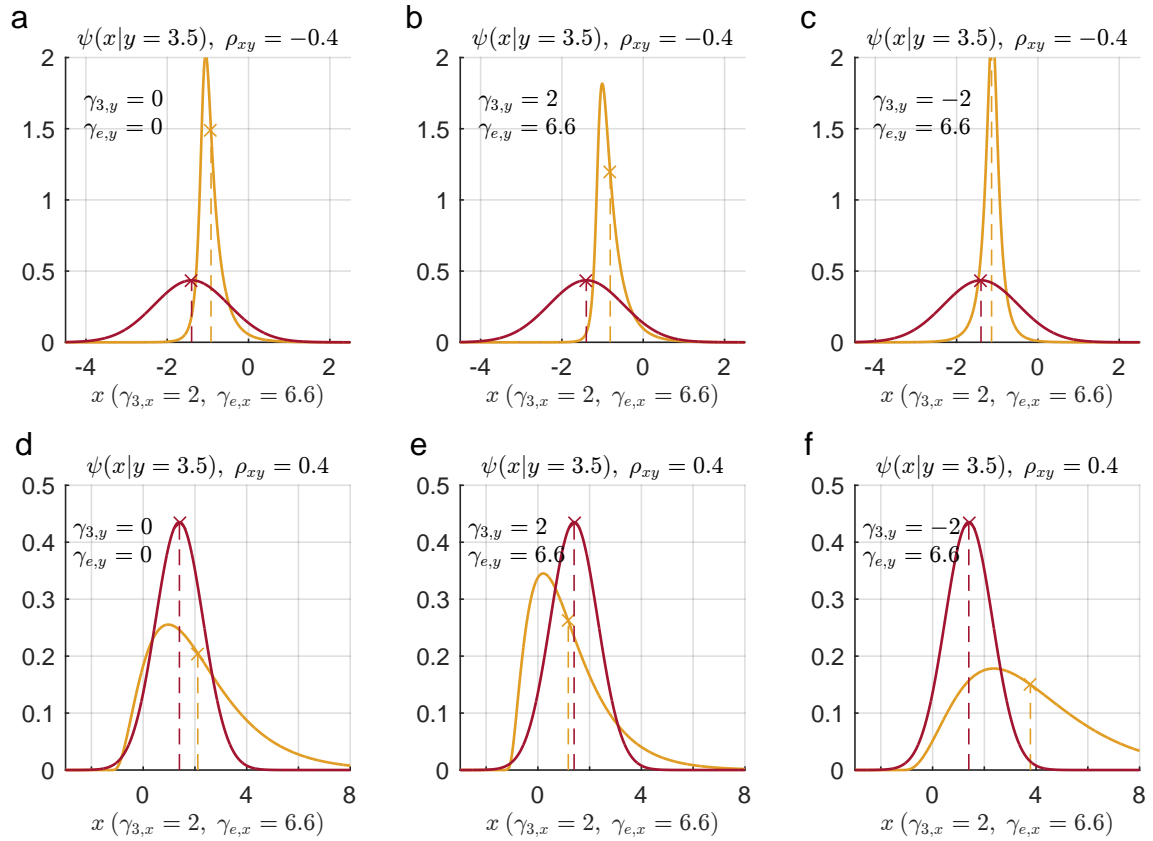


Figure IV.2: Conditional PDFs of  $x$  given  $y = 3.5$  (a typical peak value) for different couples  $(\gamma_3, \gamma_e)$  and for two correlation coefficients  $\rho_{xy} = -0.4, 0.4$ . Conditional mean values are indicated by the cross. The orange line is associated with the non-Gaussian bicubic conditional PDFs while the red line is for the normal conditional PDFs.

For standard variables  $x$  and  $y$ , Figure IV.2 illustrates the conditional PDFs of  $x$  given  $y = 3.5$  computed from (IV.8.7). Two kinds of cases are shown in Figure IV.2: the random variable  $y$  is normal and  $x$  is not, and both random variables are non-Gaussian. Significant differences between the non-Gaussian conditional mean values  $\mu_{x|y}^{\mathcal{B}}(3.5)$ , collected in Table IV.4, and the Gaussian ones,  $\mu_{x|y}^{\mathcal{N}}(3.5) = -1.75$  and  $\mu_{x|y}^{\mathcal{N}}(3.5) = 1.75$  for  $\rho_{xy} = -0.4$  and  $\rho_{xy} = 0.4$  respectively, can be observed in Figure IV.2.

|                    | $(\gamma_{3,y} = 0; \gamma_{e,y} = 0)$ | $(\gamma_{3,y} = 2; \gamma_{e,y} = 6.6)$ | $(\gamma_{3,y} = -2; \gamma_{e,y} = 6.6)$ |
|--------------------|--|--|---|
| $\rho_{xy} = -0.4$ | -0.92                                  | -0.81                                    | -1.14                                     |
| $\rho_{xy} = 0.4$  | 2.11                                   | 1.17                                     | 3.78                                      |

Table IV.4: Non-Gaussian conditional mean values  $\mu_{x|y}^B(3.5)$  associated with Figure IV.2.

For two correlation coefficients, Figure IV.3 illustrates the ratio of the conditional mean value of  $x$  given  $y = 3.5$  obtained with the bicubic model and the conditional mean value assuming Gaussian variables. The random variable  $x$  is non-Gaussian with  $\gamma_{3,x} = 2, \gamma_{e,x} = 6.6$ . The ratio increases rapidly as the distribution of  $y$  becomes left-skewed, i.e.,  $\gamma_{3,y} < 0$ , while the distribution of  $x$  remains right-skewed. For the correlation coefficient  $\rho_{xy} = 0.4$ , when the distribution of  $y$  is left-skewed and the couple  $(\gamma_{3,y}, \gamma_{e,y})$  is close to the monotone limitation, the ratio takes large values up to 3.

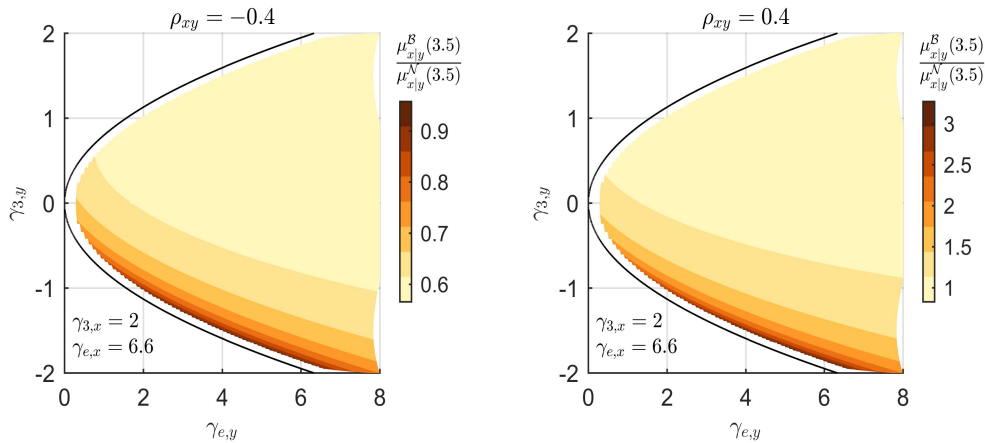


Figure IV.3: Ratio of the conditional mean value of  $x$  given  $y = 3.5$  obtained with the bicubic model and the conditional mean value assuming Gaussian variables for two correlation coefficients  $\rho_{xy} = -0.4, 0.4$ . The random variable  $x$  is non-Gaussian with  $\gamma_{3,x} = 2, \gamma_{e,x} = 6.6$ .

## IV.9 Two-step adjustment method

Section IV.7 has highlighted that the equivalent static wind loads  $\mathbf{f}^{(e,m)}$  do not necessarily satisfy the envelope value condition, nor the non-overestimation condition. These two issues can be addressed with a two-step adjustment method described next.

If the envelope value condition is not fulfilled under the *original* ESWLs  $\mathbf{f}^{(e,m)}$ , *scaled* ESWLs are defined for this purpose by

$$(\alpha\mathbf{f})^{(e,m)} := \alpha^{(e,m)}\mathbf{f}^{(e,m)}. \quad (\text{IV.9.1})$$

If the fulfillment of the non-overestimation condition fail under the *original* or *scaled* ESWLs, an *adjusted* ESWLs is defined, satisfying the 2 conditions (IV.2.3)-(IV.2.4), by

$$(\boldsymbol{\beta} \circ \alpha\mathbf{f})^{(e,m)} := \boldsymbol{\beta}^{(e,m)} \circ \alpha^{(e,m)}\mathbf{f}^{(e,m)}. \quad (\text{IV.9.2})$$

The scaling coefficient  $\alpha^{(e,m)}$  is determined to ensure the envelope value condition while the local coefficients  $\boldsymbol{\beta}^{(e,m)}$ , an  $n_t \times 1$  vector, adjust the scaled ESWLs  $(\alpha\mathbf{f})^{(e,m)}$  in order to fulfill the non-overestimation condition. For instance, if ESWLs are based on the conditional sampling technique, the load scaling coefficient  $\alpha^{(e,m)}$  may be comprehended as the ratio between the actual envelope and the one that would have been obtained from realisations. The local coefficients  $\boldsymbol{\beta}$  should slightly increase or decrease the components of the ESWL without distorting too much the scaled ESWL. In other words, these coefficients have to be as close to unity as possible but simultaneously ensure that sure the non-overestimation condition is met. Computation of the local coefficients vector  $\boldsymbol{\beta}^{(e,m)}$  is formalized here as another constrained nonlinear optimization. We want to hold the envelope value condition and to satisfy the non-overestimation condition by finding the minimum of a problem specified by

$$\min_{\boldsymbol{\beta}^{(e,m)}} \sum_{j=1}^{n_t} \left| \beta_j^{(e,m)} - 1 \right|^{\gamma_\beta}, \quad (\text{IV.9.3})$$

under the linear constraints

$$\begin{cases} +\mathbf{L} [(\boldsymbol{\beta} \circ \alpha\mathbf{f})^{(e,m)}] - \mathbf{r}^{(\max)} & \leq \mathbf{0}, \\ -\mathbf{L} [(\boldsymbol{\beta} \circ \alpha\mathbf{f})^{(e,m)}] + \mathbf{r}^{(\min)} & \leq \mathbf{0}, \\ \sum_{j=1}^{n_t} L_{ij}\beta_j^{(e,m)}\alpha^{(e,m)}f_j^{(e,m)} & = r_i^{(m)}. \end{cases} \quad (\text{IV.9.4})$$

The first two constraints in (IV.9.4) are the non-overestimation condition while the third one corresponds to the envelope value condition. The objective is to obtain adjusted ESWLs as close as possible to the scaled ones, i.e.,  $\beta_j^{(e,m)}$  as close as possible to unity, which justifies the choice of the cost function. Symbol  $\gamma_\beta$  is a positive coefficient taken here equal to 2 as an educated value. The magnitudes of  $\alpha^{(e,m)}$  and  $\boldsymbol{\beta}^{(e,m)}$  are used in the illustrations, third example (see Section VI.5), to compare ESWL formulations in a Non-Gaussian framework.

## IV.10 Envelope reconstruction problem using ESWLs

### IV.10.1 Normalization

The ESWLs, as for basic SWLs, require *normalization* before the envelope reconstruction. A *normalized* ESWL ( $m \equiv \min$ ,  $m \equiv \max$ ) is computed for each ESWL using

$$\mathbf{f}_{(i)}^{(e,m,1)} = \alpha_{(i)}^{(e,m,1)} \mathbf{f}_{(i)}^{(e,m)}, \quad (\text{IV.10.1})$$

where  $\alpha_{(i)}^{(e,m,1)}$  is a positive coefficients applied to satisfy the acceptable overestimation of the envelope (III.3.10) and *the tangency condition*. The tangency condition is such that the static responses  $\mathbf{r}_{(i)}^{(e,m,1)}$  under the ESWL  $\mathbf{f}_{(i)}^{(e,m,1)}$ , defined as

$$\mathbf{r}_{(i)}^{(e,m,1)} = \mathbf{L} \mathbf{f}_{(i)}^{(e,m,1)}, \quad (\text{IV.10.2})$$

are somewhere tangent to the envelope amplified by the acceptable overestimation  $\hat{\varepsilon}$ . Mathematically, we may write

$$\begin{aligned} \forall i, \quad (\exists j \in [1, n_r] : \mathbf{r}_{j(i)}^{(e,m,1)} = (1 + \hat{\varepsilon}) \mathbf{r}_j^{(\max)} \quad \text{or} \quad \mathbf{r}_{j(i)}^{(e,m,1)} = (1 + \hat{\varepsilon}) \mathbf{r}_j^{(\min)}) \\ \wedge \quad (1 + \hat{\varepsilon}) \mathbf{r}_j^{(\min)} \leq \mathbf{r}_{j(i)}^{(e,m,1)} \leq (1 + \hat{\varepsilon}) \mathbf{r}_j^{(\max)} \quad \forall j \in [1, n_r]. \end{aligned} \quad (\text{IV.10.3})$$

In a Gaussian framework:  $\alpha_{(i)}^{(e,\min,1)} = \alpha_{(i)}^{(e,\max,1)}$  and  $\mathbf{f}_{(i)}^{(e,\min,1)} = -\mathbf{f}_{(i)}^{(e,\max,1)}$ .

### Case of adjusted equivalent static wind loads

A *normalized* adjusted ESWL ( $m \equiv \min$ ,  $m \equiv \max$ ) is computed for each adjusted ESWL, using

$$\mathbf{f}_{(i)}^{(e,m,1)} = (1 + \hat{\varepsilon}) \left( \boldsymbol{\beta}^{(e,m)} \circ \alpha^{(e,m)} \mathbf{f}^{(e,m)} \right), \quad (\text{IV.10.4})$$

so that  $\alpha_{(i)}^{(e,m,1)} = 1 + \hat{\varepsilon}$ . It is emphasized that for adjusted ESWL, the envelope value and non-overestimation conditions are fulfilled before normalization. The vector of static responses  $\mathbf{r}_{(i)}^{(e,m,1)}$  under the ESWL  $\mathbf{f}_{(i)}^{(e,m,1)}$  is tangent to the envelope amplified by  $\hat{\varepsilon}$  for the  $i$ -th response. In other words, (IV.10.3) degenerates into

$$\begin{aligned} \forall i, \quad \mathbf{r}_{i(i)}^{(e,m,1)} = (1 + \hat{\varepsilon}) \mathbf{r}_i^{(m)} \\ \wedge \quad (1 + \hat{\varepsilon}) \mathbf{r}_j^{(\min)} \leq \mathbf{r}_{j(i)}^{(e,m,1)} \leq (1 + \hat{\varepsilon}) \mathbf{r}_j^{(\max)} \quad \forall j \in [1, n_r]. \end{aligned} \quad (\text{IV.10.5})$$

### IV.10.2 Ranking of the equivalent static wind loads

The ranking of the ESWLs in the  $n_s$ -dimensional basis used for the ERP is based on how a given ESWL is able to minimize the cost function (III.5.5) of the envelope ( $\mathbf{r}^{(\min)}$ ,  $\mathbf{r}^{(\max)}$ ) and its current approximation  $(\tilde{\mathbf{r}}_{(k)}^{(\min)}, \tilde{\mathbf{r}}_{(k)}^{(\max)})$ , recalled here

$$f \left( \left( \tilde{\mathbf{r}}_{(k)}^{(\min)}, \tilde{\mathbf{r}}_{(k)}^{(\max)} \right), \left( \mathbf{r}^{(\min)}, \mathbf{r}^{(\max)} \right) \right) := \left| \Psi_{(k)}^\gamma \right|. \quad (\text{IV.10.6})$$

The cost function aims at the minimization, at each iteration, of the overall error indicator. Figure III.8 depicts the flowchart for the ERP with ESWLs.

**Gaussian framework** The  $n_s$ -dimensional vector space of static wind loads (III.3.1) regrouping the selected ESWLs has an important feature if structural responses are Gaussian processes. For  $k$  odd, the  $k$ -th and  $(k + 1)$ -th static wind loads are identical in distribution and just differ by their sign

$$\mathbf{f}_{(k)}^{(s)} = -\mathbf{f}_{(k+1)}^{(s)}. \quad (\text{IV.10.7})$$

For  $k$  odd, if the  $k$ -th static wind load is the  $j$ -th normalized equivalent static wind load targeting the envelope max of the  $j$ -th structural response  $r_j^{(\max)}$

$$\mathbf{f}_{(k)}^{(s)} = \mathbf{f}_{(j)}^{(e,\max,1)}, \quad (\text{IV.10.8})$$

then the  $(k + 1)$ -th static wind load is the  $j$ -th normalized equivalent static wind load targeting the envelope min of the  $j$ -th structural response  $r_j^{(\min)}$

$$\mathbf{f}_{(k+1)}^{(s)} = \mathbf{f}_{(j)}^{(e,\min,1)}, \quad (\text{IV.10.9})$$

since we have  $\mathbf{f}_{(j)}^{(e,\min,1)} = -\mathbf{f}_{(j)}^{(e,\max,1)}$  in a Gaussian context. This result holds because of the symmetry of the envelope and if the reconstruction of each side of the envelope has the same weight in the cost function.

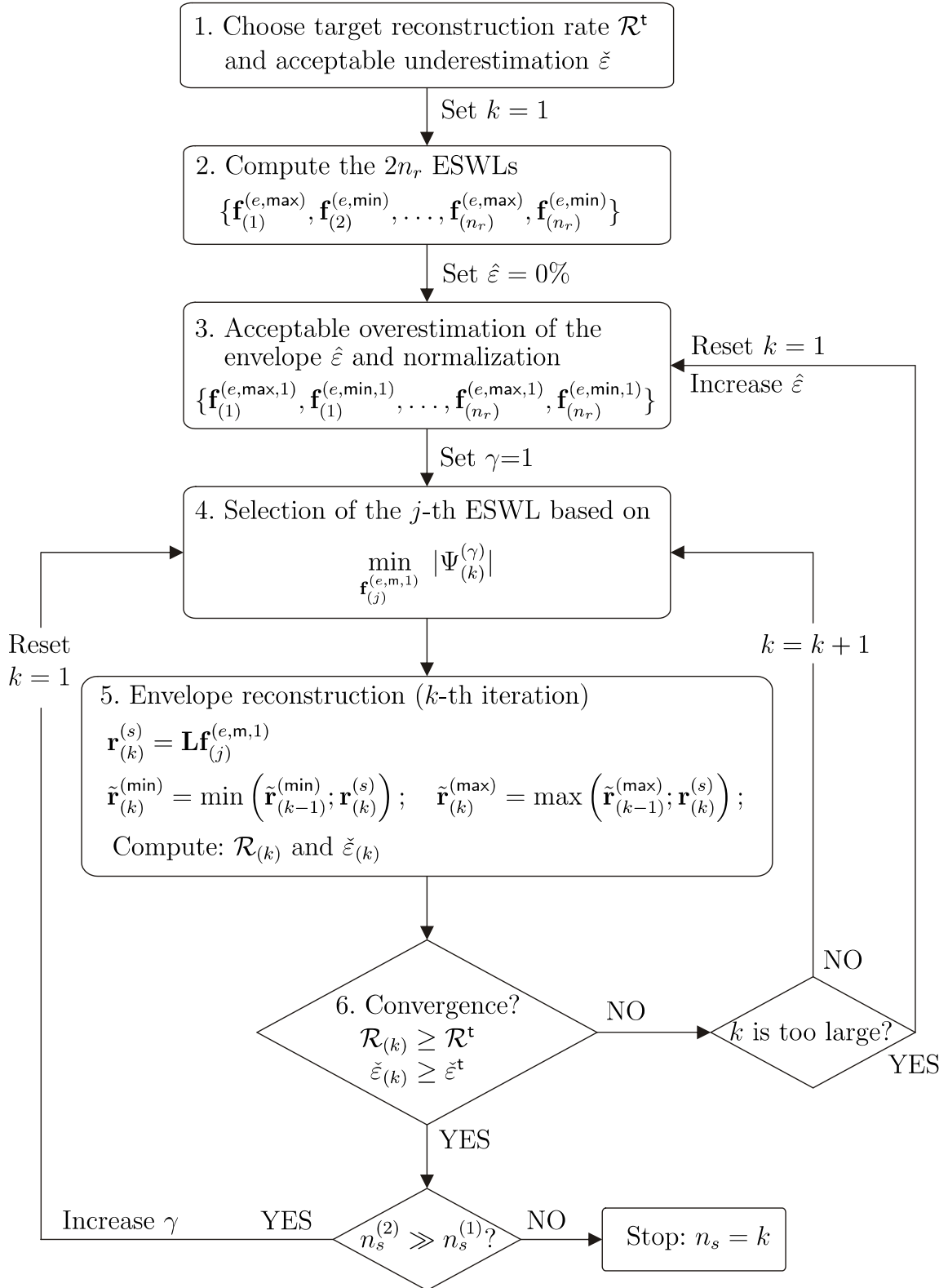


Figure IV.4: Flowchart of the envelope reconstruction problem with ESWLs.



## IV.11 Summary

Equivalent static wind loads have been derived and directly used as a valuable tool in the design of structures. Two mathematical expressions formulating them have been reviewed, namely, the load-response correlation method and the hybrid method, both developed in a Gaussian context.

With the aim to develop a formulation in the case of aerodynamic pressures and structural responses exhibiting non-Gaussianities, a conditional expected load method has been established. Inspired by the LRC method in which Gaussian conditional probability densities as well as their mean values are required, the concept of conditional expected static wind load is derived. Such loading is based on the premise that it collects the average wind loads conditioned upon recovery of the considered response. A parametric bicubic model of non-Gaussian conditional probability density is proposed for this purpose.

The conditional expected load method formulates conditional expected static wind loads

1. for any linear structural behavior; background, hybrid and mostly resonant,
2. no matter the basis used for the analysis: nodal or hybrid (nodal-modal),
3. for non-Gaussian processes by a proper recourse to the bicubic model,
4. that are relevant even if there is not a clear separation of the timescales associated with the background and resonant components of structural responses.

Figure IV.5 depicts the ways to compute conditional expected static wind load in a Gaussian or non-Gaussian context.

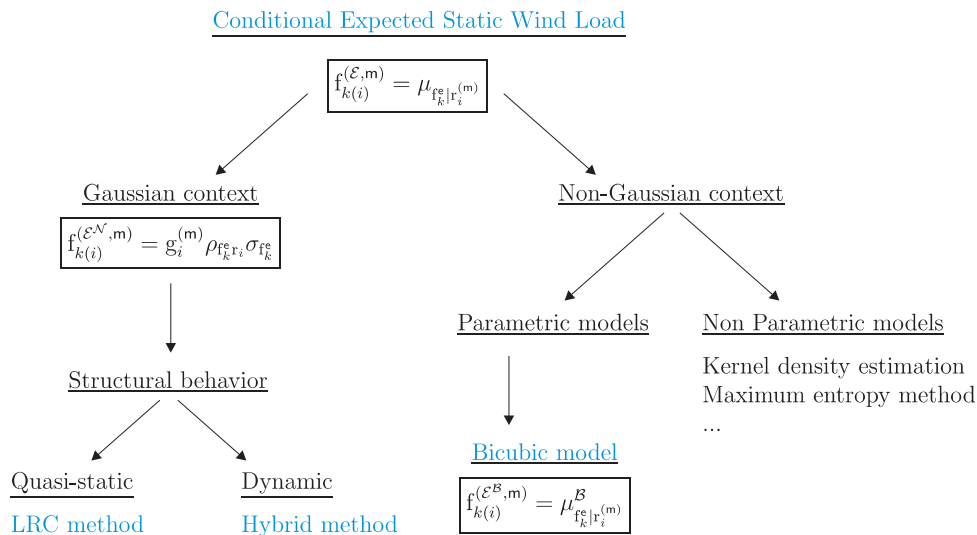


Figure IV.5: Flowchart of the concept of conditional expected static wind load.



# Chapter V

## Principal static wind loads

- 
- V.1 Introduction
  - V.2 Singular value decomposition
  - V.3 Principal static wind loads
  - V.4 Envelope reconstruction problem using PSWLs
  - V.5 Summary
-

## V.1 Introduction

One main objective of this dissertation is to study and develop methods establishing efficient bases of static wind loads  $\{\mathbf{f}_{(1)}^{(s)}, \mathbf{f}_{(2)}^{(s)}, \dots, \mathbf{f}_{(n_s)}^{(s)}\}$  for the envelope reconstruction problem.

At first glance, two basic static wind loads, the CPT loading modes and the modal inertial loads, are good candidates for two limit structural behaviors, quasi-static and resonant, respectively. As a matter of fact, no such candidate is available, see Table V.1, for hybrid structural behavior, i.e., when background and resonant components of the structural responses are similar in magnitude. Moreover both basic SWLs do not adapt when the structural responses are non-Gaussian, i.e., when the envelope becomes asymmetric. Additionally, they do not adapt to the specific set of structural responses of interest.

| Structural behavior: | Quasi-static | Dynamic<br>(Hybrid) | Resonant |
|----------------------|--------------|---------------------|----------|
| CPT loading modes    | ✓            | ✗                   | ✗        |
| Modal inertial loads | ✗            | ✗                   | ✓        |

Table V.1: Envelope reconstruction problem with two sets of basic static wind loads. Domain of applicability.

These shortcomings have motivated the study of a new concept of Principal Static Wind Load. This kind of loading is obtained with a singular value decomposition of a target set of equivalent static wind loads.

### Outline of the Chapter

In Section V.2, the singular value decomposition is reviewed and specific features of this decomposition when applied on a matrix given by the product of two other matrices are identified. This matrix decomposition is used in Section V.3 to derive the innovative concept of principal static wind load. This Section also studies the peculiar circumstances which determine if the PSWL basis degenerates into the CPT loading modes or MILs as limit cases for quasi-static and resonant structural behaviors, respectively. Finally, Section V.4 provides the elementary steps to implement PSWLs for the envelope reconstruction problem.

## V.2 Singular value decomposition

We are interested in the matrix factorization of a real rectangular  $m \times n$  matrix  $\mathbf{A}$ . There are several ways to decompose such a matrix  $\mathbf{A}$  into the product of matrices depending on their expected properties. In the problem treated hereinafter, the factorization shall produce two orthogonal matrices, a reason why we only detail next the singular value decomposition.

A real  $m \times n$  matrix  $\mathbf{A}$  can be expressed by a Singular Value Decomposition (SVD) of the form

$$\mathbf{A} = \mathbf{U}\mathbf{S}\mathbf{V}^T, \quad (\text{V.2.1})$$

where  $\mathbf{U}$  and  $\mathbf{V}$  are  $m \times r$  and  $n \times r$  real matrices whose column vectors form an orthonormal basis and  $\mathbf{S}$  is an  $r \times r$  square diagonal matrix. The diagonal elements of the square matrix  $\mathbf{S}$  are positive and ordered in decreasing values. They are known as singular values of  $\mathbf{A}$  or principal coordinates and denoted by  $\lambda_i$ , such that the matrix  $\mathbf{S}$  reads

$$\mathbf{S} = \text{diag}(\lambda_1, \dots, \lambda_r), \quad (\text{V.2.2})$$

with  $\lambda_1 \geq \lambda_2 \geq \dots \geq \lambda_r$ . The number  $r$  corresponds to the number of non-zero singular values of  $\mathbf{A}$ , that is the rank of  $\mathbf{A}$ . The singular value decomposition of  $\mathbf{A}$  is a twofold eigenvalue problem that can be written as

$$[\mathbf{A}\mathbf{A}^T] \mathbf{U}_i = \lambda_i^2 \mathbf{U}_i, \quad \forall i \in [1, r], \quad (\text{V.2.3})$$

$$[\mathbf{A}^T\mathbf{A}] \mathbf{V}_i = \lambda_i^2 \mathbf{V}_i, \quad \forall i \in [1, r]. \quad (\text{V.2.4})$$

Hence, the columns of the matrices  $\mathbf{U}$  and  $\mathbf{V}$  collect the so-called left-singular vectors and right-singular vectors of  $\mathbf{A}$ , that are the eigenvectors of  $\mathbf{A}\mathbf{A}^T$  and  $\mathbf{A}^T\mathbf{A}$ , respectively.

### Property

The left-singular vectors of an  $m \times 2n$  matrix  $\mathbf{B} = [\mathbf{A}, -\mathbf{A}]$  are identical to the left-singular vectors of the matrix  $\mathbf{A}$ . Since the product  $[\mathbf{B}\mathbf{B}^T]$  reduces to

$$\mathbf{B}\mathbf{B}^T = [\mathbf{A}, -\mathbf{A}] [\mathbf{A}, -\mathbf{A}]^T = 2\mathbf{A}\mathbf{A}^T, \quad (\text{V.2.5})$$

the left-singular vectors of the matrix  $\mathbf{B}$  are derived from the eigenvalue problem

$$[\mathbf{A}\mathbf{A}^T] \mathbf{U}_i = \frac{\lambda_i^2}{2} \mathbf{U}_i, \quad \forall i \in [1, r], \quad (\text{V.2.6})$$

that corresponds to (V.2.3). Consequently to (V.2.6), the  $r$  singular values of  $\mathbf{B}$  are scaled by  $\sqrt{2}$  in comparison with the  $r$  singular values of  $\mathbf{A}$ . The ranks of  $\mathbf{B}$  and  $\mathbf{A}$  are equal, thus both matrices have the same number of singular values.

### Special case

Eventually, in our problem treated in the sequel, the matrix  $\mathbf{A}$  is already given by the product of two matrices, such as

$$\mathbf{A} = \mathbf{P}\mathbf{W}, \quad (\text{V.2.7})$$

where  $\mathbf{P}$  is an  $m \times q$  ( $q \leq \min(m, n)$ ) real matrix and  $\mathbf{W}$  is a  $q \times n$  matrix of weighting factors. Depending on the properties of  $\mathbf{P}$  and  $\mathbf{W}$ , three cases are studied next.

**Case A** If the columns of  $\mathbf{P}$  form a set of linearly independent vectors ( $\det(\mathbf{P}) \neq 0$ ) then the number  $r$  of singular values of  $\mathbf{A}$  is equal to  $q$ .

**Case B** If the columns of  $\mathbf{P}$  and the rows of  $\mathbf{W}$  do not form orthogonal bases, the left- and right- singular vectors of the matrix  $\mathbf{A}$  can be found by first computing the left-singular vectors of the matrix  $\mathbf{W}$ , via the eigenvalue problem

$$\mathbf{W}\mathbf{W}^T\mathbf{Z} = \mathbf{Z} \text{diag}(\zeta_1^2, \dots, \zeta_r^2), \quad (\text{V.2.8})$$

where  $\mathbf{Z}$  is a  $q \times q$  square matrix of left-singular vectors and  $\text{diag}(\zeta_1^2, \dots, \zeta_r^2)$  collects the eigenvalues. From (V.2.8), the product of the matrix  $\mathbf{W}$  with its transpose is given by

$$\mathbf{W}\mathbf{W}^T = \mathbf{Z} \text{diag}(\zeta_1^2, \dots, \zeta_r^2) \mathbf{Z}^T. \quad (\text{V.2.9})$$

The left-singular vectors of the matrix  $\mathbf{A}$  are derived from (V.2.3). By inserting (V.2.7) and using (V.2.9), the eigenvalue problem is written

$$\begin{aligned} [\mathbf{A}\mathbf{A}^T] \mathbf{U} &= \mathbf{U} \text{diag}(\lambda_1^2, \dots, \lambda_r^2), \\ [\mathbf{P}\mathbf{W}\mathbf{W}^T\mathbf{P}^T] \mathbf{U} &= \mathbf{U} \text{diag}(\lambda_1^2, \dots, \lambda_r^2), \\ [\mathbf{P}\mathbf{Z} \text{diag}(\zeta_1^2, \dots, \zeta_r^2) \mathbf{Z}^T \mathbf{P}^T] \mathbf{U} &= \mathbf{U} \text{diag}(\lambda_1^2, \dots, \lambda_r^2), \end{aligned} \quad (\text{V.2.10})$$

and (V.2.10) is fulfilled if the left-singular vectors of the matrix  $\mathbf{A}$  are given by

$$\mathbf{U} = \mathbf{P}\mathbf{Z}, \quad (\text{V.2.11})$$

and the eigenvalues of the left-singular vectors of the matrices  $\mathbf{A}$  and  $\mathbf{W}$  are equal

$$\text{diag}(\zeta_1^2, \dots, \zeta_r^2) = \text{diag}(\lambda_1^2, \dots, \lambda_r^2). \quad (\text{V.2.12})$$

Inserting (V.2.11) into (V.2.7), the matrix  $\mathbf{A}$  reads

$$\mathbf{A} = \mathbf{U}\mathbf{Z}^T\mathbf{W}. \quad (\text{V.2.13})$$

Comparing (V.2.13) with (V.2.1) we write

$$\mathbf{S}\mathbf{V}^T = \mathbf{Z}^T\mathbf{W}, \quad (\text{V.2.14})$$

and the right-singular vectors of the matrix  $\mathbf{A}$  are expressed by

$$\mathbf{V} = \mathbf{W}^T\mathbf{Z}\mathbf{S}^{-1}. \quad (\text{V.2.15})$$

**Case C** If the columns of  $\mathbf{P}$  and the rows of  $\mathbf{W}$  both form orthogonal bases, i.e.,

$$\mathbf{P}^T \mathbf{P} = \text{diag}(\|\mathbf{P}_1\|, \dots, \|\mathbf{P}_q\|); \quad \mathbf{W} \mathbf{W}^T = \text{diag}(\|\mathbf{W}_{1\circ}\|, \dots, \|\mathbf{W}_{q\circ}\|), \quad (\text{V.2.16})$$

then they correspond to the left-singular and right-singular vectors of the matrix  $\mathbf{A}$ , respectively. By writing

$$\mathbf{U} = \mathbf{P} \text{diag} \left( \frac{1}{\sqrt{\|\mathbf{P}_1\|}}, \dots, \frac{1}{\sqrt{\|\mathbf{P}_q\|}} \right), \quad \mathbf{V}^T = \text{diag} \left( \frac{1}{\sqrt{\|\mathbf{W}_{1\circ}\|}}, \dots, \frac{1}{\sqrt{\|\mathbf{W}_{q\circ}\|}} \right) \mathbf{W}, \quad (\text{V.2.17})$$

the square diagonal matrix  $\mathbf{S}$  is given by

$$\mathbf{S} = \text{diag} \left( \sqrt{\|\mathbf{P}_1\|} \sqrt{\|\mathbf{W}_{1\circ}\|}, \dots, \sqrt{\|\mathbf{P}_q\|} \sqrt{\|\mathbf{W}_{q\circ}\|} \right). \quad (\text{V.2.18})$$

## V.3 Principal static wind loads

This section presents the concept of Principal Static Wind Load. They are obtained with a singular value decomposition of equivalent static wind loads. The approach followed to derive them is discussed in Section V.3.1 in a general framework. Several features are highlighted and under peculiar circumstances, the PSWL basis degenerates into the CPT loading modes or the modal inertial loads. This is demonstrated in Sections V.3.2 and V.3.3, respectively.

### V.3.1 Concept

Driven by the needs for static wind loads that could be derived for any kind of structural behavior and for non-Gaussian structural responses, the concept of PSWL is derived hereinafter.

The  $n_t \times n_r$  ESWL matrices  $\mathbf{F}^{(e,\min)}$  and  $\mathbf{F}^{(e,\max)}$  consist of columns collecting the ESWLs  $\mathbf{f}_{(i)}^{(e,m)}$ , which were computed for all envelope values, minima and maxima, respectively. We define an  $n_t \times 2n_r$  matrix  $\mathbf{F}^{(e)}$  collecting all ESWLs

$$\mathbf{F}^{(e)} = [\mathbf{F}^{(e,\min)} \mathbf{F}^{(e,\max)}]. \quad (\text{V.3.1})$$

The PSWLs  $\mathbf{F}^{(\mathcal{P})}$  are defined as the left-singular vectors resulting from the *singular value decomposition* (SVD) of  $\mathbf{F}^{(e)}$

$$\mathbf{F}^{(e)} = \mathbf{F}^{(\mathcal{P})} \mathbf{S} \mathbf{V}^T = \mathbf{F}^{(\mathcal{P})} \mathbf{W}^{(\mathcal{P})}, \quad (\text{V.3.2})$$

where  $\mathbf{F}^{(\mathcal{P})}$  is an  $n_t \times 2n_r$  real matrix, the main diagonal of  $\mathbf{S}$  gathers the principal coordinates  $\lambda_i^{(\mathcal{P})}$ , and  $\mathbf{W}^{(\mathcal{P})} = \mathbf{S} \mathbf{V}^T$  collects the weighting coefficients of each principal static wind load. As such, the PSWLs  $\mathbf{F}^{(\mathcal{P})}$  form an orthonormal basis.

- It is emphasized that PSWLs are basic SWLs since they are not associated with specific structural responses and ordered by decreasing principal coordinates  $\lambda_i^{(\mathcal{P})}$ , see Section III.4. All the methodology described in Chapter III to handle the envelope reconstruction problem with basic SWLs is therefore relevant with PSWLs.
- Contrary to CPT loading modes and MILs, PSWLs are dependent upon the set of structural responses to be reconstructed, though, they are not associated with specific structural responses as ESWLs, making a notable difference. Indeed, the matrix  $\mathbf{F}^{(e)}$  on which the SVD is applied only collects the ESWLs of structural responses considered for the ERP.
- Principal static wind loads can be seen as a manner to sort out the most important load patterns, out of a large set of ESWLs. They are the directors of an optimum basis of loadings to represent any ESWL in  $\mathbf{F}^{(e)}$ . The more structural responses are correlated and tend to be Gaussian random processes, the more ESWLs have similar distribution and the less PSWLs has to be retained for an appropriate reconstruction of  $\mathbf{F}^{(e)}$ .



- The LRC-, CST-, Hybrid-, CEL-, based ESWL formulation can be used to establish the matrix  $\mathbf{F}^{(e)}$ . The PSWLs is thence relevant for structures with quasi-static, hybrid or resonant behaviors on the condition that the appropriate ESWL formulation has been selected to compute all ESWLs.
- Under peculiar circumstances, see Sections V.3.2 and V.3.3, the PSWL basis degenerates into the CPT loading modes or MILs as limit cases for quasi-static and resonant structural behaviors, respectively.

### Gaussian case

In a Gaussian framework and for ESWLs that correspond to the conditional expected ones, the following equality holds

$$\mathbf{F}^{(e,\min)} = -\mathbf{F}^{(e,\max)}, \quad (\text{V.3.3})$$

and introducing (V.3.3) into (V.3.1), the matrix  $\mathbf{F}^{(e)}$  collecting all ESWLs can be written

$$\mathbf{F}^{(e)} = [\mathbf{F}^{(e,\min)} \quad -\mathbf{F}^{(e,\min)}] = [-\mathbf{F}^{(e,\max)} \quad \mathbf{F}^{(e,\max)}]. \quad (\text{V.3.4})$$

Consequently to the property exposed in Section V.2, the SVD with (V.3.2) in a Gaussian framework would provide the same first  $n_r$  principal static wind loads than the SVD of the matrices  $\mathbf{F}^{(e,\min)}$  or  $\mathbf{F}^{(e,\max)}$ . However, the last  $n_r$  principal loads associated with the SVD of the matrix  $\mathbf{F}^{(e)}$  have no meaning since the associated  $n_r$  principal coordinates would be equal to zero:  $S_{ii} = 0 \quad \forall i \in [n_r + 1, 2n_r]$ .

### Quasi-static structural behavior

In this case, principal static wind loads can be formulated with aerodynamic pressures rather than nodal forces. The  $n_l \times n_r$  ESWL matrices  $\mathbf{P}^{(e,\min)}$  and  $\mathbf{P}^{(e,\max)}$  consist of columns collecting the ESWLs  $\mathbf{p}_{(i)}^{(e,m)}$ , computed for all envelope values, minima and maxima, respectively. We define an  $n_l \times 2n_r$  matrix  $\mathbf{P}^{(e)}$  collecting all ESWLs

$$\mathbf{P}^{(e)} = [\mathbf{P}^{(e,\min)} \quad \mathbf{P}^{(e,\max)}]. \quad (\text{V.3.5})$$

The PSWLs in terms of aerodynamic pressures are defined as the columns of the principal  $n_l \times 2n_r$  matrix  $\mathbf{P}^{(\mathcal{P})}$  resulting from the singular value decomposition of  $\mathbf{P}^{(e)}$

$$\mathbf{P}^{(e)} = \mathbf{P}^{(\mathcal{P})} \mathbf{S} \mathbf{V}^T = \mathbf{P}^{(\mathcal{P})} \mathbf{W}^{(\mathcal{P})}. \quad (\text{V.3.6})$$

### V.3.2 LRC-based ESWLs with CPT loading modes

From (IV.4.4), the  $n_l \times n_r$  LRC-based ESWL matrix  $\mathbf{P}^{(\mathcal{L}^c,m)} = [\mathbf{p}_{(1)}^{(\mathcal{L}^c,m)}, \mathbf{p}_{(2)}^{(\mathcal{L}^c,m)}, \dots, \mathbf{p}_{(n_r)}^{(\mathcal{L}^c,m)}]$  obtained with CPT loading modes is expressed as

$$\mathbf{P}^{(\mathcal{L}^c,m)} = \mathbf{P}^{(\mathcal{C})} \mathbf{W}^{(\mathcal{C},m)}, \quad (\text{V.3.7})$$

with  $\mathbf{P}^{(C)}$  an  $n_l \times n_{cpt}$  ( $n_{cpt} \leq n_r$ ) matrix whose columns are orthonormal vectors (the retained CPT loadings modes) and  $\mathbf{W}^{(C,m)}$  an  $n_{cpt} \times n_r$  matrix of weighting factors. Since, the CPT loading modes form an orthogonal basis, the case C studied in Section V.2 indicates that the CPT loading modes are, in fact, the PSWLs

$$\mathbf{P}^{(C)} = \mathbf{P}^{(\mathcal{P})}, \quad (\text{V.3.8})$$

if the rows of the matrix  $\mathbf{W}^{(C,m)}$  are orthogonal, a condition studied next.

The  $n_r \times n_{cpt}$  matrix of structural responses under the CPT loading modes reads

$$\mathbf{R}^{(C)} = \mathbf{B}\mathbf{P}^{(C)}. \quad (\text{V.3.9})$$

Rewriting (IV.5.7) using (V.3.9), the weighting factors are expressed by

$$\mathbf{W}^{(C,m)} = \Sigma^c \left[ (\mathbf{R}^{(C)})^T \text{diag}(\mathbf{g}^{(m)} \div \boldsymbol{\sigma}_{r^b}) \right], \quad (\text{V.3.10})$$

$$= \Sigma^c \widetilde{\mathbf{W}}^{(C,m)}, \quad (\text{V.3.11})$$

and the term in brackets in (V.3.10) represents the weighting factors, denoted by  $\widetilde{\mathbf{W}}^{(C,m)} = (\mathbf{R}^{(C)})^T \text{diag}(\mathbf{g}^{(m)} \div \boldsymbol{\sigma}_{r^b})$ , before scaling by the eigenvalue of each CPT loading mode.

In general nothing guarantees that the structural responses provided by each CPT loading mode are orthogonal vectors, too.

Let us assume the  $m$  and  $n$  columns of the matrix  $\mathbf{R}^{(C)}$  are orthogonal vectors (**assumption 1**)

$$(\mathbf{R}_m^{(C)})^T \mathbf{R}_n^{(C)} = 0, \quad \forall m \neq n \quad (\text{V.3.12})$$

the dot product between the  $m$  and  $n$  rows of the scaled matrix  $\widetilde{\mathbf{W}}^{(C,m)}$  is written as

$$\left[ \widetilde{\mathbf{W}}^{(C,m)} (\widetilde{\mathbf{W}}^{(C,m)})^T \right]_{mn} = \sum_{i=1}^{n_r} \left( \frac{g_i^{(m)}}{\sigma_{r_i^b}} \right)^2 \mathbf{R}_{im}^{(C)} \mathbf{R}_{in}^{(C)}. \quad (\text{V.3.13})$$

The indices of structural responses for which the product  $\mathbf{R}_{im}^{(C)} \mathbf{R}_{in}^{(C)}$  is either positive or negative are collected such that

$$\mathbf{R}_{im}^{(C)} \mathbf{R}_{in}^{(C)} \geq 0 \quad \forall i = i^+; \quad \mathbf{R}_{im}^{(C)} \mathbf{R}_{in}^{(C)} < 0 \quad \forall i = i^-. \quad (\text{V.3.14})$$

Using (V.3.14), equation (V.3.13) is expressed as

$$\left[ \widetilde{\mathbf{W}}^{(C,m)} (\widetilde{\mathbf{W}}^{(C,m)})^T \right]_{mn} = \sum_{i^-=1} \left( \frac{g_{i^-}^{(m)}}{\sigma_{r_{i^-}^b}} \right)^2 \mathbf{R}_{i^-m}^{(C)} \mathbf{R}_{i^-n}^{(C)} + \sum_{i^+=1} \left( \frac{g_{i^+}^{(m)}}{\sigma_{r_{i^+}^b}} \right)^2 \mathbf{R}_{i^+m}^{(C)} \mathbf{R}_{i^+n}^{(C)}, \quad (\text{V.3.15})$$

and the  $m$  and  $n$  rows of the scaled matrix  $\widetilde{\mathbf{W}}^{(C,m)}$  are orthogonal vectors if equation

$$\sum_{i^-=1} \left( \frac{g_{i^-}^{(m)}}{\sigma_{r_{i^-}^b}} \right)^2 = \sum_{i^+=1} \left( \frac{g_{i^+}^{(m)}}{\sigma_{r_{i^+}^b}} \right)^2, \quad (\text{V.3.16})$$

is verified (**assumption 2**). Finally, since the matrix  $\Sigma^c$  is diagonal and if assumptions 1 and 2 are fulfilled, i.e.,

$$\left[ \widetilde{\mathbf{W}}^{(c,m)} \left( \widetilde{\mathbf{W}}^{(c,m)} \right)^\top \right]_{mn} = 0, \quad (\text{V.3.17})$$

the  $m$  and  $n$  rows of the matrix  $\mathbf{W}^{(c,m)}$  are orthogonal vectors as well.

The PSWL basis degenerates into the CPT loading modes as a limit case if the weighting factors for each CPT loading mode are orthogonal vectors. The maximum number of PSWLs is equal to the number of CPT loading modes retained for computing the LRC-based ESWLs (Case A).

### V.3.3 MIL-based ESWLs

From (IV.5.6), the  $n_t \times n_r$  MIL-based ESWL matrix  $\mathbf{F}^{(\mathcal{M},m)} = \left[ \mathbf{f}_{(1)}^{(\mathcal{M},m)}, \mathbf{f}_{(2)}^{(\mathcal{M},m)}, \dots, \mathbf{f}_{(n_r)}^{(\mathcal{M},m)} \right]$  obtained with modal inertial loads is expressed as

$$\mathbf{F}^{(\mathcal{M},m)} = \mathbf{F}^{(\mathcal{M})} \mathbf{W}^{(\mathcal{M},m)}, \quad (\text{V.3.18})$$

with  $\mathbf{F}^{(\mathcal{M})}$  an  $n_t \times n_m$  ( $n_m \leq n_r$ ) matrix whose columns are the modal inertial loads and  $\mathbf{W}^{(\mathcal{M},m)}$  an  $n_c \times n_r$  matrix of weighting factors. The case C studied in Section V.2 indicates that the MILs are the PSWLs

$$\mathbf{F}^{(\mathcal{M})} = \mathbf{F}^{(\mathcal{P})}, \quad (\text{V.3.19})$$

if the normal modes of vibration constitute an orthogonal basis and the rows of the matrix  $\mathbf{W}^{(\mathcal{M},m)}$  are orthogonal, two conditions studied next.

The  $n_r \times n_m$  matrix of structural responses under the MILs reads

$$\mathbf{R}^{(\mathcal{M})} = \mathbf{L} \mathbf{F}^{(\mathcal{M})}. \quad (\text{V.3.20})$$

Rewriting (IV.5.7) using (V.3.20), the weighting factors are expressed by

$$\mathbf{W}^{(\mathcal{M},m)} = \Sigma^q \left[ \left( \mathbf{R}^{(\mathcal{M})} \right)^\top \text{diag}(\mathbf{g}^{(m)} \div \boldsymbol{\sigma}_r) \right], \quad (\text{V.3.21})$$

$$= \Sigma^q \widetilde{\mathbf{W}}^{(\mathcal{M},m)}, \quad (\text{V.3.22})$$

and the term in brackets in (V.3.21) represents the weighting factors before left multiplication by the covariance matrix of modal amplitudes and denoted by  $\widetilde{\mathbf{W}}^{(\mathcal{M},m)} = \left( \mathbf{R}^{(\mathcal{M})} \right)^\top \text{diag}(\mathbf{g}^{(m)} \div \boldsymbol{\sigma}_r)$ .

**Assumption 1** First, under specific mass and stiffness distributions in the structure, the normal modes of vibration constitute an orthogonal basis, i.e.,

$$\boldsymbol{\Phi}_j^\top \boldsymbol{\Phi}_k = 0 \quad \forall j \neq k. \quad (\text{V.3.23})$$

This property allows to write the stiffness matrix as

$$\mathbf{K} = \boldsymbol{\Phi} \boldsymbol{\Omega} \boldsymbol{\Phi}^\top. \quad (\text{V.3.24})$$

Inserting (V.3.24) into (II.5.11), the modal inertial loads are affine to the modal shapes

$$\mathbf{F}_i^{(\mathcal{M})} = \mathbf{\Phi}\mathbf{\Omega}\mathbf{\Phi}^\top\mathbf{\Phi}_i = \mathbf{\Phi}_i\mathbf{\Omega}_{ii}, \quad (\text{V.3.25})$$

through the modal stiffness and therefore the MILs form an orthogonal basis, too

$$\left(\mathbf{F}_j^{(\mathcal{M})}\right)^\top \mathbf{F}_k^{(\mathcal{M})} = 0, \quad \forall j \neq k. \quad (\text{V.3.26})$$

**Assumption 2** Nothing guarantees the structural responses provided by each MIL are orthogonal vectors, too. Let us assume the  $m$  and  $n$  columns of the matrix  $\mathbf{R}^{(\mathcal{M})}$  are orthogonal vectors

$$\left(\mathbf{R}_m^{(\mathcal{M})}\right)^\top \mathbf{R}_n^{(\mathcal{M})} = 0, \quad (\text{V.3.27})$$

**Assumption 3** and the  $m$  and  $n$  rows of the matrix  $\widetilde{\mathbf{W}}^{(\mathcal{M},m)}$  are also orthogonal vectors if equation

$$\sum_{i^- = 1} \left(\frac{\mathbf{g}_{i^-}^{(m)}}{\sigma_{r_{i^-}}}\right)^2 = \sum_{i^+ = 1} \left(\frac{\mathbf{g}_{i^+}^{(m)}}{\sigma_{r_{i^+}}}\right)^2, \quad (\text{V.3.28})$$

is verified.

**Assumption 4** The dot product between the  $m$  and  $n$  rows of the matrix  $\mathbf{W}^{(\mathcal{M},m)}$  is given by

$$\left[\mathbf{W}^{(\mathcal{M},m)} \left(\mathbf{W}^{(\mathcal{M},m)}\right)^\top\right]_{mn} = \sum_i^{n_r} \left(\sum_k^{n_m} \sum_{mk}^q \widetilde{\mathbf{W}}_{ki}^{(\mathcal{M},m)}\right) \left(\sum_l^{n_m} \sum_{nl}^q \widetilde{\mathbf{W}}_{li}^{(\mathcal{M},m)}\right). \quad (\text{V.3.29})$$

Hence, the more the  $m$  and  $n$  modes are uncorrelated with other modes, i.e.,

$$\mathcal{R}_{mk}^q = 0 \text{ if } m \neq k \quad , \quad \mathcal{R}_{nk}^q = 0 \text{ if } n \neq k, \quad (\text{V.3.30})$$

then the more the  $m$  and  $n$  rows of the matrix  $\mathbf{W}^{(\mathcal{M},m)}$  are orthogonal.

The PSWL basis degenerates into the modal inertial load as a limit case if the weighting factors for each modal inertial load are orthogonal vectors and the modal shapes are orthogonal vectors too.

The maximum number of PSWLs is equal to the number of modal inertial load retained for computing the MIL-based ESWLs (Case A).

### V.3.4 Hybrid-based ESWLs

From (IV.6.4), the  $n_t \times n_r$  hybrid-based ESWL matrix  $\mathbf{F}^{(\mathcal{L}^b \mathcal{M}^r, m)} = \left[\mathbf{f}_{(1)}^{(\mathcal{L}^b \mathcal{M}^r, m)}, \dots, \mathbf{f}_{(n_r)}^{(\mathcal{L}^b \mathcal{M}^r, m)}\right]$  obtained with CPT loading modes and modal inertial loads is expressed as

$$\mathbf{F}^{(\mathcal{L}^b \mathcal{M}^r, m)} = \mathbf{F}^{(\mathcal{C}\mathcal{M})} \mathbf{W}^{(\mathcal{L}^b \mathcal{M}^r, m)}, \quad (\text{V.3.31})$$

with  $\mathbf{F}^{(\mathcal{CM})} = [\mathbf{F}^{(\mathcal{C})} \ \mathbf{F}^{(\mathcal{M})}]$  an  $n_t \times (n_{cpt} + n_m)$  ( $n_{cpt} + n_m \leq n_r$ ) matrix whose columns collect the CPT loading modes,  $\mathbf{F}^{(\mathcal{C})} = \mathbf{A}\mathbf{P}^{(\mathcal{C})}$ , and the modal inertial loads. The weighting factors are collected in an  $(n_{cpt} + n_m) \times n_r$  matrix  $\mathbf{W}^{(\mathcal{L}^b\mathcal{M}^r, \mathcal{m})} = [\mathbf{W}^{(\mathcal{L}^b, \mathcal{m})} \ \mathbf{W}^{(\mathcal{M}^r, \mathcal{m})}]^T$ . In addition to the aforementioned studied assumptions of (see Sections V.3.2 and V.3.3)

- orthogonality of the normal modes of vibrations,
- and orthogonality of the weighting factors  $\mathbf{W}^{(\mathcal{L}^b, \mathcal{m})}$  and  $\mathbf{W}^{(\mathcal{M}^r, \mathcal{m})}$ ,

the CPT loading modes and MILs are the PSWLs

$$\mathbf{F}^{(\mathcal{CM})} = \mathbf{F}^{(\mathcal{P})}, \quad (\text{V.3.32})$$

if we have also

- orthogonality between the CPT loading modes and MILs

$$\left(\mathbf{F}_j^{(\mathcal{C})}\right)^T \mathbf{F}_k^{(\mathcal{M})} = 0 \quad \forall j \in [1, n_{cpt}], \forall k \in [1, n_m], \quad (\text{V.3.33})$$

- and orthogonality between the weighting factors of each CPT loading modes and modal inertial loads

$$\left[\mathbf{W}^{(\mathcal{L}^b, \mathcal{m})} \left(\mathbf{W}^{(\mathcal{M}^r, \mathcal{m})}\right)^T\right]_{jk} = 0 \quad \forall j \in [1, n_{cpt}], \forall k \in [1, n_m]. \quad (\text{V.3.34})$$

## V.4 Envelope reconstruction problem using PSWLs

Figure V.1 depicts the required steps to derive the PSWL basis. First, the structural behavior is appreciated and second, the suitable ESWL formulation, see Chapter IV, is selected. Third, for each envelope value is computed the associated ESWL. At this stage, it is not necessary to compute normalized ESWLs, see Section IV.10.1. Indeed, computing the singular value decomposition of the matrix  $\mathbf{F}^{(e)}$  collecting ESWLs, step four, which are normalized or not clearly provides the same PSWLs. The order of PSWLs may however differ if significant normalization coefficients multiply the “original” ESWLs. It is therefore recommended to compute only the original ESWLs for the singular value decomposition since the normalization coefficients are not an inherent characteristic of the definition of an ESWL given by the conditional expected load method.

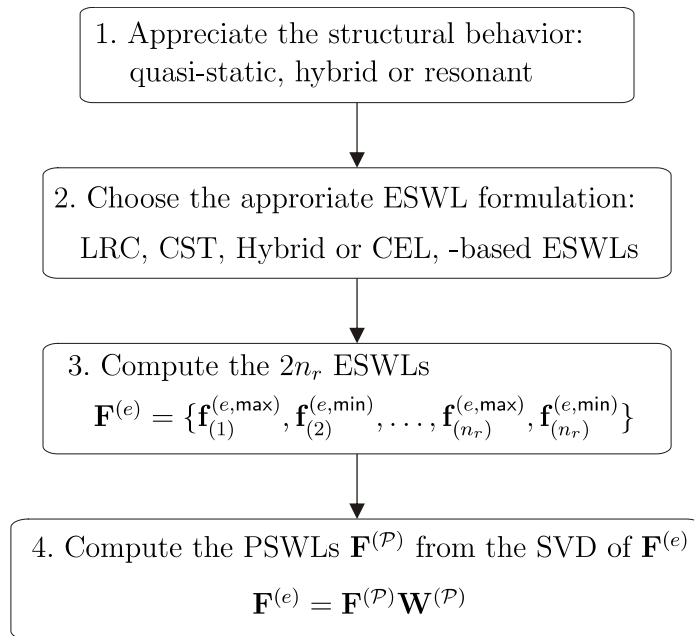


Figure V.1: Required steps to compute PSWLs.

Since PSWLs are basic SWLs, the whole methodology described in Chapter III to handle the envelope reconstruction problem is relevant. The PSWL basis, however, has the notable feature to adapt to the specific set of structural responses considered for reconstruction. Modal inertial loads or CPT loading modes do not have this feature at all. For that reason, the flowchart of the envelope reconstruction problem with combinations of basic SWLs, see Figure III.8, is adapted for PSWLs, see Figure V.2.

As illustrated in Chapter VI, the condition (III.3.12) on the overall reconstruction is more easily fulfilled than the condition (III.3.13) on the acceptable underestimation. The latter condition therefore usually drives the envelope reconstruction problem. For instance, after applying the  $k$ -th static wind load, the overall reconstruction condition is satisfied and only a small number of reconstructed structural responses has relative errors larger than the acceptable underestimation  $\varepsilon^{\dagger}$ . We define  $n_{r(k)}^{(\min)}$  and  $n_{r(k)}^{(\max)}$ , the numbers of lower (negative) and upper (positive) envelope values, with the indices  $i^-$  and  $i^+$ , respectively, that do not

fulfill the acceptable underestimation  $\tilde{\varepsilon}^t$  at the  $k$ -th iteration, i.e.,

$$\varepsilon_{i^-, (k)}^{(\min)} \leq \tilde{\varepsilon}^t \quad , \quad \varepsilon_{i^+, (k)}^{(\max)} \leq \tilde{\varepsilon}^t. \quad (\text{V.4.1})$$

The total number  $n_{r(k)}$  of envelope values that have relative errors larger than the acceptable underestimation  $\tilde{\varepsilon}^t$  at the  $k$ -th iteration is given by

$$n_{r(k)} = n_{r(k)}^{(\min)} + n_{r(k)}^{(\max)}. \quad (\text{V.4.2})$$

Through the iterations, if this number of structural responses  $n_{r(k)}$  decreases slowly even if either a large overestimation  $\hat{\varepsilon}$  is tolerated or a large number  $n_q$  of PSWLs are combined, a pertinent alternative is offered by the PSWL basis. This alternative, numbered 8 in the flowchart, consists in selecting the ESWLs associated with the structural responses for which the reconstruction has a too large relative error. A secondary basis of PSWLs is then computed by applying the singular value decomposition on these selected ESWLs. This secondary PSWL basis is used for the next iterations.

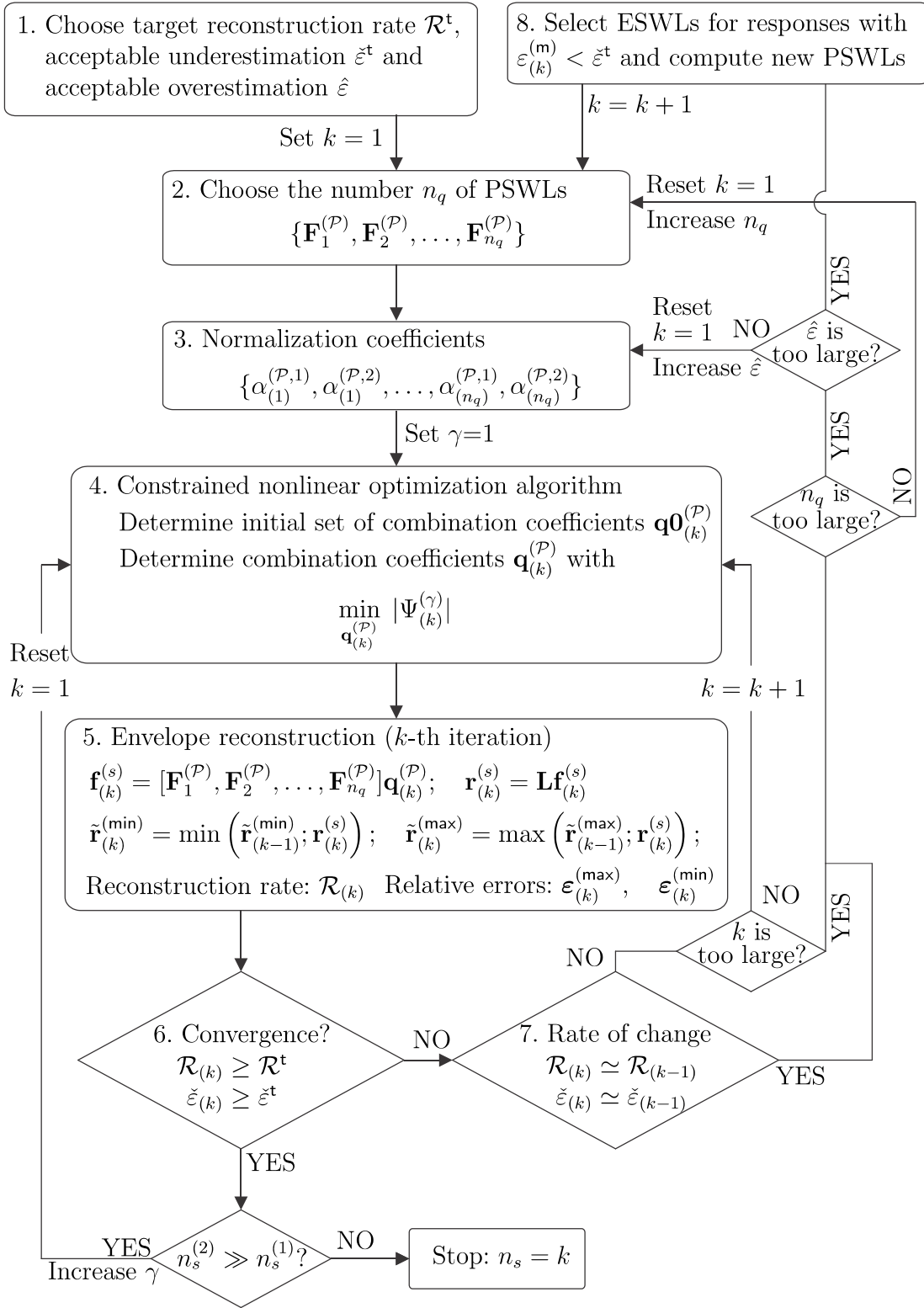


Figure V.2: Flowchart of the envelope reconstruction problem. Combinations of PSWLs are considered.



### Automatic procedure

An automatic procedure is described in Figure V.3. The number  $n_q$  of PSWLs for combinations is automatically selected such that

$$\frac{\sum_i^{n_q} \lambda_i}{\sum_i^r \lambda_i} \leq \chi^{\mathcal{P}}, \quad (\text{V.4.3})$$

with a minimum condition

$$n_q = n_{r(k)} \quad \text{if} \quad n_{r(k)} \leq 5. \quad (\text{V.4.4})$$

where  $\lambda_i$  is the  $i$ -th principal coordinate and  $\chi^{\mathcal{P}}$  is an arbitrary ratio. We recommend to set this ratio  $\chi^{\mathcal{P}}$  in the range [0.9 0.99]. This is studied in the illustrations.

After  $p$  updatings of the PSWL basis, the number  $n_{r(k)}$  of responses that do not fulfill the acceptable underestimation may have become very small, e.g. 5 or 10. These responses are expected to have a low indicator of correlation (III.3.9) and also slightly correlated with the other over-underestimated responses at the  $k$ -th iteration. Consequently, the truncated PSWL basis may no longer be efficient and the whole basis should be kept. This is the purpose of the minimum condition (V.4.4)

Figure V.3 depicts the flowchart with combinations of basic SWLs to solve the envelope reconstruction problem. At step 7 in the flowchart, if one of the two equations

$$\mathcal{R}_{(k)} = \mathcal{R}_{(k-1)}, \quad n_{r(k)} = n_{r(k-1)}, \quad (\text{V.4.5})$$

is fulfilled, this means that the PSWL basis is no longer efficient to solve the envelope reconstruction problem and has to be updated as described in step 8. At the end, the number  $n_p$  corresponds to the number of PSWL bases required to solve the envelope reconstruction problem.

This automatic procedure is especially relevant for complex envelope reconstruction problems, i.e., a problem with a low overall indicator of correlation, a large number of structural responses and a low acceptable overestimation and underestimation of the envelope. This is studied in Chapter VI.

### Convergence of the envelope reconstruction problem with very small tolerance on the acceptable relative errors

The smaller the acceptable overestimation and underestimation parameters are, the more frequent the update of the PSWL basis is and the larger the number  $n_s$  of static wind loads is. In this framework, the automatic procedure may not succeed in solving (efficiently, at least) the ERP. This is particularly true if the original ESWLs do not satisfy any of the envelope value or non-overestimation conditions. This is especially expected in a non-Gaussian framework.

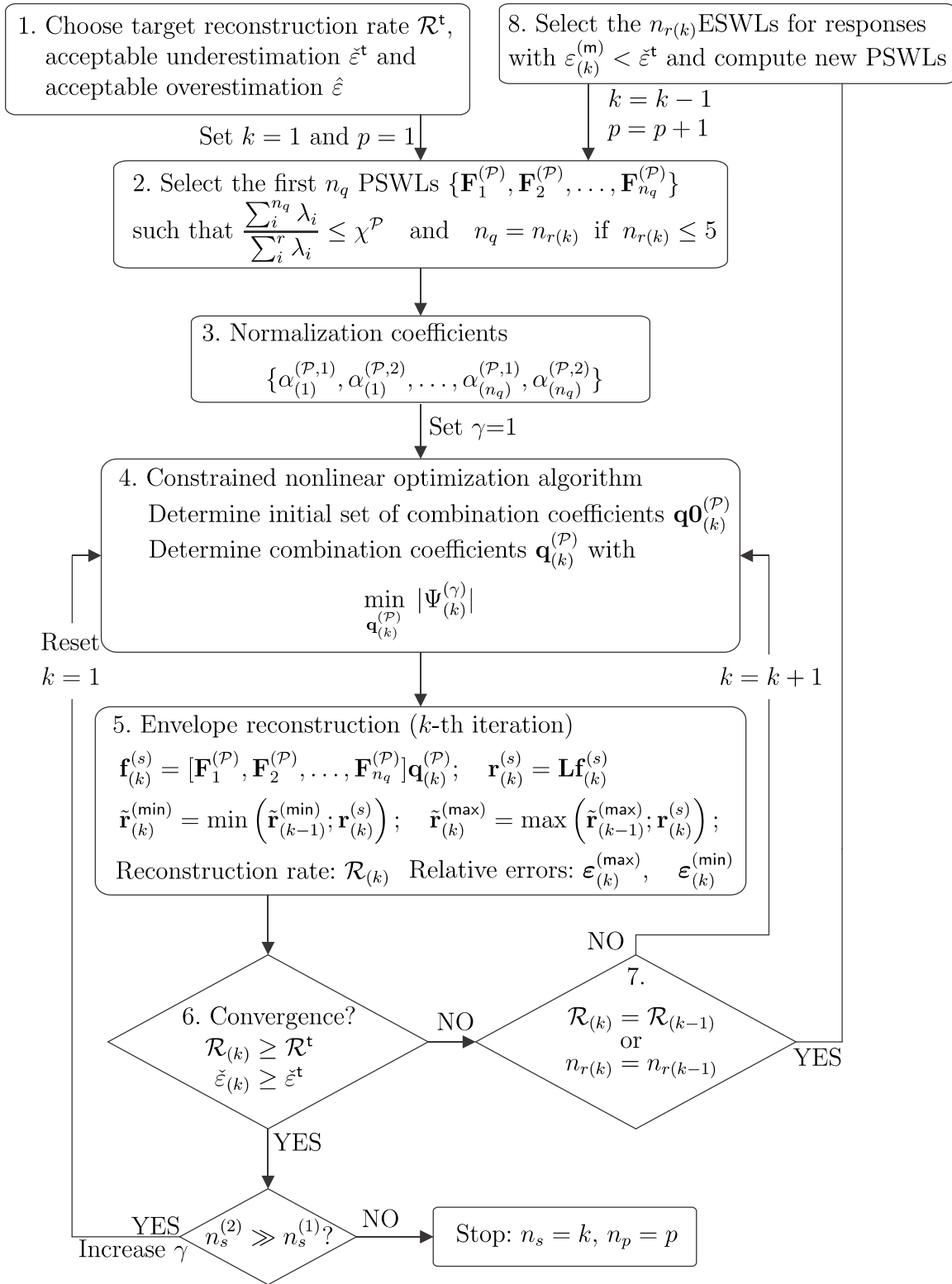


Figure V.3: Flowchart of the envelope reconstruction problem. Combinations of PSWLs and basis updating are considered.

## V.5 Summary

A new concept of Principal Static Wind Load has been established. These loadings are obtained with a singular value decomposition of equivalent static wind loads. The PSWLs are relevant for structures with quasi-static, hybrid or resonant behaviors, see Table V.2, on the condition that the appropriate ESWL formulation has been selected to compute the ESWLs.

| Structural behavior:        | Quasi-static | Dynamic<br>(Hybrid) | Resonant |
|-----------------------------|--------------|---------------------|----------|
| CPT loading modes           | ✓            | ✗                   | ✗        |
| Modal inertial loads        | ✗            | ✗                   | ✓        |
| Principal static wind loads | ✓            | ✓                   | ✓        |

Table V.2: Envelope reconstruction problem with basic static wind loads. Domain of applicability.

Contrary to the CPT loading modes and modal inertial loads, the PSWLs are dependent upon the set of structural responses to be reconstructed. The general methodology to solve the ERP described in Chapter III is improved with this distinctive feature formalized in an automatic procedure. Its efficiency is illustrated with the second and third examples in Chapter VI.

In Chapter VI is demonstrated that the PSWLs are better suited for an accurate reconstruction of the envelope than the ESWLs, CPT loading modes or the MILs, as well.



# Chapter VI

## Illustrations

### VI.1 Introduction

This Chapter illustrates the different concepts discussed in this work with three examples. The modal inertial loads (Section II.5), CPT loading modes (Section II.8.2), equivalent static wind loads (Chapter IV) and principal static wind loads (Chapter V) are considered to handle the envelope reconstruction problem stated in Chapter III by means of the general methodology described in Section III.3. Table VI.1 collects the main characteristics of each example. In the main part of the text, the envelope values (Section II.3) are computed for a reference period of 10 min. Other reference periods could also be used. This is done in the Appendix A for a reference period of 1 hour.

- First in Section VI.2, a four span bridge with pinned supports is analyzed under Gaussian lift aerodynamic forces. The ERP focuses on the bending moment diagram. Equivalent static wind loads are obtained from the conditional expected load method, derived in Section IV.7. Several specific properties of this academic example allows us to show that the PSWL basis degenerates into the CPT loading modes and the MILs as limiting cases, see Sections V.3.2 and V.3.3, respectively. This example is adapted from (Blaise and Denoël, 2013a).
- Second in Section VI.3, the methodology to handle the ERP is confronted with a real structure: the large roof of the stadium at Lille, France. Aerodynamic pressures are obtained with wind-tunnel measurements and the dynamic analysis is firstly done in a Gaussian framework. The modal analysis and in particular the estimation of modal correlation coefficients are done using the extended white noise approximation, see Section II.7. As regards the ERP, the number of envelope values to reconstruct is many times greater than in the first example and the overall correlation between responses is also lower. In this case, the benefit from combinations of SWLs, by applying the constrained nonlinear optimization algorithm described in Section III.5 is important. Moreover, the influence on the envelope reconstruction of an acceptable range of overestimation  $\hat{\varepsilon}$  is investigated. This example is adapted from (Blaise and Denoël, 2013b).
- Third in Section VI.4, the automatic procedure to handle the ERP with PSWLs is implemented for the Lille's stadium. The non-Gaussianity is taken into account to

compute the peak factors. The three options detailed in Section III.3.5 to derive SWLs ensuring no underestimation of the envelope are investigated.

- At last in Section VI.5, a rigid gable-roofed low-rise building is studied under aerodynamic pressures obtained with wind-tunnel measurements. Depending on the angle of attack of the wind, the aerodynamic pressure field for this roof configuration is known to exhibit mildly to strongly non-Gaussianities. In this context, equivalent static wind loads are derived from the conditional expected load method used in combination with the bicubic model derived in Section IV.8. These equivalent static wind loads are compared with those obtained from the conditional sampling (Section IV.3) and load-response correlation (Section IV.4) methods. The envelope value and non-overestimation conditions, introduced in Section IV.2, are extensively studied for this purpose. The impact on the PSWL basis of the methods used to compute the ESWLs and effects on the efficiency to handle the ERP are assessed. This example is adapted from (Blaise and Denoël, 2015; Blaise et al., 2016). Additionally, the automatic procedure to handle the ERP with PSWLs is implemented. The three options detailed in Section III.3.5 to derive SWLs ensuring no underestimation of the envelope are investigated as well.

|                     | Example 1<br>Four span<br>bridge | Example 2<br>Lille's stadium |              | Example 3<br>Low-rise gable roof |           |
|---------------------|----------------------------------|------------------------------|--------------|----------------------------------|-----------|
| Section             | VI.2                             | VI.3                         | VI.4         | VI.5                             | VI.5.5    |
| Methodology         | General                          | General                      | Automatic    | General                          | Automatic |
| Analysis            | Hybrid                           | Hybrid                       |              | Quasi-static                     |           |
| Framework           | Gaussian                         | Gaussian                     | Non-Gaussian | Non-Gaussian                     |           |
| Pressures           | Model                            | Wind-tunnel                  |              | Wind-tunnel                      |           |
| ERP                 | Bending moments                  | 6 internal forces            |              | Bending moments                  |           |
| ESWLs               | CEL-based                        | Hybrid-based                 |              | CST-, LRC-, CEL-                 |           |
| PSWLs               | ✓                                | ✓                            | ✓            | ✓                                |           |
| CPT, MILs           | ✓                                | ✓                            | -            | -                                |           |
| $n_r$               | 121                              | 7994                         |              | 451                              |           |
| $\bar{\rho}_r$      | [0.41, 0.47]                     | 0.16                         |              | 0.53                             |           |
| $\mathcal{R}^t$     | 95%                              | 95%                          | 100%         | 95%                              | 100%      |
| $\varepsilon^t$     | -10%                             | -25%                         | Variable     | -15%                             | Variable  |
| $\hat{\varepsilon}$ | 0%                               | [0, 25, 50]%                 | Variable     | [0, 15]%                         | Variable  |
| $\gamma$            | [1, 3, 5, 7]                     | [1, 2, 3]                    | 1            | 1                                | 1         |

Table VI.1: Characteristics of the three examples.

## VI.2 Four span bridge

### Description of the structure

A four span bridge with pinned supports is analyzed under wind actions. Each span has a length of one hundred meters. The finite element model is an assembly of classical 2-D beam elements with two DOFs per node (vertical displacement and rotation in this order). The pinned supports are modeled as springs with a large stiffness  $K = 10^{10}$  N/m compared to the bending stiffness  $EI/L^3$ , see Figure VI.1. This trick is necessary to compute elastic forces at each node with (II.4.3) in the CEL method since nodal wind forces are also applied at the supports of the finite element model.

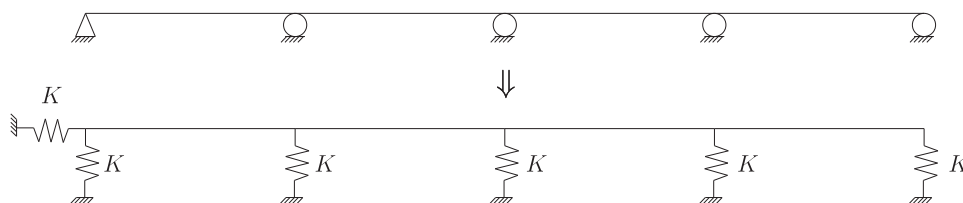


Figure VI.1: Finite element modeling of the pinned supports of the four span bridge as springs with a large stiffness  $K$ .

Each span is uniformly divided into 30 finite elements in order to obtain a fine representation of the profiles of internal forces (each finite element has a length  $\ell_e=3.33$  m). The number of DOFs is thus equal to  $n_t=242$ . Table VI.2 gives the characteristics of the deck.

| Width          | Section       | Inertia        | Young's modulus          | Mass density        | Lift coefficient |
|----------------|---------------|----------------|--------------------------|---------------------|------------------|
| $B=30\text{m}$ | $1\text{m}^2$ | $10\text{m}^4$ | $1\text{e}9\text{N/m}^2$ | $2500\text{kg/m}^3$ | $C_L=-0.15$      |

Table VI.2: Geometrical and mechanical characteristics of the deck.

The structural dynamic analysis of the wind effects is conducted in both modal (Section II.6.2) and hybrid bases (Section II.6.3). Figure VI.2 depicts the vertical displacements of the first six modes. These modes have frequencies below 1.5 Hz and are retained for the modal analysis. They are normalized to a unitary maximum.

A very specific property of the modal basis (Section II.5) in this example is that, in addition to be orthogonal vectors in the metric space of the stiffness and mass matrices ( $\mathbf{K}, \mathbf{M}$ ), they are also mutually orthogonal:  $\Phi^T \Phi = \mathbf{I}$ . This is explained by the uniform mass distribution and bending stiffness of the bridge. This is not usually the case for real bridges and the example treated here is rather academic. However, this specific feature is not mandatory for the developments in the sequel.

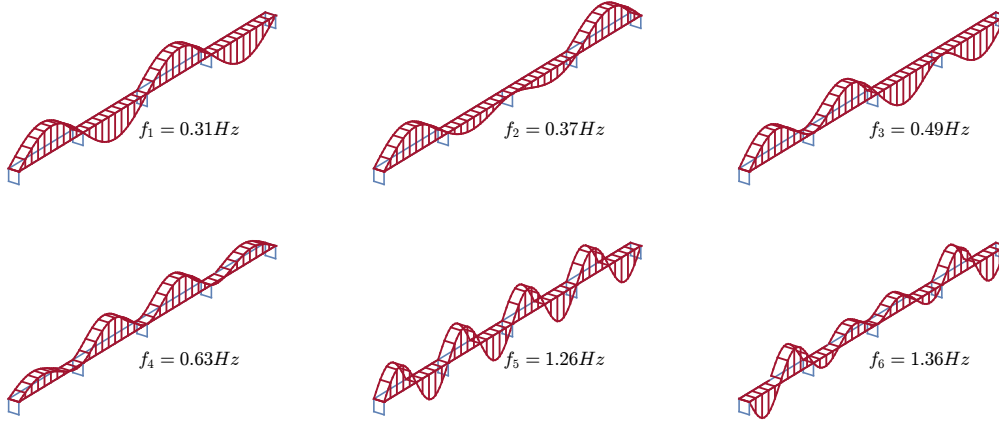


Figure VI.2: Modal vertical displacements and associated frequencies.

A Rayleigh damping matrix  $\mathbf{C}$  is constructed as

$$\mathbf{C} = \alpha\mathbf{M} + \beta\mathbf{K}, \quad (\text{VI.2.1})$$

by imposing a damping coefficient  $\xi$  in the first and fourth modes. Three damping ratios 0.5%, 1.5% and 4.5% are used to study a resonant, an intermediate background-resonant and a background-slightly resonant, behavior of the structure, respectively. The  $\alpha$  and  $\beta$  coefficients used in (VI.2.1) and obtained through (II.5.16) and (II.5.17), respectively, are reported in Table VI.3.

|                  | $\xi_1 = \xi_4$ |       |       |
|------------------|-----------------|-------|-------|
|                  | 0.5%            | 1.5%  | 4.5%  |
| $\alpha$ [rad/s] | 0.013           | 0.04  | 0.12  |
| $\beta$ [s/rad]  | 0.0017          | 0.005 | 0.015 |

Table VI.3: The  $\alpha$  and  $\beta$  coefficients used to build the Rayleigh damping matrix.

### Description of the loading

For the sake of simplicity, the loading induced by the wind takes a basic form in this example. More advanced models should obviously be considered for a real case study.

A one-dimensional longitudinal Gaussian velocity field with a mean velocity  $U$  equal to 30 m/s and a turbulence component  $u(t)$  with intensity equal to 16% is considered, that gives a variance of  $\sigma_u^2 = 23.04$  (m/s)<sup>2</sup>. The bridge is analyzed under the lift aerodynamic force given by

$$F'_L = \frac{1}{2}\rho C_L B(U^2 + 2Uu). \quad (\text{VI.2.2})$$

In (VI.2.2), the horizontal, vertical and torsional deck motions are not taken into account to derive the relative velocity of the incoming wind. Additionally, the quadratic term of the fluctuating component  $u$  is disregarded. The lift coefficient is arbitrarily chosen equal



to -0.15 and other values (Denoël, 2009b) could have been chosen without modifying the interpretation of the results.

Again, from a structural design viewpoint, the vertical component of the turbulence should also be included in the turbulence model, as much as the aerodynamic drag force and torque should also be considered.

The longitudinal turbulent component  $u$  of the velocity field is described by the following (frequency-based) power spectral density (II.2.25) from Von Karman (1958)

$$\frac{f S_u}{\sigma_u^2} = \frac{4\bar{f}L_u/z}{[1 + 70.8(\bar{f}L_u/z)^2]^{5/6}}, \quad (\text{VI.2.3})$$

with  $\sigma_u^2 = \int_{\mathbb{R}^+} S_u df$  and where  $f$  is the frequency,  $\bar{f} = fz/U$  is the Monin coordinate,  $L_u = 200m$  is the integral length scale of  $u$  and  $z = 100m$  is the height of the bridge above ground level, see Figure VI.3.

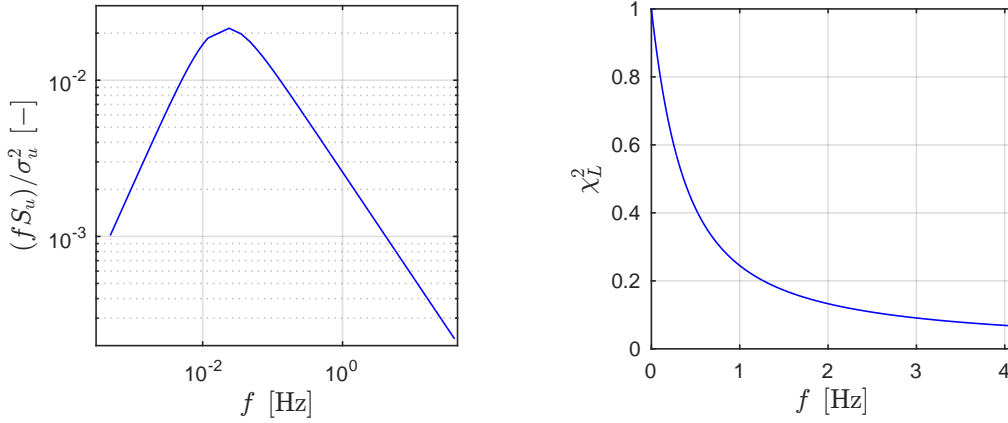


Figure VI.3: Von Karman power spectral density (left) and aerodynamic admittance for the lift aerodynamic force (right).

The real part of the spanwise coherence function (II.2.37) of  $u$  between two points of the deck separated by a length  $\ell$  is modeled by a decreasing exponential (Vickery, 1970)

$$\Gamma = \exp\left(-\frac{2fC\ell}{2U}\right), \quad (\text{VI.2.4})$$

where  $C$  is the coefficient of coherence taken equal to 8. To the author's knowledge, no generic model exists for the imaginary part of the coherence function; it is therefore not taken into account.

The average lift force per unit length,  $\mu_{L'}$ , is found as

$$\mu_{L'} = \frac{1}{2}\rho C_L B U^2 = -2531 \text{ N/m}, \quad (\text{VI.2.5})$$

with  $\rho = 1,25 \text{ kg/m}^3$ ,  $C_L$  and  $B$ , the mass density of the air, lift coefficient and deck's width, respectively, given in Table VI.2.

The  $n_t \times 1$  vector of average nodal forces,  $\boldsymbol{\mu}_{f'}$ , is given by

$$\boldsymbol{\mu}_{f'} = \mathbf{A}\mathbf{I}\mu_{L'}, \quad (\text{VI.2.6})$$

where  $\mathbf{A}=\text{diag}(\ell_e, 0, \dots, \ell_e, 0)$  is an  $n_t \times n_t$  matrix that collects the coefficients which transform the lift aerodynamic force per unit length to nodal vertical external forces for each element with a mean equal to -8437 N. The PSD of the lift aerodynamic force is

$$\frac{S_L}{\left(\frac{1}{2}\rho UB\right)^2} = 4C_L^2\chi_L^2 S_u, \quad (\text{VI.2.7})$$

where  $\chi_L^2(\omega)$  is the aerodynamic admittance proposed by [Davenport \(1962\)](#)

$$\chi_L^2 = \frac{2 \left[ \frac{7f}{U}B - 1 + \exp\left(-\frac{7f}{U}B\right) \right]}{\left(\frac{7f}{U}B\right)^2}, \quad (\text{VI.2.8})$$

shown in [Figure VI.3](#) and the variance of the lift aerodynamic force is  $\sigma_L^2=5.52 \cdot 10^5$  (N/m)<sup>2</sup>. The aerodynamic admittance relates the lift aerodynamic forces to the oncoming wind velocity.

Finally, the PSD matrix ([II.2.42](#)) of nodal forces is expressed as a function of the PSD of the lift aerodynamic force through

$$\mathbf{S}^f = \mathbf{A}\mathbf{\Gamma}S_L\mathbf{A}^\top, \quad (\text{VI.2.9})$$

where  $\mathbf{\Gamma}$  is an  $n_t \times n_t$  matrix of aerodynamic admittances taking into account the imperfect correlation of the turbulent component  $u$  of the velocity field using ([VI.2.4](#)). The variance of nodal vertical forces is  $6176 \cdot 10^6$  N<sup>2</sup>.

### Buffeting analysis in the modal basis

The white noise approximation and the proposed extension ([Section II.7](#)) are performed to compute the resonant contribution to the variances and covariance of modal amplitudes, respectively. Additionally, the residual contribution ([Section II.6.3](#)) is computed to check the timescale separation condition and so the relevancy of the white noise approximations, i.e., the mixed background/resonant contribution is negligible and the residual contribution mainly consists of the resonant one.

**Standard deviation of modal amplitudes** [Figure VI.4](#) depicts the standard deviation of modal amplitudes in modes 1 to 6 for the three studied damping cases:  $\xi=0.5\%$ ,  $1.5\%$  and  $4.5\%$ . Only the first four modes are activated and thus retained for the hybrid analysis. As expected, the timescale separation condition is fulfilled since the resonant and residual contributions are almost similar.

**Covariance of modal amplitudes** The white noise approximation of the real part of the coherence functions  $\Gamma_{mn}^{(\text{Re},\text{wn})}$  of generalized forces gives

$$\Gamma_{mn}^{(\text{Re},\text{wn})} = \begin{bmatrix} 1 & 0 & 0.01 & 0 \\ & 1 & 0 & 0 \\ & \text{Sym.} & 1 & 0 \\ & & & 1 \end{bmatrix}.$$

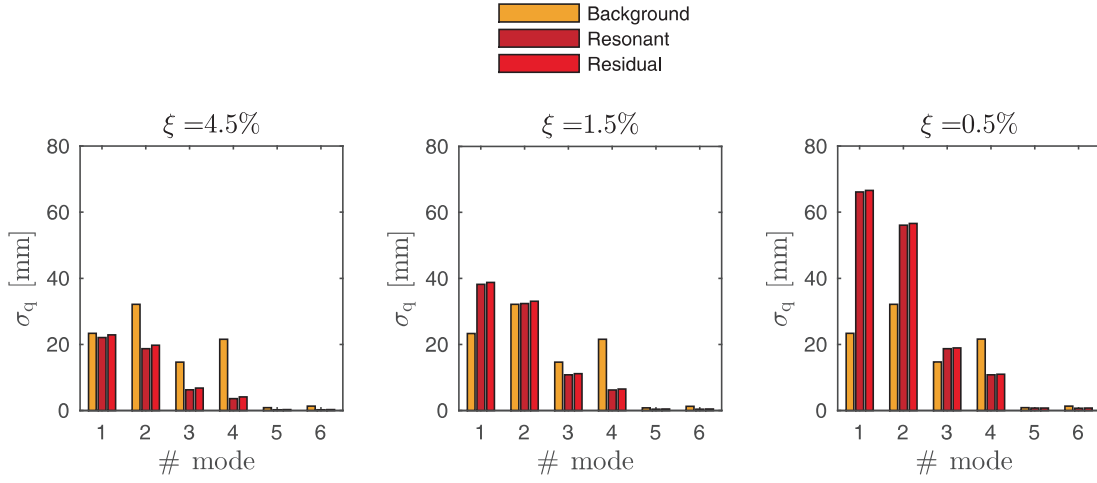


Figure VI.4: Standard deviation of the first six modal amplitudes.

In fact, there is only coherence between the first and third modes for which the white noise approximation is negligible. Therefore the resonant contribution to the correlation coefficients  $\rho_{q_m^r, q_n^r}^{(Re)}$  can be neglected and the overall correlation coefficient between modal amplitudes, see (II.7.31), simplifies as

$$\rho_{q_m q_n}^{(d)} \simeq \gamma_{mn}^b \rho_{g_m g_n} \quad \forall m \neq n. \quad (\text{VI.2.10})$$

The weighting function for the background contribution gives

$$\gamma_{mn}^b = \begin{matrix} \xi = 4.5\% & \xi = 1.5\% & \xi = 0.5\% \\ \begin{bmatrix} 0.53 & 0.63 & 0.67 & 0.72 \\ & 0.75 & 0.8 & 0.85 \\ & \text{Sym.} & 0.85 & 0.91 \\ & & & 0.97 \end{bmatrix}, & \begin{bmatrix} 0.27 & 0.37 & 0.42 & 0.5 \\ & 0.50 & 0.57 & 0.68 \\ & \text{Sym.} & 0.65 & 0.77 \\ & & & 0.92 \end{bmatrix}, & \begin{bmatrix} 0.11 & 0.17 & 0.21 & 0.3 \\ & 0.25 & 0.31 & 0.44 \\ & \text{Sym.} & 0.38 & 0.55 \\ & & & 0.80 \end{bmatrix}, \end{matrix}$$

and the correlation matrix (II.2.41) of the generalized forces is equal to

$$\rho_{g_m g_n} = \begin{bmatrix} 1 & 0 & 0.36 & 0 \\ & 1 & 0 & 0.6 \\ & \text{Sym.} & 1 & 0 \\ & & & 1 \end{bmatrix}.$$

Finally, the correlation matrix of the modal amplitudes reads

$$\rho_{q_m q_n}^{(d)} = \begin{matrix} \xi = 4.5\% & \xi = 1.5\% & \xi = 0.5\% \\ \begin{bmatrix} 1 & 0 & 0.24 & 0 \\ & 1 & 0 & 0.51 \\ & \text{Sym.} & 1 & 0 \\ & & & 1 \end{bmatrix}, & \begin{bmatrix} 1 & 0 & 0.15 & 0 \\ & 1 & 0 & 0.4 \\ & \text{Sym.} & 1 & 0 \\ & & & 1 \end{bmatrix}, & \begin{bmatrix} 1 & 0 & 0.07 & 0 \\ & 1 & 0 & 0.27 \\ & \text{Sym.} & 1 & 0 \\ & & & 1 \end{bmatrix}. \end{matrix}$$

In this case, the larger the damping, the larger the background component, and the larger the correlation between modal amplitudes.

### Determination of the envelope

In the sequel, it is chosen to focus exclusively on the bending moments but the same developments could be performed with several other types of responses (shear forces, stresses, etc). The number  $n_r$  of responses is thus equal to 121 and the bending moments are numbered from left to right, as for the spans and supports. The results hereinbelow are obtained through a hybrid analysis—see Section II.6.3—and a full modal analysis—see Section II.5—by means of the white noise approximation. The results associated with the hybrid basis are used as reference. Figure VI.5 shows the bending moments under the uniform average lift forces.

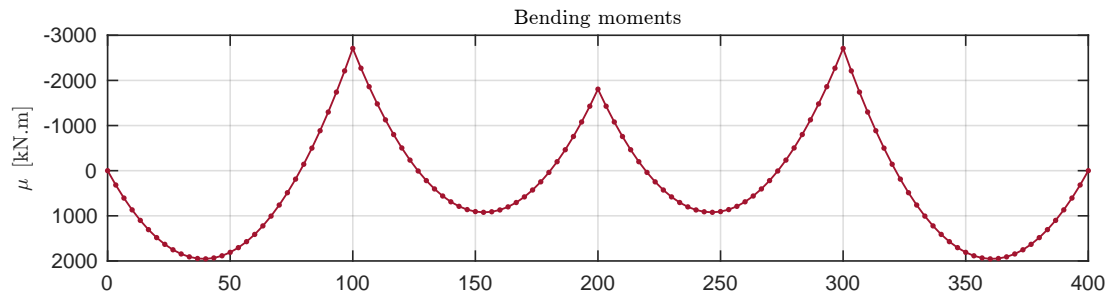


Figure VI.5: Mean bending moment diagram.

Figure VI.6-(a,b) depicts the background contribution and the total standard deviation of the bending moments, for the three studied cases.

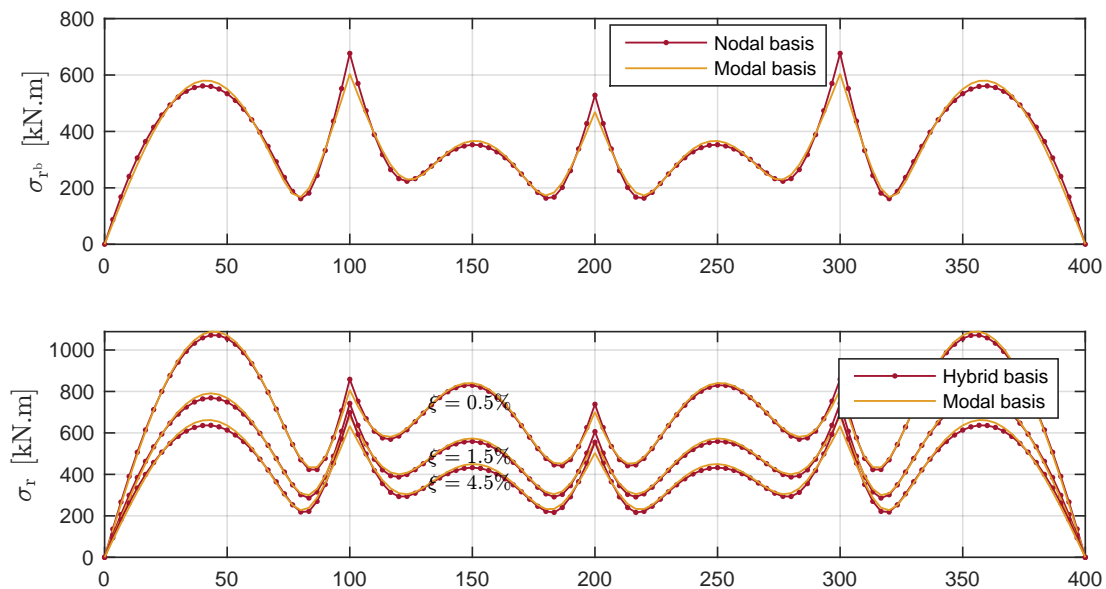


Figure VI.6: Background contribution and total standard deviations of the bending moments.

The background contribution is well-evaluated in the modal basis and the recourse to a hybrid basis for the analysis is not obligatory. As expected, maxima occur in side spans at the extremities and the resonant case,  $\xi = 0.5\%$ , provides the largest standard deviation of the bending moments.

In order to evaluate the relative importance of the background  $\sigma_{r_b}^2$  and resonant  $\sigma_r^2$  contributions in the responses, the background-resonant ratio  $b_r = \sigma_{r_b}^2 / \sigma_r^2$  for each bending moment is computed and given in Figure VI.7. These ratios show the same profile for the three cases. Near supports, the background component for each case is more important than in the span which simply results from the smallness of inertial forces near supports. This Figure justifies the choice of three damping coefficients  $\xi = 4.5\%$ ,  $\xi = 1.5\%$  and  $\xi = 0.5\%$ . Indeed, the 3 cases more or less correspond to  $b_r \gg 1$ ,  $b_r \sim 1$  and  $b_r \ll 1$ .

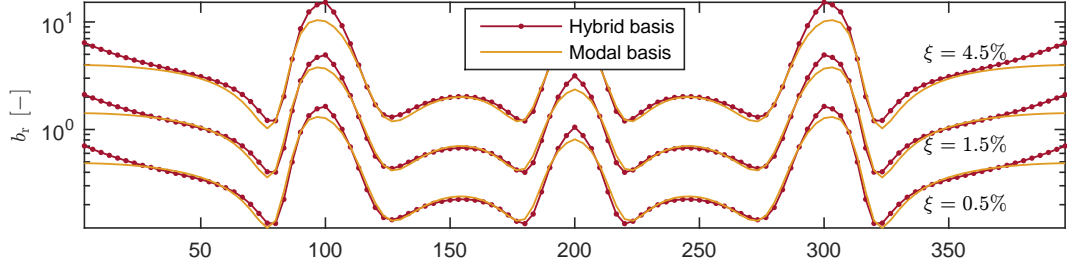


Figure VI.7: Background-resonant ratios of the bending moments.

Figure VI.8 illustrates the peak factor computed with (II.3.21). As the structural behavior is more and more dynamic, the zero-up crossing, and thus the peak factor, increase.

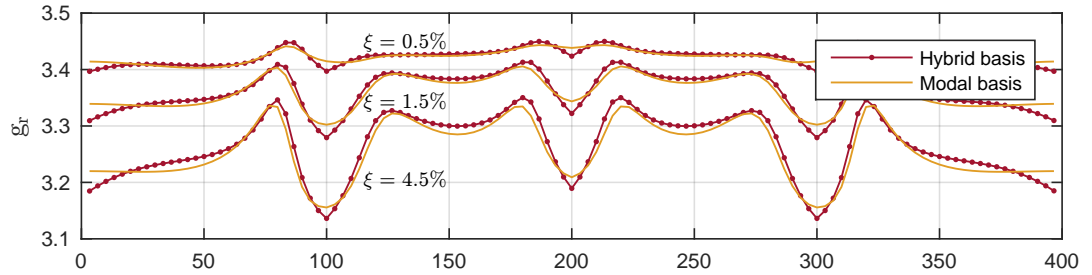


Figure VI.8: Peak factors, obtained using (II.3.21), for the three studied cases.

Figure VI.9 shows the averages of the absolute correlation coefficients defined by (III.3.9). The more dynamic the structural behavior is, the more correlated the structural responses are to each other. This is only true in the spans where the inertial forces mainly take place and lower values of  $\bar{\rho}_{r_i}$  are observed near the supports.

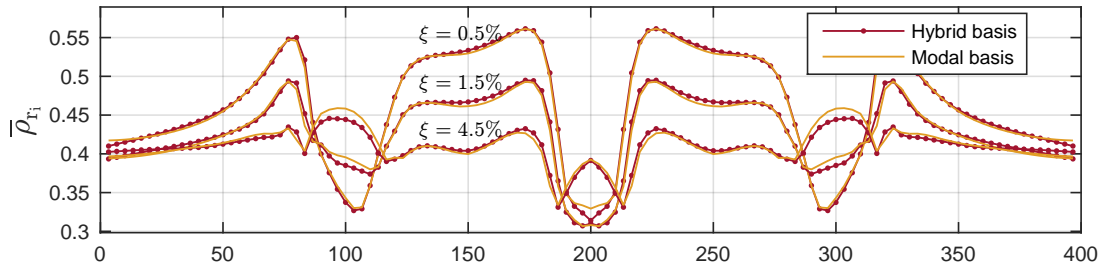


Figure VI.9: Averages of the absolute correlation coefficients, obtained using (III.3.9), for the three studied cases.

Table VI.4 gives the overall indicator of correlation. From a quasi-static to a resonant behavior of the structure, the overall correlation between the structural responses slightly increases.

| $\xi$          | 0.5% | 1.5% | 4.5% |
|----------------|------|------|------|
| $\bar{\rho}_r$ | 0.47 | 0.43 | 0.41 |

Table VI.4: Overall indicator of correlation, defined in (III.3.8), for the three different damping ratios.

Figure VI.10 depicts the envelope and total envelope for the three studied cases which we seek to reconstruct with static wind loads in the sequel.

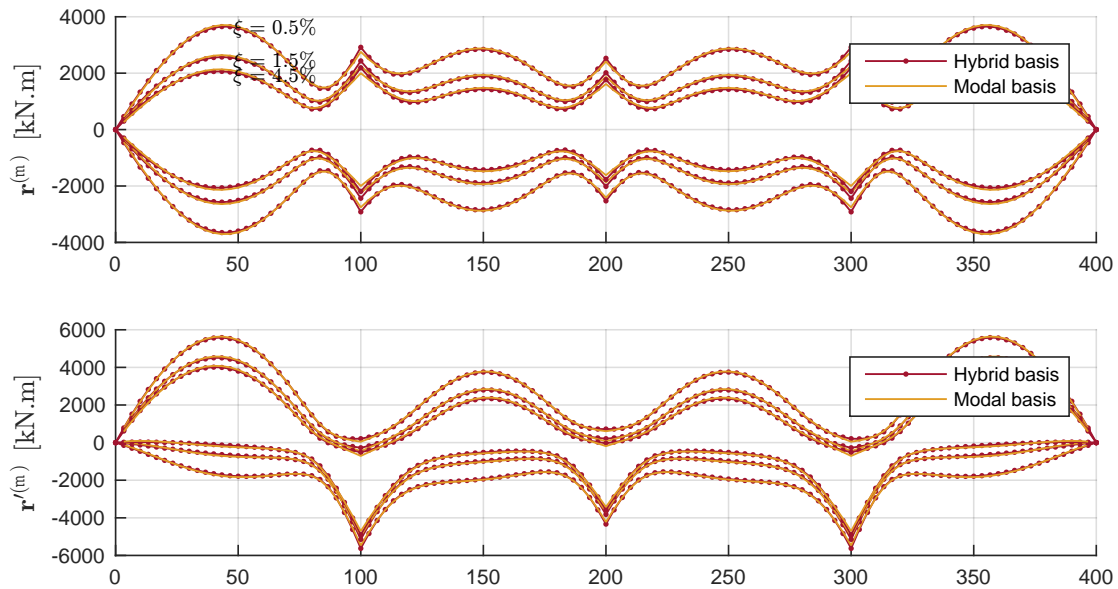


Figure VI.10: Envelope (upper graph) and total envelope (lower graph) bending moment diagrams.

### VI.2.1 CEL-based ESWLs for the case $\xi = 1.5\%$

In the illustrations hereinafter, we illustrate the conditional expected SWLs using the proposed conditional expected load method, see Section IV.7. Figure VI.11 illustrates the variance of elastic forces computed with formulation 1 in both hybrid and modal bases and the variance of the wind forces is also shown. Although elastic forces comprise both transverse forces and moments, only transverse forces are represented in Figure VI.11; the same convention holds in the following figures.

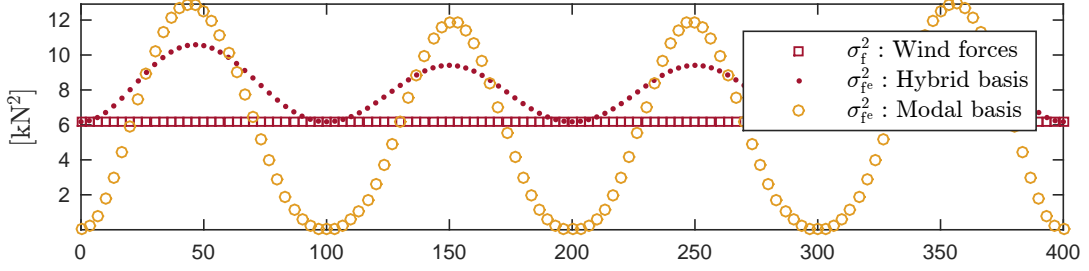


Figure VI.11: Variance of elastic forces computed with formulation 1, obtained using (IV.7.20), in a hybrid basis and in a modal basis. The variance of applied wind forces is also represented for comparison.

Large differences of variance are observable between the results obtained in a hybrid basis and those obtained in a modal basis. Actually, the modal basis with the first four modes is inappropriate to provide a relevant estimation of the variance of applied wind forces. This is explained by the profile for the variance of applied wind forces and the shapes of the modal inertial loads. The first four MILs are represented in Figure VI.12.

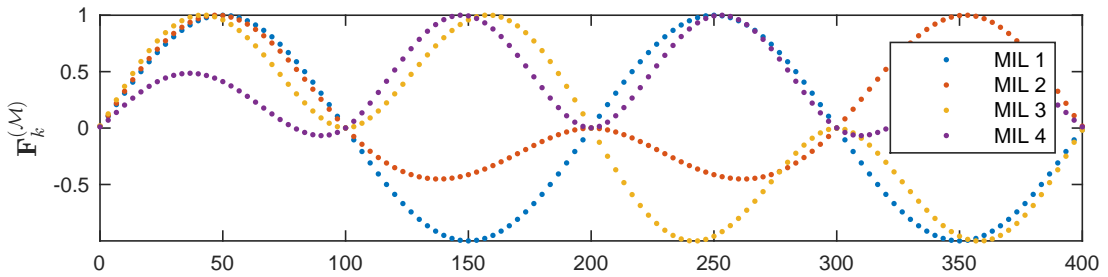


Figure VI.12: Unity-scaled modal inertial loads (vertical forces).

Figure VI.13 illustrates the approximation of the variance of wind forces  $\mathbf{f}$  with an increasing number of modal inertial loads through

$$\Sigma^{\mathbf{f}} \simeq \mathbf{K}\Phi\Sigma^{\mathbf{q}^b}\Phi^{\top}\mathbf{K}^{\top}. \quad (\text{VI.2.11})$$

Even with the first 50 MILs, there are large differences, especially close to the support where the inertial forces are low. It is thus not recommended to use the formulation 1 in a full modal basis.

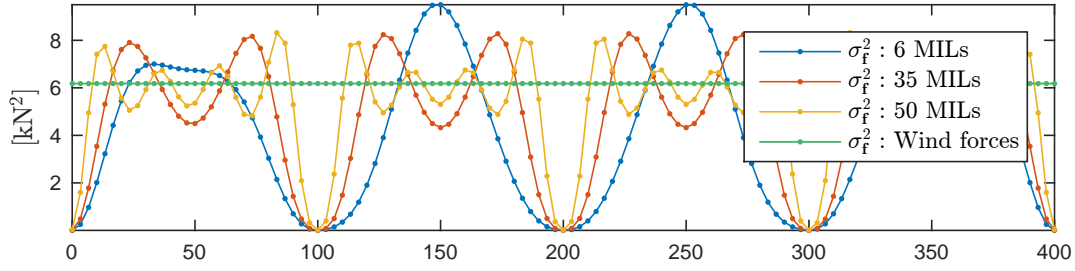


Figure VI.13: Approximation of the variance of vertical wind forces  $\sigma_{\mathbf{f}}$  with an increasing number of modal inertial loads using (VI.2.11).

In formulation 2, contributions of each covariance matrix in (IV.7.21) are studied next and rearranged here as

$$\Sigma^{\mathbf{f}^e} - \Sigma^{\mathbf{f}} = (\Sigma^{\mathbf{f}^e})_{\mathbf{A}} + (\Sigma^{\mathbf{f}^e})_{\mathbf{B}} + (\Sigma^{\mathbf{f}^e})_{\mathbf{C}}, \quad (\text{VI.2.12})$$

with  $(\Sigma^{\mathbf{f}^e})_{\mathbf{A}} = \Sigma^{\mathbf{f}} \ddot{\mathbf{x}} \mathbf{M}^{\mathbf{T}} + \mathbf{M} \Sigma^{\ddot{\mathbf{x}} \mathbf{f}}$ ,  $(\Sigma^{\mathbf{f}^e})_{\mathbf{B}} = \mathbf{M} \Sigma^{\ddot{\mathbf{x}}} \mathbf{M}^{\mathbf{T}}$  and  $(\Sigma^{\mathbf{f}^e})_{\mathbf{C}} = \mathbf{C} \Sigma^{\dot{\mathbf{x}}} \mathbf{C}^{\mathbf{T}}$ . Figure VI.14 shows contributions to the variance of elastic forces in formulation 2. As expected, the magnitude of  $(\Sigma_{ii}^{\mathbf{f}^e})_{\mathbf{B}}$  is three orders of magnitude greater than  $(\Sigma_{ii}^{\mathbf{f}^e})_{\mathbf{C}}$  and thus the contribution of the damping forces to the covariance matrix of elastic forces is negligible. However, the diagonal elements of  $(\Sigma^{\mathbf{f}^e})_{\mathbf{A}}$  are only one order of magnitude lower than  $(\Sigma_{ii}^{\mathbf{f}^e})_{\mathbf{B}}$  and therefore can not be neglected.

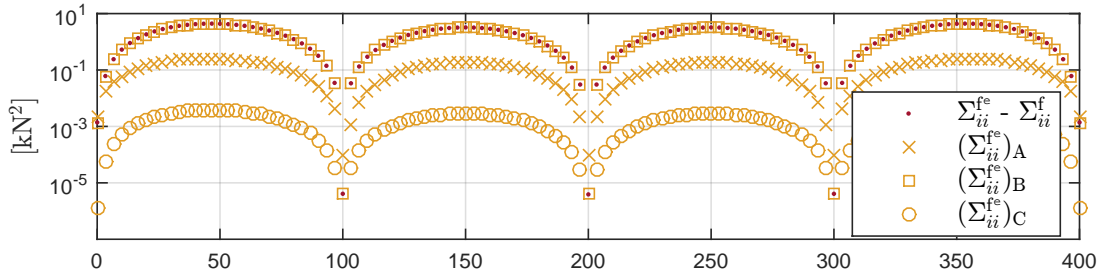


Figure VI.14: Contributions to the variance of elastic forces in formulation 2, obtained using (IV.7.21) of the CEL method.



## VI.2.2 Envelope reconstruction with ESWLs ( $\xi = 1.5\%$ )

A usual option to solve the envelope reconstruction problem is to consider the equivalent static wind loads computed here with the CEL method, see Section VI.2.1. The ESWLs are ranked depending on how a given ESWL is able to minimize the cost function, defined in (IV.10.6) and recalled here

$$f\left(\left(\tilde{\mathbf{r}}_{(k)}^{(\min)}, \tilde{\mathbf{r}}_{(k)}^{(\max)}\right), \left(\mathbf{r}^{(\min)}, \mathbf{r}^{(\max)}\right)\right) := \left|\Psi_{(k)}^{(\gamma)}\right|,$$

where  $\Psi_{(k)}^{(\gamma)}$  is the overall error indicator defined in (III.5.6). At each iteration, the ESWL providing the lower cost function is selected and applied to the structure following the flowchart depicted in Figure IV.4. The acceptable overestimation  $\hat{\varepsilon}$  is set equal to zero and the parameter  $\gamma$  to one. All ESWLs computed with the CEL method naturally satisfy the envelope value condition (IV.2.3), see Table IV.2. Moreover, the non-overestimation condition (IV.2.4) is verified and all CEL-based ESWLs fulfill it. Therefore, the ESWLs do not require normalization—see Section IV.10.1—before using them for the envelope reconstruction problem.

Figures VI.15 and VI.16 show ESWLs and the iterative reconstruction of the envelope. In a Gaussian context, the  $k$ -th and  $(k+1)$ -th static wind loads are identical in distribution and just differ by their sign for  $k$  odd, see Section IV.10.2.

Both figures also illustrates the vertical displacement component of the influence line  $\mathbf{L}_i$  corresponding to the  $i$ -th bending moment and the correlation coefficient  $\overline{\rho_{r_i}}$  between the  $i$ -th bending moment and the bending moment profile. Additionally, the structural responses under each ESWL and the sequential reconstruction of the envelope  $\tilde{\mathbf{r}}_k^{(m)}$  using the responses for the considered bending moments are depicted. Finally, the relative errors between the envelope and its reconstruction are given. As expected, the shapes of the loads are related to the influence lines of the considered responses. Actually, the loadings do not match precisely the influence line due to the coherence in the velocity field. It could be observed that the less coherence there is, the more equivalent static wind loads match the influence lines of the considered responses.

The figures illustrate that the response under a specific equivalent static wind load lies within the envelope but also partially reconstructs the envelope at other sections than the considered one, especially when the correlation is close to unity in magnitude, see (IV.3.2). To sum up, the reconstructed envelope  $\tilde{\mathbf{r}}_{(k)}^{(m)}$  monotonically converges towards the actual envelope.

The methodology to solve the ERP—see Section III.3—and particularized for ESWLs in Figure IV.4 is next applied. We choose an acceptable overall reconstruction  $\mathcal{R}^t$  of 95 % and an acceptable underestimation  $\tilde{\varepsilon}^t$  of  $-10\%$ . The overall reconstruction indicator  $\mathcal{R}_{(k)}$  gives a global picture of the whole reconstruction of the bending moments in the bridge while the largest relative error indicator  $\tilde{\varepsilon}_{(k)}$  indicates the worse reconstruction of the envelope.

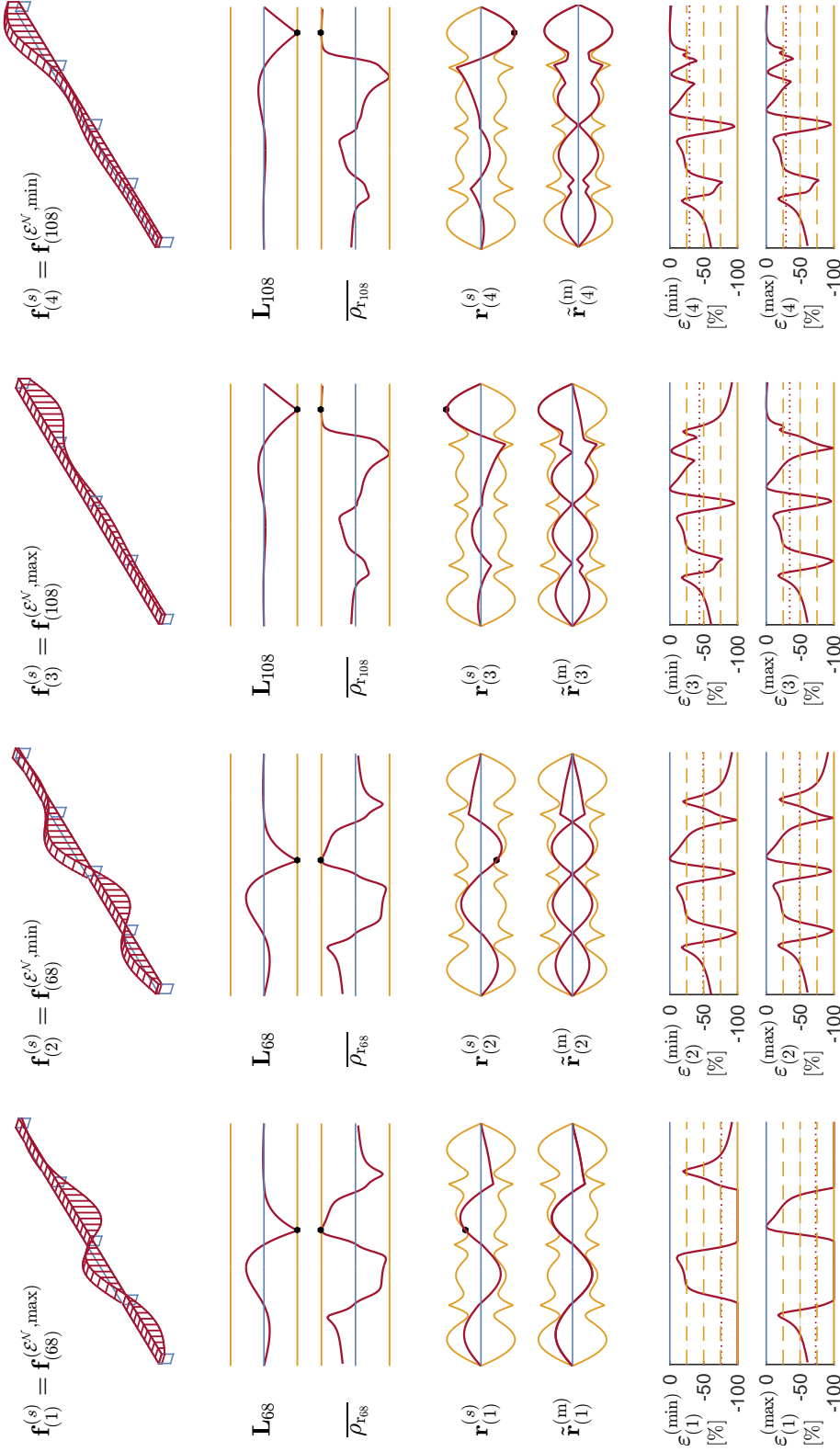


Figure VI.15: CEL-based ESWLs  $\mathbf{f}_{(i)}^{(\mathcal{E}^V, m)}$  (vertical forces at every node), influence line  $\mathbf{L}_i$  (vertical displacement component), correlation coefficients  $\overline{\rho}_{r_i}$ , static bending moments  $\mathbf{r}_{(i)}^{(s)}$ , reconstructed envelope  $\tilde{\mathbf{r}}_{(i)}^{(m)}$  and relative errors  $\epsilon_{(i)}^{(\min)}$  and  $\epsilon_{(i)}^{(\max)}$  of the reconstructed envelope. Dots identify the bending moments associated with the ESWLs. Each column corresponds to the  $k$ -th iteration in the sequential reconstruction of the envelope. Range of iteration:  $i \in [1, 4]$ .

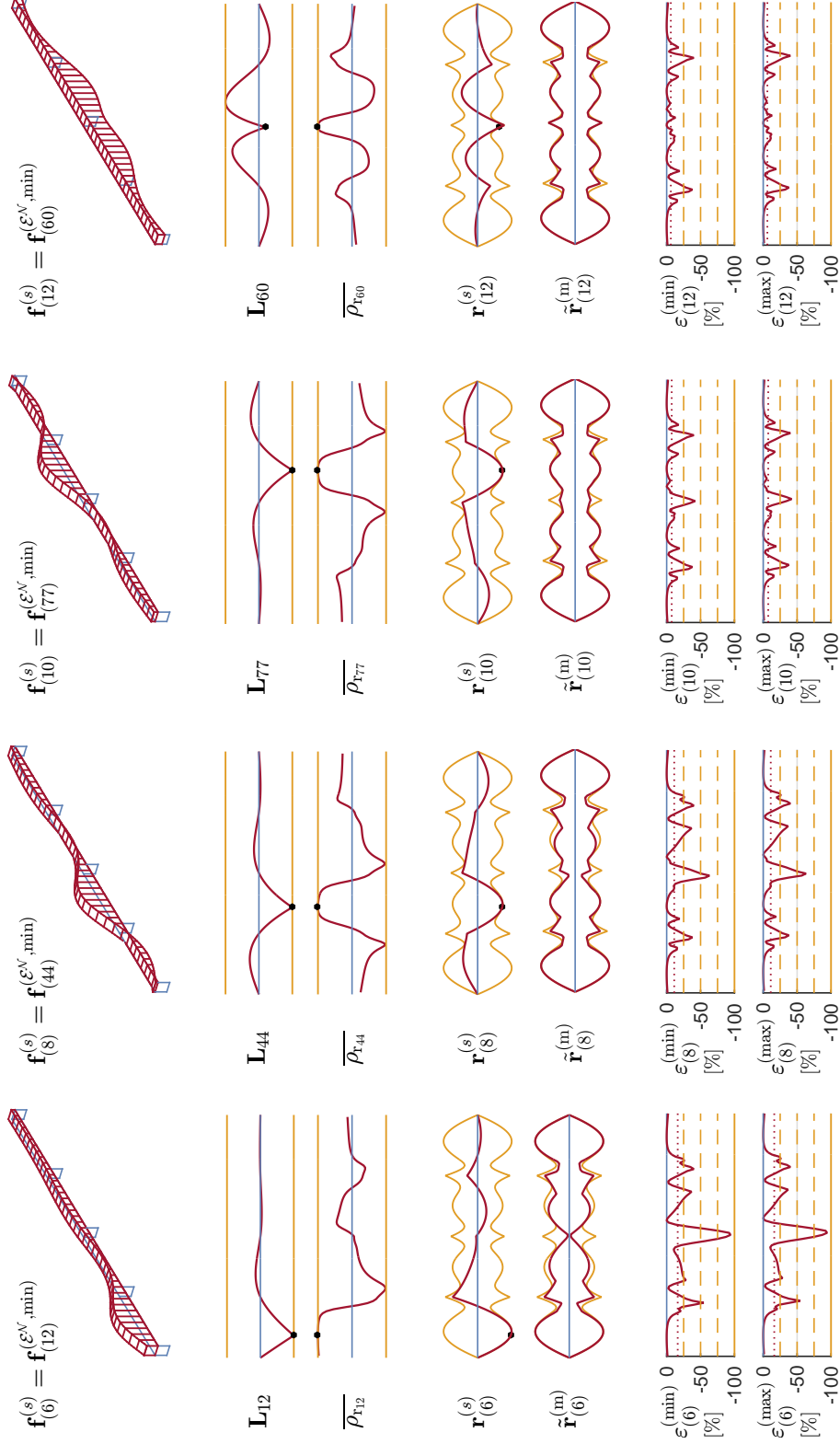


Figure VI.16: CEL-based ESWLs  $\mathbf{f}_{(i)}^{(E^N, m)}$  (vertical forces at every node), influence line  $\mathbf{L}_i$  (vertical displacement component), correlation coefficients  $\overline{\rho}_{r_i}$ , static bending moments  $\mathbf{r}_{(i)}^{(s)}$ , reconstructed envelope  $\tilde{\mathbf{r}}_{(k)}^{(m)}$  and relative errors  $\varepsilon_{(k)}^{(\min)}$  and  $\varepsilon_{(k)}^{(\max)}$  of the reconstructed envelope. Dots identify the bending moments associated with the ESWLs. Each column corresponds to the  $k$ -th iteration in the sequential reconstruction of the envelope. Range of iteration:  $i \in [1, 4]$ .

Figures VI.17 and VI.18 depict the overall reconstruction and the largest relative error indicators as a function of the number of load cases (from 1 to 35) derived by successive applications of ESWLs. The evolution of  $\mathcal{R}_{(k)}$  features a slow monotonic increase and a value of  $\mathcal{R}_{(k)}$  around 95% is obtained for  $n_s^{(1)} = 14$  ESWLs. However,  $n_s^{(2)} = 32$  ESWLs are necessary to satisfy the acceptable underestimation. Therefore, the number  $n_s$  of ESWLs to consider is equal to 32.

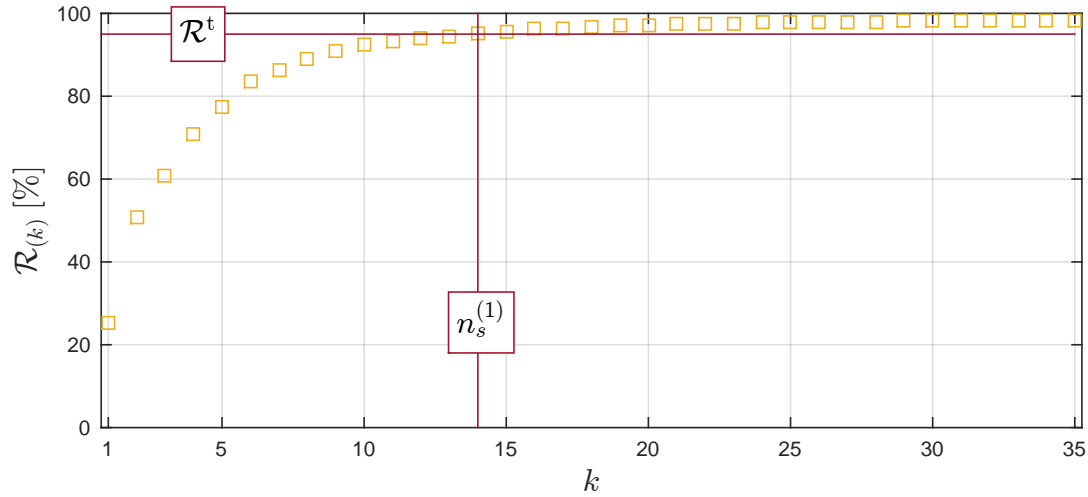


Figure VI.17: Evolution of the overall reconstruction indicator  $\mathcal{R}_{(k)}$  as a function of the number of ESWLs for the case  $\xi = 1.5\%$ . (ERP parameters:  $\hat{\varepsilon} = 0\%$ ,  $\gamma = 1$ )

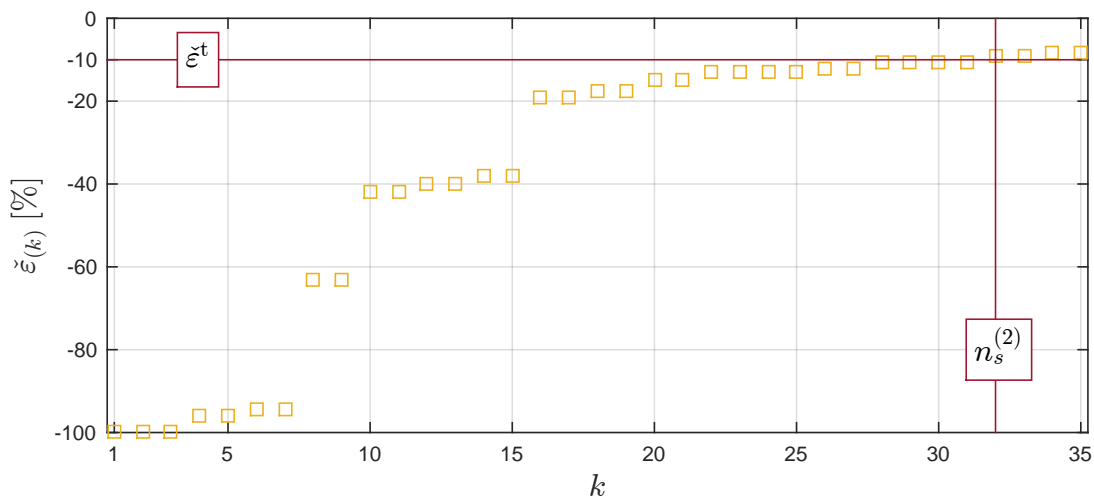


Figure VI.18: Evolution of the largest relative error indicator  $\check{\varepsilon}_{(k)}$  as a function of the number of ESWLs for the case  $\xi = 1.5\%$ . (ERP parameters:  $\hat{\varepsilon} = 0\%$ ,  $\gamma = 1$ )

### VI.2.3 PSWLs

A second option to solve the envelope reconstruction problem is to consider the principal static wind loads obtained by singular value decomposition of the equivalent static wind loads, see Chapter V.

The normalized cumulative summation of the principal coordinates  $S_{ii}$ , see (V.3.2), for the three cases are shown in Figure VI.19. The first four PSWL reproduce more than 90% of the total sum of the principal coordinates.

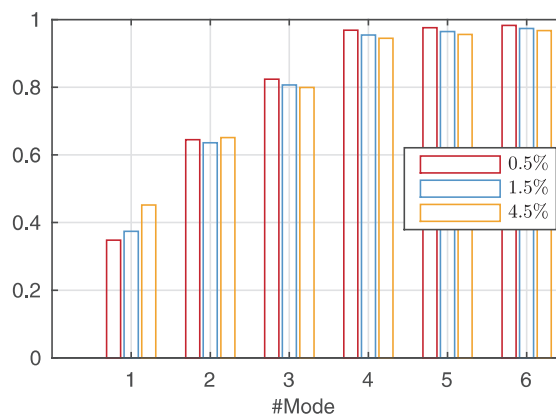


Figure VI.19: Normalized cumulative summation of the principal coordinates of the principal loadings.

The PSWLs require normalization —see Section III.4.1— before using them for the envelope reconstruction problem. Figure VI.20 shows the first four normalized principal static wind loads (computed from the 121 ESWLs) and the corresponding responses for the three studied cases. The left column in Figure VI.20, collects the static loads and responses for a structure with a dominant background behavior ( $\xi = 4.5\%$ ). In this case, similar PSWLs could be obtained by SVD of the ESWLs computed with the LRC method. The right column in Figure VI.20 corresponds to a dominant resonant behavior ( $\xi = 0.5\%$ ). The middle column in Figure VI.20, represents the basis for an intermediate background-resonant behavior. In that case, the singular value decomposition automatically provides loads with similarities with both limit cases. Also, some loadings in the three cases have close shapes but differ in position because of the behavior of the structure, see, for example, the first and second loadings for the cases  $\xi = 0.5\%$  and  $\xi = 1.5\%$ . In general, PSWLs are no longer associated with a specific bending moment but are the principal components, ordered by importance, of all the ESWLs. This is confirmed by their symmetry with respect to the vertical center of the bridge. Consequently, several extrema are recovered with a single loading.

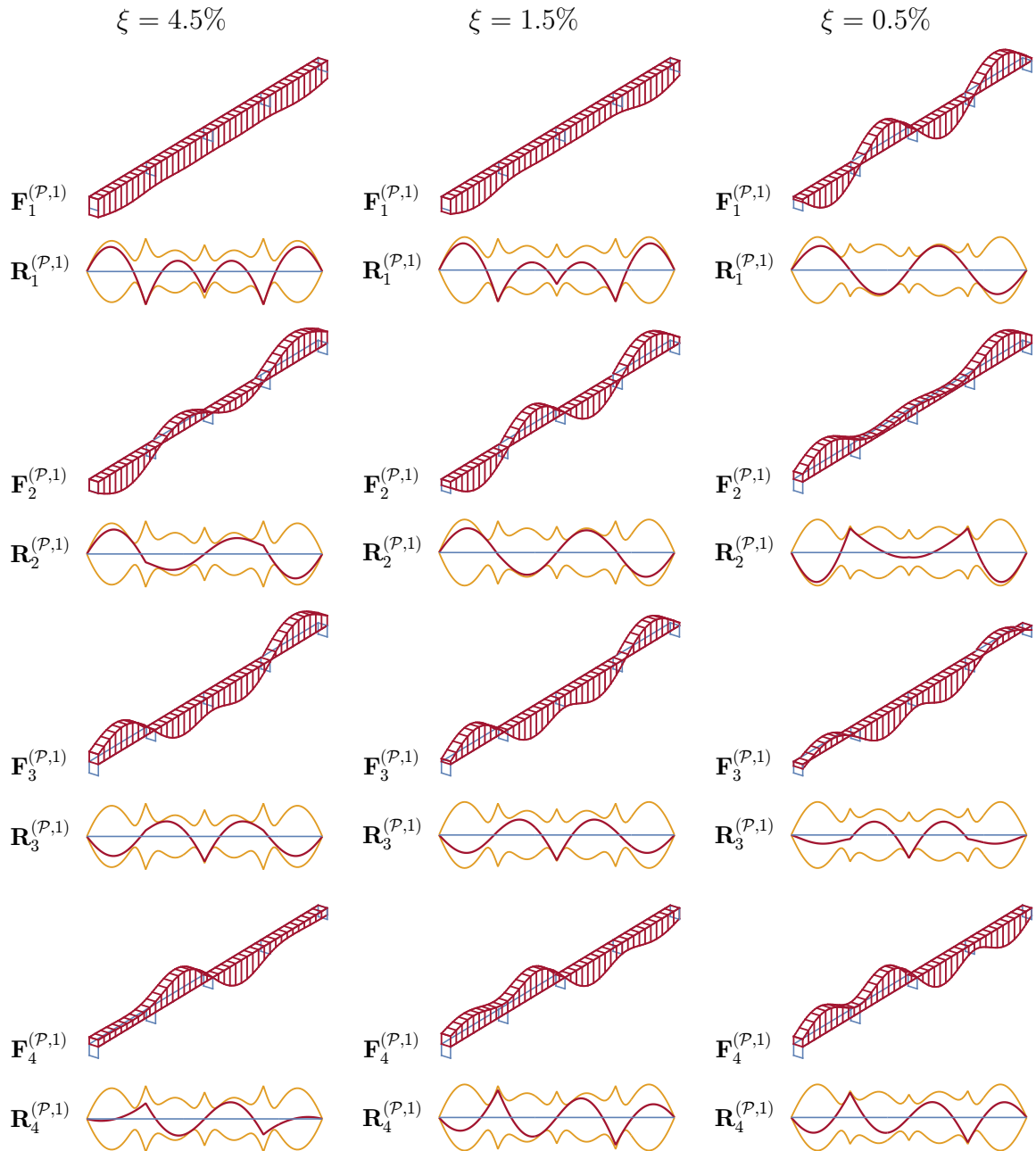


Figure VI.20: First four principal static wind loads  $\mathbf{F}_i^{(P,1)}$  and corresponding static bending moments  $\mathbf{R}_i^{(P,1)}$  for the three considered structural behaviors (strongly to slightly damped).

### VI.2.4 Limiting cases of PSWLs: CPT loading modes and MILs

We now seek to understand how the proposed PSWL basis may degenerate into the basis formed by the CPT modes and the MILs.

#### Limit quasi-static structural behavior

For the strongly damped ( $\xi = 4.5\%$ ) structural behavior, the resonant contribution is negligible and only the quasi-static contribution is considered. From (II.8.3), the covariance matrix of wind forces is approximated with a reduced set of CPT loading modes as

$$\boldsymbol{\Sigma}^{\mathbf{p}} \simeq \mathbf{P}^{(c)} \boldsymbol{\Sigma}^c (\mathbf{P}^{(c)})^{\mathbf{T}}. \quad (\text{VI.2.13})$$

Figure VI.21 illustrates the standard deviation of bending moments obtained when retaining 1, 4 or 6 CPT loading modes in (VI.2.13). Bending moments derived in the hybrid basis and in the nodal basis neglecting the resonant contribution are also shown for comparison. The first 6 CPT loading modes are retained since standard deviations of bending moments are almost recovered, i.e., the higher CPT loading modes bring minor contributions.

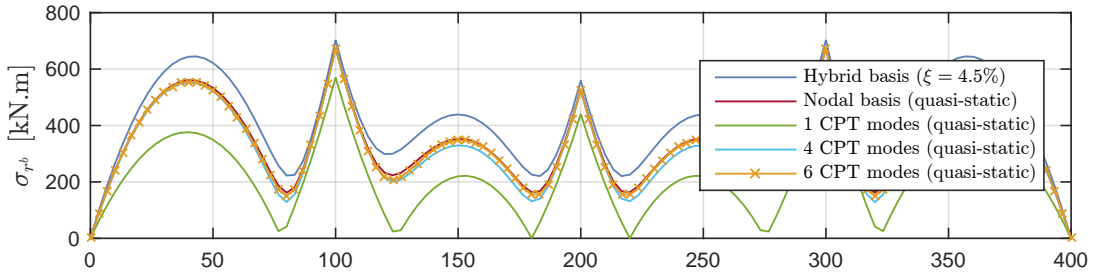


Figure VI.21: Standard deviation of bending moments derived in the hybrid basis and in the nodal basis assuming a quasi-static structural behavior. Also, results obtained with 1, 4 and 6 CPT loading modes retained to build the covariance matrix of aerodynamic pressures in a quasi-static analysis.

The establishment of ESWLs is done with the LRC method using the first six CPT loading modes ( $e \equiv \mathcal{L}^c$ )

$$\mathbf{F}^{(\mathcal{L}^c, m)} = \mathbf{F}^{(c)} \mathbf{W}^{(c, m)}, \quad (\text{VI.2.14})$$

see Section IV.4. Figure VI.22 shows the CPT loading modes with the associated static responses. The corresponding PSWLs are depicted in the second column. Also PSWLs computed in Section VI.2.3 for the strongly damped case ( $\xi = 4.5\%$ ) are shown for comparison. As a matter of fact, the two bases are nearly identical and this is explained thanks to the developments of Section V.3.2.

First, several structural responses under each CPT loading mode are orthogonal

$$\left( \|\mathbf{R}_m^{(c)}\|^{-1} \mathbf{R}_m^{(c)} \right)^\top \left( \|\mathbf{R}_n^{(c)}\|^{-1} \mathbf{R}_n^{(c)} \right) = \begin{bmatrix} 1 & 0 & -0.4 & 0 & 0.49 & 0 \\ & 1 & 0 & 0.39 & 0 & -0.01 \\ & & 1 & 0 & -0.76 & 0 \\ & & & 1 & 0 & -0.87 \\ \text{Sym.} & & & & 1 & 0 \\ & & & & & 1 \end{bmatrix},$$

and thus the first assumption (V.3.12) is nearly fulfilled. Besides, each CPT loading mode contains positive and negative parts that are symmetric with respect to the center of the bridge, except the first one. It appears that standard deviations and peak factors of bending moments investigated along the bridge present also a symmetry with respect to the center of the bridge, see Figures VI.6 and VI.8, respectively. Therefore the second assumption (V.3.16) is satisfied. Finally, the scalar products of the weighting factors for each CPT loading mode is found as

$$\left( \|\mathbf{W}_{m\circ}^{(c)}\|^{-1} \mathbf{W}_{m\circ}^{(c)} \right) \left( \|\mathbf{W}_{n\circ}^{(c)}\|^{-1} \mathbf{W}_{n\circ}^{(c)} \right)^\top = \begin{bmatrix} 1 & 0 & -0.14 & 0 & 0.36 & 0 \\ & 1 & 0 & 0.22 & 0 & 0.08 \\ & & 1 & 0 & -0.7 & 0 \\ & & & 1 & 0 & -0.91 \\ \text{Sym.} & & & & 1 & 0 \\ & & & & & 1 \end{bmatrix},$$

and even if some weighting factors are not perfectly orthogonal, the magnitude of their scalar products remain small and therefore the PSWLs have similar distributions to the CPT loading modes:  $\mathbf{F}^{(P)} \simeq \mathbf{F}^{(C)}$ .



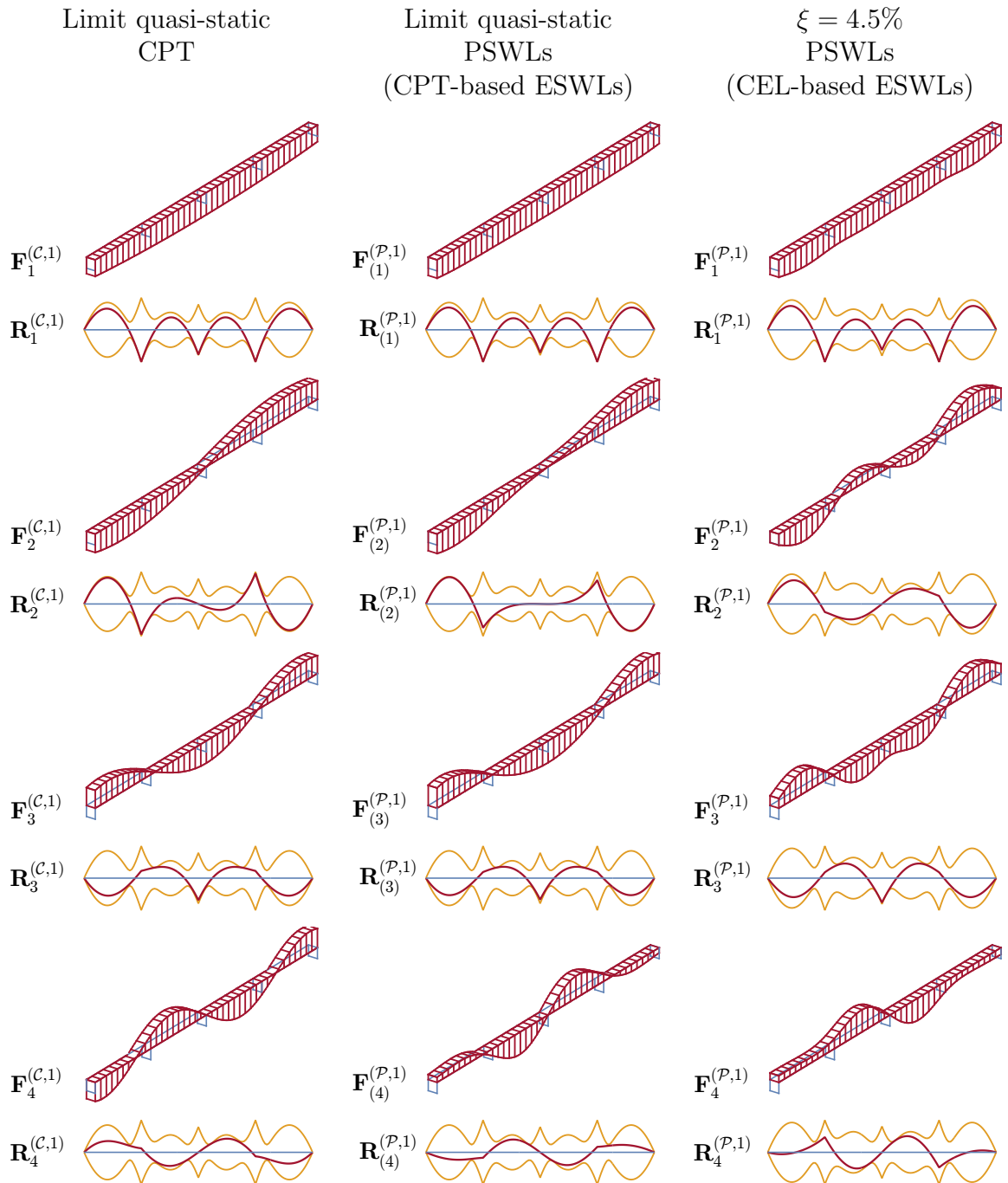


Figure VI.22: First four CPT loading modes  $\mathbf{F}_i^{(C,1)}$  and PSWLs  $\mathbf{F}_i^{(P,1)}$  for the quasi-static (CPT-based ESWLs) and strongly damped (CEL-based ESWLs) cases. The corresponding bending moments are also depicted.

In the previous case, the basis of PSWLs tends to the CPT loadings modes partly due to the symmetry of the peak factor  $\mathbf{g}^{(m)}$  and standard deviation  $\sigma_{\mathbf{r}^b}$  diagrams of the bending moments with respect to the center of the bridge. PSWLs are next derived from ESWLs only computed for half of the bending moments situated from left to the middle of the bridge (numbered 1 to 60) and the corresponding bending moments under each CPT loading mode are no longer orthogonal

$$\left( \|\mathbf{R}_m^{(c)}\|^{-1} \mathbf{R}_m^{(c)} \right)^\top \left( \|\mathbf{R}_n^{(c)}\|^{-1} \mathbf{R}_n^{(c)} \right) = \begin{bmatrix} 1 & 0.89 & -0.36 & 0.16 & 0.49 & 0.17 \\ & 1 & -0.72 & 0.39 & 0.68 & -0.01 \\ & & 1 & -0.75 & -0.74 & 0.46 \\ & & & 1 & 0.6 & -0.87 \\ \text{Sym.} & & & & 1 & -0.14 \\ & & & & & 1 \end{bmatrix},$$

and the scalar products of the weighting factors for each CPT loading mode is found as

$$\left( \|\mathbf{W}_{m\circ}^{(c)}\|^{-1} \mathbf{W}_{m\circ}^{(c)} \right) \left( \|\mathbf{W}_{n\circ}^{(c)}\|^{-1} \mathbf{W}_{n\circ}^{(c)} \right)^\top = \begin{bmatrix} 1 & 0.82 & -0.13 & -0.03 & 0.36 & 0.25 \\ & 1 & -0.65 & 0.22 & 0.68 & 0.08 \\ & & 1 & -0.66 & -0.69 & 0.43 \\ & & & 1 & 0.31 & -0.91 \\ \text{Sym.} & & & & 1 & 0.08 \\ & & & & & 1 \end{bmatrix}.$$

Therefore the PSWLs basis does not degenerate into the CPT loading modes:  $\mathbf{F}^{(P)} \neq \mathbf{F}^{(c)}$ , see Figure VI.23.

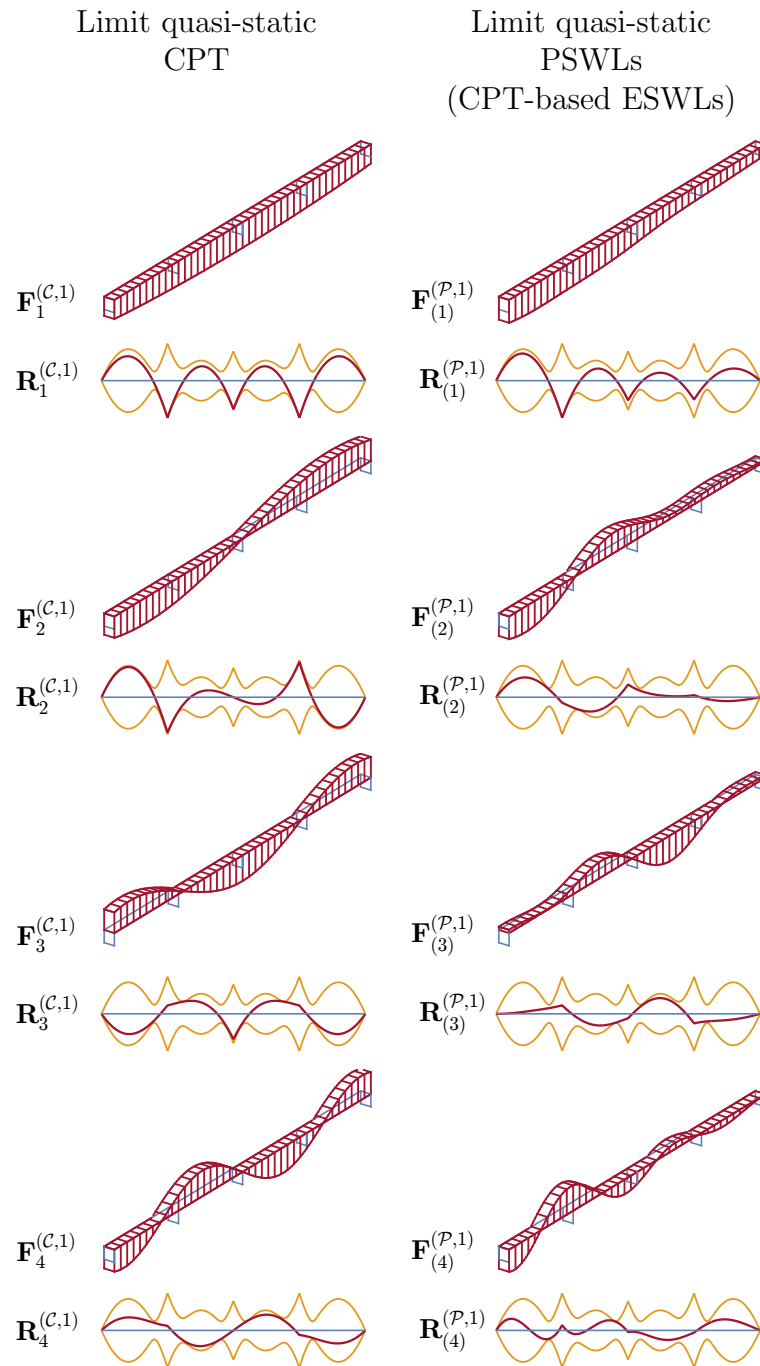


Figure VI.23: First four CPT loading modes  $\mathbf{F}_i^{(C,1)}$  and PSWLs  $\mathbf{F}_i^{(P,1)}$  for the quasi-static (CPT-based ESWLs) case. The corresponding bending moments are also depicted. PSWLs are derived from ESWLs computed only for half of the bending moments situated from left to the middle of the bridge (numbered 1 to 60).

### Slightly damped structural behavior

For the slightly damped ( $\xi = 0.5\%$ ) structural behavior, the structural analysis is performed in the modal basis. The modal analysis is done with the first four modes. Standard deviations of bending moments derived in the hybrid basis and in the modal basis are shown in Figure VI.24 for comparison.

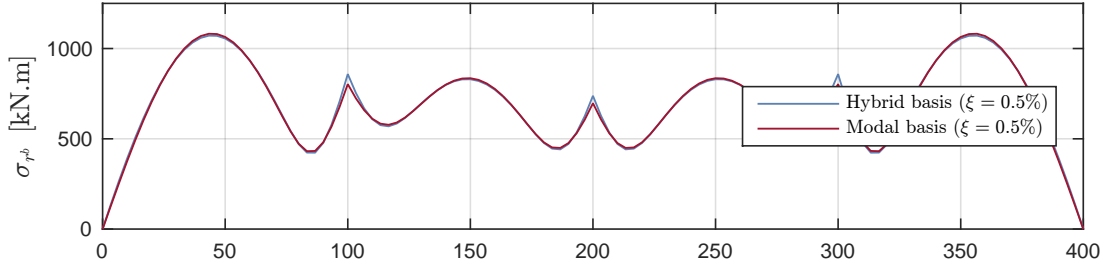


Figure VI.24: Standard deviation of bending moments derived in the hybrid basis and in the modal basis assuming a resonant structural behavior.

The MIL-based ESWLs are obtained with the first four modal inertial loads ( $e \equiv \mathcal{M}$ )

$$\mathbf{F}^{(\mathcal{M},m)} = \mathbf{F}^{(\mathcal{M})} \mathbf{W}^{(\mathcal{M},m)}, \quad (\text{VI.2.15})$$

see Section IV.5. Figure VI.25 shows the MILs with the associated static responses. PSWLs are based on the ESWLs computed with (VI.2.15) and are depicted in the second column in Figure VI.25. Also PSWLs computed in Section VI.2.3 for the slightly damped case ( $\xi = 0.5\%$ ) are shown for comparison. As a matter of fact, the bases are nearly similar and this is explained thanks to the developments of Section V.3.3.

First, in this conceptual example with uniform mass and bending stiffness, the normal modes of vibration constitute an orthogonal basis, i.e.,

$$(\Phi_j)^\top \Phi_k = 0 \quad \forall j \neq k, \quad (\text{VI.2.16})$$

and thus the first assumption (V.3.26) is fulfilled. Next, the bending moments under each MIL constitute an orthogonal basis

$$\left( \|\mathbf{R}_m^{(\mathcal{M})}\|^{-1} \mathbf{R}_m^{(\mathcal{M})} \right)^\top \left( \|\mathbf{R}_n^{(\mathcal{M})}\|^{-1} \mathbf{R}_n^{(\mathcal{M})} \right) = \begin{bmatrix} 1 & 0 & 0 & 0 \\ & 1 & 0 & 0 \\ & \text{Sym.} & 1 & 0 \\ & & & 1 \end{bmatrix},$$

and thus the second assumption (V.3.27) is entirely fulfilled. Besides, each MIL contains positive and negative parts that are symmetric with respect to the center of the bridge. It appears that standard deviations and peak factors of bending moments investigated along the bridge present also a symmetry with respect to the center of the bridge, see Figures VI.6 and VI.8, respectively. Therefore the third assumption (V.3.28) is satisfied.

The correlation matrix of modal amplitudes is given by

$$\mathbf{R}^q = \begin{bmatrix} 1 & 0 & 0.07 & 0 \\ & 1 & 0 & 0.27 \\ & \text{Sym.} & 1 & 0 \\ & & & 1 \end{bmatrix}, \quad (\text{VI.2.17})$$

indicating that the modes are almost uncorrelated, nearly satisfying the fourth assumption (V.3.30) and finally, the scalar products of the weighting factors for each MIL is found as

$$\left( \|\mathbf{W}_{m\circ}^{(\mathcal{M})}\|^{-1} \mathbf{W}_{m\circ}^{(\mathcal{M})} \right) \left( \|\mathbf{W}_{n\circ}^{(\mathcal{M})}\|^{-1} \mathbf{W}_{n\circ}^{(\mathcal{M})} \right)^T = \begin{bmatrix} 1 & 0 & -0.18 & 0 \\ & 1 & 0 & -0.14 \\ & \text{Sym.} & 1 & 0 \\ & & & 1 \end{bmatrix},$$

and even if some weighting factors are not perfectly orthogonal, the magnitude of their scalar products remains small. Therefore the PSWLs basis degenerates into the MILs:  $\mathbf{F}^{(\mathcal{P})} \simeq \mathbf{F}^{(\mathcal{M})}$ .

In the previous case, the basis of PSWLs tends to the MILs partly due to the symmetry of the peak factor  $\mathbf{g}^{(m)}$  and standard deviation  $\sigma_r$  diagrams of the bending moments with respect to the center of the bridge. If PSWLs are derived from ESWLs only computed for half of the bending moments situated from left to the middle of the bridge (numbered 1 to 60), the bending moments under each MIL are no longer orthogonal

$$\left( \|\mathbf{R}_m^{(\mathcal{M})}\|^{-1} \mathbf{R}_m^{(\mathcal{M})} \right)^T \left( \|\mathbf{R}_n^{(\mathcal{M})}\|^{-1} \mathbf{R}_n^{(\mathcal{M})} \right) = \begin{bmatrix} 1 & 0.78 & 0 & -0.18 \\ & 1 & 0.52 & -0.03 \\ & \text{Sym.} & 1 & 0.68 \\ & & & 1 \end{bmatrix},$$

and the scalar products of the weighting factors for each MIL is found as

$$\left( \|\mathbf{W}_{m\circ}^{(\mathcal{M})}\|^{-1} \mathbf{W}_{m\circ}^{(\mathcal{M})} \right) \left( \|\mathbf{W}_{n\circ}^{(\mathcal{M})}\|^{-1} \mathbf{W}_{n\circ}^{(\mathcal{M})} \right)^T = \begin{bmatrix} 1 & 0.65 & -0.18 & -0.19 \\ & 1 & 0.49 & -0.16 \\ & \text{Sym.} & 1 & 0.56 \\ & & & 1 \end{bmatrix}.$$

Therefore the PSWL basis does not degenerate into the MILs:  $\mathbf{F}^{(\mathcal{P})} \neq \mathbf{F}^{(\mathcal{M})}$ , see Figure VI.26.

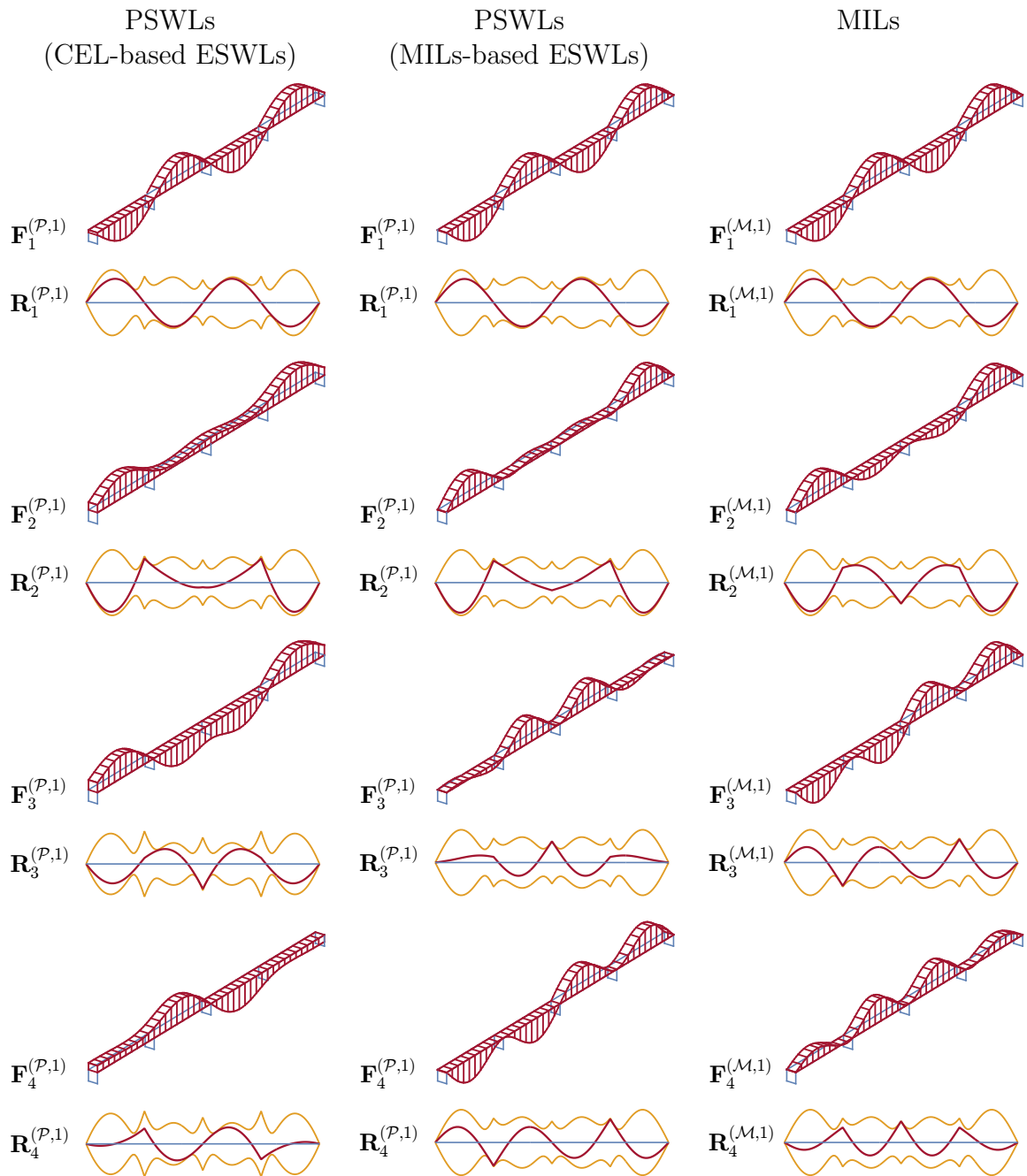


Figure VI.25: First four MILs  $F_i^{(P,1)}$  and PSWLs  $F_i^{(P,1)}$  (MILs-based ESWLs and CEL-based ESWLs). The corresponding bending moments are also depicted. Studied case:  $\xi = 0.5\%$ .

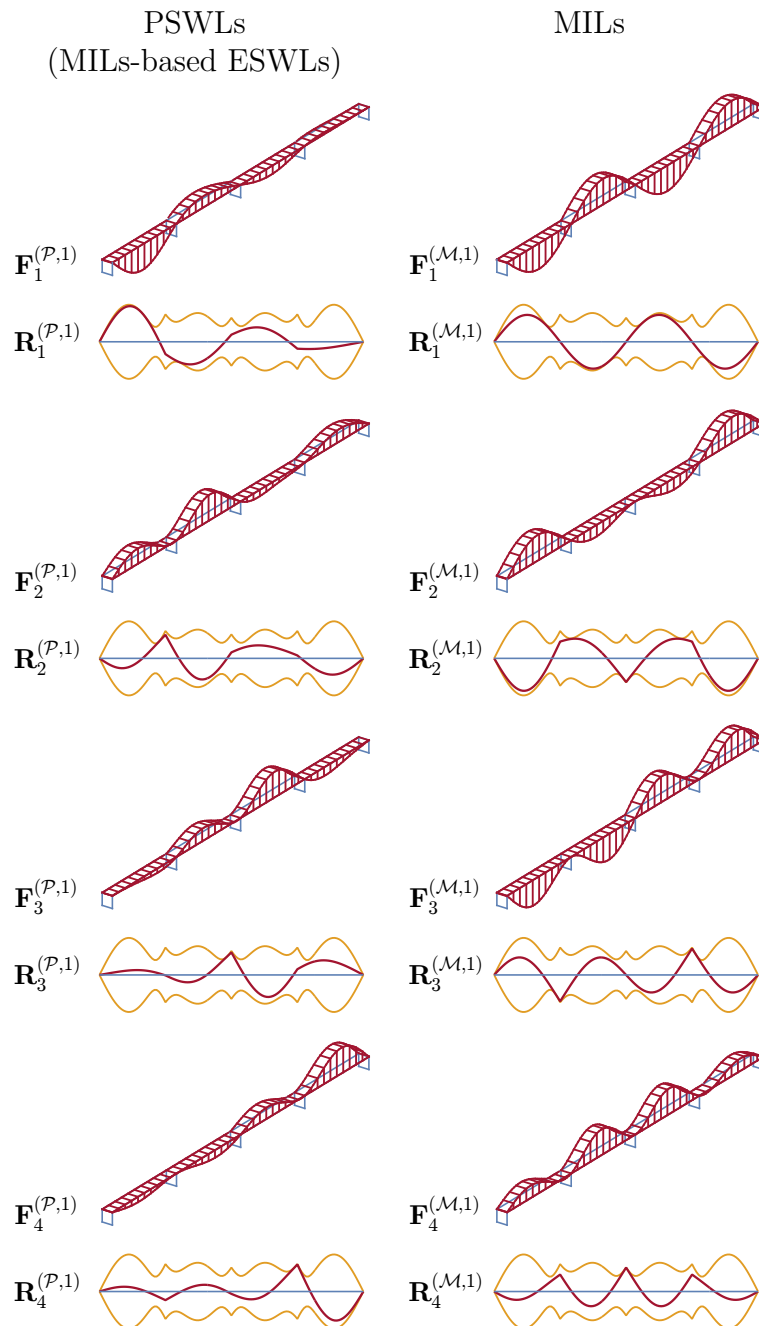


Figure VI.26: First four MILs  $\mathbf{F}_i^{(M,1)}$  and PSWLs  $\mathbf{F}_i^{(P,1)}$  (MILs-based ESWLs). The corresponding bending moments are also depicted. PSWLs are derived from ESWLs computed only for half of the bending moments situated from left to the middle of the bridge (numbered 1 to 60).

### VI.2.5 Envelope reconstruction with PSWLs $\xi = 1.5\%$

This section assesses principal static wind loads as potential candidates for the envelope reconstruction problem. Figure VI.27 illustrates the straightforward solution which is to apply successively the PSWLs without combination, see Section III.4 and applying the flowchart depicted in Figure III.7. The first three principal loadings contribute significantly to the reconstruction of the envelope. Actually, after consideration of the first three principal loadings, any additional principal loading just provides a marginal contribution. The reconstruction is fair, except in the side spans with relative errors up to -25%.

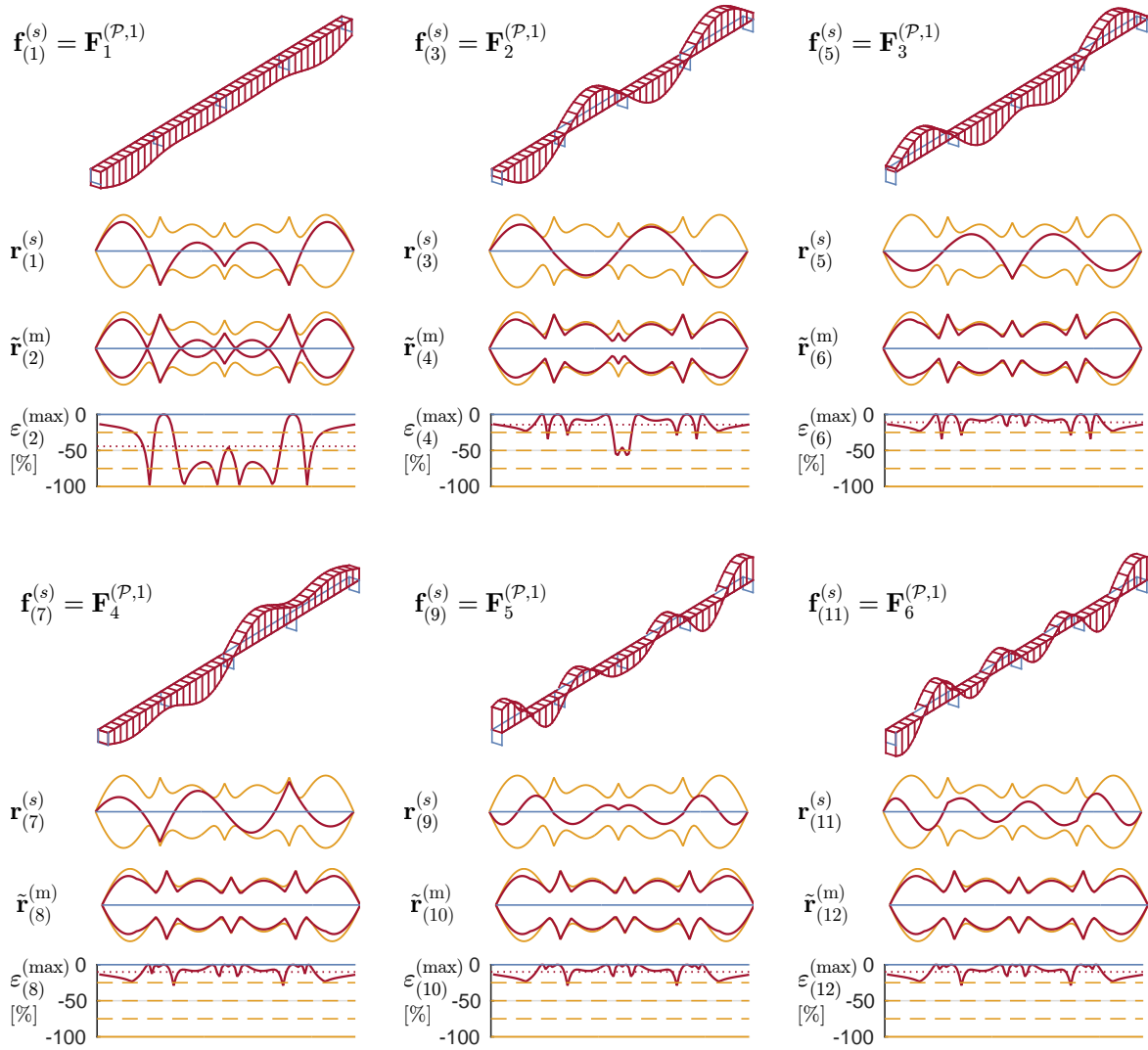


Figure VI.27: Principal static wind loads  $\mathbf{f}_k^{(s)} = \mathbf{F}_i^{(\mathcal{P},1)}$  (vertical forces at every node), static bending moments  $\mathbf{r}_k^{(s)} = \mathbf{R}_i^{(\mathcal{P},\max)}$ , reconstructed envelope  $\tilde{\mathbf{r}}_k^{(m)}$  and relative errors of the reconstructed envelope (max side)  $\varepsilon_k^{(\max)}$  for the case  $\xi = 1.5\%$ . (ERP parameters:  $\hat{\varepsilon} = 0\%$ ,  $\gamma = 1$ )

Figure VI.28 illustrates the second option where combinations of a subset of PSWLs are considered, here  $n_q = 4$  for the illustration. The combination coefficients are shown and



derived from the constrained nonlinear optimization algorithm, see Section III.5 and Figure III.8. As with ESWLs, the acceptable overestimation  $\hat{\varepsilon}$  is set equal to zero and the parameter  $\gamma$  to one.

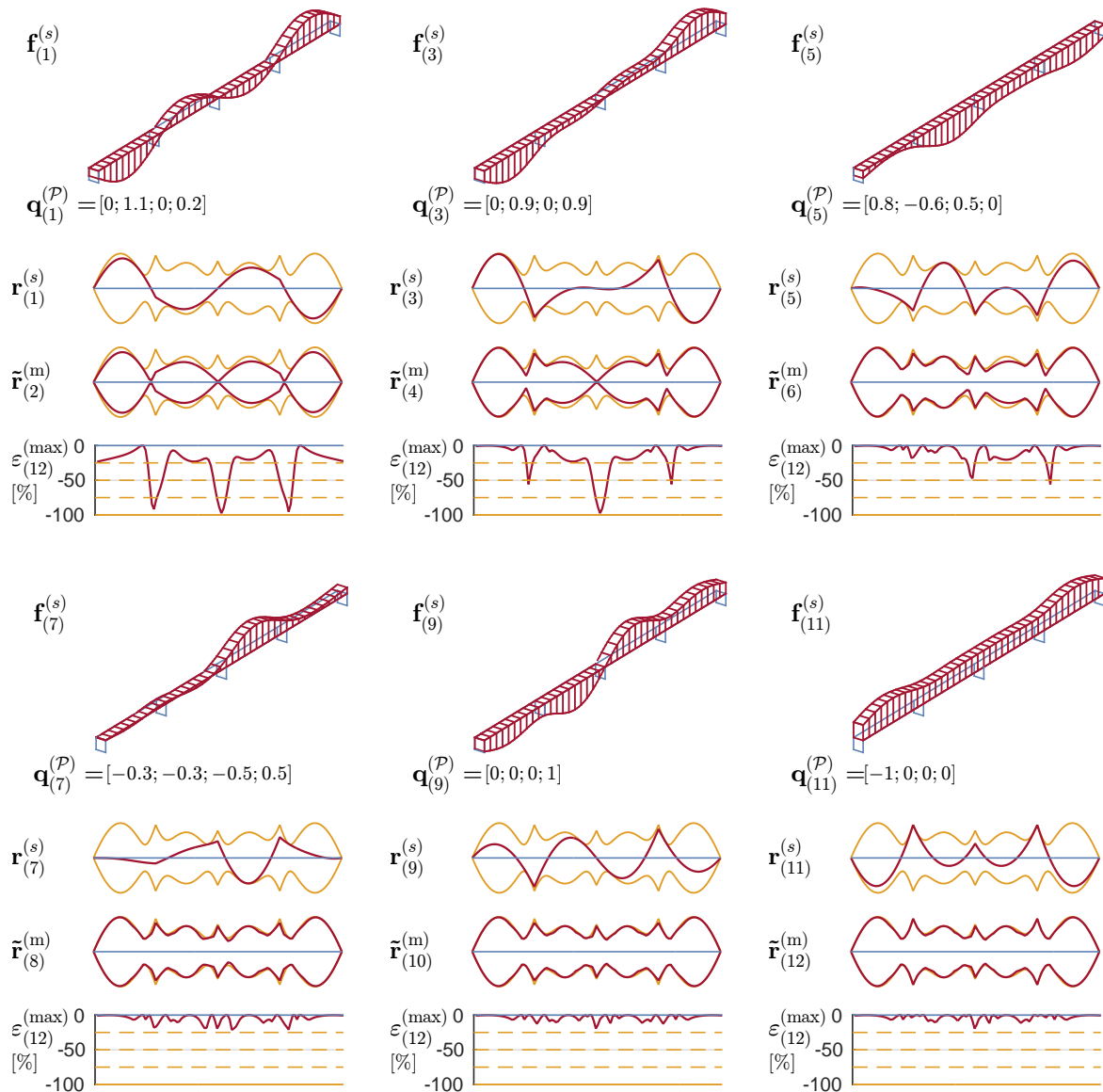


Figure VI.28: Combinations of the first four principal static wind loads  $\mathbf{f}_{(k)}^{(s)}$  (transverse forces at every node), static bending moments  $\mathbf{r}_{(k)}^{(s)}$ , reconstructed envelope  $\tilde{\mathbf{r}}_{(k)}^{(m)}$  and relative errors of the reconstructed envelope (max side)  $\varepsilon_{(k)}^{(\max)}$  for the case  $\xi = 1.5\%$ . (ERP parameters:  $\hat{\varepsilon} = 0\%$ ,  $\gamma = 1$ )

For a same number of load cases, the reconstruction of the envelope performs better by considering combinations of the first four PSWLs than applying PSWLs without combination, see Figures VI.27 and VI.28, respectively.

The number of PSWLs that should be considered for combinations may be appreciated with the reconstruction indicator  $\mathcal{R}_{(k)}$  and the largest relative error indicator  $\tilde{\varepsilon}_{(k)}$ , see Figures VI.29 and VI.30. Results obtained with ESWLs, PSWLs (no combination) and the first two, four, six and eight combined PSWLs are shown for comparison.

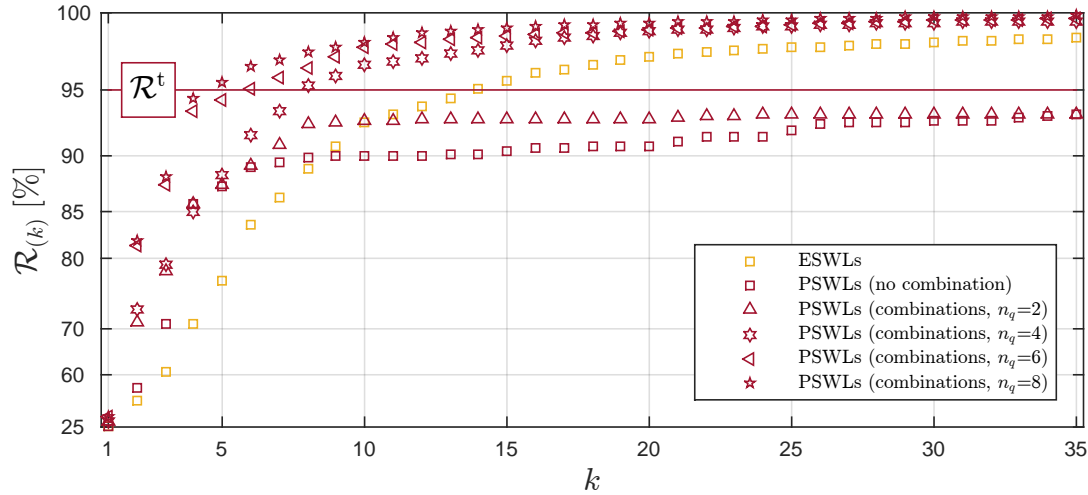


Figure VI.29: Evolution of the reconstruction indicator  $\mathcal{R}_{(k)}$  as a function of the number of load cases for the case  $\xi = 1.5\%$ . (ERP parameters:  $\hat{\varepsilon} = 0\%$ ,  $\gamma = 1$ ).

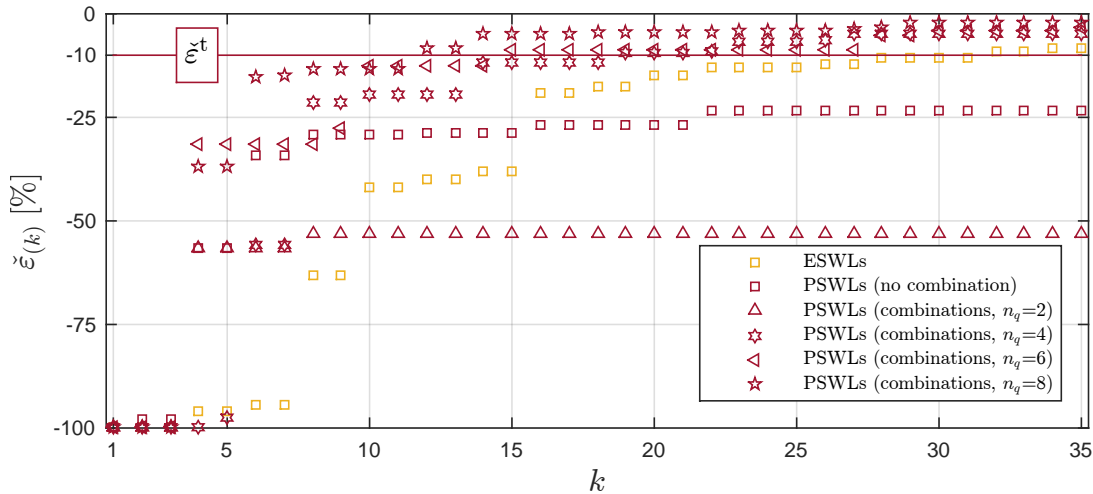


Figure VI.30: Evolution of the largest relative error indicator  $\tilde{\varepsilon}_{(k)}$  as a function of the number of load cases for the case  $\xi = 1.5\%$ . (ERP parameters:  $\hat{\varepsilon} = 0\%$ ,  $\gamma = 1$ )

After 35 load cases, applying successively PSWLs without combination does not provide the acceptable reconstruction  $\mathcal{R}^t$  nor the acceptable underestimation  $\varepsilon^t$ . It is therefore not

enough to only implement this straightforward solution and combinations of PSWLs have to be considered instead.

After 8 combinations of the first two PSWLs, considering more and more combinations do not bring any improvement to the reconstructed envelope with  $\mathcal{R}_{(k \geq 8)} \simeq 92.5\% \lesssim \mathcal{R}_{(\infty)}$  and  $\check{\varepsilon}_{(k \geq 8)} \simeq -53\% \lesssim \check{\varepsilon}_{(\infty)}$ . However, after  $n_s^{(1)} = 8, 6$  and  $5$  and  $n_s^{(2)} = 19, 15$  and  $12$  combinations of the first  $n_q = 4, 6$  and  $8$  PSWLs, the acceptable reconstruction and largest relative error indicators are satisfied, respectively. At this stage, two approaches to choose the number  $n_q$  to consider may be pointed out. On the one hand, the more  $n_q$  PSWLs are considered, the less  $n_s$  load cases are required. On the other hand, the more  $n_q$  PSWLs are considered, the less the decrease on the number of load cases  $n_s$  and the more time-consuming computations are. In other words, a lower number  $n_q$  may be sought for sake of simplicity even if it means a slightly larger number of load cases.

It is emphasized that with combinations of PSWLs, at least with  $n_q > 2$ , the reconstruction is faster than with ESWLs, i.e., for a same number of load cases, the reconstruction is better in terms of overall reconstruction and relative errors.

### Parameter $\gamma$

For both kinds of static wind loads considered so far, i.e., equivalent and principal, the number of SWLs  $n_s^{(2)}$  to fulfill the acceptable underestimation is approximately more than twice the number  $n_s^{(1)}$  necessary to check the acceptable overall reconstruction. With the purpose of decreasing this difference, the parameter  $\gamma$  in the cost function (III.5.11) is increased, see Section III.5. Its influence on  $\mathcal{R}_{(k)}$  and  $\check{\varepsilon}_{(k)}$  can be appreciated with Figures VI.31 and VI.32, respectively. As expected, an increase of  $\gamma$  corresponds to an increase of  $n_s^{(1)}$ .

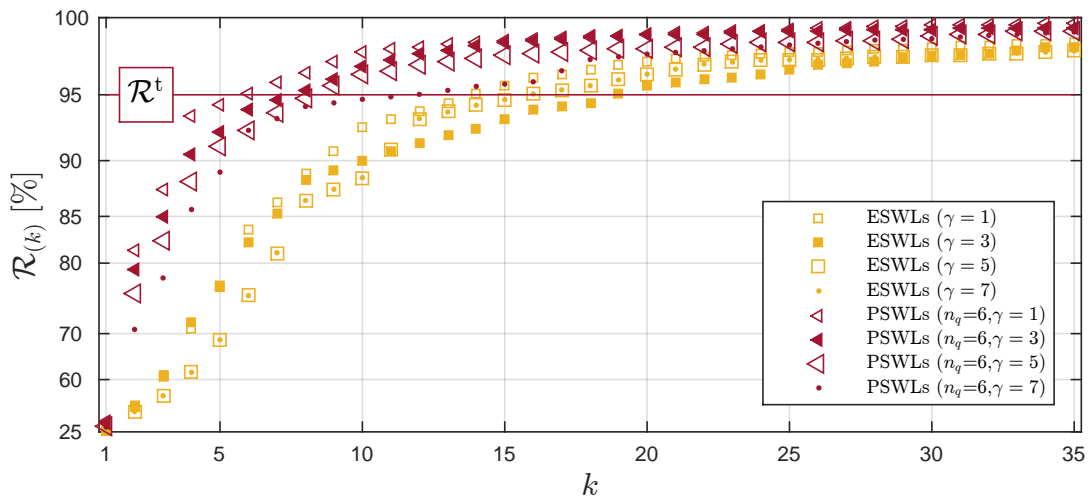


Figure VI.31: Evolution of the reconstruction indicator  $\mathcal{R}_{(k)}$  as a function of the number of load cases for the case  $\xi = 1.5\%$ . (ERP parameters:  $\hat{\varepsilon} = 0\%$ ,  $\gamma$  variable).

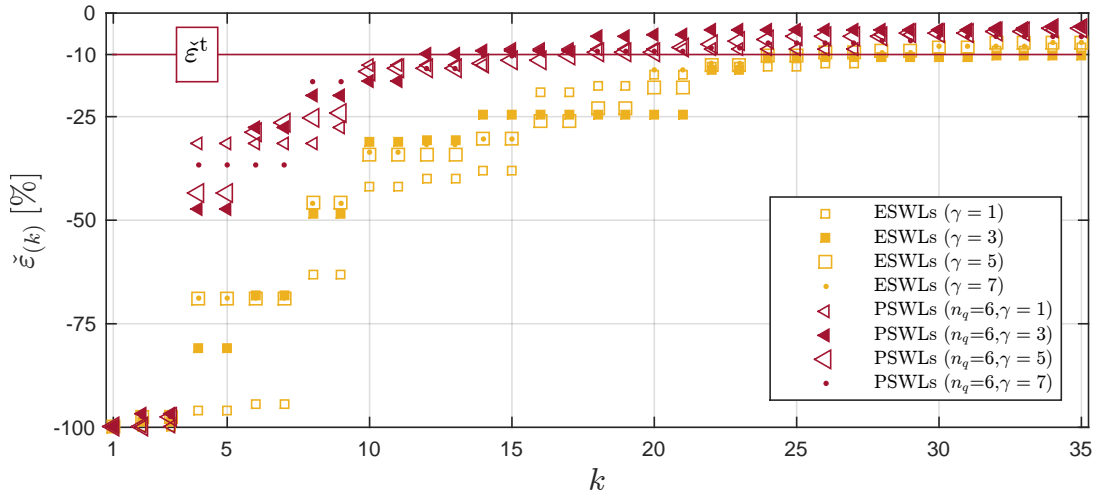


Figure VI.32: Evolution of the largest relative error indicator  $\check{\xi}(k)$  as a function of the number of load cases for the case  $\xi = 1.5\%$ . (ERP parameters:  $\hat{\varepsilon} = 0\%$ ,  $\gamma$  variable)

The impact on  $n_s^{(2)}$  is however more difficult to assess with Figure VI.32 and so Table VI.5 collects  $n_s^{(1)}$  and  $n_s^{(2)}$  for the four values of  $\gamma$  investigated. Surprisingly, an increase of  $\gamma$  does not necessary corresponds to a decrease of  $n_s^{(2)}$ : this make the optimization of this parameter rather difficult.

The larger  $\gamma$  is, the more the SWL reconstructing the envelope value associated with the largest relative error is selected. However this can be counterproductive since with a lower  $\gamma$ , another SWL, reconstructing, for instance, several envelope values with slightly lower relative errors would have been selected. This is one possible explanation. At the end, it is recommended not to blindly increase the parameter  $\gamma$  and set it to one as an educated value.

In any case, the benefit is rather low. For ESWLs,  $n_s = 32$  to 26 with  $\gamma = 5$  and for PSWLs ( $n_q = 6$ ),  $n_s = 15$  to 12 with  $\gamma = 3$ .

|                     |             | $\gamma=1$ | $\gamma=3$ | $\gamma=5$ | $\gamma=7$ |
|---------------------|-------------|------------|------------|------------|------------|
| ESWLs               | $n_s^{(1)}$ | 14         | 19         | 16         | 16         |
|                     | $n_s^{(2)}$ | 32         | > 35       | 26         | 28         |
| PSWLs ( $n_q = 6$ ) | $n_s^{(1)}$ | 6          | 8          | 9          | 12         |
|                     | $n_s^{(2)}$ | 15         | 12         | 18         | 16         |

Table VI.5: Number of SWLs  $n_s^{(1)}$  and  $n_s^{(2)}$  with ESWLs and PSWLs (combinations,  $n_q = 6$ ). (ERP parameter:  $\hat{\varepsilon} = 0\%$ ).

### VI.2.6 Comparison of envelope reconstruction with combinations of basic static wind loads

This section assesses the envelope reconstruction efficiency with combinations of a subset of CPT loading modes, MILs and PSWLs. For the three damping coefficients, Figures VI.33, VI.35, VI.37 and VI.34, VI.36, VI.38 depict the reconstruction indicator  $\mathcal{R}_{(k)}$  and the largest relative error indicator  $\tilde{\varepsilon}_{(k)}$ , respectively. Table VI.6 collects  $n_s^{(1)}$  and  $n_s^{(2)}$  for the three cases. Globally, with  $n_q = 2$  and  $n_q = 4$ , the PSWLs perform better than the CPT loading modes or the MILs: the actual envelope is better reproduced, no matter the damping coefficient. However, with  $n_q = 6$ , the three bases provide close numbers  $n_s^{(2)}$  of load cases to fulfill the acceptable underestimation.

As expected, the CPT loading modes are better suited when the structural behavior tends to be quasi-static. Surprisingly, the MILs provide approximately the same range of reconstruction of the envelope no matter the damping coefficient. This is explained by the specific property of the normal modes of vibration which constitute, in this example, an orthogonal basis, see (VI.2.16). This property allows to write the stiffness matrix as

$$\mathbf{K} = \mathbf{\Phi}\mathbf{\Omega}\mathbf{\Phi}^T, \quad (\text{VI.2.18})$$

which means that the normal modes of vibration are also the eigenvectors of the stiffness matrix  $\mathbf{K}$  and are thus well-suited to compute quasi-static structural responses, as well.

|               | ESWLs | MILs |    |    | CPT |    |    | PSWLs |    |    |
|---------------|-------|------|----|----|-----|----|----|-------|----|----|
| $n_q$         | -     | 2    | 4  | 6  | 2   | 4  | 6  | 2     | 4  | 6  |
| $\xi = 4.5\%$ |       |      |    |    |     |    |    |       |    |    |
| $n_s^{(1)}$   | 15    | -    | 11 | 7  | -   | 9  | 8  | -     | 8  | 7  |
| $n_s^{(2)}$   | 34    | -    | -  | 18 | -   | 12 | 16 | -     | 18 | 12 |
| $\xi = 1.5\%$ |       |      |    |    |     |    |    |       |    |    |
| $n_s^{(1)}$   | 14    | -    | 9  | 7  | -   | 12 | 8  | -     | 8  | 6  |
| $n_s^{(2)}$   | 32    | -    | -  | 20 | -   | -  | 14 | -     | 19 | 15 |
| $\xi = 0.5\%$ |       |      |    |    |     |    |    |       |    |    |
| $n_s^{(1)}$   | 14    | -    | 8  | 5  | -   | -  | 8  | -     | 10 | 6  |
| $n_s^{(2)}$   | 32    | -    | 18 | 14 | -   | -  | 14 | -     | 16 | 14 |

Table VI.6: Number of SWLs  $n_s^{(1)}$  and  $n_s^{(2)}$  with ESWLs, MILs, CPT loading modes and PSWLs. (ERP parameter:  $\hat{\varepsilon} = 0\%$ ,  $\gamma = 1$ ).

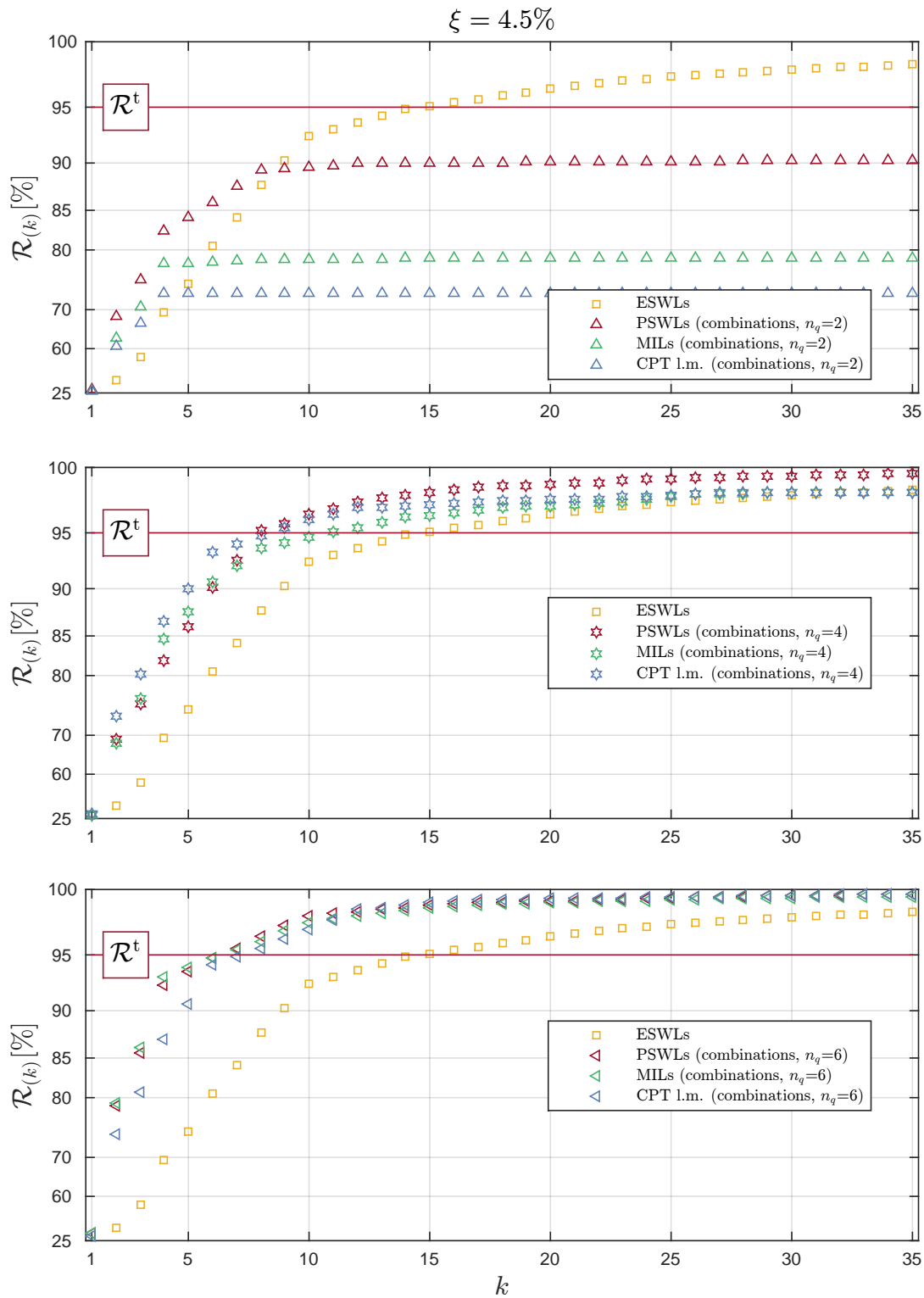


Figure VI.33: Evolution of the reconstruction indicator  $\mathcal{R}_{(k)}$  as a function of the number of load cases for the case  $\xi = 4.5\%$ . Combinations of the first 2, 4 and 6 basic SWLs are considered. (ERP parameters:  $\hat{\varepsilon} = 0\%$ ,  $\gamma = 1$ ).

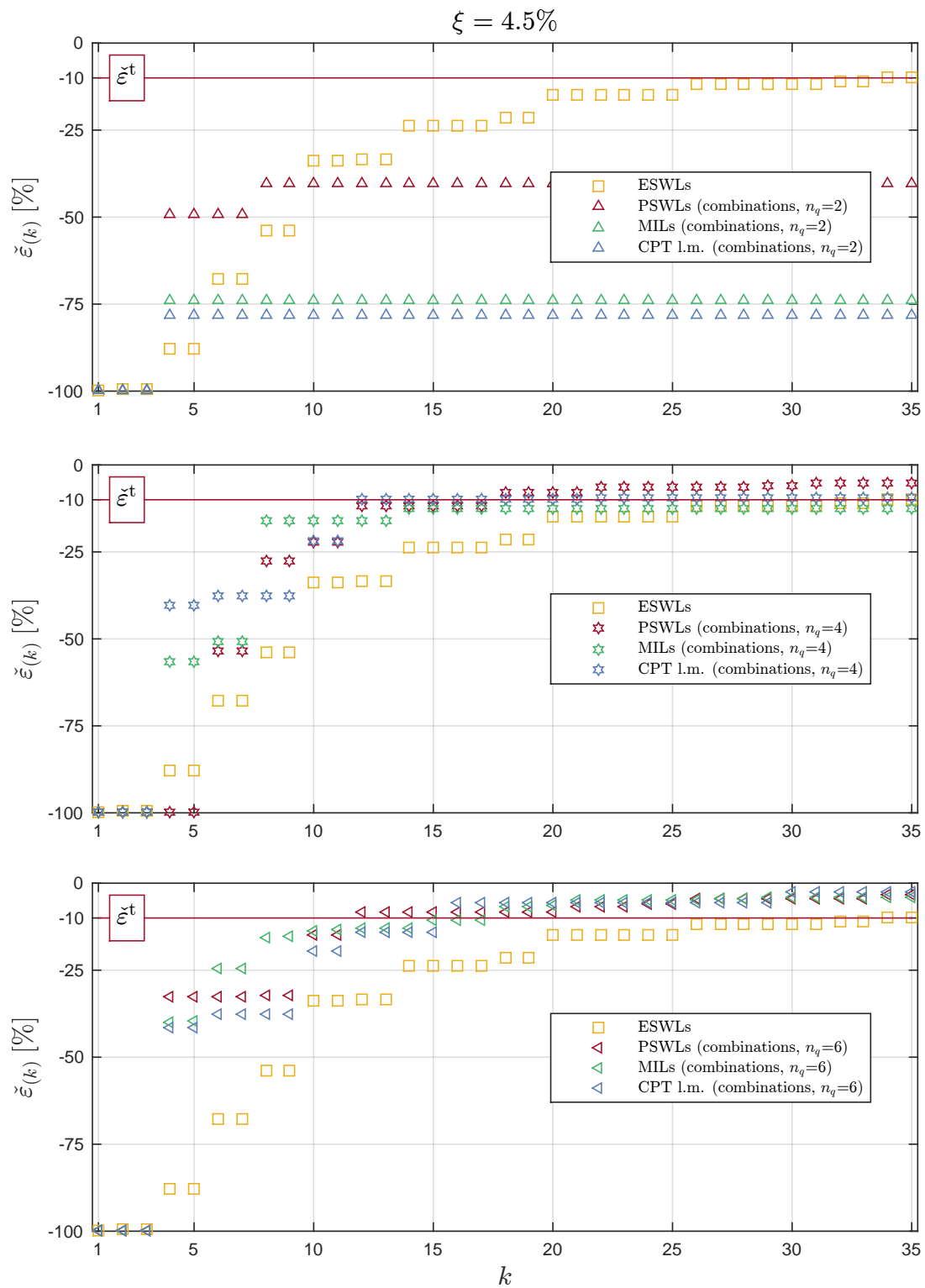


Figure VI.34: Evolution of the largest relative error indicator  $\check{\epsilon}(k)$  as a function of the number of load cases for the case  $\xi = 4.5\%$ . Combinations of the first 2, 4 and 6 basic SWLs are considered. (ERP parameters:  $\hat{\epsilon} = 0\%$ ,  $\gamma = 1$ ).

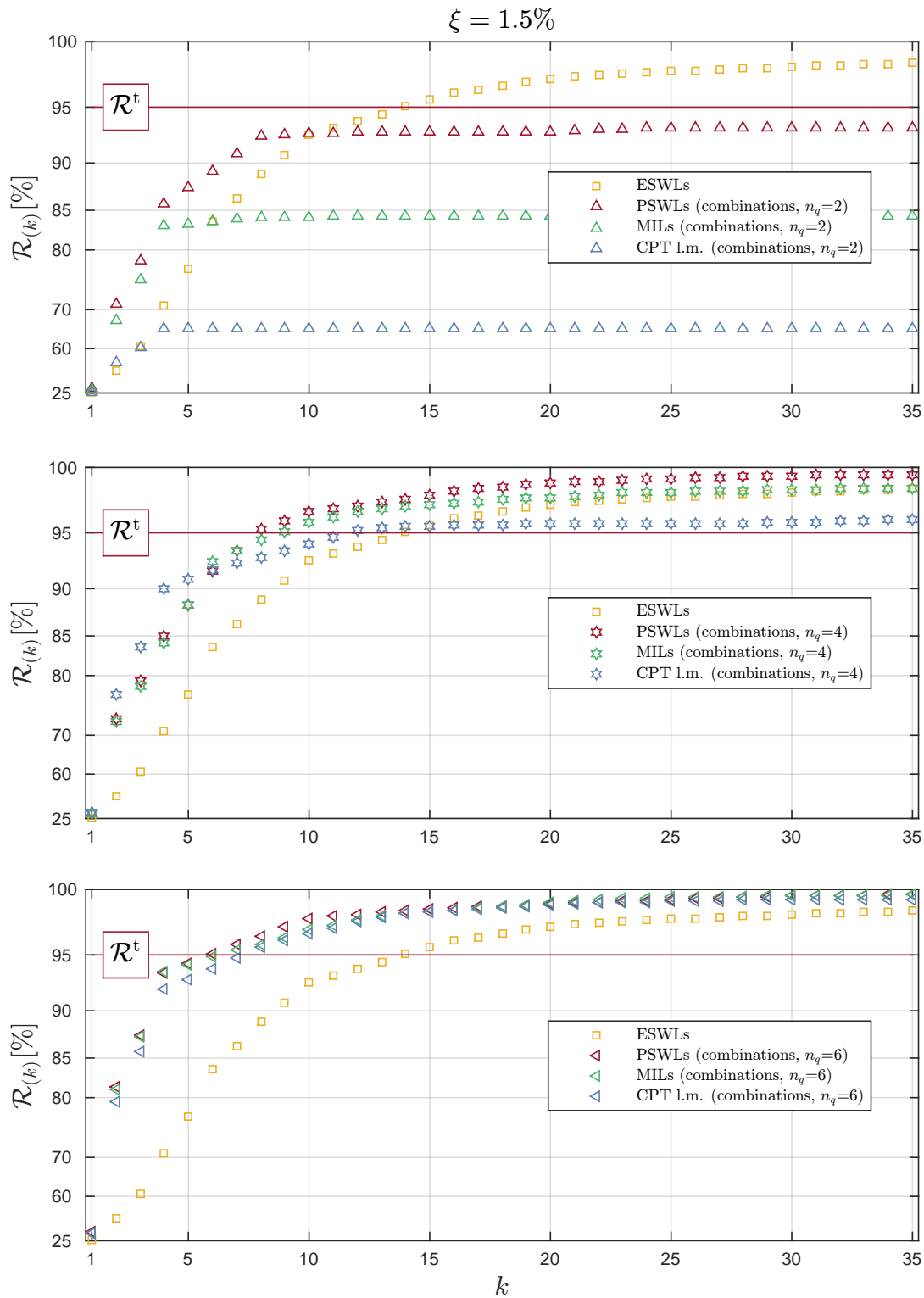


Figure VI.35: Evolution of the reconstruction indicator  $\mathcal{R}_{(k)}$  as a function of the number of load cases for the case  $\xi = 1.5\%$ . Combinations of the first 2, 4 and 6 basic SWLs are considered. (ERP parameters:  $\hat{\varepsilon} = 0\%$ ,  $\gamma = 1$ ).



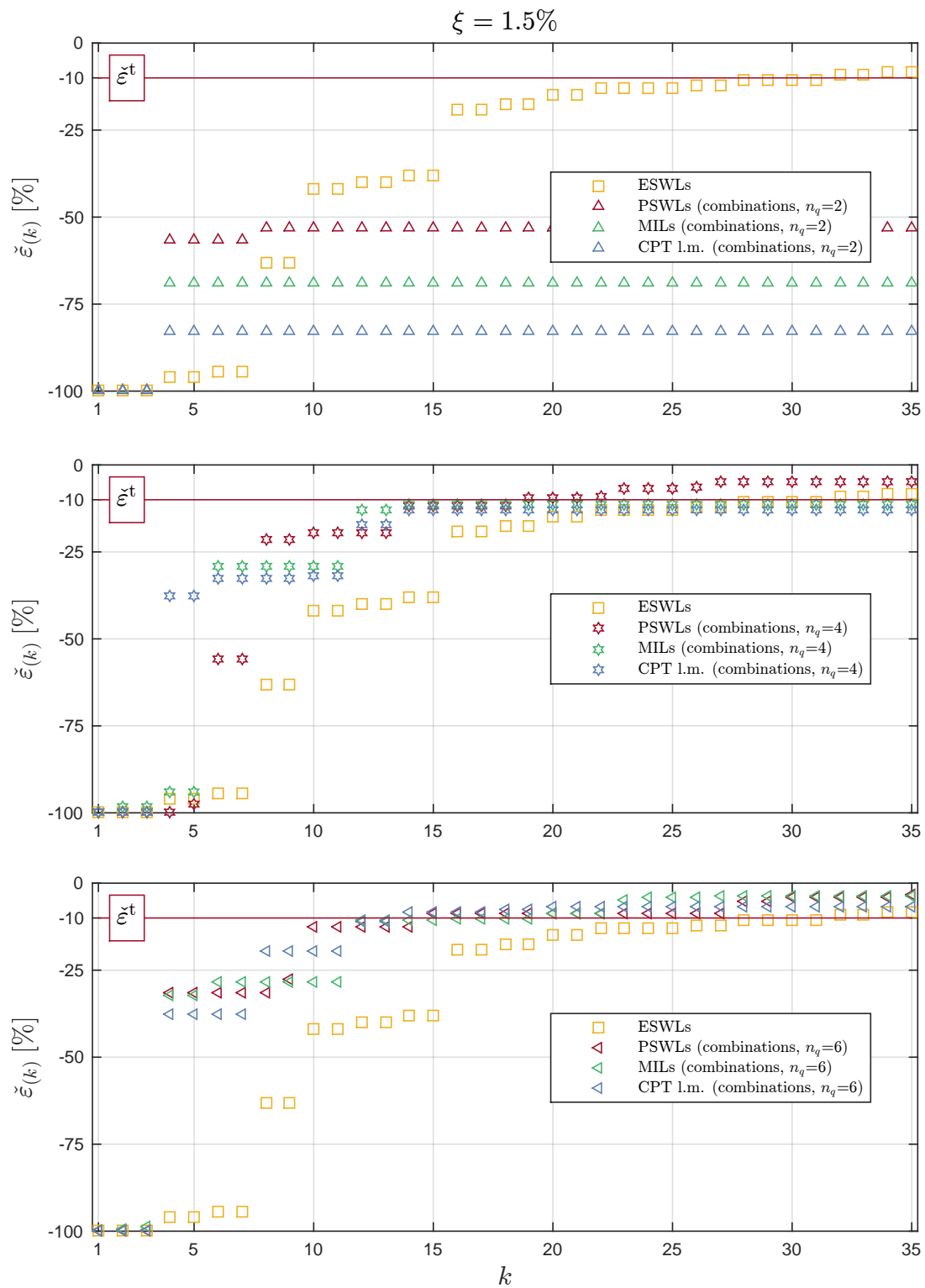


Figure VI.36: Evolution of the largest relative error indicator  $\check{\epsilon}(k)$  as a function of the number of load cases for the case  $\xi = 1.5\%$ . combinations of the first 2 and 3 basic SWLs are considered. Combinations of the first 2, 4 and 6 basic SWLs are considered. (ERP parameters:  $\hat{\epsilon} = 0\%$ ,  $\gamma = 1$ ).

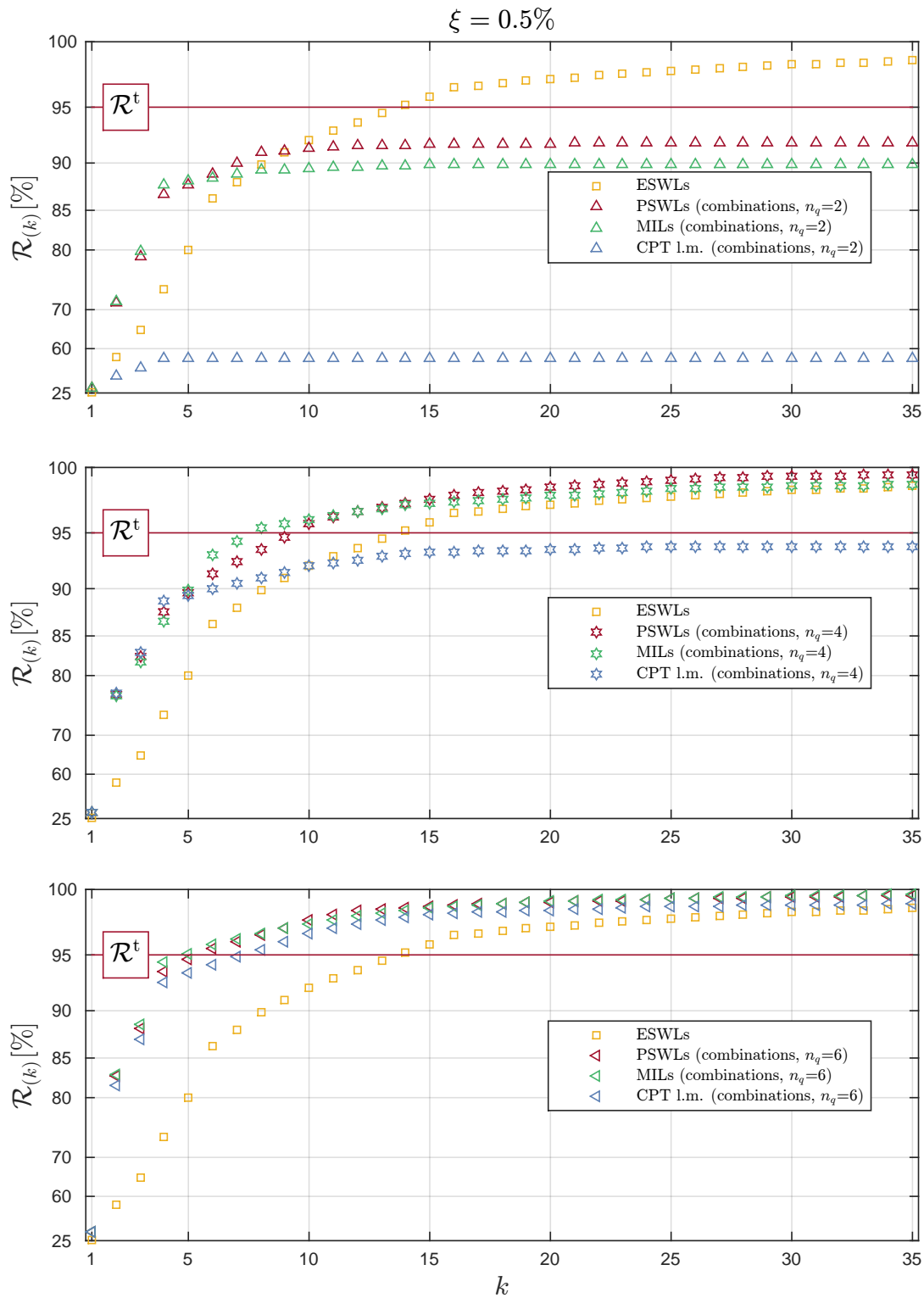


Figure VI.37: Evolution of the reconstruction indicator  $\mathcal{R}_{(k)}$  as a function of the number of load cases for the case  $\xi = 0.5\%$ . Combinations of the first 2, 4 and 6 basic SWLs are considered. (ERP parameters:  $\hat{\varepsilon} = 0\%$ ,  $\gamma = 1$ ).

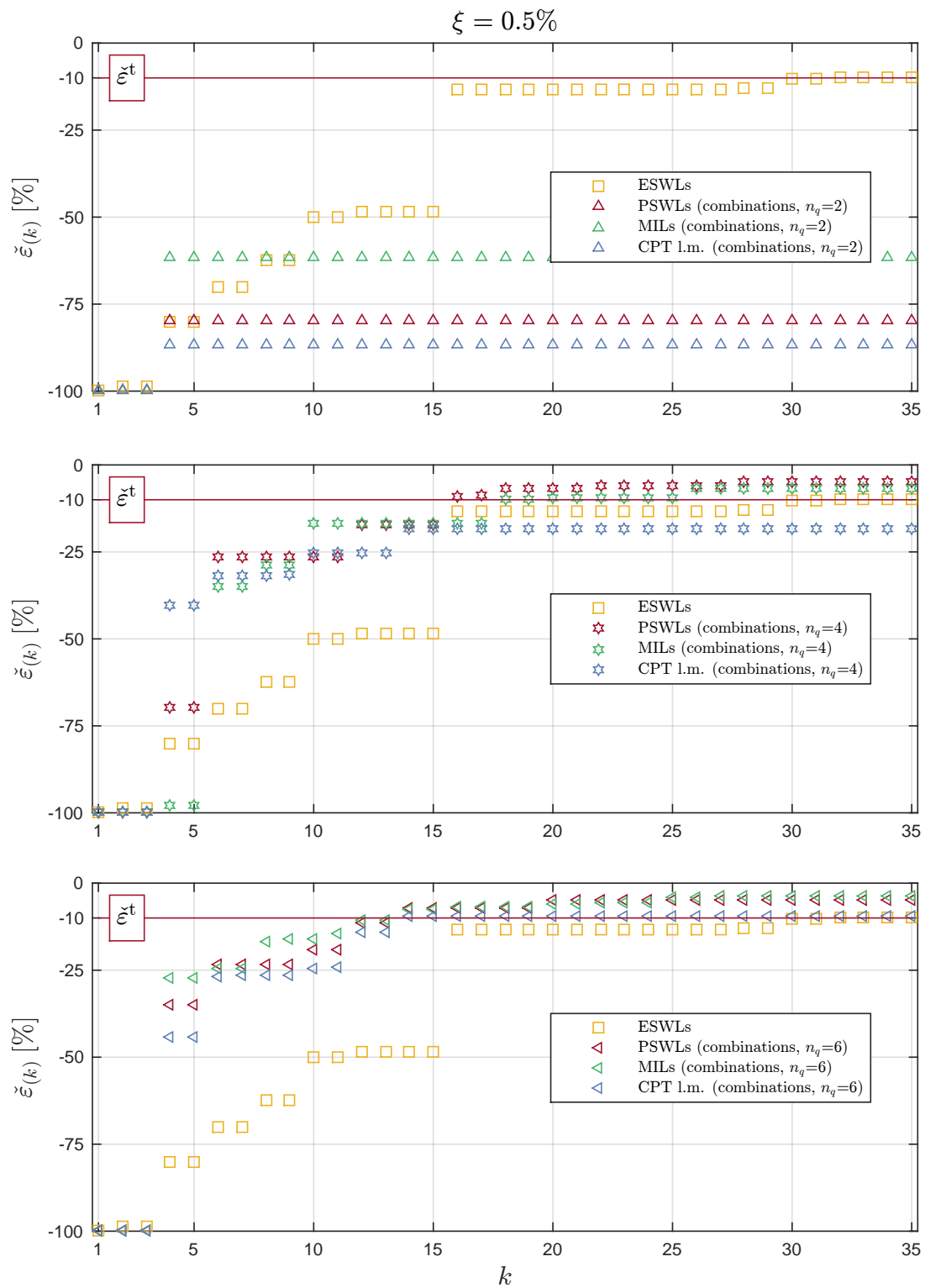


Figure VI.38: Evolution of the largest relative error indicator  $\check{\epsilon}(k)$  as a function of the number of load cases for the case  $\xi = 0.5\%$ . combinations of the first 2 and 3 basic SWLs are considered. Combinations of the first 2, 4 and 6 basic SWLs are considered. (ERP parameters:  $\hat{\epsilon} = 0\%$ ,  $\gamma = 1$ ).

### VI.2.7 Summary

In order to get accustomed to the envelope reconstruction problem, the reconstruction of the bending moment diagram of a four span bridge under lift aerodynamic forces has been considered. Several bases of SWLs have been used for comparison and the principal findings are:

- Applying successively the basic SWLs without combination does not provide a satisfactory envelope reconstruction;
- some combinations of a subset of basic SWLs based on the constrained non-linear optimization problem, developed in Chapter III provides a faster and better reconstruction of the envelope provided that a sufficiently large subset of SWLs is considered for combinations;
- combinations of CPT loading modes and the MILs are better suited for an accurate reconstruction of the envelope than the ESWLs, as well as combinations of the PSWLs no matter the structural behavior.

## VI.3 Lille's stadium (unique peak factor)

### VI.3.1 Description of the structure

The envelope reconstruction problem is now illustrated for the case of a large stadium with a retractable roof, known as “Stade Pierre-Mauroy”, in Lille, France. Figure VI.39 shows an aerial view of the stadium with its roof in the fully open configuration. A part of its design has been conducted by the design office Greisch, at Liège, Belgium. The design office is acknowledged for having provided the finite element model used for the illustrations. The finite element model has 4940 elements, 2548 nodes and  $n_t = 15288$  DOFs.



Figure VI.39: Aerial view of the “Stade Pierre-Mauroy” (courtesy of [www.info-stades.fr](http://www.info-stades.fr)).

Figure VI.40 shows three different parts of the roof: the retractable one, above the ambulatories and above the grandstands. The roof covering is composed of polycarbonate plates.

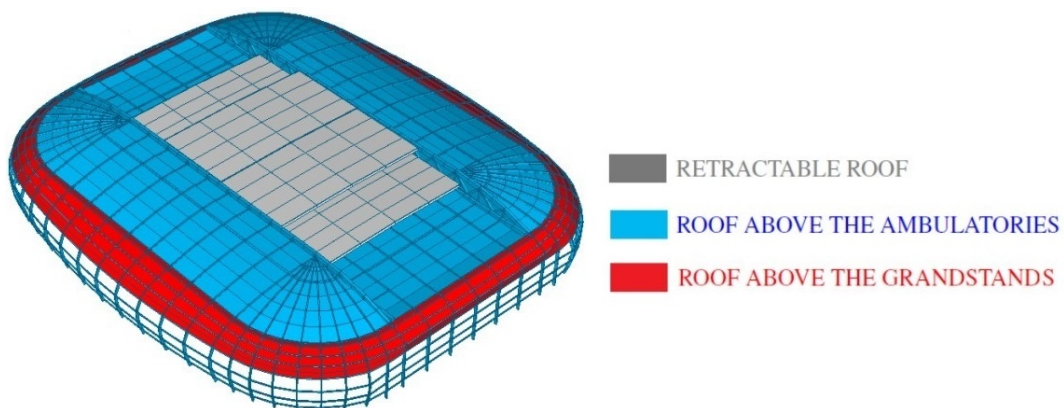


Figure VI.40: Different parts of the roof (image from [FinelG \(1999\)](#)).

The retractable roof is modeled with plates in the finite element model. Figure VI.41 shows different views of the finite element model of the load-bearing system mainly composed of steel elements.

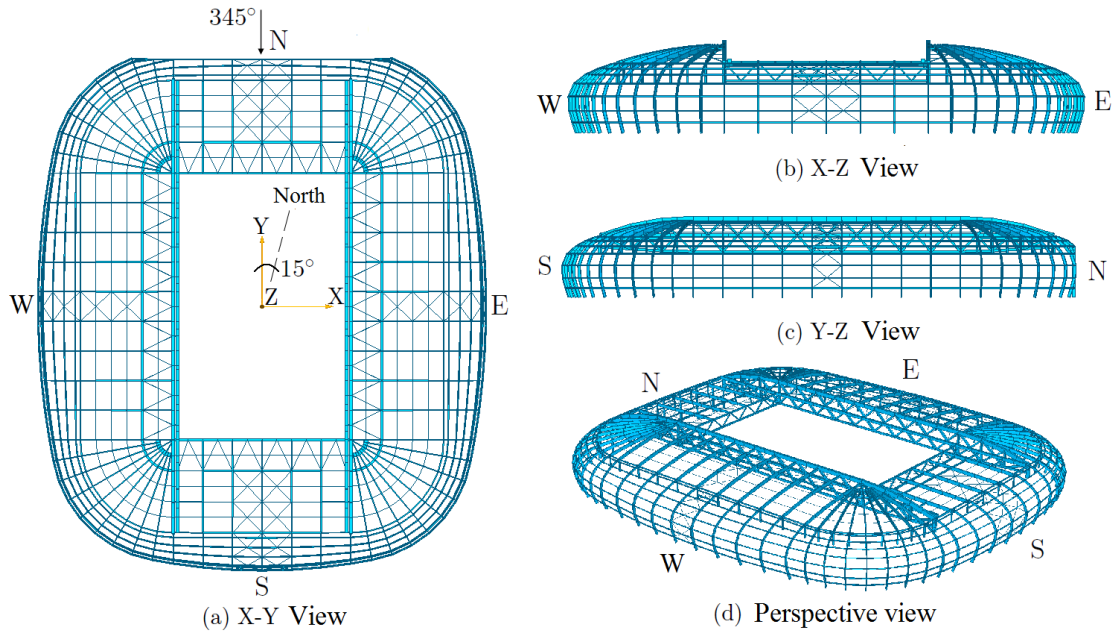


Figure VI.41: Different views of the finite element model of the load-bearing system (image from FinelG (1999)).

Two longitudinal large beams of 205 m span, see Figure VI.42-(a), support the retractable roof and the roof above grandstands. These beams are trusses, about 15 meters height, which are isostatic and pre-stressed by cables. Two cross-way beams support the South and North parts of the roof above grandstands and are connected with these longitudinal beams. These cross-way beams are also trusses with a height that reaches 8 m for a span of 80 m, see Figure VI.42-(b).

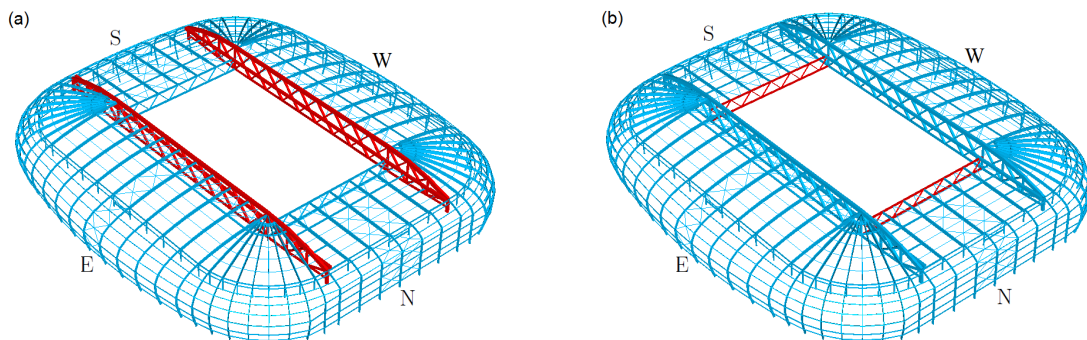


Figure VI.42: (a) Longitudinal large beams (in red) and (b) cross-way beams (in red) (image from FinelG (1999)).

Figure VI.43 shows the load-bearing system for the coverage of the stands (a)-(b) as well as the ambulatories (c) supported by columns (d) situated at the top of the grandstands. The beams are approximately spaced by 13.4 meters.

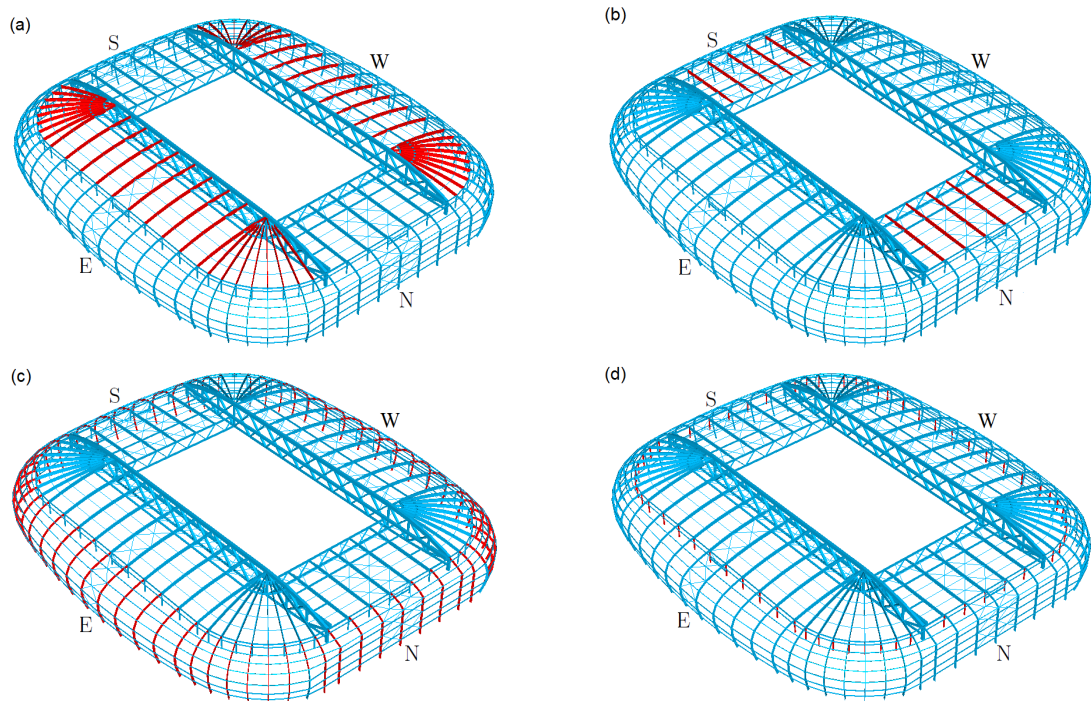


Figure VI.43: In red, beams of the (a)-(b) roof-bearing system, (c) ambulatory-bearing system and (d) Columns (image from [FinelG \(1999\)](#)).

There are four types of purlins: the ones (1) above the ambulatory in steel, (2) above the stands in wood, (3) those necessary for the retractable roof and (4) those necessary for the bracing system, see Figure VI.44.

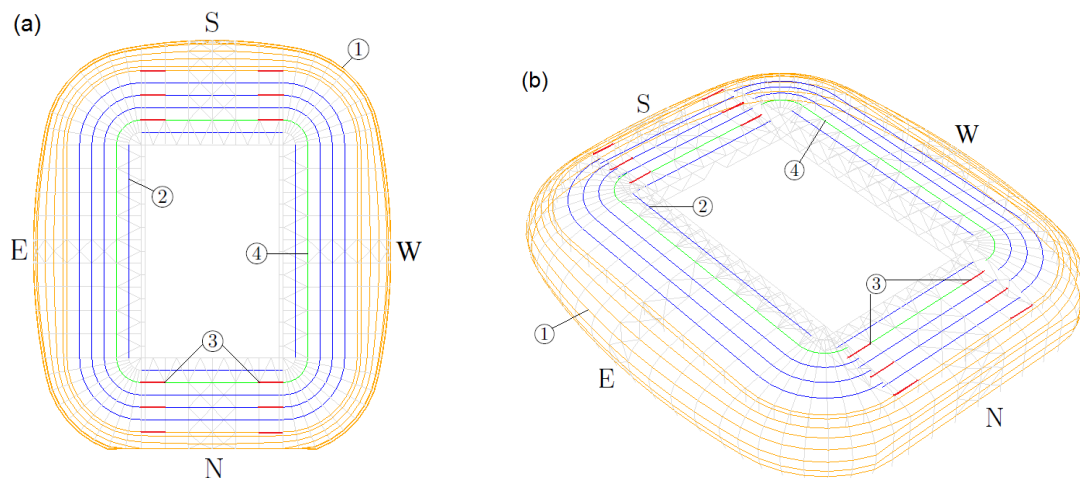


Figure VI.44: (a) Top view and (b) perspective view of different purlins (image from [Blaise \(2010\)](#)).

The overall horizontal stability of the roof is ensured by a bracing system shown in

Figure VI.45. This system transfers the horizontal forces to two vertical bracings in each principal direction. The bracing elements are metal tubes. The configuration does not provide clamping during elongations or contractions due to thermal stresses in the structural elements.

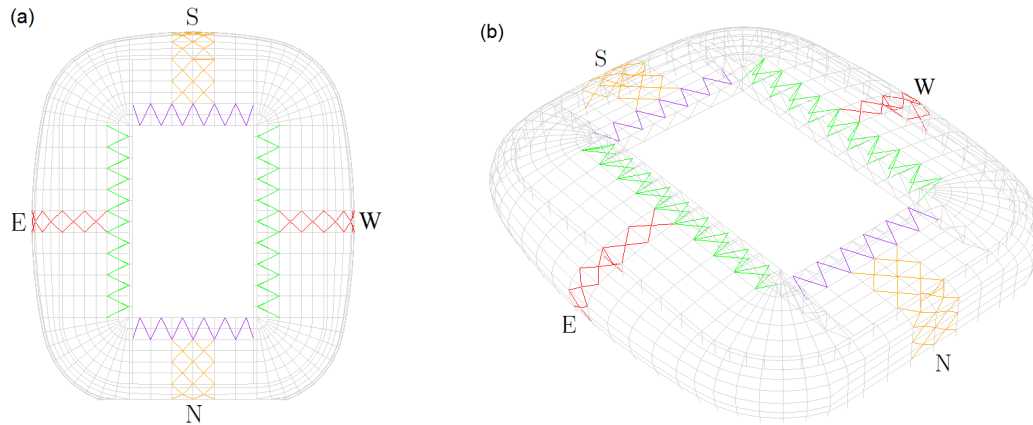


Figure VI.45: (a) Top view and (b) perspective view of the bracing system (image from [FinelG \(1999\)](#)).

### VI.3.2 Description of the wind loading

The aerodynamic loading characterization has been realized by wind tunnel measurements at the “*Centre Scientifique et Technique du Bâtiment*” (CSTB) in Nantes, France. The CSTB is acknowledged for having provided the measurements in wind tunnel used for the illustrations. Figure VI.46 depicts the 1/200 scaled model in the wind tunnel.

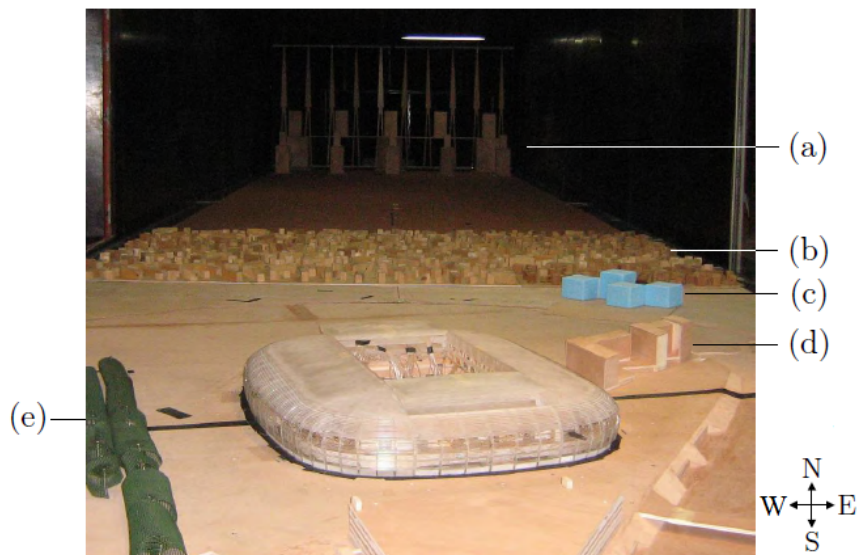


Figure VI.46: Model of the stadium in the wind tunnel. (a) View of the exit of the turbine, (b) block to create the wind velocity profile, (c) and (d) surrounding buildings, (e) surrounding woods. Also published in ([Blaise and Denoël, 2011b](#)), courtesy of CSTB.



The wind targets properties of the atmospheric boundary layer are simulated as prescribed in the Eurocodes (Eurocode, 1991a) and its French national appendix. Notably, the targeted wind loads correspond to the Service Limit State ones and a IIIa category terrain is appropriate to represent the surrounding of the stadium. The mean velocity recorded at the top of the stadium  $v_m = 28.3$  m/s accurately corresponds to the target value and thus to an expected reference velocity pressure  $p_{mean} = 491.7$  Pa.

The velocity and time scales are  $1/2.98$  and  $1/67$  respectively. The model is assumed to be infinitely rigid. The surrounding buildings and trees are also modeled to simulate a realistic environment. The instrumentation of the scaled model required approximately three hundred and fifty synchronous pressure sensors, sampled at 200 Hz, which corresponds to 2.94 Hz in full scale (or a time step equal to 0.342 seconds). Each measurement lasts about 105 minutes full scale, i.e., approximately ten times as much as the typical conventional requirements, which allows for some statistical treatment.

In a first rank context, pressures recorded at different locations in space are regarded as random variables (and therefore independently from their frequency content). The analysis of the maps of the mean and the standard deviations of the pressure coefficients offers a basic understanding of the wind flow around the structure and thence is of necessary interest for the wind tunnel engineers as well as the designing engineers.

Pressure coefficients are referenced using the mean velocity recorded at the top of the stadium  $v_m$ ; they are defined from the aerodynamic pressures by

$$\mathbf{c}_{\mathbf{p}'} = \frac{\mathbf{p}'}{\frac{1}{2}\rho v_m^2}, \quad (\text{VI.3.1})$$

where  $\rho = 1.225$  kg/m<sup>3</sup> is the air density. A positive pressure coefficient means that aerodynamic pressure acts towards the inner of the stadium while a negative coefficient indicates suction (with reference to the atmospheric pressure). They are illustrated for the considered application in Figure VI.47 for a wind coming East: 75° wind direction and a fully close roof configuration, see Figure VI.41. This configuration is used for the illustration in the sequel.

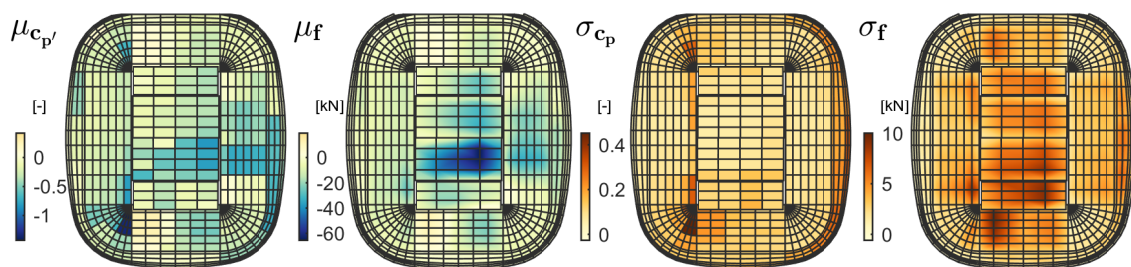


Figure VI.47: From left to right, maps of mean pressure coefficients, mean nodal forces (global vertical forces), standard deviations of pressure coefficients and standard deviations of nodal forces (global vertical forces) for the 75° wind direction.

It appears that the roof is mainly in depression (with reference to the atmospheric pressure) and that the wind loads are not symmetrically distributed with respect to the axis of the incoming flow, which is explained by the unevenness of the surrounding, see Figure VI.46. These figures also illustrate the local increase of mean pressures in zones with sharp edges. For instance, as a consequence of the high longitudinal main beam and an extra

acrotorium necessary for the moving parts to slide apart, the South-West zone exhibits very close areas with positive and negative pressures; they just result from the air flow trapped against the windward face of the vertical wall and the vortex shedding in the leeward area. Large standard deviations in this area show the substantial intensity of this shedding, and indicate the need for a proper local design of the roof in that area, for that roof configuration and wind direction.

### VI.3.3 Buffeting analysis (Gaussian assumption)

The background and resonant analyses are conducted in the nodal and modal bases respectively (Section II.6.3), and, structural responses are assumed to be Gaussian random processes as a first insight. This assumption of Gaussianity is relaxed in Section VI.4. The first 21 modes are retained for the modal analysis and are depicted in Figure VI.49. A unique modal damping coefficient  $\xi$  equal to 1% is adopted for each mode (Section II.5). The PSDs of generalized forces of modes 1 and 3 are illustrated in Figure VI.48.

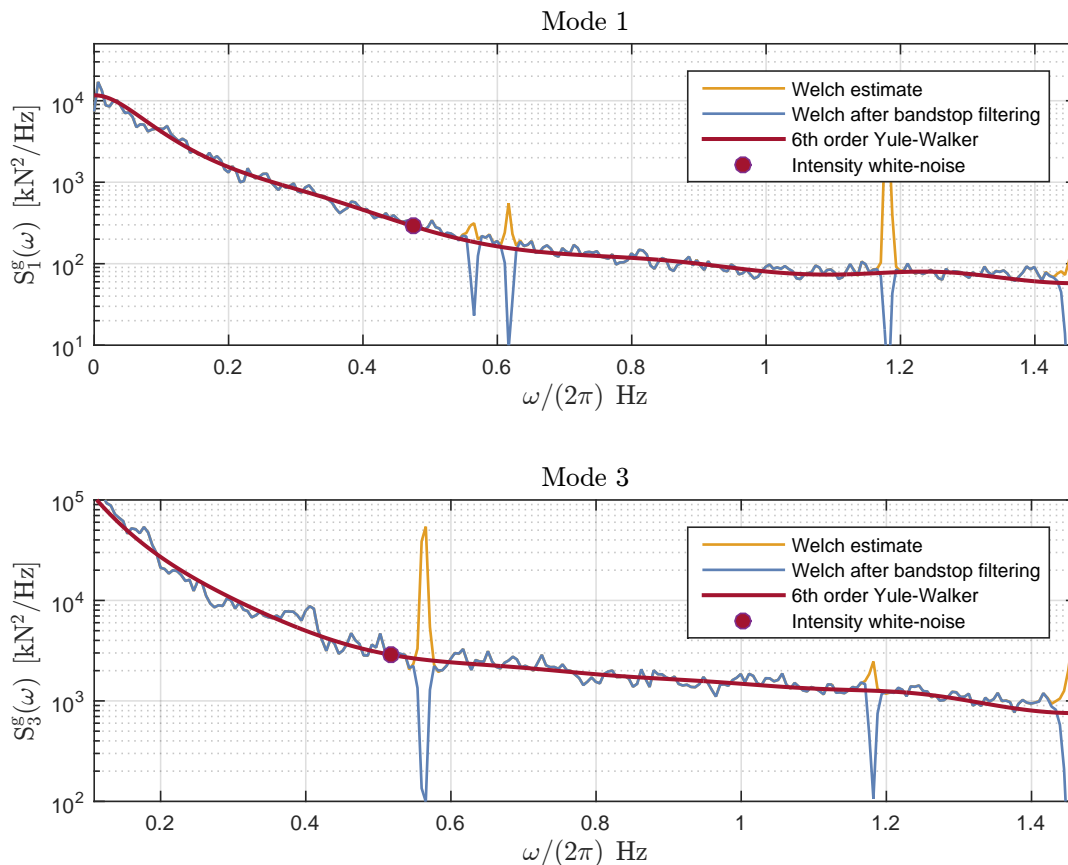


Figure VI.48: Fitting of a probabilistic model (a parametric psd estimate) to the PSDs of generalized forces of modes 1 and 3. The parametric estimate, after bandstop filtering, provides an interesting methodology offering smoothness and robustness against spurious harmonics.

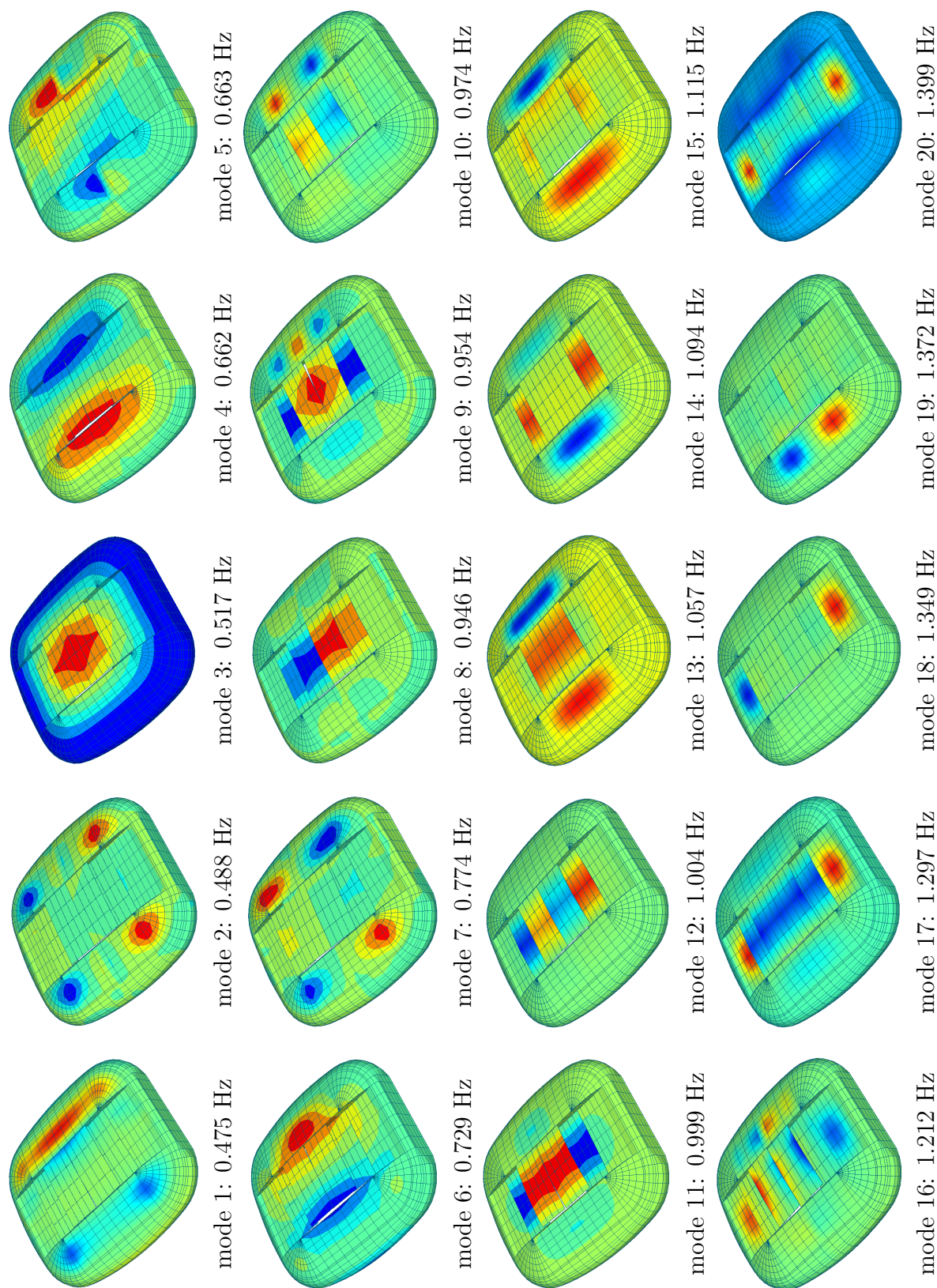


Figure VI.49: Unity-scaled modal shapes (vertical displacements) and associated frequencies. Also published in (Blaise, 2010).

The computation of modal variances and covariances is done with a proper recourse to the white noise approximation and its extension discussed in Section II.7. For this purpose, the PSDs of generalized forces are fitted with a Yule-Walker model in order to (i) smooth out spurious harmonics and (ii) provides robust estimations of the intensity of the white noise for each generalized force (Blaise and Denoël, 2011a). The fitting of a Yule-Walker model to generalized forces is illustrated in Figure VI.48 for modes 1 and 3. The orange and blue lines represent the non-parametric power spectral density estimates of the raw signal and of the bandstop filtered signal around the troublesome frequencies, respectively. The spurious peaks, see (Blaise, 2010) for their origins, are basically transformed to spurious valleys as the cutoff and order of the bandpass filter have been roughly selected. Red line represent the parametric model, a 6th-order Yule-Walker model, obtained from the raw and filtered signals, respectively. One may observe that the successive application of a bandstop filtering and parametric estimation provides a smooth acceptable power spectral density. Finally, a reliable estimation of the white-noise is done with the Yule-Walker model. A similar procedure is adopted for coherence functions of generalized forces.

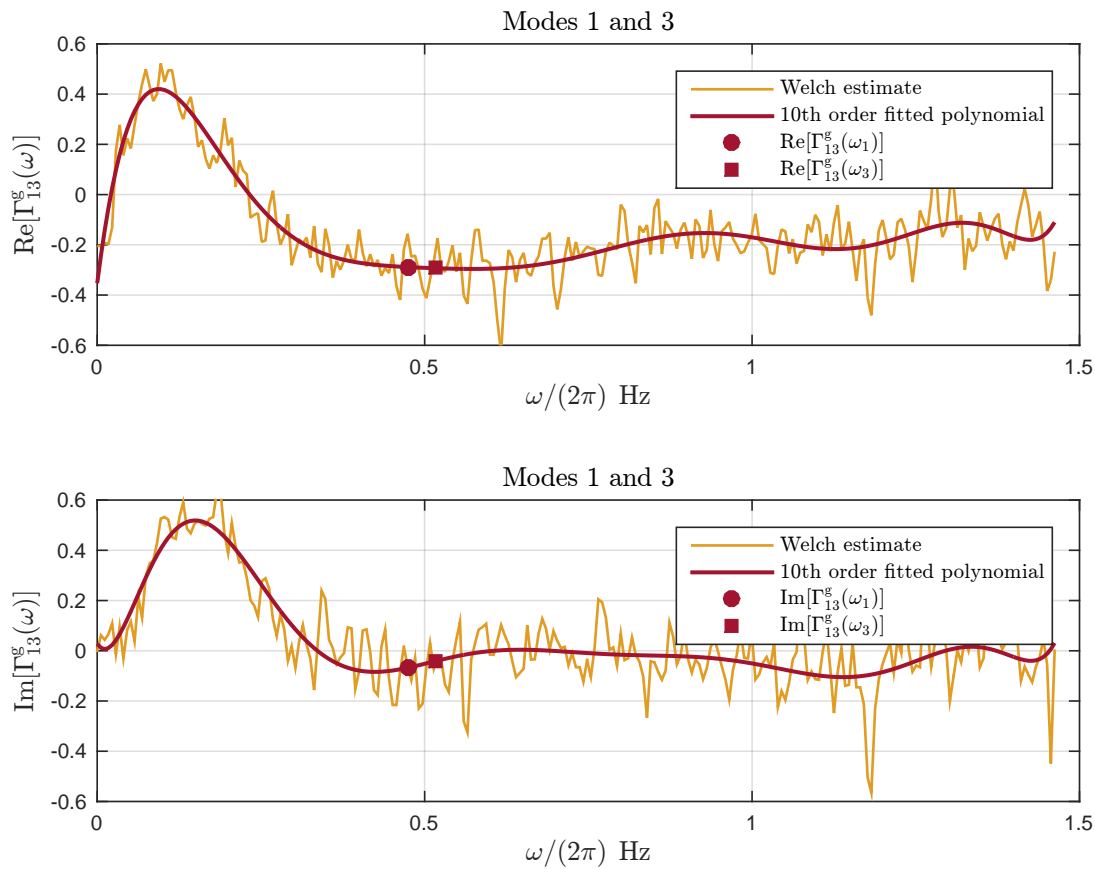


Figure VI.50: Real and imaginary parts of the coherence function (in orange) and parametric estimator (in red) of generalized forces in modes 1 and 3.

The real and imaginary parts of the coherence function between modes (1,3) are represented in Figure VI.50. They are fitted using 10th order polynomial functions that give a much smoother representation of these functions. Next, the fitted polynomial functions give reliable estimations of the real and imaginary parts of the coherence functions evaluated at the natural circular frequencies required for the extended white noise approximation (Section II.7.4). For later developments, note that for frequencies higher than 0.4Hz, the imaginary part of the coherence function between modes (1,3) is one order of magnitude lower than the real part. Even if not illustrated, this observation also applies for several other coherence functions.

The background and resonant contribution to the variance of modal amplitudes are shown in Figure VI.51. For the resonant contribution, the values obtained with the white noise approximation are very close to the results of the classical modal analysis. The structure mainly responds in the third mode which vibrates in a global vertical displacement of the roof, see Figure VI.49. The structure has a dominant resonant structural behavior since all background-to-resonant ratios are lower than one.

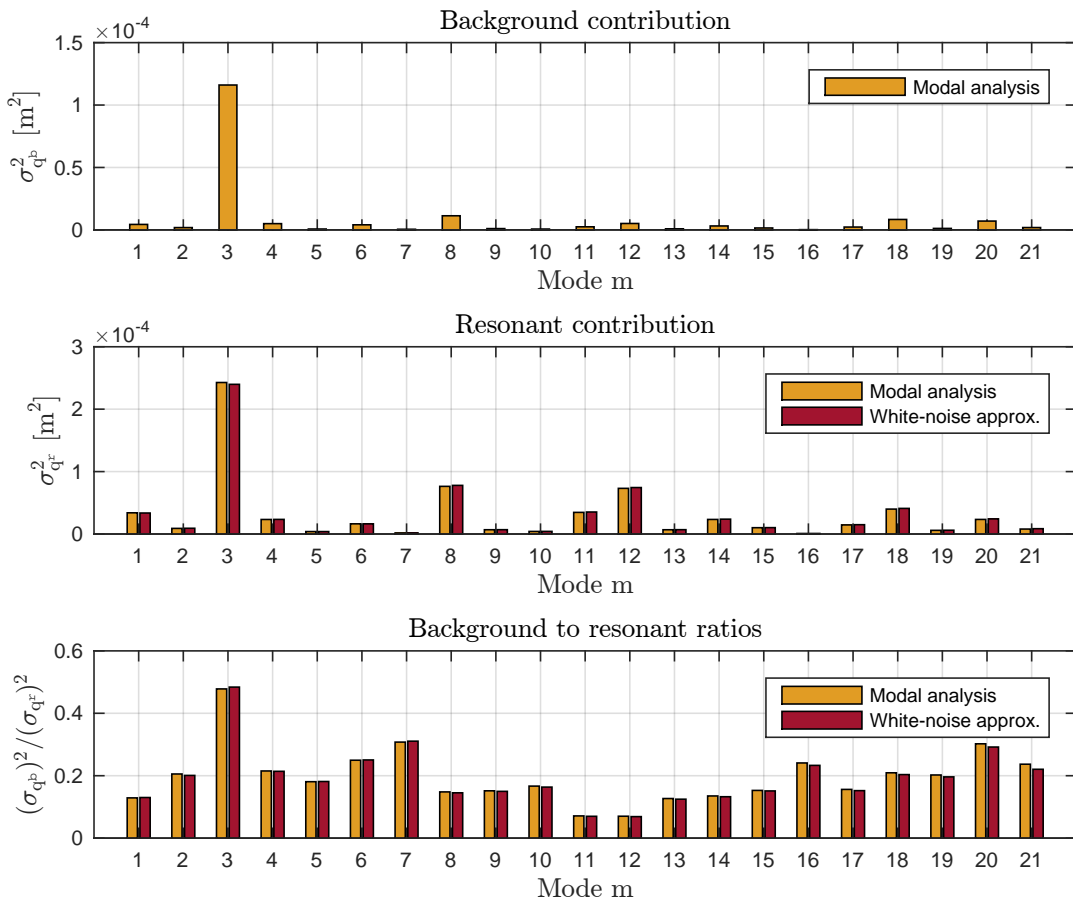


Figure VI.51: Background and resonant contribution to the variance of modal amplitudes in the first 21 modes. The background to resonant ratios indicate that the structure has a resonant structural behavior.

In the sequel, the proposed extension of the white noise approximation (Section II.7.4) to compute the resonant contribution to the (modal covariances and) correlation coefficients is applied and compared with results of the classical modal analysis.

First, the real and imaginary parts of cross-PSD of  $m$ -th and  $n$ -th generalized forces are replaced by white noises which necessitates white noise approximations of the real and imaginary parts of the coherence functions, respectively denoted by  $\Gamma_{mn}^{(\text{Re},\text{wn})}$  and  $\Gamma_{mn}^{(\text{Im},\text{wn})}$ , and depicted in Figure VI.52. The white noise approximation of the imaginary part of the coherence functions is one order of magnitude lower than the real part, as observed for the coherence functions between modes (1,3). Consequently and as commonly adopted, the contribution of the imaginary part of the cross-PSD in the covariance of modal amplitudes is negligible. This observation only holds for this specific case study.

Figure VI.52 also depicts the weighting functions for the real and imaginary parts of coherence functions. Large values are observed since the natural frequencies of the modes are sufficiently close to each other to provide resonant contribution to the correlation coefficients.

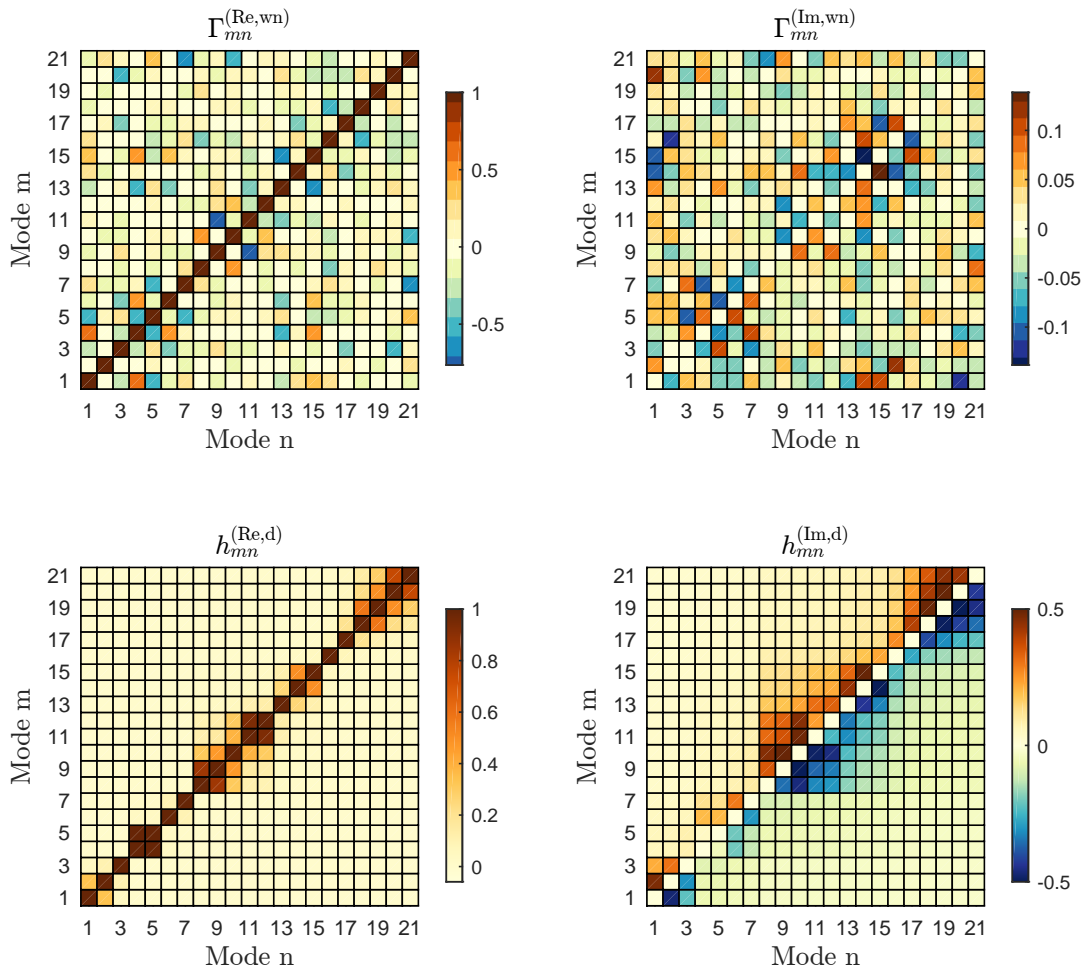


Figure VI.52: White noise approximation of the real and imaginary parts of coherence functions  $\Gamma_{mn}^{(\text{Re},\text{wn})}$  and  $\Gamma_{mn}^{(\text{Im},\text{wn})}$ . Weighting functions  $h_{mn}^{(\text{Re},\text{d})}$  and  $h_{mn}^{(\text{Im},\text{d})}$  defined in (II.7.14) and (II.7.26) for the real and imaginary parts of coherence functions.

However, since the magnitude of the white noise approximation of the real and imaginary parts of coherence functions is rather low, the resonant contribution to the correlation between modes is almost negligible, apart from correlations between modes (4,5) and (11,12) brought by the real part of coherence functions, see Figure VI.53.

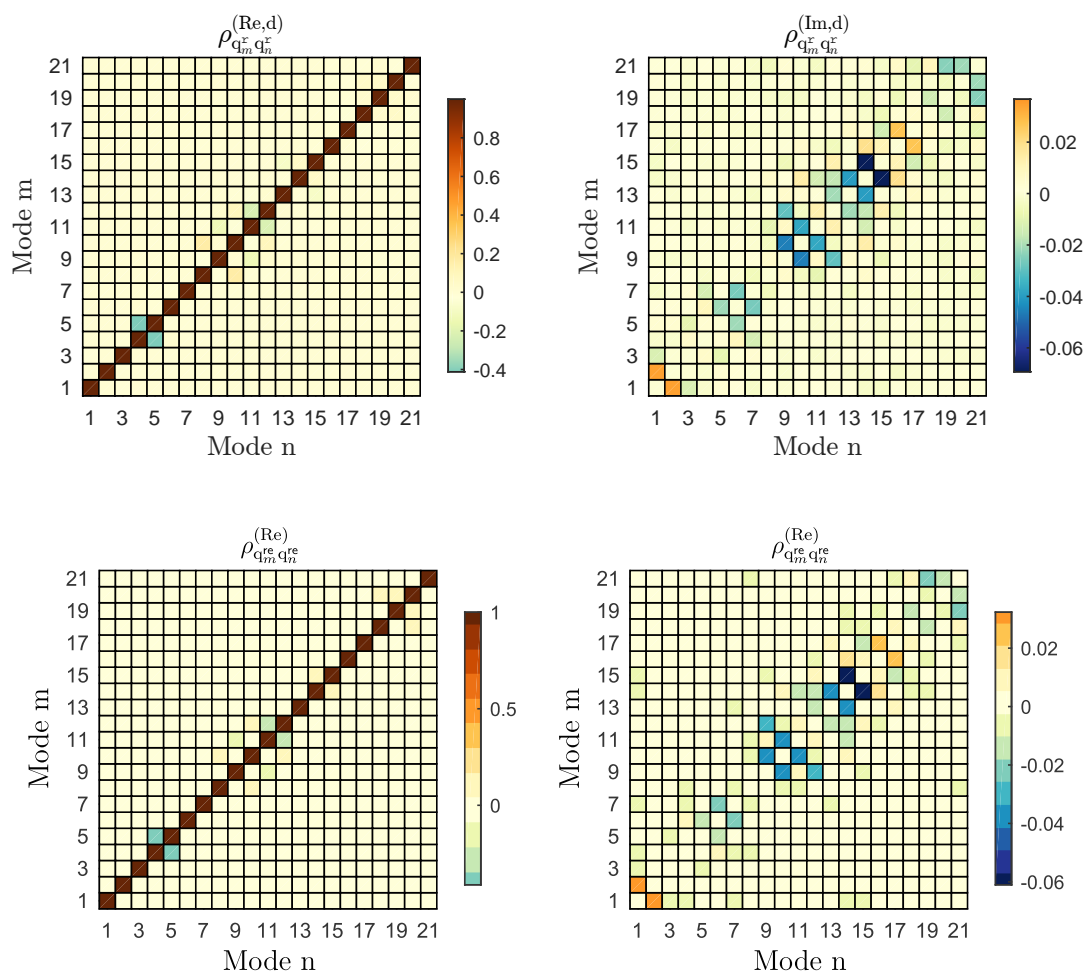


Figure VI.53: White noise approximation of the contributions  $\rho_{q_m^e, q_n^e}^{(Re,d)}$  and  $\rho_{q_m^e, q_n^e}^{(Im,d)}$ , defined in (II.7.30), of the real and imaginary parts of coherence functions to the resonant contribution of correlation coefficients. The adequacy of the white noise approximation is assessed by comparison with the residual contributions  $\rho_{q_m^e, q_n^e}^{(Re)}$  and  $\rho_{q_m^e, q_n^e}^{(Im)}$ , defined in (II.7.17).

Finally, the total correlation is obtained as a weighted combination of background and resonant contributions, see Figure VI.54.

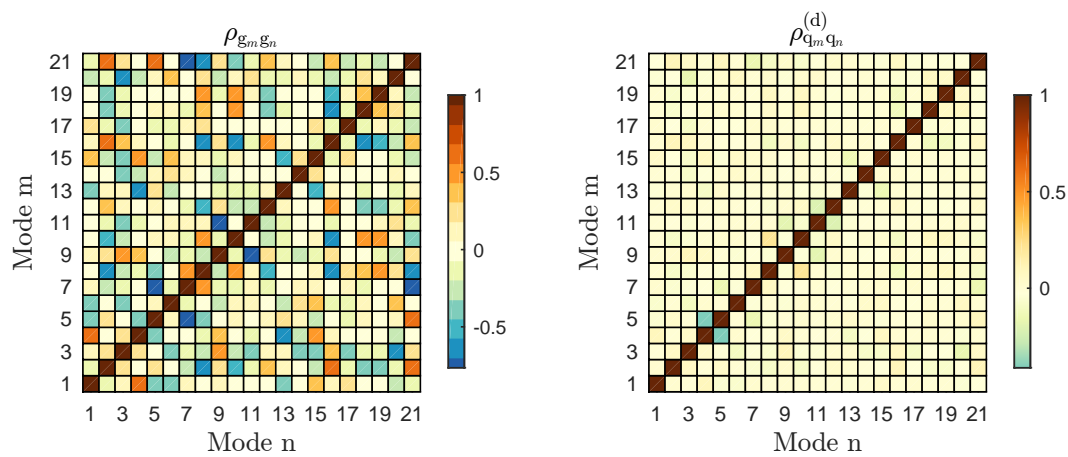


Figure VI.54: Correlation coefficients of the generalized forces and of the modal amplitudes obtained by the extended white noise approximation.



### VI.3.4 Envelope of structural responses

The envelope reconstruction problem focuses on the envelope values of internal forces in elements of the load-bearing system. Figure VI.55 identifies these structural elements and Table VI.7 collects the structural responses considered for the ERP. Structural responses are assumed to be Gaussian random processes. However, peak factors are not computed with (II.3.21). For the sake of simplicity, a unique peak factor taken equal to  $g^{(\min)} = -3.5$  and  $g^{(\max)} = 3.5$  is adopted in first approximation. Under the assumption of Gaussianity, the mean smallest minimum and the mean largest maximum only differ by their sign, i.e.,  $r^{(\min)} = -r^{(\max)}$ , and the envelope to be reconstructed is symmetric, see Section II.3.

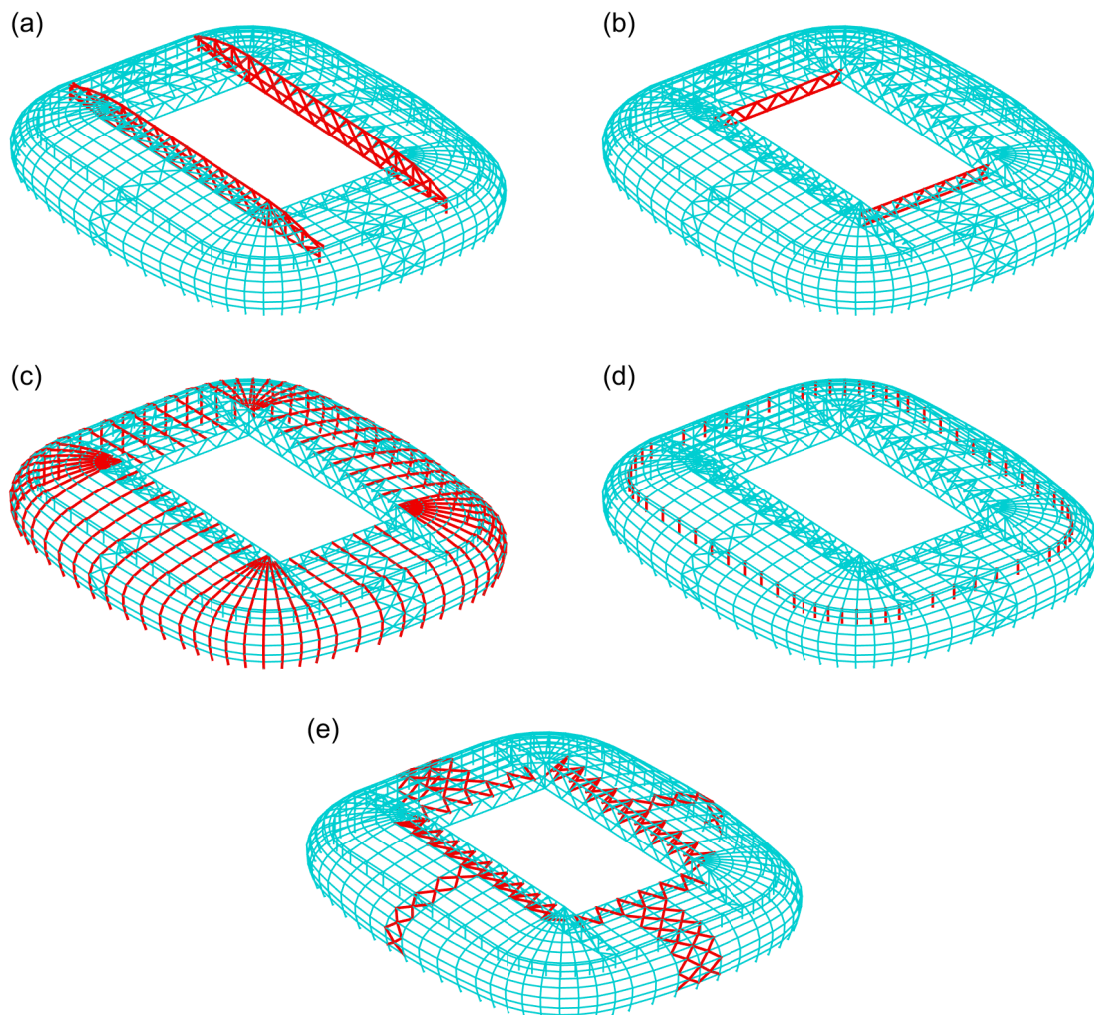


Figure VI.55: Structural elements of the load-bearing system considered for the envelope reconstruction problem.

|                                 | Type          | Elements | Forces                  | Responses  |
|---------------------------------|---------------|----------|-------------------------|------------|
| Large beams <sup>(a)</sup>      | Spatial beams | 399      | $N, M_y, M_z, T_y, T_z$ | 1995       |
| Cross-ways beams <sup>(b)</sup> | Spatial beams | 65       | $N, M_y, M_z, T_y, T_z$ | 325        |
| Beams (roof) <sup>(c)</sup>     | Spatial beams | 1070     | $N, M_y, M_z, T_y, T_z$ | 5350       |
| Columns <sup>(d)</sup>          | Spatial beams | 128      | $N$                     | 128        |
| Bracing system <sup>(e)</sup>   | Bar           | 196      | $N$                     | 196        |
|                                 |               |          |                         | $n_r=7994$ |

Table VI.7: Structural responses considered for the envelope reconstruction problem.

Table VI.8 indicates the overall indicator of correlation for each internal force taken separately and for all structural responses. For this example, the overall correlation is very low due to the large dimensions of the stadium. Additionally, the large number of structural responses make the ERP relatively challenging. The impact on the reconstruction rate is studied in the next section.

|                | $N$  | $M_y$ | $M_z$ | $T_y$ | $T_z$ | $n_r = 7994$ |
|----------------|------|-------|-------|-------|-------|--------------|
| $\bar{\rho}_r$ | 0.24 | 0.15  | 0.21  | 0.21  | 0.13  | 0.16         |

Table VI.8: Overall indicator of correlation (III.3.8) for each internal force and for all considered responses.

Because it would be impractical to illustrate the envelope reconstruction for each response, it is illustrated with six set of structural elements identified in red in Figures VI.56, VI.57, VI.58, VI.59, VI.60 and VI.61. The envelope of the considered internal force for these structural elements is also depicted. The six set of structural elements have been selected to represent each type of structural element in Table VI.7.

For the envelope reconstruction problem, we choose an acceptable overall reconstruction  $\mathcal{R}^t$  of 90 % and an acceptable underestimation  $\varepsilon^t$  of  $-25\%$ . The overall reconstruction indicator  $\mathcal{R}_{(k)}$  gives a global picture of the whole reconstruction of the structural responses in the stadium while the largest relative error indicator  $\check{\varepsilon}_{(k)}$  indicates the worse reconstruction of the envelope.

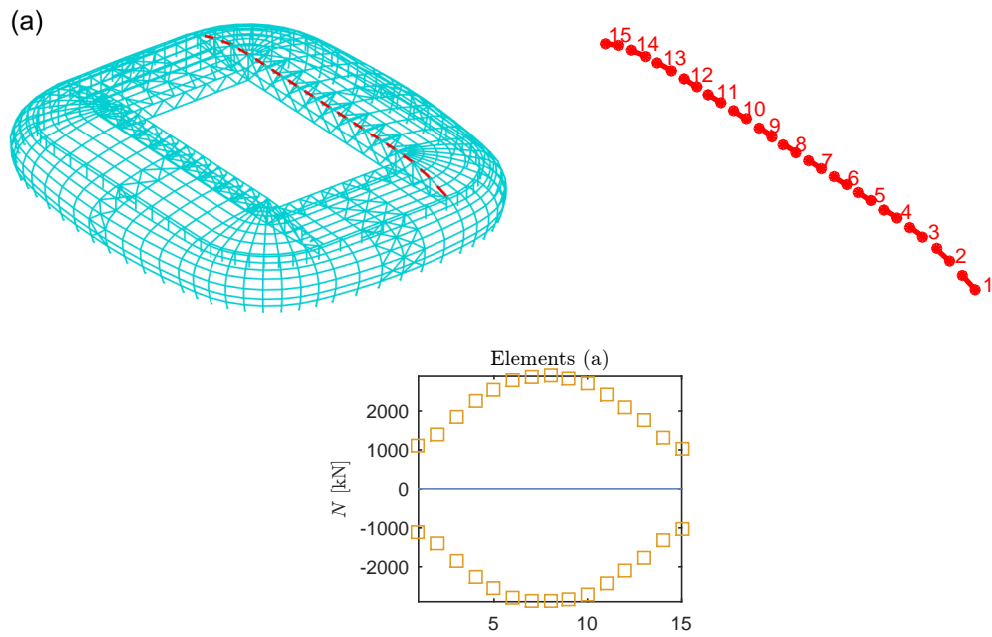


Figure VI.56: (a) Identification of 15 beam elements considered for the illustration (in red) and axial force envelope for these elements.

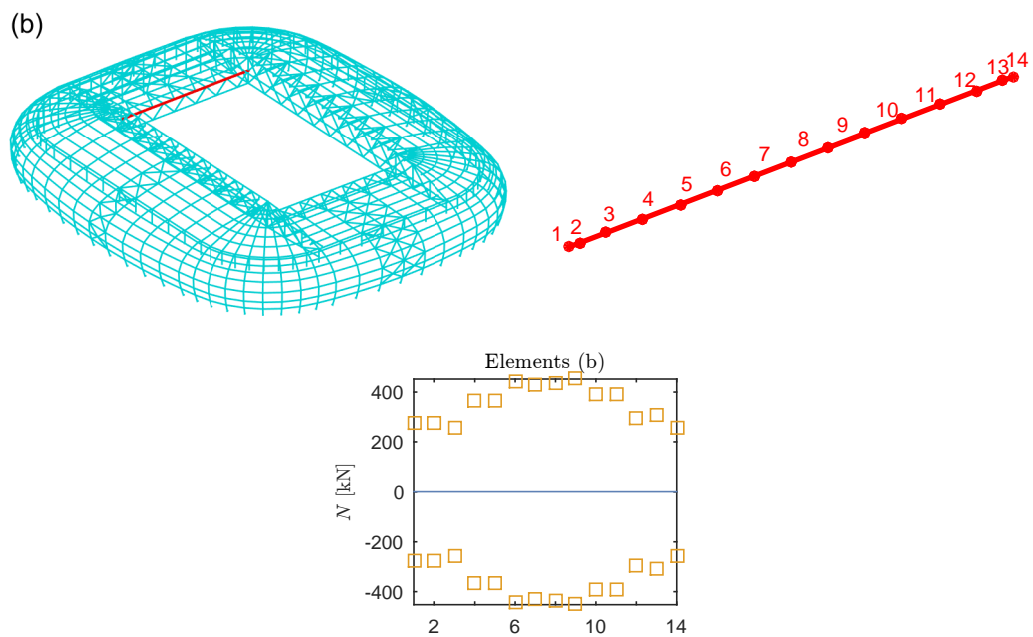


Figure VI.57: (b) Identification of 14 beam elements considered for the illustration (in red) and axial force envelope for these elements.

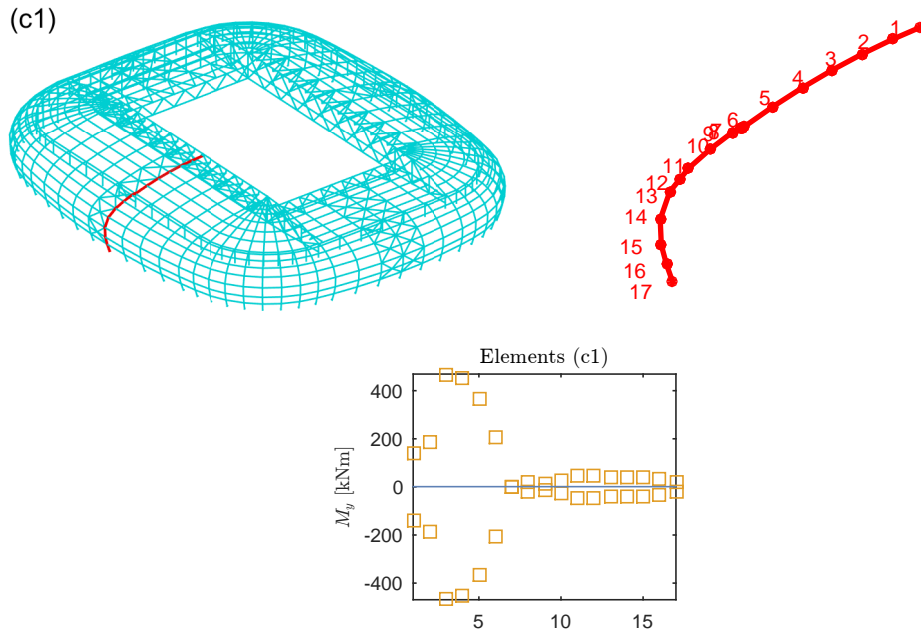


Figure VI.58: (c1) Identification of 17 beam elements considered for the illustration (in red) and bending moment envelope for these elements.

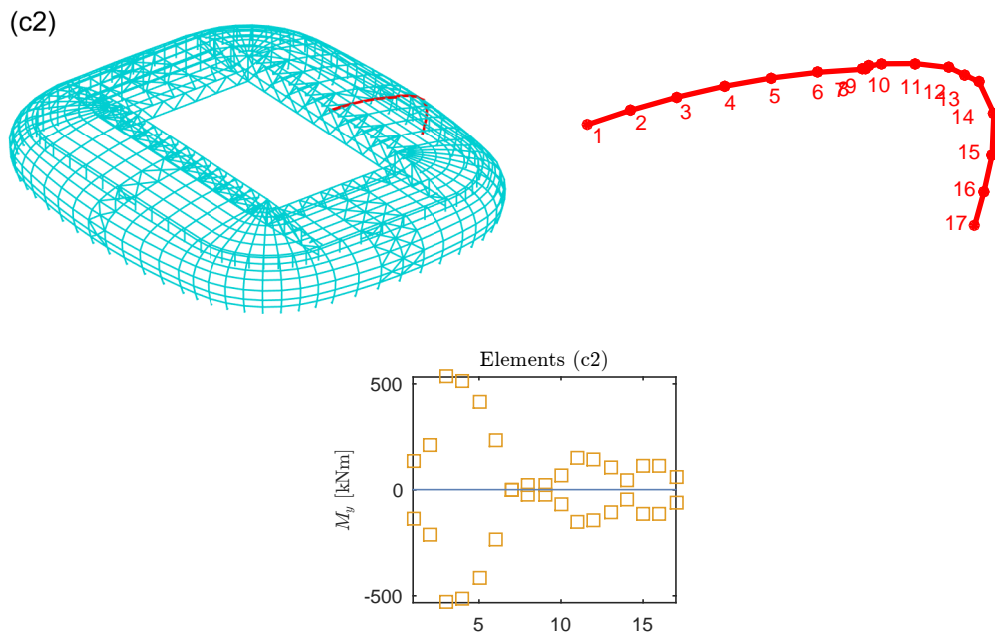


Figure VI.59: (c2) Identification of 17 beam elements considered for the illustration (in red) and bending moment envelope for these elements.

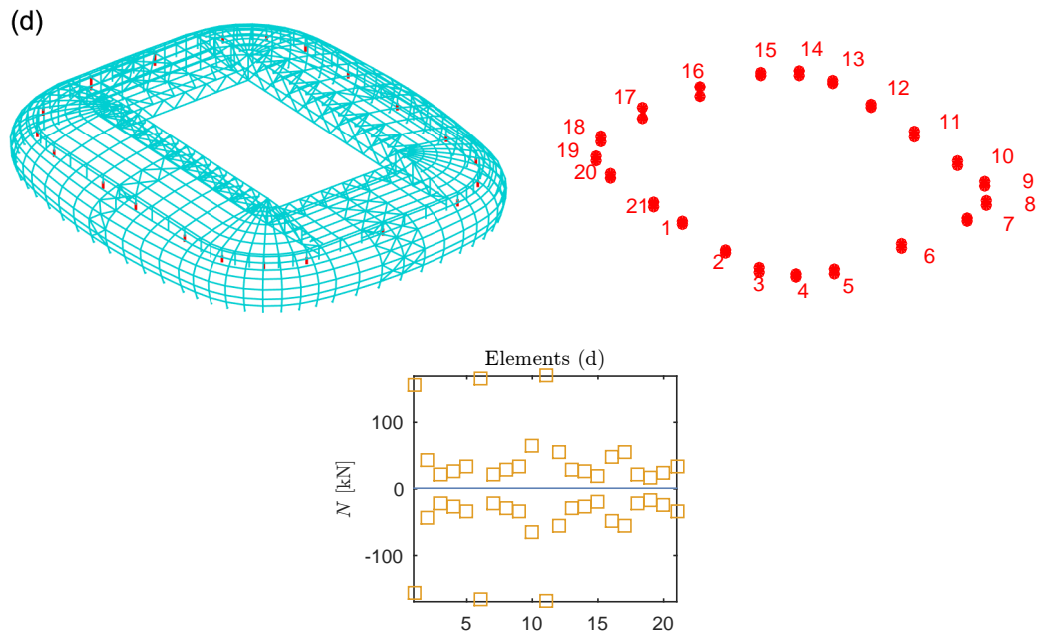


Figure VI.60: (d) Identification of 21 beam elements considered for the illustration (in red) and axial force envelope for these elements.

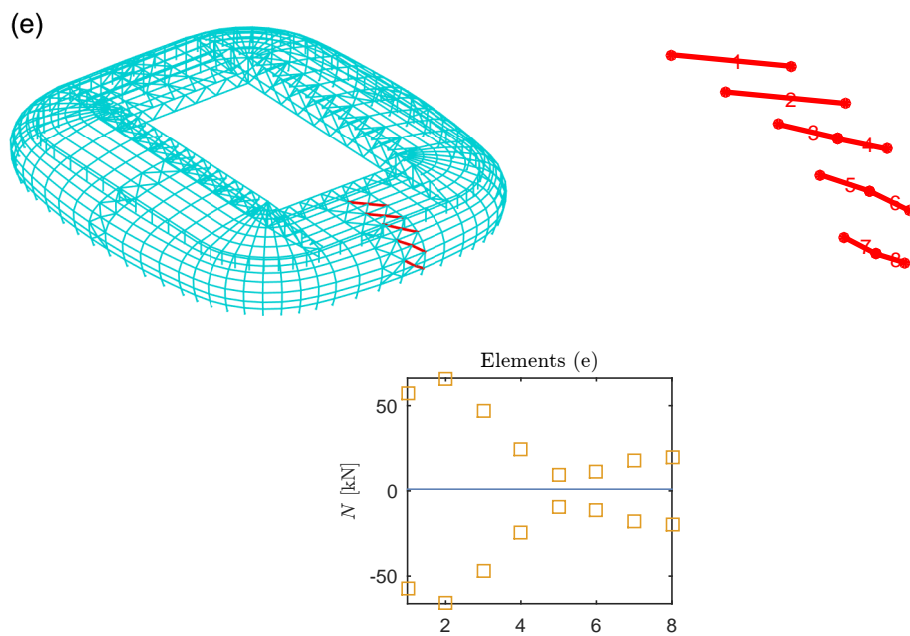


Figure VI.61: (e) Identification of 8 bars considered for the illustration (in red) and axial force envelope for these elements.

### VI.3.5 Envelope reconstruction with ESWLs

A usual option to solve the envelope reconstruction problem is to consider the equivalent static wind loads, see Section IV.10. ESWLs are obtained from the hybrid method proposed by Chen and Kareem (2001) and reviewed in Section IV.6. These hybrid-based ESWLs are formalized as weighted combinations of background ESWLs obtained with the LRC method and resonant ESWLs formulated with modal inertial loads. All ESWLs computed with the hybrid method naturally satisfy the envelope value condition (IV.2.3). Moreover, all ESWLs fulfill the non-overestimation condition (IV.2.4) since a unique peak factor is considered (IV.7.13). Therefore, the ESWLs do not require normalization (see Section IV.10.1) before using them for the envelope reconstruction problem. The ranking of ESWLs is done on how a given ESWL is able to minimize the cost function, defined in (IV.10.6). The acceptable overestimation  $\hat{\varepsilon}$  is set equal to zero and the parameter  $\gamma$  in the cost function (III.5.11) to one. Figure VI.62 only illustrates the odd static wind loads since we have in a Gaussian framework:  $\mathbf{f}_{(i)}^{(s)} = -\mathbf{f}_{(i+1)}^{(s)}$ .

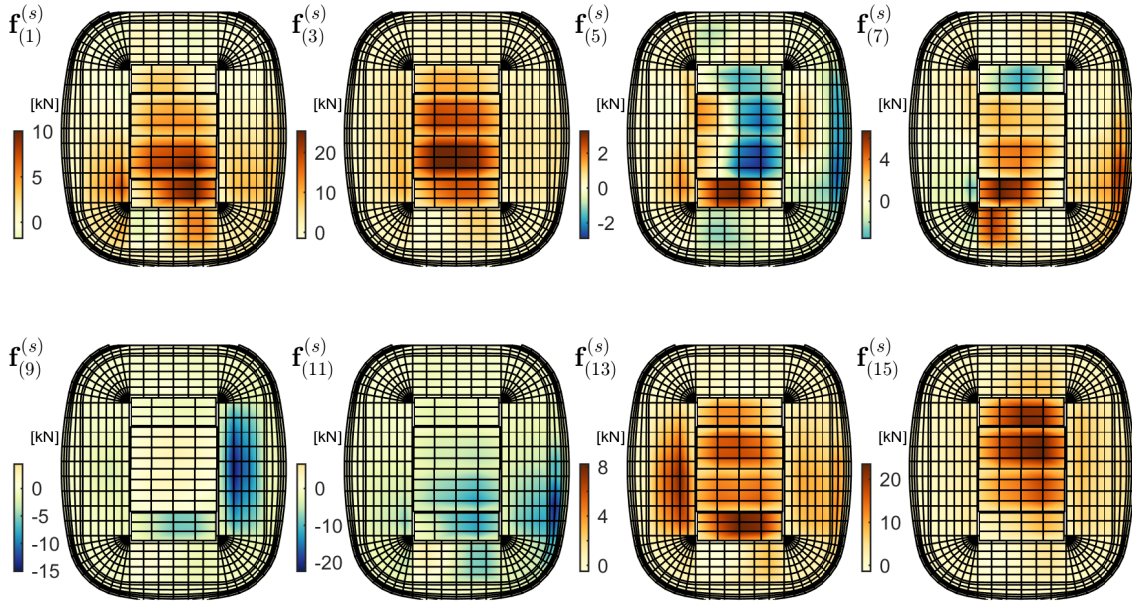


Figure VI.62: Static wind loads obtained as hybrid-based ESWLs (vertical nodal forces).

Figure VI.63 and VI.64 show the evolution of the reconstruction  $\mathcal{R}_{(k)}$  and the largest relative error  $\tilde{\varepsilon}_{(k)}$  indicators, respectively. Applying successively ESWLs provides very poor indicators  $\mathcal{R}_{(50)} = 68\%$ ,  $\tilde{\varepsilon}_{(50)} = -93\%$  with  $k = 50$  load cases.

Figure VI.65 shows the reconstructed envelope and relative errors for the six sets of structural elements with 50 load cases obtained with ESWLs. The envelope of axial forces in elements (a) of the considered large beam is very well-reconstructed while relative errors up to -70 % may be observed for structural responses in other elements. Figure VI.66 gives relative errors of reconstruction for the maximum side of the envelope for each type of internal force. For an even number of load cases, we have  $\mathcal{R}_{(50)} = \mathcal{R}_{(50)}^{(\min)} = \mathcal{R}_{(50)}^{(\max)} = 68\%$  and the average of relative errors of reconstruction is  $\Psi_{(50)}^{(\max,1)} = \mathcal{R}_{(50)}^{(\max)} - 1 = -32\%$ . Note that a large number of structural responses have relative errors  $\varepsilon_{(50)}^{(\max)}$  much larger than (in absolute

value)  $\Psi_{(50)}^{(\max,1)} = -32\%$  and even up to  $-95\%$ . These results clearly demonstrate, by way of an example, that ESWLs are not well-suited for the envelope reconstruction when a very large number of structural responses are considered.

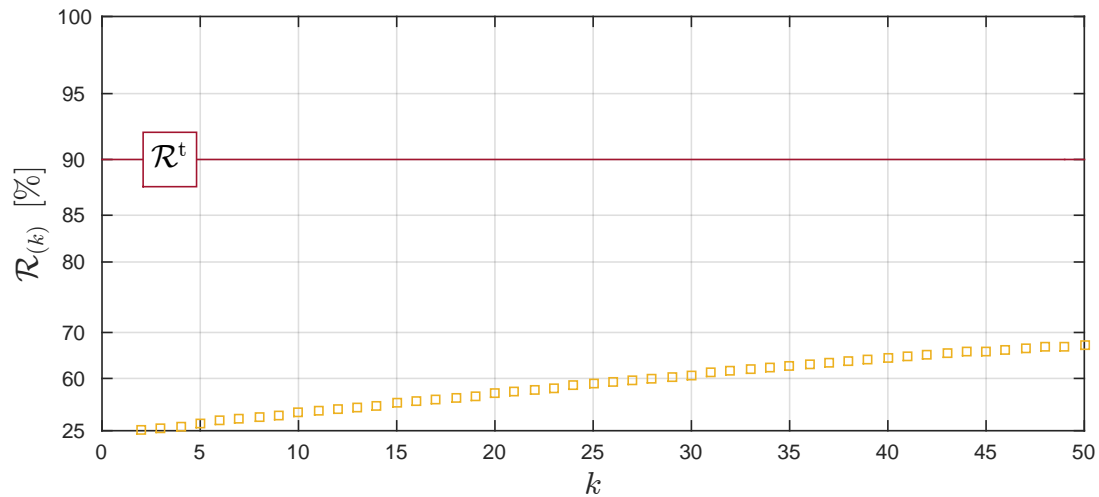


Figure VI.63: Evolution of the reconstruction indicator  $\mathcal{R}_{(k)}$  as a function of the number of load cases obtained as ESWLs. (ERP parameters:  $\hat{\varepsilon} = 0\%$ ,  $\gamma = 1$ ).

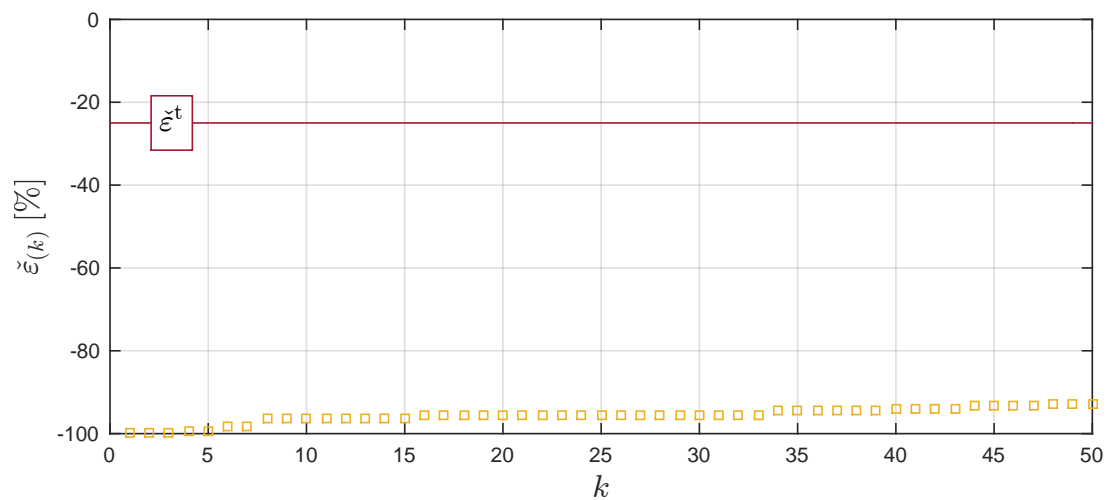


Figure VI.64: Evolution of the largest relative error indicator  $\check{\varepsilon}_{(k)}$  as a function of the number of load cases obtained as ESWLs. (ERP parameters:  $\hat{\varepsilon} = 0\%$ ,  $\gamma = 1$ ).

ESWLs,  $k = 50$ ,  $\gamma = 1$ ,  $\hat{\varepsilon} = 0\%$

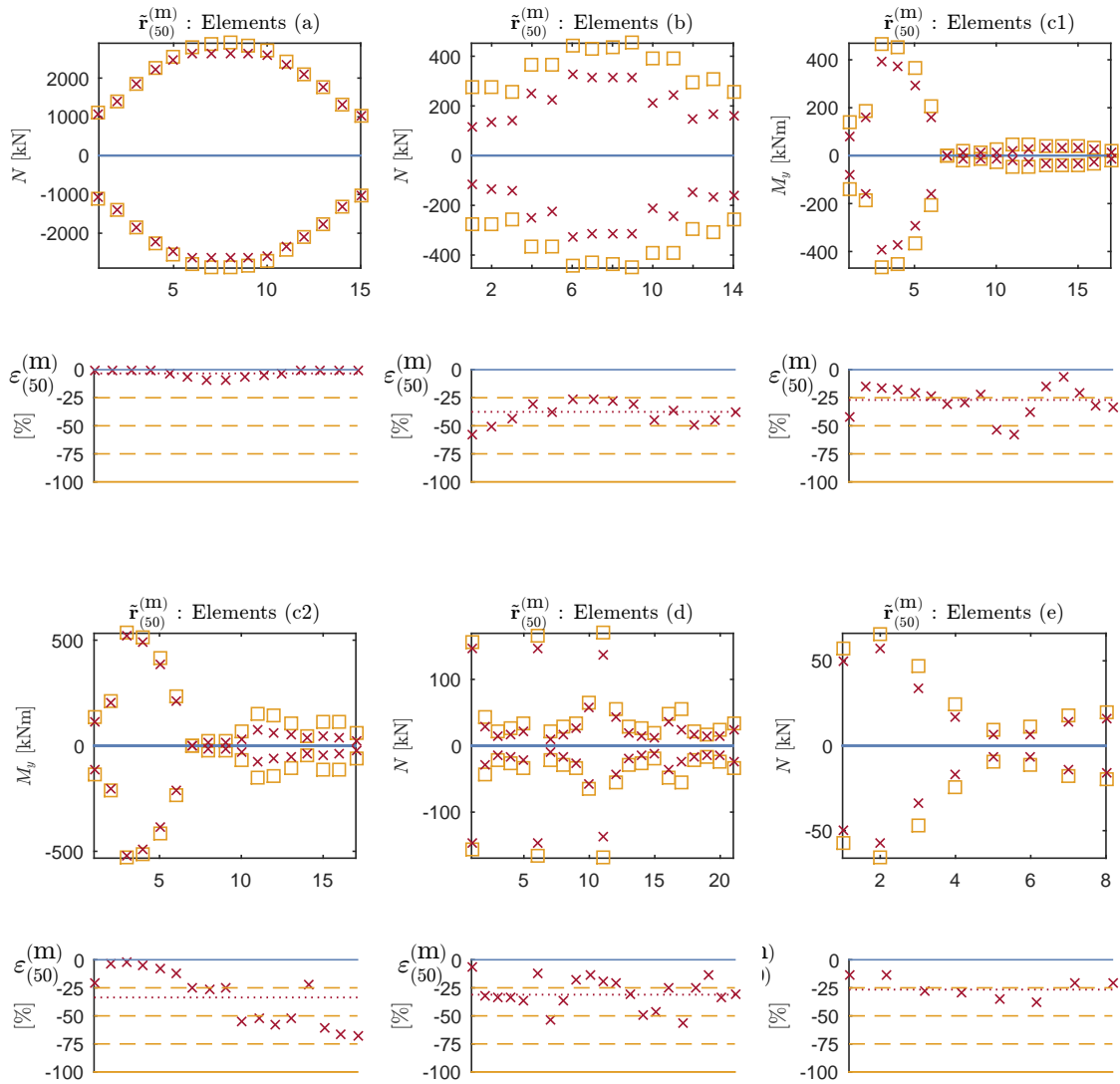


Figure VI.65: Reconstructed envelope  $\tilde{\mathbf{r}}_{(50)}^{(m)}$  (in red with x marker), actual envelope  $\mathbf{r}^{(m)}$  (in orange with square marker) and corresponding relative errors  $\varepsilon_{(50)}^{(m)}$  (in red with x marker). Results associated with  $k = 50$  load cases obtained as ESWLs. (ERP parameters:  $\hat{\varepsilon} = 0\%$ ,  $\gamma = 1$ ).



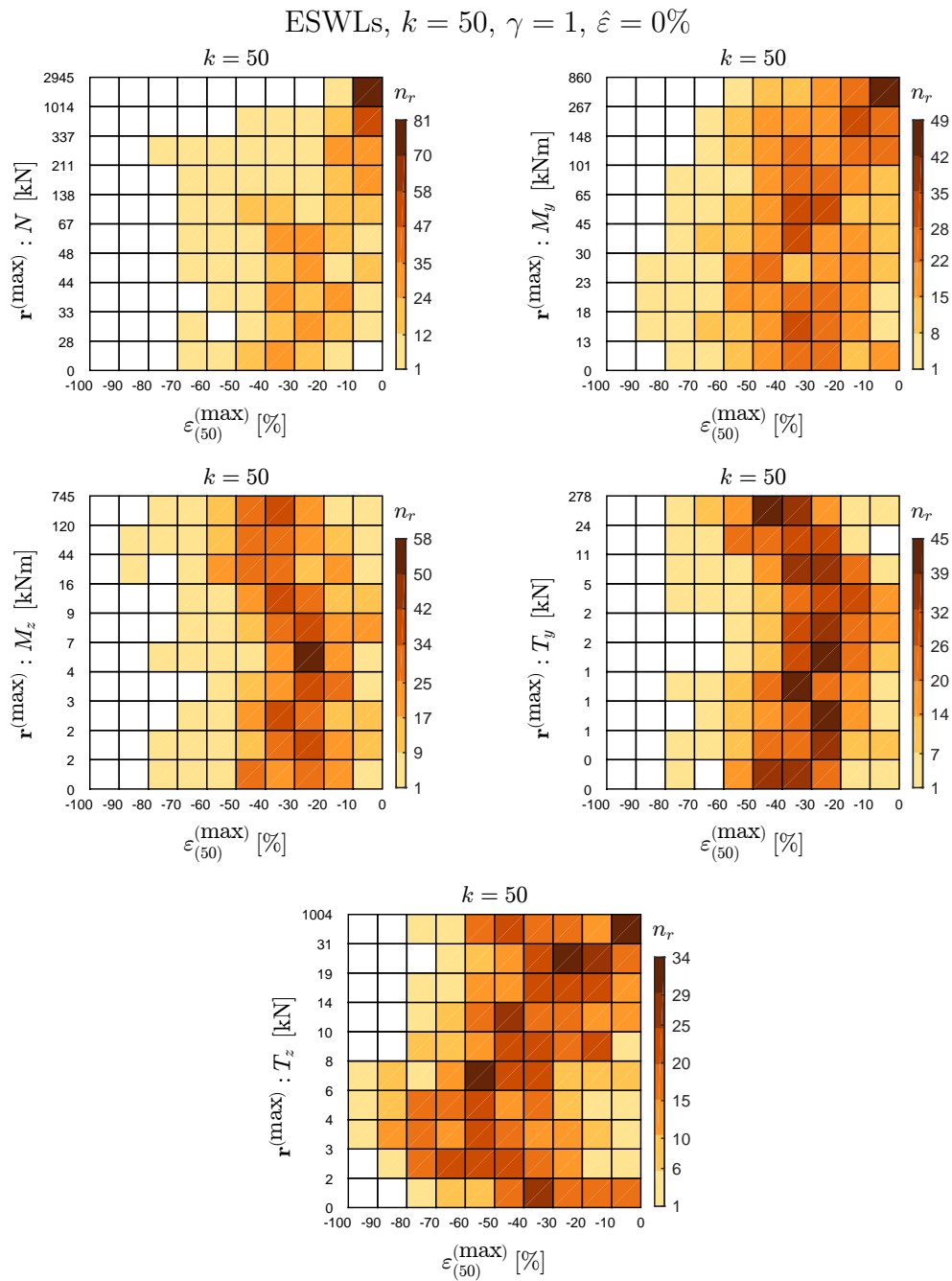


Figure VI.66: Relative errors of internal forces. Results associated with  $k = 50$  load cases obtained as ESWLs. (ERP parameters:  $\hat{\varepsilon} = 0\%$ ,  $\gamma = 1$ ).

### VI.3.6 Envelope reconstruction with PSWLs

Principal static wind loads (Chapter V) are considered in this Section for the envelope reconstruction problem. The matrix  $\mathbf{F}^{(P)}$  collecting PSWLs result from the singular value decomposition of  $\mathbf{F}^{(e)}$ , the  $15288 \times 15988$  ( $n_t \times 2n_r$ ) matrix collecting all ESWLs, see (V.3.2). PSWLs have to be first normalized before using them for the envelope reconstruction problem, see Section III.4. Figure VI.67 shows the first 8 normalized PSWLs with  $\hat{\varepsilon} = 0\%$ .

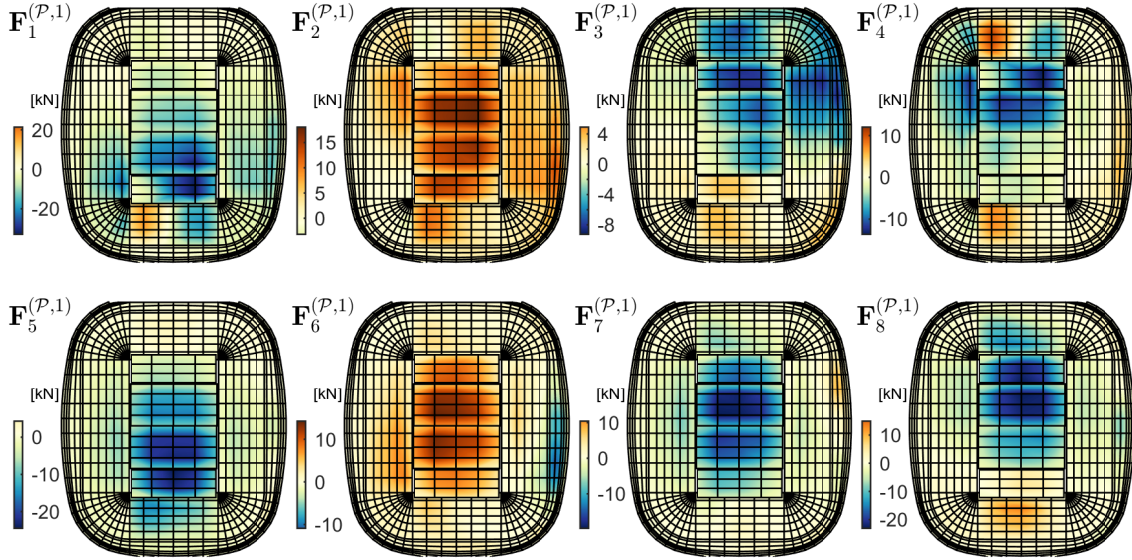


Figure VI.67: First 8 normalized PSWLs with  $\hat{\varepsilon} = 0\%$  (vertical nodal forces).

#### No overestimation of the envelope $\hat{\varepsilon} = 0\%$ and parameter $\gamma = 1$

The acceptable overestimation of the envelope, noted  $\hat{\varepsilon}$ , is first set equal to 0 as with ESWLs. For the envelope reconstruction problem, it means that there is no overestimation of the envelope anywhere.

Figure VI.68 shows the evolution of the reconstruction indicator  $\mathcal{R}_{(k)}$ . If no combination of PSWLs is considered, applying them successively provides a reconstruction  $\mathcal{R}_{(50)} = 70\%$  with 50 load cases and therefore perform only slightly better than ESWLs for which  $\mathcal{R}_{(50)} = 68\%$ . With combinations of 2 and 6 PSWLs, maximum reconstructions of  $\mathcal{R}_{(50)} = 45\% \lesssim \mathcal{R}_{(\infty)}$ ,  $\mathcal{R}_{(50)} = 71\% \lesssim \mathcal{R}_{(\infty)}$ , are respectively obtained. Consequently, a larger number of PSWLs has to be combined to produce a better reconstruction: with 15, 20, 30 and 40 PSWLs that are combined, overall reconstructions of  $\mathcal{R}_{(50)} = 84\%$ ,  $\mathcal{R}_{(50)} = 87\%$ ,  $\mathcal{R}_{(50)} = 89\%$  and  $\mathcal{R}_{(50)} = 91$  are achieved for 50 load cases, respectively. This illustrates that for a same number of load cases, combining more and more PSWLs produces a lower and lower gain on the level of reconstruction  $\mathcal{R}_{(k)}$ . With 40 PSWLs that are combined, the number  $n_s^{(1)}$  of SWLs required to fulfill the target overall reconstruction is equal to 45.

The CPU time to determine the initial set of combination coefficients to consider for one load case in the constrained nonlinear optimization algorithm may become prohibitive (Section III.5.1). In our case, the CPU time<sup>1</sup> to evaluate the cost function for one set

<sup>1</sup>Processor: Intel(R) Core(TM) i7-4600U CPU @ 2.10GHz. RAM: 16.0 Go. Programmation done in Matlab R2015a.

of combination coefficients is equal to  $t_c = 4 \cdot 10^{-4}$  sec. For a large number of PSWLs retained for combinations, considering all possible combination coefficients for each load case is time-consuming because the CPU time is prohibitive: e.g.,  $t_c \times (3^{n_q} - 1) = 387$  hours when  $n_q = 20$  PSWLs have to be combined only for one load case. To circumvent this issue, we have randomly selected  $n_c = 6000$  combination coefficients out of the  $3^{n_q} - 1$  possible combinations for  $n_q = 15, 20, 30$  and  $40$ . The number  $n_c$  has been chosen as a compromise between CPU time and reconstruction rate. The gain on  $\mathcal{R}_{(k)}$  by considering a larger  $n_c$  is in fact negligible.

Figure VI.69 depicts the largest relative error indicator  $\tilde{\varepsilon}_{(k)}$ . With 50 load cases, this indicator is still too large, up to  $-60\%$ , even by considering 50 combinations of the first 40 PSWLs. Figure VI.70 shows the number of structural responses that do not fulfill the acceptable underestimation  $\tilde{\varepsilon}^t = -25\%$ . These results demonstrate again that PSWLs are better suited than ESWLs for the ERP when the number of structural response is large and the overall correlation is very low. Indeed, PSWLs produce overall reconstructions of the envelope while ESWLs provide local reconstructions, hence the largest number of structural responses with  $\varepsilon_{(k)}^{(m)} < \tilde{\varepsilon}^t$ .

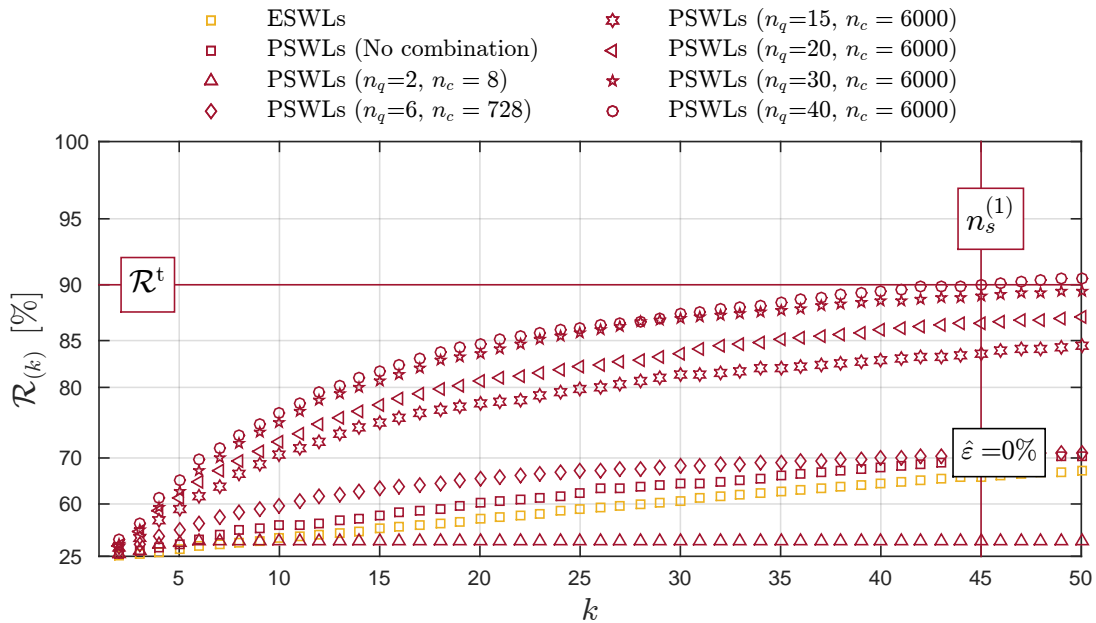


Figure VI.68: Evolution of the reconstruction indicator  $\mathcal{R}_{(k)}$  as a function of the number of load cases. (ERP parameters:  $\hat{\varepsilon} = 0\%$ ,  $\gamma = 1$ ).

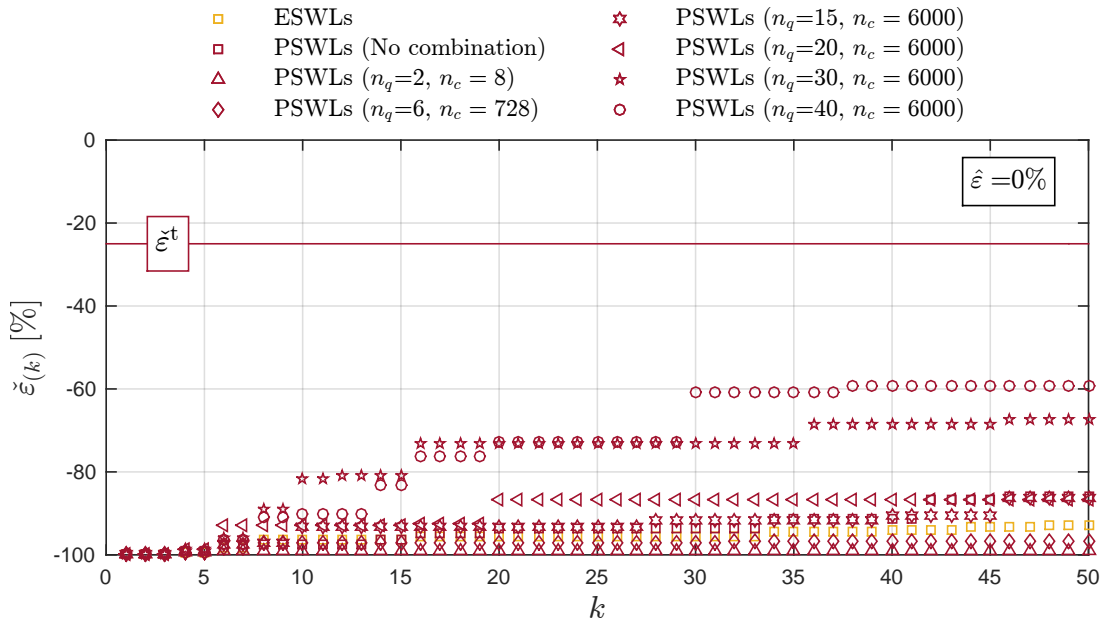


Figure VI.69: Evolution of the largest relative error indicator  $\tilde{\varepsilon}_{(k)}$  as a function of the number of load cases (ERP parameters:  $\hat{\varepsilon} = 0\%$ ,  $\gamma = 1$ ).

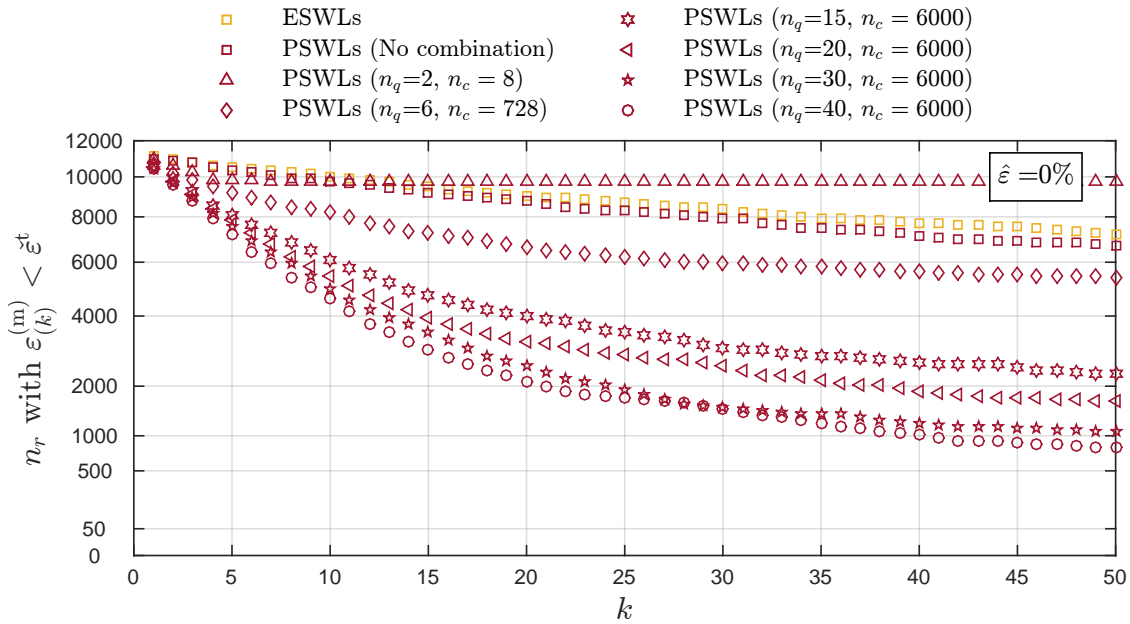


Figure VI.70: Evolution of the number of responses with  $\varepsilon_{(k)}^{(m)} < \varepsilon^t$  as a function of the number of load cases (ERP parameters:  $\hat{\varepsilon} = 0\%$ ,  $\gamma = 1$ ).

Figure VI.71 shows the reconstructed envelope and relative errors for the six sets of structural elements with 50 load cases obtained by combinations of the first 40 PSWLs. Figure VI.72 gives the distribution of relative errors of reconstruction for the maximum side of the envelope for each type of internal force with 50 load cases. With PSWLs and contrary to ESWLs, a large number of structural responses has relative errors  $\varepsilon_{(50)}^{(\max)}$  lower than (in absolute value)  $\Psi_{(50)}^{(\max)} = \mathcal{R}_{(50)}^{(\max)} - 1 = -11\%$ .

Combinations of PSWLs,  $n_q = 40$ ,  $k = 50$ ,  $\hat{\varepsilon} = 0$

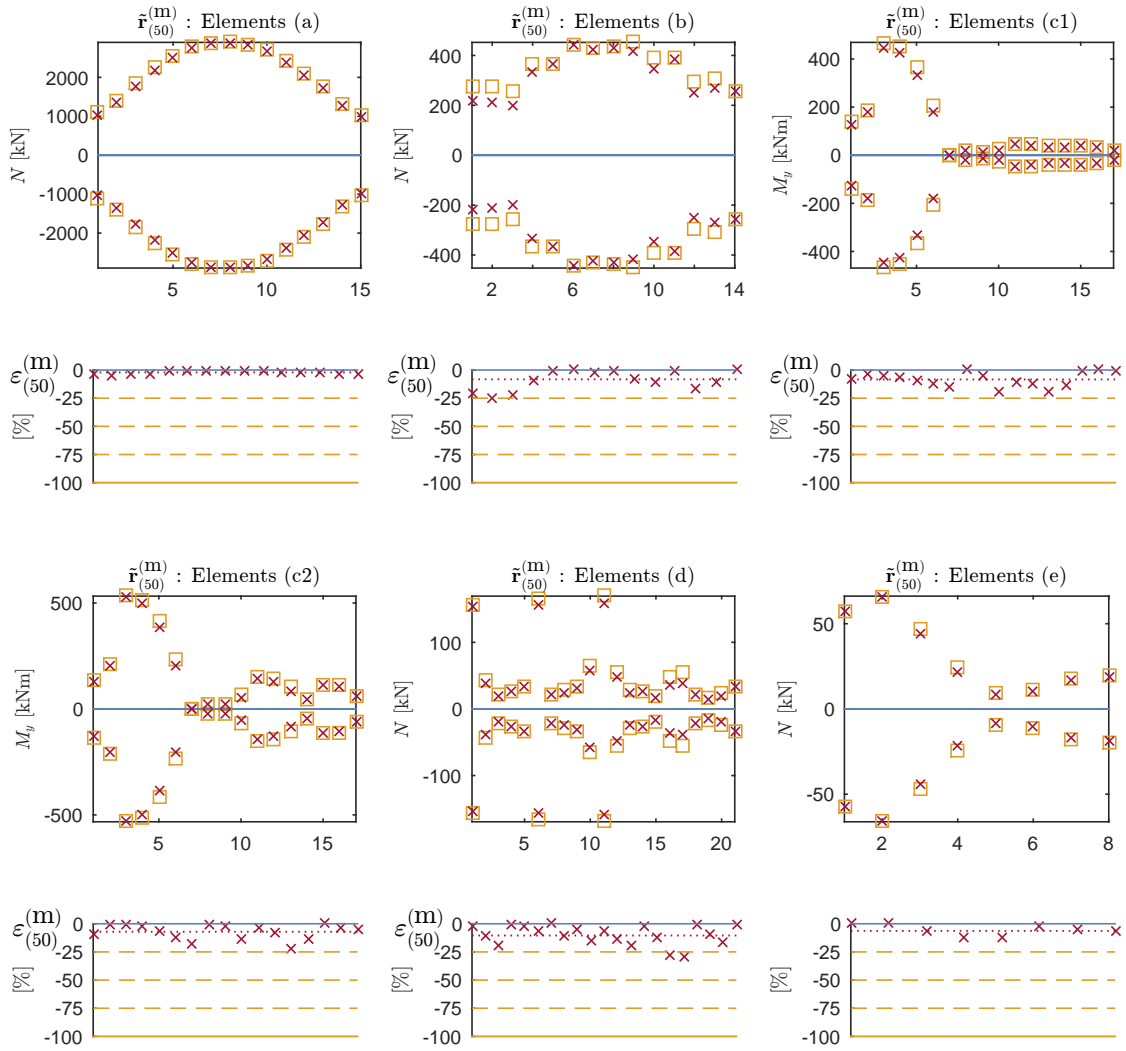


Figure VI.71: Reconstructed envelope  $\tilde{\mathbf{r}}_{(50)}^{(m)}$  (in red with x marker), actual envelope  $\mathbf{r}^{(m)}$  (in orange with square marker) and corresponding relative errors  $\varepsilon_{(50)}^{(m)}$  (in red with x marker). Results associated with  $k = 50$  load cases obtained as combinations of the first 40 PSWLs. (ERP parameters:  $\hat{\varepsilon} = 0\%$ ,  $\gamma = 1$ ).

Comparison of Figures VI.72 and VI.66 illustrates well that combinations of PSWLs perform better for the envelope reconstruction than applying successively ESWLs. Indeed, no structural response has a relative error up to -95% as with ESWLs and the reconstruction of the envelope is similar no matter the magnitude of structural responses.

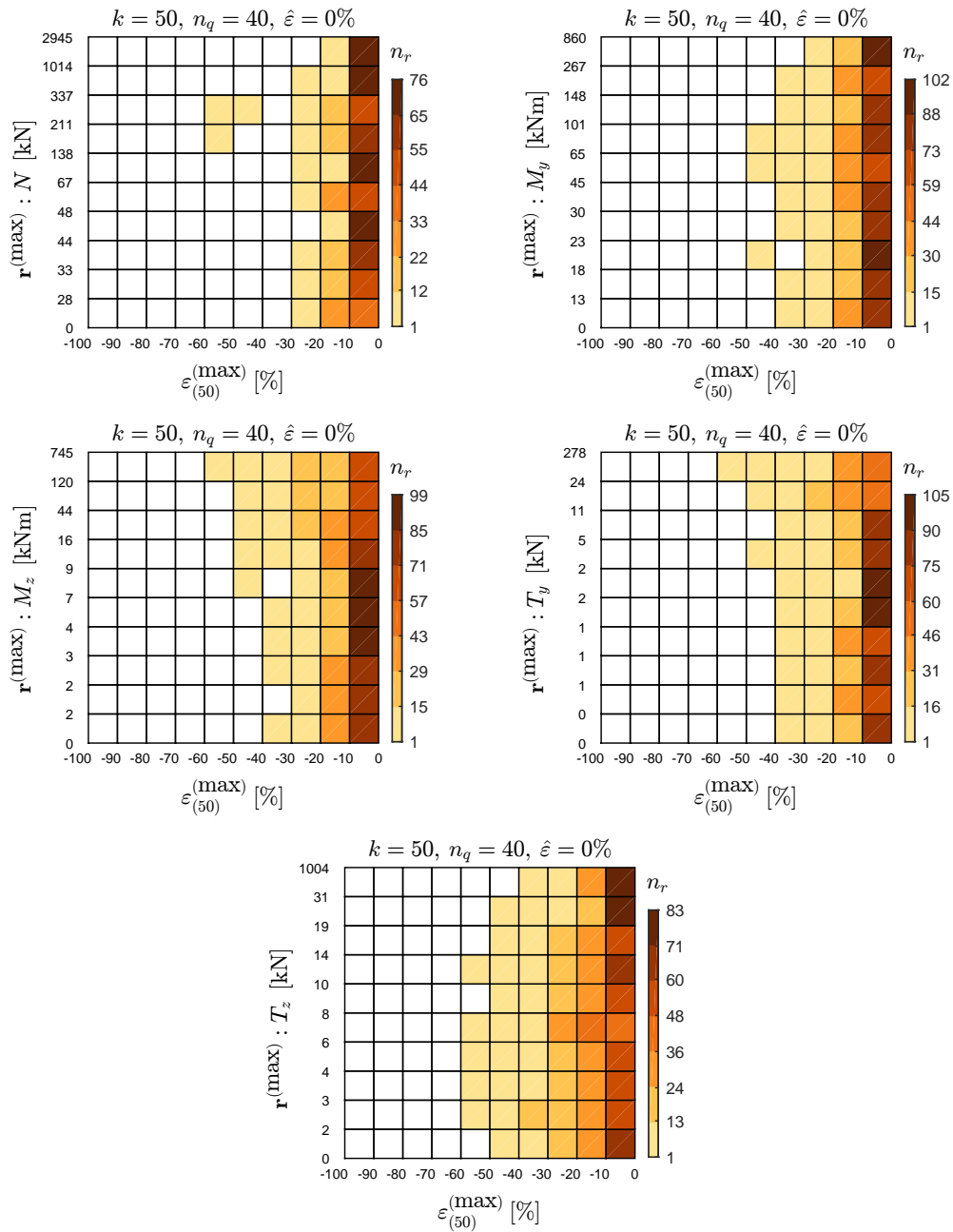


Figure VI.72: Relative errors of internal forces. Results associated with  $k = 50$  load cases obtained as combinations of the first 40 PSWLs. (ERP parameters:  $\hat{\varepsilon} = 0\%$ ,  $\gamma = 1$ ).

**Parameter  $\gamma$**  The parameter  $\gamma$  amplifies large relative errors in the cost function (III.5.5). Since the indicator  $\tilde{\varepsilon}_{(k)}$  is still large compared with  $\varepsilon^t$  and the reconstruction indicator  $\mathcal{R}_{(k)}$  is close to  $\mathcal{R}^t$ , in the previous results, the parameter  $\gamma$  is increased. Figures VI.73, VI.74 and VI.75 shows the indicators  $\mathcal{R}_{(k)}$ ,  $\tilde{\varepsilon}_{(k)}$  and the number of responses with  $\varepsilon_{(k)}^{(m)} < \varepsilon^t$  for three values of  $\gamma$ . For sake of clarity, only the results with combinations of the first 40 PSWLs are shown and results with ESWLs are plotted for comparison. With ESWLs, the influence of the parameter  $\gamma$  on  $\tilde{\varepsilon}_{(k)}$  is poor while with PSWLs, it provides a worse  $\tilde{\varepsilon}_{(50)}$ . There is no improvement and this option is therefore disregarded.

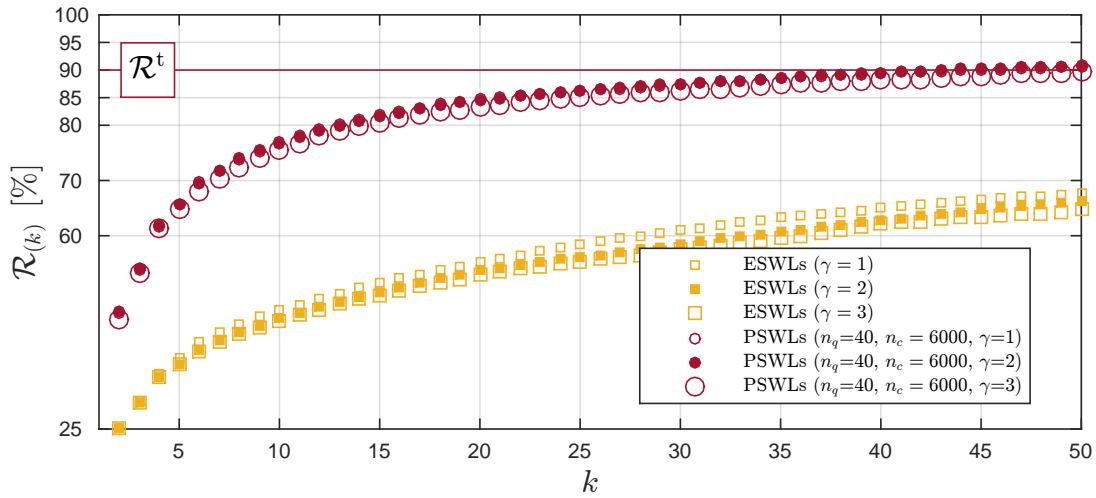


Figure VI.73: Evolution of the reconstruction indicator  $\mathcal{R}_{(k)}$  as a function of the number of load cases. (ERP parameters:  $\hat{\varepsilon} = 0$ ,  $\gamma$  variable).

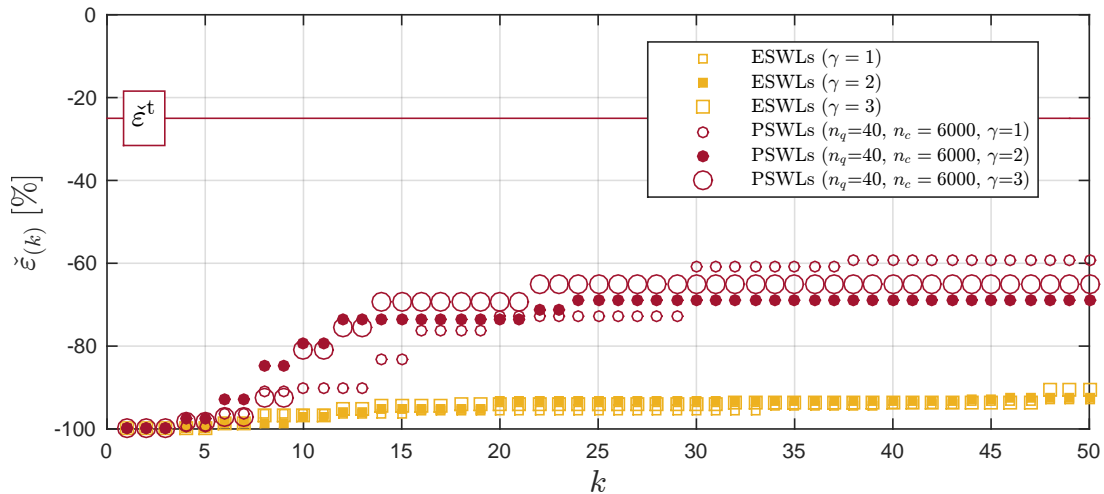


Figure VI.74: Evolution of the largest relative error indicator  $\tilde{\varepsilon}_{(k)}$  as a function of the number of load cases. (ERP parameters:  $\hat{\varepsilon} = 0$ ,  $\gamma$  variable).

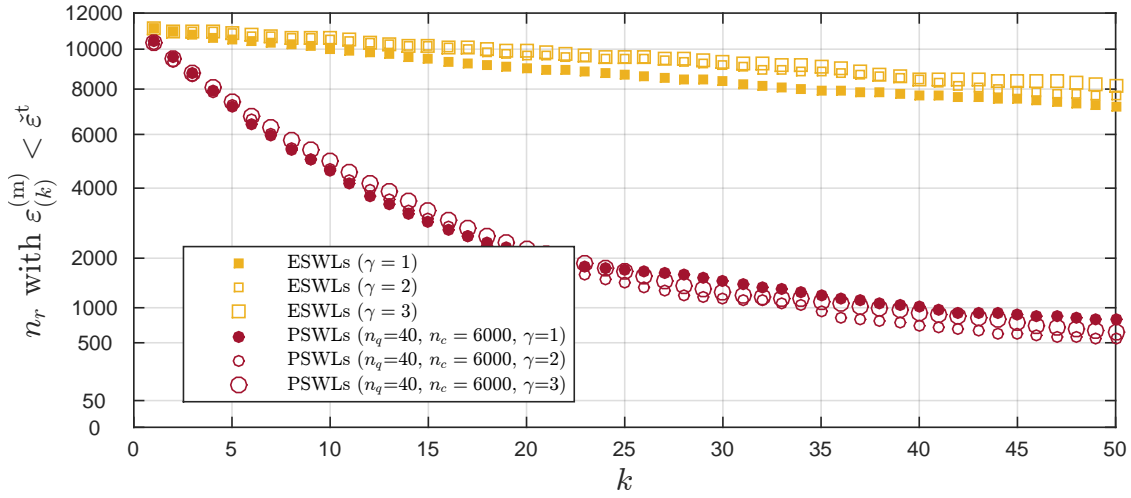


Figure VI.75: Evolution of the number of responses with  $\varepsilon_{(k)}^{(m)} < \varepsilon^t$  as a function of the number of load cases. (ERP parameters:  $\hat{\varepsilon} = 0$ ,  $\gamma$  variable).

**Acceptable overestimation of the envelope** Instead of increasing the parameter  $\gamma$ , we study the influence of the acceptable overestimation  $\hat{\varepsilon}$ . Considering 50 combinations of the first 40 PSWLs, even if a large number of structural responses has nearly reached their envelope values, see Figure VI.72, there is still an important proportion of structural responses for which relative errors are larger than  $\hat{\varepsilon}^t = -25\%$ . In order to provide a better reconstruction of the envelope with the same number of load cases and PSWLs that are combined, acceptable overestimations  $\hat{\varepsilon}$  of 25% and 50% are considered next.

Figure VI.76 depicts the reconstruction indicator  $\mathcal{R}_{(k)}$  with  $\hat{\varepsilon} = 25\%$  and  $\hat{\varepsilon} = 50\%$ . With 40 PSWLs that are combined, a reconstruction of 99% with  $\hat{\varepsilon} = 25\%$  and  $\hat{\varepsilon} = 50\%$  is achieved for 50 load cases. These results has to be compared with  $\mathcal{R}_{(50)} = 89\%$  with  $\hat{\varepsilon} = 0\%$  and the same gain of +9% of reconstruction is obtained with  $\hat{\varepsilon} = 25\%$  and  $\hat{\varepsilon} = 50\%$ .

Figures VI.77 and VI.78 show the largest relative error and the number of responses with  $\varepsilon_{(k)}^{(m)} < \varepsilon^t$ , respectively, with  $\hat{\varepsilon} = 25\%$  and  $\hat{\varepsilon} = 50\%$ . With 40 load cases, there is no improvement of these two indicators. Considering more than 40 PSWLs for combinations does not bring a significant improvement of the two indicators and those results are therefore not shown.

Table VI.9 gives the values  $\tilde{\varepsilon}$  and  $n_r$  with  $\varepsilon_{(k)}^{(m)} < \varepsilon^t$  considering 50 combinations of the first 40 PSWLs. Increasing the acceptable overestimation from 0% to 50% does not provide a significant decrease, from  $-60\%$  to  $-51\%$  of the largest relative error. However, from 0% to 25%, the number of responses with  $\varepsilon_{(k)}^{(m)} < \varepsilon^t$  is significantly decreased.

| $\hat{\varepsilon}$                                   | 0%   | 25%  | 50%  |
|---|------|------|------|
| $\tilde{\varepsilon}_{(50)}$                          | -60% | -60% | -51% |
| $n_r$ with $\varepsilon_{(50)}^{(m)} < \varepsilon^t$ | 810  | 152  | 30   |

Table VI.9: Results with 40 PSWLs that are combined for three values of  $\hat{\varepsilon}$ .



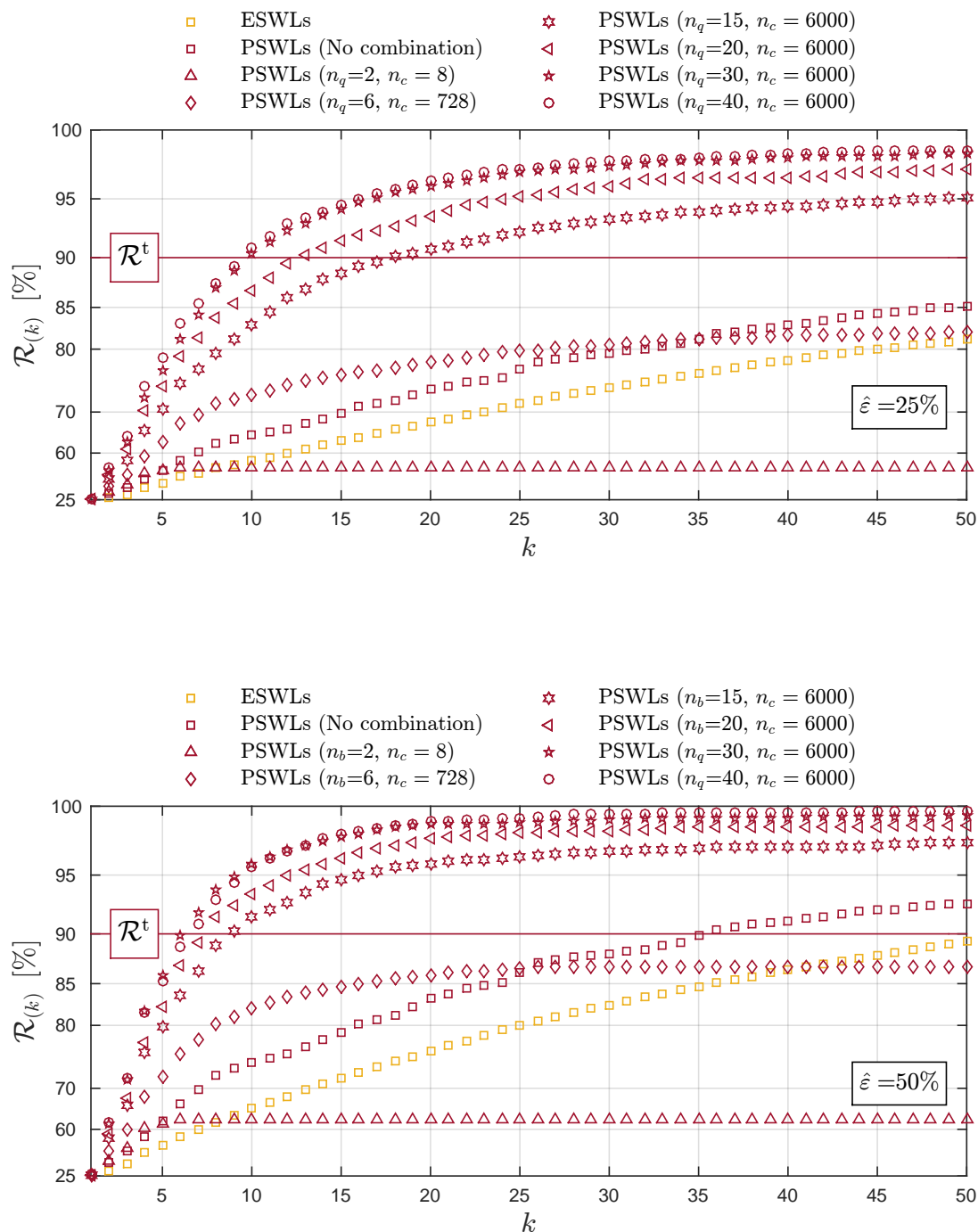


Figure VI.76: Evolution of the reconstruction indicator  $\mathcal{R}_{(k)}$  as a function of the number of load cases. (Upper graph:  $\hat{\varepsilon} = 25\%$ , lower graph:  $\hat{\varepsilon} = 50\%$ ,  $\gamma = 1$ ).

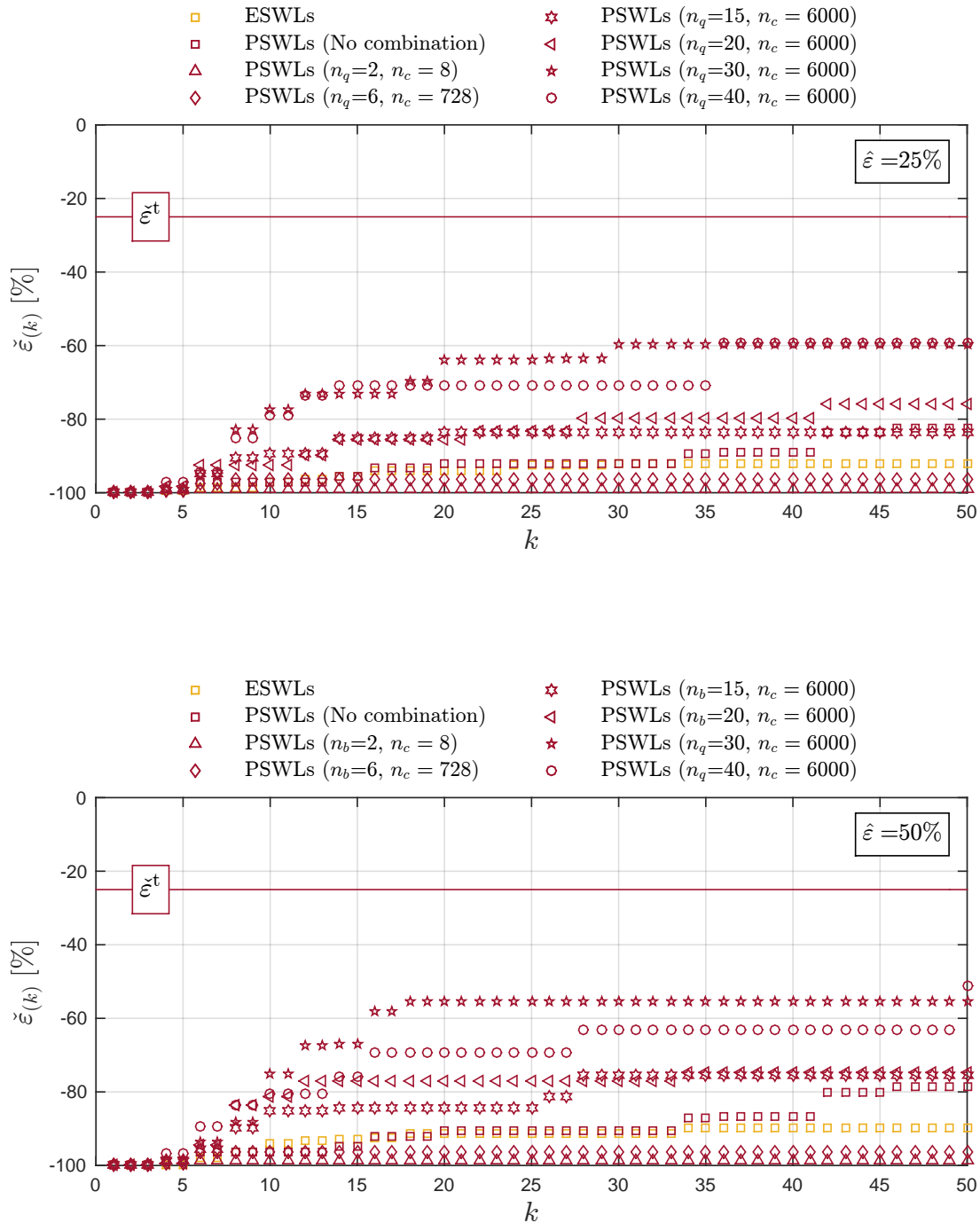


Figure VI.77: Evolution of the largest relative error indicator  $\check{\epsilon}(k)$  as a function of the number of load cases. (Upper graph:  $\hat{\epsilon} = 25\%$ , lower graph:  $\hat{\epsilon} = 50\%$ ,  $\gamma = 1$ ).

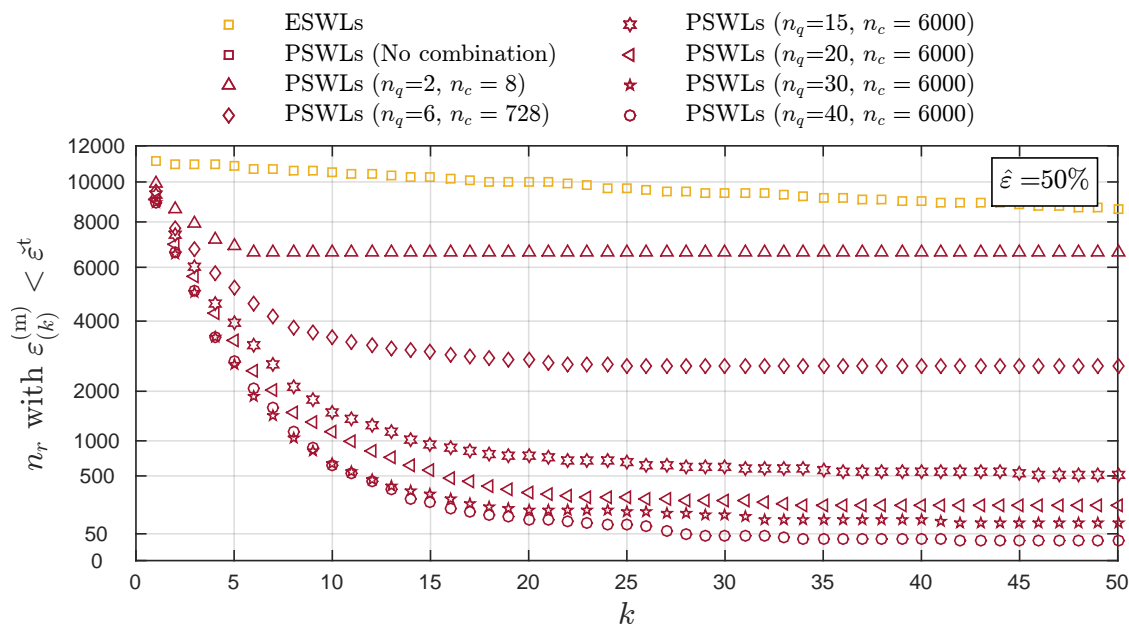
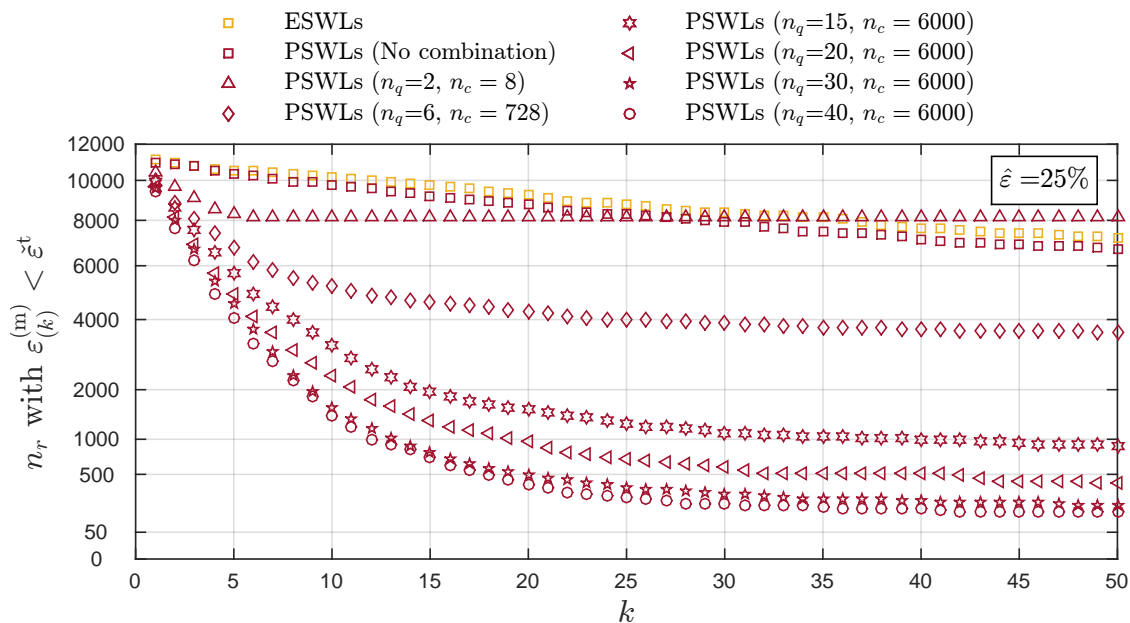


Figure VI.78: Evolution of the number of responses with  $\varepsilon_{(k)}^{(m)} < \varepsilon^t$  as a function of the number of load cases. (Upper graph:  $\hat{\varepsilon} = 25\%$ , lower graph:  $\hat{\varepsilon} = 50\%$ ,  $\gamma = 1$ ).

Figure VI.79 shows the reconstructed envelope and relative errors for the six set of structural elements with 50 load cases obtained by combinations of the first 40 PSWLs considering  $\hat{\varepsilon} = 25\%$ . Figure VI.79 gives relative errors of reconstruction for the maximum side of the envelope.

Combinations of PSWLs,  $n_q = 40$ ,  $n_s = 50$ ,  $\hat{\varepsilon} = 25\%$

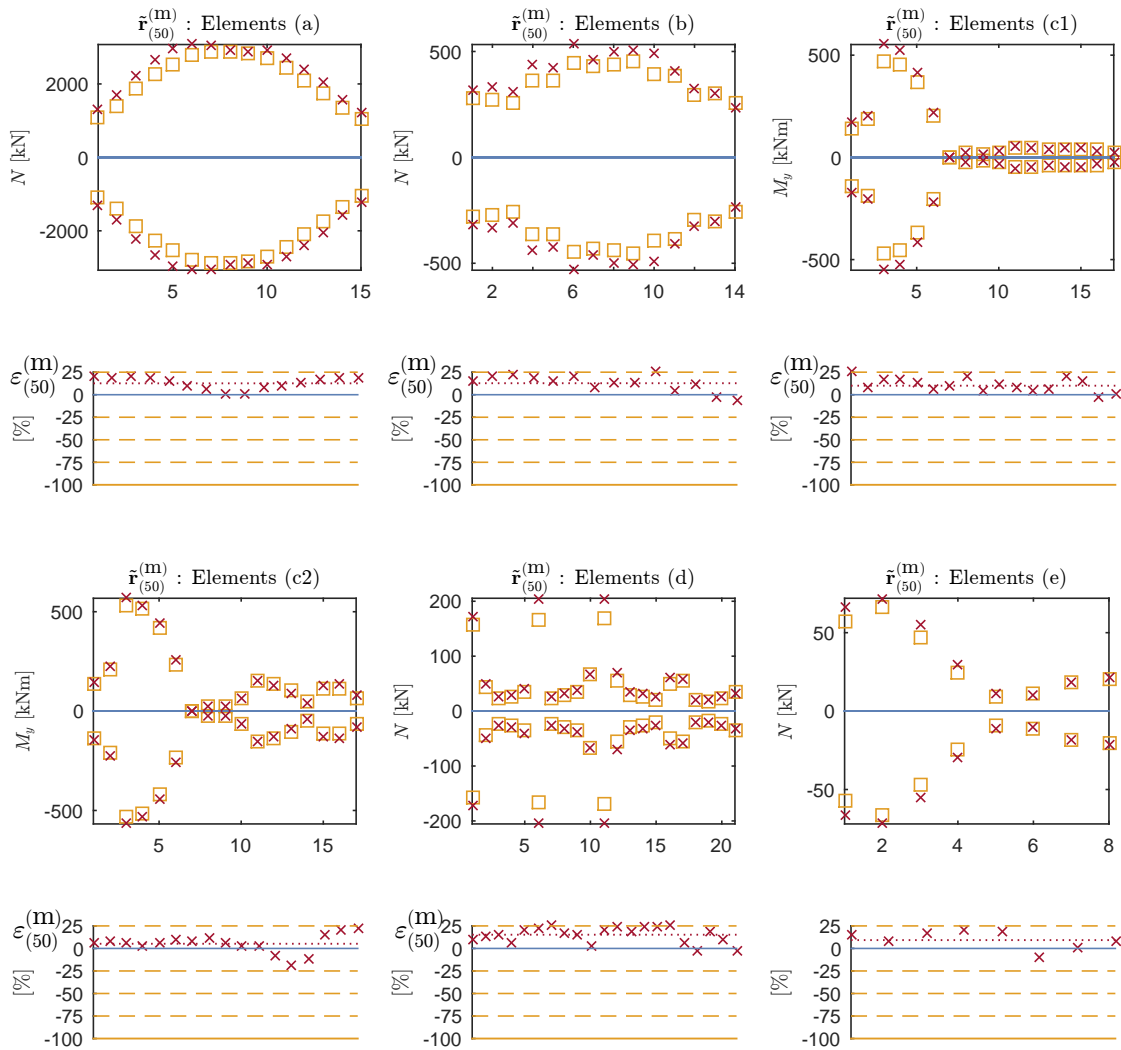


Figure VI.79: Reconstructed envelope  $\tilde{\mathbf{r}}_{(50)}^{(m)}$  (in red with x marker), actual envelope  $\mathbf{r}^{(m)}$  (in orange with square marker) and corresponding relative errors  $\varepsilon_{(50)}^{(m)}$  (in red with x marker). Results associated with  $k = 50$  load cases obtained as combinations of the first 40 PSWLs. (ERP parameters:  $\hat{\varepsilon} = 25\%$ ,  $\gamma = 1$ ).

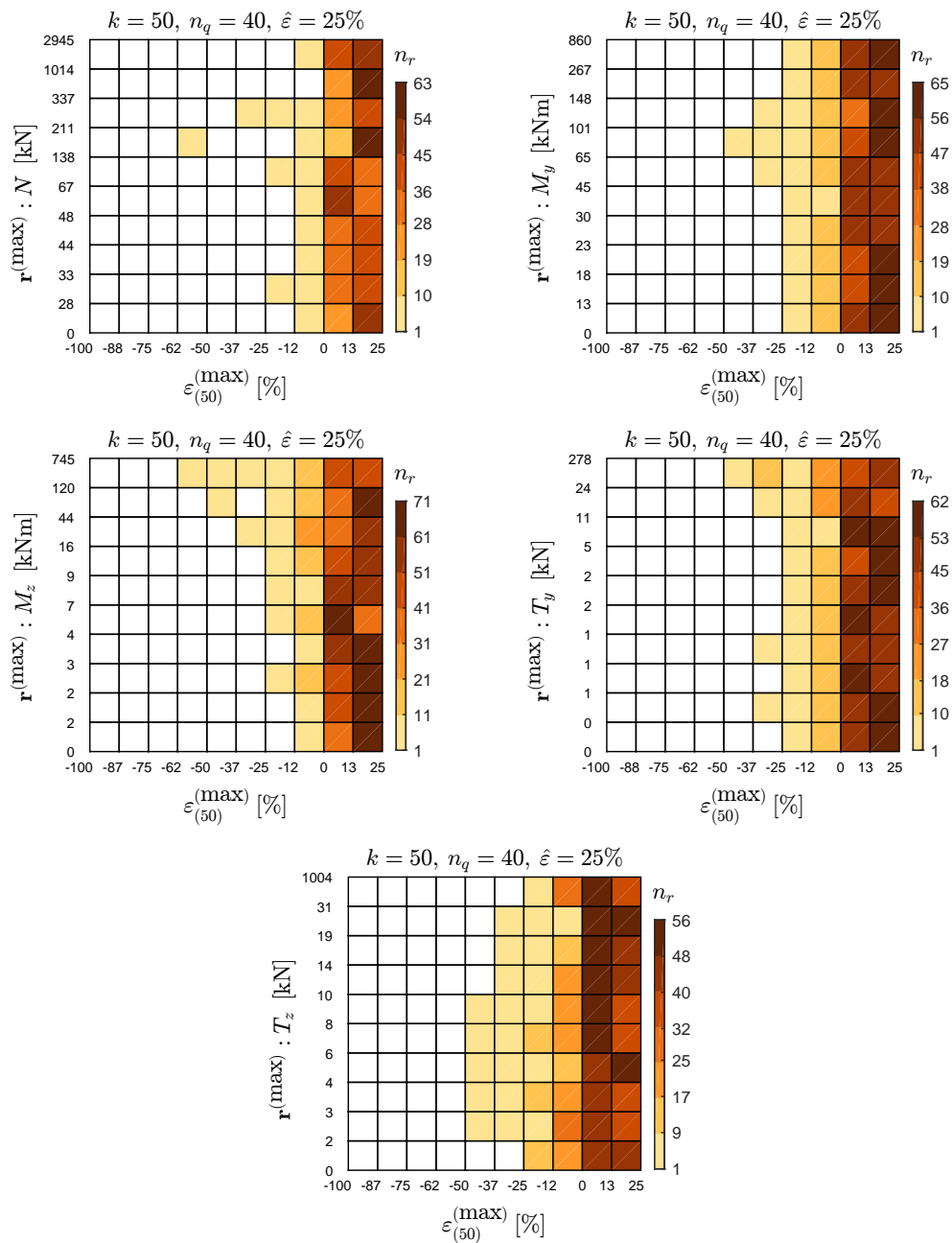


Figure VI.80: Relative errors of internal forces. Results associated with  $k=50$  load cases obtained as combinations of the first 40 PSWLs. (ERP parameters:  $\hat{\varepsilon}=25\%$ ,  $\gamma=1$ ).

**Establishing a new (secondary) PSWL basis** With  $\hat{\varepsilon} = 25\%$  and 50 combinations of the first 40 PSWLs, there is only 152 envelope values with relative errors larger than the acceptable underestimation, see Table VI.9. Instead of increasing the number  $k$  of load cases, the acceptable overestimation  $\hat{\varepsilon}$  or the number  $n_q$  of PSWLs retained for combinations, a new PSWL basis specific for these 152 envelope values is considered, see step 8 in Figure V.2. Figure VI.81 indicates in red the elements for which a reconstructed response has a relative error larger than  $\tilde{\varepsilon}^t$ .

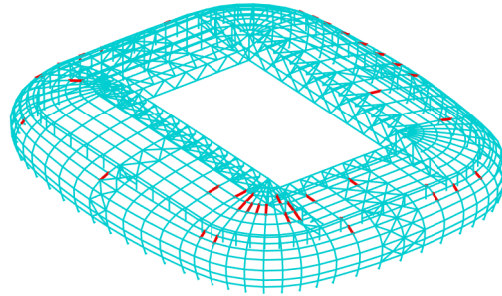


Figure VI.81: Elements (in red) for which a reconstructed response has a relative error larger than  $\tilde{\varepsilon}^t$ . (ERP parameters:  $k = 50$ ,  $\hat{\varepsilon} = 25\%$ ,  $n_q = 40$  and  $\gamma = 1$ ).

First, ESWLs associated with these 152 envelope values are collected in a  $n_t \times 152$  matrix  $\mathbf{F}^{(e)}$ . Second, a new basis of PSWLs is obtained by the singular value decomposition of this matrix  $\mathbf{F}^{(e)}$ . Third, each PSWL is normalized to satisfy the acceptable overestimation of the envelope  $\hat{\varepsilon} = 25\%$ . Fourth, the envelope reconstruction problem is solved with these new PSWLs as before. Note this option is only feasible with PSWLs since MILs and CPT loading modes are completely independent of the set of structural responses considered for reconstruction.

Figure VI.82 illustrates the first four PSWLs associated with the 152 ESWLs.

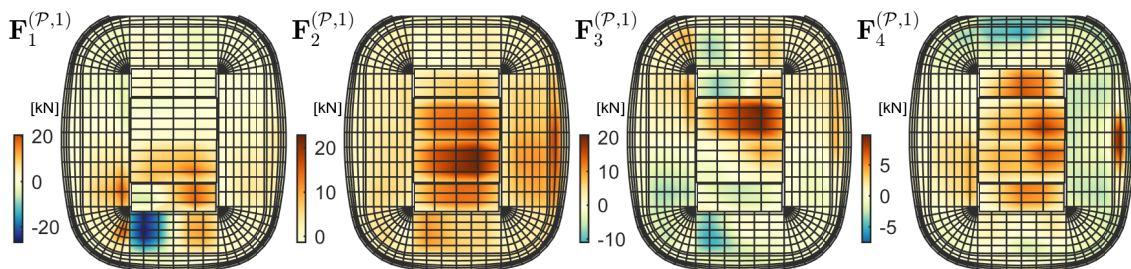


Figure VI.82: First 4 normalized PSWLs (vertical nodal forces) associated with the 152 ESWLs ( $\hat{\varepsilon} = 0\%$ ). (Secondary PSWL basis)

Figure VI.83 depicts the largest relative error indicator  $\tilde{\varepsilon}_{(k)}$ . With 18 combinations of the first 40 new PSWLs, the acceptable underestimation is fulfilled. This demonstrates the efficiency to consider a new PSWL basis. The number  $n_s^{(2)}$  to fulfill the acceptable underestimation is equal to 68.

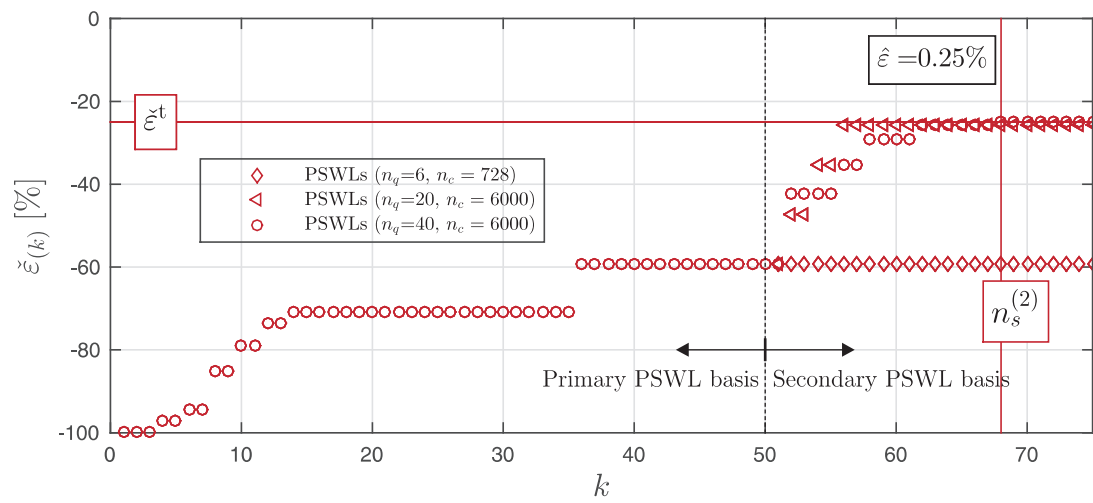


Figure VI.83: Evolution of the largest relative error indicator  $\tilde{\epsilon}(k)$  as a function of the number of load cases obtained with PSWLs. (ERP parameters:  $\hat{\epsilon} = 25\%$ ,  $\gamma = 1$ ).

Figure VI.79 gives relative errors of reconstruction for the maximum side of the envelope.

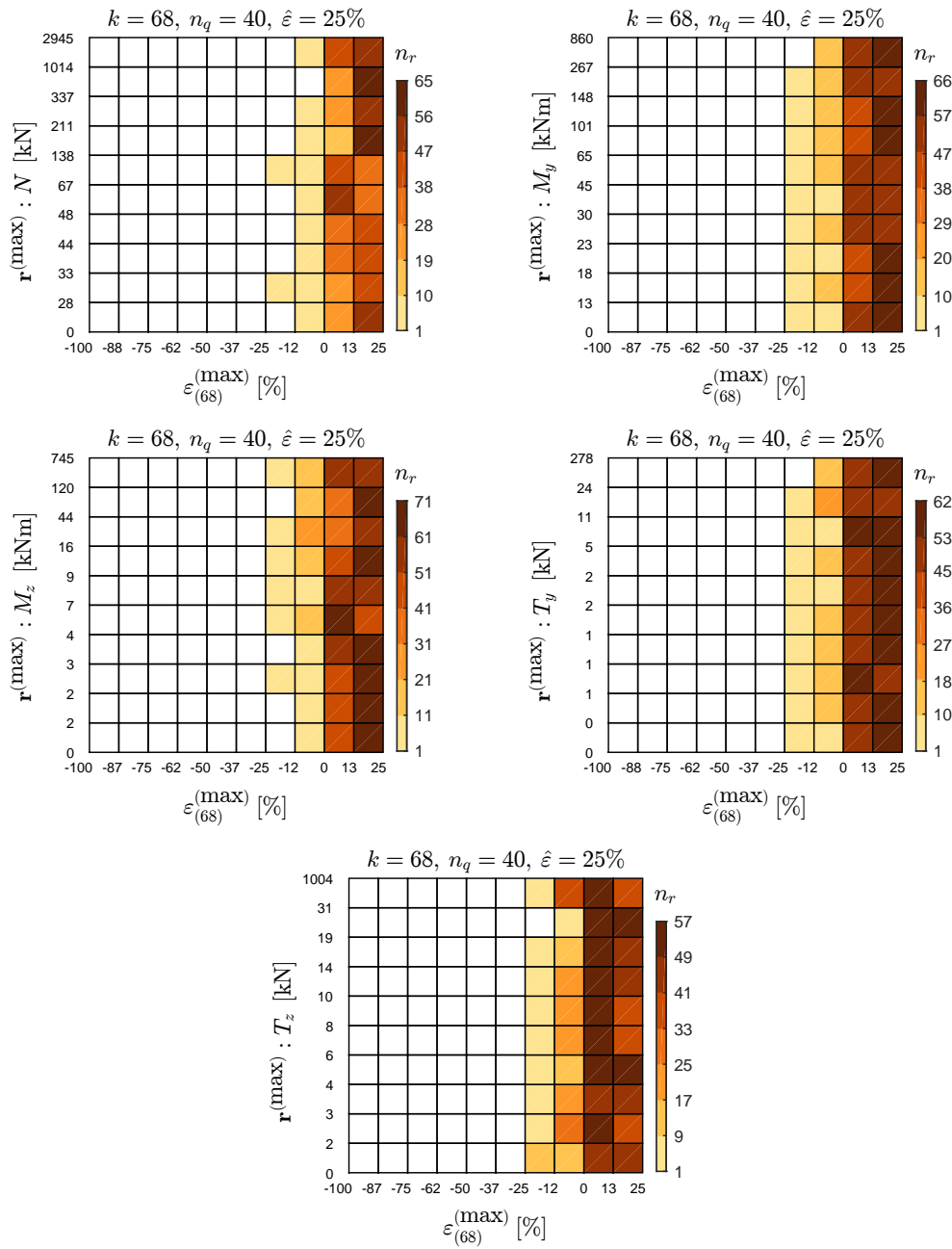


Figure VI.84: Relative errors of internal forces considering 68 combinations between the first 40 PSWLs (Two distinct PSWL bases). (ERP parameters:  $\hat{\varepsilon} = 25\%$ ,  $\gamma = 1$ ).



### VI.3.7 Envelope reconstruction with CPT loading modes and MILs

Figures VI.85 and VI.86 show the first 8 normalized CPT loading modes and MILs, respectively. These two bases are used for the envelope reconstruction and compared with PSWLs.

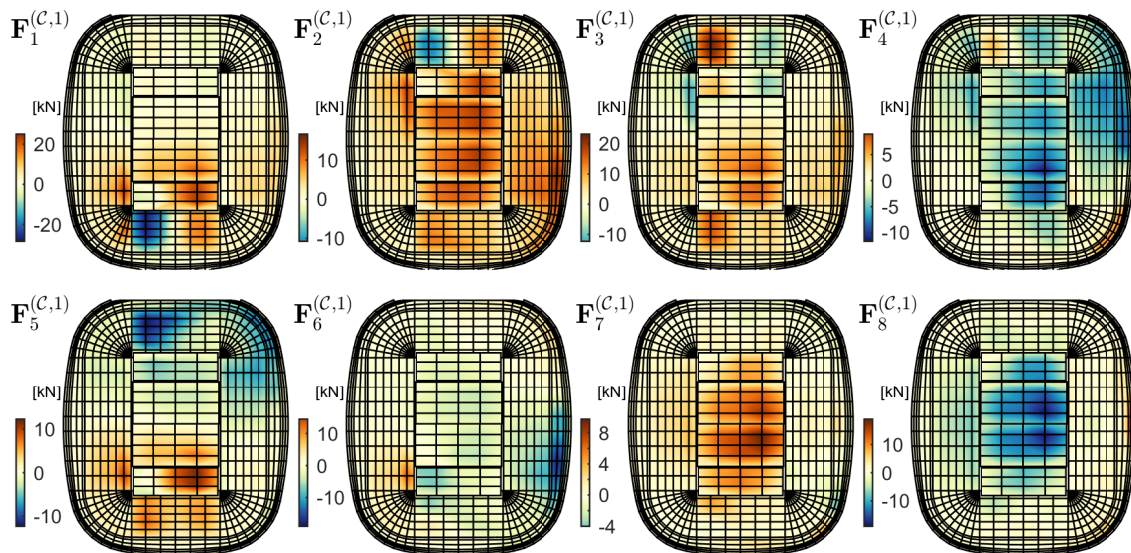


Figure VI.85: First 8 normalized CPT loading modes with  $\hat{\varepsilon} = 0\%$  (vertical nodal forces).

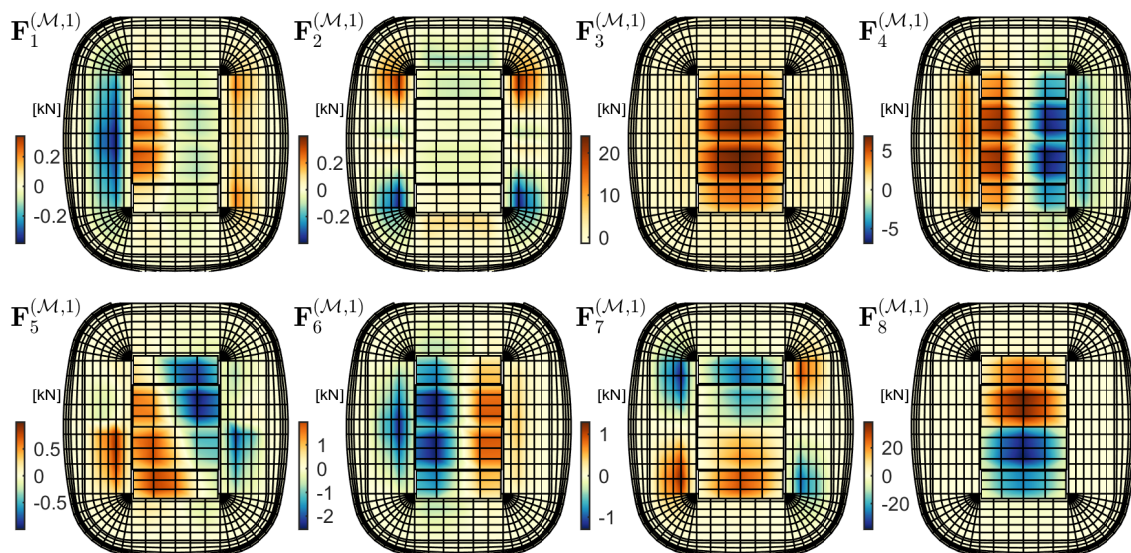


Figure VI.86: First 8 normalized MILs with  $\hat{\varepsilon} = 0\%$  (vertical nodal forces).

Figures VI.87, VI.88 and VI.89 show the evolution of the reconstruction indicator  $\mathcal{R}_{(k)}$ , the largest relative error indicator  $\check{\varepsilon}_{(k)}$  and the number of structural responses that do not

fulfill the acceptable underestimation, respectively, obtained with PSWLs, CPT l.m and MILs. For 50 load cases, Table VI.10 collects these indicators considering combinations of the first 40 basic SWLs. These results illustrate well that PSWLs are more accurate for reconstruction of the envelope than MILs or CPT loading modes are.

|   | CPT l.m. | MILs | PSWLs |
|---|----------|------|-------|
| $\mathcal{R}_{(50)}[\%]$                                      | 74%      | 70%  | 91%   |
| $\check{\varepsilon}_{(50)}[\%]$                              | -100%    | -99% | -60%  |
| $n_r$ with $\varepsilon_{(50)}^{(m)} < \check{\varepsilon}^t$ | 4500     | 6966 | 810   |

Table VI.10: Results for 50 load cases obtained with combinations of the first 40 basic SWLs.

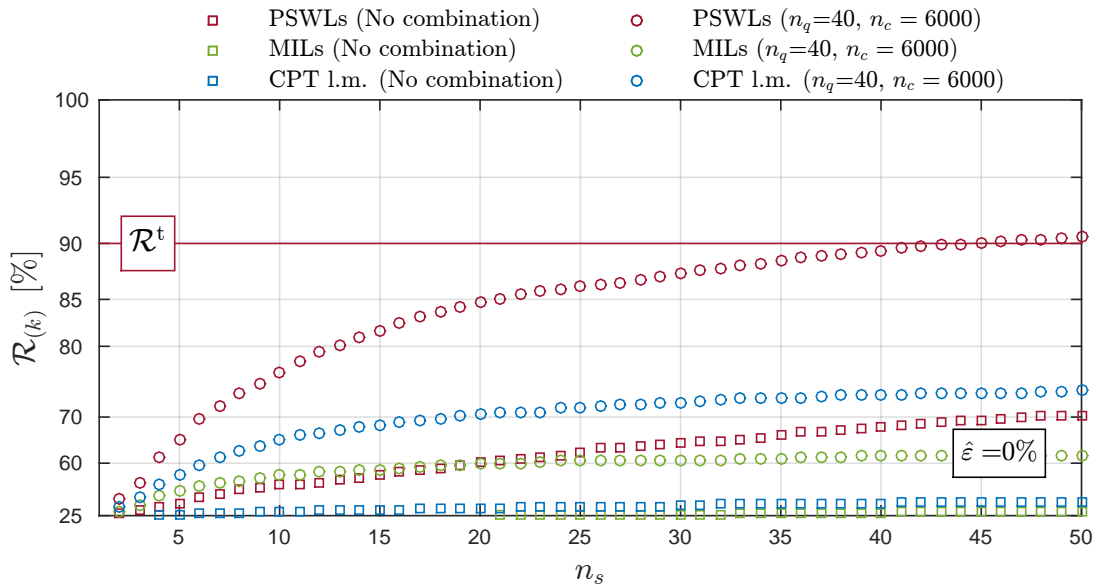


Figure VI.87: Evolution of the reconstruction indicator  $\mathcal{R}_{(k)}$  as a function of the number of load cases obtained with PSWLs, MILs and CPT loading modes. (ERP parameters:  $\hat{\varepsilon} = 0\%$ ,  $\gamma = 1$ ).

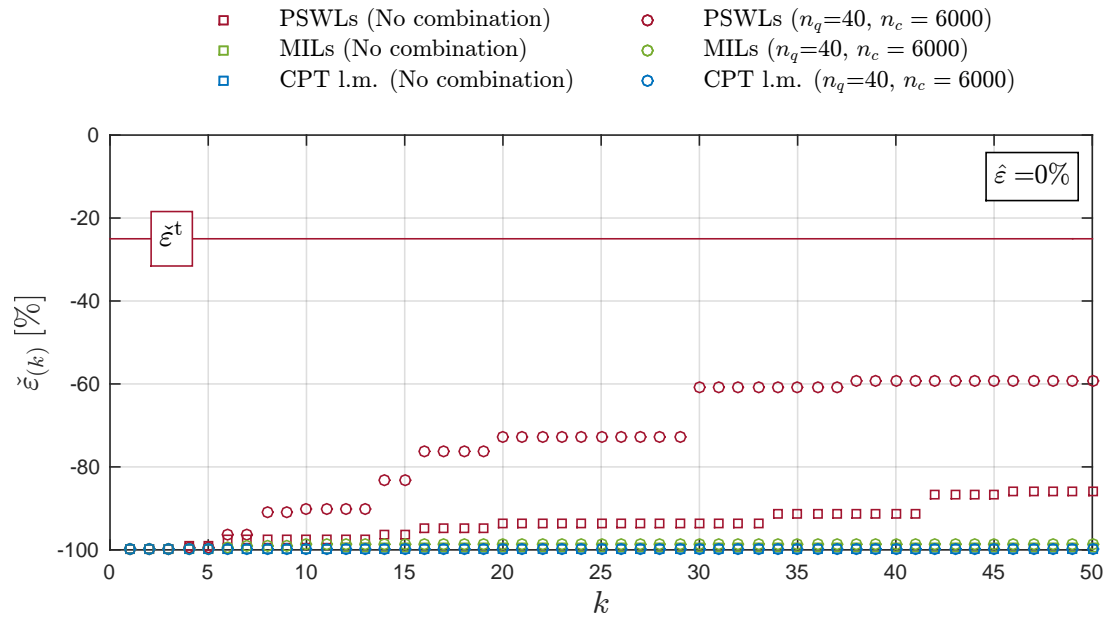


Figure VI.88: Evolution of the largest relative error indicator  $\check{\varepsilon}_{(k)}$  as a function of the number of load cases obtained with PSWLs, MILs and CPT loading modes. No overestimation of the

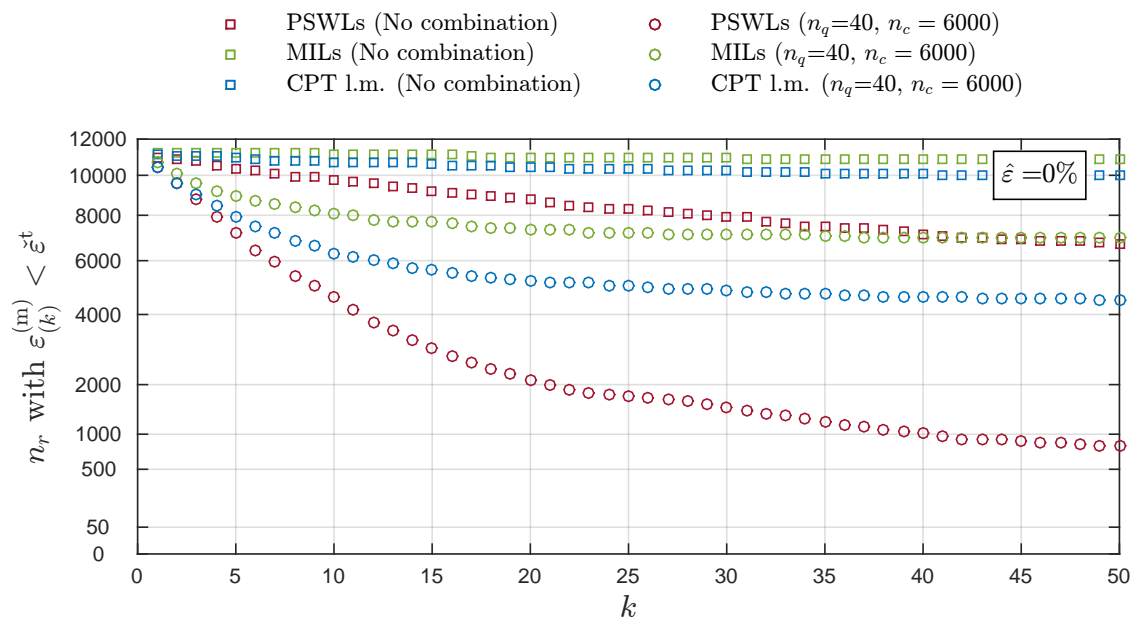


Figure VI.89: Evolution of the number of responses with  $\varepsilon_{(k)}^{(m)} < \check{\varepsilon}^t$  as a function of the number of load cases obtained with PSWLs, MILs and CPT loading modes. No overestimation of the envelope:  $\hat{\varepsilon} = 0$ . (ERP parameters:  $\hat{\varepsilon} = 0\%$ ,  $\gamma = 1$ ).

### VI.3.8 Summary

The methodology to handle the envelope reconstruction problem has been confronted with a real-life structure: the large roof of the stadium in Lille, France. Both the large number of envelope values and the low overall correlation between responses have made the envelope reconstruction challenging. The principal findings are:

- Among the overall reconstruction  $\mathcal{R}_{(k)}$  and the largest relative error  $\check{\varepsilon}_{(k)}$  indicators, the latter mainly drives the number  $n_s$  of static wind loads to be considered;
- for such a large structure, ESWLs provide local reconstructions of the envelope and therefore perform badly to provide the same order of reconstruction for all structural responses and an admissible largest relative error indicator;
- the PSWLs are better suited for an accurate reconstruction of the envelope than the CPT loading modes or the MILs;
- the parameter  $\gamma$  in the cost function (III.5.5) does not provide an improvement of the largest relative error indicator;
- the target acceptable underestimation  $\varepsilon^t$  is only fulfilled with the PSWL basis, thanks to its adaptive feature described in Section V.4.

## VI.4 Lille's stadium (Automatic procedure)

### VI.4.1 Introduction

The previous Section VI.3 has demonstrated the inefficacy of the ESWLs, CPT loading modes and MILs to solve the ERP. In this Section, the automatic procedure described in Section V.4 to solve the envelope reconstruction problem with PSWLs is studied. Additionally, the three options to establish SWLs ensuring no underestimation of the envelope, see Section III.3.5, are investigated. Finally, the impact of the non-Gaussianities on the efficiency to solve the ERP is discussed.

Indeed, the aerodynamic pressure field is mildly non-Gaussian. This can be appreciated with the maps of the skewness and the excess coefficients of aerodynamic pressures, illustrated in Figure VI.90 for a wind coming East.

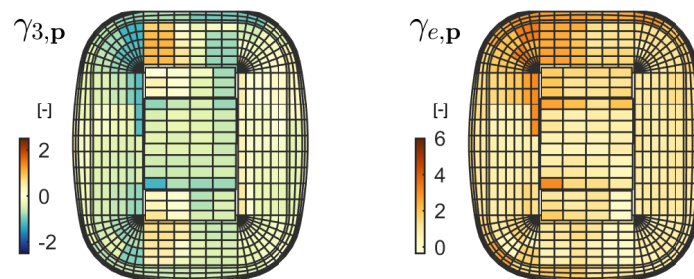


Figure VI.90: Maps of the skewness (left) and the excess (right) coefficients of aerodynamic pressures for the 75° wind direction.

### Envelope of structural responses

The cumulants (II.2.6) of the structural responses are calculated over their realizations thanks to the modal acceleration method, see Section II.5. The time-domain background analysis is done in the nodal basis with (II.4.7) while the time-domain resonant analysis is done in the modal basis by solving (II.5.5) with the Newmark's algorithm, see (Blaise and Denoël, 2011b) for further details.

The envelope reconstruction problem focuses on the envelope values of internal forces in elements of the load-bearing system. Figure VI.55 identifies these structural elements and Table VI.7 collects the structural responses considered for the ERP.

In this Section, the peak factors are computed in three different ways.

- First, a unique peak factor taken equal to  $g^{(\min)} = -3.5$  and  $g^{(\max)} = 3.5$  is adopted in first approximation as in Section VI.3 (assumption of Gaussian random processes).
- Second, the peak factors are derived from the formulation of Davenport (II.3.21) (assumption of Gaussian random processes).
- Third, the peak factors are derived from the Kareem-Zhao model (II.3.31)-(II.3.32).

Additionally, the peak factors are computed in a fourth way and for a reference period of one hour in Appendix A.

The peak factors computed with Davenport and Kareem-Zhao formulations are illustrated with the six sets of structural elements identified in red in Figures VI.92, VI.93, VI.94, VI.95, VI.96 and VI.97. The skewness coefficients, excess coefficients, standard deviation and envelope of the considered internal force for these structural elements are also depicted. The skewness and excess coefficients are small for important elements, e.g. (a)- (b)-(c1)-part of group (c2)-(e). However some elements, e.g. (d), exhibit non-Gaussianities which result in a significantly different envelope than the one obtained by assuming Gaussian random processes.

Figure VI.91 depicts the skewness and kurtosis coefficients for the structural responses considered for the ERP. Some processes are close to the monotone limitation and a few are slightly outside (60 out of 7994). When necessary, the vertical mapping consisting in finding on the monotone limitation the skewness for the exact kurtosis is applied, as recommended in (Peng et al., 2014).

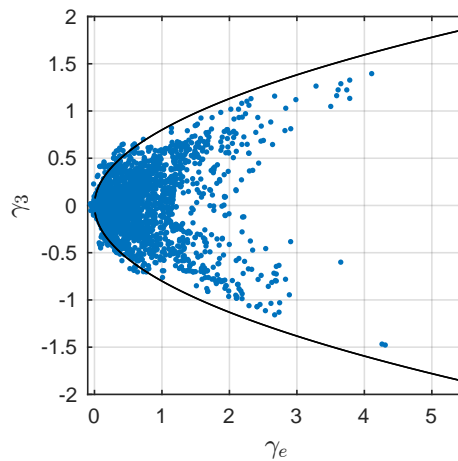


Figure VI.91: Skewness  $\gamma_3$  and kurtosis  $\gamma_e$  coefficients for the structural responses considered for the ERP. The black line corresponds to the monotone limitation.

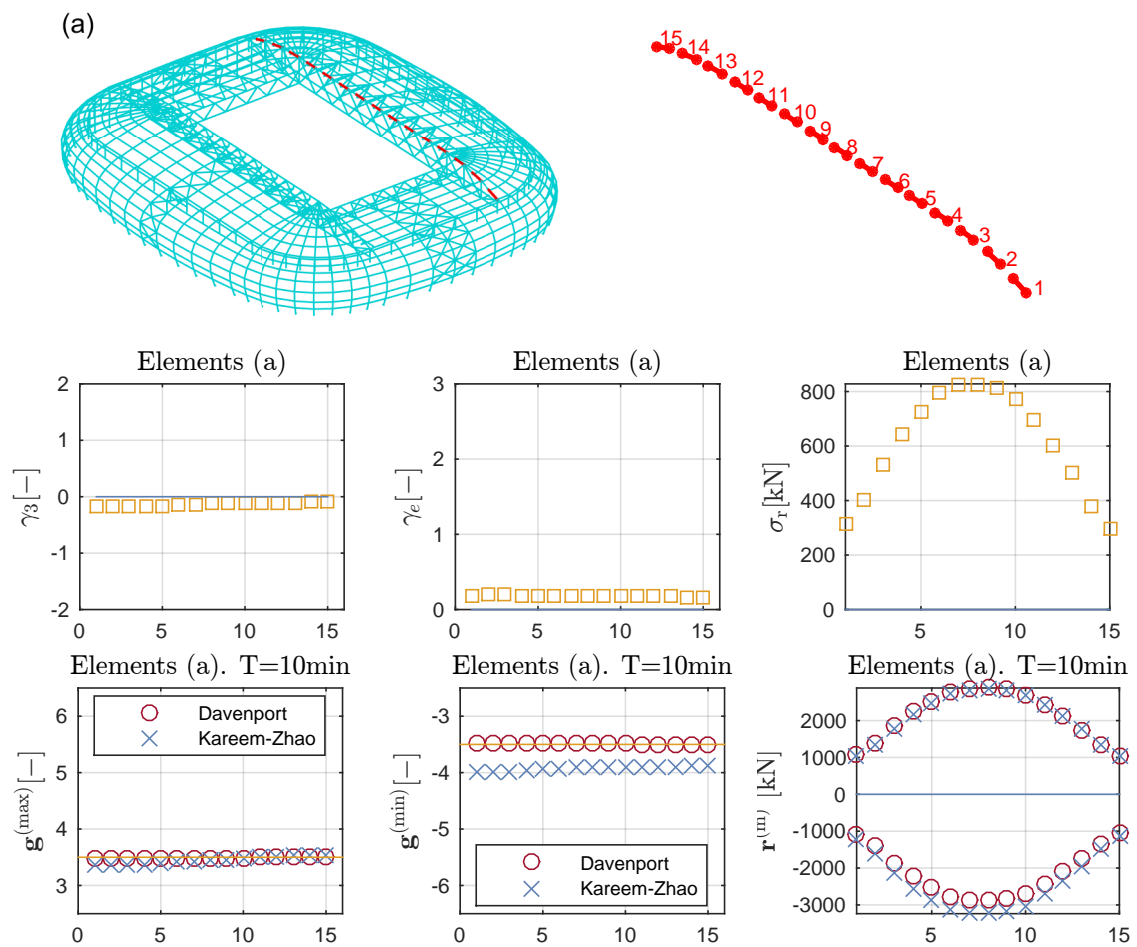


Figure VI.92: (a) Identification of 15 beam elements considered for the illustration (in red) and skewness coefficients, excess coefficients, standard deviations, peak factors and envelope values for the axial force of these elements.

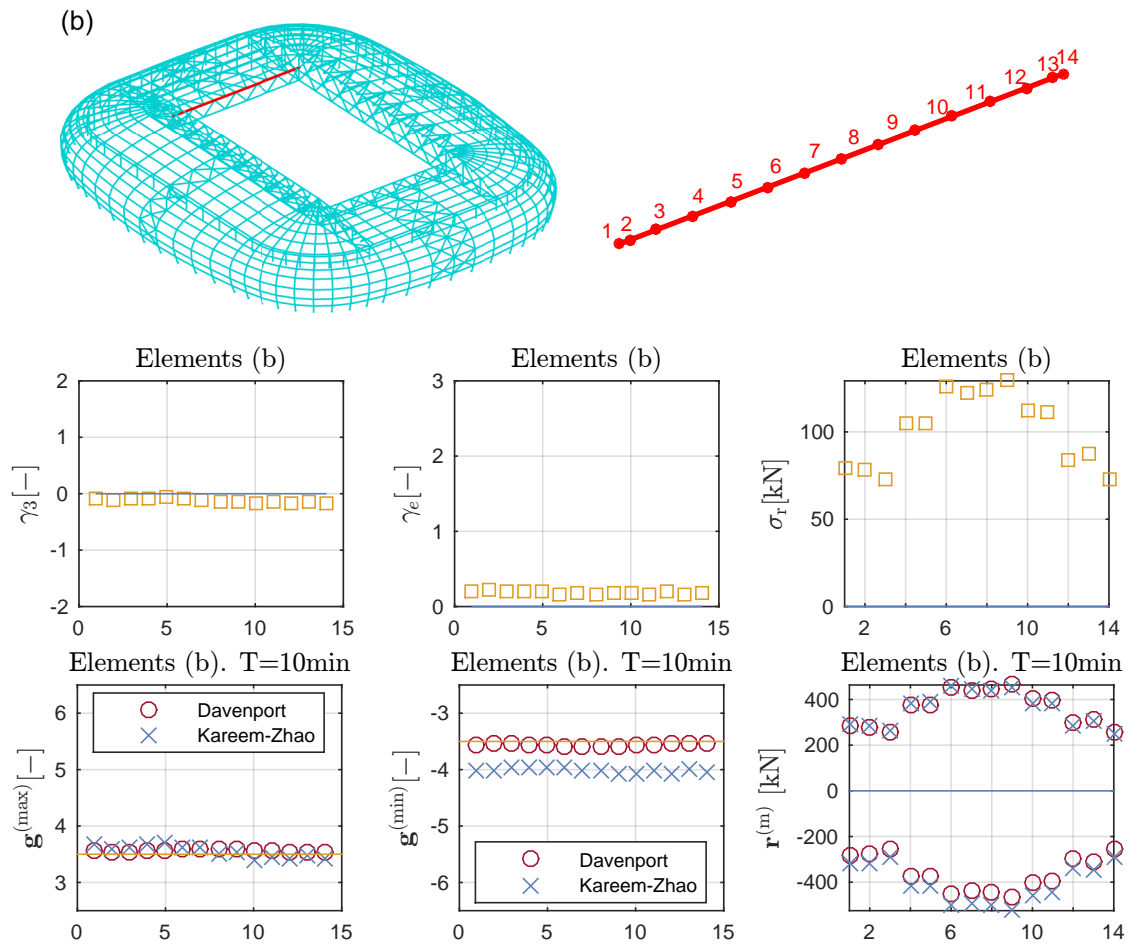


Figure VI.93: (b) Identification of 14 beam elements considered for the illustration (in red) and skewness coefficients, excess coefficients, standard deviations, peak factors and envelope values for the axial force of these elements.



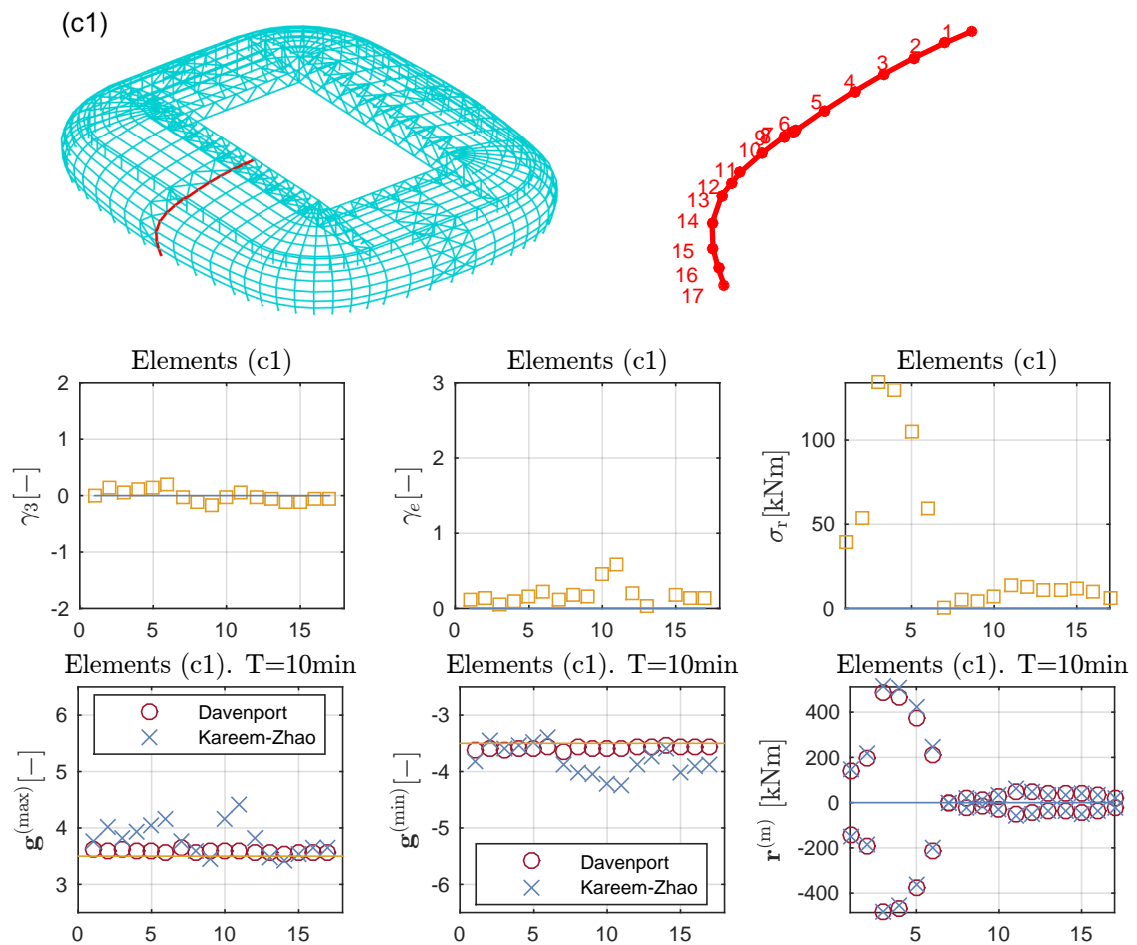


Figure VI.94: (c1) Identification of 17 beam elements considered for the illustration (in red) and skewness coefficients, excess coefficients, standard deviations, peak factors and envelope values for the bending moment of these elements.

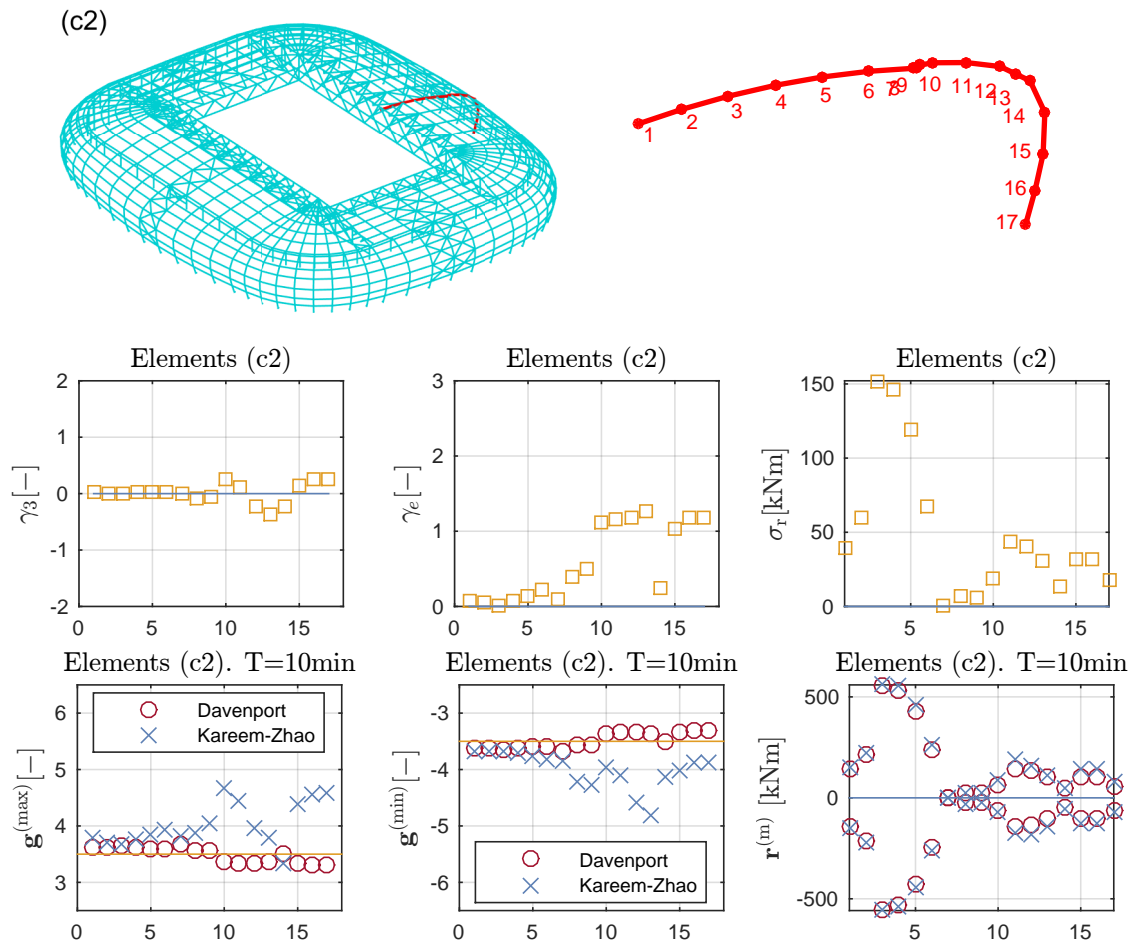


Figure VI.95: (c2) Identification of 17 beam elements considered for the illustration (in red) and skewness coefficients, excess coefficients, standard deviations, peak factors and envelope values for the bending moment of these elements.

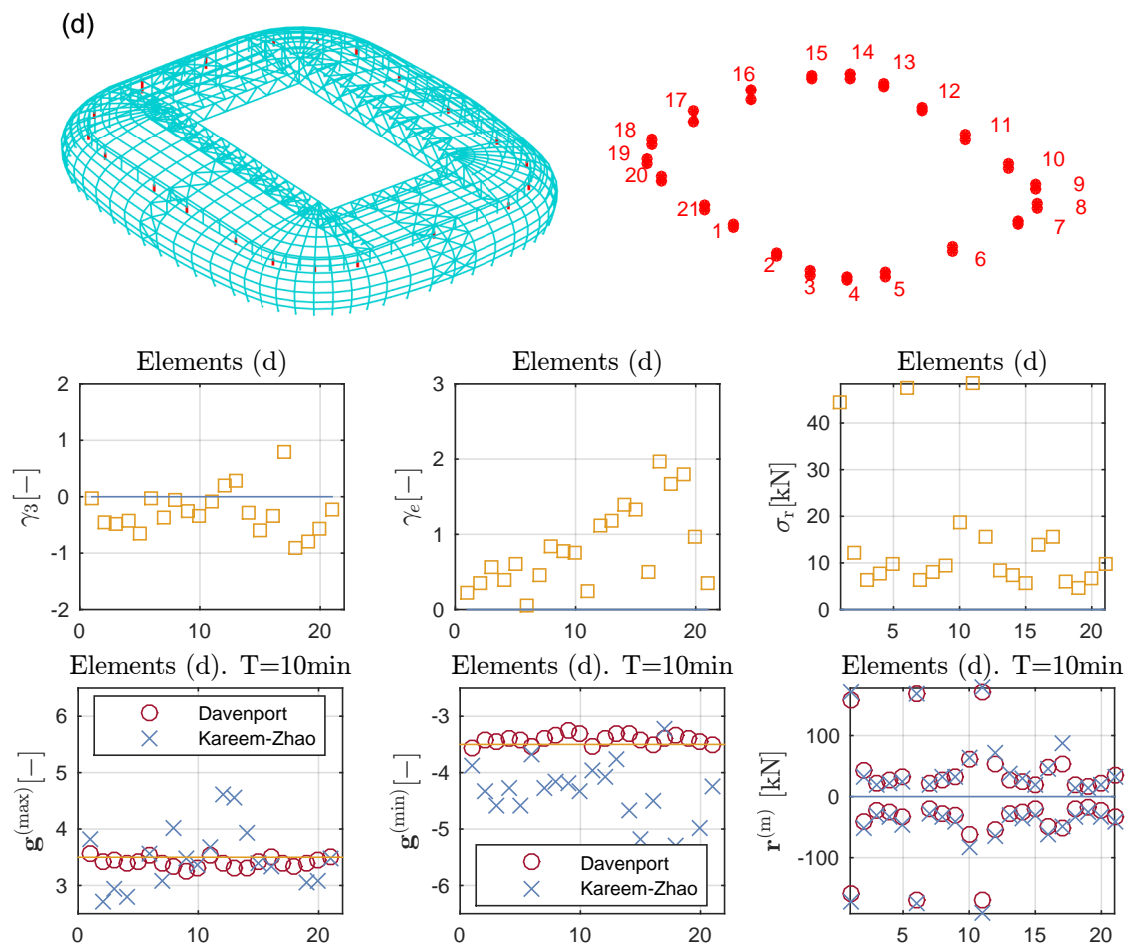


Figure VI.96: (d) Identification of 21 beam elements considered for the illustration (in red) and skewness coefficients, excess coefficients, standard deviations, peak factors and envelope values for the axial force of these elements.

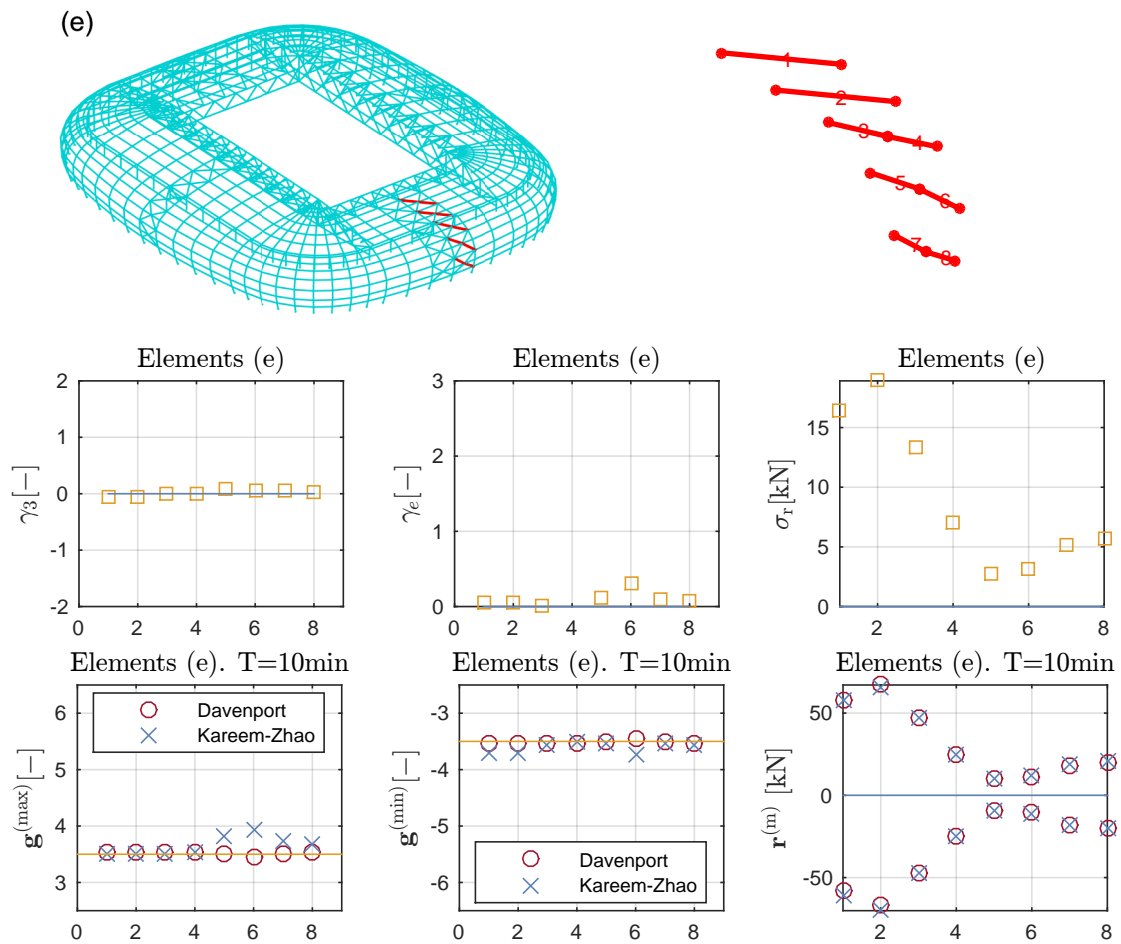


Figure VI.97: (e) Identification of 8 bars considered for the illustration (in red) and skewness coefficients, excess coefficients, standard deviations, peak factors and envelope values for the axial force of these elements.

## VI.4.2 Automatic procedure to obtain SWLs ensuring no underestimation

Principal static wind loads (Chapter V) are considered in this Section for the envelope reconstruction problem and the automatic procedure described in Section V.4 is used. The automatic procedure is applied to obtain SWLs ensuring no underestimation for two values of the final overestimation  $\hat{\varepsilon}' = 25\%$  and  $\hat{\varepsilon}' = 10\%$ . The ERP is firstly solved in a Gaussian framework and secondly in a non-Gaussian framework.

### 1. Gaussian framework (unique peak factor $g^{(m)} = \pm 3.5$ )

In Section VI.3.6, the ERP with parameters  $\varepsilon^t = -25\%$  and  $\hat{\varepsilon} = 25\%$  is solved with  $n_s=68$  combinations of the first  $n_q = 40$  PSWLs. Figure VI.98 illustrates the normalized cumulative summation of the principal coordinates  $S_{ii}$ , see (V.3.2), for the primary PSWL basis. The first  $n_q = 40$  PSWLs reproduce more than 99.5% of the total sum of the principal coordinates. The ratio  $\lambda^P$  is therefore firstly set equal to 0.995. The initial set of combination coefficients is randomly generated with  $n_c = 6000$ , see Section III.5.2.

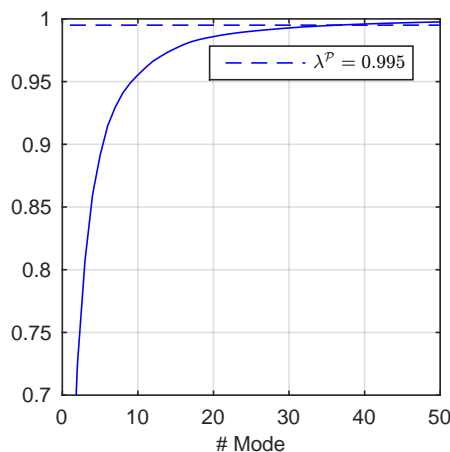


Figure VI.98: Normalized cumulative summation of the principal coordinates of the primary PSWL basis.

The three options described in Section III.3.5 to obtain SWLs ensuring no underestimation are summarized in Table VI.11. The option A performs badly in comparison with the number of SWLs obtained by applying option B or C. The option C performs slightly better than option B. The option C is only studied in the sequel. It consists in reproducing an envelope with the same over- and under- estimations, then scaling everything up.

Figure VI.99 illustrates the evolution of the number of responses  $n_{r(k)}$  with  $\varepsilon_{(k)}^{(m)} < \hat{\varepsilon}^t$  as a function of the number of load cases for the ERP parameters:  $\hat{\varepsilon} = 4.76\%$ ,  $\hat{\varepsilon}^t = -4.76\%$ .

| No underestimation and $\hat{\varepsilon}' = 25\%$ |                       |                     |            |       |             |              |                               |      |
|--|-----------------------|---------------------|------------|-------|-------------|--------------|-------------------------------|------|
| Options  | $\hat{\varepsilon}^t$ | $\hat{\varepsilon}$ | $n_s$      | $n_q$ | $n_p$       | $n_{r(n_s)}$ | $\check{\varepsilon}_{(n_s)}$ | CPU  |
| A  | 0%                    | 25%                 | 180        | 4     | [37,...,4]  | 0            | ✓                             | 5min |
| B  | -20%                  | 0%                  | 114        | 3     | [37,...,14] | 0            | ✓                             | 4min |
| C  | -11%                  | 11%                 | <b>104</b> | 3     | [37,...,6]  | 0            | ✓                             | 4min |

| No underestimation and $\hat{\varepsilon}' = 10\%$ |                       |                     |            |       |             |              |                               |       |
|--|-----------------------|---------------------|------------|-------|-------------|--------------|-------------------------------|-------|
| Options  | $\hat{\varepsilon}^t$ | $\hat{\varepsilon}$ | $n_s$      | $n_q$ | $n_p$       | $n_{r(n_s)}$ | $\check{\varepsilon}_{(n_s)}$ | CPU   |
| A  | 0%                    | 10%                 | 456        | 5     | [37,...,7]  | 0            | ✓                             | 10min |
| B  | -9.1%                 | 0%                  | 306        | 4     | [37,...,10] | 0            | ✓                             | 9min  |
| C  | -4.76%                | 4.76%               | <b>276</b> | 5     | [37,...,5]  | 0            | ✓                             | 10min |

Table VI.11: Number of SWLs to solve the ERP with the three different options (see Section III.3.5) and two values of final overestimation  $\hat{\varepsilon}'$ . ERP parameters:  $\gamma = 1$ ,  $\lambda^P = 0.995$ ,  $n_c = 6000$ . Results obtained in a Gaussian framework (unique peak factor). The symbol ✓ means that the acceptable underestimation is satisfied.

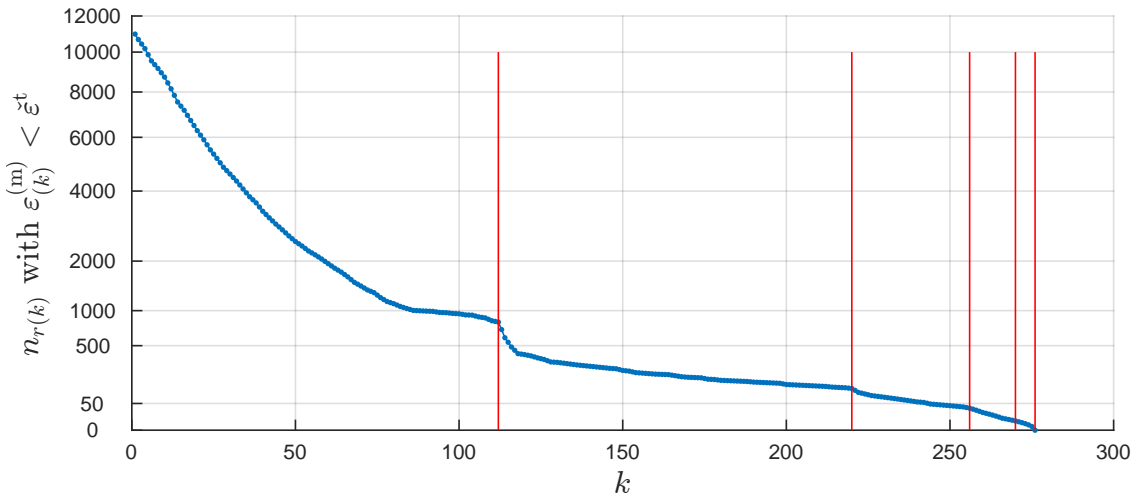


Figure VI.99: Evolution of the number of responses  $n_{r(k)}$ , see page 127, with  $\varepsilon_{(k)}^{(m)} < \hat{\varepsilon}^t$  as a function of the number of load cases. ERP parameters:  $\hat{\varepsilon} = 4.76\%$ ,  $\hat{\varepsilon}^t = -4.76\%$ ,  $\gamma = 1$ ,  $\lambda^P = 0.995$ ,  $n_c = 6000$ . Vertical red lines correspond to an updating of the PSWL basis. Results obtained in a Gaussian framework (unique peak factor).

## 2. Gaussian framework (Davenport's formulation)

The envelope values are based on the peak factors computed with (II.3.21) for a 10-min observation period. Table VI.12 presents the results with option C and Figure VI.100 shows the evolution of the number of responses as a function of the number of load cases for the ERP parameters:  $\hat{\varepsilon} = 4.76\%$ ,  $\hat{\varepsilon}^t = -4.76\%$ . The results are similar to the ones obtained

assuming a unique peak factor, see Table VI.11 and Figure VI.99.

| No underestimation and $\hat{\varepsilon}' = 25\%$ |       |              |              |                               |      | No underestimation and $\hat{\varepsilon}' = 10\%$ |       |              |              |                               |      |
|--|-------|--------------|--------------|-------------------------------|------|--|-------|--------------|--------------|-------------------------------|------|
| $n_s$  | $n_q$ | $n_p$        | $n_{r(n_s)}$ | $\check{\varepsilon}_{(n_s)}$ | CPU  | $n_s$  | $n_q$ | $n_p$        | $n_{r(n_s)}$ | $\check{\varepsilon}_{(n_s)}$ | CPU  |
| <b>120</b>   | 3     | [37, ..., 6] | 0            | ✓                             | 4min | <b>292</b>   | 5     | [37, ..., 3] | 0            | ✓                             | 9min |

Table VI.12: Number of SWLs to solve the ERP with option C (see Section III.3.5). ERP parameters:  $\hat{\varepsilon} = 4.76\%$ ,  $\hat{\varepsilon}^t = -4.76\%$ ,  $\gamma = 1$ ,  $\lambda^P = 0.995$ ,  $n_c = 6000$ . Results obtained in a Gaussian framework (Davenport's formulation for the peak factors). The symbol ✓ means that the acceptable underestimation is satisfied.

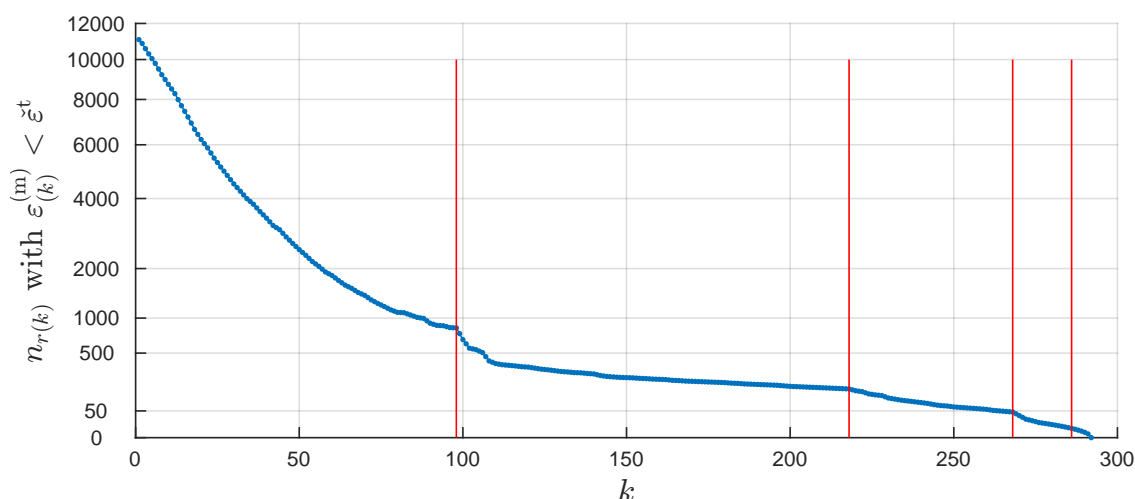


Figure VI.100: Evolution of the number of responses  $n_{r(k)}$ , see page 127, with  $\varepsilon_{(k)}^{(m)} < \varepsilon^t$  as a function of the number of load cases. ERP parameters:  $\hat{\varepsilon} = 4.76\%$ ,  $\hat{\varepsilon}^t = -4.76\%$ ,  $\gamma = 1$ ,  $\lambda^P = 0.995$ ,  $n_c = 6000$ . Vertical red lines correspond to an updating of the PSWL basis. Results obtained in a Gaussian framework (Davenport's formulation for the peak factors).

### 3. Non-Gaussian framework (Kareem-Zhao model)

The envelope values are based on the peak factors computed with (II.3.31)-(II.3.32) for a 10-min observation period. The ESWLs are still obtained from the hybrid method proposed by Chen and Kareem (2001) and reviewed in Section IV.6. All ESWLs computed with the hybrid method naturally satisfy the envelope value condition (IV.2.3). However, all ESWLs do not necessary fulfill the non-overestimation condition (IV.2.4) since the hybrid method is based on the Gaussian assumption. Figure VI.101 shows the histograms of overestimation relative errors that would be obtained if all original hybrid-based ESWLs were used for the

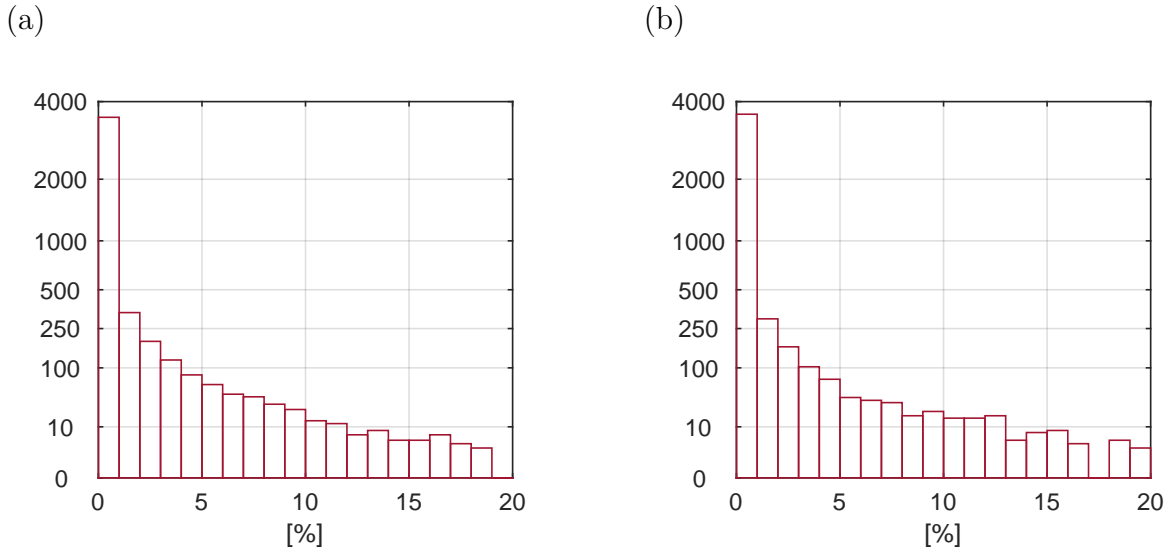


Figure VI.101: Histograms of overestimation relative errors that are obtained with the original hybrid-based ESWLs. Overestimation relative errors associated with (a) upper (positive) and (b) lower (negative) envelope values.

ERP. There are approximately 9000 envelope values out of 15988 that would be overestimated in the range  $[0,20\%]$ . This is a first hint that these ESWLs are not well-suited to tightly reconstruct the envelope.

Table VI.13 presents the results with option C and Figure VI.102 shows the evolution of the number of responses as a function of the number of load cases for the ERP parameters:  $\hat{\varepsilon} = 4.76\%$ ,  $\hat{\varepsilon}^t = -4.76\%$ . For the final overestimation parameter  $\hat{\varepsilon}' = 25\%$ , the number of SWLs is approximately the same but the number of PSWL bases increased from 3, in Table VI.12, to 7. For the value  $\hat{\varepsilon}' = 10\%$ , both the number of SWLs to solve the ERP and the number of PSWL basis increase, respectively from 292 and 5, in Table VI.12, to 411 and 10.

This example shows that, if ESWLs based on Gaussian assumption are used for the ERP, the level of complexity is increased by taking into account non-Gaussian peak factors, especially for small ranges of target underestimation and acceptable overestimation. However, the automatic procedure proves to be efficient even if the original ESWLs do not satisfy the non-overestimation condition.

| No underestimation and $\hat{\varepsilon}' = 25\%$ |       |            |              |                               |       | No underestimation and $\hat{\varepsilon}' = 10\%$ |       |            |              |                               |       |
|--|-------|------------|--------------|-------------------------------|-------|--|-------|------------|--------------|-------------------------------|-------|
| $n_s$  | $n_q$ | $n_p$      | $n_{r(n_s)}$ | $\check{\varepsilon}_{(n_s)}$ | CPU   | $n_s$  | $n_q$ | $n_p$      | $n_{r(n_s)}$ | $\check{\varepsilon}_{(n_s)}$ | CPU   |
| <b>121</b>   | 7     | [39,...,4] | 0            | ✓                             | 12min | <b>411</b>   | 10    | [39,...,7] | 0            | ✓                             | 22min |

Table VI.13: Number of SWLs to solve the ERP with option C (see Section III.3.5). ERP parameters :  $\hat{\varepsilon} = 4.76\%$ ,  $\hat{\varepsilon}^t = -4.76\%$ ,  $\gamma = 1$ ,  $\lambda^p = 0.995$ ,  $n_c = 6000$ . Results obtained in a non-Gaussian framework (Kareem-Zhao model for the peak factors). The symbol ✓ means that the acceptable underestimation is satisfied.



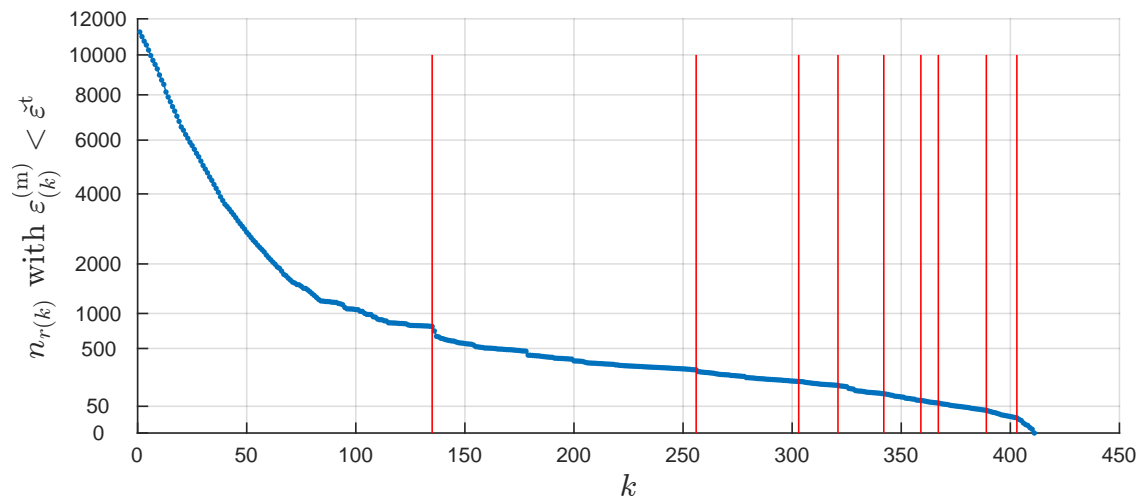


Figure VI.102: Evolution of the number of responses  $n_{r(k)}$ , see page 127, with  $\varepsilon_{(k)}^{(m)} < \varepsilon^t$  as a function of the number of load cases. ERP parameters:  $\hat{\varepsilon} = 4.76\%$ ,  $\varepsilon^t = -4.76\%$ ,  $\gamma = 1$ ,  $\lambda^P = 0.995$ ,  $n_c = 6000$ . Vertical red lines correspond to an updating of the PSWL basis. Results obtained in a non-Gaussian framework (Kareem-Zhao model for the peak factors).

### VI.4.3 Summary

In Gaussian and non-Gaussian frameworks, the automatic procedure to handle the envelope reconstruction problem with PSWL basis has been assessed to Lille's stadium and has proven to be efficient. The three options to establish SWLs ensuring no underestimation of the envelope have been investigated and the option C performs better. Only 121 SWLs are required to obtain a reconstructed envelope without underestimation of the actual 15988 envelope values and with overestimation lower than 25%. This proves the remarkable relevance of the automatic procedure.

## VI.5 Low-rise gable roof building

A rigid gable-roofed low-rise building is analyzed under wind actions. Extensive wind-tunnel tests have been performed to study the aerodynamic pressure field on these usual structures<sup>2</sup>. For normal dimensions, this type of structure is common to design and to build, being thence attractive for many applications, mainly residential and industrial. The structure used for illustrations has sharp edges between the vertical walls and the roof. Depending on the angle of attack of the wind, the aerodynamic pressure field for this roof configuration is known to exhibit mildly to strongly non-Gaussianities. Contrary to the first two examples, the envelope to be reconstructed is now asymmetric (II.4.17) since the non-Gaussianity of the structural responses is taken into account through a quasi-static time-domain analysis. The roof is supported by a collection of frames and we focus on two specific ones for the illustrations.

### Wind tunnel tests

The dimensions of the structure are a width of 36.6 m (120 ft), an eave height of 3.65 m (12 ft), a length of 57.2 m (187.5 ft) and a roof slope of 1:12. Wind-tunnel measurements have been done at the Boundary Layer Wind Tunnel Laboratory (BLWTL) of the University of Western Ontario (Ho et al., 2005), see the scaled model in Figure VI.103.

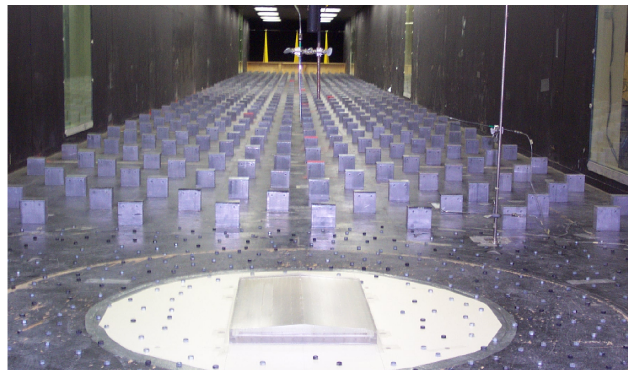


Figure VI.103: Picture of the rigid gable-roofed building in the wind-tunnel. From wind-Pressure (Main and Fritz, 2006).

The pressure time series are available from (Main, 2006)<sup>3</sup> and can be used through wind-Pressure (Main and Fritz, 2006), a Matlab-based Database-Assisted Design software available on the internet. The length scale is 1:100, the sampling frequency in the wind-tunnel is 500 Hz and the terrain condition is suburban, corresponding to a roughness length of 0.3 m. The mean wind speed at eave height is equal to 5.91 m/s in the wind tunnel. In full scale, the mean wind speed  $V$  at eave height is equal to 14.73 m/s and the velocity and time scales are 1/2.5 and 1/40.1, respectively. The sampling frequency corresponds to 12.5 Hz in full scale (a time step equal to 0.08 seconds). Each measurement lasts about 66.6 minutes full scale. The leakage case is no opening in the building.

<sup>2</sup>Luca Caracoglia is acknowledged for recommending us the National Institute of Standards and Technology aerodynamic database for the illustration of our study.

<sup>3</sup>Joseph A. Main is acknowledged for having provided several explanations of the data sets.

Pressure coefficients are usually referenced using the mean wind speed  $V$  at a given reference height; they are defined from the aerodynamic pressures by

$$c'_p = \frac{p'}{\frac{1}{2}\rho V^2}, \quad (\text{VI.5.1})$$

where  $\rho = 1.225 \text{ kg/m}^3$  is the air density. A positive pressure coefficient means that aerodynamic pressure acts towards the inner of the building while a negative coefficient indicates suction (with reference to the atmospheric pressure). For convenience, ESWLs as well as PSWLs are illustrated with the pressure coefficients.

Figure VI.104 shows in an exploded view the tap array (indicated by the dots) as well as tributary areas for each pressure tap on the vertical faces along the length of the building and on the roof.

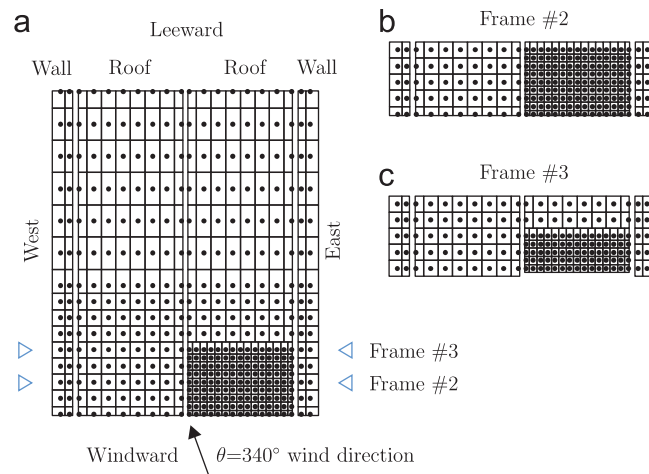


Figure VI.104: (a) Exploded view of the tap array with varying tap density, the triangles identify two frames considered for illustrations. Only aerodynamic pressures measured at the taps contributing to the reaction forces of the girts and purlins attached to (b) Frame #2 and (c) Frame #3 are used, respectively, for illustrations. The wind direction  $\theta = 340^\circ$  is studied.

The vertical faces and the two slopes of the roof are slightly shifted relative to each other for clarity. Taps on the vertical faces along the width of the building are disregarded in the structural analysis and are thus not shown in Figure VI.104. The wind direction convention is shown in Figure VI.104. The wind direction  $\theta = 340^\circ$  is chosen for illustration.

Figure VI.105 shows the maps of the mean and standard deviations along with the skewness and excess coefficients of the pressure coefficients. The roof is mainly loaded close to the sharp edge roof connection with the gable end about a quarter of the length of the building, along Frame #2. The mean loading is suction and large standard deviations close to the gable end is explained by the flow detachment intensity which is important on this windward side of the roof because the air flow encounters the structure's roof with its sharp edge connection between the horizontal and vertical parts. The aerodynamic pressure field exhibits also large skewness and excess coefficients, up to -2 and 8, respectively. This must be taken into account in a non-Gaussian analysis. The cumulants (II.2.6) and cross-central moments (II.2.12) of random processes are calculated over their realizations. Figure VI.105

also shows, for instance, the peak factors for the mean largest maximum and mean smallest minimum of the pressure coefficients computed with the “non-Gaussian” model exposed in Section II.3. For negative skewness coefficient, the peak factor for the mean largest minimum is larger than the peak factor for the mean smallest maximum (in absolute value), i.e.,  $-g^{(\min)} > g^{(\max)}$ .

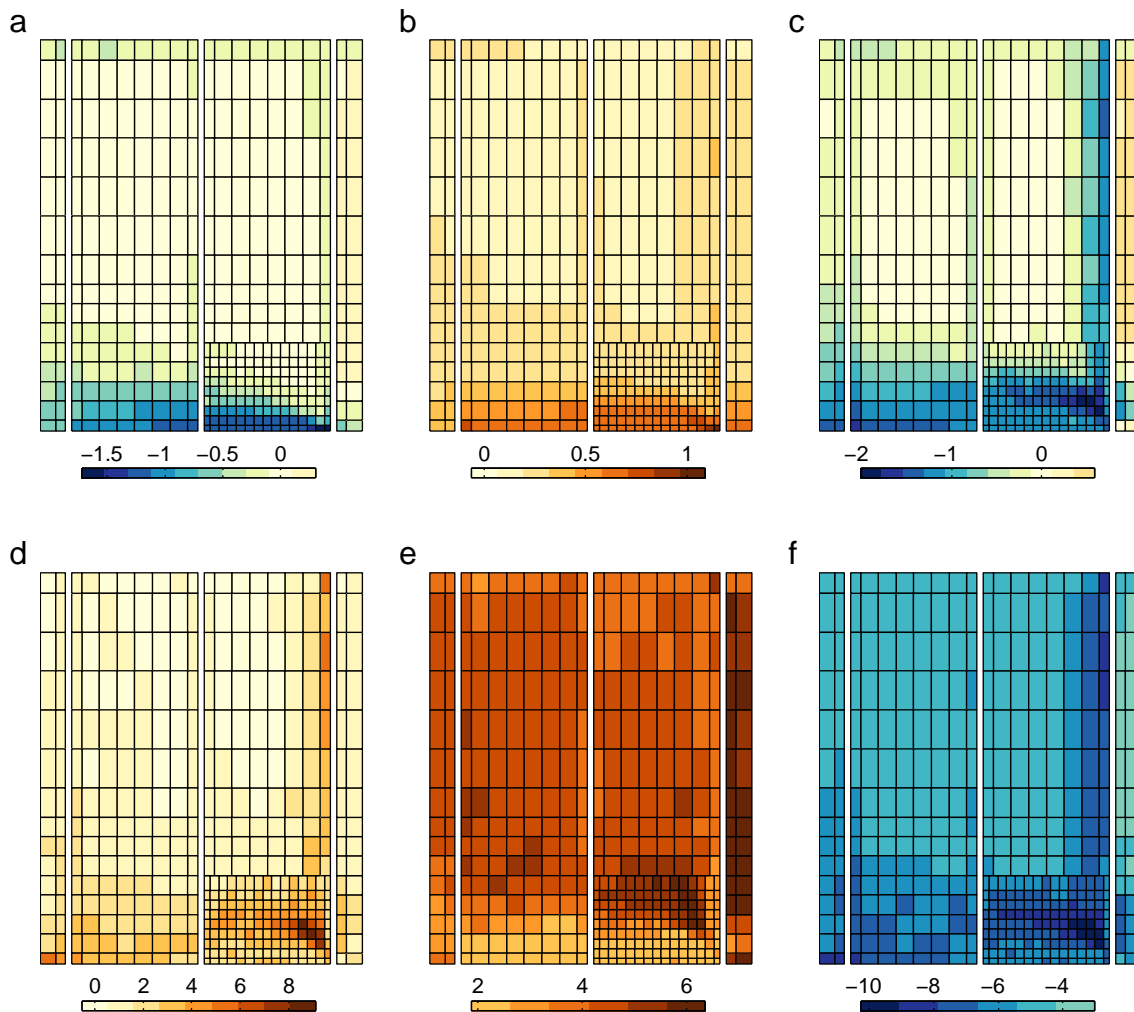


Figure VI.105: Maps of (a) mean, (b) standard deviation, (c) skewness (d) kurtosis, peak factors (e)  $g^{(\max)}$  (II.3.31) and (f)  $g^{(\min)}$  (II.3.32) of the pressure coefficients for a 340° wind direction.

### Description of the structure

The roof is supported by 11 fixed-base frames placed every 5.72 m. The second and third internal structural frames are used for illustrations and their positions are identified with triangles in Figure VI.104, numbered from bottom to top in the figure.

Each frame is clamped and the connections are considered as infinitely rigid. Columns are HE 450 AA and beams are IPE 450 with a 235 MPa steel grade and a 205000 MPa Young's modulus. The finite element model of one frame, see Figure VI.106, is an assembly of classical 2-D beam elements with three degrees of freedom per node (rotation, horizontal and vertical displacements).

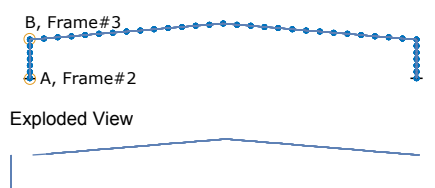


Figure VI.106: Elevation of a Frame. The dots identify the nodes of the finite element model. The bending moments at the two nodes A and B and identified by the circles are considered for the illustrations of ESWLs. The exploded view is used for the illustrations.

Each frame is divided into 40 finite elements and the number of degrees of freedom is thus equal to 123 per frame. The aerodynamic pressure field acting on the cladding is transferred by the girts and purlins to each frame of the building (Main and Fritz, 2006). Girts and purlins, considered as hinged-hinged beams, are not modeled and each frame is analyzed separately. The design of the steel frames has been done following the Eurocode (2005).

### Determination of the envelope

The bending moments at each node of the model are considered for the envelope reconstruction problem and the computation of the PSWLs. The number of structural responses considered is  $n_r = 451$ . The bending moments at the nodes identified in Figure VI.106 and labeled A and B, in the two distinct frames #2 and #3, see Figure VI.104, are considered to illustrate ESWLs. The envelope reconstruction using PSWLs is illustrated with both considered frames, as well.

Figure VI.107 represents each step to compute the total envelope of the bending moments. For sake of clarity, only a scale is given for each graph and the numerical values for the two considered bending moments are given in Table VI.14. The total envelope results from an element-by-element multiplication of the peak factors and the standard deviations and by adding the mean component, see equations (II.4.15)-(II.4.19). Bending moments in the second frame exhibit large skewness and kurtosis coefficients resulting in an asymmetric envelope. On the opposite, bending moments in the third frame exhibit moderate skewness and kurtosis coefficients resulting in a nearly symmetric envelope, close to the limit case for Gaussian structural responses. Indeed, the aerodynamic pressure field acting on the third frame is nearly Gaussian.

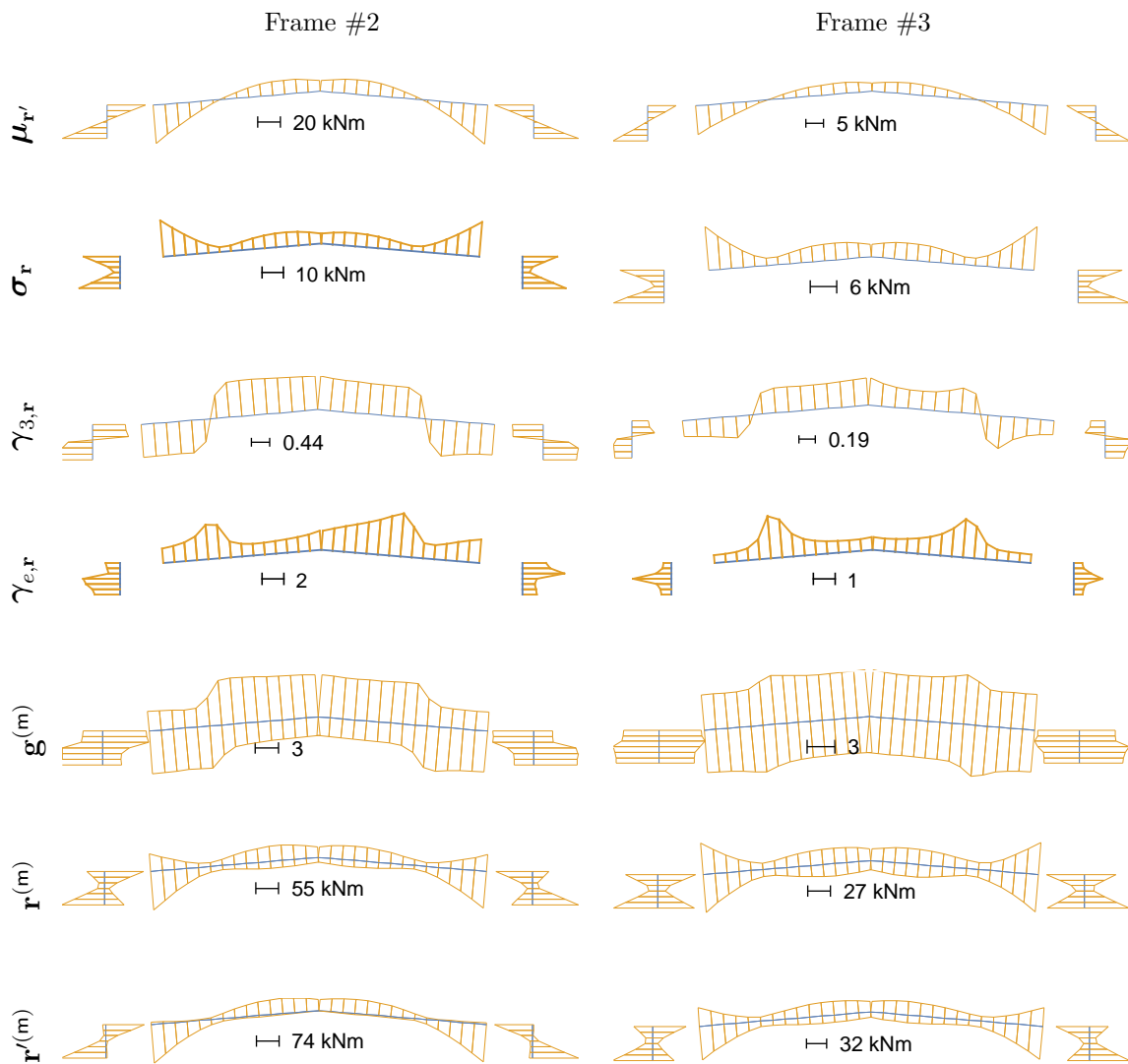


Figure VI.107: Mean, standard deviation, skewness coefficient, kurtosis coefficient, peak factors (II.3.31)-(II.3.32), envelope and total envelope for the bendings moments of both considered frames.

|         | $\mu_{r'}$ | $\sigma_r$ | $\gamma_{3,r}$ | $\gamma_{e,r}$ | $g^{(max)}$ | $g^{(min)}$ | $r^{(max)}$ | $r^{(min)}$ |
|---------|------------|------------|----------------|----------------|-------------|-------------|-------------|-------------|
|         | [kNm]      | [kNm]      | [-]            | [-]            | [-]         | [-]         | [kNm]       | [kNm]       |
| A (min) | 32.8       | 19.0       | 1.0            | 2.3            | 6.4         | -3.0        | 121.5       | -57.9       |
| B (max) | -9.4       | 9.9        | -0.2           | 0.4            | 3.9         | -4.6        | 38.8        | -45.2       |

Table VI.14: Numerical data associated with the two bending moments in Frame #2 and Frame #3, respectively.

Figure VI.108 depicts the skewness and kurtosis coefficients for the recorded aerodynamic pressures and the bending moments. Some processes are close to the monotone limitation and a few are slightly outside. When necessary, the vertical mapping consisting in finding

on the monotone limitation the skewness for the exact kurtosis is applied, as recommended in (Peng et al., 2014).

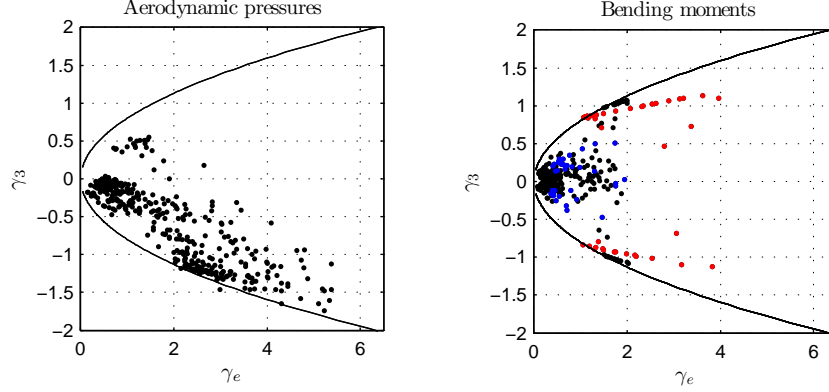


Figure VI.108: Skewness  $\gamma_3$  and kurtosis  $\gamma_e$  coefficients for aerodynamic pressures (left) and for bending moments (right), in red for Frame #2, in blue for Frame #3 and in black for the nine remaining frames. The black line corresponds to the monotone limitation.

### VI.5.1 Two-step adjustment method

Chapter IV has highlighted that the equivalent static wind loads  $\mathbf{p}^{(e,m)}$  in a non-Gaussian context do not necessarily satisfy the envelope value condition, nor the non-overestimation condition. These two issues are addressed with a two-step adjustment method described in Section IV.9. The method is particularized next in the case of a quasi-static structural behavior.

If the envelope value condition is not fulfilled (except in the case of LRC-based ESWLs where the envelope value condition is naturally satisfied) under the *original* ESWLs  $\mathbf{p}^{(e,m)}$ , *scaled* ESWLs are defined for this purpose by

$$(\alpha\mathbf{p})^{(e,m)} := \alpha^{(e,m)}\mathbf{p}^{(e,m)}. \quad (\text{VI.5.2})$$

If the fulfillment of the non-overestimation condition fail under the *original* or *scaled* ESWLs, an *adjusted* ESWLs is defined, satisfying the 2 conditions (IV.2.3)-(IV.2.4), by

$$(\beta \circ \alpha\mathbf{p})^{(e,m)} := \beta^{(e,m)} \circ \alpha^{(e,m)}\mathbf{p}^{(e,m)}. \quad (\text{VI.5.3})$$

The scaling coefficient  $\alpha^{(e,m)}$  is determined to ensure the envelope value condition while the local coefficients  $\beta^{(e,m)}$ , an  $n_l \times 1$  vector, adjust the scaled ESWLs  $(\alpha\mathbf{p})^{(e,m)}$  in order to fulfill the non-overestimation condition. We want to hold the envelope value condition and to satisfy the non-overestimation condition by finding the minimum of a problem specified by

$$\min_{\beta^{(e,m)}} \sum_{j=1}^{n_l} \left| \beta_j^{(e,m)} - 1 \right|^{\gamma_\beta}, \quad (\text{VI.5.4})$$

under the linear constraints

$$\begin{cases} +\mathbf{B} [(\boldsymbol{\beta} \circ \alpha \mathbf{p})^{(e,m)}] - \mathbf{r}^{(\max)} & \leq \mathbf{0}, \\ -\mathbf{B} [(\boldsymbol{\beta} \circ \alpha \mathbf{p})^{(e,m)}] + \mathbf{r}^{(\min)} & \leq \mathbf{0}, \\ \sum_{j=1}^{n_i} B_{ij} \beta_j^{(e,m)} \alpha^{(e,m)} p_j^{(e,m)} & = r_i^{(m)}. \end{cases} \quad (\text{VI.5.5})$$

Symbol  $\gamma_\beta$  is a positive coefficient taken here equal to 2 as a compromise between accuracy and convergence of the optimization. In the sequel, the magnitudes of  $\alpha^{(e,m)}$  and  $\beta^{(e,m)}$  are used in the illustrations to compare ESWL formulations in a Non-Gaussian framework.

## VI.5.2 Bicubic model

In this Section, the parametric bicubic model (IV.8) for joint load-response PDFs is assessed. The considered responses for illustrations are the two bending moments identified in Figure VI.106. Where flow detachments occur and lead to non-Gaussianities, three aerodynamic pressures, labeled A B and C, are considered and identified in Figure VI.109.

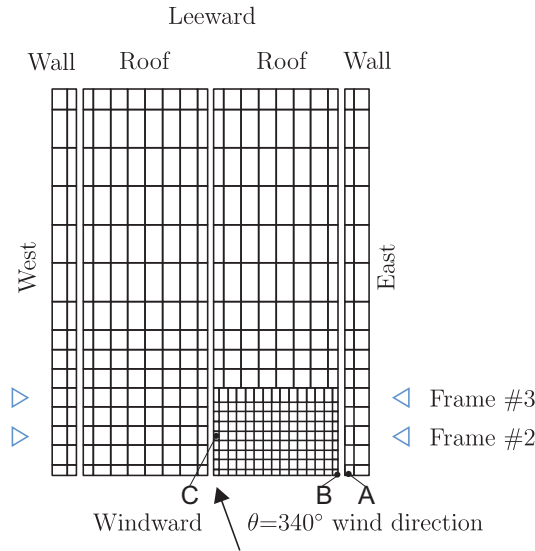


Figure VI.109: Localization of the three aerodynamic pressures A, B and C considered for the illustration of joint load-response PDFs.

Figures VI.110 and VI.111 illustrate the PDFs of the selected bending moments and aerodynamic pressures, respectively. The matching of the histogram and the cubic model PDF shows that the model is fine for representing these non-Gaussian responses and pressures. This was already observed in (Gurley et al., 1997).



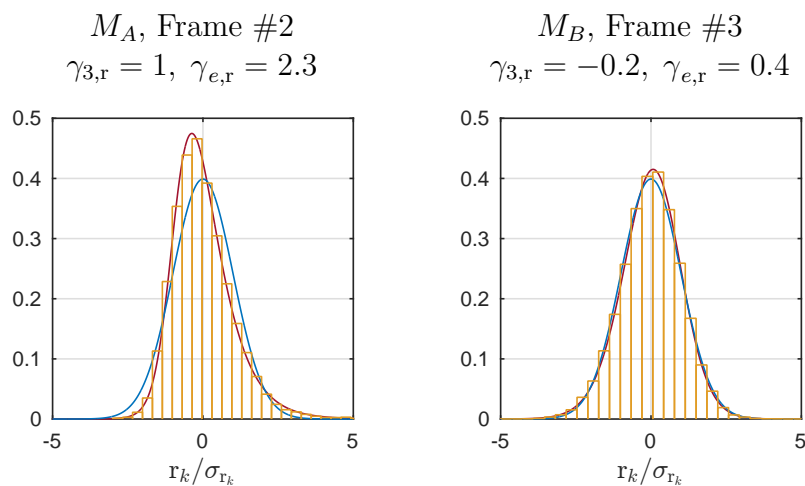


Figure VI.110: PDFs of the selected bending moments. Histograms in orange, Gaussian PDFs in blue and PDFs obtained with the Hermite moment model in burgundy.

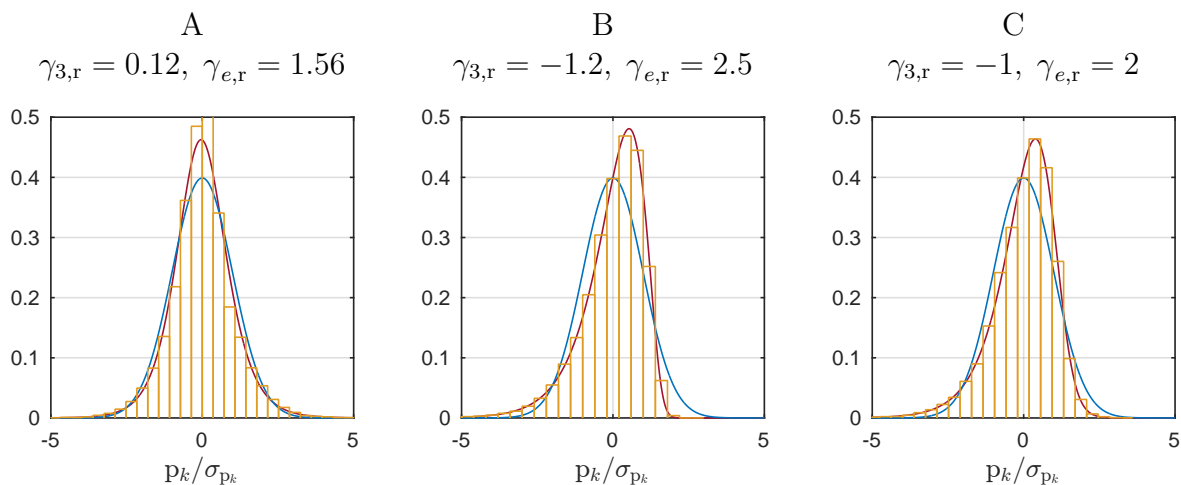


Figure VI.111: PDFs of the selected aerodynamic pressures. Histograms in orange, Gaussian PDFs in blue and PDFs obtained with the Hermite moment model in burgundy.

Figures VI.112 and VI.113 depict the joint PDFs obtained with a kernel density estimator (Botev et al., 2010) along with the Gaussian joint PDFs and the joint PDFs obtained with the bicubic model, respectively. The joint PDFs are represented by contours associated with constant values taken by the bivariate distributions. A constant step spaces the contour lines. These contours help to get some insight into the form of these joint PDFs and assess whether or not the bicubic model performs well. Compared to the Gaussian joint PDFs, it can be seen that the bicubic model succeed to localized the mode of the kernel bivariate density estimation. Moreover, the contours associated with the same value match very well, which is not the case with the Gaussian joint PDFs. For softening random processes, the bicubic model is therefore easy to be implemented, useful for representing joint PDFs, and accurate to represent various joint PDFs.

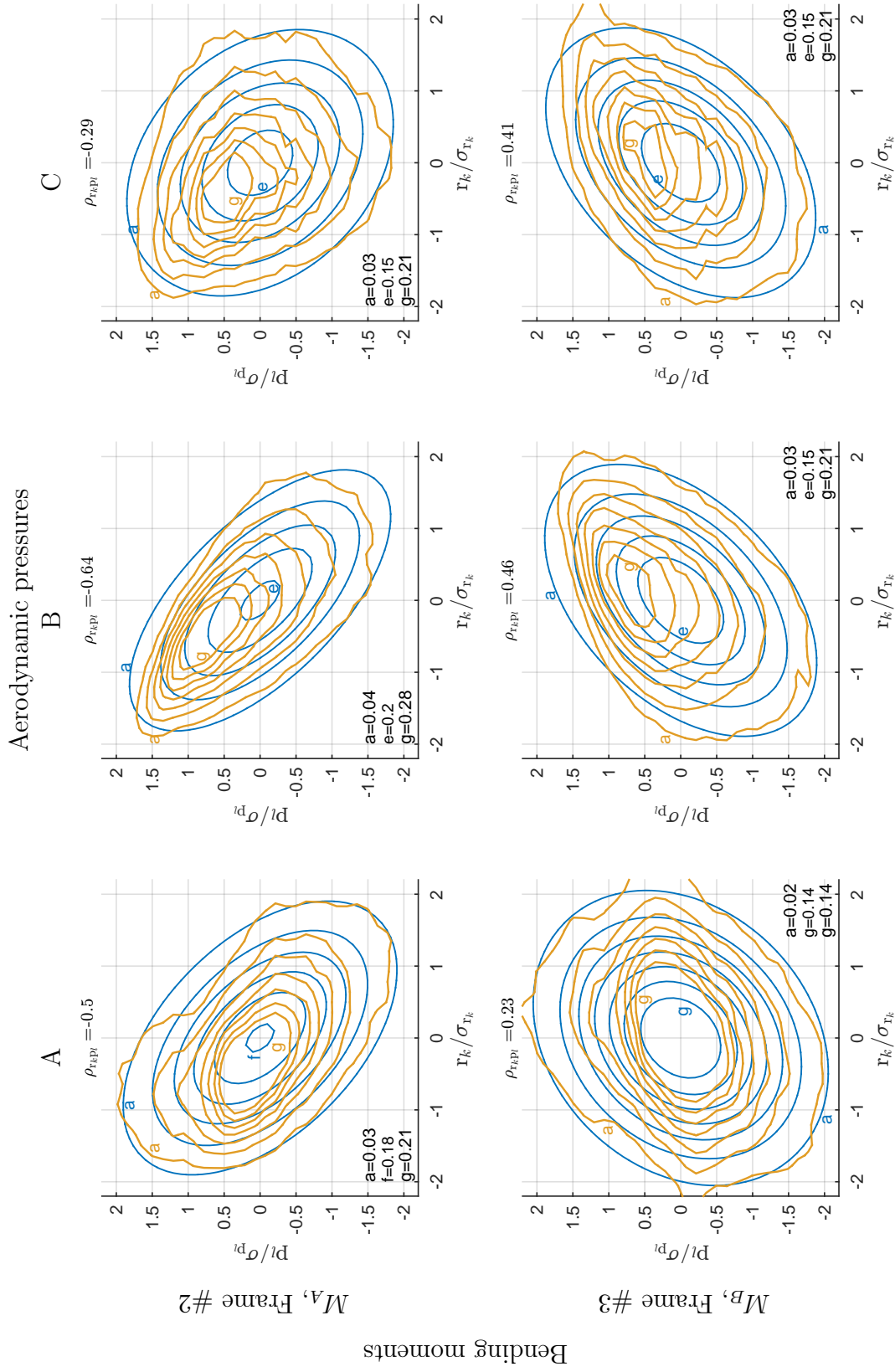


Figure VI.112: Contours of joint load-response PDFs. Kernel density estimator (obtained with the kd2d Matlab function freely available, [Botev et al. \(2010\)](#)) in orange and Gaussian joint PDFs in blue.

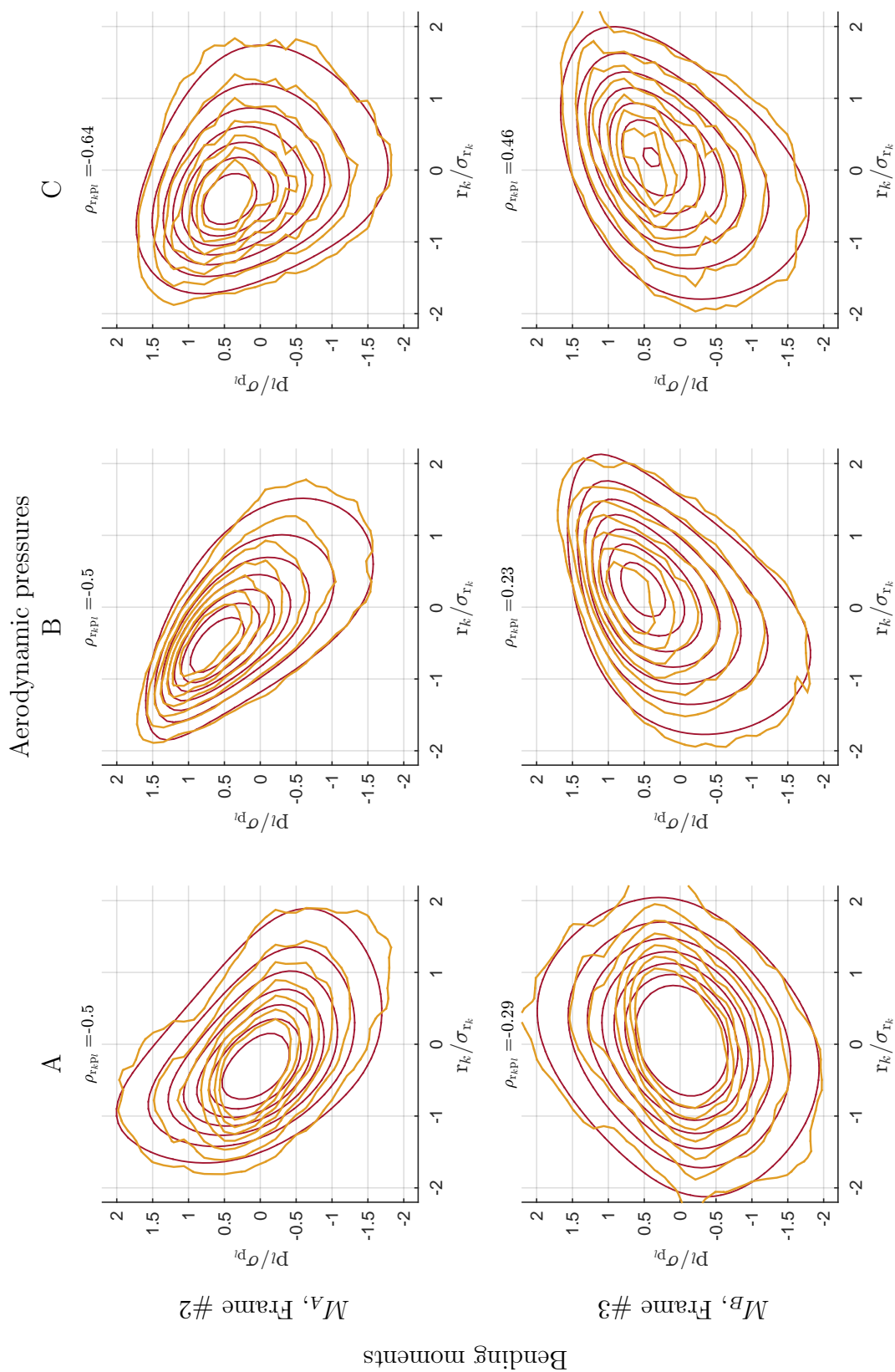


Figure VI.113: Contours of joint load-response PDFs. Kernel density estimator (obtained with the kd2d Matlab function freely available, [Botev et al. \(2010\)](#)) in orange and bicubic model for the joint PDFs in burgundy.

### VI.5.3 ESWLs

This example aims at comparing ESWLs computed with 3 different methods: the common conditional sampling technique, the Gaussian (LRC method) and the non-Gaussian formulation (CEL method with bicubic model), see Sections IV.3, IV.4 and IV.7, respectively. The magnitude of the coefficients,  $\alpha^{(e,m)}$  and  $\beta^{(e,m)}$ , applied to satisfy the envelope and non-overestimation conditions are compared to assess the formulation efficiency, i.e., those with the coefficients closest to unity are considered as more efficient. For the usual sampling technique, the load scaling coefficient  $\alpha^{(e,m)}$  has to be understood as the ratio between the envelope and the one that would have been obtained from realisations.

Figure VI.114 illustrates the surfaces of influence, load-response correlation coefficients and response-response correlation coefficients for the two considered bending moments A (min) and B (max). The load-response correlation and the response-response correlation coefficients help understanding the ESWL and structural response patterns, respectively. For example, the ESWL associated with response A produces the envelope value of the bending moment at the left support (Frame #2); furthermore bending moments close to their envelope values are also expected in both frames at the connection between columns and beams and at mid-span where the correlation coefficients are large. This is confirmed in Figure VI.116.

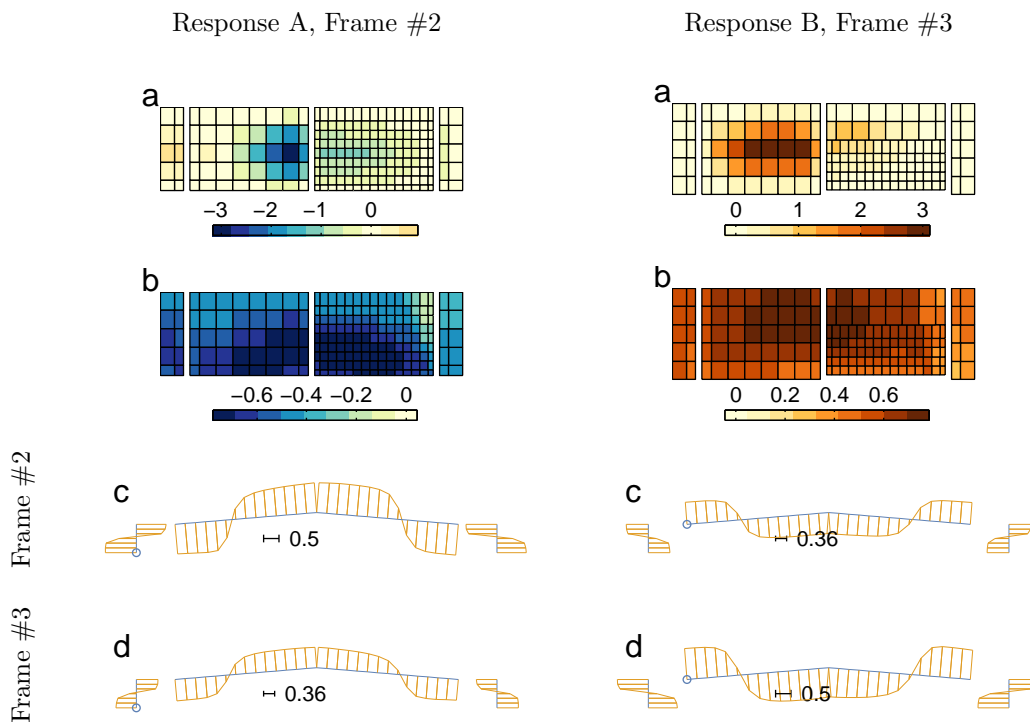


Figure VI.114: (a) Surface of influence, (b) load-response correlation coefficients and response-response correlation coefficients in (c) Frame #2 and in (d) Frame #3.

Figure VI.115 illustrates the ESWLs  $\mathbf{c}_p^{(e,m)}$  associated with the mean largest minimum and maximum of the considered responses A and B, respectively. First, third and fourth columns illustrate the original ESWLs, the coefficients  $\beta^{(e,m)}$  and the adjusted ESWLs. Also the coefficients  $\alpha^{(e,m)}$  are given for each method. For response A, the three methods

produce original (unadjusted) ESWLs which have similar patterns with slight differences in magnitude. This is not the case for the response B, for which the leading edge is less loaded with the ESWL computed from the sampling technique (a) than with the two other methods (b,c).

The target bending moment A is underestimated with the original ESWLs  $\mathbf{c}_p^{(e,\min)}$ , i.e., the envelope value condition is satisfied with scaling coefficients larger than one, namely  $\alpha^{(e,\min)} = 1.13$  for the sampling technique and  $\alpha^{(e,\min)} = 1.10$  for the CEL method. Nevertheless the target bending moment B is underestimated with the sampling technique ( $\alpha^{(e,\max)} = 1.12$ ) and slightly overestimated ( $\alpha^{(e,\max)} = 0.98$ ) with the CEL method.

The range of variation for coefficients  $\beta^{(e,m)}$  is also larger for response A (up to 1.8) than for response B. For both responses, the coefficients  $\beta^{(e,m)}$  obtained with the sampling technique and the CEL method are lower than those necessary for the LRC method. For response B, the coefficients  $\beta^{(e,m)}$  obtained with the sampling technique and the CEL method are close to one, i.e., the non-overestimation condition is nearly fulfilled under the scaled ESWL  $(\alpha \mathbf{c}_p)^{(e,\max)}$ ; slight adjustments are sufficient. Conversely for the LRC method, a larger range of variation for the coefficients  $\beta^{(e,m)}$  is necessary.

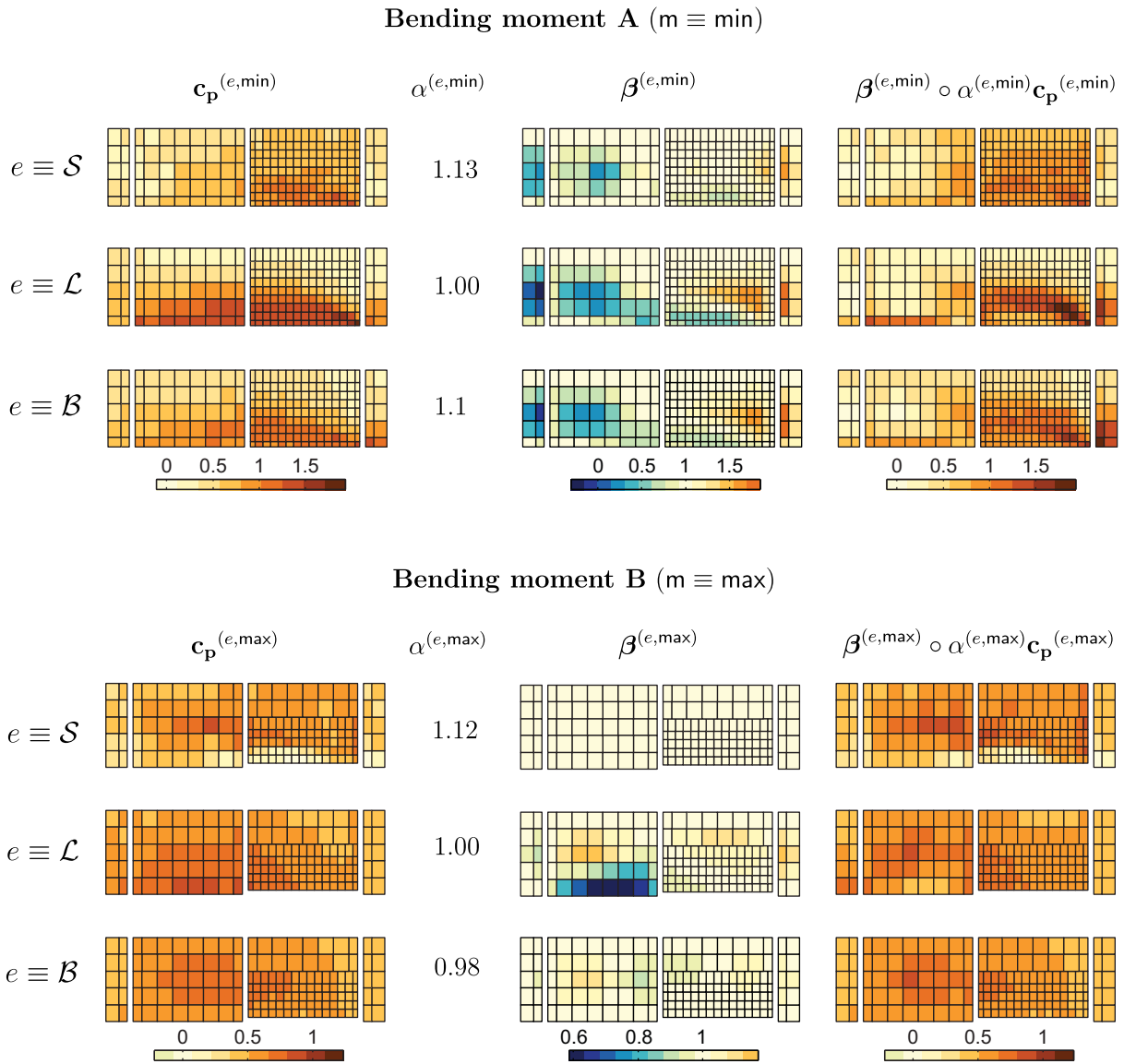


Figure VI.115: original (left) and adjusted (right) ESWLs and coefficients  $\alpha^{(e,m)}$  and  $\beta^{(e,m)}$  for the bending moments A ( $m \equiv \min$ ) and B ( $m \equiv \max$ ). Conditional sampling technique ( $e \equiv \mathcal{S}$ ), LRC method ( $e \equiv \mathcal{L}$ ) and conditional expected load method with the bicubic model ( $e \equiv \mathcal{B}$ ).

Figures VI.116-VI.117 illustrate the static bending moments in the structure under the two scaled ESWLs  $(\alpha \mathbf{c}_p)^{(e,m)}$  associated with the bending moments A and B, respectively. The bending moments under the original ESWL and under the adjusted ESWL provide very similar profiles. The responses under the three kinds of loadings (original, scaled and adjusted) are distinguished with a discrepancy indicator  $\varepsilon^{(e)}$  that measures the relative differences between the envelopes  $(\mathbf{r}^{(\max)}, \mathbf{r}^{(\min)})$  and the responses  $\mathbf{r}^{(e,m)}$  under the ESWLs, such as

$$\varepsilon^{(e)} = \max\{(\mathbf{r}^{(e,m)} - \mathbf{r}^{(\min)}) \div \mathbf{r}^{(\min)}, (\mathbf{r}^{(e,m)} - \mathbf{r}^{(\max)}) \div \mathbf{r}^{(\max)}\},$$

where division is performed element by element. Three such indicators exist and are represented in Figs. VI.116 and VI.117 with the following markers under : original ESWL  $\mathbf{c}_p^{(e,m)}$  (x marker), scaled ESWL  $(\alpha \mathbf{c}_p)^{(e,m)}$  (o marker) and adjusted ESWL  $(\beta \circ \alpha \mathbf{c}_p)^{(e,m)}$  (square marker).

For the bending moment A (in Frame #2) and before adjustment (Figure VI.116, o markers), overestimations do not occur in sections adjacent to the considered bending moment but in other parts of Frame #2, where the correlation with the bending moment A is large. No overestimation occurs in Frame #3 when considering the ESWLs associated with bending moment A.

For the bending moment B (in Frame #3) and before adjustment (Figure VI.117, o markers), largest overestimations occur with the LRC method, hence the highest range of variation for the coefficients  $\beta^{(e,\max)}$ . With the LRC method, no overestimation occurs in Frame #3 but very large overestimations (nearly 40%) occur in Frame #2. These overestimations take place where (i) correlation with the bending moment B is large, Figure VI.114, and (ii) peak factors, Figure VI.107, are very different, as demonstrated by (IV.7.13).

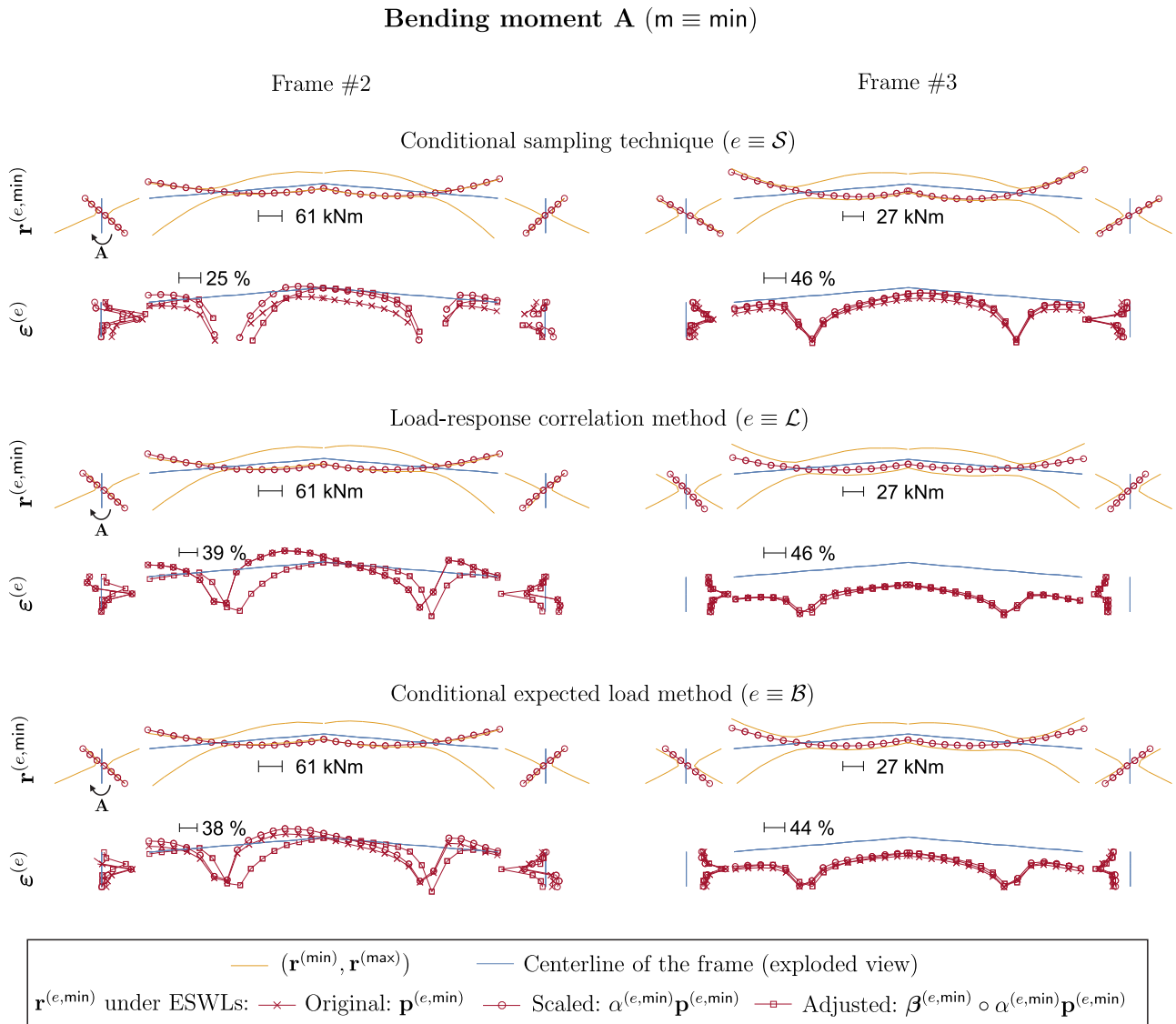


Figure VI.116: Static bending moments  $\mathbf{r}^{(e, \min)}$  under scaled ESWLs associated with bending moment A. Relative differences  $\varepsilon^{(e)}$  between the envelope of the bending moments and the bending moments obtained under the original, the scaled and the adjusted ESWLs. Positive relative differences (overestimations) are depicted outside the frame. Large (unimportant) negative relative differences (depicted inside the frame) are not shown for sake of clarity.



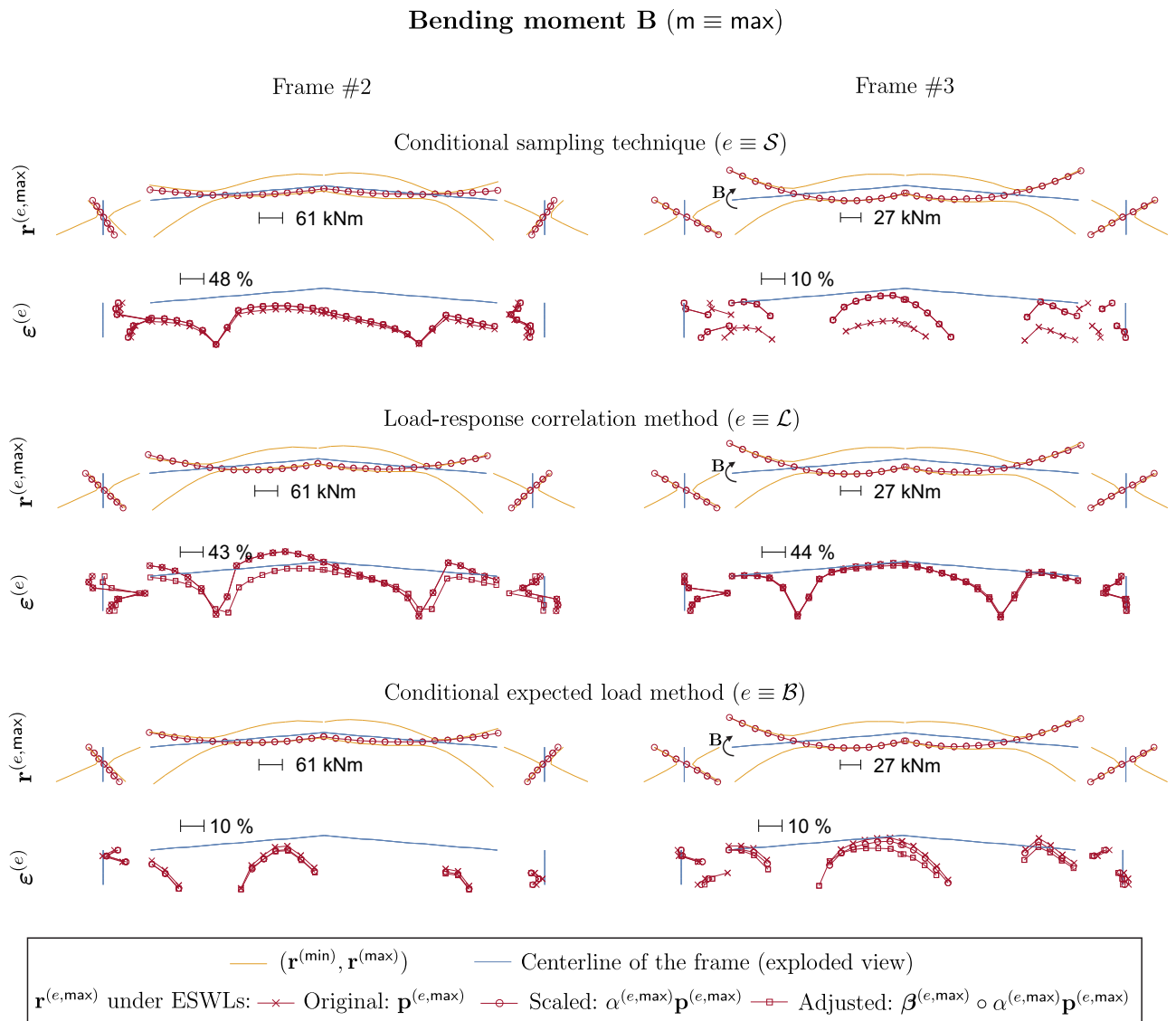


Figure VI.117: Static bending moments  $\mathbf{r}^{(e, \max)}$  under scaled ESWLs associated with bending moment  $B$ . Relative differences  $\varepsilon^{(e)}$  between the envelope of the bending moments and the bending moments obtained under the original, the scaled and the adjusted ESWLs. Positive relative differences (overestimations) are depicted inside the frame. Large (unimportant) negative relative differences (depicted inside the frame) are not shown for sake of clarity.

We have also computed the ESWLs for each bending moment (in Frames #2 and #3) and for both envelopes (min and max). Figure (VI.118) illustrates the associated scaling coefficients  $\alpha^{(e,m)}$  and also maximum of the relative differences  $\epsilon^{(e)}$  to the envelope of the static responses under the scaled ESWLs ( $\alpha \mathbf{c}_p$ )<sup>(e,m)</sup>. Similar range of variation for the scaling coefficients  $\alpha^{(e,m)}$  are observed for the sampling technique (filled dot marker) and the CEL method (filled square marker). The fact that the envelope value condition is not fulfilled is an inherent drawback of the CEL method while it is due to the low number of 10-min observation windows for the sampling technique. Indeed, provided that the peak factor used for the envelope is the same as the actual one, i.e.,  $\mathbf{g}^{(m)} = \mathbf{g}^{(\mathcal{S},m)}$ , no scaling coefficient would be needed. We also recall that the scaling coefficients  $\alpha^{(e,m)}$  are exactly equal to unity for the LRC method. In terms of overestimation of the envelopes  $\mathbf{r}^{(e,m)}$  under the scaled ESWLs ( $\alpha \mathbf{c}_p$ )<sup>(e,m)</sup>, it is observed that (i) in Frame #2, larger overestimations are observed (up to 50%) with the LRC-method (cross markers) than with the two other methods and (ii) in Frame #3, large overestimations are only observed with the LRC-method while the other two methods perform very well. Note that the sampling technique performs slightly better than the CEL method, especially for the bending moments in Frame #2.

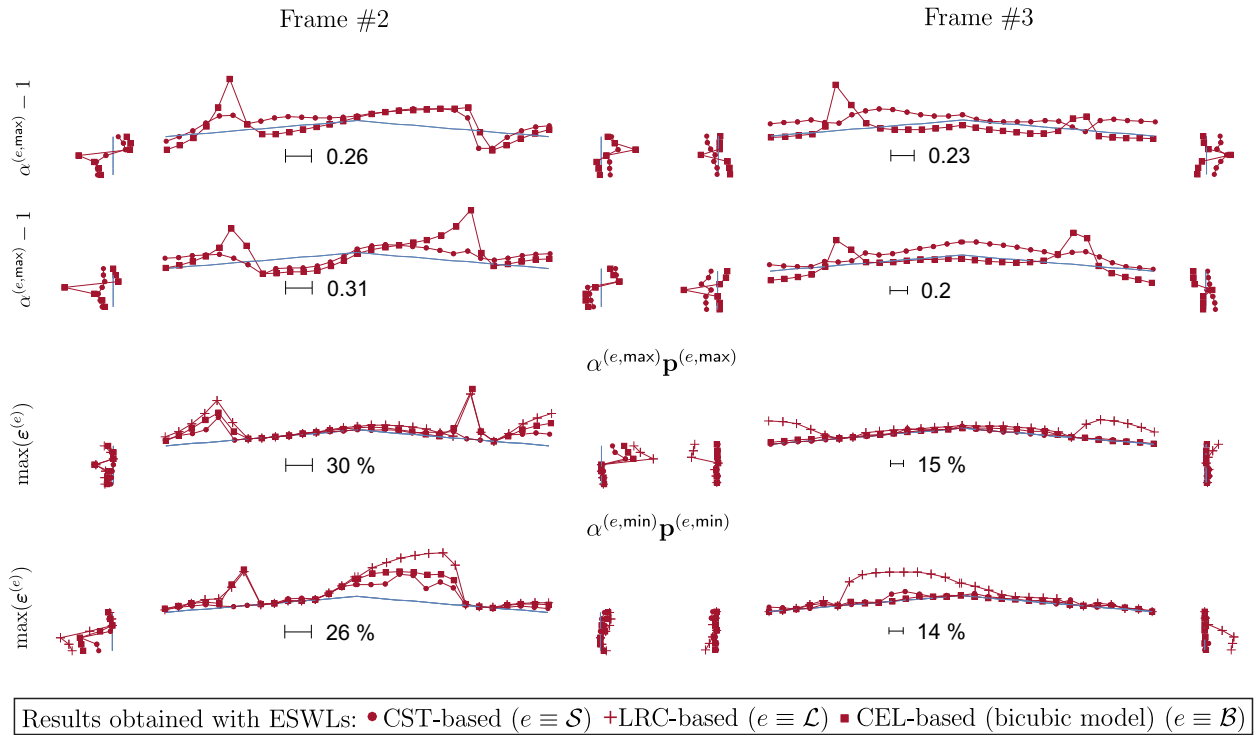


Figure VI.118: Coefficients  $\alpha^{(e,m)}$  that scale the original ESWLs computed for both envelope values for each bending moment in Frame #2 and Frame #3. Maximum of the relative differences  $\epsilon^{(e)}$  to the envelope of the static responses under scaled ESWLs computed for each bending moment in Frame #2 and Frame #3.

To summarize, the non-overestimation condition seems to be more easily fulfilled with the ESWLs derived from the sampling technique and the CEL method than with the LRC method. The extension of the original LRC method to a non-Gaussian formalism improves the fulfillment of the non-overestimation condition, i.e., smaller coefficients  $\beta^{(e,m)}$  are necessary than those obtained with the LRC method.

In the light of these results, the use of ESWLs with non-Gaussian structural responses should receive more attention and we should opt for the ESWLs derived from the sampling technique or the proposed CEL method instead of the LRC method.

#### VI.5.4 Envelope reconstruction with PSWLs

In this Section PSWLs are not derived from adjusted ESWLs but from the original ones. Indeed, even if ESWLs do not fulfill the envelope value nor the non-overestimation condition, PSWLs anyway have to be normalized to fulfill the tangency condition (III.4.4). Furthermore in case of large non-Gaussianity, adjusted loadings may be significantly different from the original ones, as shown in the previous Section. However, both ESWL bases are investigated in Section VI.5.5 and it was observed that the efficiency of the PSWLs for the envelope reconstruction problem is worse, considering adjusted ESWLs rather than the original ones for the SVD operation. There is, in our understanding, no mathematical proof that adjustment of ESWL prior to the SVD decomposition provides a faster reconstruction of the envelope. The demanding computation of the local coefficients  $\beta^{(e,m)}$  is therefore not justified. Thence we recommend the use of the original ESWLs for computing PSWLs and only this approach is illustrated in the sequel.

For the envelope reconstruction problem, we choose an acceptable overall reconstruction  $\mathcal{R}^t$  of 95% and an acceptable underestimation  $\tilde{\epsilon}^t$  of  $-15\%$ .

#### Envelope reconstruction

This section assesses the envelope reconstruction efficiency of the bending moments in the eleven frames using combinations of a limited number of PSWLs. The normalized cumulative summation of the principal coordinates  $S_{ii}$  is shown in Figure VI.119.

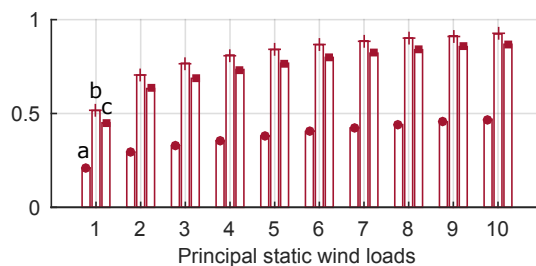


Figure VI.119: Normalized cumulative summation of the principal coordinates of the principal loadings. (a) Conditional sampling technique, (b) LRC method, and (c) CEL method (bicubic model) based PSWLs.

The LRC method has the largest principal coordinates while the sampling technique has the smallest. The ESWL basis obtained with the conditional sampling technique are actually more dissimilar than in the two other approaches. This is explained by the fact that the ESWLs are sampled from pressure field and the limitation on the small number of 10-min observation windows. It makes it such that there is more variability in the ESWLs associated with different responses, than what the LRC or the CEL approaches—based on smooth models—provide. A solution to address the issue is the (costly) repetition of

experiments. For example, if the number  $n_T$  was increased, the variability of the wind load patterns  $\mathbf{p}^{(S,m)}$  between structural responses that are well correlated would decrease.

Figure VI.120 illustrates the first four normalized PSWLs  $\mathbf{C}_{\mathbf{p}}^{(\mathcal{P},1)}$  with coefficients  $\alpha_i^{(\mathcal{P},1)}$ , see (III.4.2). The first three principal loadings show important similarities in their pattern and magnitude for the three methods while the fourth principal loading obtained with the sampling technique is completely different. The first principal loading produces a suction on the entire roof while the second and third exhibit asymmetric patterns, between the windward edge and the roof behind and between the western and eastern parts of the roof, respectively. The second normalization for any PSWL is obtained with

$$\mathbf{C}_{\mathbf{p},i}^{(\mathcal{P},2)} = -\frac{\alpha_i^{(\mathcal{P},2)}}{\alpha_i^{(\mathcal{P},1)}} \mathbf{C}_{\mathbf{p},i}^{(\mathcal{P},1)},$$

see (III.4.2). Note that the ratio  $\alpha_i^{(\mathcal{P},2)}/\alpha_i^{(\mathcal{P},1)}$ , given in Figure VI.120, has a large range of variation [0.49 1.79] here while it is equal to one in a Gaussian framework.

Figure VI.121 illustrates the static bending moments under  $\mathbf{C}_{\mathbf{p},1}^{(\mathcal{P},1)}$ ,  $\mathbf{C}_{\mathbf{p},1}^{(\mathcal{P},2)}$ ,  $\mathbf{C}_{\mathbf{p},3}^{(\mathcal{P},1)}$  and  $\mathbf{C}_{\mathbf{p},3}^{(\mathcal{P},2)}$  in Frames #2 and #3 as well as relative differences between the static responses  $\mathbf{R}_i^{(\mathcal{P},1)}$  and the envelope, defined as

$$\varepsilon_i^{(\mathcal{P},1)} = \max\left\{\left(\mathbf{R}_i^{(\mathcal{P},1)} - \mathbf{r}^{(\min)}\right) \div \mathbf{r}^{(\min)}, \left(\mathbf{R}_i^{(\mathcal{P},1)} - \mathbf{r}^{(\max)}\right) \div \mathbf{r}^{(\max)}\right\}.$$

Bending moments under the PSWLs computed with the LRC-method and the CEL method are almost similar while disparities are observed with the bending moments under  $\mathbf{C}_{\mathbf{p},1}^{(\mathcal{P},1)}$  and  $\mathbf{C}_{\mathbf{p},1}^{(\mathcal{P},2)}$  computed with the conditional sampling technique. For the sampling technique, lower relative differences are observed under  $\mathbf{C}_{\mathbf{p},1}^{(\mathcal{P},1)}$  in comparison with the two other methods, but larger relative differences are observed under  $\mathbf{C}_{\mathbf{p},1}^{(\mathcal{P},2)}$ . Notice that the PSWLs  $\mathbf{C}_{\mathbf{p},3}^{(\mathcal{P},1)}$  and  $\mathbf{C}_{\mathbf{p},3}^{(\mathcal{P},2)}$  produce large bending moments at the specific sections where the bending moments under  $\mathbf{C}_{\mathbf{p},1}^{(\mathcal{P},1)}$  and  $\mathbf{C}_{\mathbf{p},1}^{(\mathcal{P},2)}$  are rather low, e.g., at mid-height of the columns and at quarter-span and three quarter-span of the roof.

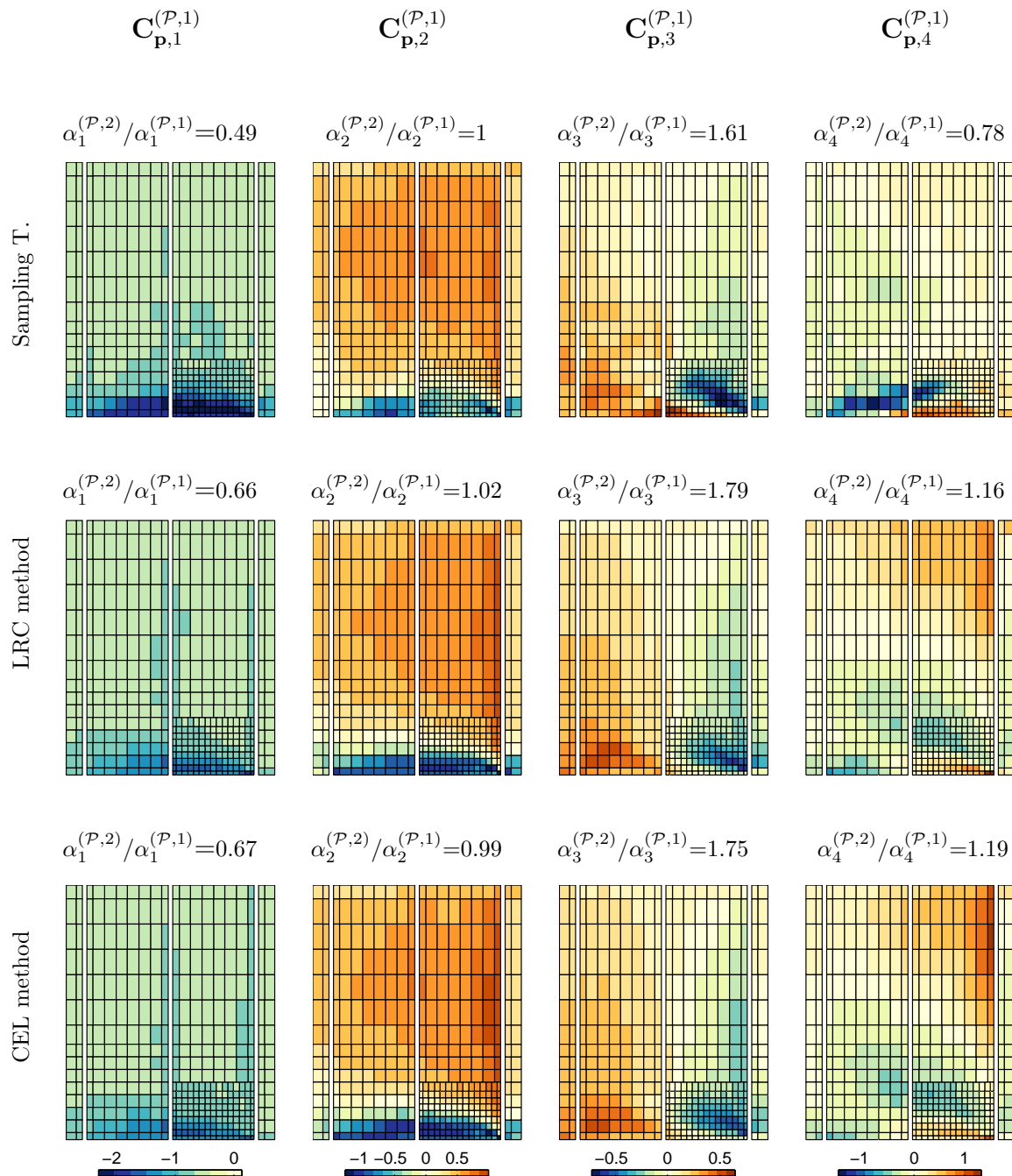


Figure VI.120: Aerodynamic coefficients for the first four normalized PSWLs (the PSWL normalized by  $\alpha_i^{(P,1)}$ , see (III.4.2), are represented; the PSWL normalized by  $\alpha_i^{(P,2)}$  are obtained by multiplication by  $-\alpha_i^{(P,2)}/\alpha_i^{(P,1)}$ ). Normalization is done with  $\hat{\varepsilon} = 0\%$ .

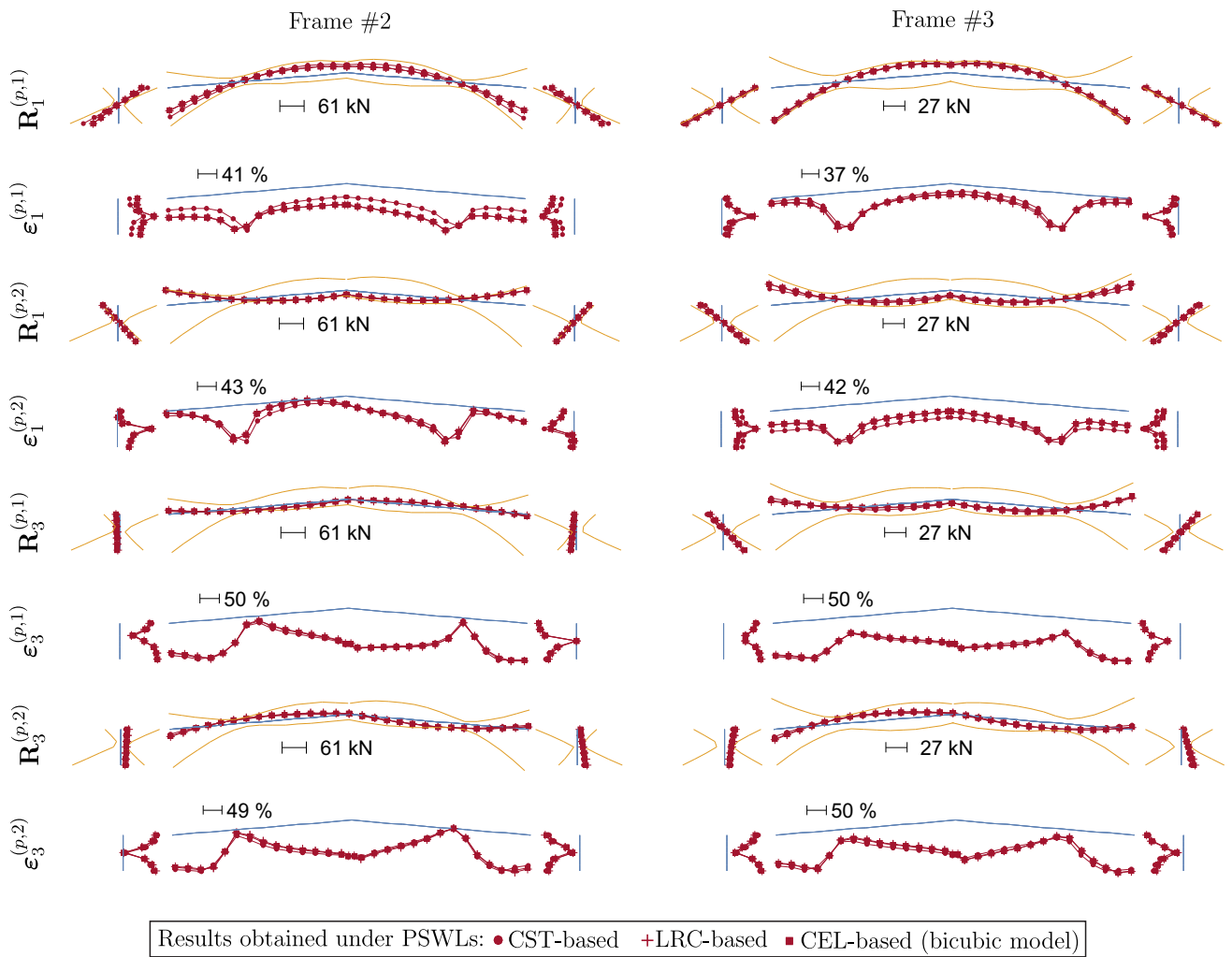


Figure VI.121: Static bending moments and relative differences with the envelope under  $C_{p,1}^{(p,1)}$ ,  $C_{p,1}^{(p,2)}$ ,  $C_{p,3}^{(p,1)}$  and  $C_{p,3}^{(p,2)}$  in Frames #2 and #3. (ERP parameter:  $\hat{\varepsilon} = 0\%$ ).

Figure VI.122 illustrates the reconstructed envelope with ten load cases: (i) the first five PSWLs along with both normalizations are applied successively (no combinations) and (ii) with optimized combinations of the first four PSWLs. As expected, the reconstructed envelopes in both frames have the same range of relative errors, since PSWLs and combinations thereof aim at a global reconstruction of the bending moments in the whole structure (eleven frames). The reconstructed envelope is not satisfactory applying the first 5 PSWLs without combination: relative errors are large, up to -65%. For the same number of load cases, ten combinations of the first 4 PSWLs produce a satisfactory reconstruction of the envelope; the largest relative errors, up to -40%, are observed in sections where the bending moments are low.

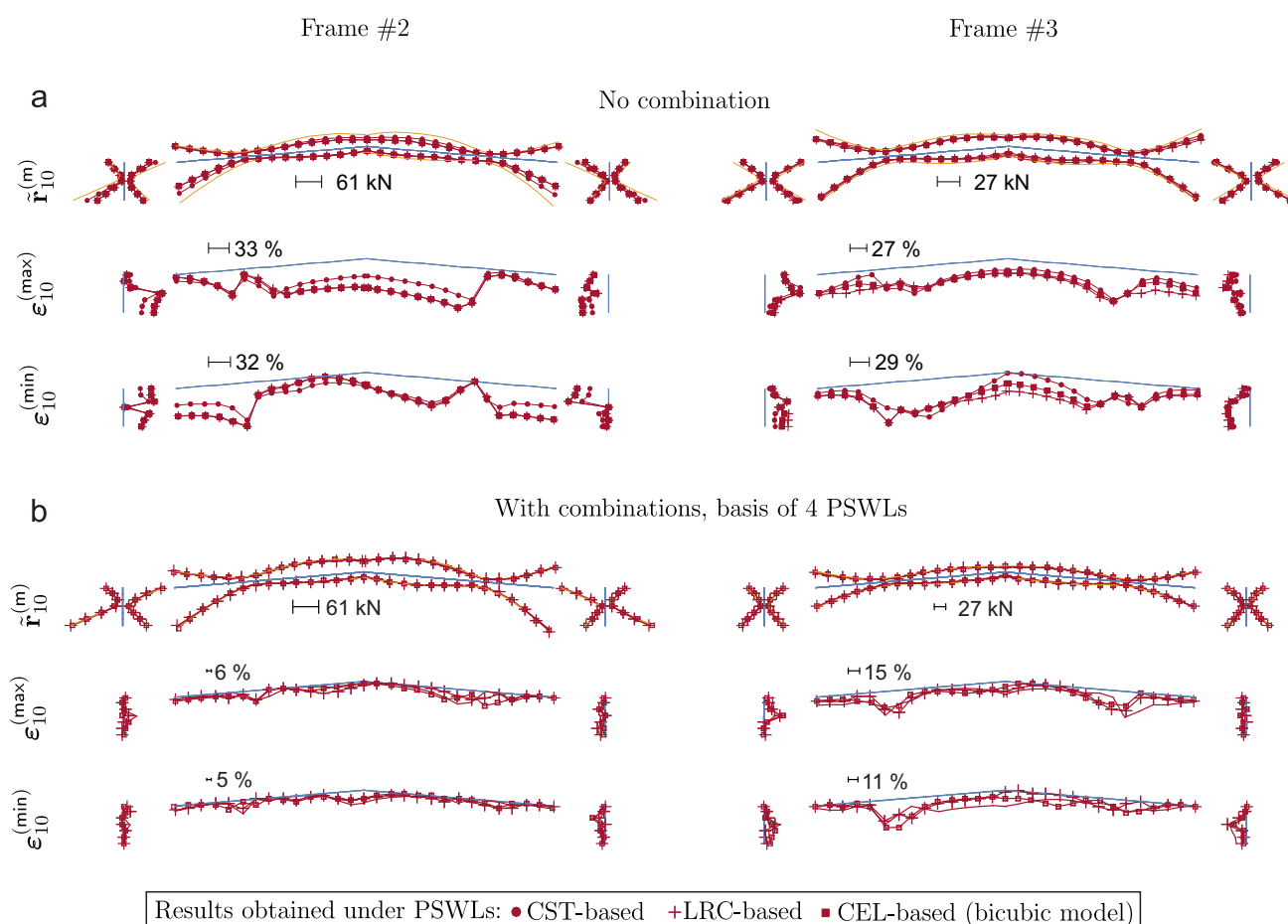


Figure VI.122: Reconstructed envelope and associated relative errors with ten load cases. (ERP parameter:  $\hat{\epsilon} = 0\%$ ,  $\gamma = 1$ ).

Even if the largest relative errors are identified for small bending moments, they are larger than the acceptable underestimation  $\tilde{\varepsilon}^t = -15\%$ . An acceptable overestimation of  $\hat{\varepsilon} = 15\%$  is therefore accepted next to satisfy more easily the underestimation condition.

The indicator of reconstruction  $\mathcal{R}_{(k)}$  gives a global picture of the whole reconstruction of the bending moments in the entire structure, i.e., in all eleven frames. The evolution of  $\mathcal{R}_{(k)}$  is depicted as a function of the number of load cases (from 1 to 25) derived by successive applications of ESWLs, PSWLs (no combinations) and combinations thereof (2, 4, 6 and 8 PSWLs are combined), see Figure VI.123. The evolution of  $\mathcal{R}_{(k)}$  features a slow monotonic increase.

PSWLs obtained with the conditional sampling technique performs slightly worse than with the two other approaches but this is not significant. Applying PSWLs without combination gives a value of  $\mathcal{R}_{(k)}$  around 80% for 10 load cases and 10 combinations of the first 2 PSWLs bring a significant improvement of +10%. Four or five combinations of at least 4 PSWLs are required to satisfy the target reconstruction  $\mathcal{R}^t = 95\%$  and this is three times lower than the number of ESWLs required for the same purpose.

Figure VI.124 shows the largest relative error indicator. PSWLs obtained the conditional sampling technique performs worse than the two others since the underestimation condition is not fulfilled with 25 load cases. The underestimation condition is fulfilled with 20 and 11 load cases by considering combinations of the first 8 PSWLs obtained with the LRC and CEL methods, respectively. Therefore, the latter PSWL basis obtained with CEL-based ESWLs perform better than the two other PSWLs bases obtained with CST-based and LRC-based ESWLs.



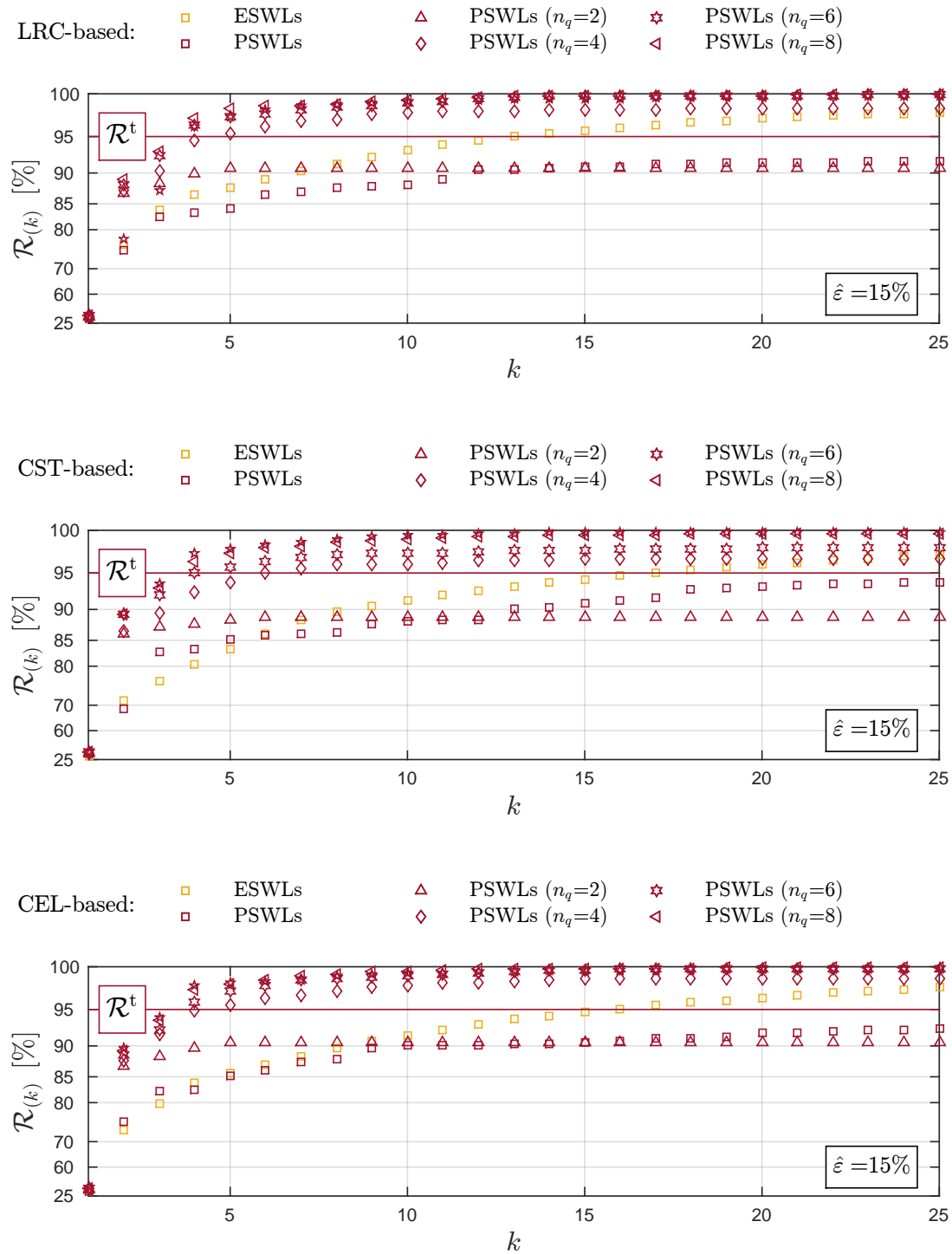


Figure VI.123: Evolution of the reconstruction indicator  $\mathcal{R}_{(k)}$  as a function of the number of load cases. (ERP parameters:  $\hat{\varepsilon} = 15\%$ ,  $\gamma = 1$ ).

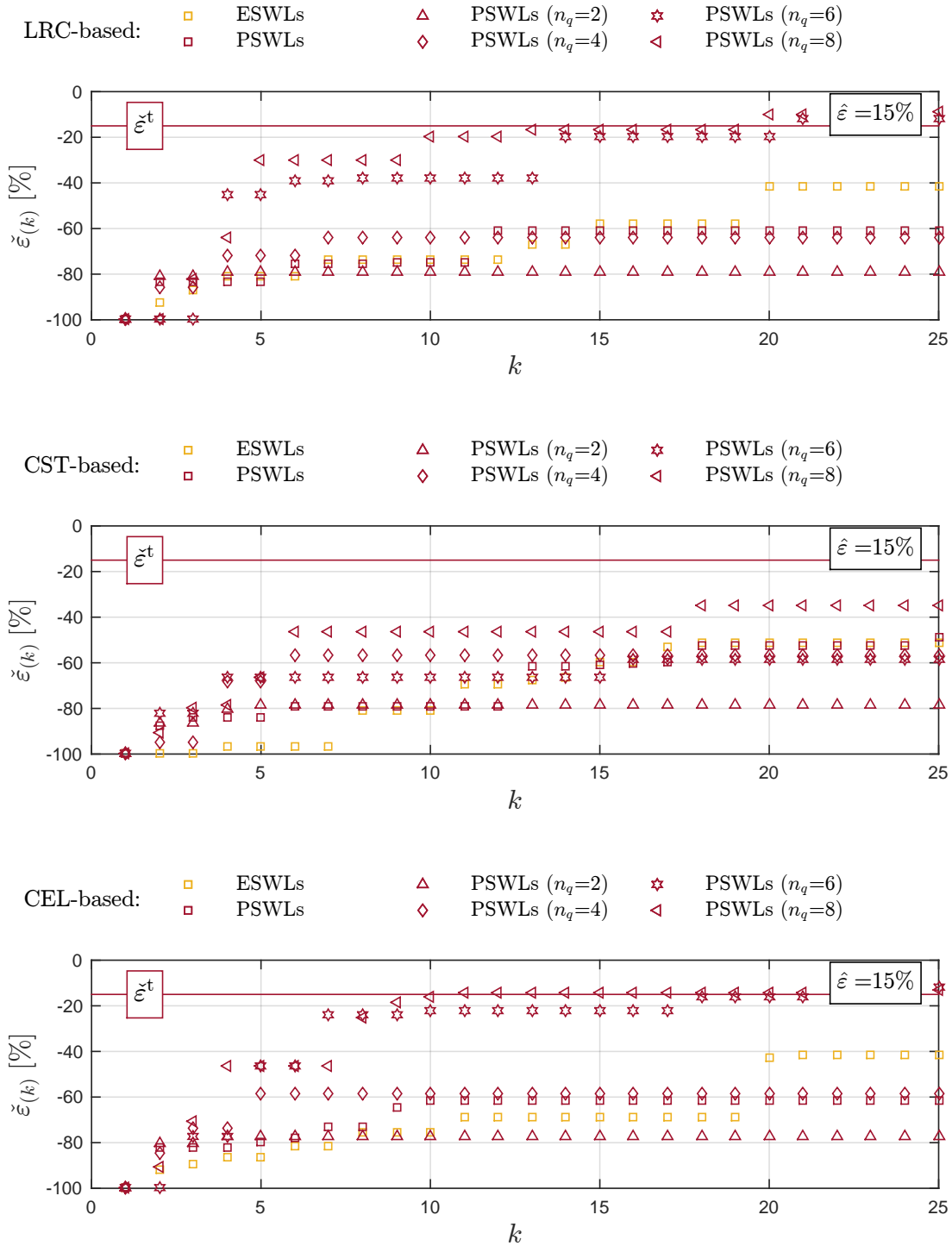


Figure VI.124: Evolution of the largest relative error indicator  $\tilde{\epsilon}(k)$  as a function of the number of load cases. (ERP parameters:  $\hat{\epsilon} = 15\%$ ,  $\gamma = 1$ ).

### VI.5.5 Automatic procedure to obtain SWLs ensuring no underestimation

The automatic procedure described in Section V.4 is implemented. In Section VI.3.6, the ERP with parameters  $\tilde{\varepsilon}^t = -15\%$  and  $\hat{\varepsilon} = 15\%$  is solved with combinations of the first  $n_q = 8$  PSWLs. Figure VI.119 illustrates the normalized cumulative summation of the principal coordinates  $S_{ii}$ , see (V.3.2), for the primary PSWL basis. The first  $n_q = 8$  PSWLs reproduce approximately 90% of the total sum of the principal coordinates. The ratio  $\lambda^P$  is therefore firstly set equal to 0.90. The initial set of combination coefficients is randomly generated with  $n_c = 6000$ , see Section III.5.2.

Table VI.15 gives the number of SWLs to solve the ERP with the three different options (detailed in Section III.3.5) and for two values of the final acceptable overestimation  $\hat{\varepsilon}'$ . These results are obtained with original CEL-based PSWLs. The option B fails to satisfy the target acceptable underestimation  $\tilde{\varepsilon}^t$ , see the largest relative error indicator  $\tilde{\varepsilon}_{(k)}$  for  $k = n_s$ . The option A performs badly in comparison with the number of SWLs obtained by applying option C. In the sequel, the option C is therefore only studied. Globally, two updatings of the PSWL basis are sufficient.

| Options | No underestimation and $\hat{\varepsilon}' = 25\%$ |                     |           |       |          |              |                               |      |
|---------|--|---------------------|-----------|-------|----------|--------------|-------------------------------|------|
|         | $\tilde{\varepsilon}^t$                            | $\hat{\varepsilon}$ | $n_s$     | $n_p$ | $n_q$    | $n_{r(n_s)}$ | $\tilde{\varepsilon}_{(n_s)}$ | CPU  |
| A       | 0%   | 25%                 | 27        | 2     | [14,1]   | 0            | 0%                            | 1min |
| B       | -20%   | 0%                  | 19        | 3     | [14,5,1] | 1            | -23%                          | 1min |
| C       | -11%   | 11%                 | <b>14</b> | 2     | [14,5]   | 0            | ✓                             | 1min |

| Options | No underestimation and $\hat{\varepsilon}' = 10\%$ |                     |           |       |          |              |                               |      |
|---------|--|---------------------|-----------|-------|----------|--------------|-------------------------------|------|
|         | $\tilde{\varepsilon}^t$                            | $\hat{\varepsilon}$ | $n_s$     | $n_p$ | $n_q$    | $n_{r(n_s)}$ | $\tilde{\varepsilon}_{(n_s)}$ | CPU  |
| A       | 0%   | 10%                 | 44        | 2     | [14,5]   | 0            | ✓                             | 1min |
| B       | -9.1%  | 0%                  | 28        | 3     | [14,7,1] | 1            | -14%                          | 1min |
| C       | -4.76%   | 4.76%               | <b>30</b> | 2     | [14,5]   | 0            | ✓                             | 1min |

Table VI.15: Number of SWLs to solve the ERP with the three different options (see Section III.3.5) and for two values of the final acceptable overestimation  $\hat{\varepsilon}'$ . ERP parameters:  $\hat{\varepsilon} = 4.76\%$ ,  $\tilde{\varepsilon}^t = -4.76\%$ ,  $\gamma = 1$ ,  $\lambda^P = 0.90$  and  $n_c = 6000$ . The symbol ✓ means that the acceptable underestimation is satisfied. Results obtained with combinations of the original CEL-based PSWLs.

Figure VI.125 illustrates the evolution of the number of responses  $n_{r(k)}$  with  $\varepsilon_{(k)}^{(m)} < \tilde{\varepsilon}^t$  as a function of the number of load cases,  $\varepsilon$  for the ERP parameters  $\hat{\varepsilon} = 4.76\%$ ,  $\tilde{\varepsilon}^t = -4.76\%$ .

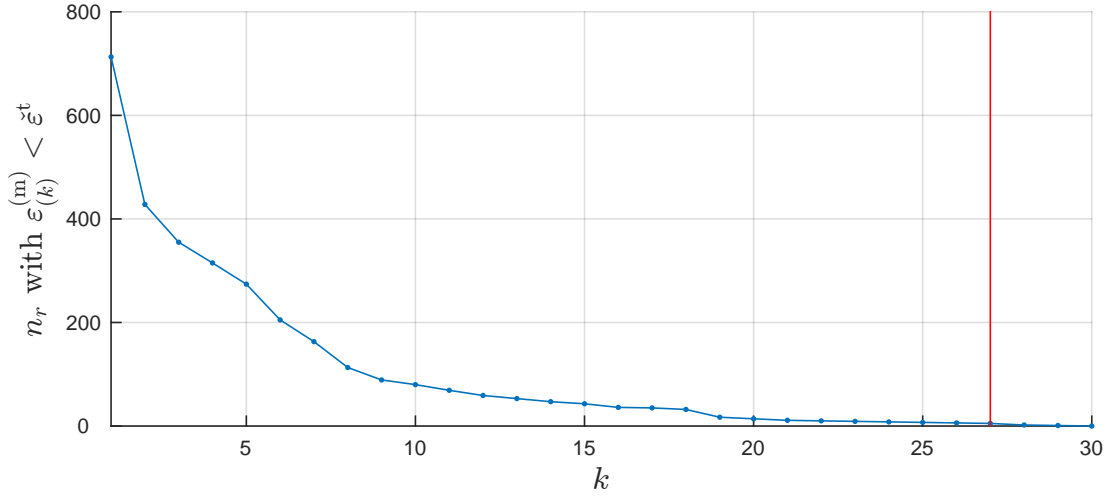


Figure VI.125: Evolution of the number of responses  $n_{r(k)}$ , see page 127, with  $\varepsilon_{(k)}^{(m)} < \varepsilon^t$  as a function of the number of load cases. ERP parameters:  $\hat{\varepsilon} = 4.76\%$ ,  $\varepsilon^t = -4.76\%$ ,  $\gamma = 1$ ,  $\lambda^P = 0.90$ ,  $n_c = 6000$ . Vertical red lines correspond to an updating of the PSWL basis. Results obtained with combinations of original CEL-based PSWLs.

The influence of the ERP parameters  $\lambda^P$  and  $n_c$  on the number of SWLs  $n_s$  is reported in Table VI.16. With  $\lambda^P = 0.85$ , the automatic procedure fails to satisfy the target acceptable underestimation  $\varepsilon^t = -4.76\%$ . Additionally, an increase of the parameter  $\lambda^P$  or  $n_c$  does not necessarily correspond to a decrease of the number of SWLs  $n_s$ . The ERP parameters  $\lambda^P=0.90$  and  $n_c = 6000$  chosen at first are satisfactory.

| $\lambda^P$ | $n_c$ | No underestimation and $\hat{\varepsilon}' = 25\%$ |       |              |                               |      | No underestimation and $\hat{\varepsilon}' = 10\%$ |       |              |                               |      |
|-------------|-------|--|-------|--------------|-------------------------------|------|--|-------|--------------|-------------------------------|------|
|             |       | $n_s$  | $n_q$ | $n_{r(n_s)}$ | $\check{\varepsilon}_{(n_s)}$ | CPU  | $n_s$  | $n_q$ | $n_{r(n_s)}$ | $\check{\varepsilon}_{(n_s)}$ | CPU  |
| 0.85        | 6000  | 13   | 1     | 0            | ✓                             | 1min | 42   | 4     | 1            | -6%                           | 1min |
|             | 12000 | 13   | 1     | 0            | ✓                             | 1min | 42   | 4     | 1            | -6%                           | 1min |
| 0.90        | 6000  | <b>14</b>  | 2     | 0            | ✓                             | 1min | <b>30</b>  | 2     | 0            | ✓                             | 1min |
|             | 12000 | 10   | 1     | 0            | ✓                             | 1min | 29   | 2     | 0            | ✓                             | 1min |
| 0.95        | 6000  | 12   | 2     | 0            | ✓                             | 1min | 35   | 3     | 0            | ✓                             | 1min |
|             | 12000 | 13   | 2     | 0            | ✓                             | 1min | 31   | 1     | 0            | ✓                             | 1min |

Table VI.16: Number of SWLs to solve the ERP with option C (see Section III.3.5). Study of the influence of the ERP parameters  $\lambda^P$  and  $n_c$ . The symbol ✓ means that the acceptable underestimation is satisfied. Results obtained with combinations of original CEL-based PSWLs.

The efficiency of the envelope reconstruction problem based on combinations of PSWLs derived from original or adjusted ESWLs obtained with the LRC, CST or CEL methods is

summarized in Table VI.17. It is observed that the efficiency of the PSWLs for the envelope reconstruction problem is worse, considering adjusted ESWLs rather than the original ones for the SVD operation. Finally, the PSWL bases obtained with ESWLs derived from the conditional expected load and load-response correlation methods perform better than the PSWL basis obtained with ESWLs derived from the conditional sampling technique.

| PSWL basis         | No underestimation and $\hat{\varepsilon}' = 10\%$ |       |              |                               |      |
|--------------------|--|-------|--------------|-------------------------------|------|
|                    | $n_s$  | $n_q$ | $n_{r(n_s)}$ | $\check{\varepsilon}_{(n_s)}$ | CPU  |
| original LRC-based | 30   | 2     | 0            | ✓                             | 1min |
| adjusted LRC-based | 49   | 4     | 0            | ✓                             | 1min |
| original CST-based | 60   | 3     | 0            | ✓                             | 2min |
| adjusted CST-based | 64   | 4     | 0            | ✓                             | 2min |
| original CEL-based | 30   | 2     | 0            | ✓                             | 1min |
| adjusted CEL-based | 52   | 3     | 0            | ✓                             | 1min |

Table VI.17: Number of SWLs to solve the ERP with option C (see Section III.3.5). ERP parameters:  $\hat{\varepsilon} = 4.76\%$ ,  $\check{\varepsilon}^t = -4.76\%$ ,  $\gamma = 1$ ,  $\lambda^p = 0.90$ ,  $n_c = 6000$ . The symbol ✓ means that the acceptable underestimation is satisfied.

### VI.5.6 Summary

The non-Gaussianity of the aerodynamic pressures and the structural responses is accounted for in this third example. The problem of the reconstruction of an asymmetric envelope has been therefore investigated.

- First, three formulations of ESWLs have been studied. Inspired by the LRC method in which Gaussian conditional probability densities as well as their mean values are required, conditional expected SWLs obtained from a bicubic model have been derived, see Sections IV.7 and IV.8. Two other methods have been considered for comparison: the conditional sampling pressure technique and the original LRC method, see Sections IV.3 and IV.4, respectively.
- Second, in order to compare those methods, the two required properties of an ESWL have been investigated: the envelope value and non-overestimation conditions, see Section IV.2. Indeed, the studied ESWL formulations may not naturally satisfy these two conditions and a procedure in Section VI.5.1 is proposed to scale and adjust original ESWLs whenever necessary.
- Third, it has been illustrated that the LRC method may encounter some difficulties to satisfy the non-overestimation condition, i.e., large local coefficients have to be applied to the original ESWLs. Actually, the conditional sampling technique and the proposed CEL method with the bicubic model are better suited: they satisfy the non-overestimation condition without excessively distorting original ESWLs, i.e., adjusted ESWLs remain close to the original ones. Computing ESWLs and using them as such, we thus recommend the use of the CEL method or the sampling technique instead of the LRC method in case of non-Gaussian structural responses.
- Fourth, concerning the envelope reconstruction efficiency, no significant differences on the overall reconstruction are observed between PSWLs obtained with the three investigated methods formulating ESWLs. However, the PSWL basis obtained with ESWLs derived from the conditional expected load and load-response correlation methods perform better to ensure the acceptable underestimation condition for all responses.
- Fifth, the automatic procedure to handle the envelope reconstruction problem with PSWL basis has proven to be efficient. The three options to establish SWLs ensuring no underestimation of the envelope have been investigated and the option C performs better.

## VI.6 Summary

The methodology to solve the envelope reconstruction problem described in Chapter III has been applied in the present Chapter to three different structures: a four-span bridge, a real-life stadium roof and a low-rise building. The methodology has demonstrated to be efficient, particularly with principal static wind loads in comparison with equivalent static wind loads, CPT loading modes or modal inertial loads. The intrinsic controllability of two pertinent parameters which are

- the acceptable overestimation  $\hat{\varepsilon}$  and
- the number  $n_q$  of basic static wind loads to be combined

makes the methodology flexible to specific envelope reconstruction requirements, chosen as

- the acceptable overall reconstruction indicator  $\mathcal{R}^t$  and
- the acceptable underestimation  $\tilde{\varepsilon}^t$ .

For instance, the choice of the acceptable overestimation and the largest relative error may depend on the structural design phase, at the early stages of pre-design or at the final stages of structural verification. In the former case, largest values for  $\hat{\varepsilon}$  and  $\tilde{\varepsilon}^t$  may be considered than in the latter phase of structural verification. This choice may also depend on the magnitude of the structural responses under the mean wind loading and permanent loads and if the wind load scenario prevails or not. From this perspective, the flexibility of the methodology to user-defined over- and underestimation of the actual envelope is an appreciable advantage.

The proposed methodology is general. The procedure is the same no matter the kind of structure, its load-bearing system, its dynamical structural behavior and the level of non-Gaussianity of the responses involved in the problem.

Finally, the automatic procedure to handle the envelope reconstruction problem with PSWL bases has proven to be efficient in case of very small tolerance on the acceptable relative errors. The three options to establish SWLs ensuring no underestimation of the envelope have been investigated and the option C performs better.





# Chapter VII

## Conclusions

---

**VII.1 Introduction**

**VII.2 Theoretical implications**

**VII.3 Practical implications**

**VII.4 Limitations of the study**

**VII.5 Recommendations for further research**

**VII.6 Conclusion**

---

## VII.1 Introduction

### Context of the study

Static wind loads are being used for the design of civil structures subjected to the buffeting action of the wind. The corresponding static analyses have to provide structural responses similar to the extreme values that would be provided by a buffeting analysis. Once static wind loads are known, they are readily applied to the structure and structural engineers can effectively focus on the structural design. If the structure under investigation is beyond the scope of actual standards, advanced methods are required to produce relevant static wind loads for the design. This brought us to formulate the following two research questions.

#### 1. How to establish ESWLs in a theoretical and general framework?

*Equivalent static wind loads* (ESWLs) are usually considered for the purpose of the design. The concept has been reviewed and two main gaps have been highlighted. First, there is no consensual view of the theoretical definition of an ESWL. This is essential to extend the concept in a non-Gaussian context. Second, each formulation is given in the specific basis—nodal, modal or hybrid—in which the structural analysis is performed instead of being general no matter the basis used.

#### 2. Which methodology to produce reliable static wind loads for the design?

Other kinds of static wind loads than the equivalent ones have been studied. The challenge consists in deriving a set of static wind loads that could efficiently reconstruct the extreme values of structural responses. The term “efficient” may cover a large range of features that would be required for these static wind loads. An optimum reconstruction for all responses of interest with a minimum number of loadings is considered as the main objective. This issue constitutes the core of the studies undertaken in this dissertation.

### Outline of the present Chapter

Section VII.2 discusses the three main theoretical implications of this thesis and how these developments offer a new insight into the concept of equivalent static wind loads. Section VII.3 focuses on the formulation of the envelope reconstruction problem and the notion of principal static wind loads as a potential tool for design in everyday practice. Section VII.4 reports the limitations of the present study and Section VII.5 gives recommendations for future researches. Finally, Section VII.6 points out how the present work has contributed to the body of knowledge in the field of wind engineering.

## VII.2 Theoretical implications

### Conditional Expected Static Wind Load

Since 1970's, several formulations of equivalent static wind loads have been established depending on the structural behavior: quasi-static, hybrid or resonant and for some of them assuming Gaussian random processes. Driven by the necessity to derive such ESWLs in a non-Gaussian context, we have formally introduced the concept of *conditional expected static*

*wind load*. In our opinion, ESWL should be based on the premise that it collects the average wind loads conditioned upon recovery of the considered response. This meaningful definition of an ESWL impinges on the understanding of existing methods since they formulate ESWLs which are actually conditional expected SWLs in a Gaussian framework. Moreover, it is a solid concept for the developments of further methods in a non-Gaussian context.

### Bicubic model for the joint and conditional PDFs

A bicubic model for the joint and conditional PDFs of two non-Gaussian variables is derived based on the Hermite moment model (Winterstein, 1988). This bicubic model is the cornerstone to establish conditional expected SWLs for non-Gaussian processes. We believe the bicubic model is directly accessible for practitioners since the Hermite moment model is already well-known in the wind engineering community for different applications, e.g., the model for “non-Gaussian” peak factor developed by Kareem and Zhao (1994). It is also important to stress that the bicubic model is utterly general—within its domain of applicability—in the sense that it could be applied to any set of two random processes: for instance, two structural responses or two loads.

## VII.3 Practical implications

### Conditional Expected Load method

Thanks to the *conditional expected load method*, conditional expected static wind loads are formulated for (i) all kinds of linear structural behaviors (background, hybrid and resonant), (ii) irrespective of the basis used for the analysis (nodal, hybrid and modal), (iii) able to handle mixed background/resonant contributions and (iv) relevant for non-Gaussian processes. Under specific circumstances, this novel method degenerates into existing pioneering theories such as the load-response correlation method (Kasperski, 1992) and what we called hybrid-based ESWLs (Chen and Kareem, 2001). Moreover, its aptitude to naturally handle mixed background/resonant contributions is a pertinent feature since a recent study proposed an ESWL formulation to this end (Ke et al., 2012).

### Robust methodology for the envelope reconstruction problem

The wind effects on structures by means of static wind loads may be understood as an *envelope reconstruction problem* (ERP). The proposed iterative procedure, is a general concept (i) no matter the structure, (ii) its load-bearing system and (iii) dynamical behavior (quasi-static, hybrid or resonant). It is relevant for (iv) Gaussian and non-Gaussian structural responses, as well. Moreover, we have highlighted that a more elaborated approach is based on combinations of static wind loads. The combination coefficients are determined with a robust constrained nonlinear optimization algorithm.

It should be emphasized that our iterative procedure departs from the prevailing approaches where one or two static wind loads are computed. However, we firmly believe it is an essential requirement of a general approach and makes the proposed methodology relevant for the envelope reconstruction problem.

### Principal Static Wind Loads for design

One key-finding from our study is the meaningful concept of *Principal Static Wind Load* (PSWL). They are determined by singular value decomposition of a large set of Equivalent Static Wind Loads and therefore can be seen as a manner to sort out the most important load patterns. They are the directors of an optimum basis of loadings to represent large sets of ESWLs. The more structural responses are correlated, the more ESWLs have similar distributions and the smaller number of PSWLs has to be retained. Also, they are still dependent upon the set of structural responses to be reconstructed, though they are not associated with specific structural responses which is the main limitation of ESWLs. Finally, the PSWLs are relevant for structures with quasi-static, hybrid or resonant behaviors on the condition that the appropriate ESWL formulation has been selected to compute all ESWLs on which the singular value decomposition is applied.

The key-idea has been to use PSWLs for the envelope reconstruction problem instead of having recourse to ESWLs, covariance proper transformation loading modes or modal inertial loads, as usual. The three examples used for illustrations have shown that the envelope reconstruction accuracy is considerably improved with PSWLs and by combinations thereof. They are, indeed, better suited than equivalent static wind loads, covariance proper transformation loading modes or modal inertial loads.

In the near future, we are convinced that the concept of PSWL is a pertinent candidate to those who want to handle the envelope reconstruction problem of large and complex-shaped structures.

## VII.4 Limitations of the study

Only synoptic winds are considered in this work. The wind loads resulting from these kinds of winds are assumed as stationary on a restricted period, representative for the wind effects on structures. Moreover, this work focuses on the analysis of structures for which a linear behavior under wind actions can be reasonably assumed. Also, we only consider in this work structural responses that are obtained by linear combinations of the nodal displacements.

## VII.5 Recommendations for further research

### Conditional expected static wind load

In a Gaussian context, the general formulation of the conditional expected SWL degenerates into a closed-form expression. The LRC and hybrid methods already formulated this kind of loading. They are being commonly used so far by the practitioners for the design. Moreover, they are also used for structural responses exhibiting non-Gaussianities. This work has shown that using the “Gaussian” formulation with non-Gaussian structural responses can lead to important overestimations of the envelope values of other responses in the structure. This may result in an uneconomical design. This observation inspires the two following research tracks.

Indeed, this work has investigated a bicubic model to formulate such SWL in a non-Gaussian context. Its limitations—only one cross-moment is considered in the parametric joint PDF and the monotone limitation—restrict, however, its accuracy and applicability.

Further research is therefore required to provide reliable estimations of the “non-Gaussian” conditional expected static wind load by means of other parametric or non-parametric approaches. It may be anticipated that the more moments and cross-moments are considered, the more parametric models would be complex or would even fail to satisfy all the imposed statistical moments. In this sense, we recommend the non-parametric estimations of joint and conditional PDFs, for instance, through the maximum entropy method or the recourse to kernel density estimation.

Second, in both cases, the number of statistical moments to be considered should be studied as a first step. Indeed, the shape of a PDF is not unique even if, for instance, the first four moments are imposed. This statement also holds for the joint and marginal PDFs. The influence of such variation on the conditional expected value should therefore be studied first. In other words, the question is how many moments and cross-moments have to be considered for a robust estimation of the “non-Gaussian” conditional expected value. From this perspective, the confidence intervals from realizations of the statistical moments must also be estimated. The larger the order of the statistical moment, the larger number of realizations is required. Indeed, it does not make sense to account for a statistical moment if its confidence interval is too large.

In conclusion, there is an important need for further guidelines to derive with confidence “non-Gaussian” conditional expected static wind load.

### **Envelope reconstruction problem**

The structural wind design of buildings is usually done for several wind directions and we could apply the methodology developed in this work for each wind direction. The number of envelope reconstruction problems is thus equal to the number of studied wind directions. However, a design office usually seeks to derive representative static wind loads covering all wind directions. This new problem remains, from our point of view, an open question. For example, the covariance proper transformation loading modes are not well-suited since they are specific for each wind direction. Moreover, the envelope reconstruction has to be reformulated. We recommend that the envelope reconstruction problem focuses on the reconstruction of the total envelope covering all wind directions since the mean component of responses is no longer associated with a unique mean loading. Accordingly, the concept of PSWLs has to be adapted. In such cases, they should be obtained with a singular value decomposition of the total equivalent static wind loads.

## **VII.6 Conclusion**

The main objective of this research work is to propose novel concepts of static wind load for the purpose of design. Due to the great significance of the subject matter under discussion, several pioneering methods are already available and have been extensively reviewed. Several potential improvements have been identified and two research questions were formulated in the introduction of this Chapter. The present study has offered novel responses to them summarized hereinafter.

**1. How to establish ESWLs in a theoretical and general framework?**

By reference to the definition of a conditional expected static wind load and the Conditional Expected Load method formulating them with elastic forces.

**2. Which methodology to produce reliable static wind loads for the design?**

By adopting the Envelope Reconstruction Problem formulation and by recourse to the Principal Static Wind Loads and combinations thereof.

The illustrations proved how the aforementioned outcomes offered new profound methods with direct theoretical and practical implications.

# Bibliography

- Adcock, C., 2010. Asset pricing and portfolio selection based on the multivariate extended skew-student-t distribution. *Annals of Operations Research* 176, 221–234.
- Arellano-Valle, R.B., Genton, M.G., 2010. Multivariate extended skew-t distributions and related families. *Metron* 68, 201–234.
- Armitt, J., 1968. Eigenvector analysis of pressure fluctuations on the west burton instrumented cooling tower. Central Electricity Research Laboratories (UK) Internal Report RD/LN/ 11/68.
- Atta, C., 1974. Sampling techniques in turbulence measurements. *Annual Review of Fluid Mechanics* 6, 75–91.
- Azzalini, A., Bowman, A.W., 1997. Applied smoothing techniques for data analysis: the kernel approach with S-Plus illustrations. Oxford University Press Oxford.
- Azzalini, A., Capitanio, A., 2003. Distributions generated by perturbation of symmetry with emphasis on a multivariate skew t-distribution. *Journal of the Royal Statistical Society. Series B: Statistical Methodology* 65, 367–389.
- Azzalini, A., Dalla Valle, A., 1996. The multivariate skew-normal distribution. *Biometrika* 83, 715–726.
- Benfratello, S., Muscolino, G., 1999. Filter approach to the stochastic analysis of mdof wind-excited structures. *Probabilistic Engineering Mechanics* 14, 311–321.
- Best, R.J., Holmes, J.D., 1983. Use of eigenvalues in the covariance integration method for determination of wind load effects. *Journal of Wind Engineering and Industrial Aerodynamics* 13, 359–370.
- Bienkiewicz, B., 1996. New tools in wind engineering. *Journal of Wind Engineering and Industrial Aerodynamics* 65, 279–300.
- Bienkiewicz, B., Ham, H.J., Sun, Y., 1993. Proper orthogonal decomposition of roof pressure. *Journal of Wind Engineering and Industrial Aerodynamics* 50, 193–202.
- Blaise, N., 2010. Study of a large roof structure submitted to turbulent wind. Thesis.
- Blaise, N., Canor, T., Denoël, V., 2016. Reconstruction of the envelope of non-gaussian structural responses with principal static wind loads. *Journal of Wind Engineering and Industrial Aerodynamics* 149, 59–76.

- Blaise, N., Denoël, V., 2011a. Optimal Processing of Wind Tunnel Measurements in View of Stochastic Structural Design of Large Flexible Structures. *Wind Tunnels and Experimental Fluid Dynamic Research*, edited by J. C. Lerner and U. Boldes, , InTech, ISBN 978-953-307-623-2.
- Blaise, N., Denoël, V., 2011b. Optimal Processing of Wind Tunnel Measurements in View of Stochastic Structural Design of Large Flexible Structures. *Wind Tunnels and Experimental Fluid Dynamic Research*, edited by J. C. Lerner and U. Boldes, , InTech, ISBN 978-953-307-623-2.
- Blaise, N., Denoël, V., 2013a. Principal static wind loads. *Journal of Wind Engineering and Industrial Aerodynamics* 113, 29–39.
- Blaise, N., Denoël, V., 2013b. Principal static wind loads, in: *European-African Conference on Wind Engineering*.
- Blaise, N., Denoël, V., 2015. Adjusted equivalent static wind loads for non-gaussian linear static analysis, in: *14th international conference on wind engineering*.
- Blaise, N., Hamra, L., Denoël, V., 2012. Principal static wind loads on a large roof structure, in: *Proceedings of the 12th ANIV conference of wind engineering In Vento*.
- Boggs, P.T., Tolle, J.W., 1995. Sequential quadratic programming. *Acta numerica* 4, 1–51.
- Botev, Z., Grotowski, J., Kroese, D., 2010. Kernel density estimation via diffusion. *The Annals of Statistics* 38, 2916–2957.
- Canor, T., Blaise, N., Denoël, V., 2012. Efficient uncoupled stochastic analysis with non-proportional damping. *Journal of Sound and Vibration* 331, 5283–5291.
- Carassale, L., 2005. Pod-based filters for the representation of random loads on structures. *Probabilistic Engineering Mechanics* 20, 263–280.
- Carassale, L., Piccardo, G., Solari, G., 2001. Double modal transformation and wind engineering applications. *Journal Of Engineering Mechanics-Asce* 127, 432–439.
- Carassale, L., Solari, G., 2002. Wind modes for structural dynamics: A continuous approach. *Probabilistic Engineering Mechanics* 17, 157–166.
- Carassale, L., Solari, G., Tubino, F., 2007. Proper orthogonal decomposition in wind engineering. part 2: Theoretical aspects and some applications. *Wind and Structures* 10, 177–208.
- Cartwright, D., Longuet-Higgins, M.S., 1956. The statistical distribution of the maxima of a random function. *Proceedings of the Royal Society of London. Series A. Mathematical and Physical Sciences* 237, 212–232.
- Chen, F.B., Li, Q.S., Wu, J.R., Fu, J.Y., 2011. Wind effects on a long-span beam string roof structure: Wind tunnel test, field measurement and numerical analysis. *Journal of Constructional Steel Research* 67, 1591–1604.



- Chen, X., Kareem, A., 2001. Equivalent static wind loads for buffeting response of bridges. *Journal of Structural Engineering-Asce* 127, 1467–1475.
- Chen, X., Kareem, A., 2005. Coupled dynamic analysis and equivalent static wind loads on buildings with three-dimensional modes. *Journal of Structural Engineering-Asce* 131, 1071–1082.
- Chen, X., Zhou, N., 2007. Equivalent static wind loads on low-rise buildings based on full-scale pressure measurements. *Engineering Structures* 29, 2563–2575.
- Choi, M., Sweetman, B., 2010. The hermite moment model for highly skewed response with application to tension leg platforms. *Journal of Offshore Mechanics and Arctic Engineering* 132, 021602.
- Clough, R.W., Penzien, J., 1993. *Dynamics of structures*. McGraw-Hill, New-York. 2nd edition edition.
- Davenport, A.G., 1962. The response of slender line-like structures to a gusty wind. In: *Proceedings of the Institution of Civil Engineers* 23, 389–408.
- Davenport, A.G., 1964a. Note on the distribution of the largest value of a random function with application to gust loading, in: *ICE Proceedings*, Thomas Telford. pp. 187–196.
- Davenport, A.G., 1964b. The buffeting of large superficial structures by atmospheric turbulence. *Annals of the New York Academy of Sciences* 116, 135–160.
- Davenport, A.G., 1967. Gust loading factors. *Journal of Institute of Civil Engineering, ASCE* 93, 11–34.
- Davenport, A.G., 1985. The representation of the dynamic effects of turbulent wind by equivalent static wind loads, in: *Proceedings of the Int. Engineering Symposium on Structural Steel*, pp. 1–13.
- Davenport, A.G., 1995. How can we simplify and generalize wind loads. *Journal of Wind Engineering and Industrial Aerodynamics* 54, 657–669.
- Denoël, V., 2009a. Estimation of modal correlation coefficients from background and resonant responses. *Structural Engineering And Mechanics* 32, 725–740.
- Denoël, V., 2009b. Polynomial approximation of aerodynamic coefficients based on the statistical description of the wind incidence. *Probabilistic Engineering Mechanics* 24, 179–189.
- Denoël, V., 2015. Multiple timescale spectral analysis. *Probabilistic Engineering Mechanics* 39, 69–86.
- Denoël, V., Degée, H., 2009. Asymptotic expansion of slightly coupled modal dynamic transfer functions. *Journal of Sound and Vibration* 328, 1–8.
- Der Kiureghian, A., 1980. Structural response to stationary excitation. *Journal of the Engineering Mechanics Division* 106, 1195–1213.

- Di Paola, M., 1998. Digital simulation of wind field velocity. *Journal of Wind Engineering and Industrial Aerodynamics* 74-76, 91–109.
- Di Paola, M., Gullo, I., 2001. Digital generation of multivariate wind field processes. *Probabilistic Engineering Mechanics* 16, 1–10.
- Dickens, J.M., Nakagawa, J.M., Wittbrodt, M.J., 1997. A critique of mode acceleration and modal truncation augmentation methods for modal response analysis. *Computers & Structures* 62, 985–998.
- Ding, J., Chen, X., 2014. Assessment of methods for extreme value analysis of non-gaussian wind effects with short-term time history samples. *Engineering Structures* 80, 75–88.
- Eurocode, E., 1991a. EN 1991-1-3: Actions on structures-General actions-Densities, self-weight, imposed loads for buildings. European Committee for Standardization.
- Eurocode, E., 1991b. EN 1991-1-3: Actions on structures-General actions-Wind actions. European Committee for Standardization.
- Eurocode, E., 2005. EN 1993-1-1: Eurocode 3: Design of Steel Structures. Part 1-1: General Rules and Rules for Buildings. European Committee for Standardization.
- FinelG, 1999. User's manual, version 8.2. Département M & S - Bureau d'études Greisch .
- Fiore, A., Monaco, P., 2009. Pod-based representation of the alongwind equivalent static force for long-span bridges. *Wind and Structures, An International Journal* 12, 239–257.
- Floris, C., Iseppi, L.D., 1998. The peak factor for gust loading: A review and some new proposals. *Meccanica* 33, 319–330.
- Fu, J.Y., Xie, Z.N., Li, Q.S., 2008. Equivalent static wind loads on long-span roof structures. *Journal of Structural Engineering-Asce* 134, 1115–1128.
- Gérardin, M., Rixen, D.J., 2014. *Mechanical vibrations: theory and application to structural dynamics*. John Wiley & Sons.
- Giofrè, M., Grigoriu, M., Kasperski, M., Simiu, E., 2000. Wind-induced peak bending moments in low-rise building frames. *Journal of engineering mechanics* 126, 879–881.
- Grigoriu, M., 2013. *Stochastic calculus: applications in science and engineering*. Springer Science & Business Media.
- Gu, M., Zhou, X.Y., 2009. An approximation method for resonant response with coupling modes of structures under wind action. *Journal of Wind Engineering and Industrial Aerodynamics* 97, 573–580.
- Gurley, K.R., Tognarelli, M.A., Kareem, A., 1997. Analysis and simulation tools for wind engineering. *Probabilistic Engineering Mechanics* 12, 9–31. Times Cited: 21.
- Han, D., Li, J., 2009. Application of proper orthogonal decomposition method in wind field simulation for roof structures. *Journal of Engineering Mechanics* 135, 786–795.

- Hansteen, O.E., Bell, K., 1979. On the accuracy of mode superposition analysis in structural dynamics. *Earthquake Engineering & Structural Dynamics* 7, 405–411.
- Ho, T.C.E., Davenport, A.G., Surry, D., 1995. Characteristic pressure distribution shapes and load repetitions for the wind loading of low building roof panels. *Journal of Wind Engineering and Industrial Aerodynamics* 57, 261–279.
- Ho, T.C.E., Surry, D., Morrish, D., Kopp, G.A., 2005. The uwo contribution to the nist aerodynamic database for wind loads on low buildings: Part 1. archiving format and basic aerodynamic data. *Journal of Wind Engineering and Industrial Aerodynamics* 93, 1–30.
- Holmes, J., Wood, G., 2001. The determination of structural wind loads for the roofs of several venues for the 2000 olympics.
- Holmes, J.D., 1988. Distribution of peak wind loads on a low-rise building. *Journal Of Wind Engineering and Industrial Aerodynamics* 29, 59–67.
- Holmes, J.D., 1992. Optimized peak load distributions. *Journal of Wind Engineering and Industrial Aerodynamics* 41, 267–276.
- Holmes, J.D., 1994. Along-wind response of lattice towers: part i - derivation of expressions for gust response factors. *Engineering Structures* 16, 287–292.
- Holmes, J.D., 1996. Along-wind response of lattice towers - iii. effective load distributions. *Engineering Structures* 18, 489–494.
- Holmes, J.D., 2007. *Wind Loading on Structures*. SponPress, London. 2nd edition edition.
- Holmes, J.D., Best, R.J., 1981. An approach to the determination of wind load effects on low-rise buildings. *Journal of Wind Engineering and Industrial Aerodynamics* 7, 273–287.
- Holmes, J.D., Sankaran, R., Kwok, K.C.S., Syme, M.J., 1997. Eigenvector modes of fluctuating pressures on low-rise building models. *Journal of Wind Engineering and Industrial Aerodynamics* 71, 697–707.
- Holmes, J.D., Syme, M.J., Kasperski, M., 1995. Optimised design of a low-rise industrial building for wind loads. *Journal of Wind Engineering and Industrial Aerodynamics* 57, 391–401.
- Huang, G., Chen, X., 2007. Wind load effects and equivalent static wind loads of tall buildings based on synchronous pressure measurements. *Engineering Structures* 29, 2641–2653.
- International Standards Organization, 2009. ISO 4354 - Wind actions on structures.
- Jolliffe, I., 2005. Principal Component Analysis. *Encyclopedia of Statistics in Behavioral Science*, John Wiley & Sons, Ltd.
- Kareem, A., Zhao, J., 1994. Analysis of non-gaussian surge response of tension leg platforms under wind loads. *Journal of Offshore Mechanics and Arctic Engineering* 116, 137–144.
- Kareem, A., Zhou, Y., 2003. Gust loading factor - past, present and future. *Journal of Wind Engineering and Industrial Aerodynamics* 91, 1301–1328.

- Kasperski, M., 1992. Extreme wind load distributions for linear and nonlinear design. *Engineering Structures* 14, 27–34.
- Kasperski, M., 1993. Aerodynamics of low-rise buildings and codification. *Journal of Wind Engineering and Industrial Aerodynamics* 50, 253–262.
- Kasperski, M., 2009. Incorporation of the lrc-method into codified wind load distributions, in: *Proceedings of The Seventh Asia-Pacific Conference on Wind Engineering*.
- Kasperski, M., Niemann, H.J., 1992. The l.r.c. (load-response-correlation) - method a general method of estimating unfavourable wind load distributions for linear and non-linear structural behaviour. *Journal of Wind Engineering and Industrial Aerodynamics* 43, 1753–1763.
- Katsumura, A., Tamura, Y., Nakamura, O., 2007. Universal wind load distribution simultaneously reproducing largest load effects in all subject members on large-span cantilevered roof. *Journal of Wind Engineering and Industrial Aerodynamics* 95, 1145–1165.
- Katsumura, A., Tamura, Y., Nakamura, O., 2011. Application of universal equivalent static wind load. *Proceedings of the 13th ICWE, Amsterdam, The Netherlands* .
- Ke, S.T., Ge, Y.J., Zhao, L., Tamura, Y., 2012. A new methodology for analysis of equivalent static wind loads on super-large cooling towers. *Journal of Wind Engineering and Industrial Aerodynamics* 111, 30–39.
- Lang, S., Mathematician, F., 1987. *Calculus of several variables*. Springer-Verlag New York.
- Letchford, C.W., Iverson, R.E., McDonald, J.R., 1993. The application of the quasi-steady theory to full scale measurements on the texas tech building. *Journal of Wind Engineering and Industrial Aerodynamics* 48, 111–132.
- Letchford, C.W., Killen, G.P., 2002. Equivalent static wind loads for cantilevered grandstand roofs. *Engineering Structures* 24, 207–217.
- Li, Y., Bao, L., Wang, L., Shen, Z., . Wind tunnel test and equivalent static wind load of a single layered reticulated shell, in: *13th International Conference on Wind Engineering*, July 10-15, 2011.
- Li, Y.Q., Tamura, Y., 2005. Equivalent static wind load estimation in wind-resistant design of single-layer reticulated shells. *Wind and Structures, An International Journal* 8, 443–454.
- Li, Y.Q., Wang, L., Tamura, Y., Shen, Z.Y., 2009. Universal equivalent static wind load estimation for spatial structures based on wind-induced envelope responses, in: *Symposium of the International Association for Shell and Spatial Structures (50th. Valencia)*.
- Lin, Y.K., 1976. *Probabilistic theory of structural dynamics*. Krieger Publishing Company.
- Liu, H., Qu, W.L., Li, Q.S., 2011. Comparison between wind load by wind tunnel test and in-site measurement of long-span spatial structure. *Wind and Structures, An International Journal* 14, 301–319.

- Loeve, M., 1977. Probability theory I, 4th eddition. Probability theory I, 4th eddition, Springer-Verlag.
- Lumley, J.L., 1967. The Structure of Inhomogeneous Turbulent Flows, in: Yaglom, A.M., Tatarski, V.I. (Eds.), Atmospheric turbulence and radio propagation. Nauka, Moscow, pp. 166–178.
- Maddox, N., 1975. On the number of modes necessary for accurate response and resulting forces in dynamic analyses. *Journal of Applied Mechanics* 42, 516–517.
- Main, J.A., 2006. University of western ontario data sets.
- Main, J.A., Fritz, W.P., 2006. Database-assisted design for wind: concepts, software, and examples for rigid and flexible buildings. National Institute of Standards and Technology, Technology Administration, US Department of Commerce.
- Morzfeld, M., Ajavakom, N., Ma, F., 2009. Diagonal dominance of damping and the decoupling approximation in linear vibratory systems. *Journal of Sound and Vibration* 320, 406–420.
- Papoulis, A., 1965. Probability, Random Variables, and Stochastic Processes. McGraw Hill, New York.
- Peng, X., Yang, L., Gavanski, E., Gurley, K., Prevatt, D., 2014. A comparison of methods to estimate peak wind loads on buildings. *Journal of Wind Engineering and Industrial Aerodynamics* 126, 11–23.
- Piccardo, G., Solari, G., 2002. 3-d gust effect factor for slender vertical structures. *Probabilistic Engineering Mechanics* 17, 143–155.
- Preumont, A., 1994. Random Vibration and Spectral Analysis. Kluwer Academic Publishers.
- Rayleigh, J.W.S., 1945. The theory of sound, vol. 1. New York: McMillan 34.
- Repetto, M.P., Solari, G., 2004. Equivalent static wind actions on vertical structures. *Journal of Wind Engineering and Industrial Aerodynamics* 92, 335–357.
- Rice, S., 1945. Mathematical analysis of random noise. *Bell System Technical Journal* 24, 45–156.
- Rizzo, F., D’Asdia, P., Lazzari, M., Olivato, G., 2009. Aerodynamic behaviour of hyperbolic paraboloid shaped roofs: Pod and cfd analysis.
- Rosenblatt, M., 1956. Remarks on some nonparametric estimates of a density function , 832–837.
- Sadek, F., Simiu, E., 2002. Peak non-gaussian wind effects for database-assisted low-rise building design. *Journal of Engineering Mechanics* 128, 530–539.
- Scanlan, R.H., Jones, N.P., 1999. A form of aerodynamic admittance for use in bridge aeroelastic analysis. *Journal Of Fluids And Structures* 13, 1017–1027.

- Seo, D.W., Caracoglia, L., 2010. Derivation of equivalent gust effect factors for wind loading on low-rise buildings through database-assisted-design approach. *Engineering Structures* 32, 328–336.
- Shannon, C.E., Weaver, W., 1948. A mathematical theory of communication. American Telephone and Telegraph Company.
- Shinozuka, M., Yun, C.B., Seya, H., 1990. Stochastic methods in wind engineering. *Journal of Wind Engineering and Industrial Aerodynamics* 36, 829–843.
- Simiu, E., 1973. Gust factors and alongwind pressure correlations. *ASCE J Struct Div* 99, 773–783.
- Simiu, E., Scanlan, R., 1996. *Wind Effects On Structures*. John Wiley and Sons. 3rd edition.
- Solari, G., 1993a. Gust buffeting. i: peak wind velocity and equivalent pressure. *Journal of structural engineering* New York, N.Y. 119, 365–382.
- Solari, G., 1993b. Gust buffeting. ii: Dynamic alongwing response. *Journal of structural engineering* New York, N.Y. 119, 383–398.
- Solari, G., Carassale, L., 2000. Modal transformation tools in structural dynamics and wind engineering. *Wind And Structures* 3, 221–241.
- Solari, G., Carassale, L., Tubino, F., 2007. Proper orthogonal decomposition in wind engineering. part 1: A state-of-the-art and some prospects. *Wind And Structures* 10, 153–176.
- Solari, G., Kareem, A., 1998. On the formulation of asce7-95 gust effect factor. *Journal of Wind Engineering and Industrial Aerodynamics* 77-78, 673–684.
- Solari, G., Tubino, F., 2002. A turbulence model based on principal components. *Probabilistic Engineering Mechanics* 17, 327–335.
- Spanos, P.D., Ghanem, R., 1989. Stochastic finite element expansion for random media. *Journal of Engineering Mechanics* 115, 1035–1053.
- Stathopoulos, T., 1984. Wind loads on low-rise buildings: a review of the state of the art. *Engineering Structures* 6, 119–135.
- Tamura, Y., Fujii, K., Ueda, H., 1992. Design wind loads for beams supporting flat roofs. *Journal of Wind Engineering and Industrial Aerodynamics* 43, 1841–1852.
- Tamura, Y., Katsumura, A., 2012. Universal equivalent static wind load for structures, in: *The Seventh International Colloquium on Bluff Body Aerodynamics and Applications (BBAA7)*.
- Tamura, Y., Kikuchi, H., Hibi, K., 2001. Extreme wind pressure distributions on low-rise building models. *Journal of Wind Engineering and Industrial Aerodynamics* 89, 1635–1646.
- Tamura, Y., Kikuchi, H., Hibi, K., 2002. Actual extreme pressure distributions and lrc formula. *Journal of Wind Engineering and Industrial Aerodynamics* 90, 1959–1971.

- Tamura, Y., Suganuma, S., Kikuchi, H., Hibi, K., 1999. Proper orthogonal decomposition of random wind pressure field. *Journal of Fluids and Structures* 13, 1069–1095.
- Tubino, F., Solari, G., 2005. Double proper orthogonal decomposition for representing and simulating turbulence fields. *Journal of Engineering Mechanics-Asce* 131, 1302–1312.
- Tubino, F., Solari, G., 2007. Gust buffeting of long span bridges: Double modal transformation and effective turbulence. *Engineering Structures* 29, 1698–1707.
- Uematsu, Y., Moteki, T., Hongo, T., 2008. Model of wind pressure field on circular flat roofs and its application to load estimation. *Journal of Wind Engineering and Industrial Aerodynamics* 96, 1003–1014. Cited By (since 1996): 8 Export Date: 5 March 2013 Source: Scopus.
- Uematsu, Y., Watanabe, K., Sasaki, A., Yamada, M., Hongo, T., 1999. Wind-induced dynamic response and resultant load estimation of a circular flat roof. *Journal of Wind Engineering and Industrial Aerodynamics* 83, 251–261.
- Uematsu, Y., Yamada, M., Karasu, A., 1997. Design wind loads for structural frames of flat long-span roofs: Gust loading factor for the beams supporting roofs. *Journal of Wind Engineering and Industrial Aerodynamics* 66, 35–50.
- Uematsu, Y., Yamada, M., Sasaki, A., 1996. Wind-induced dynamic response and resultant load estimation for a flat long-span roof. *Journal of Wind Engineering and Industrial Aerodynamics* 65, 155–166.
- Van Trees, H.L., 1968. Detection, estimation and modulation theory, Part 1. New York, N.Y.
- Vellozzi, J., Cohen, E., 1968. Gust response factors. *Journal of the structural division* .
- Vickery, B., 1970. On the reliability of gust loading factors. proceedings of the Technical Meet Concerning Wind Loads on Buildings and Structures, National Bureau of Standards, Washington , 93–104.
- Von Karman, T., 1958. Progress in the statistical theory of turbulence. *Proc Natl Acad Sci USA* 34, 530–539.
- Winterstein, S.R., 1988. Nonlinear vibration models for extremes and fatigue. *Journal of Engineering Mechanics* 114, 1772–1790.
- Winterstein, S.R., Kashef, T., 2000. Moment-based load and response models with wind engineering applications. *Journal of solar energy engineering* 122, 122–128.
- Yang, L., Gurley, K.R., Prevatt, D.O., 2013. Probabilistic modeling of wind pressure on low-rise buildings. *Journal of Wind Engineering and Industrial Aerodynamics* 114, 18–26.
- Zhou, X., Gu, M., Li, G., 2011. Application research of constrained least-squares method in computing equivalent static wind loads, in: Proceedings of the 13th International Conference on Wind Engineering.

- Zhou, Y., Gu, M., Xiang, H., 1999. Alongwind static equivalent wind loads and responses of tall buildings. part i: Unfavorable distributions of static equivalent wind loads. *Journal of Wind Engineering and Industrial Aerodynamics* 79, 135–150.
- Zhou, Y., Kareem, A., Gu, M., 2000. Equivalent static buffeting loads on structures. *Journal of Structural Engineering-Asce* 126, 989–992.
- Zhou, Y., Kijewski, T., Kareem, A., 2002. Along-wind load effects on tall buildings: Comparative study of major international codes and standards. *Journal of Structural Engineering* 128, 788–796.
- Zienkiewicz, O.C., Taylor, R.L., 1991. *The finite element method*. McGraw-Hill, U.K.. fourth edition.







# Appendix A

## Alternative estimation of representative extreme values

In this Appendix, we would like to show that the automatic procedure also performs well in case of another reference period and alternative estimation method of representative extreme values.

### A.1 Introduction

Firstly, this appendix assesses the envelope reconstruction problem efficiency when the peak factors (obtained using the Kareem-Zhao model) are associated with a reference period of 1 hour instead of 10 min. Secondly, the methodology communicated by Dr. Kasperski, see Section A.2, is used to compute the peak factors and the efficiency of the envelope reconstruction problem is investigated, as well. Only the automatic procedure, see Section V.4, is illustrated since the conclusion of the illustration Chapter has emphasized its advantages in case of small tolerance on relative errors. The option C is applied to obtain SWLs ensuring no underestimation for two values of the final overestimation  $\hat{\varepsilon}' = 25\%$  and  $\hat{\varepsilon}' = 10\%$ , see Section III.2 and Table III.2.

Section A.2 reproduces the methodology communicated by Dr. Kasperski to estimate peak factors for a reference period of 1 hour. Sections A.3 and A.4 illustrate the envelope reconstruction problem for the Lille's stadium example, see Sections VI.3-VI.4, and for the low-rise building example, see Section VI.5. Section A.5 summarizes the main findings.

### A.2 Methodology communicated by Dr. Kasperski

1. Let assume we have  $n$  observation windows of 10 minutes. We denote by  $\check{r}_i$  and  $\hat{r}_i$ , the largest minimum value and the largest maximum value, respectively, observed on the  $i$ -th observation window.
2.  $\text{cmean}(10\text{min})^- = \text{mean value of extremes (min}^- \text{ or max}^+)$  for reference period 10 minutes

$$\text{cmean}(10\text{min})^- = \frac{1}{n} \sum_{i=1}^n \check{r}_i, \quad \text{cmean}(10\text{min})^+ = \frac{1}{n} \sum_{i=1}^n \hat{r}_i, \quad (\text{A.2.1})$$

3. csdev= standard deviation of extremes (min or max) (independent of reference period)

$$\text{csdev}^- = \sqrt{\frac{1}{n-1} \sum_{i=1}^n (\check{r}_i - \text{cmean}^-)^2}, \quad \text{csdev}^+ = \sqrt{\frac{1}{n-1} \sum_{i=1}^n (\hat{r}_i - \text{cmean}^+)^2}, \quad (\text{A.2.2})$$

4. cmean(1 hour)= mean value of extremes (min<sup>-</sup> or max<sup>+</sup>) for reference period 1 hour

$$\text{cmean}(1\text{hour})^- = \text{cmean}(10\text{min})^- - 1.3970 \times \text{csdev}^-, \quad (\text{A.2.3})$$

$$\text{cmean}(1\text{hour})^+ = \text{cmean}(10\text{min})^+ + 1.3970 \times \text{csdev}^+, \quad (\text{A.2.4})$$

5. cov(c)

$$\text{cov}(c)^- = \text{csdev}^- / |\text{cmean}(1\text{hour})^-|, \quad \text{cov}(c)^+ = \text{csdev}^+ / \text{cmean}(1\text{hour})^+, \quad (\text{A.2.5})$$

6. cdesred(1hour) based on the graph

$$\text{cdesred}(1\text{hour})^- = f(\text{cov}(c)^-), \quad \text{cdesred}(1\text{hour})^+ = f(\text{cov}(c)^+), \quad (\text{A.2.6})$$

7. cdes=design value for reference period 1 hour

$$\text{cdes}(1\text{hour})^- = \text{cmean}(1\text{hour})^- - \text{cdesred}(1\text{hour})^- \text{csdev}^-, \quad (\text{A.2.7})$$

$$\text{cdes}(1\text{hour})^+ = \text{cmean}(1\text{hour})^+ + \text{cdesred}(1\text{hour})^+ \text{csdev}^+, \quad (\text{A.2.8})$$

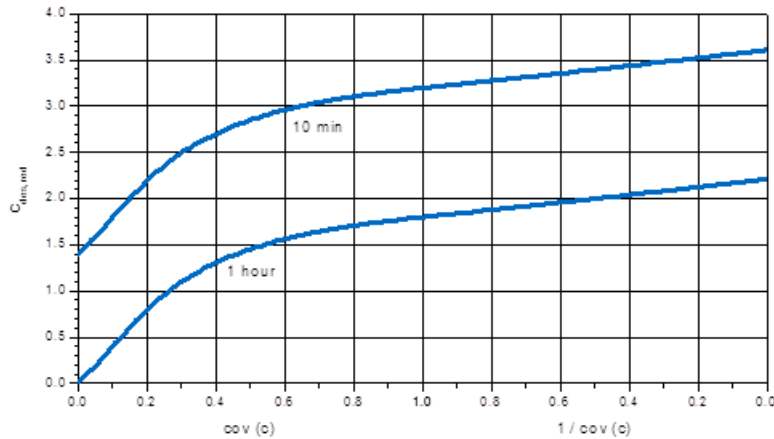


Figure A.1:  $\text{cdesred}(1\text{hour}) = f(\text{cov}(c))$ .

8. peak factors for reference period 1 hour

$$g^{(\min)} = \frac{\text{cdes}(1\text{hour})^-}{\sigma_r}, \quad (\text{A.2.9})$$

$$g^{(\max)} = \frac{\text{cdes}(1\text{hour})^+}{\sigma_r}. \quad (\text{A.2.10})$$

## A.3 Lille's stadium example

### A.3.1 Establishment of the envelope (Reference period 1 hour)

For a reference period of one hour, the peak factors computed with Kareem-Zhao and Kasperski formulations are illustrated with the six sets of structural elements identified in red in Figures A.3, A.4, A.5, A.6, A.7 and A.8. The skewness coefficients, excess coefficients, standard deviation and envelope of the considered internal force for these structural elements are also depicted. Figure A.2 shows the peaks factors obtained with the Kareem-Zhao model versus the peak factors obtained with Kasperski's methodology. In the assessment of different methods for extreme value analysis, Ding and Chen (2014) have shown that for mildly softening non-Gaussian processes (the example in the article is a random process with  $\gamma_{3,r} = 0.7$ ,  $\gamma_{e,r} = 4.3$ ), the cubic transformation method, on which is based the Kareem-Zhao model for peak factors, works very fine. They also shown that for strongly softening non-Gaussian processes (the example in the article is a random process with  $\gamma_{3,r} = 2.22$ ,  $\gamma_{e,r} = 14.71!$ ), the cubic transformation method produces relative errors of about 10% for the estimation of the mean largest maximum. For the Lille's stadium, the majority of the random processes can be classified as slightly to mildly non-Gaussian, see Figure VI.91 and a hundred (out of 7994) as strongly ones. Also, these relative differences can be partially attributed to the small number of 10-min observation windows, here 10. Indeed, the current trends in research concerning Kasperski's methodology recommend several hundred and ideally more than 1000 observation windows of 10 minutes to obtain good estimates, in the sense of confidence intervals, of the peak factors. These two remarks help to appreciate the relative differences in the range  $[-20\%, 20\%]$  between the non-Gaussian peak factors computed with the Kareem-Zhao model and Kasperski's methodology.

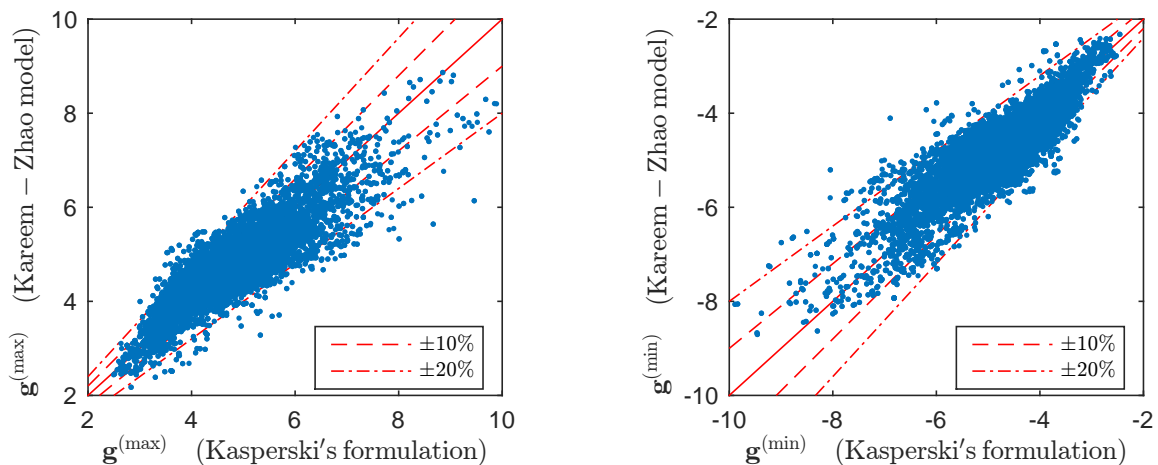


Figure A.2: Scatter plot of peak factors obtained with the Kareem-Zhao model versus the peak factors obtained with Kasperski's formulation.

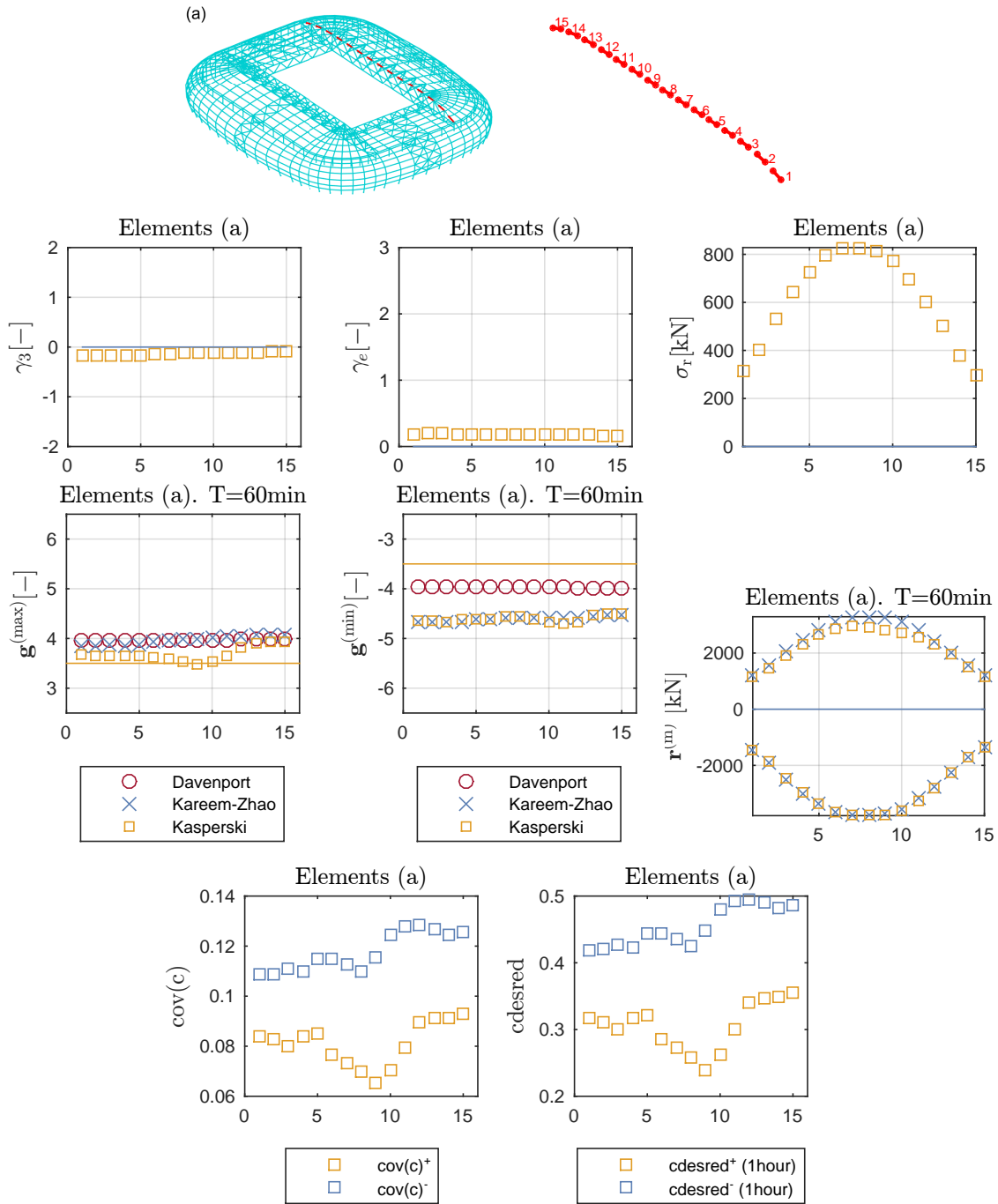


Figure A.3: Establishment of the envelope for 15 beam elements considered for the illustration (in red) and axial force envelope for these elements.

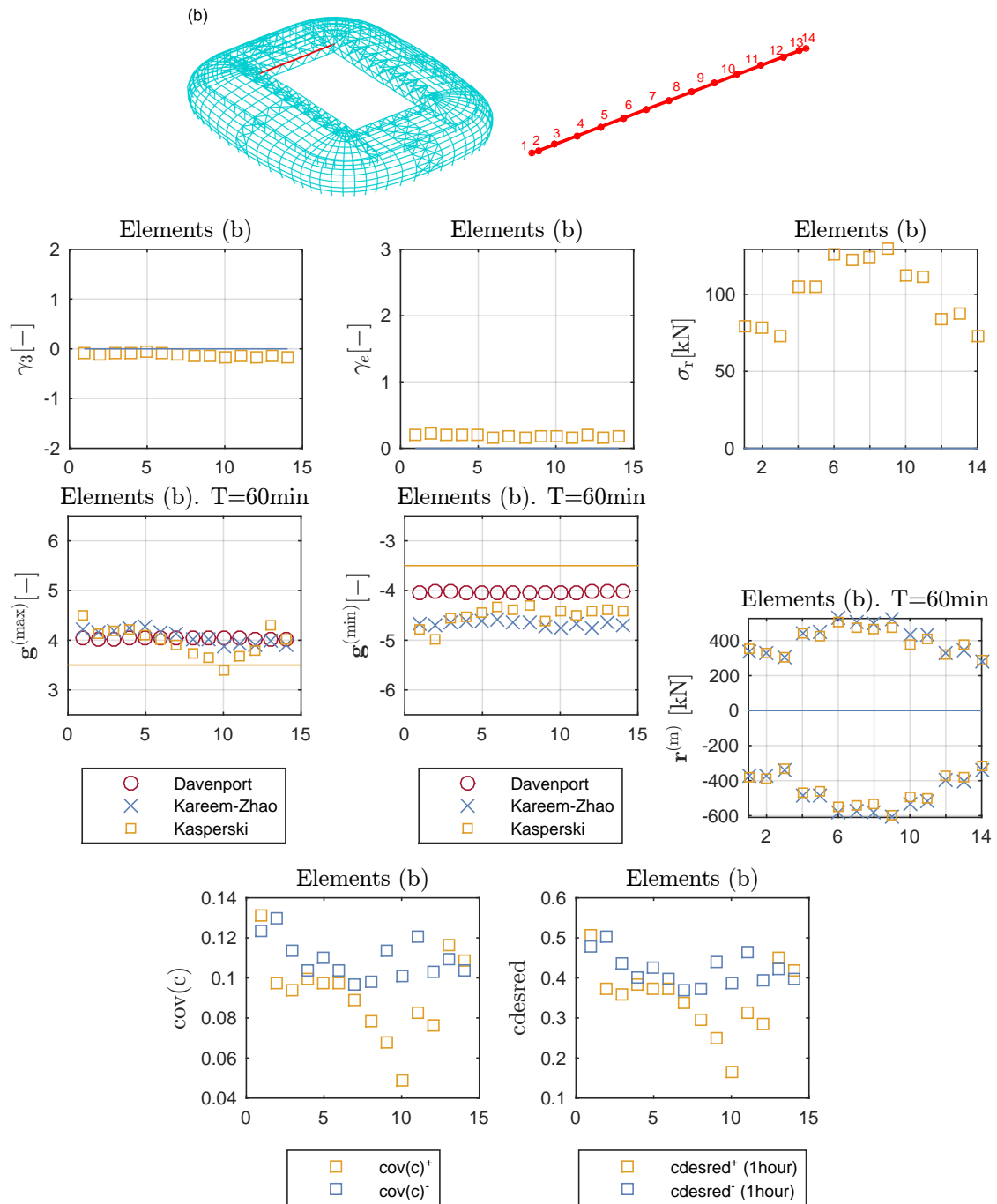


Figure A.4: Establishment of the envelope for 14 beam elements considered for the illustration (in red) and axial force envelope for these elements.

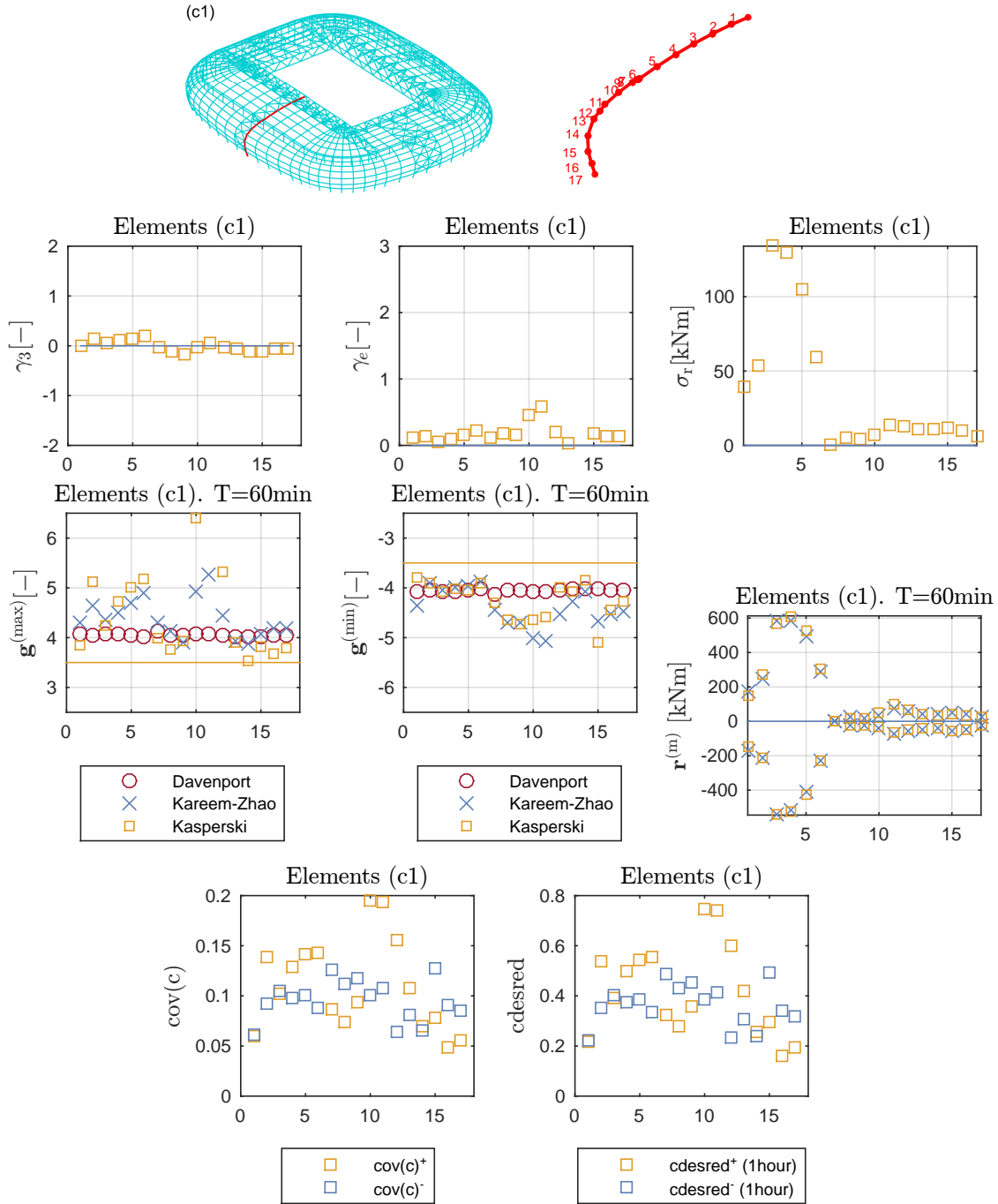


Figure A.5: Establishment of the envelope for 17 beam elements considered for the illustration (in red) and bending moment envelope for these elements.



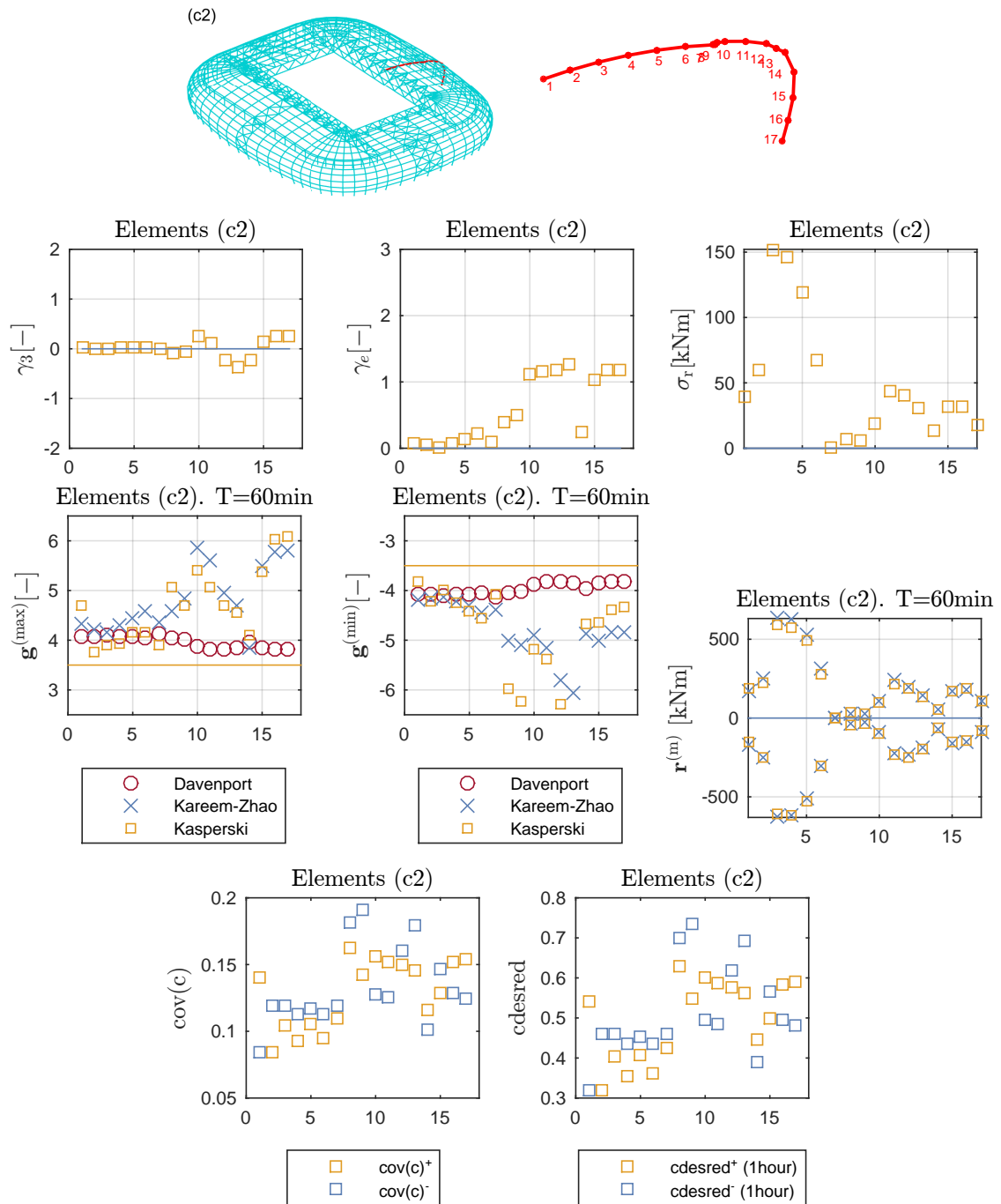


Figure A.6: Establishment of the envelope for 17 beam elements considered for the illustration (in red) and bending moment envelope for these elements.

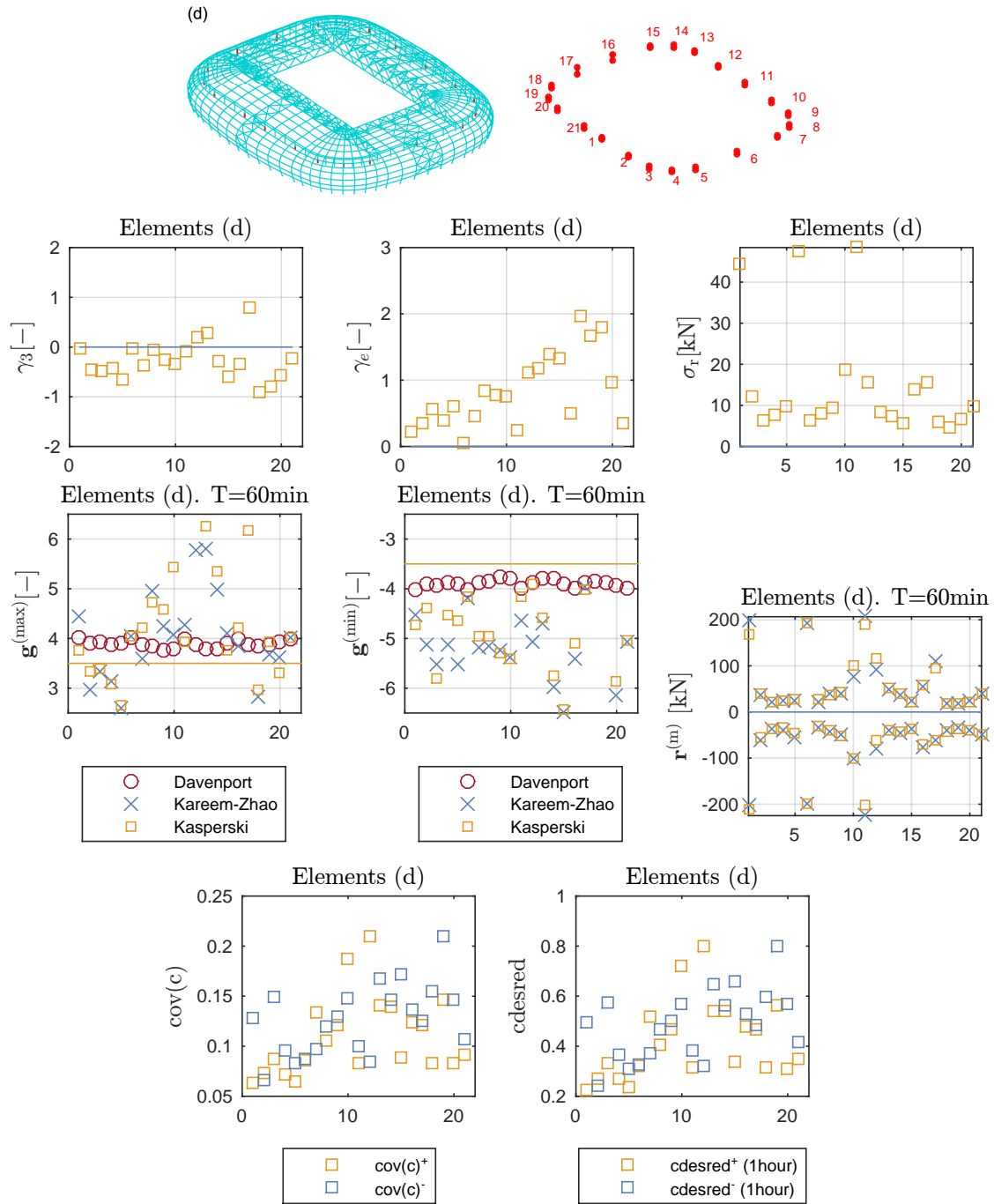


Figure A.7: Establishment of the envelope for 21 beam elements considered for the illustration (in red) and axial force envelope for these elements.

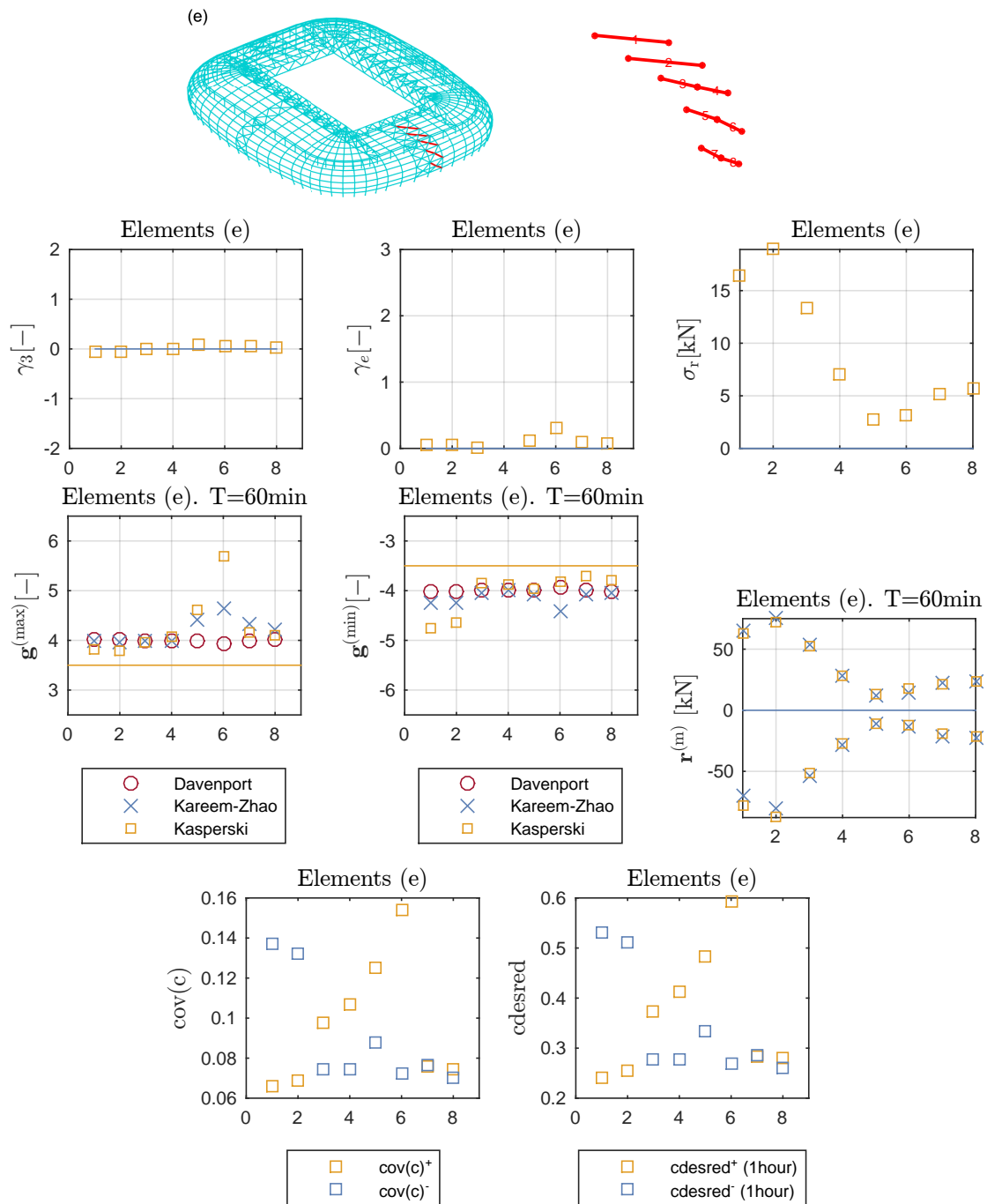


Figure A.8: Establishment of the envelope for 8 bars considered for the illustration (in red) and axial force envelope for these elements.

### A.3.2 Automatic procedure (Kareem-Zhao model for peak factors)

The ESWLs are obtained from the hybrid method proposed by (Chen and Kareem, 2001) and reviewed in Section IV.6. Figure A.9 shows the histograms of overestimation relative errors that would be obtained if all original hybrid-based ESWLs were used for the ERP. There are approximately 9778 envelope values out of 15988 that would be overestimated in the range  $[0,30\%]$ . This range of overestimation is slightly larger than the one obtained when considering a 10-min observation period, see Section VI.4.

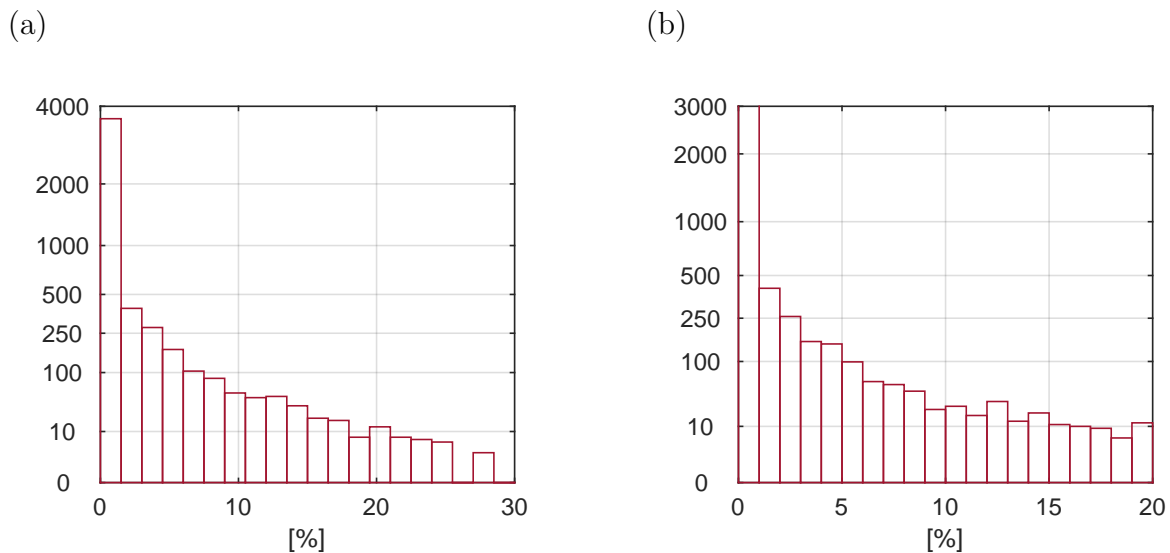


Figure A.9: Histograms of overestimation relative errors that are obtained with the original hybrid-based ESWLs. Overestimation relative errors associated with (a) upper (positive) and (b) lower (negative) envelope values. Results obtained in a non-Gaussian framework (Kareem-Zhao model for peak factors, observation period 1 hour).

Table A.1 presents the results of the ERP and Figure A.10 shows the evolution of the number of responses as a function of the number of load cases for the final overestimation  $\varepsilon' = 10\%$ . The same ratio  $\lambda^P = 0.995$  and number of initial set of combinations  $n_c = 6000$  as in Section VI.4 are used.

By comparison with the results associated with a reference period of 10min, see Table VI.13, the level of complexity of the ERP is not significantly increased by taking into account another observation period or, another envelope. Once again, the automatic procedure proves to be efficient even if the original ESWLs do not satisfy at first, the non-overestimation condition. It is just more difficult to achieve very small tolerances on the reconstruction.

| No underestimation and $\hat{\varepsilon}' = 25\%$ |       |            |              |                               |      | No underestimation and $\hat{\varepsilon}' = 10\%$ |       |            |              |                               |       |
|--|-------|------------|--------------|-------------------------------|------|--|-------|------------|--------------|-------------------------------|-------|
| $n_s$  | $n_q$ | $n_p$      | $n_{r(n_s)}$ | $\check{\varepsilon}_{(n_s)}$ | CPU  | $n_s$  | $n_q$ | $n_p$      | $n_{r(n_s)}$ | $\check{\varepsilon}_{(n_s)}$ | CPU   |
| 151  | 7     | [39,...,3] | 0            | ✓                             | 9min | 399  | 16    | [39,...,6] | 0            | ✓                             | 18min |

Table A.1: Number of SWLs to solve the ERP with option C (see Section III.3.5). ERP parameters:  $\gamma = 1$ ,  $\lambda^P = 0.995$ ,  $n_c = 6000$ . The symbol ✓ means that the acceptable underestimation is satisfied. Results obtained in a non-Gaussian framework (Kareem-Zhao model for peak factors, observation period 1 hour).

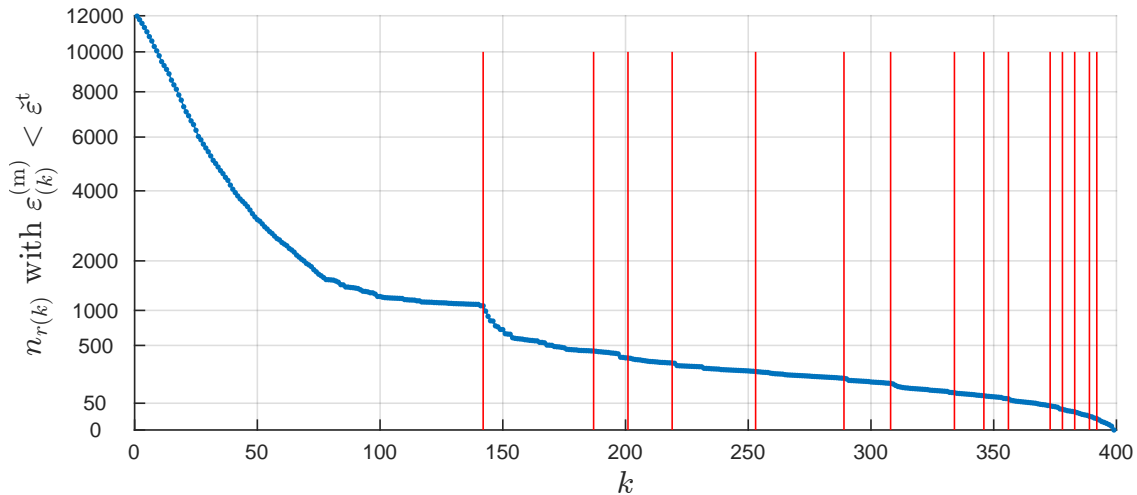


Figure A.10: Evolution of the number of responses  $n_{r(k)}$ , see 127 with  $\varepsilon_{(k)}^{(m)} < \check{\varepsilon}^t$  as a function of the number of load cases. ERP parameters:  $\hat{\varepsilon} = 4.76\%$ ,  $\check{\varepsilon}^t = -4.76\%$ ,  $\gamma = 1$ ,  $\lambda^P = 0.995$ ,  $n_c = 6000$ . Vertical red lines correspond to an updating of the PSWL basis. Results obtained in a non-Gaussian framework (Kareem-Zhao model for peak factors, observation period 1 hour).

### A.3.3 Automatic procedure (Kasperski’s methodology for peak factors)

The ESWLs are obtained with the hybrid method proposed by (Chen and Kareem, 2001) and reviewed in Section IV.6. Figure A.11 shows the histograms of overestimation relative errors that would be obtained if all original hybrid-based ESWLs were used for the ERP. There is approximately 11000 envelope values out of 15988 that would be overestimated in the range [0,60%]. This range of overestimation has doubled in comparison to the range [0,30%] obtained with Kareem-Zhao model for peak factors, see the previous Section. The envelope reconstruction problem is expected to be more complex with such large overestimations associated with the original hybrid-based ESWLs. The origin of these overestimations is

twofold. First, all ESWLs do not necessary fulfill the non-overestimation condition (IV.2.4) since the hybrid method is based on a Gaussian assumption. Secondly, the small number of observation windows<sup>1</sup>, 10, increases considerably the confidence intervals on the peak factors computed with Kasperski's methodology. The larger the errors on the estimation of the mean largest maximum and mean smallest minimum, the larger the expected overestimations associated with original ESWLs.

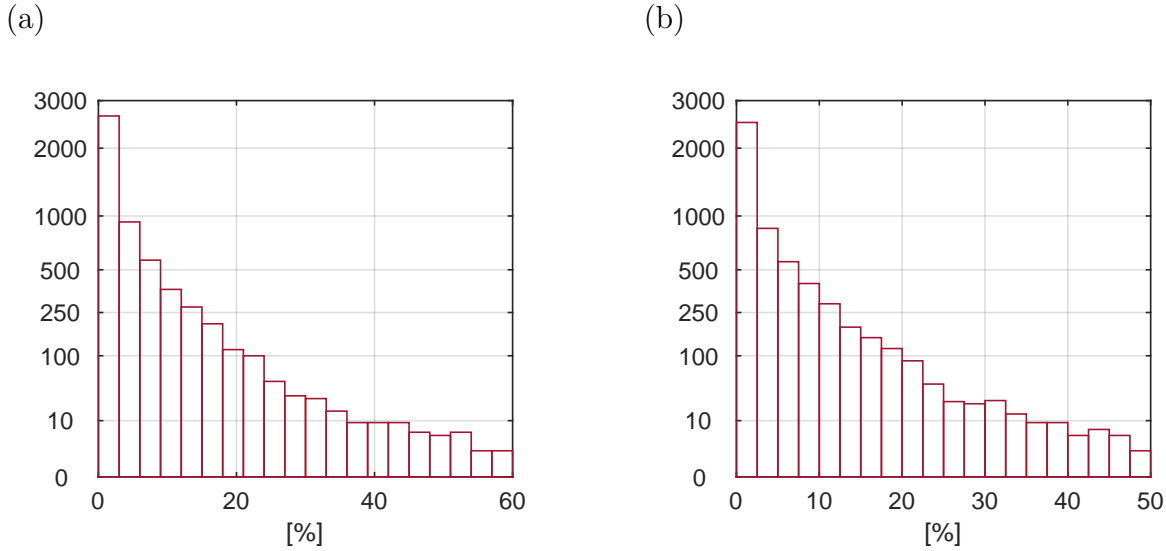


Figure A.11: Histograms of overestimation relative errors that are obtained with the original hybrid-based ESWLs. Overestimation relative errors associated with (a) upper (positive) and (b) lower (negative) envelope values. Results obtained in a non-Gaussian framework (Kasperski's methodology for peak factors, observation period 1 hour).

Table A.2 presents the results with option C and Figure A.12 shows the evolution of the number of responses as a function of the number of load cases for the final overestimation  $\hat{\varepsilon}' = 10\%$ . For the final overestimation  $\hat{\varepsilon}' = 25\%$ , the acceptable underestimation  $\hat{\varepsilon}^t = -11\%$  is not satisfied even when increasing the ratio  $\lambda^P$  from 0.995 to 0.999 and the number  $n_c$  from 6000 to 50000. The last PSWL basis is not able to solve entirely the ERP since the SVD operation is made on the original hybrid-based ESWLs which strongly violate the non-overestimation condition. On the other hand, the number of responses that do not satisfy the acceptable underestimation is very small and equal to one (out of 15988) for the parameters  $\lambda^P = 0.999$  and  $n_c = 50000$ . In this last case, the sole PSWL corresponds to the ESWL and there is simply no optimization to deal with the overestimations larger than 11% associated with this last ESWL. Additionally, it is emphasized that the largest relative indicator remains close to the target acceptable underestimation, e.g., -16.5% instead of -11% for the parameters  $\lambda^P = 0.999$  and  $n_c = 50000$ . For the final overestimation  $\hat{\varepsilon}' = 10\%$ , the number of responses that do not satisfy the acceptable underestimation is greater, 134 out of 15988 for the parameters  $\lambda^P = 0.995$  and  $n_c = 12000$ . For this specific example and envelope, adjusted ESWLs can be derived for all responses before the first SVD operation to obtain

<sup>1</sup>The current trends in research concerning the approach presented in Appendix A.2 recommends more than 1000 observation windows of 10 minutes to obtain good estimates, in the sense of confidence intervals, of the peak factors.

PSWLs or after the optimization for the remaining responses with too large underestimations.

|             |       | No underestimation and $\hat{\varepsilon}' = 25\%$ |       |            |              |                               |       |
|-------------|-------|--|-------|------------|--------------|-------------------------------|-------|
| $\lambda^P$ | $n_c$ | $n_s$  | $n_q$ | $n_p$      | $n_{r(n_s)}$ | $\check{\varepsilon}_{(n_s)}$ | CPU   |
| 0.995       | 6000  | 145  | 7     | [38,...,5] | 24           | -26%                          | 12min |
|             | 12000 | 172  | 10    | [38,...,5] | 5            | -22%                          | 21min |
|             | 50000 | 158  | 7     | [38,...,5] | 9            | -17%                          | 55min |
| 0.999       | 25000 | 144  | 11    | [68,...,4] | 4            | -15%                          | 26min |
|             | 50000 | 159  | 9     | [68,...,1] | 1            | -16.5%                        | 47min |

|             |       | No underestimation and $\hat{\varepsilon}' = 10\%$ |       |             |              |                               |       |
|-------------|-------|--|-------|-------------|--------------|-------------------------------|-------|
| $\lambda^P$ | $n_c$ | $n_s$  | $n_q$ | $n_p$       | $n_{r(n_s)}$ | $\check{\varepsilon}_{(n_s)}$ | CPU   |
| 0.995       | 6000  | 386  | 28    | [38,...,27] | 208          | -32%                          | 22min |
| 0.995       | 12000 | 465  | 45    | [38,...,22] | 134          | -25%                          | 32min |

Table A.2: Number of SWLs to solve the ERP with option C (see Section III.3.5). Results obtained in a non-Gaussian framework (Kasperski's methodology for peak factors, observation period of 1 hour).

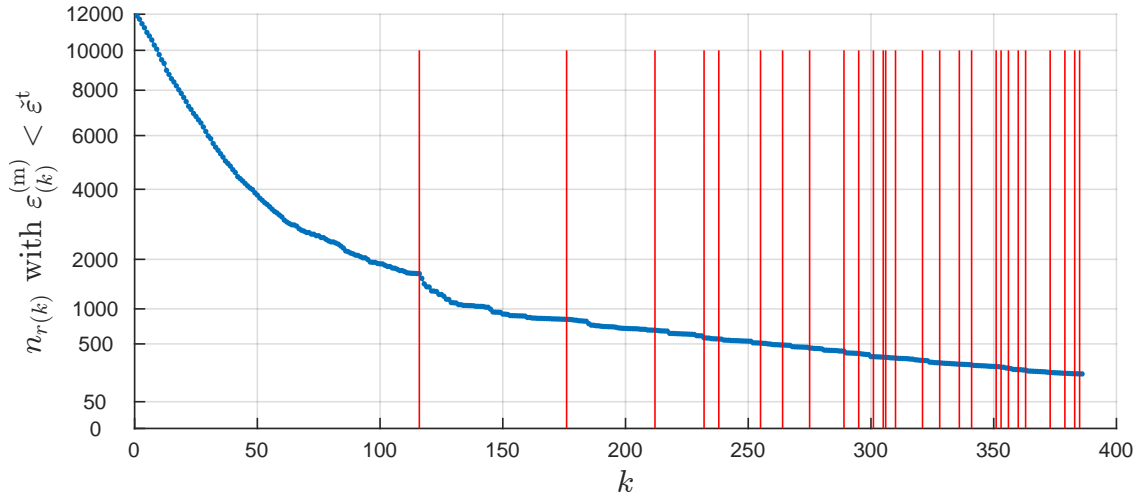


Figure A.12: Evolution of the number of responses  $n_{r(k)}$ , see page 127 with  $\varepsilon_{(k)}^{(m)} < \varepsilon^t$  as a function of the number of load cases. ERP parameters:  $\hat{\varepsilon} = 4.76\%$ ,  $\check{\varepsilon}^t = -4.76\%$ ,  $\gamma = 1$ ,  $\lambda^P = 0.995$ ,  $n_c = 6000$ . Vertical red lines correspond to an updating of the PSWL basis. Results obtained in a non-Gaussian framework (Kasperski's methodology for peak factors, observation period of 1 hour).

## A.4 Low-rise gable roof building example

### A.4.1 Establishment of the envelope (reference period 1 hour)

The envelope values are firstly computed with Kasperski's methodology, as described in Section A.2. Figure A.13 shows the  $\text{cov}(c)$  (A.2.5) and  $\text{cdesred}$  (A.2.6) parameters as well as the peak factors (A.2.9)-(A.2.10) and the envelope values (II.4.15).

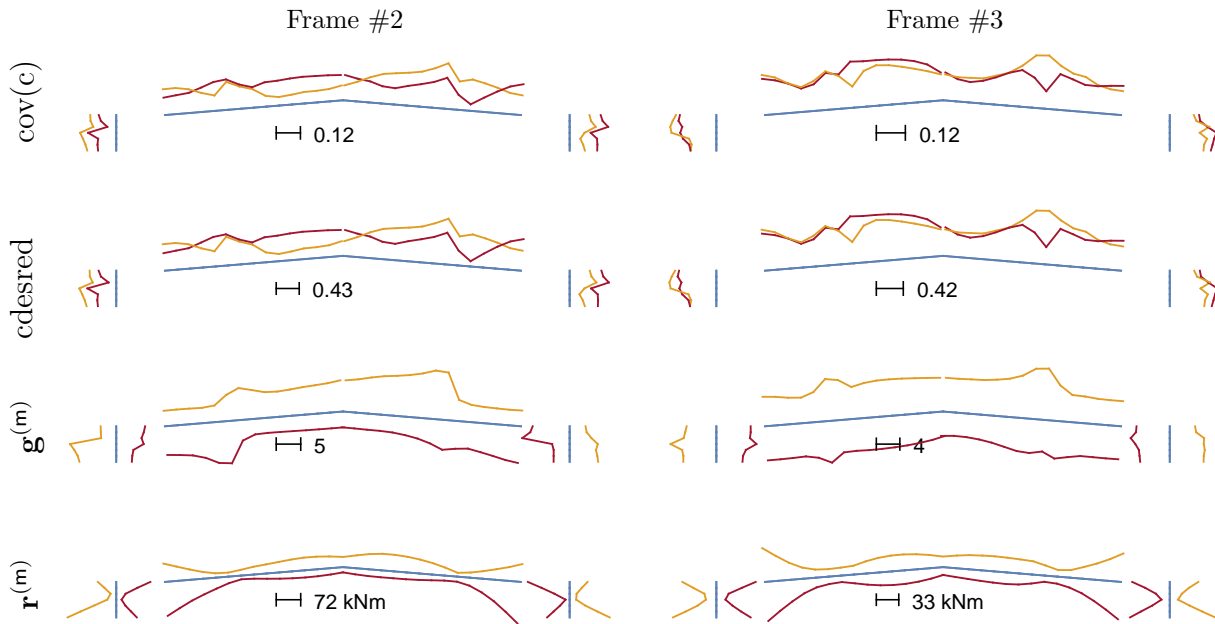


Figure A.13: Parameters:  $\text{cov}(c)$  (A.2.5) and  $\text{cdesred}$  (A.2.6), the peak factors (A.2.9)-(A.2.10) and the envelope values (II.4.15) for both considered frames. The results in orange and red are respectively associated with the positive (upper) and negative (lower) envelope values.

Figure A.14 compares the peak factors and envelope values obtained with the aforementioned methodology and with the Kareem-Zhao model (II.3.31)-(II.3.32). The two approaches showed very good agreement.

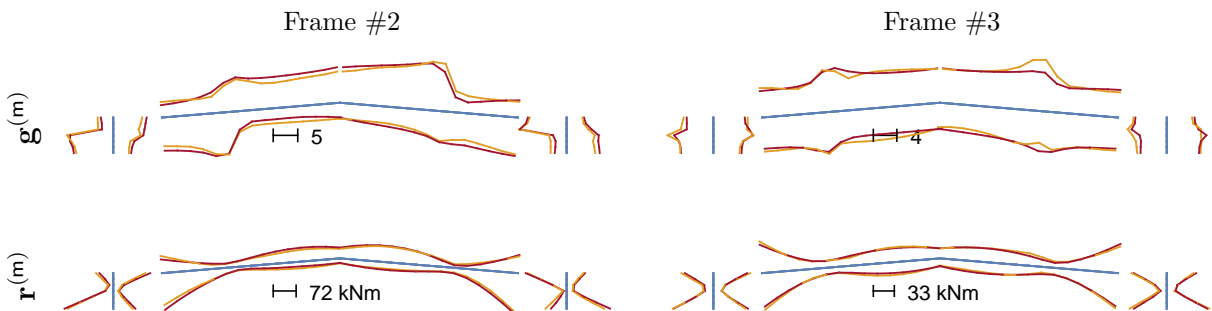


Figure A.14: Comparison of peak factors and envelope values obtained with Kasperski's methodology in orange (Section A.2) and Kareem-Zhao model in red (Section II.3.2).



Figure A.15 shows the peaks factors obtained with the Kareem-Zhao model versus the peak factors obtained with Kasperski's methodology. The relative differences are globally in the range  $[-20\% 20\%]$  as for the Lille's stadium and the same comments formulated in Section A.3.1 applied here.

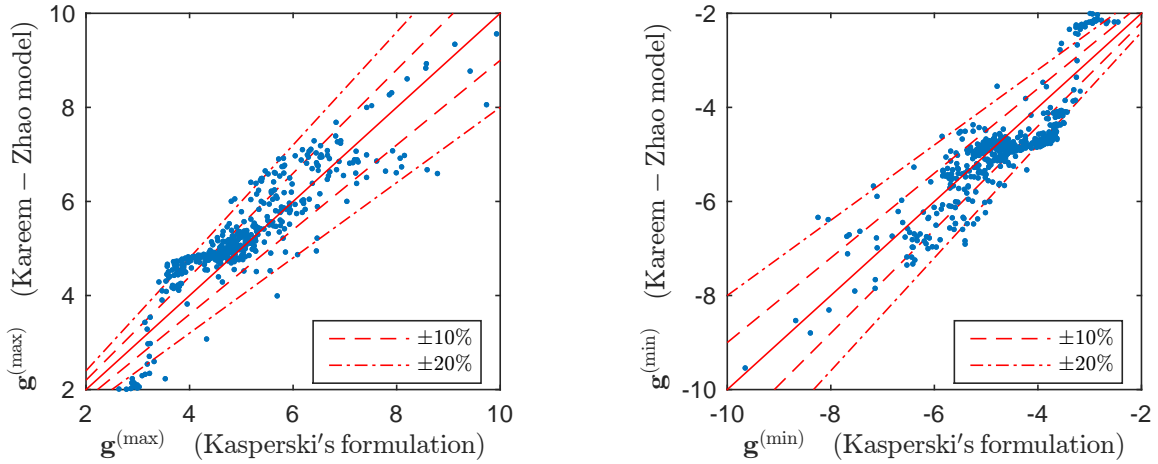


Figure A.15: Scatter plot of peaks factors obtained with the Kareem-Zhao model versus the peak factors obtained with Kasperski's formulation.

### A.4.2 Automatic procedure (Kareem-Zhao model for peak factors)

The influence of the ERP parameters  $\lambda^P$  and  $n_c$  on the number of SWLs  $n_s$  is reported in Table A.3. The results are obtained with combinations of original CEL-based PSWLs. The ERP parameters  $\lambda^P=0.90$  and  $n_c = 6000$  chosen in Section VI.5.5 are satisfactory and kept in the sequel.

| $\lambda^P$ | $n_c$ | No underestimation and $\hat{\varepsilon}' = 25\%$ |       |              |                               |      | No underestimation and $\hat{\varepsilon}' = 10\%$ |       |              |                               |      |
|-------------|-------|--|-------|--------------|-------------------------------|------|--|-------|--------------|-------------------------------|------|
|             |       | $n_s$  | $n_q$ | $n_{r(n_s)}$ | $\check{\varepsilon}_{(n_s)}$ | CPU  | $n_s$  | $n_q$ | $n_{r(n_s)}$ | $\check{\varepsilon}_{(n_s)}$ | CPU  |
| 0.85        | 6000  | 14   | 1     | 0            | ✓                             | 1min | 32   | 2     | 0            | ✓                             | 1min |
|             | 12000 | 14   | 1     | 0            | ✓                             | 1min | 32   | 2     | 0            | ✓                             | 1min |
| 0.90        | 6000  | <b>14</b>  | 2     | 0            | ✓                             | 1min | <b>16</b>  | 1     | 0            | ✓                             | 1min |
|             | 12000 | <b>12</b>  | 1     | 0            | ✓                             | 1min | <b>14</b>  | 2     | 0            | ✓                             | 1min |
| 0.95        | 6000  | 16   | 2     | 0            | ✓                             | 1min | 24   | 2     | 0            | ✓                             | 1min |
|             | 12000 | 16   | 1     | 0            | ✓                             | 1min | 22   | 1     | 0            | ✓                             | 1min |

Table A.3: Number of SWLs to solve the ERP with option C (see Section III.3.5). Study of the influence of the ERP parameters  $\lambda^P$  and  $n_c$ . The symbol ✓ means that the acceptable underestimation is satisfied. Results obtained with combinations of original CEL-based PSWLs (Kareem-Zhao model for the peak factors, observation period of 1 hour).

The efficiency of the envelope reconstruction problem based on combinations of PSWLs derived from original or adjusted ESWLs obtained with the LRC, CST or CEL methods is reported in Table A.4. It is observed that the efficiency of the PSWLs for the envelope reconstruction problem is slightly worse, considering adjusted ESWLs rather than the original ones for the SVD operation. Finally, the PSWL bases obtained with ESWLs derived from the conditional expected load and load-response correlation methods perform better than the PSWL basis obtained with ESWLs derived from the conditional sampling technique.

| PSWL basis         | No underestimation and $\hat{\varepsilon}' = 10\%$ |       |              |                            |      |
|--------------------|--|-------|--------------|----------------------------|------|
|                    | $n_s$  | $n_q$ | $n_{r(n_s)}$ | $\tilde{\varepsilon}(n_s)$ | CPU  |
| original LRC-based | 22   | 1     | 0            | ✓                          | 1min |
| adjusted LRC-based | 22   | 1     | 0            | ✓                          | 1min |
| original CST-based | 56   | 3     | 0            | ✓                          | 2min |
| adjusted CST-based | 72   | 2     | 0            | ✓                          | 2min |
| original CEL-based | <b>16</b>  | 1     | 0            | ✓                          | 1min |
| adjusted CEL-based | 24   | 3     | 0            | ✓                          | 1min |

Table A.4: Number of SWLs to solve the ERP with option C (see Section III.3.5). ERP parameters:  $\hat{\varepsilon} = 4.76\%$ ,  $\hat{\varepsilon}^t = -4.76\%$ ,  $\gamma = 1$ ,  $\lambda^P = 0.90$ ,  $n_c = 6000$ . The symbol ✓ means that the acceptable underestimation is satisfied. (Kareem-Zhao model for peak factors, observation period of 1 hour)

Figure A.16 shows the evolution of the number of responses as a function of the number of load cases for the final overestimation  $\hat{\varepsilon}' = 10\%$ . The results are obtained in a non-Gaussian framework with PSWLs based on original CEL-based ESWLs.

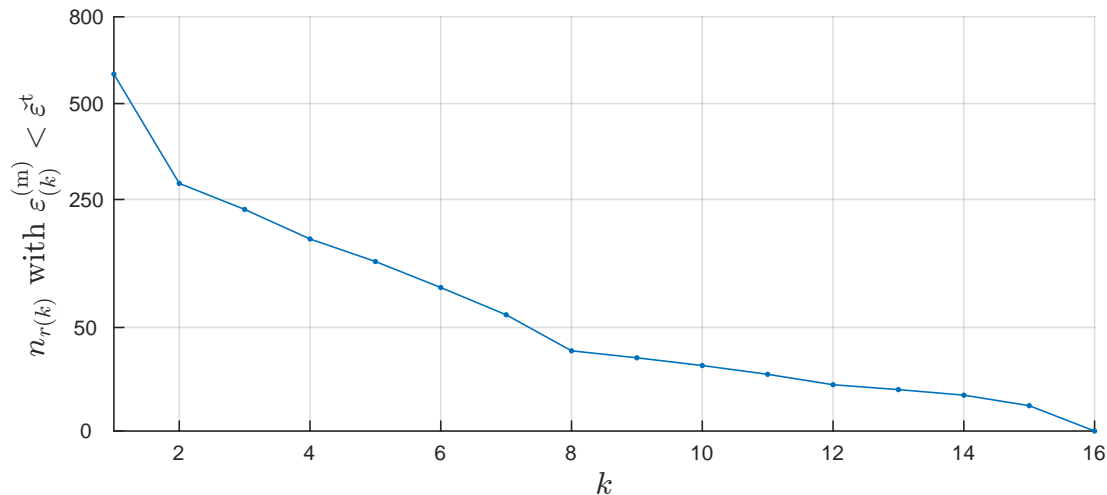


Figure A.16: Evolution of the number of responses  $n_{r(k)}$ , see page 127 with  $\varepsilon_{(k)}^{(m)} < \varepsilon^t$  as a function of the number of load cases. ERP parameters:  $\hat{\varepsilon} = 4.76\%$ ,  $\check{\varepsilon}^t = -4.76\%$ ,  $\gamma = 1$ ,  $\lambda^P = 0.90$ ,  $n_c = 6000$ . Vertical red lines correspond to an updating of the PSWL basis. Results obtained in a non-Gaussian framework with PSWLs based on original CEL-based ESWLs (Kareem-Zhao model for peak factors, observation period of 1 hour).

### A.4.3 Automatic procedure (Kasperski’s methodology for peak factors)

The influence of the ERP parameters  $\lambda^P$  and  $n_c$  on the number of SWLs  $n_s$  and the convergence on the ERP is reported in Table A.5. The ERP parameters  $\lambda^P=0.90$  and  $n_c = 12000$  are chosen for the subsequent computations.

| $\lambda^P$ | $n_c$ | No underestimation and $\hat{\varepsilon}' = 25\%$ |       |              |                               |      | No underestimation and $\hat{\varepsilon}' = 10\%$ |       |              |                               |      |
|-------------|-------|--|-------|--------------|-------------------------------|------|--|-------|--------------|-------------------------------|------|
|             |       | $n_s$  | $n_q$ | $n_{r(n_s)}$ | $\check{\varepsilon}_{(n_s)}$ | CPU  | $n_s$  | $n_q$ | $n_{r(n_s)}$ | $\check{\varepsilon}_{(n_s)}$ | CPU  |
| 0.85        | 6000  | 20   | 2     | 0            | ✓                             | 1min | 53   | 5     | 0            | ✓                             | 1min |
|             | 12000 | 22   | 4     | 1            | -13%                          | 1min | 50   | 4     | 0            | ✓                             | 1min |
| 0.90        | 6000  | 18   | 2     | 0            | ✓                             | 1min | 54   | 7     | 2            | -8%                           | 1min |
|             | 12000 | <b>16</b>  | 2     | 0            | ✓                             | 1min | <b>46</b>  | 2     | 0            | ✓                             | 1min |
| 0.95        | 6000  | 20   | 2     | 0            | ✓                             | 1min | 37   | 4     | 1            | -5.9%                         | 1min |
|             | 12000 | 16   | 3     | 1            | -12.9%                        | 1min | 42   | 3     | 1            | -6.9%                         | 1min |

Table A.5: Number of SWLs to solve the ERP with option C (see Section III.3.5). Study of the influence of the ERP parameters  $\lambda^P$  and  $n_c$ . The symbol ✓ means that the acceptable underestimation is satisfied. Results obtained with combinations of original CEL-based PSWLs (Kasperski’s methodology for peak factors, observation period of 1 hour).

The efficiency of the envelope reconstruction problem based on combinations of PSWLs derived from original or adjusted ESWLs obtained with the LRC, CST or CEL methods is studied in Table A.6. It is observed that the efficiency of the PSWLs for the envelope reconstruction problem is better, considering adjusted ESWLs rather than the original ones for the SVD operation. This statement is all the more true when the PSWLs based on the original ESWLs fail to solve the ERP, i.e., fail to satisfy the acceptable underestimation (LRC-, CST-based). In such cases, we thence recommend the use of the adjusted ESWLs for computing PSWLs.

Finally, if only original ESWLs had to be considered, the PSWL basis obtained with ESWLs derived from the conditional expected load performs better than original ESWLs derived from the load-response correlation method or the conditional sampling technique.

| PSWL basis         | No underestimation and $\hat{\varepsilon}' = 10\%$ |       |              |                               |      |
|--------------------|--|-------|--------------|-------------------------------|------|
|                    | $n_s$  | $n_q$ | $n_{r(n_s)}$ | $\check{\varepsilon}_{(n_s)}$ | CPU  |
| original LRC-based | 56   | 8     | 4            | -9.5%                         | 1min |
| adjusted LRC-based | 38   | 3     | 0            | ✓                             | 1min |
| original CST-based | 49   | 3     | 2            | -8.9%                         | 2min |
| adjusted CST-based | 55   | 3     | 0            | ✓                             | 2min |
| original CEL-based | 46   | 2     | 0            | ✓                             | 1min |
| adjusted CEL-based | 46   | 4     | 0            | ✓                             | 1min |

Table A.6: Number of SWLs to solve the ERP with option C (see Section III.3.5). ERP parameters:  $\lambda^P = 0.90$ ,  $n_c = 12000$ . (Kasperski's methodology for peak factors, observation period of 1 hour)

Figure A.17 shows the evolution of the number of responses as a function of the number of load cases for the final overestimation  $\hat{\varepsilon}' = 10\%$ . The results are obtained in a non-Gaussian framework with PSWLs based on original CEL-based ESWLs.

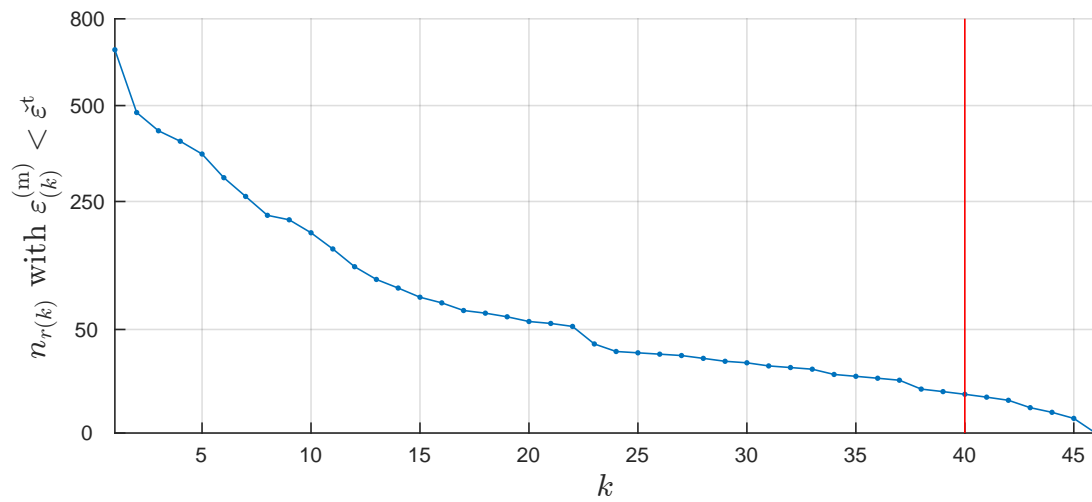


Figure A.17: Evolution of the number of responses  $n_{r(k)}$ , see page 127 with  $\varepsilon_{(k)}^{(m)} < \check{\varepsilon}^t$  as a function of the number of load cases. ERP parameters:  $\hat{\varepsilon} = 4.76\%$ ,  $\check{\varepsilon}^t = -4.76\%$ ,  $\gamma = 1$ ,  $\lambda^P = 0.90$ ,  $n_c = 12000$ . Vertical red lines correspond to an updating of the PSWL basis. Results obtained in a non-Gaussian framework with PSWLs based on original CEL-based ESWLs (Kasperski's methodology for peak factors, observation period of 1 hour).

## A.5 Conclusion

The principal findings are:

- the automatic procedure performs well in case of another reference period and alternative estimation method of representative extreme values;
- the reference period has a very small influence on the envelope reconstruction problem efficiency;
- for small tolerance on the relative errors, if the PSWLs based on original ESWLs do not solve the ERP, it means that the original ESWLs strongly violate the non-overestimation condition. This emphasizes the importance to accurately estimate the mean of the extremes and/or to derive CEL-based ESWLs.
- If the automatic procedure does not succeed to satisfy the acceptable under- and over- estimations, adjusted ESWLs should be used for the SVD operation establishing PSWLs.







# Appendix B

## Curriculum vitae

### Education

- PhD in Civil Engineering, Ulg  
Sept 2010 - 2016
- MSc in Applied Sciences: Civil Engineering, Ulg  
Sept 2008 - June 2010  
Master's thesis: *"Étude du comportement d'une toiture de grandes dimensions soumise à un vent turbulent. Application : le Grand Stade de Lille Métropole"*  
Great distinction
- BSc in Applied Sciences: Civil Engineering, Ulg  
Sept 2005 - June 2008  
Distinction
- Secondary education, Athénée Royal Air Pur, Seraing  
Sept 1999 - June 2005

### Professional experience

Teaching assistant, Argenco Department - Structural and Stochastic Dynamics sector.  
Sept 2010 - Sept 2016

### Publications

#### Papers published or accepted for publication in ISI journals

1. Blaise, N., Canor, T., Denoël, V. (2015). Reconstruction of the envelope of non-Gaussian structural responses with principal static wind loads. *Journal of Wind Engineering and Industrial Aerodynamics*, 149, 59-76.

2. Canor, T., Blaise, N., Denoël, V. (2014). An asymptotic expansion-based method for a spectral approach in equivalent statistical linearization. *Probabilistic Engineering Mechanics*, 38, 1-12.
3. Blaise, N., Denoël, V. (2013). Principal Static Wind Loads. *Journal of Wind Engineering and Industrial Aerodynamics*, 113, 29-39.
4. Canor, T., Blaise, N., Denoël, V. (2012). Efficient uncoupled stochastic analysis with non-proportional damping. *Journal of Sound and Vibration*, 331(24), 5283-5291.

### Chapter of a book

1. Blaise, N., Denoël, V., (2011). Optimal processing of wind tunnel measurements in view of stochastic structural design of large flexible structures *Wind Tunnels and Experimental Fluid Dynamic Research* edited by J. C. Lerner and U. Boldes, ISBN 978-953-307-623-2, InTech.

### Papers published in the proceedings of international conferences

1. Blaise N., Denoël V., (2015). Adjusted Equivalent Static Wind Loads for non-Gaussian linear static analysis. 14th International Conference on Wind Engineering, Porto Alegre, Brazil.
2. Canor, T., Blaise, N., Denoël, V. (2014). A Fast Newton-Raphson Method in Stochastic Linearization. Ninth International Conference on Structural Dynamics Eurodyn 2014.
3. Blaise, N., Canor, T., Denoël, V. (2014). Calculation of third order joint acceptance function for line-like structures. XIII Conference of the Italian Association for Wind Engineering-In Vento.
4. Canor, T., Blaise N., Denoël V. (2013). Uncoupled spectral analysis with non-proportional damping. European-African Conference on Wind Engineering.
5. Blaise, N., Canor, T., Denoël V. (2013). Equivalent static wind loads for structures with non-proportional damping. 11th International Conference on Recent Advances in Structural dynamics.
6. Blaise, N., Canor T., Denoël, V. (2013). Equivalent static wind loads for structures with non-proportional damping. Fifth International Conference on Structural Engineering, Mechanics & Computation, Cape Town, South Africa.
7. Blaise, N., Hamra, L., Denoël, V. (2012). Principal Static Wind Loads on a large roof structure. Proceedings of the 12th ANIV conference of wind engineering In Vento, Venice, Italy.
8. Blaise, N., Denoël, V. (2011). Envelope approximation using equivalent static wind loads. Fifth International Conference on Advanced COmputational Methods in ENgineering, Liege, Belgium.

9. Blaise, N., Denoël, V. (2011). Optimal processing of wind tunnel measurements in view of stochastic structural. Proceedings of the 13th International Conference on Wind Engineering, Amsterdam, The Netherlands.
10. Blaise, N., Grillaud, G., De Ville de Goyet, V., Denoël, V. (2011). Application of deterministic and stochastic analysis to calculate a stadium with pressure measurements in wind tunnel, Proceedings of the 8th International Conference on Structural Dynamics, Leuven, Belgium.